Department of Spatial Sciences

New Generation GNSS/RNSS: Algorithms, Numerical Analyses and Applications

Safoora Zaminpardaz

This thesis is presented for the Degree of
Doctor of Philosophy
of
Curtin University

January 2018

DECLARATION

To the best of my knowledge and belief this thesis contains no material previously published by any other person except where due acknowledgment has been made. This thesis contains no material which has been accepted for the award of any other degree or diploma in any university.

Safoora Zaminpardaz
11 January 2018

ABSTRACT

Global/Regional Navigation Satellite Systems (GNSSs/RNSSs) serve, as the prime positioning technology, a wide range of applications with different levels of accuracy in the broad fields of surveying, navigation, remote sensing and geodesy. With the advent of new GNSSs/RNSSs, and the corresponding proliferation of satellites and signals, combination and integration of the different systems has become an important goal, thereby aiming for the opportunities to create stronger models with improved ambiguity resolution, a prerequisite for exploiting the very precise carrier-phase measurements. In this thesis, our aim is to provide an understanding and demonstration of the improved capabilities the new generation GNSSs/RNSSs has to offer. For this purpose we develop mathematical algorithms and conduct numerical data analyses for several of these new systems, stand-alone as well as in combination. The corresponding results are presented in the context of several single- and multi-GNSS observational models for various types of application, such as single-point positioning (SPP), maritime navigation, real-time kinematic (RTK) positioning, attitude determination and ionospheric gradient monitoring. We focus our attention specifically to the Indian IRNSS/NavIC, the American GPS Block IIF, the Russian GLONASS series M and K, and the European Galileo, as they are new additions to the satellite-based navigation systems. Several single-frequency assessments of the IRNSS, as a standalone system and in combination with the GPS Block IIF, are provided, that cover SPP, RTK positioning and attitude determination. A proper integration of different constellations requires knowledge of the differential inter-system biases (DISBs) between their signals. We therefore characterize these DISBs for the shared frequency between IRNSS, GPS, Galileo and QZSS. The new GLONASS code-division multiple access (CDMA) signals are analysed in terms of their stochastic properties, ambiguity resolution and positioning performance. A stochastic analysis of the Galileo signals, considering different receiver/antenna types, is presented, followed by an evaluation of the Galileo single-frequency RTK performance. As the ionosphere is one of the most challenging error sources affecting the GNSS positioning accuracy, we also study the detectability of the ionospheric spatial gradient using the concept of uniformly most powerful invariant (UMPI) test.

ACKNOWLEDGMENTS

I would like to express my sincere gratitude to my supervisor, Professor Peter J.G. Teunissen, who has provided continued support and strong motivation to keep enhancing the quality of my PhD study. This thesis could not be realized without his valuable suggestions and strong scientific points.

I would also like to thank my co-supervisor, Dr Nandakumaran Nadarajah, for his technical support in data analysis and software development. My grateful thanks are also extended to my colleagues at the Curtin GNSS Research Centre, especially Dr Amir Khodabandeh. Their support is greatly appreciated.

Finally, special thanks should be given to my family for their encouragement and support during all the stages of my life.

LIST OF PUBLICATIONS

This PhD thesis by publication comprises 1 single-author, 8 first-author, and 1 third-author peer-reviewed publications and 2 first-author peer-reviewed technical articles. These articles have been published/accepted in the following journals, proceedings and magazines. The reader may be referred to Appendix A for copyright authorization, Appendix B for signed declarations for author contributions to the co-authored publications, and Appendix C for the proof that all the publications are peer-reviewed and have been published/accepted.

1. **Zaminpardaz S.**, Teunissen P.J.G., Nadarajah N. (2016a) IRNSS stand-alone positioning: first results in Australia. Journal of Spatial Science, Taylor & Francis, 61(1):5-27

2. **Zaminpardaz S.**, Teunissen P.J.G., Nadarajah N. (2017a) IRNSS/NavIC Single-Point Positioning: A Service Area Precision Analysis. Marine Geodesy, Taylor & Francis, 40(4):259-274

3. Odijk D., Nadarajah N., **Zaminpardaz S.**, Teunissen P.J.G. (2017) GPS, Galileo, QZSS and IRNSS differential ISBs: estimation and application. GPS Solutions, Springer, 21(2):439-450

4. **Zaminpardaz S.**, Teunissen P.J.G., Nadarajah N. (2017b) IRNSS/NavIC and GPS: A Single and Dual System L5 Analysis. Journal of Geodesy, Springer, 91(8):915-931

5. **Zaminpardaz S.**, Teunissen P.J.G., Nadarajah N. (2017c) L5 RTK Over India: IRNSS and GPS. Inside GNSS, 12(1):48-55

6. **Zaminpardaz S.**, Teunissen P.J.G., Nadarajah N. (2017d) IRNSS/NavIC L5 Attitude Determination. Sensors, MDPI, 17(2), 274, DOI 10.3390/s17020274

7. **Zaminpardaz S.**, Teunissen P.J.G., Nadarajah N. (2017e) Single-frequency L5 attitude determination from IRNSS/NavIC and GPS: a single- and dual-system analysis. Journal of Geodesy, Springer, 91(12):1415-1433

8. **Zaminpardaz S.**, Teunissen P.J.G., Nadarajah N. (2017f) GLONASS CDMA L3 ambiguity resolution and positioning. GPS Solutions, Springer, 21(2): 535-549

9. **Zaminpardaz S.**, Teunissen P.J.G., Nadarajah N. (2016b) GLONASS CDMA L3 Ambiguity Resolution. Inside GNSS, 11(4):44-47

10. **Zaminpardaz S.**, Teunissen P.J.G. (2017) Analysis of Galileo IOV+FOC Signals and E5 RTK performance. GPS Solutions, Springer, 21(4):1855-1870

11. **Zaminpardaz S.**, Teunissen P.J.G., Nadarajah N., Khodabandeh A. (2015) GNSS Array-Based Ionospheric Spatial Gradient Monitoring: Precision and Integrity Analysis. ION Pacific PNT 2015, pp. 799-814. The Institute of Navigation, Honolulu, Hawaii

12. **Zaminpardaz S.** (2016) Horizon-to-elevation Mask: A Potential Benefit to Ionospheric Gradient Monitoring. ION GNSS+ 2016, pp. 1764-1779. The Institute of Navigation, Portland, Oregon

TABLE OF CONTENTS

1 INTRODUCTION

1.1 Background

As the prime positioning technology, Global/Regional Navigation Satellite Systems (GNSSs/RNSSs) serve a wide range of applications with different levels of accuracy requirements such as navigation of cars and marine vessels, geodesy and surveying, precision agriculture and atmospheric studies. Depending on the required accuracy, code observables of decimetre-level precision and/or carrier-phase observables of millimetre-level precision are employed.

At the moment (January 2018), there are *four* GNSSs available, namely the American GPS (Global Positioning System), the Russian GLONASS (Global'naja Nawigatsionnaja Sputnikowaya Sistema), the Chinese BeiDou (Chinese for the "Big Dipper") and the European Galileo. Becoming fully-operational since 1995, the GPS constellation nominally contains 24 satellites orbiting in six Medium Earth Orbit (MEO) planes at an altitude of 20200 km. In order to maintain the global coverage however, usually more than 24 satellites are put into the constellation such that currently 31 satellites are operating in GPS constellation (GPS 2017).

GLONASS has also a nominal constellation of 24 satellites distributed in three MEO planes at an altitude of 19100 km. Although reaching its full operational capability in 1995 (ICD-GLONASS 2008), GLONASS encountered a decrease in the number of its operational satellites down to seven till 2001 (Urlichich et al. 2011). In 2002, it was again re-established and the fully-operational 24-satellite constellation was retrieved in 2011. The navigation signals of the GLONASS system are traditionally transmitted using the frequency division multiple access (FDMA) technique. Since 2011, as part of GLONASS modernization, the Russian satellite system has commenced sending signals using the technique used by the other GNSSs, i.e. code division multiple access (CDMA) technique. Currently, only three GLONASS satellites are capable of transmitting both CDMA and FDMA signals.

The development of BeiDou consists of three steps (Ran 2011; CSNO 2013); BeiDou-1: the experimental system with a constellation of three Geostationary Earth Orbit (GEO) satellites; BeiDou-2 (previously referred to as Compass): the regional system which became operational in 2012 with five GEO satellites, five Inclined Geo-Synchronous Orbit (IGSO) satellites and four MEO satellites providing service over China and Asia-Pacific region; BeiDou-3: the final system with the global

coverage to be accomplished by 2020 consisting of five GEO, five IGSO and 27 MEO satellites.

The full constellation of Galileo, expected to be realized by 2020, is planned to comprise 24 satellites plus at most six spares orbiting in three MEO planes at an altitude of 23222 km (ESA 2016a,b). Galileo deployment procedure contains three phases; GIOVE (Galileo In-Orbit Validation Element): planned to characterize the performance of the novel Galileo signals with two experimental satellites—finalized in 2012; IOV (In-Orbit Validation): planned to conduct the initial validation of the Galileo system based on four satellites—finalized in 2014; FOC (Full Operational Capability): planned to realize the fully-operational system such that a minimum of four satellites be always visible at any location—still ongoing.

In addition to the above-mentioned GNSSs, two RNSSs are also in operation with the aim of serving specified regional areas. These are the Japanese QZSS (Quasi-Zenith Satellite System) and the Indian IRNSS (Indian Regional Navigation Satellite System) with the operational name of NavIC (Navigation with Indian Constellation). The current QZSS constellation comprises three HEO (Highly inclined Elliptical Orbit) satellites and one GEO satellite, which is going to be extended to four HEO and three GEO satellites by 2023 (Murai 2015). The orbital parameters of these satellites are designed in such a way that a better visibility at high elevation angles in Japan is guaranteed and navigation service is provided to East Asia and Oceania region. IRNSS became fully operational with a constellation of three GEO and four IGSO satellites in May 2016, covering latitudes between 30° S and 50° N, and longitudes between 30° E and 130° E (ISRO 2014). This means that a large part of the IRNSS service area accommodates the Indian Ocean. Therefore, such satellite system would be of high interest to different maritime applications over the Indian Ocean. At the moment, one of the IGSO satellites (satellite I1) is not operational due to its clock failures.

The advent of new GNSSs/RNSSs has led to a proliferation of satellites and signals. Integration of different GNSSs/RNSSs makes the underlying model stronger, thereby expediting the successful ambiguity resolution, a prerequisite for exploiting the very precise carrier-phase measurements. This would however be hindered if, in multi-system integration, one neglects the differences between constellations. Among the currently transmitted frequencies, there are subsets which are shared by some constellations allowing the inter-system differencing of the observations, thus

increasing the number of DD observations compared to classical differencing (differencing per constellation). For this case, one should however take into account the differential inter-system biases (DISBs) which emerge due to a difference in receiver hardware delays between the signals of different constellations (Hegarty et al. 2004). The overlap of one frequency between several satellite systems implies that the low-cost multi-GNSS single-frequency receivers—tracking two or more constellations at the same time—are able to track a multitude of satellites. This, in turn, reveals that even by means of low-cost single-frequency receivers, successful ambiguity resolution can be achieved (almost) instantaneously (Odolinski and Teunissen 2016; Zaminpardaz et al. 2017c).

1.2 Literature Review

In recent years, one has witnessed a rapid development of GNSSs/RNSSs in the form of the establishment of new constellations, modernized signals and multi-GNSS capable receivers. The modernisation phase of GPS has commenced upon launching Block IIR-M in 2005 and then Block IIF in 2010 which, respectively, added the civil signals L2 (1227.60 MHz) and L5 (1176.45 MHz) to legacy L1 (1575.42 MHz) (GPS Directorate, 2011). As the latest generation of GPS, Block IIF with12 MEO satellites became fully-operational on February 2016. Thus far, a few studies have been devoted to analysing the GPS L5 real-world data. The first data-based assessment of GPS L5-signal noise characteristics is given by de Bakker et al. (2012) considering several combinations of the GPS data. Tegedor and Øvstedal (2014) employs the GPS measurements on triple frequencies L1, L2 and L5 to analyse the precise point positioning (PPP) performance.

The frequency L5 overlaps between GPS Block IIF, Galileo, QZSS and IRNSS, making them interoperable. An optimal integration of these constellations requires a comprehensive investigation of the DISBs between their signals (Hegarty et al. 2004). Such study is provided by Odijk and Teunissen (2013a) for the constellation pair GPS-Galileo, which is then extended by Odijk and Teunissen (2013b) via including QZSS as well. The first results of the DISBs on L5 frequency between IRNSS and GPS, Galileo and QZSS are presented in (Odijk et al. 2017). There, it is shown that for the constellation pair GPS-IRNSS, the L5 DISBs are absent for the baselines of identical receivers (of the same manufacturer), and present

but temporally-stable for the baselines of mixed receivers. In case the DISBs are either absent or can be calibrated, the underlying model strengthens and the ambiguity resolution performance improves dramatically. Results of such improvements can be found in, e.g. (Paziewski and Wielgosz 2015, Odijk et al. 2017).

The newly-established IRNSS, with the operational name of NavIC, reached its full operational capability in May 2016 consisting of three GEOs and four IGSOs (ISRO, 2014). During the IRNSS development, several studies have been published on the basis of the IRNSS real data. Thoelert et al. (2014) assesses the clock stability of satellite I1. Using the I1 and I2 observations, while Kumari et al. (2015) tests the accuracy of a precise model for solar radiation pressure, Montenbruck and Steigenberger (2015) investigates the quality of the IRNSS navigation messages. The data of I1, I2 and I3 are used by Babu et al. (2015) for comparison of the orbit determination methods, and by Chandrasekhar et al. (2015) to validate the orbit accuracy with the modernized ephemeris parameters. The first positioning results based on the data of I1, I2, I3, and I4 over India are presented in (Ganeshan et al. 2015) and over Australia in (Zaminpardaz et al. 2016a). The first results of the single-frequency (L5) *fully-operational* IRNSS+GPS are provided by Zaminpardaz et al. (2017b, c) for real-time kinematic (RTK) positioning and by Zaminpardaz et al. (2017e) for attitude determination. The attitude determination performance of the L5-signal of IRNSS, GPS, Galileo and QZSS is evaluated by Nadarajah et al. (2015). However, their assessment is based on only *two* IRNSS and *seven* GPS Block IIF satellites.

As part of its modernization program, GLONASS has embarked on transmitting CDMA signals on the brand-new L3 frequency (1202.025 MHz) since 2011, following the launch of the first GLONASS-K1 satellite (Urlichich et al. 2010; Thoelert et al. 2011; Oleynik 2012). The satellites of the Russian system traditionally transmit signals on the basis of the FDMA technique (ICD-GLONASS 2008). The integer ambiguity resolution of the FDMA signals is hindered by the presence of the inherent inter-frequency biases (Leick et al. 2015; Hofmann-Wellenhof et al. 2013). To tackle this issue, special calibration procedures have been proposed aimed at realizing GLONASS FDMA integer ambiguity resolution (Takac 2009; Yamada et al. 2010; Reussner and Wanninger 2011; Wanninger 2009). GLONASS CDMA signals however are not confronted with this impediment such that the optimal

methods of integer ambiguity resolution can directly be applied to them. Currently, there are three GLONASS satellites in orbit equipped with the CDMA signals. An overview of the CDMA signals is presented in (Urlichich et al. 2010, 2011; Karutin 2012), and the quality of them is assessed in (Thoelert et al. 2011). The first real-data analysis of the ambiguity resolution and positioning performance is provided in (Zaminpardaz et al. 2016b, 2017f) where the measurements of two GLONASS CDMA-transmitting satellites are used.

The Galileo signals are of the advanced code modulation schemes and transmitted on five frequencies E1 (1575.420 MHz), E5a (1176.450 MHz), E5b (1207.140 MHz), E5 (1191.795 MHz) and E6 (1278.750 MHz). Having AltBOC (Alternative Binary Offset Carrier) modulation, the high-performance Galileo E5 signal is a wideband signal consisting of two sub-carriers, i.e. E5a and E5b, which can be tracked either as two independent BPSK(10) (Binary Phase Shift Keying) modulations at respective center frequencies of 1176.45 MHz and 1207.14 MHz, or coherently as one signal centered at 1191.795 MHz, leading to the E5 signal (Simsky et al, 2006). The characterization of the Galileo signals has been carried out in several studies (Simsky et al. 2006, 2008a, b; de Bakker et al. 2009, 2012; Cai et al. 2016; Odijk et al. 2014; Zaminpardaz and Teunissen 2017). Galileo, either in standalone mode or in combination with other GNSSs/RNSSs, has been studied for a variety of application fields such as precise point positioning (PPP) (Langley et al. 2012; Tegedor et al. 2014, 2015; Afifi and El-Rabbany 2014; Cai et al. 2015; Li et al. 2015; Lou et al. 2016; Guo et al. 2017), short-baseline RTK positioning (Odijk et al. 2012, 2014; Odolinski et al. 2015; Zaminpardaz and Teunissen 2017), single point positioning (SPP) (Steigenberger et al, 2013; Cai et al, 2014; Gioia et al, 2015; Gaglione et al, 2015; Steigenberger and Montenbruck, 2016; Pan et al, 2017; Liu et al, 2017), and attitude determination (Nadarajah et al, 2013, 2015; Nadarajah and Teunissen, 2014).

1.3 Thesis objectives and outline

The objective of this thesis is to provide an understanding of the new generation GNSSs/RNSSs for which we develop mathematical algorithms and conduct numerical data analyses. The corresponding results are presented in the framework of several single- and multi-GNSS observational models for various types of application such as single-point positioning (SPP), marine navigation, RTK

positioning, attitude determination and ionospheric gradient monitoring. Our focus is on the IRNSS/NavIC (L5), GPS Block IIF (L5), GLONASS series M and K (CDMA L3), and Galileo (E5AltBOC) as they are new additions to the satellite-based navigation systems.

We provide, on the basis of real-world data, the very first results of the four-satellite IRNSS positioning capability over Australia. We identify the occurrence of poor receiver-satellite geometries, consisting of the "cone-like" geometry, where all the receiver-satellite unit direction vectors lie on a cone with the same symmetry axis. To elaborate on such geometry, the cones formed by the unit direction vectors are illustrated through an innovative visualization in the skyplot view of the satellites. Comprising mostly the Indian Ocean, the IRNSS service area is then assessed in terms of the IRNSS SPP performance for maritime applications. It is also shown how the performance of the IRNSS can be improved through height-constraining.

The L5/E5a frequency is shared by IRNSS, GPS, Galileo and QZSS, thus making these satellite systems interoperable. The optimal integration of these constellations requires the knowledge of the DISBs between their signals. We study the magnitude and stability of the DISBs between different constellation pairs for both identical-receiver and mixed-receiver baselines. It is shown that the interpretation of the estimable DISBs differs for short-baseline and long-baseline observational model. The DISBs on L5 between IRNSS and GPS is estimated to be negligible when working with the identical-receiver baselines. This enables us, instead of the classical differencing, to form the inter-system differencing which results in higher ambiguity resolution success rates. Throughout the thesis, our analyses of the combined IRNSS+GPS L5 are carried out for identical-receiver baselines where the DISBs can be neglected.

We present the first ambiguity resolution and positioning performance assessment of the *fully-operational* IRNSS in standalone mode and when integrated with the *fully-operational* GPS Block IIF and the future GPS III. The underlying models cover the unconstrained and height-constrained single-frequency RTK scenarios. Along with the real-world evaluations in Australia, also the formal analysis over the IRNSS service area with the aid of the boxplot concept is provided. In addition to the RTK application, we also consider the IRNSS capability for instantaneous precise attitude determination. It is shown that the standalone IRNSS

can provide *almost* instantaneous precise attitude determination. Its performance improves remarkably when combined with GPS Block IIF.

GLONASS CDMA-transmitting satellites (series M and K) have joined the GNSSs since 2011. GLONASS signals are traditionally transmitted on the basis of the FDMA technique which hampers the DD ambiguity resolution due to the inherent inter-frequency biases (Leick et al. 2015; Hofmann-Wellenhof et al. 2013). The newly added CDMA signals however circumvent this problem such that the optimal methods of integer ambiguity resolution can directly be applied. As the first study, we provide the ambiguity resolution and the corresponding positioning performance of the GLONASS CDMA L3-signal based on the data of *two* satellites, and compare them with their counterparts based on GPS L1- and L5-signal. Our results show similar stochastic properties for GLONASS L3 and GPS L5, but better than GPS L1.

Galileo is currently in the last phase of its deployment. The fully-operational system is planned in such a way that a minimum of four satellites are always visible at any location (ESA 2016b). Using the mixture of IOV and FOC constellations, we study the stochastic properties of the Galileo signals on all the five frequencies E1, E5a, E5b, E5 and E6. Excelling in the noise and multipath performance, E5-signal is further analysed for short-baseline RTK application. Our findings reveal that the Galileo E5 data, if corrected for the multipath effect, can make (almost) instantaneous ambiguity resolution feasible.

The GNSS observational model links the code and carrier-phase measurements to a set of unknown parameters, e.g., baseline components, clocks, instrumental biases and ambiguities. Determination of the parameters set to be included in the model to appropriately describe the observed data is of high importance and is driven by the underlying circumstances. The significance of the parameters can be quantified through a testing procedure based on UMPI (uniformly most powerful invariant) test concept. For example, under nominal ionospheric condition (no ionospheric front or storm), it can be assumed that the differential ionospheric delays between two receivers of short baseline are zero. This is not the case however if the GNSS observations are affected by a hazardous ionospheric front. The resultant ionospheric spatial gradient needs then to be tested for its significance particularly for safety-critical applications like civil aviation. We study the detectability of the ionospheric spatial gradient by means of the UMPI test. The

novelty of our study lies in using multiple baselines instead of a single baseline, using multiple satellites instead of one satellite pair, and incorporating the code measurements in addition to the carrier phase observations. The corresponding UMPI MDBs (minimal detectable biases) are presented in analytical closed form so as to clearly distinguish the roles of different contributing factors. Although our numerical analyses are conducted for the GPS-only scenario, our analytical assessments are valid for both the single-system as well as the multi-system scenario provided that the DISBs between the constellations involved can either be neglected or calibrated. We also present the first analysis of the ionospheric gradient detection improvement upon employing the *horizon-to-elevation mask* data—the data collected prior to a satellite rising above the elevation mask.

This thesis is structured by the chapters coming in the following. The chapters include the publications covering the objectives discussed below. The conclusions of each chapter can be found in the respective papers. The thesis conclusions can be found at the end of this chapter so as to bind the publications into a collective piece of work.

Chapter 2: IRNSS positioning performance in Australia

This chapter is covered by the following publication:

- Zaminpardaz S., Teunissen P.J.G., Nadarajah N. (2016a) IRNSS stand-alone positioning: first results in Australia. Journal of Spatial Science, Taylor & Francis, 61(1):5-27

This contribution provides the very first results of the IRNSS stand-alone positioning capabilities over Australia based on the data of four satellites. During the 24-hour period, there are some intervals over which the number of visible satellites reaches three, less than the minimum required number of satellites (four) for positioning. The IRNSS-based positioning during these intervals can still be realized through constraining the height component. Therefore, our analysis is conducted in the framework of the height-constrained model. We first analyse the visibility of the IRNSS satellites at three different locations in Australia lying in the IRNSS secondary service area. The strength of the IRNSS receiver-satellite geometry for positioning is then investigated through the time series of position dilution of precision (PDOP). When the receiver-satellite unit direction vectors all lie on a cone

with the same symmetry axis, the corresponding receiver-satellite geometry, consisting of the "cone-like" geometry, is considered to be poor from positioning point of view. This paper, for the first time, identifies the occurrence of the cone-like geometry, explains it mathematically and presents it graphically in the skyplot view. The single-point positioning (SPP) and relative-point positioning (RPP) performance of four-satellite IRNSS are, empirically and formally, investigated for Christmas Island, Perth and Darwin, from West to East of Australia. In addition, a formal analysis of the SPP precision on the basis of the simulated fully-operational IRNSS constellation is given. The underlying models vary from code-only to carrier-phase-smoothed code observational model. It is shown how the IRNSS positioning performance gets poorer the more eastward the Australian user is located.

Chapter 3: IRNSS positioning performance over its service area

This chapter is covered by the following publication:

- Zaminpardaz S., Teunissen P.J.G., Nadarajah N. (2017a) IRNSS/NavIC Single-Point Positioning: A Service Area Precision Analysis. Marine Geodesy, Taylor & Francis, 40(4):259-274

In this contribution, the first analysis of the SPP performance of the fully-operational IRNSS (based on real orbital parameters) is provided for different locations in its two service areas, i.e. primary and secondary service area. The SPP model of observations for both the unconstrained and height-constrained scenarios is described. A detailed dilution of precision (DOP) analysis of IRNSS's two service areas, including the identification, in location and time, of poor receiver-satellite geometries is given. It is demonstrated how height-constraining can mitigate the impact of some of these poor receiver-satellite geometries. The SPP precision for a grid of locations over the two service areas is given. It includes easy-to-use representative day-averaged values of the positioning precision. It is hereby shown that location ($\varphi = 0^\circ$, $\lambda = 83^\circ$), being the IRNSS ground tracks symmetry point, has the best precision and that how the precision gets poorer in North/South direction the further one departs from the equator and likewise poorer in East/West direction the further one departs from this location in such East/West direction.

Chapter 4: GNSSs/RNSSs differential ISBs analysis

This chapter is covered by the following publication:

- Odijk D., Nadarajah N., Zaminpardaz S., Teunissen P.J.G. (2017) GPS, Galileo, QZSS and IRNSS differential ISBs: estimation and application. GPS Solutions, Springer, 21(2):439-450

This contribution investigates the magnitude and stability of DISBs corresponding to the signals of different constellations transmitted at identical frequencies. This research is motivated by the launches of new satellites of IRNSS, GPS Block IIF and Galileo. For the four-satellite IRNSS (I1, I2, I3 and I4), this article presents the first analysis of the DISBs when integrating its L5 signal with the L5/E5a signals of GPS, Galileo and QZSS for both the identical-receiver and mixed-receiver baselines. The estimability and the interpretation of the DISBs are explained for both the short-baseline and the long-baseline model, the difference thereof lies in the presence of the differential ionospheric delays. It is shown that the DISBs determined from short baselines can be used to calibrate those of the long-baseline. This strengthens the model and benefits ambiguity resolution and the position estimation, which is indeed confirmed by the presented empirical results. The DISB analysis shows that for the identical-receiver baseline model, the misalignment between IRNSS and the other constellations is indeed absent. For the mixed-receiver baseline model however, the DISBs are present but temporally stable.

Chapter 5: IRNSS+GPS L5 RTK performance (Part 1: An analysis of survey-grade receivers)

This chapter is covered by the following publication:

- Zaminpardaz S., Teunissen P.J.G., Nadarajah N. (2017b) IRNSS/NavIC and GPS: A Single and Dual System L5 Analysis. Journal of Geodesy, Springer, 91(8):915-931

This publication is the first of two parts. We provide, for the fully-operational IRNSS as a standalone system and also in combination with GPS, a first assessment of L5 integer ambiguity resolution and positioning performance. The data in use are collected from two (survey-grade) receivers of a short baseline at Curtin University, Perth, Australia. The noise characteristics of the L5-signal for both the IRNSS and GPS are studied by means of the carrier-to-noise density, measurement precision and

time correlation. The results show that the GPS data are of better precision compared to the IRNSS data. Upon applying the multipath corrections to the data, we have shown that the time correlation for both the constellations can be neglected even if 1-second data are used. For our analysis, the underlying models cover the unconstrained/height-constrained and single-system/dual-system identical-receiver single-baseline model. The advantage of the integration of IRNSS with GPS over the standalone IRNSS is demonstrated in the form of the ambiguity resolution success rate and positioning precision. Due to the agreement between our empirical and formal results, we, with the aid of the boxplot concept, conduct a formal analysis of the number of epochs needed to successfully fix the DD ambiguities over the IRNSS service area. This L5 analysis is performed for IRNSS, IRNSS+GPS Block IIF and IRNSS+GPS III.

Chapter 6: IRNSS+GPS L5 RTK performance (Part 2: An analysis of survey-grade and low-cost receivers)

This chapter is covered by the following publication:

- Zaminpardaz S., Teunissen P.J.G., Nadarajah N. (2017c) L5 RTK Over India: IRNSS and GPS. Inside GNSS, 12(1):48-55

This publication is the second of two parts. In this contribution, the L5 ambiguity resolution performance analysis of the fully-operational IRNSS and GPS are presented considering both the geodetic survey-grade receivers as well as the low-cost receivers. The potential of the single-frequency (L5) single-epoch RTK positioning is evaluated for different underlying models including standalone IRNSS, IRNSS+GPS Block IIF, standalone GPS III and IRNSS+GPS III. Using the survey-grade receivers, it is shown that the standalone IRNSS user needs quite a long time to successfully fix the DD ambiguities, while the IRNSS+GPS Block IIF as well as the standalone GPS III user can do it almost instantaneously during the whole day for most of the locations within the IRNSS primary service area. It is furthermore shown that the single-epoch RTK becomes feasible upon integration of IRNSS with GPS III at any location within the IRNSS service area even if low-cost receivers are employed.

Chapter 7: IRNSS L5 attitude determination

This chapter is covered by the following publication:

- Zaminpardaz S., Teunissen P.J.G., Nadarajah N. (2017d) IRNSS/NavIC L5 Attitude Determination. Sensors, MDPI, 17(2), 274, DOI 10.3390/s17020274

In this contribution, we study, for the first time, the IRNSS L5 capability to realize the instantaneous precise attitude determination. In doing so, use is made of the data of a linear array of two antennas and a planar array of three antennas. Since successful ambiguity resolution is the key to precise and fast GNSS-based attitude determination, we investigate the integer ambiguity resolution performance through the well-known LAMBDA (Least-squares AMBiguity Decorrelation Adjustment) and its multivariate-constrained counterpart, i.e. MC-LAMBDA. The latter is advantageous over the former due to the rigorous incorporation of the known local antenna geometry. The high MC-LAMBDA success rates for the linear array (90%) and planar array (almost 100%) show that the standalone IRNSS can realize 24-h *almost* instantaneous precise attitude determination. Since these success rates are already large, only a few more epochs are needed for successful ambiguity resolution.

Chapter 8: IRNSS+GPS L5 attitude determination

This chapter is covered by the following publication:

- Zaminpardaz S., Teunissen P.J.G., Nadarajah N. (2017e) Single-frequency L5 attitude determination from IRNSS/NavIC and GPS: a single- and dual-system analysis. Journal of Geodesy, Springer, 91(12):1415-1433

This paper, for the first time, presents the L5 attitude determination performance of the *fully-operational* IRNSS+GPS Block IIF in comparison with the standalone IRNSS. The underlying GNSS attitude model is explained for a linear array of two antennas and a planar array of three antennas. Our analysis is conducted on the basis of both the original and multipath-corrected GNSS data. It is shown that the multipath correction improves the results. The ambiguity resolution results show that upon integrating IRNSS with GPS Block IIF, a MC-LAMBDA success rate of almost 100% is achievable for both types of array. The constraint (rotation matrix orthonormality) involved in the GNSS attitude model is of a nonlinear nature which depends on the baseline length and the GNSS data precision. This nonlinearity is

elaborated, both mathematically and visually, through a comprehensible example. It is explained how the behaviour of the attitude angles precision changes as function of the satellites geometry and the baseline orientation. An overview, in the form of colour maps, of the formal attitude determination performance is also given over the IRNSS service area.

Chapter 9: GLONASS CDMA L3 performance (Part 1: Ambiguity resolution and positioning in comparison with GPS L1)

This chapter is covered by the following publication:

- Zaminpardaz S., Teunissen P.J.G., Nadarajah N. (2017f) GLONASS CDMA L3 ambiguity resolution and positioning. GPS Solutions, Springer, 21(2):535-549

This publication is the first of two parts. It provides, for the first time, an assessment of GLONASS CDMA L3 ambiguity resolution and positioning performance based on the data of two CDMA-transmitting satellites, i.e. SVNs 755 and 801, tracked by two stations at Curtin University, Perth, Australia. We also compare the GLONASS results with those based on L1 of two GPS satellites with the same trajectories as of the GLONASS satellites. The noise characteristics of the L1- and L3-signal are studied, confirming better precision for L3 compared to L1. This difference is not only seen in the noise levels but also in their onward propagation to the ambiguity time series and ambiguity residuals distribution. Since the data of only two satellites are available, our analyses are carried out in the framework of the two-satellite observational models including: the geometry-free model, the geometry-based model, the height-constrained geometry-based model, and the geometry-fixed model. The periodic impact of multipath on the GLONASS and GPS code and phase observations is shown and then corrected for all the remaining analyses. In order for positioning to become possible based on the data of two satellites, we divide the whole period into three segments from which one code and one phase observation are taken each time. This allows sufficient change of receiver-satellite geometry. Comparing the ambiguity resolution and the positioning performance, the conclusion is that while a receiver-satellite geometry may perform poorly for positioning, it can still be strong enough for ambiguity resolution.

Chapter 10: GLONASS CDMA L3 performance (Part 2: Ambiguity resolution in comparison with GPS L5)

This chapter is covered by the following publication:

- Zaminpardaz S., Teunissen P.J.G., Nadarajah N. (2016b) GLONASS CDMA L3 Ambiguity Resolution. Inside GNSS, 11(4):44-47

This publication is the second of two parts. In the frame-work of the geometry-free and geometry-fixed model of observations, the ambiguity resolution performance of the two GLONASS CDMA-transmitting satellites on L3 is compared with that of two GPS Block IIF satellites on L5. The stochastic properties of both signals are shown to be of similar signature. Based on the data of two stations of a short baseline, the GPS L5 ambiguity resolution outperforms that of the GLONASS L3. This is attributed to the higher elevations of the GPS satellites in use.

Chapter 11: Galileo IOV+FOC signal analysis

This chapter is covered by the following publication:

- Zaminpardaz S., Teunissen P.J.G. (2017) Analysis of Galileo IOV+FOC Signals and E5 RTK performance. GPS Solutions, Springer, 21(4):1855-1870

The focus of this contribution is on analysing the stochastic properties (power, multipath, noise) of the Galileo E1-, E5a-, E5b-, E5- and E6-signal transmitted by both the IOV and FOC satellites. The data in use are collected by four baselines varying in length (6m, 350m, 3.6km and 7.9km) and receiver/antenna type in Perth, Australia as well as the Netherlands. Excluding E5, the Galileo signals demonstrate different relative noise and multipath performance for different receiver/antenna types. The E5 signal, in contrast, shows a weak dependency on the type of receiver/antenna, and a significantly lower level of multipath and noise compared to the other Galileo signals. Estimations of the E5 code standard deviation based on the data of each of the mentioned baselines corroborates a value of ≈6cm, further reduced to ≈1cm upon applying multipath correction to the data in use. Since E5 outperforms the other Galileo signals in terms of noise and multipath characteristics, we further provide the short-baseline RTK performance analysis of the Galileo E5 measurements. Our conclusion is that the Galileo E5 data, if corrected for the multipath effect, can make (almost) instantaneous ambiguity resolution feasible.

Chapter 12: Array-based ionospheric spatial gradient monitoring

This chapter is covered by the following publication:

- Zaminpardaz S., Teunissen P.J.G., Nadarajah N., Khodabandeh A. (2015) GNSS Array-Based Ionospheric Spatial Gradient Monitoring: Precision and Integrity Analysis. ION Pacific PNT 2015, pp. 799-814. The Institute of Navigation, Honolulu, Hawaii

As the ionosphere is known to decorrelate as function of the separation between two receivers, this paper studies the GNSS array-based ionospheric spatial gradient monitoring. While the precision of the ionospheric spatial gradient estimator is evaluated through its formal variance matrix, its detectability is studied by means of its minimal detectable bias (MDB). The MDBs in this contribution are computed on the basis of the uniformly most powerful invariant (UMPI) test. The ionospheric spatial gradient multivariate variance matrix and MDB are presented analytically in such a way that the role of different contributing factors, e.g. number of antennas and number of frequencies are clearly distinguished. Such presentation allows one to conduct an a priori analysis before an actual measurement campaign is launched. The underlying model is the double-differenced (DD) short-baseline ambiguity-float/fixed model with known position for the antennas in the array, taking into account both the code and carrier-phase observables. To assess the significance of the ionospheric gradient, we test the assumptions of having zero versus linear spatial changes of the ionospheric delays corresponding with a specific satellite. Our analytical formulation is accompanied by numerical results considering several array configurations and satellite geometries. Although our numerical analyses are provided for the single-system scenario (GPS), our analytical assessments can be generalized to the multi-system scenario provided that the DISBs between the involved constellations can either be neglected or calibrated.

Chapter 13: The potential benefit of the horizon-to-elevation mask data to the ionospheric gradient detectability

This chapter is covered by the following publication:

- Zaminpardaz S. (2016) Horizon-to-elevation Mask: A Potential Benefit to Ionospheric Gradient Monitoring. ION GNSS+ 2016, pp. 1764-1779. The Institute of Navigation, Portland, Oregon. ***Best Student Paper Award***

This contribution concentrates, from an ionospheric spatial gradient monitoring point of view, on the potential benefit of *horizon-to-elevation mask* data—that could be collected during the period when the satellite elevation is increasing from horizon to elevation mask. Such analysis becomes of more importance for the satellites that have just risen above the elevation mask. Ground Based Augmentation System (GBAS) monitors are required to instantaneously detect the hazardous ionospheric gradients. When a satellite rises above the elevation mask, the GBAS-monitors' ability to detect hazardous ionospheric spatial gradients depends on the data of only that epoch since no observations were recorded beforehand. We explore the potential benefits of using horizon-to-elevation mask data in terms of ionospheric spatial gradient detectability with the aid of UMPI concept. The underlying model is the same as that explained in Chapter 12. Considering a poor GPS receiver-satellite geometry (in terms of ionospheric gradient detectability), our evaluations are carried out for several array configurations as well as number of frequencies. Setting 5° to be the elevation mask, it is shown that using the data recorded between 2° of elevation and the elevation mask, it is possible to resolve the integer DD ambiguities with the failure rate of 10^{-6} using eight antennas for single-frequency scenario and four antennas for dual-frequency scenario. The ambiguity-resolved MDB of 300 mm/km can in turn be achieved even if the antennas of the array form baselines shorter than 500 meters.

1.4 Summary and Conclusions

In this thesis, we provided an insight into the new generation GNSSs/RNSSs for which we developed algorithms and models and carried out data analyses for a broad range of applications including SPP, marine navigation, RTK positioning, attitude determination and ionospheric gradient monitoring. We mainly concentrated on the IRNSS/NavIC (L5), GPS Block IIF (L5), GLONASS series M and K (CDMA L3), and Galileo (E5AltBOC) as they are new additions to the satellite-based navigation systems. The standalone IRNSS positioning performance over Australia based on the

data of four satellites were assessed in the context of SPP and RPP. For our analysis, we considered both the code-only and the carrier-phase-smoothed code observational model. A new visualisation method was employed to explain the positioning-wise poor receiver-satellite geometry, referred to as *cone-like* geometry. An overview of the SPP performance together with a detailed DOP analysis of the fully-operational IRNSS (based on real orbital parameters) were provided over the IRNSS service area which is largely formed by the Indian continent and its surrounding areas as well as the Indian Ocean. The corresponding results were presented in the framework of the unconstrained and height-constrained model of observations.

As the IRNSS shares the L5 frequency with GPS, Galileo and QZSS, we investigated the behaviour of the DISBs on L5 when integrating these satellite systems. It was shown that the DISBs between IRNSS and the aforementioned constellations can be considered zero for the identical-receiver baselines, and non-zero but temporally stable for mixed-receiver baselines. For high-precision applications including the RTK positioning and attitude determination, we presented the standalone IRNSS L5 as well as IRNSS+GPS L5 results.

On the basis of real-world data (identical-receiver baseline) in Australia, we evaluated the L5 ambiguity resolution and positioning performance for the fully-operational IRNSS and IRNSS+GPS Block IIF. It was demonstrated that from single-system to dual-system scenario, a dramatic improvement in the instantaneous resolution of the ambiguities is achieved. A formal analysis of the ambiguity resolution performance over the IRNSS service area was also provided for IRNSS, IRNSS+GPS Block IIF, GPS III and IRNSS+GPS III. Our assessment for the survey-grade receivers confirmed that the 24-hour almost instantaneous ambiguity resolution and RTK can be realized for the locations inside the IRNSS *primary* service area using IRNSS+GPS Block IIF, and in addition for the IRNSS *secondary* service area using IRNSS+GPS III. The low-cost receivers demonstrated similar performance as the survey-grade receivers for IRNSS+GPS III. In addition to RTK, the L5-based instantaneous precise attitude determination was also assessed using the fully-operational IRNSS and IRNSS+GPS Block IIF. In doing so, the data of a linear and a planar array was used. We analysed the possibility of the 24-hour *instantaneous* successful ambiguity resolution using MC-LAMBDA method. This was shown to be achievable for the planar array in case of standalone IRNSS, and for both the linear and planar array in case of IRNSS+GPS Block IIF.

Next to the IRNSS and GPS Block IIF L5-signal, we also carried out the very first assessment of the GLONASS CDMA L3-signal. We based our analyses on the measurements of two GLONASS CDMA-transmitting satellites. Several two-satellite observational models were considered, i.e., geometry-free, geometry-based, height-constrained geometry-based and geometry-fixed model. To make the two-satellite positioning feasible, we divided the whole period into three segments from which one code and one phase observation are taken each time such that a sufficient change of receiver-satellite geometry is realized. The corresponding results of the ambiguity resolution were compared to their counterparts based on the GPS L1- and L5-signal. Our outcomes showed similar noise characteristics for GLONASS L3 and GPS L5, but better than GPS L1.

The power, noise and multipath characteristics of Galileo signals on all the five frequencies E1, E5a, E5b, E5 and E6 were studied using the observations of both the IOV and FOC satellites. In order to have representative conclusions, we made use of the data collected by four short baselines of different lengths and receiver/antenna types in Perth, Australia as well as the Netherlands. The outcomes of our analysis confirmed an outstanding noise and multipath performance for E5 signal, a cut above remaining Galileo signals. Due to its superiority, E5 was further investigated for the short-baseline RTK positioning application. It was shown that if the multipath on the E5 data can be mitigated to a large extent, then the Galileo E5-based successful ambiguity resolution can be realized almost instantaneously.

We concluded the thesis by assessing the ionospheric spatial gradient detectability, which is of high importance for safety-critical applications. The novelty of our study lies in the uptake of multiple baselines/satellites instead of a single baseline/satellite pair, and also incorporating the code measurements in addition to the carrier phase observations. Applying the UMPI test concept to the GNSS array-based observational model with known receivers' coordinates, we provided closed-form expressions of the ionospheric gradient MDB for different scenarios, in which the role of different contributing factors was distinguished. This presentation allows one to characterize the impact of the contributing factors and, in turn, conduct an a priori analysis before an actual measurement campaign is launched. Assuming that a satellite has just risen above the elevation mask, we assessed the ionospheric gradient instantaneous detectability for such satellite using the aforementioned UMPI test statistic. For this case, we investigated the circumstances under which the

incorporation of the horizon-to-elevation mask data can benefit the instantaneous detection of the ionospheric spatial gradient.

The main innovative contributions of this thesis are highlighted below:

- The very first results of the four-satellite IRNSS positioning capability over Australia are presented.
- For the first time, the occurrence of the cone-like geometry, for the IRNSS and GLONASS, is identified, analytically explained and graphically presented in the skyplot view.
- For the first time, the signature of DISBs on L5 between IRNSS and other satellite systems, i.e. GPS, Galileo and QZSS, is investigated.
- The first real-data-based L5 ambiguity resolution and positioning performance assessment of the fully-operational IRNSS as standalone and in combination with the fully-operational GPS Block IIF is provided. Instantaneous L5-based RTK feasibility is presented for both the survey-grade and low-cost receivers using IRNSS, GPS block IIF and GPS III, in a standalone manner and also in combination with each other.
- For the first time, the standalone IRNSS L5 and IRNSS+GPS Block IIF L5 capability for the precise attitude determination is studied both formally and empirically. A service area overview is also provided.
- As the first study, the GLONASS CDMA signals of two satellites are assessed in terms of stochastic properties, ambiguity resolution and positioning performance.
- For the first time, the Galileo signals are characterized based on the data of both the IOV and FOC satellites, and the corresponding Galileo E5-based RTK positioning results are provided.
- A new expression is given for the UMPI MDB of the ionospheric spatial gradient based on the double-differenced short-baseline model. The novelty of our study lies in using multiple baselines instead of single baseline, using multiple satellites instead of one satellite pair, and incorporating the code measurements in addition to the carrier phase observations.
- The concept of horizon-to-elevation mask is introduced for the ionospheric spatial gradient monitoring.

2 IRNSS positioning performance in Australia

This chapter is covered by the following publication:

Zaminpardaz S., Teunissen P.J.G., Nadarajah N. (2016a) IRNSS stand-alone positioning: first results in Australia. Journal of Spatial Science, Taylor & Francis, 61(1):5-27

Journal of Spatial Science

ISSN: 1449-8596 (Print) 1836-5655 (Online) Journal homepage: http://www.tandfonline.com/loi/tjss20

IRNSS stand-alone positioning: first results in Australia

Safoora Zaminpardaz, Peter J.G. Teunissen & Nandakumaran Nadarajah

To cite this article: Safoora Zaminpardaz, Peter J.G. Teunissen & Nandakumaran Nadarajah (2016) IRNSS stand-alone positioning: first results in Australia, Journal of Spatial Science, 61:1, 5-27, DOI: 10.1080/14498596.2016.1142398

To link to this article: http://dx.doi.org/10.1080/14498596.2016.1142398

Published online: 10 Apr 2016.

Journal of Spatial Science, 2016
Vol. 61, No. 1, 5–27, http://dx.doi.org/10.1080/14498596.2016.1142398

Taylor & Francis
Taylor & Francis Group

IRNSS stand-alone positioning: first results in Australia

Safoora Zaminpardaz*, Peter J.G. Teunissen and Nandakumaran Nadarajah

GNSS Research Centre, Curtin University, GPO Box U1987, Perth, 6845, Australia

The Indian Regional Navigation Satellite System (IRNSS) currently under development is expected to reach full operational capability before 2017. As a large part of the Australian continent lies in IRNSS's service area, it is important to gain an understanding of its navigational potential and actual positioning capabilities for Australian users. The goals of this contribution are therefore to provide insight into IRNSS, to demonstrate its current positioning performance using actual L5 pseudorange tracking data, and to analyse its expected positioning performance for when the system is fully operational. As such this contribution provides the very first results of the IRNSS stand-alone positioning capabilities over Australia.

Keywords: Indian Regional Navigation Satellite System (IRNSS); position dilution of precision (PDOP); single-point positioning (SPP); relative-point positioning (RPP); L5 pseudorange; phase-smoothed pseudorange

1. Introduction

The Indian Regional Navigation Satellite System (IRNSS) is a satellite-based navigation system currently under development by the Indian Space Research Organisation (ISRO). IRNSS will consist of three geosynchronous orbit (GEO) satellites and four inclined geosynchronous orbit (IGSO) satellites (see Figure 1(a),(b)), providing two types of services: a standard positioning service (SPS) for civilian users and a restricted service (RS) for authorised users (ISRO 2014a). The expected positioning accuracy of IRNSS is 10 m (2σ) over the Indian landmass and 20 m over the Indian Ocean, covering regions located up to 1500 km from India between longitude 30°E and 130°E and between latitude 30°S and 50°N (Sarma *et al.* 2010; Ganeshan 2012; Saikiran & Vikram 2013).

A few published studies have hitherto been devoted to the IRNSS. Next to the simulation-based studies (Garcia *et al.* 2010; Sarma *et al.* 2010; Sekar *et al.* 2012; Rethika *et al.* 2013; Rao 2013), some newer studies make use of real IRNSS data. Thoelert *et al.* (2014) characterised the IRNSS signals by means of data from a high-gain antenna, and assessed the clock stability of IRNSS-1A. In Kumari *et al.* (2015), a precise model for solar radiation pressure was proposed, of which the accuracy was then tested using the IRNSS-1A and 1B observations.

Babu *et al.* (2015) compared orbit determination methods for IRNSS-1A, 1B and 1C. In order to validate the orbit accuracy with modernised ephemeris parameters, Chandrasekhar *et al.* (2015) made use of the IRNSS-1A, 1B and 1C real measurements. Montenbruck *et al.* (2015) used the observations of the IRNSS-1A and 1B to investigate the quality of the IRNSS navigation messages and Nadarajah *et al.* (2015), after assessing the IRNSS noise characteristics, combined the L5/E5 signals of IRNSS, GPS, Galileo and QZSS for instantaneous attitude determination.

*Corresponding author. Email: safoora.zaminpardaz@curtin.edu.au

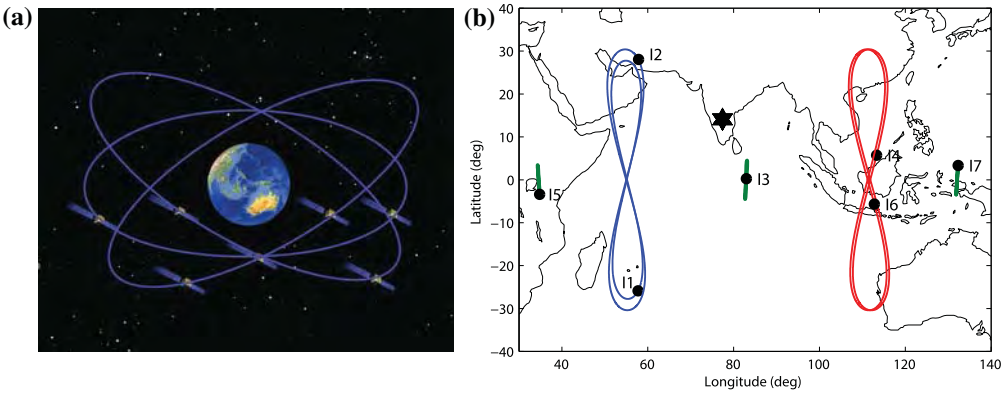

Figure 1. (a) The 7 satellite IRNSS constellation when fully operational. (b) The three GEO and four IGSO satellite ground tracks of fully operational IRNSS.

As IRNSS will soon become fully operational (before the end of 2016), it is important to gain an understanding of its navigational potential and actual positioning capabilities. This is not only of general interest, but also specifically for Australian users since a large part of the Australian continent lies in IRNSS's service area. The goals of this contribution are therefore to provide insight into IRNSS, to demonstrate its current positioning performance using actual L5 tracking data, and to analyse its expected positioning performance for when the system is fully operational. As such this contribution provides the very first results of the IRNSS stand-alone positioning capabilities over Australia.

This contribution is organised as follows. The IRNSS system is briefly described in section 2. In section 3 we formulate the single-point positioning (SPP) model of observation equations and analyse the observability of the current IRNSS constellation for several Australian locations in its secondary service area. This analysis includes the identification and explanation of occurring periods of poor receiver-satellite geometries. In section 4 we analyse, formally as well as empirically, the SPP precision that can be achieved with the current constellation. In an analogous fashion, section 5 presents a formal and empirical analysis of the relative-point positioning (RPP) precision that is achievable with the current constellation. Here we also show by how much the results can be further improved when use is made of carrier-phase smoothing on the observed L5 pseudoranges. The expected performance of the fully operational system is presented in section 6, first through a PDOP analysis and then by means of a positioning precision analysis with and without carrier-phase smoothing. Finally, the main results are summarised in section 7.

2. The IRNSS system

The Indian Regional Navigation Satellite System (IRNSS) is a satellite-based navigation system being developed by India. IRNSS is planned to consist of *three* geosynchronous orbit (GEO) satellites and *four* inclined geosynchronous orbit (IGSO) satellites, providing two services: a standard positioning service (SPS) for civilian users and a restricted service (RS) for authorised users (ISRO 2014a).

The IRNSS satellites transmit navigation signals, based on code division multiple access (CDMA), on L5 (1176.45 MHz) and on S (2492.028 MHz), with a binary phase-shift key (BPSK (1)) modulation for SPS users, and with a binary offset carrier (BOC (5,2)) modulation for RS users (ISRO 2014a). The orbital period of the IRNSS satellites is one sidereal

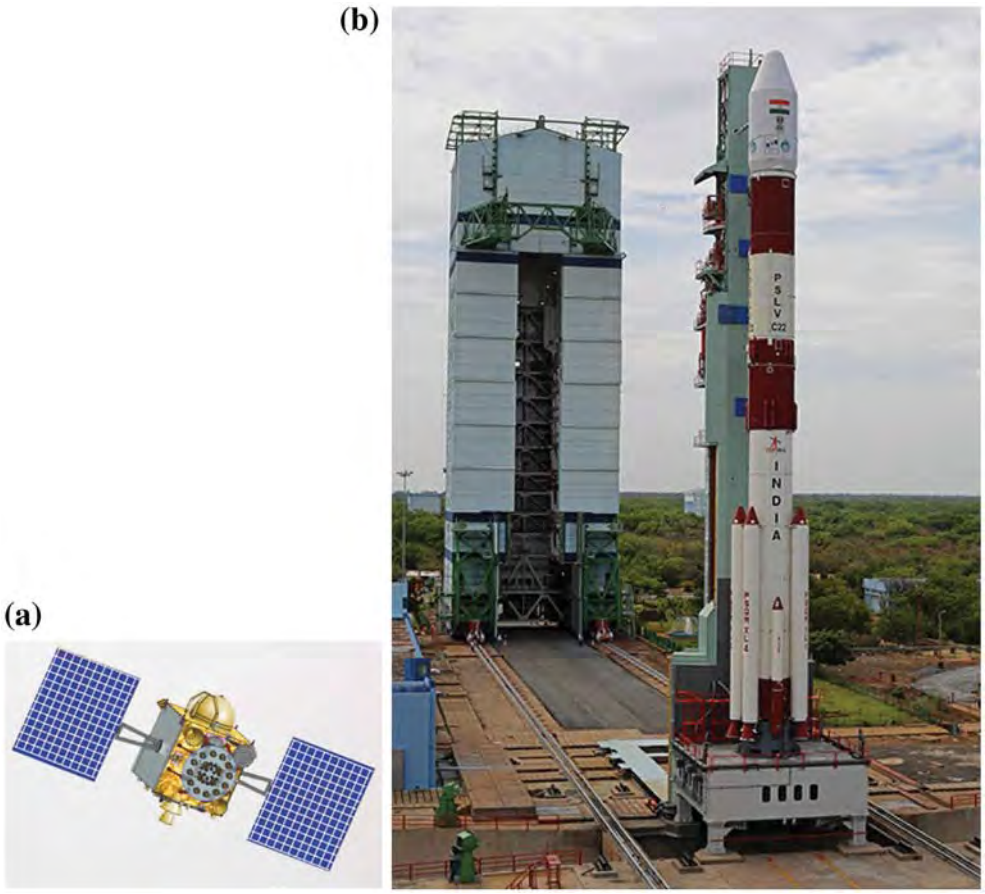

Figure 2. (a) Artistic view of satellite I1. (b) The PSLV-C22 rocket used to launch I1 (images credit: ISRO).

day (23 h and 56 min), such that the IRNSS satellite ground tracks repeat every solar day (24 h) four minutes earlier.

Figure 1(a) and (b) show the fully operational seven-satellite IRNSS constellation together with the corresponding ground tracks, respectively. Three satellites will be placed as GEOs located at longitudes 32.5°E, 83°E and 131.5°E, respectively, while the remaining four satellites will be IGSOs, in pairs, placed at an inclination angle of 29° w.r.t. the equator, with their longitude crossings at 55°E and 111.75°E, respectively (ISRO 2014a). The complete system is planned to be fully operational by the end of 2016 (GPS World 2015).

The *current* operational IRNSS constellation (November 2015) comprises three IGSO satellites, IRNSS-1A/1B/1D (I1/I2/I4), and one GEO satellite, IRNSS-1C (I3). The satellites I1, I2, I3 and I4 were launched by the launchers PSLV-C22, PSLV-C24, PSLV-C26 and PSLV-C27 on 1 July 2013, 4 April 2014, 16 October 2014 and 28 March 2015, respectively (ISRO 2014b,c,d, 2015). The launches for the remaining three satellites are planned in the following periods: IRNSS-1E (January 2016), IRNSS-1F (February–March 2016) and IRNSS-1G (March–April 2016). Figure 2(a) and (b) show satellite I1 and the launch vehicle PSLV-C22, respectively (ISRO 2014b).

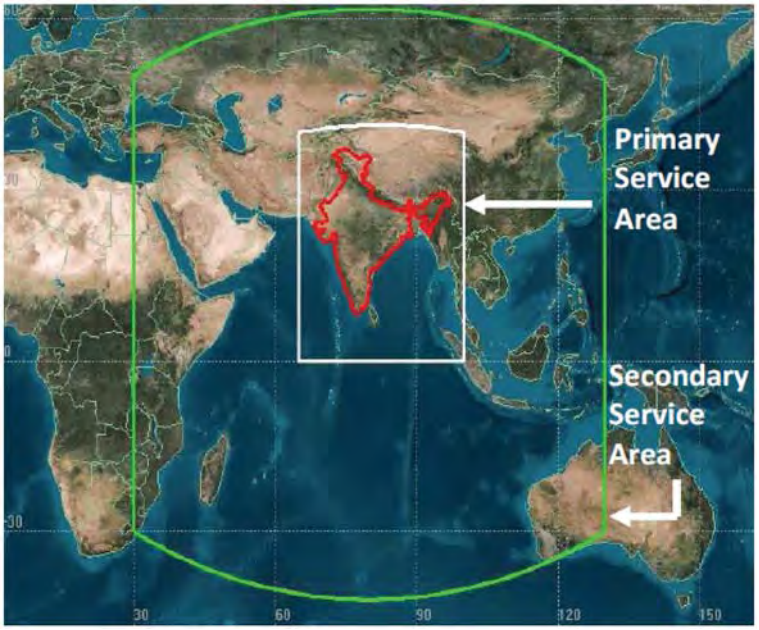

Figure 3. IRNSS primary and secondary service area (image credit: ISRO).

The IRNSS is established with the objective of offering positioning, navigation and timing (PNT) services to the users in its service area. The IRNSS classifies its service areas broadly into the two regions shown in Figure 3. The primary service area of IRNSS encompasses the Indian landmass and a region lying within a distance of 1500 km from its geo-political boundary. In this area the system is designed to provide its users with a position accuracy of less than 10 m (2σ). The secondary service area extends between latitudes 30°S to 50°N and longitudes 30°E to 130°E with an expected positioning accuracy of 20 m over the Indian ocean (Sarma *et al*. 2010; Ganeshan 2012; Saikiran & Vikram 2013).

3. IRNSS L5 single-point positioning (SPP)

In this section we formulate the SPP model of observation equations and analyse the observability of the current IRNSS constellation for several Australian locations in its secondary service area.

Single-epoch pseudorange-only SPP model

We assume that a single receiver r is tracking m IRNSS satellites on frequency L5. The single-epoch, single-frequency linearised SPP observation equations can then be formulated in vector-matrix form as

$$\begin{aligned} E\{\Delta \underline{p}_r\} &= [G_r \quad e_m] \begin{bmatrix} \Delta x_r \\ dt_r \end{bmatrix} \\ D\{\Delta \underline{p}_r\} &= \sigma^2 W_r^{-1} \end{aligned} \tag{1}$$

where $E\{.\}$ and $D\{.\}$ denote the expectation and dispersion operators, respectively. The m-vector $\Delta \underline{p}_r$ contains the observed-minus-computed pseudorange observables to the m IRNSS satellites, and underscore is used to indicate its random nature. They are a priori corrected for the ionospheric delays using the

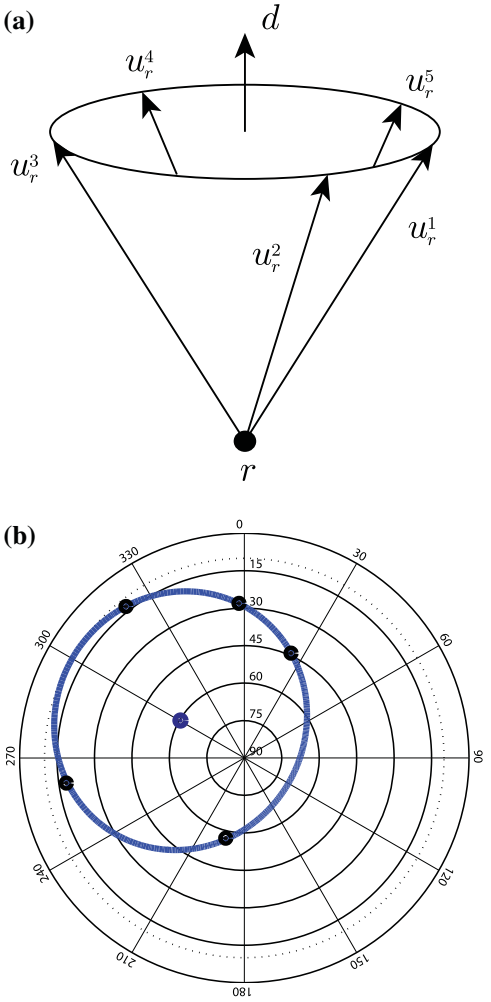

Figure 4. (a) SPP positioning is indeterminate in direction if the receiver-satellite direction vectors u_r^s, s = 1, …, *m*, all lie on a cone having d as its symmetry axis (Teunissen 1990). (b) Skyplot showing a cone with symmetry axis d having an azimuth of 300° and an elevation of 60°.

Global Ionosphere Map GIM (CODE 2015) and for the dry tropospheric delays using the Saastamoinen model (Saastamoinen 1972).

The $m \times 3$ matrix $G_r = [-u_r^1, \ldots, -u_r^m]^T$ contains the unit direction vectors u_r^i, $i = 1, \ldots, m$, from the receiver antenna to the m tracked IRNSS satellites and e_m is the m-vector of ones. The 3-vector Δx_r is the receiver position increment, and the scalar dt_r is the increment of the receiver clock error biased by the receiver code hardware delay.

The parameter σ denotes the zenith-referenced user range accuracy which captures the observables noise characteristics as well as the remaining unmodelled effects. The $m \times m$ diagonal weight matrix $W_r = \mathrm{diag}(w_r^1, \ldots, w_r^m)$ contains the elevation-dependent weights (Odolinski *et al.* 2014),

$$w_r^s = \left(\frac{1.02}{sin\varepsilon_r^s + 0.02}\right)^{-2} \tag{2}$$

with ε_r^s being the elevation of the satellite s with respect to receiver r.

Assuming that the design matrix $[G_r, e_m]$ is of full rank, the SPP weighted least-squares solution of the position vector is given as

$$\begin{aligned} \Delta\hat{x}_r &= (G_r^T W_D G_r)^{-1} G_r^T W_D \Delta p_r \\ Q_{\hat{x}_r\hat{x}_r} &= \sigma^2 (G_r^T W_D G_r)^{-1} \end{aligned} \tag{3}$$

in which $W_D = D_m (D_m^T W_r^{-1} D_m)^{-1} D_m^T$ and the range space of the $m \times (m-1)$ difference matrix D_m spans the orthogonal complement of e_m, i.e. $D_m^T e_m = 0$. Note that Δp_r of (3) is a realisation of the random observable $\Delta \underline{p}_r$.

Rank-defect receiver-satellite geometries

As the IRNSS system is currently still in a built-up phase, one can expect that there will be occasions of poor receiver satellite geometries. To understand what they look like, we now give a geometric interpretation to the occurrence of a rank defect in the $m \times 4$ SPP design matrix $[G_r, e_m]$. The design matrix is rank defect if linear combinations of its column vectors exist that equal the zero vector, i.e. if a vector $d \in \mathbb{R}^3$ and a scalar $\lambda \in \mathbb{R}$ can be found such that

$$G_r d + e_m \lambda = 0 \tag{4}$$

As the columns of $-G_r^T$ are given by the receiver-satellite unit direction vectors u_r^s, $s = 1, \ldots, m$, we may write (4) also as $(u_r^s)^T d = \lambda$ for $s = 1, \ldots, m$, or, by using the cosine rule with $const = \lambda / ||d||$, as

$$cos\angle(u_r^s, d) = const \quad for \quad s = 1, \ldots, m \quad (5)$$

Hence, the design matrix is rank defect if the unit direction vectors of the satellites u_r^s all have the same constant angle to vector d. Geometrically this means that this rank deficiency occurs when all these unit direction vectors lie on a cone having d as its symmetry axis (see Figure 4(a)). The symmetry axis of the cone, i.e. the vector d, is then the direction in which the position solution has become indeterminate. Thus if d points towards the zenith, as in Figure 4(a) for example, then it is the height component that has become indeterminate. Figure 4(b) shows a skyplot example in which the receiver-satellite direction vectors all lie on a cone with symmetry axis having an azimuth of 300°and an elevation of 60°.

Another case of (5) which is relevant for IRNSS is when *const* = 0. In that case all receiver-satellite direction vectors u_r^i lie in a plane with d as its normal vector. Thus if, for example, all satellites lie in an east-west oriented plane, then the indeterminate direction vector d would point in the north-south direction. Hence, if the receiver-satellite geometry is such that the geometric extent is smallest in north-south direction, then it is also that direction in which positioning will perform most poorly. This may happen with IRNSS, for instance, if the IGSO satellites are closest to the equatorial plane in which the GEO satellites already reside.

Current satellite visibility

The current constellation consists of three IGSOs and one GEO satellite. Their visibility is depicted in Figure 5 for three different Australian locations, Christmas Island, Perth and Darwin, on DOY 166 of 2015 using cut-off elevation angles of 5° and 10°. The number of satellites that can be tracked from these three locations is shown in Figure 5(a), (c) and (e), while Figure 5(b), (d) and (f) show the corresponding 24-h IRNSS ground tracks for a cut-off elevation angle of 10°.

As Figure 5 shows, the number of current satellites that can be tracked reduces the more eastward the Australian user is located. Although four satellites can be still tracked on a continuous basis at Christmas island, there are periods in Perth and Darwin when this number drops to three and in Darwin even to two. Although the durations of these periods can be shortened somewhat by using 5° instead of 10° cut-off elevations, they remain present when tracking from Perth and Darwin.

To remedy the situation that continuous SPP positioning is currently not possible at these locations, we investigate what the inclusion of a soft height constraint in the SPP model brings in terms of its positioning capability. Assuming that the geodetic height h_r of the receiver antenna is known with a certain standard deviation σ_{h_r} and that Δx_r is represented in the local East-North-Up (ENU) frame, the SPP model (1) is extended with

$$E\{\Delta \underline{h}_r\} = c^T \Delta x_r \quad , \quad D\{\Delta \underline{h}_r\} = \sigma_{h_r}^2 \quad (6)$$

in which c denotes the canonical unit 3-vector, having 1 as its third element. With the inclusion of such a weighted constraint, SPP becomes possible in principle with only three tracked satellites.

PDOP and the receiver-satellite geometry

We use the position dilution of precision (PDOP) as a scalar measure to diagnose the strength of the receiver-satellite geometry. The PDOP is defined as (Teunissen 1998; Hofmann-Wellenhof *et al.* 2013)

$$\mathrm{PDOP} = \mathrm{trace}\left([G_r^T W_D G_r]^{-1}\right) \quad (7)$$

where $W_D = D_m(D_m^T W_r^{-1} D_m)^{-1} D_m^T$. For the weighted height-constrained case, matrices G_r and W_D are adopted to take (6) into account. The corresponding 24-h PDOP time series are given in Figure 6 for Christmas Island, Perth and Darwin for DOY 166 of 2015. Note that the signatures of these time series are repre-

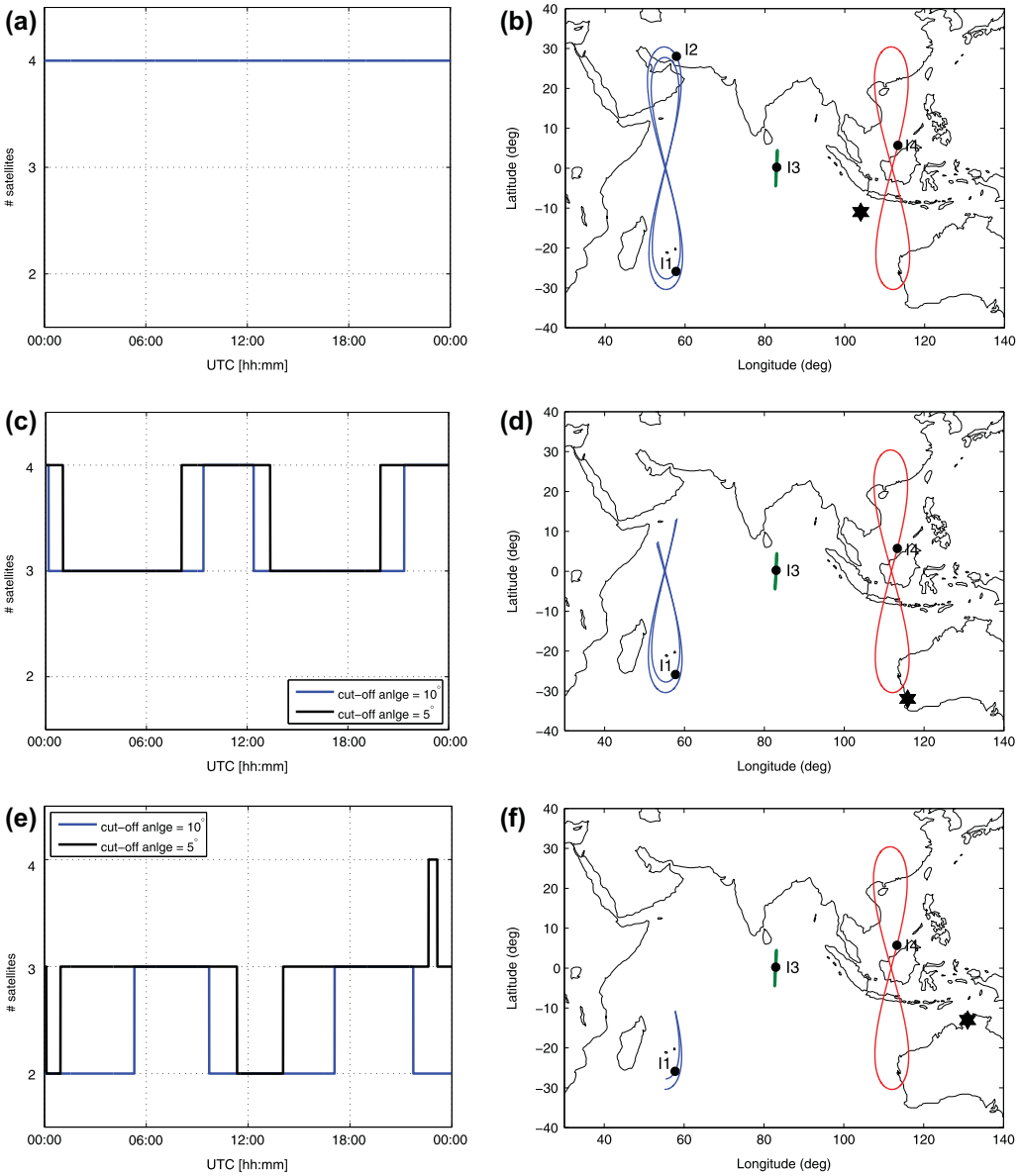

Figure 5. Current IRNSS satellite visibility at Christmas Island, Perth and Darwin. (a) Number of satellites that can be tracked at Christmas Island, (c) at Perth and (e) at Darwin on DOY 166 of 2015, using cut-off elevation angles of 5° and 10°, respectively. (b), (d) and (f) Corresponding satellite ground tracks on DOY 166 of 2015 for 10° cut-off elevation angle. The GEO I3 ground track is shown in green, the I1 and I2 IGSOs (figures-of-eight) ground tracks are shown in blue, and the I4 IGSO ground track is shown in red. The satellite positions at UTC 06:40 are indicated by dots. The location of the users are indicated by the star symbol.

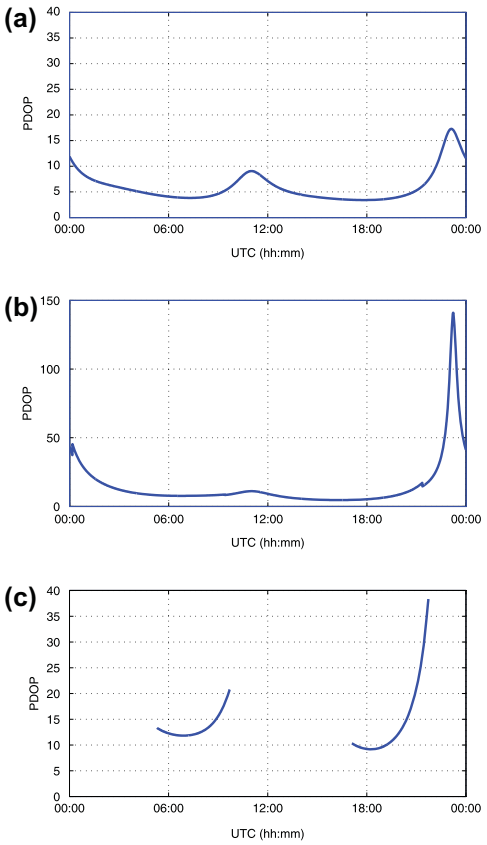

Figure 6. Height constrained PDOPs on DOY 166 of 2015 for (a) Christmas Island, (b) Perth, and (c) Darwin, with 10° cut-off elevation.

sentable for any day as the receiver-satellite geometry repeats itself every day four minutes earlier w.r.t. the previous day.

As Figure 6 shows, the PDOPs become larger, and thus the receiver-satellite geometry weaker, when one changes location from Christmas Island to Perth and then to Darwin. The PDOPs of Darwin are only shown for the two periods that three satellites are visible (see Figure 5). Note that the PDOP time series of Christmas Island is relatively flat except for two distinct peaks that built up in the UTC periods 09:16:00–13:18:00 and 20:51:00–00:00:00. They can also be recognised in the Perth PDOP time series, albeit in a somewhat distorted way. Prior to the peaks in the Perth PDOP times series, the PDOP shows a sudden drop in value due to the inclusion of a fourth satellite at UTC times 09:23:30 and 21:21:00 (see Figure 5). Thus although one is observing the maximum number of available satellites in those two periods in Perth, the receiver-satellite geometry is apparently such that it still weakens the model, thereby increasing the PDOP values.

To get a better understanding of this phenomenon, we analyse the Perth receiver-satellite geometry for the UTC period 21:21:00–00:04:00, which is 05:21:00–08:04:00 local time. Figure 7(a) shows the skyplot of the IRNSS satellites for this period. The peak in the Perth PDOP time series of Figure 6 occurs when the two satellites I1 and I2 occupy the same skyplot position. The corresponding skyplot of this instant is shown in Figure 7(b). In it we have shown the direction d (cf. 4 and 5), indicated as a *blue* dot in the north-westerly direction, in which the receiver position is the poorest estimatable, i.e. it has the largest variance and two contour lines of unit vectors that make 36° resp. 38° angles with this poorest estimatable direction. As the skyplot shows, the receiver-satellite direction vectors of all the four satellites are on or near these contour lines, thus showing that the receiver-satellite geometry comes close to the rank-defect geometry as described in previous subsections.

Another way to illustrate this poor position estimatability is as follows. As the direction vector d lies in the horizontal plane (due to the imposed height constraint), the projections onto the horizontal plane of the unit vectors on the 36° resp. 38° cones will form a straight line. Figure 7(c) shows the projections onto the horizontal plane of the actual receiver-satellite direction vectors at 07:13:00 Perth local time on DOY 166. The fact that they all lie on or close to a straight line again indicates that the corresponding design matrix in this period is near singular.

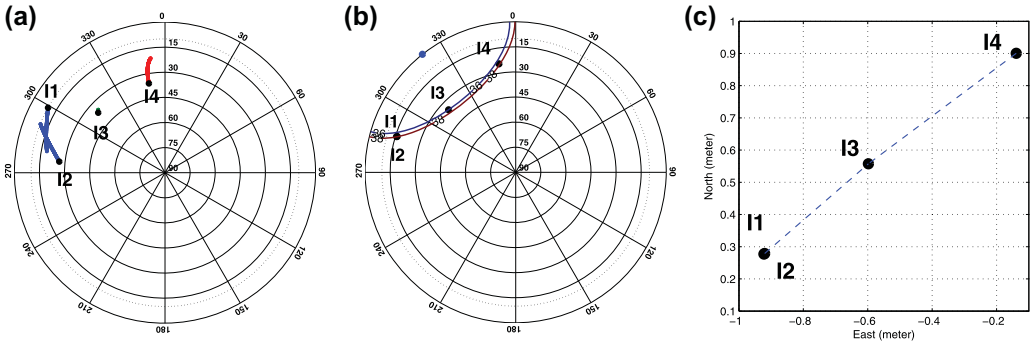

Figure 7. (a) IRNSS skyplot for Perth, on DOY 166 of 2015 during [05:21:00–08:04:00] Perth local time. The black dots show the location of the visible satellites at the first epoch of the mentioned time interval. (b) IRNSS skyplot for Perth, at 07:13:00 Perth local time on DOY 166 of 2015. The blue dot illustrates the direction d along which the receiver position is poorest estimable. The two colored contour lines show the loci of the unit vectors that make the same 36 resp. 38 degree angle with d. (c) The projections onto the horizontal plane of the four Perth receiver-satellite direction vectors lie approximately on a straight line at 07:13:00 Perth local time on DOY 166 of 2015.

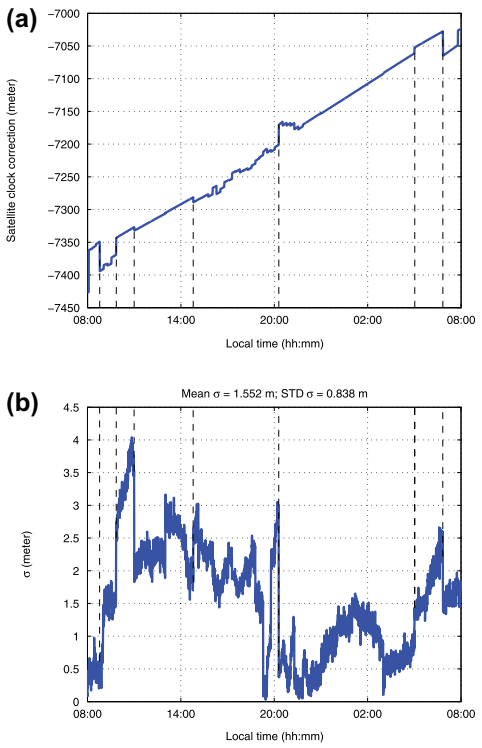

Figure 8. (a) Time series of the I4 satellite clock corrections as provided by the broadcast ephemerides on DOY 200 of 2015. (b) The $\hat{\sigma}(i)$ time series as obtained from the CUT3 data on DOY 200 of 2015 with 10° cut-off elevation.

4. IRNSS SPP precision

In this section we analyse, formally as well as empirically, the SPP precision that can be achieved with the current constellation.

Noise characteristics

To analyse the SPP precision we first need a representative value for the zenith-referenced σ^2 of (1). The estimation of σ^2 can be done by means of variance component estimation (VCE) provided redundancy is present (Teunissen & Amiri-Simkooei 2008). To create redundancy for the present constellation, we use data from a tracking station of which the coordinates are known. With the receiver coordinate vector x_r known, the redundancy equals $m - 1$, thus providing single-epoch redundancy for two or more satellites. With the receiver position known, the single-epoch misclosure vector of the SPP model becomes

$$\underline{s} = D_m^T \, \Delta \underline{p}_r \tag{8}$$

having zero expectation, $E\{\underline{s}\} = 0$ and dispersion $D\{\underline{s}\} = \sigma^2 \, D_m^T W_r^{-1} D_m$. The estimated variance component based on the misclosure vector of epoch i follows then as

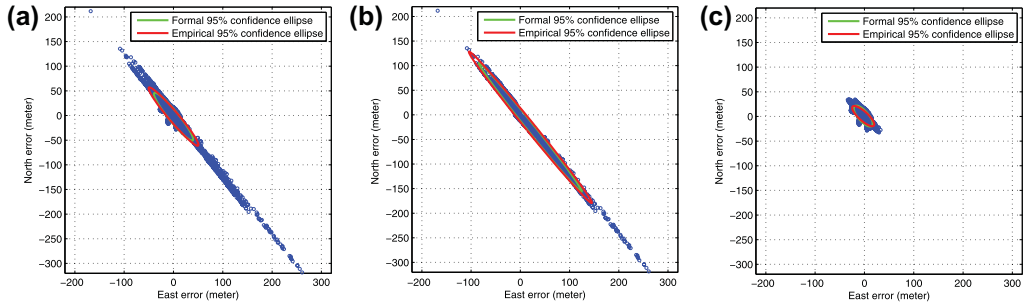

Figure 9. IRNSS height-constrained SPP horizontal scatter plots (h_r = 24 m and σ_{h_r} = 1 m) for (a) time window 1, (b) time window 2 and (c) time window 3, based on 10° cut-off elevation CUT3 data collected on DOYs 182, 195, 200, 201, 205 and 207 of the year 2015.

$$\underline{\hat{\sigma}}^2(i) = \frac{\underline{s}^T(i)\, C_s^{-1}(i)\underline{s}(i)}{(m_i - 1)} \qquad (9)$$

with $C_s(i) = D_{m_i}^T W_r^{-1}(i) D_{m_i}$. We used this estimator to determine a $\hat{\sigma}(i)$ time series. A 10-day data-set was used, collected by CUT3, a static JAVAD TRE_G3TH_8 receiver at Curtin University, employing a 30 s sampling rate and a 10° cut-off elevation angle. The so obtained $\hat{\sigma}(i)$ time series is shown in Figure 8(b) for DOY 200 of 2015.

For the relatively crude pseudorange-only SPP model, the estimates $\hat{\sigma}(i)$ will include all remaining unmodelled effects, such as e.g. satellite orbital errors, satellite clock errors and residual atmospheric delays. However, the $\hat{\sigma}(i)$ time series of Figure 8(b) also shows some peculiar jumps. We were able to trace these jumps back to the performance of satellite I4, in particular to its on-board frequency. Figure 8(a) shows the time series of the I4 satellite clock correction provided by the broadcast ephemerides on DOY 200 of 2015. By means of the vertical dashed lines, highlighting the jumps, it can be observed that most of the jumps in the clock time series correspond to those of the $\hat{\sigma}(i)$ time series. This finding of the jumps in the on-board frequency of satellite I4 is consistent with that of Babu *et al.* (2015).

After having removed the impact of satellite I4 from the data-set, the corresponding jumps in the $\hat{\sigma}(i)$ time series disappeared and an average value of 1 m was obtained. This is the value that we used for our SPP positioning precision analysis.

SPP positioning precision: formal and empirical

We now determine the instantaneous SPP positioning precision that can be achieved with the current constellation by the use of a data-set collected on DOYs 182, 195, 200, 201, 205 and 207 of 2015 at the rate of 30 s and with the cut-off elevation angle of 10°. This cannot, however, be captured by using a single averaged precision value, since the receiver-satellite geometry, as observed in Perth, changes rather significantly over a 24 h period. Therefore, to illustrate this, we will work with three different time windows:

(1) *time window 1:* this covers the whole 24 h of a day;
(2) *time window 2:* this covers the local time period 04:19:30–07:02:30 of DOY 182 and its counterparts on the other days;
(3) *time window 3:* this covers time window 1 with the exclusion of time window 2.

Note that the receiver-satellite geometries in time window 2 are the same as those during 05:21:00–08:04:00 on DOY 166 (cf. Figure 7). In Figure 9, the scatter plots of the positioning errors are shown for the time windows 1,

Table 1. IRNSS single-epoch SPP empirical and formal standard deviations based on L5 data collected by station CUT3 in Perth (10° cut-off elevation), on DOYs 182, 195, 200, 201, 205 and 207 of 2015.

		σ_N (m)		σ_E (m)	
Height precision	Time window	emp	form	emp	form
$\sigma_{h_r} = 1$ m	1	24.16	19.81	20.62	16.23
	2	62.94	53.45	51.07	42.74
	3	8.41	8.67	9.17	7.88
$\sigma_{h_r} = 5$ m	1	25.26	21.04	21.55	17.37
	2	66.67	56.86	53.77	45.33
	3	8.93	9.13	9.92	8.71
$\sigma_{h_r} = 10$ m	1	27.84	24.02	23.66	20.17
	2	75.46	64.93	60.20	51.47
	3	9.85	10.41	11.34	10.87

Note: emp: empirical; form: formal; time window 1: outcomes based on all the observations; time window 2: outcomes based on the observations made during the local time period 04:19:30–07:02:30 on DOY 182 and its counterparts on other days; time window 3: outcomes based on time window 1 with the exclusion of time window 2.

2 and 3, along with their empirical and formal 95% confidence ellipses. Note that the scatter plots are elongated in the north-westerly direction, which conforms to the direction of the symmetry axis of the cone shown in Figure 7. Note that the first two scatter plots of Figure 9 are quite similar, whereas the third is much smaller in extent. The fact that the first two scatter plots do not differ by much in extent is due to the overwhelming influence of the poor receiver-satellite geometry of the time window 2. The scatter plot of time window 3 is much smaller as it corresponds to periods of much better receiver-satellite geometries; see also Figure 6.

Table 1 lists the formal and empirical standard deviations for different values of σ_{h_r} using the data of the above-mentioned six DOYs. The formal standard deviations are obtained from taking the average of all the single-epoch least-squares position variance matrices. The empirical standard deviations are obtained from the differences of the estimated SPP positions and the available ground truth of CUT3.

The results of Table 1 show that the best precision is achieved in time window 3, while the worst is achieved in time window 2, which indeed is the period in which the receiver-satellite geometry is poorest (see Figures 6 and 7). The results also show a reasonable consistency between the empirical and formal values, with the best matches being obtained for time window 3. This consistency shows that the easy-to-compute formal values can indeed be used to predict the expected precision with which SPP positioning can be achieved. In summary, the results of Table 1 show that a single-epoch, pseudorange-only positioning standard deviation in North and East of about 10 m can be achieved with the current constellation.

5. IRNSS relative-point positioning (RPP)

In this section we discuss the IRNSS current relative-point positioning performance for both the pseudorange-only case and the phase-smoothed case.

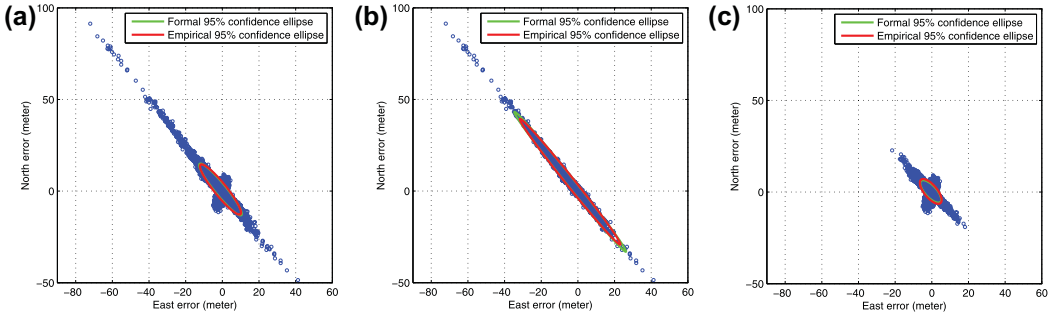

Figure 10. IRNSS height-constrained RPP horizontal scatter plots ($\sigma_{h_{12}} = 1$ m) for (a) time window 1, (b) time window 2 and (c) and time window 3, based on 10° cut-off elevation using SD pseudorange data of CUT3 and CUBB collected on DOYs 182, 195, 200, 201, 205 and 207 of the year 2015.

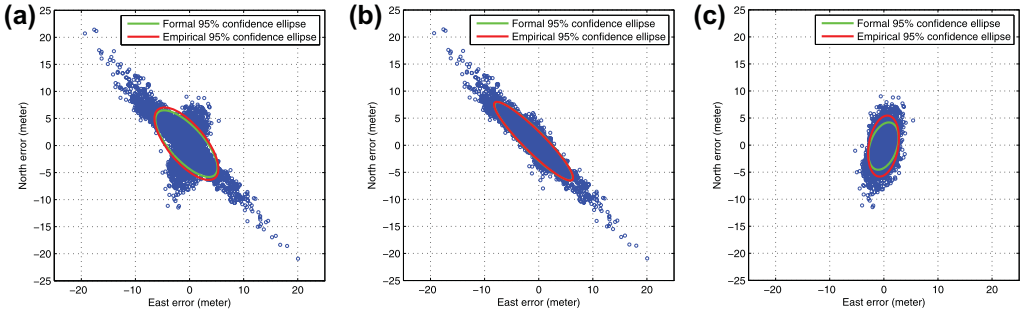

Figure 11. IRNSS single-frequency height-constrained single-frequency RPP ($\sigma_{h_{12}} = 1$ m) results of time window 3: (a) Whole period of time window 3, (b) [16:19:00–01:33:00] Perth local time on DOY 182 and its counterparts on other days, (c) Remaining part of the whole time window 3.

Pseudorange-only single-frequency RPP

The linearised RPP model of observation equations read

$$E\{\Delta \underline{p}_{12}\} = [G \quad e_m] \begin{bmatrix} \Delta x_{12} \\ dt_{12} \end{bmatrix} \qquad (10)$$

$$D\{\Delta \underline{p}_{12}\} = 2\sigma_p^2 \, W^{-1}$$

in which $(.)_{12} = (.)_2 - (.)_1$ is used to denote the between-receiver single-differenced (SD) observations and parameters. Δx_{12} is the between-receiver baseline increment, while σ_p is the zenith-referenced pseudorange standard deviation. As the unmodelled effects common to both receivers become eliminated in the between-receiver differencing, a large part of the residual biases present in the SPP model are absent in the RPP model. This also implies that in the case of the RPP model, σ_p mainly consists of the pseudorange measurement noise, which in our case was determined as 0.2 m (Nadarajah *et al.* 2015).

To illustrate how the RPP model succeeds in eliminating the large biases present in the SPP model, Figure 10 shows the RPP equivalent of Figure 9. A comparison between the two figures shows that the scatters have become smaller and that the large excursions in the SPP scatters of Figure 9 have disappeared. The lack of homogeneity in the scatters of Figure 10 seems to indicate

Table 2. IRNSS single-epoch, pseudorange-only RPP empirical and formal standard deviations based on L5 data collected for station pairs CUT3-CUBB (emp1) and CUAA-SPA7 (emp2) in Perth (10° cut-off elevation), on DOYs 182, 195, 200, 201, 205 and 207 of 2015.

		σ_N (m)			σ_E (m)		
Height precision	Time window	emp1	emp2	form	emp1	emp2	form
$\sigma_{h_{12}} = 1$ m	1	5.82	5.86	5.78	4.73	4.74	4.75
	2	14.77	15.57	15.60	11.78	12.29	12.46
	3	2.74	2.58	2.52	2.41	2.35	2.34
$\sigma_{h_{12}} = 5$ m	1	8.30	7.86	8.35	7.12	6.86	7.21
	2	21.63	20.42	22.35	16.98	16.00	17.62
	3	3.91	3.98	3.78	4.31	4.47	4.33
$\sigma_{h_{12}} = 10$ m	1	10.94	11.03	11.86	10.12	10.19	10.79
	2	27.03	27.55	30.48	21.15	21.51	23.92
	3	6.33	6.26	6.25	7.57	7.59	7.59

Note:emp: empirical; form: formal; time window 1: outcomes based on all the observations; time window 2: outcomes based on the observations made during the local time period 04:19:30–07:02:30 on DOY 182 and its counterparts on other days; time window 3: outcomes based on time window 1 with the exclusion of time window 2.

that there are still some significant unmodelled effects left. This, however, is not due to the presence of biases, but rather to the significant change that the receiver-satellite geometry undergoes in these time windows. We have illustrated this in Figure 11. This figure shows the time window 3 scatter (a), split out in a scatter for the local time window 16:19:00–01:33:00 on DOY 182 and its counterparts in other days (b), and the remaining period of time window 3 (c). Due to the significant change in receiver-satellite geometry, we indeed see the two quite different scatter signatures in the last two scatters of Figure 11.

Pseudorange-only RPP positioning precision: formal and empirical

We now determine the precision that can be achieved with the current constellation using the RPP model (10). Two independent sets of data were used: one data-set was obtained from the IRNSS tracking station pair CUT3-CUBB and the other from the pair CUAA-SPA7, all of JAVAD TRE_G3TH_8 type. Both sets of data were collected on DOYs 182, 195, 200, 201, 205 and 207 of 2015 at the rate of 30 s with the cut-off elevation angle of 10°.

Table 2 lists the formal and empirical standard deviations for different values of $\sigma_{h_{12}}$ using the two data sets of the above-mentioned six DOYs. The entries in this table have been determined in the same way as the entries in Table 1. Comparison with the SPP results of Table 1 shows that the precision has improved and that the factor of improvement is indeed approximately $5/\sqrt{2}$. The results show agreement between the empirical results ('emp1' and 'emp2' of Table 2) and also a reasonable consistency between the empirical and formal values. In summary, the results of Table 2 show that a single-epoch, L5 pseudorange-only RPP positioning standard deviation in North and East of about 7 m can be achieved with the current IRNSS constellation.

Table 3. IRNSS single-epoch, phase-smoothed RPP empirical and formal standard deviations based on L5 data collected for station pair CUT3-CUBB in Perth (10° cut-off elevation), on DOYs 182, 195, 200, 201, 205 and 207 of 2015.

		$\sigma_{N,50}[\sigma_{N,100}]$ (m)		$\sigma_{E,50}[\sigma_{E,100}]$ (m)	
Height precision	Time window	emp	form	emp	form
$\sigma_{h_{12}} = 1$ m	1	2.55[2.52]	1.39[1.19]	2.23[2.29]	1.23[1.08]
	2	5.57[5.97]	3.65[3.04]	4.56[4.95]	2.87[2.38]
	3	1.42[1.13]	0.63[0.55]	1.41[1.33]	0.77[0.71]
$\sigma_{h_{12}} = 5$ m	1	4.16[3.74]	3.83[3.53]	4.17[4.04]	3.93[3.75]
	2	8.56[7.03]	8.02[6.74]	6.79[5.67]	6.27[5.27]
	3	2.86[2.60]	2.57[2.38]	3.78[3.46]	3.31[3.15]
$\sigma_{h_{12}} = 10$ m	1	6.42[6.12]	6.59[6.25]	7.04[6.96]	7.19[7.00]
	2	10.80[9.38]	11.33[9.49]	8.52[7.44]	8.86[7.41]
	3	4.94[4.57]	5.08[4.73]	6.35[6.17]	6.52[6.23]

Note:emp: empirical; form: formal; time window 1: outcomes based on all the observations; time window 2: outcomes based on the observations made during the local time period 04:19:30–07:02:30 on DOY 182 and its counterparts on other days; time window 3: outcomes based on time window 1 with the exclusion of time window 2..

Phase-smoothed RPP positioning precision: formal and empirical

In this section we study the impact of replacing the raw pseudorange observations by their more precise carrier-phase-smoothed counterparts. The phase-smoothed pseudoranges, denoted here as $\bar{p}_r(i)$, are computed recursively from the original pseudoranges $p_r(i)$ and carrier-phases $\varphi_r(i)$ as (Hatch 1982, 1986; Teunissen 1991):

$$\bar{p}_r(i) = \frac{1}{k} p_r(i) + \frac{k-1}{k}[\bar{p}_r(i-1) + \varphi_r(i) - \varphi_r(i-1)] \tag{11}$$

with initialisation $\bar{p}_r(1) = p_r(1)$. The smoothing can be done on the basis of a chosen window length wl. With the window length wl specified, the factor k in (11) is taken as

$$k = \begin{cases} i \quad , & i \leq wl \\ wl \quad , & i > wl \end{cases} \tag{12}$$

Note that if, during the period in which the IRNSS observations are being made, one of the satellites sets and rises again, then smoothing for the data of that satellite should be reinitialised by setting $i = 1$ for the epoch in which the satellite rises again. This can be explained as follows. The phase integer ambiguity after satellite rise is not necessarily the same as that before satellite set. Therefore, if one makes use of the observations recorded before satellite set to smooth the code observations after satellite rise, the phase-smoothed code observables will become biased by the above-mentioned integer ambiguity differences.

Table 3 displays the phase-smoothed counterparts of the entries in Table 2 for the station pair CUT3-CUBB, and for the window lengths of $wl = 50$ and $wl = 100$. Upon comparing these two tables, we note that both empirical and formal precisions have improved, especially those corresponding to time window 2. However, it can also be observed that there is some discrepancy still between the empirical and formal results, especially when a harder con-

Table 4. IRNSS day-differenced single-epoch, phase-smoothed RPP empirical and formal standard deviations based on L5 data collected for station pair CUT3-CUBB in Perth (10° cut-off elevation), on DOYs 182, 195, 200, 201, 205 and 207 of 2015.

		$\sigma_{N,50}[\sigma_{N,100}]$ (m)		$\sigma_{E,50}[\sigma_{E,100}]$ (m)	
Height precision	Time window	emp	form	emp	form
$\sigma_{h_{12}} = 1$ m	1	1.97[1.70]	1.97[1.68]	1.80[1.62]	1.75[1.54]
	2	4.79[3.99]	5.15[4.28]	3.78[3.13]	4.04[3.35]
	3	1.03[0.81]	0.89[0.76]	1.22[1.13]	1.08[0.99]
$\sigma_{h_{12}} = 5$ m	1	5.26[4.97]	5.41[4.99]	5.42[5.32]	5.58[5.30]
	2	10.65[9.40]	11.30[9.50]	8.33[7.35]	8.83[7.43]
	3	3.58[3.23]	3.55[3.23]	4.56[4.41]	4.62[4.36]
$\sigma_{h_{12}} = 10$ m	1	9.36[8.90]	9.31[8.84]	10.17[9.96]	10.17[9.89]
	2	15.07[12.43]	15.98[13.41]	11.79[9.71]	12.48[10.47]
	3	7.19[6.60]	7.02[6.41]	9.11[8.72]	9.10[8.62]

Note:emp: empirical; form: formal; time window 1: outcomes based on all the observations; time window 2: outcomes based on the observations made during the local time period 04:19:30–07:02:30 on DOY 182 and its counterparts on other days; time window 3: outcomes based on time window 1 with the exclusion of time window 2.

straint is imposed on the height of the receiver. This is due to the accumulation in the smoothing procedure of a residual multipath (Kim & Langley 2000; Park *et al.* 2008; Zhao *et al.* 2009). This also explains the increment of the empirical standard deviations after increasing the smoothing window length from $wl = 50$ to $wl = 100$.

As the IRNSS constellation repeats itself every sidereal day, the stations multipath can also be expected to repeat every sidereal day. Hence, one can expect to eliminate the effect of multipaths by differencing the observations between days associated with the same satellite geometry. Listed in Table 4 are the day-differenced counterparts of Table 3. Table 4 does indeed show not only that this differencing results in a better consistency between empirical and formal precisions, but also that the previously noted accumulation effect for longer window lengths is now absent in the empirical standard deviations. The results of Table 4, divided by $\sqrt{2}$, are therefore representative for a multipath-free RPP positioning performance. In summary, the results show that a single-epoch, carrier-phase-smoothed pseudorange RPP positioning standard deviation in North and East of about 5 m can be achieved with the current IRNSS constellation.

6. Fully operational IRNSS performance

In this section we extend the previous analysis to the near-future case where the IRNSS has reached its full operational capability. The following investigations are based on the IRNSS geometry on DOY 166 of 2015. The orbits of the satellites I5, I6 and I7 are simulated. For simulation, the orbital parameters are determined such that they have respective nominated longitudes (ISRO 2014a) and have similar ground tracks to the respective types of existing satellites.

PDOP analysis

We start with a full-constellation PDOP analysis of the same three Australian locations as considered in the previous sections, Christmas

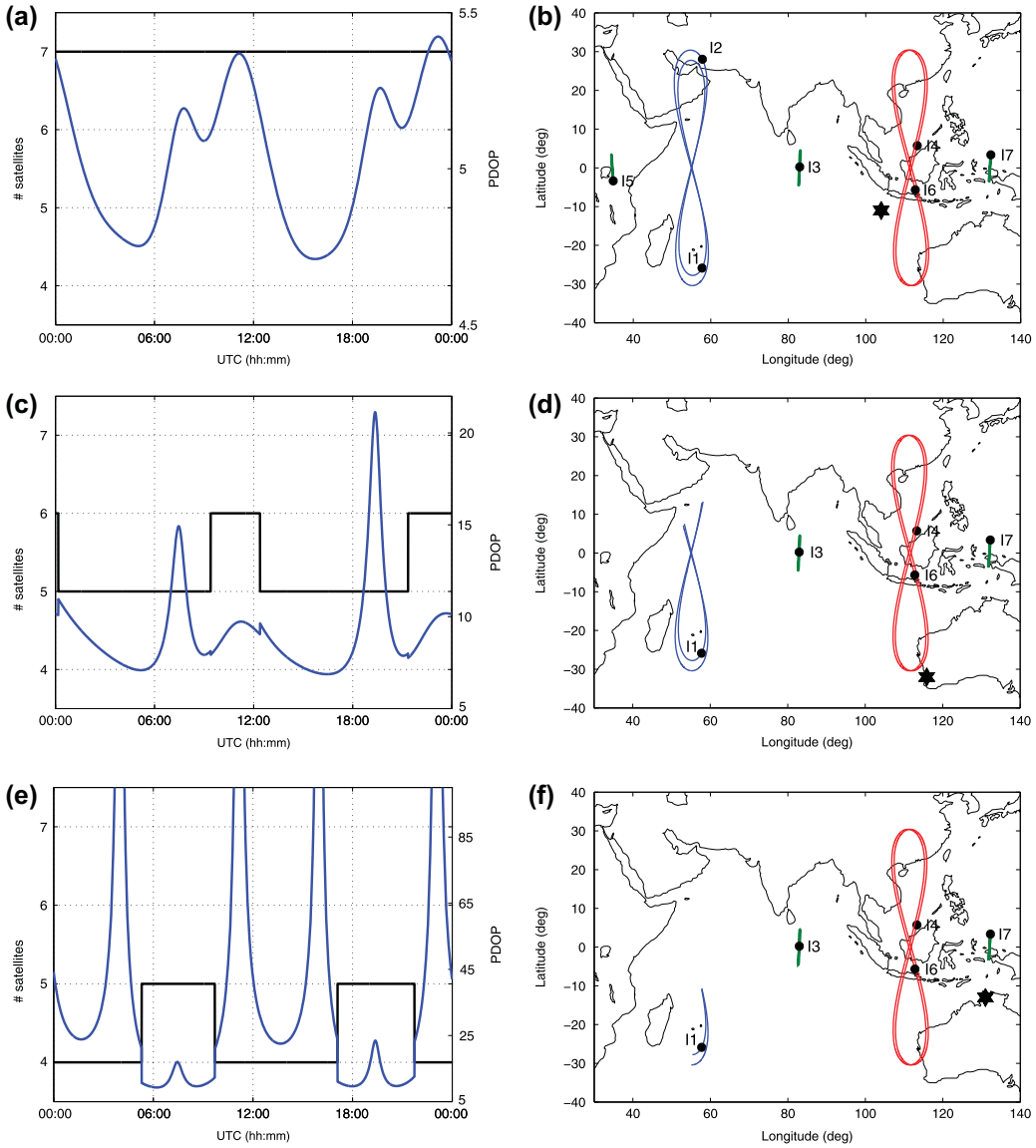

Figure 12. Full constellation PDOPs and satellite groundtracks for Christmas Island, Perth and Darwin. (a) PDOPs and number of satellites that can be tracked at Christmas Island, (c) at Perth and (e) at Darwin, on DOY 166 of 2015, using 10° cut-off elevation angle. (b), (d) and (f) Corresponding satellite ground tracks on DOY 166 of 2015 for 10° cut-off elevation angle. The GEO ground tracks are shown in green, the I1 and I2 IGSOs (figures-of-eight) ground tracks are shown in blue, and the I4 and I6 IGSO ground tracks are shown in red. The satellite positions at UTC 06:40 are indicated by dots. The location of the users are indicated by the star symbol.

Island, Perth and Darwin. The satellite visibility and 24-h PDOP time series are shown in Figure 12(a), (c) and (e), while the corresponding satellite ground tracks are shown in Figure 12(b), (d) and (f). Note that the three PDOP time series each behave almost sim-

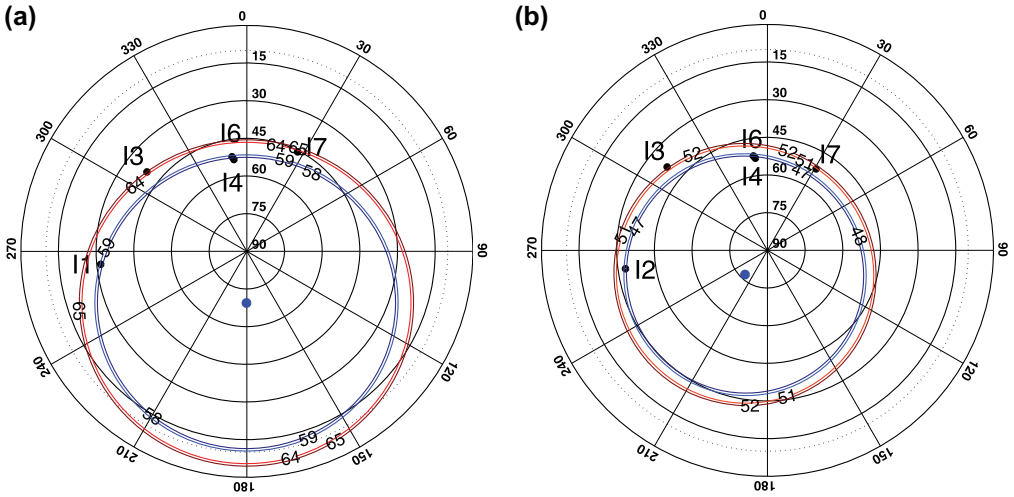

Figure 13. (a) Fully operational IRNSS skyplot for Perth on DOY 166 of 2015 at UTC 07:27:00 and (b) UTC 19:21:00. The blue dot in each figure denotes the symmetry axis *d* of the cone, i.e. the direction in which the receiver position is poorest estimable. The colored contour plots show the loci of unit vectors that make a constant angle with *d*.

ilarly in the periods UTC 00:00–12:00 and UTC 12:00–00:00. This is due to the fact that the IRNSS satellite configuration in the period UTC 00:00–12:00 is similar to that in UTC 12:00–00:00, albeit in the second period the positions of I1 and I2 and of I4 and I6 have interchanged.

The figure also shows that with a fully operational IRNSS, all seven satellites are visible from Christmas Island, but five and sometimes six from Perth, and only four or five from Darwin. Users in Perth would not be able to track the GEO I5 and most of the time also not the north-westerly IGSO (either I1 or I2), while users in Darwin additionally would lose most of the time track of the south-westerly IGSO also. With a reduction in number of satellites tracked, the PDOP value generally increases and the positioning precision decreases. With a lower cut-off elevation angle than 10° the situation would improve, but not by much. For Perth, for instance, a 5° cut-off elevation would not increase the maximum number of visible satellites, but it would lengthen the period that five satellites are visible somewhat.

In the Perth PDOP time series, there are two peaks visible, one at UTC 07:27 and another at 19:21. Although these peaks are not the same as shown in the earlier height-constrained PDOP time series for Perth (see Figure 6), they can again be explained by the occurrence of an approximate ‘cone-like’ receiver-satellite geometry. This is shown in the skyplots of Figure 13. In these two skyplots the symmetry axes of the two cones are also shown, i.e. the direction *d* (cf. 4 and 5) along which the position is the poorest estimatable (*blue* dot). Since these directions are near zenith in both cases, it is particularly the Up component that is poorly estimatable. The coloured contour plots in Figure 13 are the loci of unit vectors that make a constant angle with the cone’s symmetry axis, i.e. with direction *d*. For the first epoch UTC 07:27, the receiver-satellite direction vectors are located on the contours with values of 58°, 59°, 64° and 65°, respectively, and for the second epoch UTC 19:21 they are on the contours with values of 47°, 48°, 51° and 52°, respectively. As the variability in angles of the first set is larger than that of the sec-

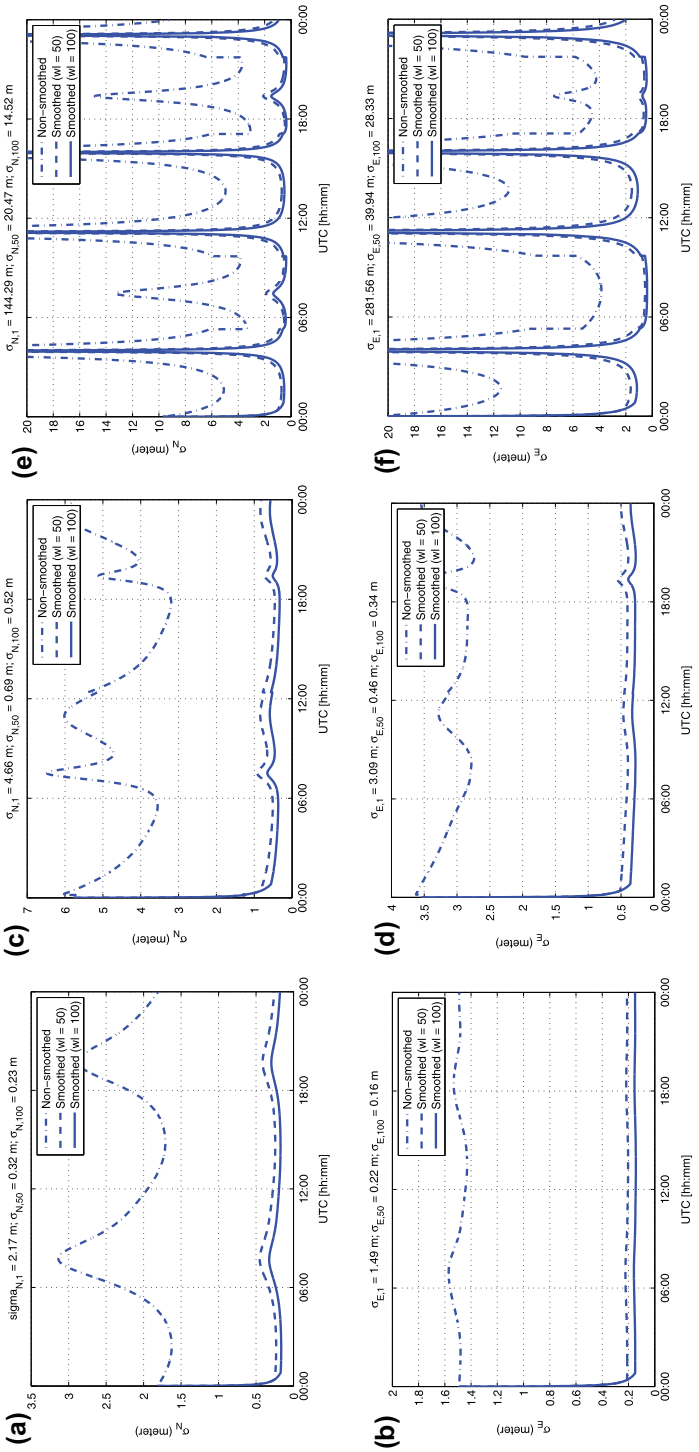

Figure 14. Full constellation, single-epoch, horizontal SPP precision for (a) & (b) Christmas Island (c) & (d) Perth and (e) & (f) Darwin. 'Non-smoothed' is the single-epoch, pseudorange-only SPP precision; 'smoothed (wl=50)' is the carrier-phase smoothed pseudorange SPP precision with window length of 50 epochs; 'smoothed (wl=100)' is the carrier-phase smoothed pseudorange SPP precision with window length of 100 epochs. Note the differences in σ-scale between the three locations. The average values of the time series are given on top of the graphs.

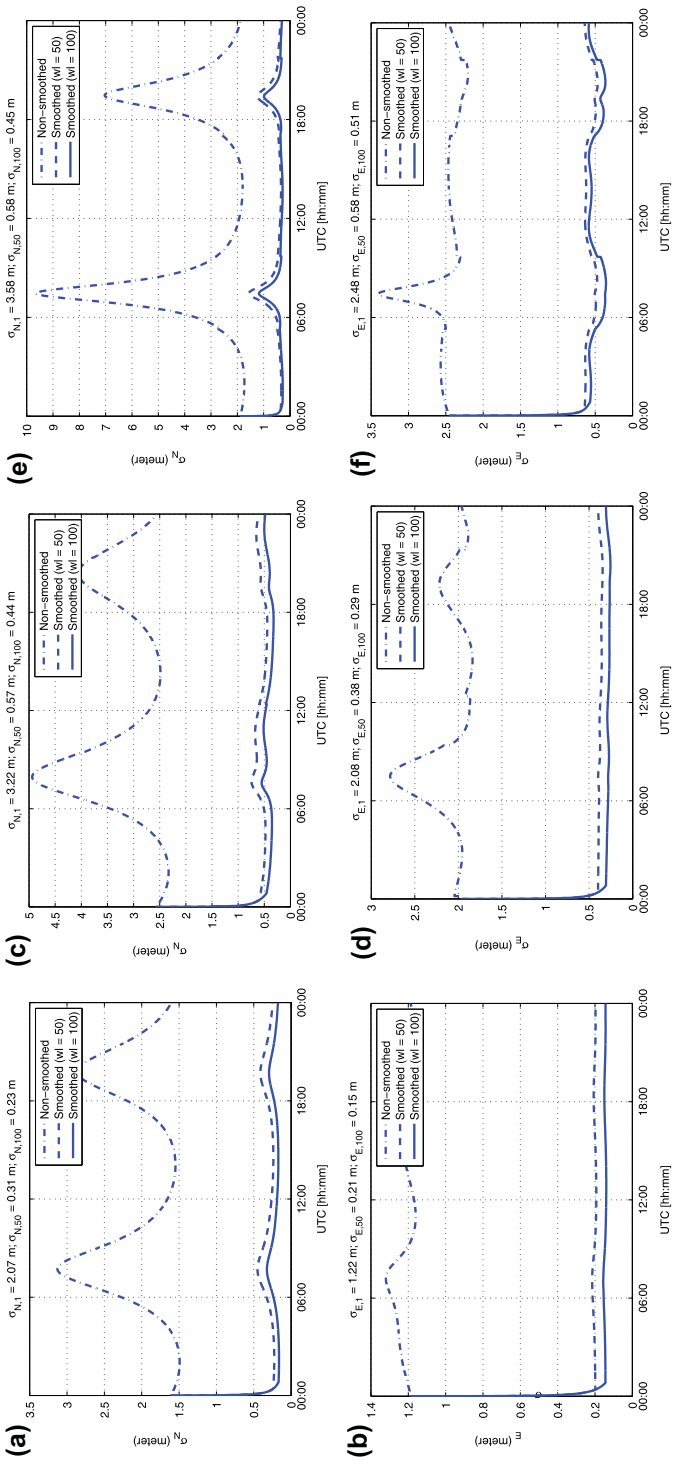

Figure 15. Full constellation, height-constrained ($\sigma_{h_i} = 5$ m), horizontal SPP precision for (a) & (b) Christmas Island (c) & (d) Perth and (e) & (f) Darwin. 'Non-smoothed' is the single epoch, pseudorange-only SPP precision; 'smoothed (wl=50)' is the carrier-phase smoothed pseudorange SPP precision with window length of 50 epochs; 'smoothed (wl=100)' is the carrier-phase smoothed pseudorange SPP precision with window length of 100 epochs. Note the differences in σ -scale between the three locations. The average values of the time series are given on top of the graphs.

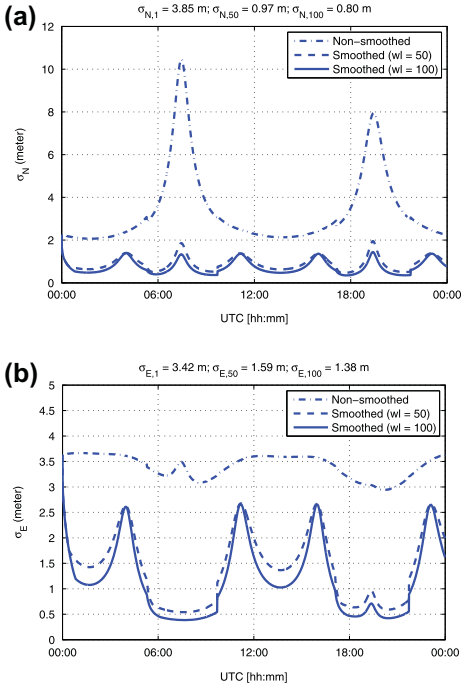

Figure 16. Full constellation, height-constrained (σ_{h_r} = 5 m), horizontal SPP precision for Darwin. 'Non-smoothed' is the single epoch, pseudorange-only SPP precision; 'smoothed (wl = 50)' is the carrier-phase smoothed pseudorange SPP precision with window length of 50 epochs; 'smoothed (wl = 100)' is the carrier-phase smoothed pseudorange SPP precision with window length of 100 epochs.

ond set, the deviation of the receiver-satellite geometry from a conical geometry is larger at UTC 07:27 than at UTC 19:20. This is why the value of the PDOP is smaller at UTC 07:27 than at UTC 19:21.

If we compare the PDOP time series of Darwin with that of Perth, we note, next to the generally much larger PDOP values in Darwin, that there are four periods when the Darwin PDOP values reach extreme values. During these four periods the receiver-satellite geometry is such that not only are a mere four satellites, namely I3, I4, I6 and I7, visible, but that two of them, namely I4 and I6, also have almost the same skyplot location. Hence, since all these four receiver-satellite direction vectors will then approximately span a plane, the columns of the receiver-satellite geometry matrix G_r of (1) will become near linearly dependent, thus leading to very large PDOP values.

Positioning precision

We now determine the positioning precision that one can expect to have once the full IRNSS constellation is operational. The expected single-epoch SPP precision over a whole day is shown in Figure 14 for Christmas Island, Perth and Darwin. The precision clearly deteriorates when moving eastwards, i.e. the precision is best at Christmas Island and poorest in Darwin. Each graph in Figure 14 shows three time series, one based on pseudoranges only ('non-smoothed') and another two based on carrier-phase-smoothed pseudoranges ('smoothed'), with window lengths of wl = 50 and wl = 100, respectively (cf. 11). The average values of the time series are given on top of the graphs.

The carrier-phase smoothing clearly has a very beneficial effect on the positioning precision, particularly for Christmas Island and Perth. We see not only a significant improvement in precision of approximately one order of magnitude, but also, in the case of Christmas Island and Perth, a flattening of the time series, thus making the positioning precision almost independent of the time of day. The two peaks in the time series of the Christmas Island North standard deviation are due to a reduced extent in north-southerly direction of the satellite locations at those instances.

As Figure 14(e) and (f) show, the positioning precision at Darwin is problematic, even when carrier-phase smoothing is used. Although the carrier-phase smoothing does help to lower the standard deviations and make the durations of the peaks briefer, the carrier-phase smoothing does not eliminate the large peaks. Hence, in Darwin there will remain four periods during the day when SPP positioning better than a few meters will not

be possible, even with the full IRNSS constellation operational.

The four periods that the standard deviations at Darwin will be smaller than 2 m are given in local time for DOY 166 as [09:58:00, 12:11:30], [14:21:00, 19:44:00], [22:00:30, 00:17:00], [02:19:00, 07:38:00] for window length wl = 50 and as [09:58:00, 12:40:30], [14:06:30, 19:59:30], [21:30:30, 00:43:00], [02:05:00, 07:53:30] for window length wl = 100. These periods can be transferred to other days as well knowing that the IRNSS geometry repeats every day four minutes earlier. For example, if one is interested in finding the counterparts of these periods on DOY 25 of 2016, the day differences between this day and DOY 166 of 2015, which is 224 days, should be multiplied by four minutes, and then subtracted from these periods.

The above results refer to the unconstrained case. We now consider the height-constrained case. With a weighted height constraint of $\sigma_{h_r} = 1$ m, the results of Figure 14 improve to those of Figure 15. These results show that positioning at Christmas Island and Perth marginally benefits from the constraint, but that Darwin, on the other hand, benefits significantly. With the carrier-phase smoothing included, the positioning precision at Darwin even approaches that of Chrismas Island and Perth.

One may argue of course, that for some applications a height constraint of $\sigma_{h_r} = 1$ m is overly restrictive. We therefore also show the results for Darwin when the much softer constraint of $\sigma_{h_r} = 5$ m is used; see Figure 16. These results show that positioning at Darwin can still benefit considerably even with such a much softer constraint. With carrier-phase smoothing the precision is about at the 2 m level, which is a dramatic improvement over the Darwin results of Figure 14.

7. Summary

As IRNSS will soon become fully operational, it is important to gain an understanding of its navigational potential and actual positioning capabilities. We therefore studied in this contribution the IRNSS stand-alone positioning performance for Australian stations located in the IRNSSs service area. This is the first such study performed. After a brief introduction to the IRNSS system, we described the positioning model that formed the basis for our analysis. We determined the zenith-referenced range error to be 1 m for SPP and 0.2 m for RPP. In the first part of our analysis we focussed on the currently achievable positioning performance. We identified and explained the occurrence of some poor receiver-satellite geometries and demonstrated with real IRNSS L5 data that instantaneous positioning better than 10 m for SPP and better than 7 m for RPP is currently feasible at the west-coast (e.g. Perth). These results are expected to improve significantly when IRNSS reaches its full operational capability. The instantaneous SPP precision for Perth was shown to improve then to 4 m on average and even down to 0.5 m if carrier-phase smoothing is included. These results get even better, due to the impact of IRNSSs receiver-satellite geometry, the more westward one moves, i.e. for marine navigation and positioning on the Indian Ocean. When moving eastwards, however, the results get poorer. At Darwin, for instance, the receiver-satellite geometry is such that every day four periods exist during which the positioning precision is poor, even when carrier-phase smoothing is used. Outside these four periods, however, the positioning precision is good and comparable with that of Perth. And as demonstrated, reduction of the impact of the four periods at Darwin is possible through the inclusion of soft height constraining ($\sigma_{h_r} = 5$m) combined with carrier-phase smoothing. In this case positioning at Darwin will be around 2 m or better for the whole day and thus still able to service a whole range of important applications.

Acknowledgements

This work has been done in the context of the Positioning Program Project 1.19 'Multi-GNSS PPP-RTK Network' of the Cooperative Research Centre for Spatial Information (CRC-SI). The second author is the recipient of an Australian Research Council (ARC) Federation Fellowship (project number FF0883188).

References

Babu, R., Mula, P., Ratnakara, S.C., Ganeshan, A.S., 2015. IRNSS satellite parameter estimation using combination strategy. *Global Journal of Science Frontier Research*, 15 (3), 87–95.

Chandrasekhar, M.V., Rajarajan, D., Satyanarayana, G., Tirmal, N., Rathnakara, S.C., Ganeshan, A.S., 2015. Modernized IRNSS broadcast ephemeris parameters. *Control Theory and Informatics*, 5 (2), 1–9.

CODE, 2015. *Global ionosphere maps produced by CODE* [online]. Available from: ftp://ftp.unibe.ch/aiub/CODE/2015 [Accessed 2 September 2015].

Ganeshan, A.S., 2012. Overview of GNSS and Indian Navigation Program. *In*: GNSS User Meeting, 23 Feb. 2012, ISRO Satellite Center, Bangalore.

GPS World, 2015. *ISRO: All 7 IRNSS Satellites in Orbit by March* [online]. Available from: http://gpsworld.com/isro-all-7-irnss-satellites-in-orbit-by-march [Accessed 2 November 2015].

Garcia, A.M., Piriz, R., Samper, M.D.L., Merino, M.M.R., 2010. Multisystem real time precise-point-positioning, today with GPS+GLONASS in the near future also with QZSS, Galileo, Compass, IRNSS. *In:* International Symposium on GPS/GNSS, 26–28 Oct 2010, Taipei, Taiwan.

Hatch, R., 1982. The synergism of GPS code and carrier measurements. *In*: 3rd International geodetic symposium on satellite Doppler positioning, 8–12 Feb 1982, Las Cruses, New Mexico, 2, 1213–1231

Hatch, R., 1986. Dynamic differential GPS at the centimeter level. *In*: Proceedings of the 4th International Geodetic Symposium on Satellite Positioning, 28 Apr–2 May 1986, Austin, Texas, 2, 1287–1298

Hofmann-Wellenhof, B., Lichtenegger, H., and Collins, J., 2013. *Global positioning system: theory and practice*. New York: Springer Science & Business Media.

ISRO, 2014 a. Indian regional navigation satellite system: signal in space ICD for standard positioning service, Version 1.0. ISRO Satellite Centre, June 2014.

ISRO, 2014 b. *PSLV-C22/IRNSS-1A* [online]. Available from: http://www.isro.gov.in/sites/default/files/pdf/pslv-brochures/PSLVC22.pdf [Accessed 1 September 2015].

ISRO, 2014 d. *PSLV-C26/IRNSS-1C* [online]. Available from: http://www.isro.gov.in/sites/default/files/pdf/pslv-brochures/PSLV-C26SS-1C [Accessed 1 September 2015].

ISRO, 2014c. *PSLV-C24/IRNSS-1B* [online]. Available from: http://www.isro.gov.in/sites/default/files/pslv-c24-brochure.pdf [Accessed 1 September 2015].

ISRO, 2015. *PSLV-C27/IRNSS-1D* [online]. Available from: http://www.isro.gov.in/sites/default/files/pdf/pslv-brochures/PSLV-C27-IRNSS-1D-BROCHURE.pdf [Accessed 1 September 2015].

Kim, D. and Langley, R.B., 2000. The multipath divergence problem in gps carrier-smoothed code pseudorange. Proceedings of 47th Annual Conference of the Canadian Aeronautics and Space Institute, 30 Apr–3 May 2000, Canadian Aeronautics and Space Institute, Ottawa, Ont., 161–163.

Kumari, A., Samal, K., Rajarajan, D., Swami, U., Babu, R., Kartik, A., Rathnakara, S.C., Ganeshan, A.S., 2015. Precise modeling of solar radiation pressure for IRNSS satellite. *Journal of Natural Sciences Research*, 5 (3), 35–43.

Montenbruck, O., Steigenberger, P. and Riley, S., 2015. IRNSS orbit determination and broadcast ephemeris assessment. Proceedings of the 2015 International Technical Meeting of The Institute of Navigation, 26–28 Jan 2015, CA: Dana Point, 185–193.

Nadarajah, N., Khodabandeh, A. and Teunissen, P.J.G., 2015. Assessing the IRNSS L5-signal in combination with GPS, Galileo, and QZSS L5/E5a-signals for positioning and navigation. *GPS Solutions*, 1–9, doi: http://dx.doi.org/10.1007/s10291-015-0450-8.

Odolinski, R., Teunissen, P.J.G. and Odijk, D., 2014. First combined COMPASS/BeiDou-2 and GPS positioning results in Australia. Part I: single-receiver and relative code-only positioning. *Journal of Spatial Science*, 59 (1), 3–24.

Park, B., Sohn, K. and Kee, C., 2008. Optimal hatch filter with an adaptive smoothing window width. *Journal of Navigation*, 61 (03), 435–454.

Rao, V.G., 2013. *Proposed LOS fast TTFF signal design for IRNSS*. Thesis (PhD). University of Calgary.

Rethika, T., Mishra, S., Nirmala, S.Rathnakara, S.C., Ganeshan, A.S., 2013. Single frequency ionospheric error correction using coefficients generated from regional ionospheric data for IRNSS. *Indian Journal of radio & Space Physics*, 42 (3), 125–130.

Saastamoinen, J., 1972. Atmospheric correction for the troposphere and stratosphere in radio ranging satellites. *In*: S.W. Henriksen, A. Mancini and B.H. Chovitz, eds. *The use of artificial satellites for geodesy*. Washington, DC: American Geophysical Union, 247–251.

Saikiran, B. and Vikram, V., 2013. IRNSS architecture and applications. *Journal of Comm & Electron*, 1 (3), 21–27.

Sarma, A.D., Sultana, Q. and Srinivas, V.S., 2010. Augmentation of Indian regional navigation satellite system to improve dilution of precision. *Journal of Navigation*, 63 (02), 313–321.

Sekar, S.B., Sengupta, S., and Bandyopadhyay, K., 2012. Spectral compatibility of BOC (5, 2) modulation with existing GNSS signals. *In:* Position Location and Navigation Symposium (PLANS), 2012 IEEE/ION, IEEE, 886–890.

Teunissen, P.J.G., 1990. GPS op afstand bekeken. *In:* een halve eeuw in de goede richting . Lustrumboek Snellius 1985-1990, DUM Delft, 215–233.

Teunissen, P.J.G., 1991. The GPS phase-adjusted pseudo-range. *In*: K. Linkwitz and U. Hangleiter, eds. *Proceedings of the 2nd International Workshop on High Precision Navigation*. Bonn: Dummler, 115–125.

Teunissen, P.J.G., 1998. A proof of Nielsen's conjecture on the relationship between dilution of precision for point positioning and for relative positioning with GPS. *IEEE on Aerospace and Electronic Systems*, 34 (2), 693–695.

Teunissen, P.J.G. and Amiri-Simkooei, A.R., 2008. Least-squares variance component estimation. *Journal of Geodesy*, 82 (2), 65–82.

Thoelert, S., Montenbruck, O. and Meurer, M., 2014. IRNSS-1A: signal and clock characterization of the Indian regional navigation system. *GPS Solutions*, 18 (1), 147–152.

Zhao, L., Li, L., and Zhao, X., 2009. An adaptive Hatch filter to minimize the effects of ionosphere and multipath for GPS single point positioning. *In:* International Conference on Mechatronics and Automation, 2009. ICMA 2009. IEEE, 4167–4172.

3 IRNSS positioning performance over its service area

This chapter is covered by the following publication:

Zaminpardaz S., Teunissen P.J.G., Nadarajah N. (2017a) IRNSS/NavIC Single-Point Positioning: A Service Area Precision Analysis. Marine Geodesy, Taylor & Francis, 40(4):259-274

Marine Geodesy

ISSN: 0149-0419 (Print) 1521-060X (Online) Journal homepage: http://www.tandfonline.com/loi/umgd20

IRNSS/NavIC Single-Point Positioning: A Service Area Precision Analysis

Safoora Zaminpardaz, Peter J. G. Teunissen & Nandakumaran Nadarajah

To cite this article: Safoora Zaminpardaz, Peter J. G. Teunissen & Nandakumaran Nadarajah (2016): IRNSS/NavIC Single-Point Positioning: A Service Area Precision Analysis, Marine Geodesy, DOI: 10.1080/01490419.2016.1269034

To link to this article: http://dx.doi.org/10.1080/01490419.2016.1269034

Accepted author version posted online: 12 Dec 2016.
Published online: 12 Dec 2016.

MARINE GEODESY
2017, VOL. 40, NO. 4, 259–274
http://dx.doi.org/10.1080/01490419.2016.1269034

Taylor & Francis
Taylor & Francis Group

IRNSS/NavIC Single-Point Positioning: A Service Area Precision Analysis

Safoora Zaminpardaz, Peter J. G. Teunissen, and Nandakumaran Nadarajah

GNSS Research Centre, Curtin University, Perth, Australia

ABSTRACT

The Indian Regional Navigation Satellite System (IRNSS) has recently (as of May 2016) become operational. The system has been developed with the objective of offering positioning, navigation, and timing (PNT) to users in its two service areas, covering the Indian landmass and the Indian Ocean, respectively. It is the goal of this contribution to provide further insight into the full-constellation L5 pseudorange single-point positioning (SPP) capabilities of the system. A detailed dilution of precision (DOP) analysis of its two service areas, including the identification, in location and time, of poor receiver-satellite geometries is provided. It is hereby demonstrated how the impact of some of these poor receiver-satellite geometries can be mitigated by means of height-constraining. An overview and analysis of the SPP precision is also provided including easy-to-use representative day-averaged values for a grid of locations covering the two service areas.

ARTICLE HISTORY
Received 18 July 2016
Accepted 1 December 2016

KEYWORDS
Dilution of precision (DOP); Indian Regional Navigation Satellite System (IRNSS); L5 pseudorange; Navigation with Indian Constellation (NavIC); single-point positioning (SPP)

Introduction

The Indian Regional Navigation Satellite System (IRNSS) has recently (May 2016) become operational and provided with the operational name of Navigation with Indian Constellation (NavIC). It has been developed by the Indian Space Research Organization (ISRO) with the objective of offering positioning, navigation, and timing (PNT) to the users in its service area. It thereby provides two types of services: a standard positioning service (SPS) for civilian users and a restricted service (RS) for authorized users (ISRO 2014).

As IRNSS has recently become fully operational, it is important to gain an understanding of its navigational potential and actual positioning capabilities for civilian users. This is not only of general interest, but also specifically for users operating in its service area. There are to date only a few published studies on IRNSS's positioning performance and none are based on the full constellation. Among the published IRNSS studies, several are simulation-based (Mozo Garcia et al. 2010; Sarma et al. 2010; Sekar et al. 2012; Rethika et al. 2013; Rao 2013; Su et al. 2012), while some are based on real data, such as Thoelert et al. (2014) in which the clock stability of IRNSS-1A is assessed. The accuracy of a precise model for solar radiation pressure is tested using the IRNSS-1A and 1B observations in Kumari et al. (2015). Babu

CONTACT Safoora Zaminpardaz safoora.zaminpardaz@postgrad.curtin.edu.au GNSS Research Centre, Curtin University, GPO Box U1987, Perth 6845, Australia.

Color versions of one or more of the figures in the article can be found online at www.tandfonline.com/umgd.

et al. (2015) compares orbit determination methods for IRNSS-1A, 1B, and 1C. In order to validate the orbit accuracy with modernized ephemeris parameters, Chandrasekhar et al. (2015) employs the IRNSS-1A, 1B, and 1C real data. Montenbruck and Steigenberger (2015) use the observations of the IRNSS-1A and 1B to investigate the quality of the IRNSS navigation messages. Nadarajah et al. (2015), after assessing the IRNSS noise characteristics, combines the L5/E5 signals of IRNSS, GPS, Galileo, and the Quasi-Zenith Satellite System (QZSS) for instantaneous attitude determination. Some positioning results over India based on the 4-satellite data of I1, I2, I3, and I4 are presented by Ganeshan et al. (2015), and Pal and Ganeshan (2015), and the position accuracy of two IRNSS satellites integrated with the other satellite systems is presented by Thombre et al. (2016). Zaminpardaz et al. (2016) present the first IRNSS standalone positioning results over Australia and Odijk et al. (2016) present the first analysis of the differential inter-system biases between L5 signal of IRNSS with respect to the L5/E5a signals of GPS, Galileo, and QZSS.

The goals of this contribution are to provide insight into IRNSS and to demonstrate its full-constellation single-point positioning (SPP) performance. As such, this contribution provides the first IRNSS standalone positioning performance analysis for different locations in its two service areas.

This contribution is organized as follows. First, the full IRNSS constellation with its two service areas are described as well as the SPP model that forms the basis of our analyses. A detailed dilution of precision (DOP) analysis of IRNSS's two service areas, including the identification, in location and time, of poor receiver-satellite geometries is then provided. It is hereby also demonstrated how the impact of some of these poor receiver-satellite geometries can be mitigated by means of height-constraining. Next, an overview and analysis of the SPP precision for a grid of locations over the two service areas is given. It includes easy-to-use representative day-averaged values of the positioning precision.

The IRNSS/NavIC system

In this section, we describe the IRNSS constellation with its two service areas as well as the SPP model that forms the basis of our analyses.

The IRNSS constellation

The IRNSS constellation consists of three geostationary orbit (GEO) satellites and four inclined geosynchronous orbit (IGSO) satellites (see Figure 1 and Table 1). The orbital period of the IRNSS satellites is one sidereal day (23 hours and 56 minutes), such that the IRNSS satellite ground tracks repeat every solar day (24 hours) 4 minutes earlier. The IRNSS satellites transmit navigation signals, based on Code Division Multiple Access, on L5 (1176.45 MHz), and on S (2492.028 MHz), with a Binary Phase-Shift Keying (BPSK (1)) modulation for standard positioning service (SPS) users, and with a Binary Offset Carrier (BOC (5,2)) modulation for restricted service (RS) users (ISRO 2014).

The IRNSS is established with the objective of offering PNT services to the users in its service area. The IRNSS classifies its service areas broadly into the two regions shown in Figure 2. The primary service area of IRNSS encompasses the Indian landmass and a region lying within a distance of 1500 km from its geo-political boundary, and the secondary service area extends between latitudes 30° S to 50° N and longitudes 30° E to 130° E (Sarma et al. 2010;

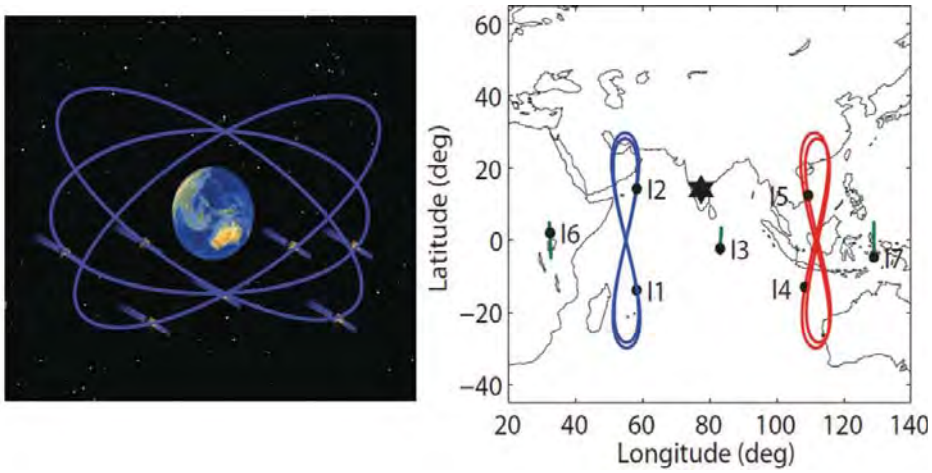

Figure 1. The 7-satellite IRNSS constellation (Left). The 3 GEO and 4 IGSO satellite ground tracks of IRNSS (Right).

Ganeshan 2012; Saikiran and Vikram 2013). Also, the secondary service area is important as it covers the Indian Ocean— one of the busiest oceans. The Indian Ocean is the third largest of the world's oceanic divisions, covering approximately 20% of the water on the Earth's surface. It contains major sea routes connecting the Middle East, Africa, and East Asia with Europe and the Americas, and it provides an estimated 40% of the world's offshore oil production.

The single-epoch SPP model

We assume that a single receiver r is tracking m IRNSS satellites on frequency L5. The single-epoch, single-frequency linearized SPP observation equations can then be formulated in vector-matrix form as

$$\begin{aligned} E\{\Delta p_r\} &= [G_r \quad e_m] \begin{bmatrix} \Delta x_r \\ dt_r \end{bmatrix} \\ D\{\Delta p_r\} &= \sigma^2 \, W_r^{-1} \end{aligned} \tag{1}$$

where $E\{.\}$ and $D\{.\}$ denote the expectation and dispersion operators, respectively. The m-vector Δp_r contains the observed-minus-computed pseudorange observables to the m IRNSS satellites. They are a priori corrected for the ionospheric delays and for the dry tropospheric delays.

Table 1. Information on the IRNSS satellites (ISRO 2016).

Satellite	Type	Longitude	Inclination	Launch date
IRNSS-1A (I1)	IGSO	55° E	29.0°	July 2013
IRNSS-1B (I2)	IGSO	55° E	31.0°	April 2014
IRNSS-1C (I3)	GEO	83° E	—	October 2014
IRNSS-1D (I4)	IGSO	111.75° E	30.5°	March 2015
IRNSS-1E (I5)	IGSO	111.75° E	28.1°	January 2016
IRNSS-1F (I6)	GEO	32.5° E	—	March 2016
IRNSS-1G (I7)	GEO	129.5° E	—	April 2016

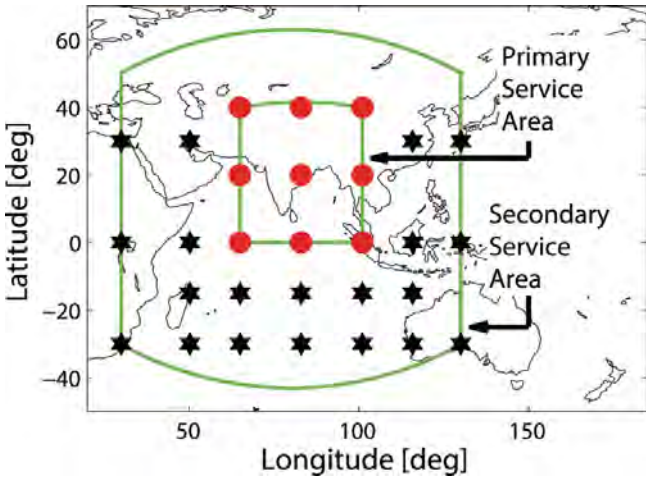

Figure 2. Primary (*red*) and secondary (*black*) service area locations. The inner and outer *green* boundaries indicate the border of the primary and secondary service areas, respectively.

The $m\times 3$ matrix $G_r = [-u_r^1, \ldots, -u_r^m]^T$ contains the unit direction vectors u_r^s, $s = 1, \ldots, m$, from the receiver antenna to the m tracked IRNSS satellites and e_m is the m-vector of ones. The 3-vector Δx_r is the receiver position increment, and the scalar dt_r is the increment of the receiver clock error biased by the receiver code hardware delay.

The parameter σ denotes the zenith-referenced user range accuracy, which captures the observables noise characteristics as well as the remaining unmodelled effects. The $m\times m$ diagonal weight matrix $W_r = \text{diag}(w_r^1, \ldots, w_r^m)$ contains the elevation-dependent weights (Euler and Goad 1991),

$$w_r^s = \left[1 + 10\,\exp\left(-\frac{\varepsilon_r^s}{10}\right)\right]^{-2} \tag{2}$$

with ε_r^s being the elevation of the satellite s with respect to receiver r.

Assuming that the design matrix $[G_r, e_m]$ is of full rank, the SPP weighted least-squares solution of the position vector is given as

$$\begin{aligned} \Delta\hat{x}_r &= (G_r^T W_D G_r)^{-1} G_r^T W_D \Delta p_r \\ Q_{\hat{x}_r\hat{x}_r} &= \sigma^2 (G_r^T W_D G_r)^{-1} \end{aligned} \tag{3}$$

in which $W_D = D_m (D_m^T W_r^{-1} D_m)^{-1} D_m^T$ and the range space of the $m\times(m-1)$ difference matrix D_m spans the orthogonal complement of e_m, i.e. $D_m^T e_m = 0$. By making use of the matrix identity $W_D = W_r\ (I_m - e_m (e_m^T W_r e_m)^{-1} e_m^T\ W_r)$, the variance matrix of $\Delta\hat{x}_r$ can also be expressed as

$$Q_{\hat{x}_r\hat{x}_r} = \sigma^2 \left(\sum_{s=1}^{m} w_r^s\ [u_r^s - \overline{u}_r][u_r^s - \overline{u}_r]^T\right)^{-1} \tag{4}$$

with the weighted average $\overline{u}_r = \sum_{s=1}^{m} w_r^s u_r^s / \sum_{s=1}^{m} w_r^s$. This expression now explicitly shows how the receiver-satellite unit direction vectors and their corresponding satellite elevation weighting contribute to the variance matrix.

Height-constrained model

As we will see in the following, there are situations for which the IRNSS SPP model turns out to be too weak to provide accurate positioning. Height-constraining of the model would then be a possible remedy. Information on the height component could be provided if the vertical user position would be known on average and not vary too much. Examples of such applications are marine positioning, bathymetric surveying, and kinematic positioning over small areas with low height fluctuations (Zhu and Santerre 2002; Godha and Cannon 2007). When enforcing the weighted height constraint, the observational model in (1) is extended with

$$E\{\delta h\} = \begin{bmatrix} 0, & 0, & 1 \end{bmatrix} \Delta x_r, \quad D\{\delta h\} = \sigma_h^2 \tag{5}$$

in which δh denotes the height constraint corrected for an initial height value and σ_h is the a priori standard deviation of the height constraint.

IRNSS PDOP-HDOP analysis

In this section, we provide a SPP dilution of precision (DOP) analysis for a grid of locations covering IRNSS's two service areas.

Horizontal dilution of precision

We use the DOP as a scalar measure to diagnose the strength of the receiver-satellite geometry. The Position DOP (PDOP) is defined as (Teunissen 1998; Hofmann-Wellenhof et al. 2013)

$$\text{PDOP} = \text{trace}\left(\left[G_r^T W_D G_r\right]^{-1}\right)^{0.5} = \frac{1}{\sigma} \text{trace}(Q_{\hat{x}_r \hat{x}_r})^{0.5} \tag{6}$$

The PDOP considers the impact of the receiver-satellite geometry on all three receiver coordinates. The Horizontal DOP (HDOP) is obtained in case only the horizontal receiver coordinates are considered.

In the following, we provide the 24-hour PDOP and HDOP time series for different locations over the two service areas. As the IRNSS receiver-satellite geometry repeats itself every day 4 minutes earlier with respect to the previous day, the signatures of these time series are representable for any day. Figure 2 shows the selected locations, for the primary service area in *red* and for the secondary service area in *black*.

Primary service HDOP

Figure 3 shows the time series of the number of visible satellites (*black*), the PDOP (*red*), and the HDOP (*blue*) for the primary service area locations (see Figure 2). It can be seen that the

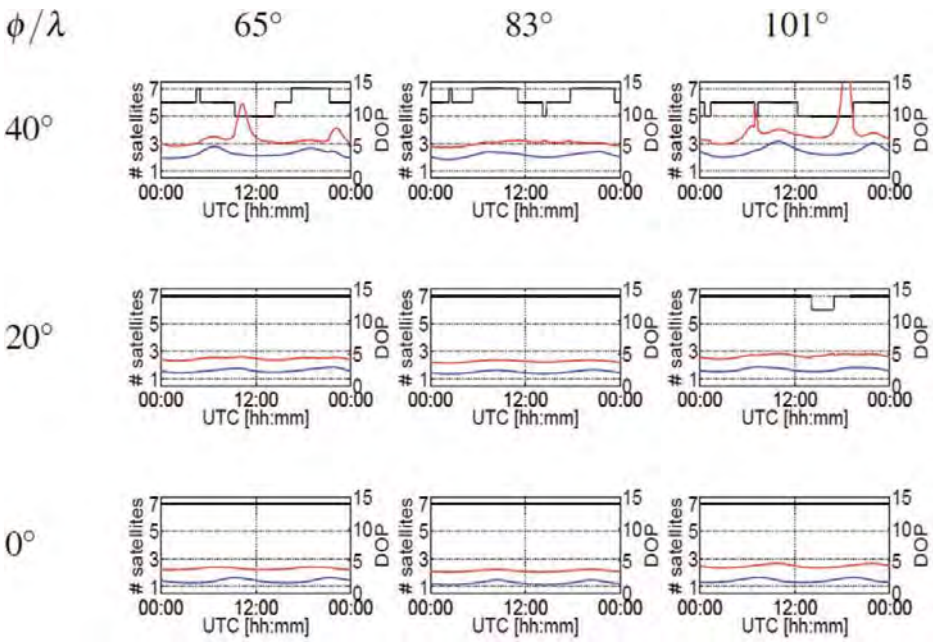

Figure 3. Primary service area time series of the number of visible IRNSS satellites (*black*) on DOY 153 of 2016, with 10° cut-off angle, and the corresponding PDOP (*red*) and HDOP (*blue*) values.

PDOP and HDOP values are reasonably constant over the day for the locations at latitudes of 0° and 20°, with PDOP ≈ 4 and HDOP ≈ 2.

For locations ($\varphi = 40°, \lambda = 65°$) and ($\varphi = 40°, \lambda = 101°$) we note a difference in satellite visibility, despite their symmetry with respect to the location of satellite I3. This is due to the fact that the distribution of the other four IGSOs and two GEOs is not symmetric with respect to the I3 location. For example, I6 is located 50.5° to the West of I3, whereas I7 is located 46.5° to the East of I3. Therefore, location ($\varphi = 40°, \lambda = 65°$) has a longer visibility of I7 than location ($\varphi = 40°$, $\lambda = 101°$) has of I6. Still, except for a distinct peak in the PDOP time series of location ($\varphi = 40°$, $\lambda = 101°$) over the period UTC [17:32:00–19:23:00], the PDOP and HDOP values are comparable to those of locations ($\varphi = 40°, \lambda = 65°$) and ($\varphi = 40°, \lambda = 83°$), with PDOP ≈ 6 and HDOP ≈ 4.

The occurrence of the PDOP peak at location ($\varphi = 40°$, $\lambda = 101°$) can be explained through the corresponding receiver-satellite geometry. Figure 4 depicts the satellites skyplot at UTC 18:30:30, which is the moment the PDOP peak occurs at location ($\varphi = 40°$, $\lambda = 101°$). It can be seen that at this moment in time the receiver-satellite line-of-sight unit vectors of all five satellites I1, I3, I4, I5, and I7 form a cone-like geometry (Teunissen 1990; Zaminpardaz et al. 2016), thus leading to a near-rank-defect SPP design matrix and hence large PDOP values. Note that the poorest estimable direction, i.e., the direction of the cone symmetry axis, has almost no component in the horizontal plane. This explains why the large peak in the PDOP at location ($\varphi = 40°, \lambda = 101°$) (see Figure 3) is absent from the HDOP.

Secondary service HDOP

Figure 5 shows the time series of the number of visible satellites (*black*), the PDOP (*red*), and the HDOP (*blue*) for the secondary service area locations (see Figure 2). When we consider

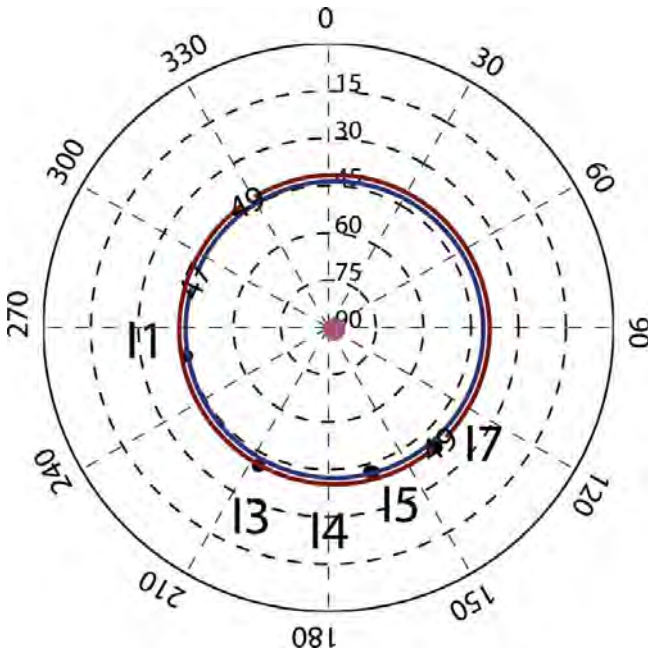

Figure 4. IRNSS satellites skyplot at UTC 18:30:30 of primary service area location ($\varphi = 40°$, $\lambda = 101°$) on DOY 153 of 2016, with 10° cut-off angle. The circles and the straight lines are the axes for the elevation and azimuth, respectively. The cone symmetry axis (poorest estimable direction) is identified by the *purple* dot and the circular contour lines show the loci of the directions that make angles of 47° and 49° with this symmetry axis.

the behaviour of the DOP values, four different categories of locations can be discriminated: **I, II, III**, and **IV**.

For the locations in category **I**, the DOP values are almost constant and similar to those of the primary service area, PDOP $\approx$ 4, and HDOP $\approx$ 2.5. Also, the DOP values of the locations within category **II** are reasonably constant, although somewhat more irregular than those of **I**. The first time that we really see a PDOP peak occurring is at the locations of category **III**, the explanation of which is the same as given for primary service area location ($\varphi = 40°$, $\lambda = 101°$). More frequent and more extreme DOP values, both for PDOP and HDOP, occur when we go to the border of the secondary service area at location, inside category **IV**. At these locations proper positioning is really becoming troublesome.

The large DOP values at the border locations can be mitigated by imposing a height constraint (cf. 5). In Figure 6, the height-constrained ($\sigma_h / \sigma = 1$), practically coinciding PDOP and HDOP time series are presented for border locations in category **IV**. It can be seen that upon constraining the height component, non-equator locations indeed obtain a reasonably smooth DOP behaviour for the whole 24-hour period. However, for the equator locations, there still exist two time intervals over which the height-constrained DOP reaches large values. This is due to the fact that at these two locations only four satellites, two GEOs and two IGSOs, are visible and therefore there are two periods when the two IGSOs occupy (almost) the same skyplot position, thus leading to a poor receiver-satellite geometry with corresponding large DOP values.

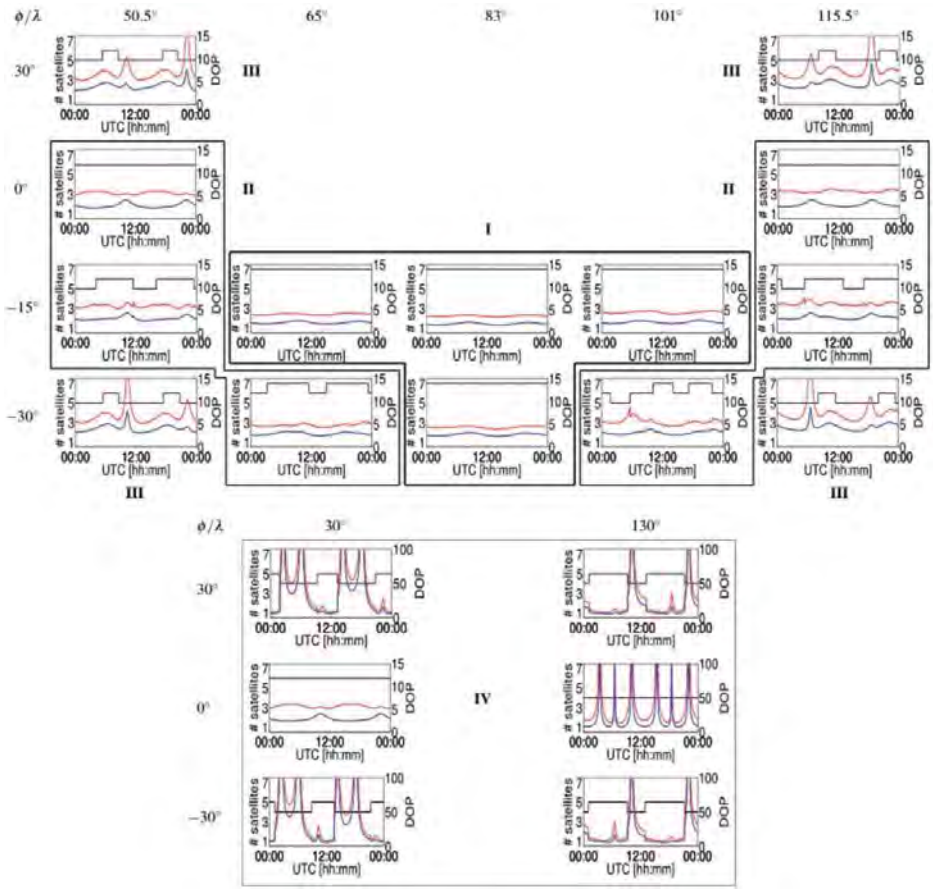

Figure 5. Secondary service area time series of the number of visible IRNSS satellites (*black*) on DOY 153 of 2016, with 10° cut-off angle, and the corresponding PDOP (*red*) and HDOP (*blue*) values.

Day-averaged HDOP map

With the above given insight into the daily PDOP and HDOP behaviour of the selected locations in the primary and secondary service areas, we now present a more fluid representation of the spatial HDOP variability. Figure 7 shows the 24-hour average IRNSS HDOP colour map over its service areas. As the IRNSS receiver-satellite geometry repeats itself approximately every day, this average HDOP map can be considered a useful day-average. When using this value as an approximation to the actual HDOP, one should keep in mind though that this approximation will be poorer for locations that show a greater HDOP time variability, such as when one gets closer to the borders of the secondary service area. The map can be used to compute the average horizontal positioning standard deviation for a particular location l as

$$\overline{\sigma}_l = \frac{\sigma}{\sqrt{2}} \overline{\mathrm{HDOP}}_l \tag{7}$$

in which $\overline{\mathrm{HDOP}}_l$ denotes the average HDOP value of that location.

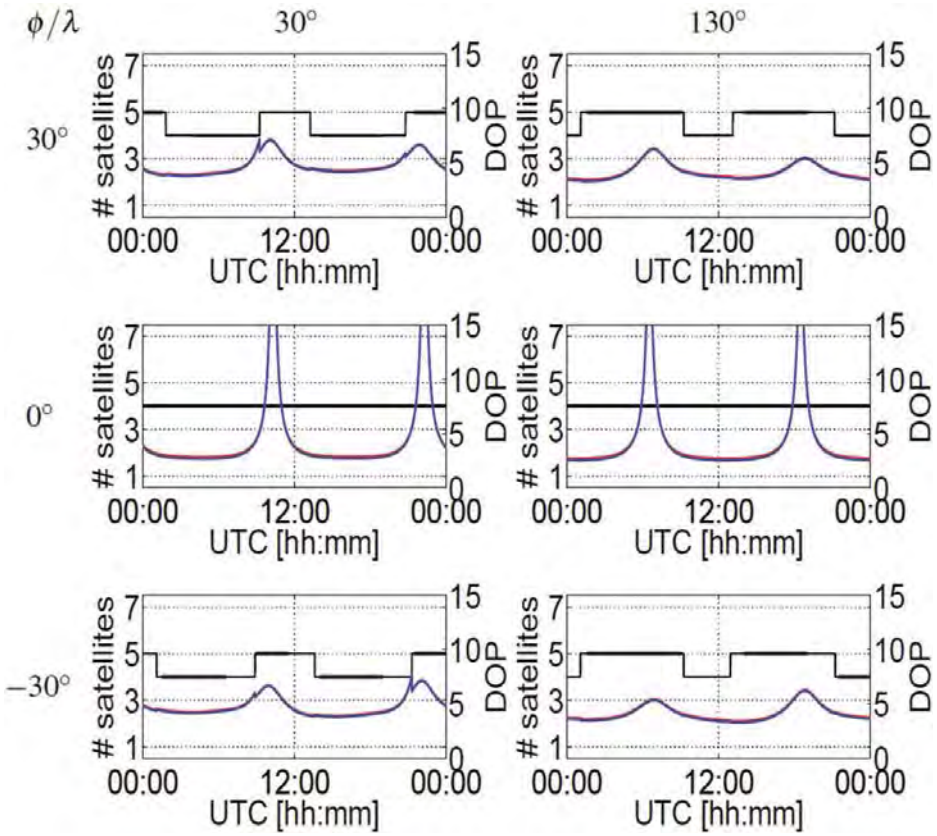

Figure 6. Time series of the number of visible IRNSS satellites and the corresponding height-constrained PDOP (*red*) and HDOP (*blue*) with $\sigma_h / \sigma = 1$ over the secondary service area, on DOY 153 of 2016 with 10° cut-off angle.

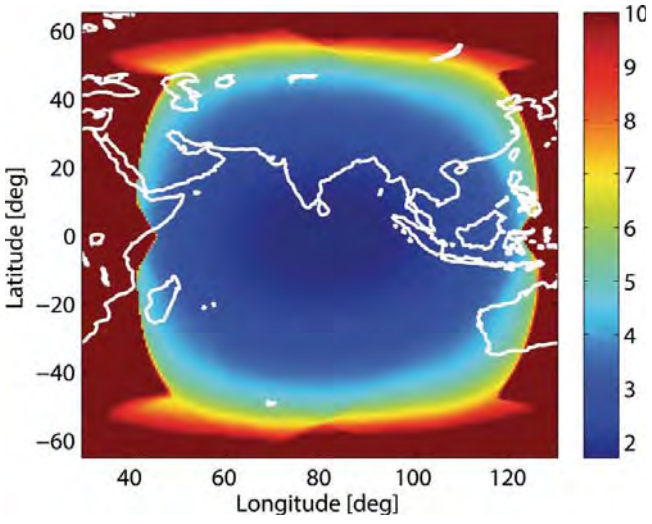

Figure 7. Day-averaged IRNSS HDOP colour map for DOY 153 of 2016 with 10° cut-off angle.

IRNSS SPP precision

In this section, an overview is provided for the expected IRNSS's SPP precision over the two service areas.

SPP scatterplots and confidence ellipses

To get a first impression of the SPP repeatability, we have processed 5 days of 30-second IRNSS data collected with the cut-off elevation angle of 10° at two different stations in Western Australia. The two stations are Perth ($\varphi = -32°, \lambda = 115.89°$) and Fitzroy ($\varphi = -18.13°, \lambda = 125.80°$), which are equipped with JAVAD TRE_G3TH_8 receiver and Septentrio PolaRx5 receiver, respectively. Perth is close to the location ($\varphi = -30°, \lambda = 115.5°$) of the secondary service area, while Fitzroy is east of the location ($\varphi = -15°, \lambda = 115.5°$) and close to the border of the secondary service area. The data are a priori corrected for the ionospheric delays using the predicted Global Ionosphere Map (CODE 2016) and for the dry tropospheric delays using the Saastamoinen model (Saastamoinen 1972). Their user range accuracies were determined as $\sigma = 1.80$m for Perth and $\sigma = 2.30$m for Fitzroy by means of variance component estimation (Teunissen and Amiri-Simkooei 2008). For the relatively crude pseudorange-only SPP model, these estimates will include all the remaining unmodelled effects, such as satellite orbital errors, satellite clock errors, and residual atmospheric delays. That of Fitzroy is somewhat larger due to the additional ionospheric uncertainty. The single-epoch SPP scatterplots of the two stations are shown in Figure 8a and c. Superimposed on the scatterplots are also shown the formal (*green*) and empirical (*red*) 95% confidence ellipses, which show a reasonably good agreement. But note that the two SPP scatterplots are not as homogeneous as one would expect if data would be coming from a normal distribution. The reason for this lack of homogeneity lies in the presence of mismodelled effects, particularly due to the satellite clocks and ionospheric delays. These effects would be absent if one would consider relative point positioning (RPP) between two nearby stations. This is demonstrated in Figure 8b, which shows the RPP scatterplot of Perth and a closeby station.

Note that the Fitzroy scatterplot is far more elongated than the one of Perth (Figure 8a and c). This is due to the relatively poor receiver-satellite geometry of Fitzroy, being so close to the border of the secondary service area. Considerable improvement is possible though if

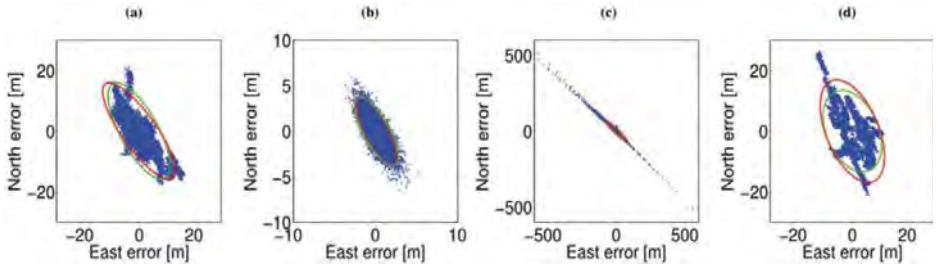

Figure 8. Single-epoch (30-second sampling rate) scatterplots for five DOYs of 2016 with 10° cut-off angle. Formal (*green*) and empirical (*red*) 95% confidence ellipses are also shown. (a) Perth SPP scatterplot (close to location ($\varphi = -30°, \lambda = 115.5°$) of secondary service area); (b) Perth RPP scatterplot; (c) Fitzroy SPP scatterplot (east of location ($\varphi = -15°, \lambda = 115.5°$) close to border of secondary service area); (d) Fitzroy height-constrained SPP scatterplot ($\sigma_h = 1$m).

one applies a height constraint. Figure 8d shows the Fitzroy scatterplot when a height constraint of $\sigma_h = 1\text{m}$ is applied.

Also note that all confidence ellipses of Figure 8 are oriented in a northwesterly direction. This can be explained by means of the receiver-satellite geometry and its impact on the confidence ellipse of $\hat{x}_r$,

$$(\hat{x}_r - x_r)^T Q^{-1}_{\hat{x}_r\hat{x}_r} (\hat{x}_r - x_r) = r^2 \tag{8}$$

in which the constant r^2 is chosen such that a certain confidence level is reached. As the direction of elongation is given by the direction of the eigenvector of $Q^{-1}_{\hat{x}_r\hat{x}_r}$ corresponding to its smallest eigenvalue, it follows with the aid of (4) that this direction is given by

$$\begin{aligned} f &= \underset{\tilde{f}}{\text{argmin}} \; \tilde{f}^T Q^{-1}_{\hat{x}_r\hat{x}_r} \tilde{f} \\ &= \underset{\tilde{f}}{\text{argmin}} \sum_{s=1}^{m} w_r^s \left[\tilde{f}^T (u_r^s - \overline{u}_r)\right]^2 \end{aligned} \tag{9}$$

Figure 9 depicts the day-averaged skyplot position of the IRNSS satellites as well as that of the weighted average $\overline{u}_r$ at Perth on day of year (DOY) 153 of 2016 with cut-off angle of 10°. As the differences $(u_r^s - \overline{u}_r)$ are mainly oriented along the north-

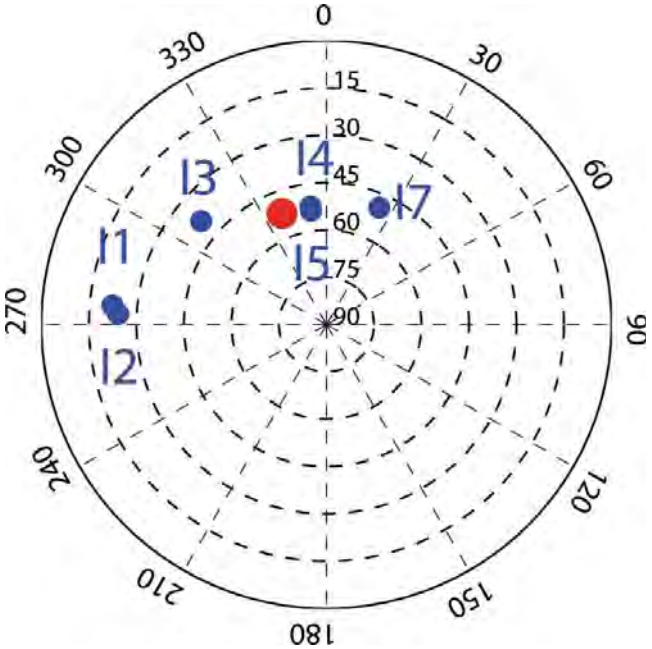

Figure 9. Day-averaged IRNSS skyplot at Perth for DOY 153 of 2016 with 10° cut-off angle. The circles and the straight lines are the axes for the elevation and azimuth, respectively. The *red* circle indicates the skyplot position of vector $\overline{u}_r$ (cf. (4), (9)).

east direction, the direction f that minimizes their contribution to (9) will mainly lie in a northwesterly direction.

Primary service area

We now provide an overview of the SPP precision for the primary service area. Table 2 gives for the primary service area locations (within the *grey* box and the secondary service area locations), the day-averaged values of their north and east standard deviations, σ_N and σ_E, and the corresponding correlation coefficients ρ_{NE}. For each location, there are two rows of values; the first row corresponds to the unconstrained scenario with $\sigma = 1$m, while the second row corresponds to the height-constrained scenario with $\sigma = 1$m and $\sigma_h/\sigma = 1$. Given the user range accuracy of $\sigma = 1$m, the rate of change of the horizontal precision with respect to the variation of the ratio σ_h/σ can be described considering two cases $\sigma_h/\sigma > 1$ and $\sigma_h/\sigma < 1$. The average rate of change of the horizontal precision with respect to $\sigma_h/\sigma > 1$ is zero for the locations within $(-30^\circ < \varphi < 40^\circ, 65^\circ < \lambda < 101^\circ)$ and 0.01, 0.25, 0.14, 0.43 and 0.22 for the locations within $(\lambda = 50.5^\circ, 115.5^\circ)$, $(\varphi < 40^\circ, \lambda = 30^\circ)$, $(\varphi < 40^\circ, \lambda = 130^\circ)$, $(\varphi = 40^\circ, \lambda = 30^\circ)$ and $(\varphi = 40^\circ, \lambda = 130^\circ)$, respectively. The average rate of change of the horizontal precision with respect to $\sigma_h/\sigma < 1$ is 0.07, 0.03, 0.02, 0.02, 0.02, 0.04, and 0.06 for the locations on $(\lambda = 30^\circ, 50.5^\circ, 65^\circ, 83^\circ, 110^\circ, 155.5^\circ$, and $130^\circ)$, respectively. For any other values of user range accuracy σ, one can scale these rates of change and the results in Table 2 accordingly. For example, for $\sigma = 3$m, these values should be multiplied by 3. The table values can be considered representative for the whole day as their HDOP time series showed a rather stable behaviour over the 24-hour period, see Figure 3.

It follows from Table 2 that location $(\varphi = 0^\circ, \lambda = 83^\circ)$, being the ground tracks symmetry point, has the best precision and that the precision gets poorer in north/south direction the further one departs from the equator and likewise poorer in east/west direction the further one departs from this location in such east/west direction. As the impact of height-constraining is larger the poorer the unconstrained precision, its effect increases the further one is located from $(\varphi = 0^\circ, \lambda = 83^\circ)$. But overall the effect of height-constraining on these primary service area locations is only marginal.

Secondary service area

We now provide an overview of the SPP precision for the secondary service area. Table 2, outside the *grey* box, gives an overview for the secondary service area locations. All the day-averaged entries of the table can be considered representative for the whole day as their corresponding HDOP time series are shown to be sufficiently stable, see Figure 5. Note that the formal results given for location $(\varphi = -30^\circ, \lambda = 115.5^\circ)$, which is close to Perth, is indeed consistent with the empirical results obtained for Perth (Figure 8a).

As was mentioned for the primary service area locations, the results of the secondary service area show the general tendency that the SPP precision gets poorer the further one moves away from the central location $(\varphi = 0^\circ, \lambda = 83^\circ)$. However, for the locations on the border of the secondary service area, with longitudes of $\lambda = 30^\circ, 130^\circ$, the worsening in the SPP precision is such that no representative day-average can be given. As their unconstrained HDOP values show very large excursions over the day (cf. Figure 5), no day-averaged values have been given for these locations in Table 2. For their height-constrained case, the situation is

Table 2. IRNSS L5 single-epoch SPP north-east formal standard deviations, σ_N and σ_E, and correlation coefficients, $\rho_{NE}$with the cut-off elevation angle of 10° over the IRNSS service area.

$\varphi\lambda$	30°	50.5°	65°	83°	101°	115.5°	130°
40°	—	4.58,2.49, −0.71	3.57,1.52,−0.52	3.41,1.21,0.00	3.95,1.67, 0.58	4.79,3.13, 0.74	—
	4.82,4.16, −0.73	3.28,1.90,−0.57	3.03,1.40,−0.42	3.02,1.19, 0.01	3.08,1.47, 0.44	3.30,2.08, 0.61	4.05,3.53, 0.68
30°	—	3.53,2.16, −0.58	2.66,1.29, −0.50	2.56,0.98, 0.01	2.86,1.42, 0.56	3.62,2.71, 0.56	—
	3.74,3.00, −0.55	2.56,1.59, −0.47	2.34,1.18, −0.38	2.26,0.98, 0.01	2.36,1.25, 0.40	2.59,1.73, 0.50	3.19,2.72, 0.52
20°	—	3.01,2.01, −0.41	2.11,1.18, −0.42	1.99,0.86, 0.01	2.18,1.32, 0.48	2.83,2.44, 0.47	—
	—	2.28,1.44, −0.38	1.94,1.04, −0.31	1.80,0.86, 0.01	1.94,1.09, 0.33	2.27,1.56, 0.41	—
0°	—	2.16,1.93, 0.00	1.65,1.12, 0.00	1.49,0.78, 0.00	1.63,1.26, 0.00	2.11,2.31, 0.00	—
	—	2.16,1.31, 0.00	1.65,0.93, 0.00	1.49,0.78, 0.00	1.63,0.97, 0.00	2.11,1.40, 0.00	—
−15°	—	2.50,1.97, 0.38	1.92,1.15, 0.35	1.78,0.82, −0.01	1.95,1.29, −0.40	2.47,2.37, −0.41	—
	—	2.21,1.39, 0.31	1.81,0.99, 0.25	1.66,0.82, 0.00	1.80,1.04, −0.26	2.19,1.49, −0.33	—
−30°	—	3.56,2.15, 0.58	2.66,1.29, 0.50	2.56,0.98, −0.01	2.86,1.42, −0.56	3.59,2.71, −0.56	—
	3.77,3.01, 0.55	2.56,1.59, 0.48	2.34,1.18, 0.39	2.26,0.98, −0.01	2.36,1.24, −0.41	2.58,1.73, −0.51	3.18,2.71, −0.53

There are two rows of values for each location; first row corresponds to the unconstrained scenario ($\sigma = 1$m) and second row to the height-constrained scenario ($\sigma = 1$m and $\sigma_h / \sigma = 1$). On each row, three values are given which are (from left to right) σ_N [m], σ_E [m], and ρ_{NE}. These values are the day-averaged values for DOY 153 of 2016. The *grey* box contains the results of the primary service area.

Table 3. IRNSS L5 single-epoch SPP north-east formal standard deviations, σ_N and σ_E, and correlation coefficients, ρ_{NE} with the cut-off elevation angle of 10° on the IRNSS secondary service area border.

φ	λ	24-hour period excluding two sub-periods (UTC [hh:mm])	σ_N [m], σ_E [m], ρ_{NE}
20°	30°	[09:00–11:41] & [20:56–23:17]	2.47,2.48, −0.32
20°	130°	[05:40–07:38] & [17:50–19:23]	2.41,2.30, 0.31
0°	30°	[09:12–11:25] & [21:11–23:23]	2.15,2.23, 0.01
0°	130°	[05:01–07:35] & [17:26–19:32]	2.05,2.12, 0.00
−15°	30°	[09:06–11:29] & [21:04–23:31]	2.31,2.36, 0.24
−15°	130°	[05:47–07:24] & [17:37–19:31]	2.29,2.21, −0.23

These values are the day-averaged values (excluding the mentioned periods) for DOY 153 of 2016 for height-constrained scenario ($\sigma = 1$m and $\sigma_h / \sigma = 1$).

different. Upon constraining the height component, the HDOP time series at locations with latitudes of $\varphi = -30°, 30°, 40°$ becomes almost flat and the corresponding day-averaged precision can be considered representative again (cf. Figure 6). This is however not the case for the equator and near-equator locations with latitudes of $\varphi = -15°, 0°, 20°$. Their height-constrained day-averaged values are therefore excluded from Table 2. To have a better description of their precision, we divided the 24-hour period into two sub-periods; one sub-period accommodating the large peaks for the HDOP and one containing the remaining part of the 24-hour period (cf. Figure 6). Note that these sub-periods are similar for locations with the same longitude. Table 3 lists the average height-constrained north, east standard deviations and correlation coefficients for these locations over the sub-periods with smooth HDOP behaviour.

The east-north correlation coefficients given in Tables 2 and 3 show that for those locations with the same longitude or the same latitude of central location ($\varphi = 0°, \lambda = 83°$) of primary service area, east and north components can be considered uncorrelated. Comparing the east and north standard deviations for these locations, it can be said that their corresponding horizontal confidence ellipses are vertically or horizontally elongated towards location ($\varphi = 0°, \lambda = 83°$) of primary service area. For the locations with different latitude and longitude from those of location ($\varphi = 0°, \lambda = 83°$) of primary service area, the east-north correlation is such that their corresponding confidence ellipses are elongated towards this point.

Finally we note that, although the IRNSS satellite ground tracks do not exactly have a 24-hour repeat cycle, the day-averaged values provided in the prior tables can still be considered representative for any arbitrary day. The unconstrained mean values given in Tables 2 and 3 can vary for any other arbitrary day by at most 2 cm in north and 4 cm in east for the user range accuracy of $\sigma = 1$m. Theses variations get smaller when the underlying model is strengthened by a weighted height constraint. Irrespective of the value of σ_h, the largest variation in the mean north and east standard deviations is 1 cm in case $\sigma = 1$m.

Summary and conclusion

As IRNSS has recently (May 2016) become operational, it is important to gain an understanding of its navigational potential and actual positioning capabilities for civilian users. This contribution has provided for that purpose a first full-constellation IRNSS SPP precision analysis over its two service areas. A DOP analysis of daily PDOP and HDOP time

series was given, including the identification, in location and time, of poor receiver-satellite geometries. The nature of these geometries was explained and it was demonstrated how the impact of some of these poor receiver-satellite geometries can be mitigated by means of height-constraining. We also provided an overview and analysis of the SPP precision for a grid of locations covering the two service areas. It includes, with the exception of six locations, easy-to-use representative day-averaged values of the positioning precision, unconstrained as well as height-constrained. For the six exempted locations, on and near the equator on the border of the secondary service area, sub-day averages were given.

Funding

The second author is the recipient of an Australian Research Council Federation Fellowship (project number FF0883188). A part of the IRNSS date was provided by Geoscience Australia. This support is gratefully acknowledged.

ORCID

Safoora Zaminpardaz http://orcid.org/0000-0003-0719-674X

References

Babu, R., P. Mula, S. C. Ratnakara, and A. S. Ganeshan. 2015. IRNSS satellite parameter estimation using combination strategy. *Global Journal of Science Frontier Research* 15(3):87–95.

Chandrasekhar, M. V., D. Rajarajan, G. Satyanarayana, N. Tirmal, S. C. Rathnakara, and A. S. Ganeshan. 2015. Modernized IRNSS broadcast ephemeris parameters. *Control Theory and Informatics* 5 (2):1–9.

CODE. 2016. *Global Ionosphere Maps Produced by CODE.* Available at ftp://ftp.unibe.ch/aiub/CODE/2015. Last accessed July 2016.

Euler, H. J., C. C. Goad 1991. On optimal filtering of GPS dual frequency observations without using orbit information. *Bulletin Geodesique* 65(2):130–143.

Ganeshan, A. S. 2012. Overview of GNSS and Indian Navigation ProgramPaper presented at GNSS User Meeting, ISRO Satellite Center, Bangalore, Februery 23.

Ganeshan, A. S., S. C. Ratnakara, N. Srinivasan, B. Rajaram, N. Tirmal, and K. Anbalagan. 2015. First Position Fix with IRNSS. *Inside GNSS*, July/August 2015. Available at http://www.insidegnss.com/node/4545. Accessed April 2016.

Godha, S., and M. Cannon. 2007. GPS/MEMS INS integrated system for navigation in urban areas. *GPS Solutions* 11(3):193–203.

Hofmann-Wellenhof, B., H. Lichtenegger, and J. Collins. 2013. *Global Positioning System: Theory and Practice*. New York: Springer Science & Business Media.

ISRO. 2014. Indian regional navigation satellite system: Signal in space ICD for standard positioning service, Version 1.0. *ISRO Satellite Centre*, June 2014.

ISRO. 2016. PSLV-C33/IRNSS-1G. Available at http://www.isro.gov.in/sites/default/files/pslv-c33-brochure.pdf. Accessed July 2016.

Kumari, A., K. Samal, D. Rajarajan, U. Swami, R. Babu, A. Kartik, S. C. Rathnakara, and A. S. Ganeshan. 2015. Precise modeling of solar radiation pressure for IRNSS satellite. *Journal of Natural Sciences Research* 5(3) 35–43.

Montenbruck, O., P. Steigenberger, and S. Riley. 2015. IRNSS orbit determination and broadcast ephemeris assessment. *Paper presented at International Technical Meeting of The Institute of Navigation*, Dana Point, CA, January 26–28, 185–193.

Mozo Garcia, A., R. Piriz, M. D. Lainez Samper, and M. M. Romay Merino. 2010. Multisystem Real Time Precise-Point-Positioning, today with GPS+GLONASS in the near future also with QZSS, Galileo, Compass, IRNSS. *Paper presented at International Symposium on GPS/GNSS*, Taipei, Taiwan, October 26–28.

Nadarajah, N., A. Khodabandeh, and P. J. G. Teunissen. 2015. Assessing the IRNSS L5-signal in combination with GPS, Galileo, and QZSS L5/E5a-signals for positioning and navigation. *GPS Solutions* 20:289–297.

Odijk, D., N. Nadarajah, S. Zaminpardaz, and P. J. G. Teunissen 2016. GPS, Galileo, BDS, QZSS and IRNSS differential ISBs: Estimation and application. *GPS Solutions*. Advance online publication. doi:10.1007/s10291-016-0536-y.

Pal, S., and A. S. Ganeshan.2015. Indian GNSS Paradigm. *PNT Symposium*, Standford, CA, 12–13 November 2015.

Rao, V. G. 2013. Proposed LOS fast TTFF signal design for IRNSS. PhD diss. Calgary, Canada: University of Calgary.

Rethika, T., S. Mishra, S. Nirmala, S. C. Rathnakara, and A. S. Ganeshan. 2013. Single frequency ionospheric error correction using coefficients generated from regional ionospheric data for IRNSS. *Indian Journal of Radio and Space Physics* 42(3):125–130.

Saastamoinen, J. 1972. Atmospheric correction for the troposphere and stratosphere in radio ranging satellites. In *The use of artificial satellites for geodesy*, Henriksen, S. W., A. Mancini, and B. H. Chovitz (eds.), 247–251. Washington, DC: American Geophysical Union.

Saikiran, B., and V. Vikram. 2013. IRNSS architecture and applications. *Journal of Communication and Electronics* 1(3):21–27.

Sarma, A. D., Q. Sultana, and V. S. Srinivas. 2010. Augmentation of indian regional navigation satellite system to improve dilution of precision. *Journal of Navigation* 63(2):313–321.

Sekar, S. B., S. Sengupta, and K. Bandyopadhyay. 2012. Spectral compatibility of BOC (5, 2) modulation with existing GNSS signals. *Paper presented at IEEE/ION Position Location and Navigation Symposium (PLANS)*, IEEE. 886–890.

Su, X. L., X. Q. Zhan, M. C. Niu, and Y. H. Zhang. 2012. Performance comparison for combined navigation satellite systems in asia-pacific region. *Journal of Aeronautics, Astronautics and Aviation. Series A* 44(4):249–257.

Teunissen, P. J. G. 1990. GPS op afstand bekeken. *In*: *een halve eeuw in de goede richting. Lustrumboek Snellius 1985–1990*, DUM Delft, 215–233.

Teunissen, P. J. G. 1998. A proof of Nielsen's conjecture on the relationship between dilution of precision for point positioning and for relative positioning with GPS. *IEEE Transactions on Aerospace and Electronic Systems* 34(2):693–695.

Teunissen, P. J. G., and A. R. Amiri-Simkooei. 2008. Least-squares variance component estimation. *Journal of Geodesy* 82(2):65–82

Thoelert, S., O. Montenbruck, and M. Meurer. 2014. IRNSS-1A: Signal and clock characterization of the Indian regional navigation system. *GPS Solutions* 18(1):147–152.

Thombre, S., M. Z. H. Bhuiyan, S. Söderholm, M. Kirkko-Jaakkola, L. Ruotsalainen, and H. Kuusniemi. 2016. A software multi-GNSS receiver implementation for the Indian Regional Navigation Satellite System. *IETE Journal of Research* 62(2):246–256.

Zaminpardaz, S., P. J. G. Teunissen, and N. Nadarajah. 2016. IRNSS stand-alone positioning: First results in Australia. *Journal of Spatial Science* 61(1):5–27.

Zhu, J., and R. Santerre. 2002. Improvement of GPS phase ambiguity resolution using prior height information as a quasi-observation. *Geomatica* 56(3):211–221.

4 GNSSs/RNSSs differential ISBs analysis

This chapter is covered by the following publication:

- Odijk D., Nadarajah N., Zaminpardaz S., Teunissen P.J.G. (2017) GPS, Galileo, QZSS and IRNSS differential ISBs: estimation and application. GPS Solutions, Springer, 21(2):439-450

GPS Solut (2017) 21:439–450
DOI 10.1007/s10291-016-0536-y

ORIGINAL ARTICLE

GPS, Galileo, QZSS and IRNSS differential ISBs: estimation and application

Dennis Odijk[1] · Nandakumaran Nadarajah[1] · Safoora Zaminpardaz[1] · Peter J. G. Teunissen[1,2]

Received: 25 February 2016 / Accepted: 31 March 2016 / Published online: 16 April 2016

Abstract Knowledge of inter-system biases (ISBs) is essential to combine observations of multiple global and regional navigation satellite systems (GNSS/RNSS) in an optimal way. Earlier studies based on GPS, Galileo, BDS and QZSS have demonstrated that the performance of multi-GNSS real-time kinematic positioning is improved when the differential ISBs (DISBs) corresponding to signals of different constellations but transmitted at identical frequencies can be calibrated, such that only one common pivot satellite is sufficient for inter-system ambiguity resolution at that particular frequency. Recently, many new GNSS satellites have been launched. At the beginning of 2016, there were 12 Galileo IOV/FOC satellites and 12 GPS Block IIF satellites in orbit, while the Indian Regional Navigation Satellite System (IRNSS) had five satellites launched of which four are operational. More launches are scheduled for the coming years. As a continuation of the earlier studies, we analyze the magnitude and stability of the DISBs corresponding to these new satellites. For IRNSS this article presents for the first time DISBs with respect to the L5/E5a signals of GPS, Galileo and QZSS for a mixed-receiver baseline. It is furthermore demonstrated that single-frequency (L5/E5a) ambiguity resolution is tremendously improved when the multi-GNSS observations are all differenced with respect to a common pivot satellite, compared to classical differencing for which a pivot satellite is selected for each constellation.

Keywords GPS · Galileo · QZSS · IRNSS · Multi-GNSS · Differential inter-system bias (DISB) · RTK

Introduction

With the multitude of global and regional navigation satellite systems (GNSS/RNSS) being modernized or developed, many more satellites and frequencies are becoming available that benefit high-precision relative applications, such as real-time kinematic (RTK) positioning. Having a subset of frequencies that are shared between the constellations allows differencing of observations between these constellations (also referred to as tightly or inter-system differencing), resulting in additional double-differenced (DD) observations compared to differencing the observations of each constellation independently (Julien et al. 2003). Hence, this results in a stronger positioning model and better performance of integer ambiguity resolution, which is the key to high-precision positioning.

However, when differencing observations between constellations one has to account for inter-system biases (ISBs), due to a difference in receiver hardware delays between the signals of different constellations, as well as a difference in system time between constellations (Hegarty et al. 2004). As this article is restricted to relative positioning, we do not have to bother about this system time offset since it gets eliminated. More details on the determination of absolute ISBs can be found in Torre and Caporali (2015) and Jiang et al. (2016). Concerning the relative or differential ISBs (DISBs), Odijk and Teunissen (2013a, b) demonstrated that for combinations of GPS,

✉ Dennis Odijk
d.odijk@curtin.edu.au

[1] GNSS Research Centre, Curtin University, GPO Box U1987, Perth, WA 6845, Australia

[2] Department of Geoscience and Remote Sensing, Delft University of Technology, PO Box 5048, 2600 GA Delft, The Netherlands

Galileo, BDS and QZSS observations these cancel for baselines with receiver pairs of the same manufacturer. These DISBs do in principle not cancel when the baseline is formed by receivers of different manufacturers, i.e., mixed receivers. Fortunately, Odijk and Teunissen (2013a, b), Melgard et al. (2013) and Paziewski and Wielgosz (2015) demonstrated that these mixed-receiver DISBs are very stable in time and can be calibrated. As a consequence, also mixed-receiver baselines can be processed in the same way as baselines consisting of identical receivers. Results of improved RTK ambiguity resolution with calibrated DISBs are given in Odijk and Teunissen (2013a), Odolinski et al. (2015) and Nadarajah et al. (2015).

This research is motivated by the recent launches of new GNSS satellites. By the end of 2015, 8 Galileo full-operational capability (FOC) satellites were in orbit next to the four in-orbit validation (IOV) satellites. In addition to these new Galileo satellites, during the recent years also GPS Block IIF satellites were launched, bringing the number of GPS satellites transmitting the L5 signal to 12 at the beginning of 2016. Moreover, five satellites of the Indian Regional Navigational Satellite System (IRNSS) have been put in orbit since 2013, of which four satellites are operational. So far these new satellites were not yet included in the DISB analyses, and for IRNSS it is even the first time that DISBs are estimated relative to the other constellations.

As the DISB analyses are restricted to CDMA signals between constellations that have identical frequencies, Table 1 gives an overview of those frequencies of GPS, GLONASS, Galileo, BDS, QZSS and IRNSS. This research is restricted to DISBs for the L5/E5a frequency that is shared between GPS, Galileo, QZSS and IRNSS; see the right column of Table 1.

The next section reviews the mixed-constellation GNSS model that underlies the estimation and application of the DISBs. In the subsequent section, the outcomes of the DISB estimation based on real GPS, Galileo, QZSS and IRNSS data are presented. That section also gives examples of the performance of integer ambiguity resolution and relative positioning for a short baseline for which a priori knowledge on the DISBs is incorporated.

Mixed-constellation GNSS model: estimation and application of DISBs

This section first reviews the estimation of DISB parameters and after that their application. We distinguish between estimation and application for short baselines, ignoring the differential ionospheric delays, and long baselines, for which these delays cannot be ignored.

Estimation of DISBs

Assume two GNSS constellations, denoted as A and B, of which signals are tracked on identical frequencies. For relative GNSS positioning applications, it is a common procedure to eliminate receiver and satellite specific biases by double differencing the code and phase observations with respect to a pivot satellite and a pivot receiver. In a multi-GNSS environment, this then relates to selecting a pivot satellite for each constellation: In case of two constellations A and B, these are denoted as 1_A and 1_B, as shown in Fig. 1 (left). This double differencing separately per constellation is referred to as the classical differencing approach.

Alternatively, instead of this classical differencing, one could difference the code and phase observations between constellations such that the model is based on inter-system differencing. Assuming the pivot for both constellations A and B to be satellite 1_A, the model of mixed-constellation DD observation equations can be given as follows, for a short baseline, assuming differential atmospheric delays to be absent (Odijk and Teunissen 2013a):

$$\begin{aligned} E\left(\phi_j^{1_A u}\right) &= \rho^{1_A u} + \lambda_j a_j^{1_A u} \\ E\left(\phi_j^{1_A v}\right) &= \rho^{1_A v} + \lambda_j a_j^{1_B v} + \lambda_j \bar{\delta}_j^{AB} \\ E\left(p_j^{1_A u}\right) &= \rho^{1_A u} \\ E\left(p_j^{1_A v}\right) &= \rho^{1_A v} + d_j^{AB} \end{aligned} \tag{1}$$

Here $E(.)$ denotes the mathematical expectation, $\phi_j^{1_A u}$ and $p_j^{1_A u}$ the vectors of DD phase and code observables at frequency j for constellation A, with satellite index

Table 1 Overview of GNSS frequencies (CDMA signals)

Frequency (MHz)	2492.028	1575.42	1561.098	1278.75	1268.52	1227.60	1207.14	1202.025	1191.795	1176.45
GPS (G)		L1				L2				L5
GLONASS (R)								L3		
Galileo (E)		E1		E6			E5b		E5	E5a
BDS (C)			B1		B3		B2			
QZSS (J)		L1		LEX		L2				L5
IRNSS (I)	S									L5

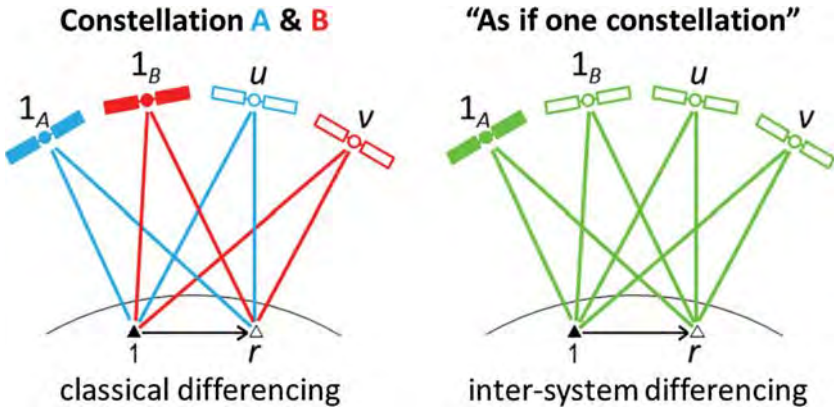

Fig. 1 Multi-constellation differencing: (*left*) a pivot satellite per constellation, i.e., satellite 1_A for constellation A and satellite 1_B for constellation B; (*right*) one pivot satellite 1_A for both constellations. Satellite u belongs to constellation A and satellite v to constellation B. The pivot receiver is denoted as 1 and the rover receiver as r

$u = 2_A, \ldots, m_A$. $\phi_j^{1_A v}$ and $p_j^{1_A v}$ are their counterparts for constellation B, with satellite index $v = 1_B, \ldots, m_B$. $\rho^{1_A u}$ and $\rho^{1_A v}$ denote the lumped combination of DD ranges and DD tropospheric delays for both constellations, λ_j the wavelength corresponding to frequency j, $a_j^{1_A u}$ and $a_j^{1_B v}$ the DD ambiguities for both constellations, and finally $\bar{\delta}_j^{AB}$ and d_j^{AB} the phase and code DISB parameters. Note that all above DD observables and parameters are receiver-dependent, but for notational convenience the receiver indices have been omitted. The estimable DD ambiguities, i.e., $a_j^{1_A u}$ and $a_j^{1_B v}$, have the property to be integer, and resolving these integers is the key to high-precision RTK positioning solutions.

The estimable DISB parameters in (1) are defined as:

$$\begin{aligned} &\bar{\delta}_j^{AB} = \bar{\delta}_j^B - \bar{\delta}_j^A; \quad \text{with} \quad \bar{\delta}_j^S = \delta_j^S + a_j^{1_S}, \quad j \geq 1 \\ &d_j^{AB} = d_j^B - d_j^A, \quad j \geq 1 \end{aligned} \tag{2}$$

Here δ_j^S and d_j^S, with $S \in \{A, B\}$, denote the frequency- and constellation-dependent receiver phase and code hardware biases. The phase DISB parameter is denoted using a bar, i.e., $\bar{\delta}_j^{AB}$, as it can only be estimated lumped to the DD ambiguity $a_j^{1_A 1_B}$. This is due to a rank deficiency in the model based on the observation Eq. (1). As a consequence, satellite 1_B does not have an estimable ambiguity parameter, as it is lumped to the phase DISB. The estimable DISBs can thus be interpreted as double differences, but then between receivers and constellations. Compared to the classical DD model, the inter-system model has two more observables for each frequency, corresponding to the pivot satellite of B, but it also has two more unknown parameters per frequency, i.e., the phase and code DISBs. Also note that the DD observables between the two constellations in the inter-system model become correlated, as they all share the same pivot satellite. Furthermore, note that the model based on (1) cannot be directly used to solve the receiver position, as the observation equations need to be linearized.

The observation model based on (1) is only valid for sufficiently short baselines, typically of a few kilometers at maximum. For longer baselines, the ionospheric delays need to be parametrized as well, resulting in the following inter-system DD observation equations (Teunissen et al. 2016):

$$\begin{aligned} E\left(\phi_j^{1_A u}\right) &= \rho^{1_A u} + \lambda_j a_j^{1_A u} - \mu_j I^{1_A u} \\ E\left(\phi_j^{1_A v}\right) &= \rho^{1_A v} + \lambda_j a_j^{1_B v} + \lambda_j \bar{\delta}_j^{AB} - \mu_j \bar{I}^{1_A v} \\ E\left(p_j^{1_A u}\right) &= \rho^{1_A u} + \mu_j I^{1_A u} \\ E\left(p_j^{1_A v}\right) &= \rho^{1_A v} + d_{IF}^{AB} + \bar{d}_j^{AB} + \mu_j \bar{I}^{1_A v} \end{aligned} \tag{3}$$

Because of the ionospheric parameters, this long-baseline model requires at least two shared frequencies, whereas the model based on (1) is already solvable using a single frequency. The estimable DD ionospheric parameters are denoted as $I^{1_A u}$ for constellation A. It is assumed that these ionospheric parameters apply to the first frequency (i.e., $j = 1$). For the other frequencies, these ionospheric parameters need to be multiplied by a frequency-dependent coefficient, denoted as $\mu_j = \lambda_j^2/\lambda_1^2$. The presence of the ionospheric parameters adds a rank deficiency to the model, which has as consequence that the interpretation and the estimability of the phase and code ISB parameters, as well as of the ionospheric parameters of constellation B, are changed:

$$\begin{aligned} &\bar{\bar{\delta}}_j^{AB} = \bar{\bar{\delta}}_j^B - \bar{\bar{\delta}}_j^A; \quad \text{with} \quad \bar{\bar{\delta}}_j^S = \delta_j^S + \frac{\mu_j}{\lambda_j} d_{GF}^S + a_j^{1_S}, \quad j \geq 1 \\ &d_{IF}^{AB} = d_{IF}^B - d_{IF}^A \\ &\bar{\bar{d}}_j^{AB} = \bar{\bar{d}}_j^B - \bar{\bar{d}}_j^A; \quad \text{with} \quad \bar{\bar{d}}_j^S = d_j^S - \left(\mu_j d_{GF}^S + d_{IF}^S\right), \quad j \geq 3 \\ &\bar{\bar{I}}^{1_A v} = I^{1_A v} + d_{GF}^B - d_{GF}^A \end{aligned} \tag{4}$$

To distinguish the estimable phase and code DISB parameters from their counterparts in the short-baseline model (1), in the long-baseline model (3) they are denoted using a double bar. Also the estimable ionospheric parameter for constellation B gets a double bar. Furthermore, in (4) the geometry-free and ionospheric-free differential receiver code biases for one constellation $S \in \{A, B\}$ are defined as:

$$\begin{aligned} d^S_{GF} &= -\frac{1}{\mu_2 - \mu_1}\left(d^S_1 - d^S_2\right) \quad \text{and} \\ d^S_{IF} &= \frac{\mu_2}{\mu_2 - \mu_1} d^S_1 - \frac{\mu_1}{\mu_2 - \mu_1} d^S_2 \end{aligned} \tag{5}$$

Note that the difference $d^S_1 - d^S_2$ is also known as the between-receiver differential code bias (DCB) between the first two frequencies (Zhang and Teunissen 2015).

The ionospheric-free code DISB, i.e., d^{AB}_{IF}, is one of the estimable parameters in the long-baseline model, as shown in (3), but this is not the case for the geometry-free code DISB, i.e., d^{AB}_{GF}. This geometry-free code DISB is inestimable, as it is constrained to overcome the rank deficiency in the long-baseline model (as S-basis; see Odijk et al. 2016). Consequently, its scaled version is lumped to the parameters that are involved in the rank deficiency, i.e., the phase and code DISBs and the ionospheric parameters of constellation B, as shown in (4). It follows from (5) that the estimable ionospheric-free code DISB is also a function of this geometry-free code DISB:

$$d^{AB}_{IF} = d^{AB}_j - \mu_j d^{AB}_{GF}, \quad j = 1, 2 \tag{6}$$

Because of this relation, there are different types of code DISB parameters in the long-baseline model (3). The first type is d^{AB}_{IF} and is always estimable with at least two frequencies. With more than two frequencies available, a second type of code DISB parameter becomes estimable, denoted as $\bar{\bar{d}}^{AB}_j, j \geq 3$. It is noted that the first type corresponds to the ionospheric-free code DISB parameter given in Montenbruck et al. (2011), with the difference that here we assume that both constellations track identical frequencies. In Montenbruck et al. (2011), this is not necessarily the case, as their DISB corresponds to the L1 and L2 frequencies of GPS and the E1 and E5a frequencies of Galileo. Finally, we note that, instead of the multi-GNSS long-baseline model (3), other ionospheric-float parametrizations exist as well, such as those given by Odolinski et al. (2014) and Yuan and Zhang (2014).

In the case one has multi-GNSS data of more than two constellations that share identical frequencies, the models (1) and (3) can be easily extended, parameterizing DISBs per combination of two constellations (e.g., GPS + Galileo; GPS + QZSS; GPS + IRNSS).

Application of DISBs

From the previous section, it follows that the DISB parameters have a different estimability and interpretation depending on whether the observation equations for a short baseline (1) or for a long baseline (3) are applied for their determination. This difference has influence on their applicability, and this can be shown as follows. First, consider the following relations between the estimable short-baseline DISB parameters, i.e., $\bar{\delta}^{AB}_{j\geq 1}$ and $d^{AB}_{j\geq 1}$ at the left side of the equal sign, and the long-baseline DISB parameters, i.e., $\bar{\bar{\delta}}^{AB}_{j\geq 1}$, d^{AB}_{IF} and $\bar{\bar{d}}^{AB}_{j\geq 3}$ at the right side of the equal sign:

$$\begin{aligned} \bar{\delta}^{AB}_{j\geq 1} &= \bar{\bar{\delta}}^{AB}_{j\geq 1} - \frac{\mu_j}{\lambda_j} d^{AB}_{GF} \\ d^{AB}_{j\geq 1} &= d^{AB}_{IF} + \bar{\bar{d}}^{AB}_{j\geq 3} + \mu_j d^{AB}_{GF} \end{aligned} \tag{7}$$

From the above, it follows that the short-baseline DISB for phase is equal to its long-baseline counterparts, minus the (scaled) geometry-free DISB, i.e., d^{AB}_{GF}. The short-baseline DISB for code is equal to ionospheric-free DISB from the long-baseline model, plus, in case of more than two frequencies, a code DISB, and the (scaled) geometry-free DISB as well. Thus, to convert the long-baseline DISBs to their short-baseline counterparts the geometry-free DISB is required for both phase and code. Unfortunately, this term cannot be determined from the long-baseline model, as it is fixed in order to remove the rank deficiency of the model. This also explains why the long-baseline model has one estimable DISB parameter less than the short-baseline model. It is therefore not possible to calibrate short baselines with DISBs that are determined from a long-baseline model.

The other way around, i.e., calibrating long baselines by using short-baseline DISBs, is a different story. In that case one does not need to know the geometry-free DISB term. The reason for this is that this geometry-free DISB parameter is multiplied by the ionospheric coefficient vector $-\mu_j$ for phase and μ_j for code, as shown in (7), which implies that it will be lumped to the estimable ionospheric parameters in the long-baseline model. Alternatively, it will be eliminated when the ionospheric-free combination is taken. Thus, the DISBs that are determined from short baselines can be applied to long-baseline models.

Let us now assume that DISBs that are estimated from the short-baseline model can be used to calibrate another baseline, such that we have the following DISB corrections available per frequency: $\bar{\delta}^{AB}_j$ and d^{AB}_j. Recall from the previous subsection that the phase DISB correction is biased by an ambiguity, which is integer but unknown. However, this is not a problem, as we may subtract an arbitrary integer from the correction and apply a fractional

correction for the phase DISB. Thus, let the fractional phase DISB correction be denoted as $\Delta\delta_j^{AB} = \bar{\delta}_j^{AB} - \bar{a}_j^{1_A 1_B}$, with $\bar{a}_j^{1_A 1_B}$ the arbitrary integer, which is usually the closest integer, the mixed-constellation DD observation equations can be given as follows, applying the short-baseline DISB corrections to the observations of B:

$$\begin{aligned} E\left(\phi_j^{1_A u}\right) &= \rho^{1_A u} + \lambda_j a_j^{1_A u}\left[-\mu_j I^{1_A u}\right] \\ E\left(\phi_j^{1_A v} - \lambda_j \Delta\delta_j^{AB}\right) &= \rho^{1_A v} + \lambda_j \bar{a}_j^{1_A v}\left[-\mu_j I^{1_A v}\right] \\ E\left(p_j^{1_A u}\right) &= \rho^{1_A u}\left[+\mu_j I^{1_A u}\right] \\ E\left(p_j^{1_A v} - d_j^{AB}\right) &= \rho^{1_A v}\left[+\mu_j I^{1_A v}\right] \end{aligned} \tag{8}$$

The above DISB-corrected model now applies to both short and long baselines, where in case of short baselines the DD ionospheric parameters are absent, while these are present for long baselines. To distinguish this, in (8) these parameters are denoted using square brackets. The absence or presence of these ionosphere parameters does, however, not affect the interpretation of the other parameters. The estimable ambiguities of constellation B have the following interpretation: $\bar{a}_j^{1_A v} = a_j^{1_B v} + \bar{a}_j^{1_A 1_B}$; i.e., they are a combination of the DD ambiguity having the pivot satellite of B and the arbitrarily chosen integer. If this chosen integer actually equals the true integer, the estimable ambiguities of B are the true DD ambiguities of this constellation with respect to A; i.e., $\bar{a}_j^{1_A v} = a_j^{1_A v}$. However, irrespective of the actual choice for $\bar{a}_j^{1_A 1_B}$, as long as it is an integer, $\bar{a}_j^{1_A v}$ is an integer parameter as well.

Note that the inter-system DD observation equations in (8) are all relative to pivot satellite 1_A of constellation A, and thus, the observations of both constellations at the identical frequencies can be processed as if one constellation, as shown in Fig. 1 (right). In fact, this means that one additional satellite is available compared to models (1) and (3). This strengthens the model and benefits ambiguity resolution and the position estimation. As a consequence of knowing the short-baseline DISBs, the differential ionospheric delays corresponding to constellation B are freed from the geometry-free code DISB. That is why the estimable DD ionospheric parameters corresponding to constellation B, denoted using a double bar in (3), have been replaced by DD ionospheric parameters without bar in the observation Eq. (8).

Estimation and application of DISBs between GPS, Galileo, QZSS and IRNSS

In this section, the estimation of code and phase DISBs is applied to the shared L5/E5a frequencies between GPS, Galileo, QZSS and IRNSS. Similar to earlier DISB studies, zero and very short baselines are measured, with the differential receiver position either absent or known, such that a strong model remains for the estimation of DISBs, which can be carried out in epoch-by-epoch mode.

IRNSS data are tracked by some of the multi-GNSS receivers stationed at the campus of Curtin University in Perth (Australia), such as listed in Table 2 and shown in Fig. 2. Of the IRNSS-enabled receivers CUT3, CUAA and CUCC are Javad TRE-G3TH receivers, whereas CUCS is a Septentrio PolaRx5, the latest generation of Septentrio multi-GNSS receivers at the time of this writing. Note that CUCC and CUCS are connected to the same antenna and thus form a zero baseline. Receivers CUT3 and CUAA are separated by about 8 m. Note from Table 2 that Javad uses combined data and pilot tracking for GPS, Galileo and QZSS, while Septentrio employs pilot-only signals. For IRNSS, however, both Javad and Septentrio track data-only signals.

Estimation of the DISBs

First, for the 8 m baseline CUT3-CUAA it is verified whether the DISBs are indeed zero, as is expected for a pair of identical receiver types. Next, DISBs for the mixed zero-baseline CUCS-CUCC are estimated.

Figure 3 depicts sky plots, i.e., azimuth versus elevation, at CUT3 for the four constellations during the day of November 21, 2015. In particular, the 8-shaped Highly inclined Elliptical Orbit (HEO) of the QZSS satellite is visible, as well as the three satellites of IRNSS that have Inclined Geosynchronous Satellite Orbits (IGSO). The fourth IRNSS satellite, i.e., I03 in Fig. 3, is a geostationary (GEO) satellite. The sky plots only show those satellites that are actually used for the DISB estimation. Thus, for GPS only the Block IIF satellites that transmit L5 are shown. As Galileo's fourth IOV satellite, i.e., E20, is not

Table 2 Used multi-GNSS receivers and the constellations they observe (G = GPS, E = Galileo, J = QZSS, I = IRNSS), together with their observables including tracking mode (corresponding to their RINEX 3.03 notation; IGS and RTCM-SC104 2015)

Receiver ID	Receiver type	G	E	J	I
CUT3	Javad TRE-G3TH	L5X	L5X	L5X	L5I*
CUAA	Javad TRE-G3TH	L5X	L5X	L5X	L5I*
CUCS	Septentrio PolaRx5	L5Q	L5Q	L5Q	L5A
CUCC	Javad TRE-G3TH	L5X	L5X	L5X	L5I*

Explanation of the tracking modes: L5X = data + pilot signal for GPS, Galileo and QZSS; L5Q = pilot signal for GPS, Galileo and QZSS; L5I/L5A = data signal for IRNSS

* L5I as tracked by the Javad receivers is not conform RINEX 3.03. According to Javad, this is equivalent to L5A, i.e., the data signal of IRNSS (Javad 2016)

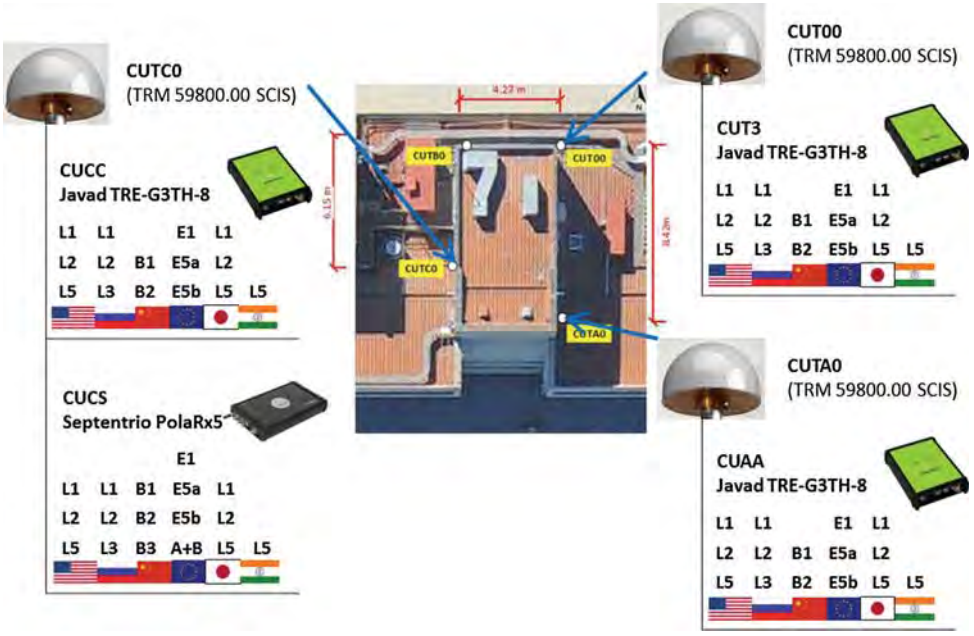

Fig. 2 Some of the multi-GNSS receivers stationed at the roof of building 402 at the campus of Curtin University in Perth

transmitting on the E5a frequency, but only on E1 due to a loss of power that occurred in 2014 (Cameron and Reynolds 2014), it is not shown here. Galileo FOC satellite E14, which is shown in the sky plot, is one of the two satellites that were originally injected in an anomalous orbit (Hellemans 2014). Because of this, there are no broadcast ephemerides available for this satellite, and therefore, we used the precise orbit product from CODE (Center for Orbit Determination in Europe) for the purpose of DISB estimation.

Figure 4 (top left) shows the number of GPS, Galileo, QZSS and IRNSS satellites tracked at CUT3 above 5° cutoff elevation. From the figure, it can be seen that the number of GPS satellites varies between 3 and 6, whereas the number of Galileo satellites varies between 0 during some part of the day and 3. The QZSS satellite is tracked the entire day, although there are no data tracked at one instance close to epoch 500, at which the QZSS satellite is close to the horizon. The number of tracked IRNSS satellites is 3–4. The other graphs in Fig. 4 show the estimated DISBs for GPS–IRNSS, Galileo–IRNSS and QZSS–IRNSS, all based on a data sampling interval of 30 s. Although the mean of these DISBs over the day is close to zero indeed, it can be seen that—especially for the combinations Galileo–IRNSS and QZSS–IRNSS—at certain times the estimated DISBs show quite a noisy behavior, for example around 3:00 hours UTC, as well as around 6:00 hours UTC for the code DISBs of QZSS–IRNSS. The cause for this is the low elevation of the satellites during these times. Between 3:00 and 6:00 hours UTC the elevation of the QZSS satellite is only between 5° and 10° (see Fig. 4; bottom right) causing high noise on the QZSS observations, possibly in combination with low-elevation multi-path biases. A similar behavior applies to Galileo satellite E26 around 3:00 hours UTC, which is tracked just above the cutoff elevation of 5°, in local southeast, as shown in Fig. 3.

The estimated DISBs for the mixed-receiver zero-baseline CUCS-CUCC during January 17, 2016, are shown in Fig. 5, again based on a sampling interval of 30 s. This more recent day was chosen since these receivers were only installed at the beginning of 2016. From the top left graph, it follows that toward the end of this day there were no Galileo satellites tracked above the 5° cutoff elevation, which explains the gap in the Galileo–IRNSS DISB time series. As this is a zero baseline for which differential atmospheric errors are completely absent and multi-path errors are very minor, the noise in these ISB time series is less than in those of the nonzero-baseline CUT3-CUAA. As summarized in Table 3, for this Septentrio–Javad combination the estimated-phase DISBs are 0.50 cycle for both GPS–IRNSS and QZSS–IRNSS, while it is estimated as zero for the Galileo–IRNSS combination. The code DISBs of the three constellations with respect to IRNSS are

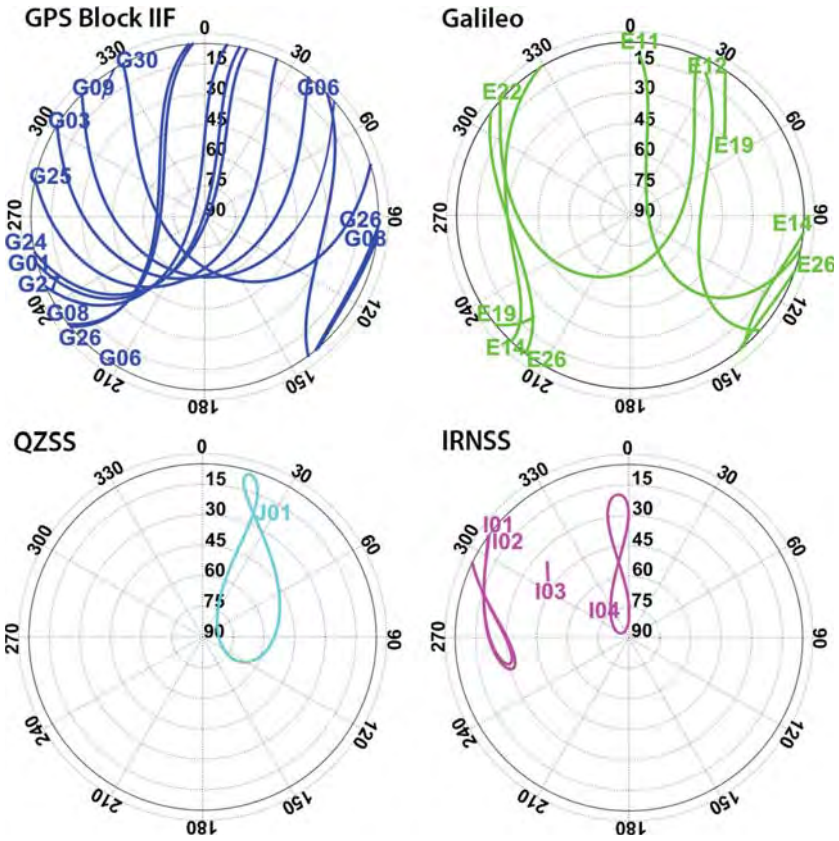

Fig. 3 Sky plots at CUT3 of used GPS Block IIF (*top left*), Galileo (*top right*), QZSS (*bottom left*) and IRNSS (*bottom right*) satellites, during November 21, 2015, above a cutoff elevation of 5°

all estimated within the level of 1.3–1.4 m. It is noted that the phase DISBs in Table 3 are rounded to two decimals (in cycle), as 0.01 cyc equals about 2 mm, which corresponds to the standard deviation of an undifferenced phase observation (in zenith). For the code DISBs one decimal is sufficient, as it corresponds to 1 dm and thus falls within the precision level of a few decimeters for an undifferenced code observation.

Application of the DISBs

As mentioned earlier, the whole purpose of DISB calibration is to improve the performance of multi-GNSS ambiguity resolution which is essential to high-precision mixed-constellation RTK positioning. This is tested for a short, i.e., 352 m, mixed baseline measured at the campus of Curtin University, measured during the full day of January 17, 2016, between stations CUCS (Septentrio PolaRx5) and SPA7 (Javad TRE-G3TH). Both receivers are tracking GPS, Galileo, QZSS and IRNSS data, and for the purpose of demonstration, we only used the L5/E5a observations of each constellation. Broadcast ephemerides were used for all constellations.

In order to evaluate the performance of multi-GNSS, single-frequency ambiguity resolution, we first computed a reference set of integer ambiguities during the full day by solving the short-baseline model with both receiver positions fixed, as precise coordinates for them are available. These reference ambiguities are then used to compare the outcomes of epoch-by-epoch ambiguity resolution, first based on a model in which each constellation defines its own pivot satellite, i.e., classical differencing, as shown in (1), and next based on a model in which all constellations are differenced relative to the pivot satellite of GPS, i.e., inter-system differencing, as shown in (8). The phase and code DISBs are calibrated to the values in Table 3. Table 4 presents the results of ambiguity resolution in terms of empirical success rates, starting with GPS only and then adding the other constellations one by one. The success rate is defined as the number of epochs with correctly

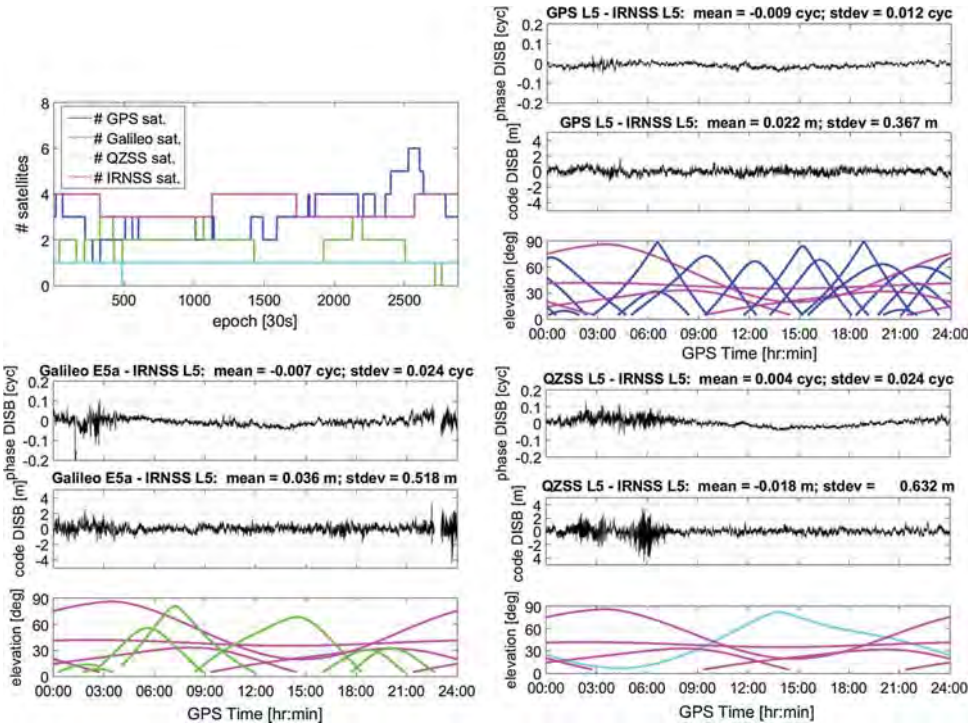

Fig. 4 Number of GPS Block IIF, Galileo, QZSS and IRNSS satellites tracked on November 21, 2015, above 5° cutoff elevation (*top left*) versus estimated GPS–IRNSS DISBs (*top right*), Galileo–IRNSS DISBs (*bottom left*) and QZSS–IRNSS DISBs (*bottom right*) for 8 m baseline CUT3–CUAA based on identical Javad TRE-G3TH receivers. For each GNSS combination, the phase DISB is shown in the *upper* graph, the code DISB in the *middle* graph and the elevations in the *bottom* graph

resolved integer ambiguities divided by the total number of epochs. Cutoff elevation is set to 5°, and the data sampling interval is 30 s.

For GPS only, for 2.5 % of the epochs during the day the correct ambiguities could be resolved. This poor performance is particularly due to having 4 or less GPS Block IIF satellites available for most of the time during the day (see also Fig. 5; top left). With Galileo added the empirical ambiguity success rate increases slightly to 2.7 % when based on classical differencing. This marginal improvement is due to the 1–2 Galileo satellites that are at most in view during most parts of the day. A higher success rate of 12.8 % is achieved, however, when the Galileo data are differenced with respect to the GPS pivot satellite. Adding QZSS data to GPS + Galileo with classical differencing results in a success rate that is identical to GPS + Galileo, i.e., 2.7 %. The reason is that in this case the QZSS data do not contribute, as there is only one satellite and thus no differences can be formed. The QZSS data clearly contribute when they are differenced relative to the GPS pivot satellite, tremendously increasing the success rate to 38.2 %. The best results are obtained when the 3–4 IRNSS satellites are added to GPS + Galileo + QZSS. With classical differencing the success rate increases to 28.9 %, but when the observations are inter-system differenced, the success rate is a large 95.7 %, which means for almost all epochs during the day the ambiguities are correctly resolved.

Figure 6 shows the horizontal position scatter and the vertical position time series of SPA7 based on inter-system differencing for the four cases investigated, i.e., GPS, GPS + Galileo, GPS + Galileo + QZSS and GPS + Galileo + QZSS + IRNSS. The graphs depict both float and fixed position solutions, with the fixed positions also showing the solutions based on the wrong integer ambiguities, next to the correct solutions. From the graphs it can be seen that the availability of the positioning solutions clearly increases when going from one to multiple constellations. The improvement in precision of the float solution is also visible: In case of GPS only, the root mean

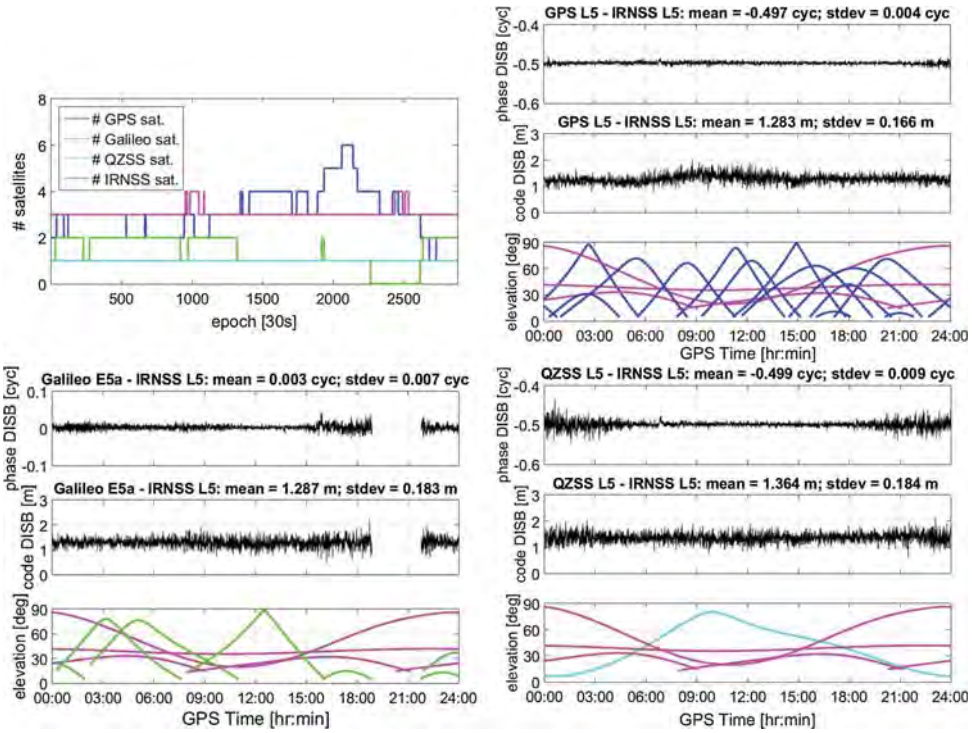

Fig. 5 Number of GPS Block IIF, Galileo, QZSS and IRNSS satellites tracked above 5° cutoff elevation (*top left*) versus estimated GPS–IRNSS DISBs (*top right*), Galileo–IRNSS DISBs (*bottom left*) and QZSS–IRNSS DISBs (*bottom right*) for zero-baseline CUCS–CUCC based on Septentrio PolaRx5 and Javad TRE-G3TH receivers. For each GNSS combination, the phase DISB is shown in the *upper* graph, the code DISB in the *middle* graph and the elevations in the *bottom* graph

Table 3 Estimated L5/E5a DISBs for phase (in cycles) and code (in meters) between GPS, Galileo, QZSS and IRNSS, based on the Septentrio–Javad receiver combination

	GPS	Galileo	QZSS
Galileo	0.50 cyc		
	0.0 m		
QZSS	0.00 cyc	0.50 cyc	
	0.0 m	0.0 m	
IRNSS	0.50 cyc	0.00 cyc	0.50 cyc
	−1.3 m	−1.3 m	−1.4 m

An empty cell means a zero DISB for combinations of same constellations, or opposite of sign for combinations of mixed constellations

square (RMS) of the horizontal components is at the level of 1 m, whereas for GPS + Galileo + QZSS + IRNSS it is improved to a level of 30–40 cm. After correct ambiguity fixing, in all cases the horizontal RMS is about 5 mm (in East and North component) and the vertical RMS is at the level of 1 cm.

Conclusions

We extended the determination of differential ISBs (DISBs) between multi-GNSS phase and code observations to new GNSS satellites, following the recent launches of GPS Block IIF satellites, Galileo FOC satellites and regional IRNSS satellites. For IRNSS we presented for the first time estimated DISBs at its L5 frequency and relative to GPS L5, Galileo E5a and QZSS L5. For a baseline with identical receiver pairs, it could be confirmed that the DISBs of IRNSS with respect to the other constellations are indeed absent. The DISBs based on a mixed-receiver combination are estimated as nonzero but seem to be stable, which is in line with the DISBs for mixed receivers based on combinations of GPS, BDS, Galileo and QZSS. In addition to the estimation, we focused on the applicability of DISBs. It was first theoretically demonstrated that DISBs which are determined from zero or short baselines can also be applied to calibrate long baselines for which the differential ionospheric delays cannot be ignored. The other way around, the calibration of short baselines using

Table 4 Empirical integer ambiguity success rates for short-baseline CUCS-SPA7 based on L5/E5a data only

	Classical differencing (%)	Inter-system differencing (%)
GPS only	72/2880 = 2.5	–
GPS + Galileo	77/2880 = 2.7	368/2880 = 12.8
GPS + Galileo + QZSS	77/2880 = 2.7	1100/2880 = 38.2
GPS + Galileo + QZSS + IRNSS	831/2880 = 28.9	2755/2880 = 95.7

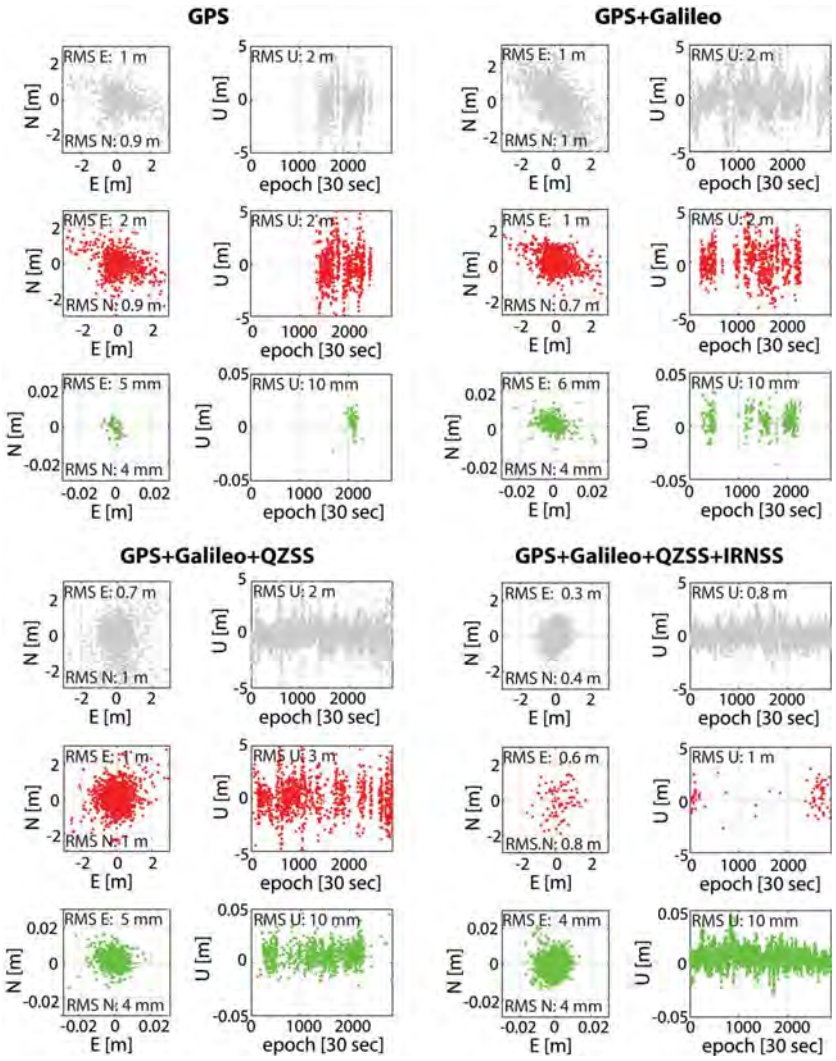

Fig. 6 *Horizontal* (E = East vs. N = North) position *scatter* and *vertical* (U = Up) time series for station SPA7, based on GPS only (*top left*), GPS + Galileo (*top right*), GPS + Galileo + QZSS (*bottom left*) and GPS + Galileo + QZSS + IRNSS (*bottom right*), with the multi-GNSS position solutions based on *inter-system differencing*. The float solutions are depicted in *gray*, whereas the fixed solutions are in either *red* (wrong integer solutions) or *green* (correct integer solutions)

DISBs determined from long baselines, is however not possible, which is due to a lack of information, as the geometry-free combination of the code DISBs on the first two frequencies is needed for that. Application of nonzero DISBs estimated from a zero baseline to a 1-km baseline consisting of mixed receivers demonstrated that the success

rate of single-frequency (L5/E5a) GPS + Galileo + QZSS + IRNSS ambiguity resolution based on inter-system differencing, i.e., relative to the pivot satellite of GPS, is tremendously, i.e., 67 %, higher than the ambiguity success rate corresponding to classically differenced observations, where a pivot satellite is selected for each of the four constellations. Also the availability of positioning improves with inter-system differencing, which is benefitting RTK in environments where GNSS signals are obstructed.

Acknowledgments Part of this work has been carried out in the context of the Positioning Program Project 1.19 "Multi-GNSS PPP-RTK Network Processing" of the Cooperative Research Centre for Spatial Information (CRC-SI) in Australia. P.J.G. Teunissen is the recipient of an Australian Research Council (ARC) Federation Fellowship (Project No. FF0883188). This support is gratefully acknowledged.

References

Cameron A, Reynolds T (2014) Power loss created trouble aboard Galileo satellite. http://www.gpsworld.com/trouble-aboard-galileo-satellite/

Hegarty C, Powers E, Fonville B (2004) Accounting for timing biases between GPS, modernized GPS, and Galileo signals. In: Proceedings of 36th annual Precise Time and Time Interval (PTTI) meeting, Washington, DC, 7–9 Dec, pp. 307–317

Hellemans A (2014) A simple plumbing problem sent Galileo satellites into wrong orbits. http://spectrum.ieee.org/tech-talk/aerospace/satellites/a-simple-plumbing-problem-sent-galileo-satellites-into-wrong-orbits

IGS and RTCM-SC104 (2015) RINEX—The receiver independent exchange format, Version 3.03, 14 July. International GNSS Service (IGS), RINEX Working Group and Radio Technical Commission for Maritime Services Special Committee

Javad (2016) Personal communication with the helpdesk of Javad GNSS Inc. Feb 2016

Jiang N, Xu Y, Xu T, Xu G, Sun Z, Schuh H (2016) GPS/BDS short-term ISB modelling and prediction. GPS Solut. doi:10.1007/s10291-015-0513-x

Julien O, Alves P, Cannon ME, Zhang W (2003) A tightly coupled GPS/GALILEO combination for improved ambiguity resolution. In: Proceedings of ENC-GNSS 2003, Graz, Austria, 22–25 April

Melgard T, Tegedor J, Jong K de, Lapucha D, Lachapelle G (2013) Interchangeable integration of GPS and Galileo by using a common system clock in PPP. In: Proceedings of ION GNSS + 2013, Nashville, TN, 16–20 Sept, pp. 1198–1206

Montenbruck O, Hauschild A, Hessels U (2011) Characterization of GPS/GIOVE sensor stations in the CONGO network. GPS Solut 15(3):193–205

Nadarajah N, Khodabandeh A, Teunissen PJG (2015) Assessing the IRNSS L5-signal in combination with GPS, Galileo, and QZSS L5/E5a-signals for positioning and navigation. GPS Solut 20(2):289–297

Odijk D, Teunissen PJG (2013a) Characterization of between-receiver GPS-Galileo inter-system biases and their effect on mixed ambiguity resolution. GPS Solut 17(4):521–533

Odijk D, Teunissen PJG (2013b) Estimation of differential inter-system biases between the overlapping frequencies of GPS, Galileo, BeiDou and QZSS. In: Proceedings of 4th international colloquium scientific and fundamental aspects of the Galileo programme, Prague, Czech Republic, 4–6 Dec, p 8

Odijk D, Zhang B, Khodabandeh A, Odolinski R, Teunissen PJG (2016) On the estimability of parameters in undifferenced, uncombined GNSS network and PPP-RTK user models by means of S-system theory. J Geodesy 90(1):15–44

Odolinski R, Teunissen PJG, Odijk D (2014) Combined GPS + BDS + Galileo + QZSS for long baseline RTK positioning. In: Proceedings of ION GNSS + 2014, Tampa, FL, 8–12 Sept, pp 2326–2340

Odolinski R, Teunissen PJG, Odijk D (2015) Combined BDS, Galileo, QZSS and GPS single-frequency RTK. GPS Solut 19(1):151–163

Paziewski J, Wielgosz P (2015) Accounting for Galileo-GPS inter-system biases in precise satellite positioning. J Geodesy 89(1):81–93

Teunissen PJG, Khodabandeh A, Zhang B (2016) Multi-GNSS PPP-RTK: mixed-receiver network and user scenarios. In: International association of geodesy (IAG) symposia series, 26th IUGG General Assembly 2015, Prague, Czech Republic, 22 June–2 July **(under review)**

Torre AD, Caporali A (2015) An analysis of intersystem biases for multi-GNSS positioning. GPS Solut 19(2):297–307

Yuan Y, Zhang B (2014) Retrieval of inter-system biases (ISBs) using a network of multi-GNSS receivers. J Glob Position Syst 13(1):22–29

Zhang B, Teunissen PJG (2015) Characterization of multi-GNSS between-receiver differential code biases using zero and short baselines. Sci Bull 60(21):1840–1849

Dennis Odijk received his MSc and PhD in Geodesy from Delft University of Technology, the Netherlands. Currently, he works as a research fellow at GNSS Research Centre, Curtin University. His research is focused on high-precision GNSS positioning, multi-GNSS inter-operability, data quality control and prototype software development.

Nandakumaran Nadarajah received his MSc and PhD in Electrical and Computer Engineering from McMaster University, Canada. Currently, he is working as a research fellow at GNSS Research Centre, Curtin University. His research interests are in multi-GNSS attitude determination and relative navigation, signal processing and target tracking.

Safoora Zaminpardaz received her MSc in Geodesy from University of Tehran. She has been pursuing her PhD since July 2014 at the GNSS Research Centre, Curtin University, Australia. Her research interests include array-based multi-GNSS positioning, ionosphere sensing and integrity monitoring.

Peter J. G. Teunissen is Professor of Geodesy and Navigation, Head of Curtin University's GNSS Research Centre and Science Director of the Cooperative Research Centre for Spatial Information. His current research focuses on multi-GNSS and the modelling of next-generation GNSS for high-precision positioning, navigation and timing applications.

5 IRNSS+GPS L5 RTK performance (Part 1: An analysis of survey-grade receivers)

This chapter is covered by the following publication:

Zaminpardaz S., Teunissen P.J.G., Nadarajah N. (2017b) IRNSS/NavIC and GPS: A Single and Dual System L5 Analysis. Journal of Geodesy, Springer, 91(8):915-931

J Geod (2017) 91:915–931
DOI 10.1007/s00190-016-0996-4

ORIGINAL ARTICLE

IRNSS/NavIC and GPS: a single- and dual-system L5 analysis

S. Zaminpardaz[1] · P. J. G. Teunissen[1,2] · N. Nadarajah[1]

Received: 17 August 2016 / Accepted: 28 December 2016 / Published online: 11 February 2017

Abstract The Indian Regional Navigation Satellite System (IRNSS) has recently (May 2016) become fully operational. In this contribution, for the fully operational IRNSS as a stand-alone system and also in combination with GPS, we provide a first assessment of L5 integer ambiguity resolution and positioning performance. While our empirical analyses are based on the data collected by two JAVAD receivers at Curtin University, Perth, Australia, our formal analyses are carried out for various onshore locations within the IRNSS service area. We study the noise characteristics (carrier-to-noise density, measurement precision, time correlation), the integer ambiguity resolution performance (success rates and ambiguity dilution of precision), and the positioning performance (ambiguity float and ambiguity fixed). The results show that our empirical outcomes are consistent with their formal counterparts and that the GPS L5-data have a lower noise level than that of IRNSS L5-data, particularly in case of the code data. The underlying model in our assessments varies from stand-alone IRNSS (L5) to IRNSS + GPS (L5), from unconstrained to height-constrained and from kinematic to static. Significant improvements in ambiguity resolution and positioning performance are achievable upon integrating L5-data of IRNSS with GPS.

Keywords Indian Regional Navigation Satellite System (IRNSS) · Navigation with Indian Constellation (NavIC) · GPS block IIF · Integer ambiguity resolution · ADOP

✉ S. Zaminpardaz
safoora.zaminpardaz@curtin.edu.au

[1] Department of Spatial Sciences, GNSS Research Centre, Curtin University, Perth, Australia

[2] Department of Geoscience and Remote Sensing, Delft University of Technology, Delft, The Netherlands

1 Introduction

The Indian Regional Navigation Satellite System (IRNSS) has recently (May 2016) become fully operational and provided with the operational name of NavIC (Navigation with Indian Constellation). It has been developed by the Indian Space Research Organization (ISRO) with the objective of offering positioning, navigation, and timing (PNT) to the users in its service area. The IRNSS satellites transmit navigation signals, based on code division multiple access (CDMA), on L5 (1176.45 MHz) with a binary phase-shift key (BPSK (1)) modulation for standard positioning service (SPS) users, and with a binary offset carrier (BOC (5,2)) modulation for restricted service (RS) users (ISRO 2014a). The fully operational IRNSS constellation has recently been realized, consisting of three geostationary orbit (GEO) satellites and four inclined geosynchronous orbit (IGSO) satellites. The orbital period of the IRNSS satellites is one sidereal day (23 h and 56 min), such that the IRNSS satellite ground tracks repeat every solar day (24 h) 4 min earlier. Table 1 gives information on the full IRNSS constellation.

Among the published studies on the IRNSS, while some are simulation-based (Mozo Garcia et al. 2010; Sarma et al. 2010; Sekar et al. 2012; Rethika et al. 2013; Rao 2013), the others are based on using real data. Thoelert et al. (2014) assesses the clock stability of IRNSS-1A, while the accuracy of a precise model for solar radiation pressure is tested using the IRNSS-1A and 1B observations in Kumari et al. (2015). Babu et al. (2015) compares orbit determination methods for IRNSS-1A, 1B and 1C, and in order to validate the orbit accuracy with modernized ephemeris parameters, Chandrasekhar et al. (2015) employs the IRNSS-1A, 1B and 1C real data. Montenbruck and Steigenberger (2015) uses the observations of the IRNSS-1A and 1B to investigate the quality of the IRNSS navigation messages. Nadarajah et al. (2015),

Table 1 Information on the IRNSS/NavIC satellites (ISRO 2014b, c, d, 2015, 2016a, b, c)

Satellite	Type	Longitude	Inclination	Launch date
IRNSS-1A (I1)	IGSO	55°E	29.0°	July 2013
IRNSS-1B (I2)	IGSO	55°E	31.0°	April 2014
IRNSS-1C (I3)	GEO	83°E	–	October 2014
IRNSS-1D (I4)	IGSO	111.75°E	30.5°	March 2015
IRNSS-1E (I5)	IGSO	111.75°E	28.1°	January 2016
IRNSS-1F (I6)	GEO	32.5°E	–	March 2016
IRNSS-1G (I7)	GEO	129.5°E	–	April 2016

after assessing the IRNSS noise characteristics, combines the L5/E5 signals of IRNSS, GPS, Galileo and QZSS for instantaneous attitude determination. The positioning results over India based on the data of I1, I2, I3, and I4 are presented in Ganeshan et al. (2015). The first IRNSS stand-alone positioning results over Australia are presented in Zaminpardaz et al. (2016b), and Odijk et al. (2016) presents the first analysis of the differential inter-system biases (DISBs) between L5 signal of IRNSS and the L5/E5a signals of GPS, Galileo and QZSS.

Transmitting L5 frequency shared by three other GNSSs (Global Navigation Satellite Systems), i.e., GPS, Galileo, and QZSS, makes the IRNSS interoperable with those systems. All the satellites belonging to the latest generation of GPS, called Block IIF, have been sending out the L5 signal since 2010 as part of the GPS modernization (GPS Directorate 2011). With the launch of the last satellite of Block IIF on February 2016, it now has all its 12 satellites operational. There exists a few number of studies in the literature making use of the GPS L5 real data. An analysis of the GPS L5 stochastic properties through different GNSS observables combinations is provided by de Bakker et al. (2012). The GPS L5-based precise point positioning (PPP) results are presented in Tegedor and Øvstedal (2014). In Odijk and Teunissen (2013); Odijk et al. (2016), the DISBs between GPS L5 and the same signal of other systems are characterized, and Nadarajah et al. (2015) combines the L5/E5 signals of GPS, IRNSS, Galileo and QZSS for instantaneous attitude determination.

In this contribution, we provide the very first L5 ambiguity resolution results of the fully operational IRNSS as a stand-alone system and also in combination with the fully operational GPS Block IIF together with the corresponding positioning results. This contribution is organized as follows. In Sect. 2, the unconstrained and weighted height-constrained single-frequency GNSS model of the combined IRNSS + GPS and stand-alone IRNSS is formulated. The noise characteristics of the IRNSS and GPS L5-signal are presented in Sect. 3 through the carrier-to-noise density, the estimated measurement precision and time correlation. A formal analysis of the position dilution of precision (PDOP) corresponding with the stand-alone IRNSS and IRNSS + GPS is also provided. This analysis includes the identification and explanation of occurring periods of poor receiver-satellite geometries. Section 4 contains the formal and empirical ambiguity resolution performance analyses on an epoch-by-epoch and multi-epoch basis. This is done for the unconstrained and height-constrained model, and for single-system IRNSS and dual-system IRNSS + GPS. The corresponding positioning performance is investigated in Sect. 5, both for ambiguity-float and ambiguity-fixed scenarios. Finally, a summary and conclusions are given in Sect. 6.

2 GNSS model of observations

In this section, we formulate the single-baseline single-frequency GNSS model for the combined IRNSS and GPS, from which the stand-alone IRNSS model follows as a special case. In the sequel, we refer to the IRNSS-specific parameters and the GPS-specific parameters using the subscripts $_I$ and $_G$, respectively.

2.1 Unconstrained model

Suppose that two receivers are simultaneously tracking m_I IRNSS plus m_G GPS satellites on frequency L5 with the wavelength λ. We assume that the two receivers form a short baseline such that the atmospheric delays and orbital errors are common to both of them, thereby becoming eliminated through between-receiver differencing. We further assume that both receivers are of the same manufacturer (receiver make, type and firmware), thus allowing us to assume that the IRNSS-GPS ISBs are zero (Odijk et al. 2012, 2016). Therefore, instead of classical double-differencing per constellation, inter-system double-differencing can be used, resulting in a higher level of redundancy. For such a setup, the corresponding full-rank single-epoch model of linearized double-differenced (DD) observation equations reads

$$
\begin{aligned}
E\begin{bmatrix} D_m^{\mathrm{T}} p \\ D_m^{\mathrm{T}} \phi \end{bmatrix} &= \begin{bmatrix} D_m^{\mathrm{T}} G & 0 \\ D_m^{\mathrm{T}} G & \lambda I_{m-1} \end{bmatrix} \begin{bmatrix} b \\ a \end{bmatrix} \\
D\begin{bmatrix} D_m^{\mathrm{T}} p \\ D_m^{\mathrm{T}} \phi \end{bmatrix} &= \begin{bmatrix} D_m^{\mathrm{T}} Q_{pp} D_m & 0 \\ 0 & D_m^{\mathrm{T}} Q_{\phi\phi} D_m \end{bmatrix}
\end{aligned} \tag{1}
$$

where $E[.]$ and $D[.]$ denote the expectation and dispersion operator, respectively. With $m = m_I + m_G$, the $(m-1) \times m$ matrix $D_m^{\mathrm{T}} = [-e_{m-1},\ I_{m-1}]$ represents the inter-system differencing operator, where e_{m-1} and I_{m-1} are the $(m-1)$-vector of ones and the identity matrix of $(m-1)$ dimension, respectively. The combined vectors and matrices can be split into system-specific parts as

$$p = \left[p_I^{\mathrm{T}}, p_G^{\mathrm{T}}\right]^{\mathrm{T}}, \phi = \left[\phi_I^{\mathrm{T}}, \phi_G^{\mathrm{T}}\right]^{\mathrm{T}}, G = \left[G_I^{\mathrm{T}}, G_G^{\mathrm{T}}\right]^{\mathrm{T}}$$
$$Q_{pp} = 2 \times \mathrm{blkdiag}\left(\sigma_{p_I}^2 W_I^{-1}, \quad \sigma_{p_G}^2 W_G^{-1}\right)$$
$$Q_{\phi\phi} = 2 \times \mathrm{blkdiag}\left(\sigma_{\phi_I}^2 W_I^{-1}, \quad \sigma_{\phi_G}^2 W_G^{-1}\right)$$

with $* = \{I, G\}$, p_* and ϕ_* denote, respectively, the m_*-vectors of between-receiver single-differenced (SD) "observed-minus-computed" code and phase observables. The $m_* \times 3$ matrix $G_* = [-u^{1*}, \ldots, -u^{m*}]^{\mathrm{T}}$ includes the undifferenced receiver-satellite unit direction vectors $u^{s_*^{\mathrm{T}}}$ as its rows. The zenith-referenced standard deviation of the undifferenced code and phase observables are denoted as σ_{p_*} and σ_{ϕ_*}, respectively. $W_* = \mathrm{diag}(w^{1*}, \ldots, w^{m*})$ is the $m_* \times m_*$ diagonal matrix which captures the elevation dependency of the GNSS observables. In this contribution, the satellite elevation-dependent weight w^{s*} takes the form of the exponential weighting function as

$$w^{s*} = \left[1 + 10 \exp\left(-\frac{\theta^{s*}}{10}\right)\right]^{-2} \tag{2}$$

where θ^{s*} is the elevation of the satellite s_* in degrees (Euler and Goad 1991). The unknowns to be estimated are the real-valued 3-vector of baseline increment b and the integer-valued $(m-1)$-vector of inter-system DD ambiguities a. Their corresponding single-epoch weighted least-squares float solutions, $\hat{b}$ and $\hat{a}$, are given as

$$\hat{b} = Q_{\hat{b}\hat{b}}\, G^{\mathrm{T}} P_{D_m} Q_{pp}^{-1}\, p, \;\; Q_{\hat{b}\hat{b}} = (G^{\mathrm{T}} P_{D_m} Q_{pp}^{-1}\, G)^{-1}$$
$$\hat{a} = \frac{1}{\lambda} D_m^{\mathrm{T}}(\phi - G\hat{b}), \;\; Q_{\hat{a}\hat{a}} = \frac{1}{\lambda^2} D_m^{\mathrm{T}} \left(Q_{\phi\phi} + G Q_{\hat{b}\hat{b}} G^{\mathrm{T}}\right) D_m \tag{3}$$

with $P_{D_m} = D_m (D_m^{\mathrm{T}} Q_{pp} D_m)^{-1} D_m^{\mathrm{T}} Q_{pp}$. Since, in the case of a single epoch, the number of DD ambiguities equals that of the DD phase observables, uncorrelated with the DD code observables, the DD phase observables are fully reserved for the ambiguity estimation. Therefore, the single-epoch estimation of the baseline components does not benefit from the high precision phase observables unless the DD ambiguities are resolved to their integer values. Upon fixing the DD ambiguities, the phase observations act as the very precise code observations and improve the baseline estimation and precision. The fixed baseline estimation and its corresponding variance matrix are then given by

$$\check{b} = Q_{\check{b}\check{b}}\, G^{\mathrm{T}} P_{D_m} \left(Q_{pp}^{-1}\, p + Q_{\phi\phi}^{-1}\, \phi\right)$$
$$Q_{\check{b}\check{b}} = \left(G^{\mathrm{T}} P_{D_m} (Q_{pp}^{-1} + Q_{\phi\phi}^{-1})\, G\right)^{-1} \tag{4}$$

To obtain the stand-alone IRNSS observational model from (1), it is enough to put $m_G = 0$. The redundancy and solvability for IRNSS and IRNSS + GPS are as follows

IRNSS	redundancy : $m_I - 4$
	solvability : $m_I \geq 4$
IRNSS + GPS	redundancy : $m_I + m_G - 4$
	solvability : $m_I + m_G \geq 4$.

This implies that when the IRNSS is integrated with GPS, (1) would be solvable even if less than four satellites of each system are in view. Note that the redundancy and solvability of the IRNSS + GPS model would be different if the receivers are of different manufacturers and the ISBs are in turn present.

2.2 Height-constrained model

For some GNSS applications where the vertical position of the user does not vary considerably, information on the height component can be provided to strengthen the model of observations. Examples of such applications are bathymetric surveying (Zhu and Santerre 2002), and kinematic positioning over small areas with low height fluctuations (Godha and Cannon 2007). Enforcing a weighted height constraint, the observational model in (1) is extended with

$$E[\delta h] = [0, \;\; 0, \;\; 1]\, b; \qquad D[\delta h] = \sigma_h^2 \tag{5}$$

with δh being the height constraint corrected for an initial value of the height component, and σ_h the a priori standard deviation of the height constraint.

3 Measurement setup

The data used in this study were taken from the two static stations CUBB and CUCC of a short baseline at Curtin University, Perth, Australia (Fig. 1). Each station is equipped with a JAVAD TRE_ G3TH_8 receiver and connected to a TRM59800.00 SCIS antenna. The dataset contains the 1-s IRNSS L5 and GPS L5 observations collected with a cut-off elevation angle of 10° on DOY (Day Of Year) 156 of 2016. Most of our analyses are conducted on an epoch-by-epoch basis, and since the satellites geometry has a low rate of change over time, our conclusions would be valid even for lower sampling rates, like 30 s. For both constellations, the broadcast ephemeris is used. Figure 2 illustrates the 24-h skyplot of IRNSS and GPS Block IIF at Perth.

3.1 Stochastic properties

Prior to our analyses, we need to consider representative values for the zenith-referenced standard deviations in (1), i.e., $\{\sigma_{p_I}, \sigma_{\phi_I}, \sigma_{p_G}, \sigma_{\phi_G}\}$. These values will capture the measurement noise as well as any remaining mis-modeled effects like

Fig. 1 CUCC (*left*) and CUBB (*right*) stations at Curtin University equipped with JAVAD TRE_G3TH_8 receivers, connected to TRM59800.00 SCIS antennas

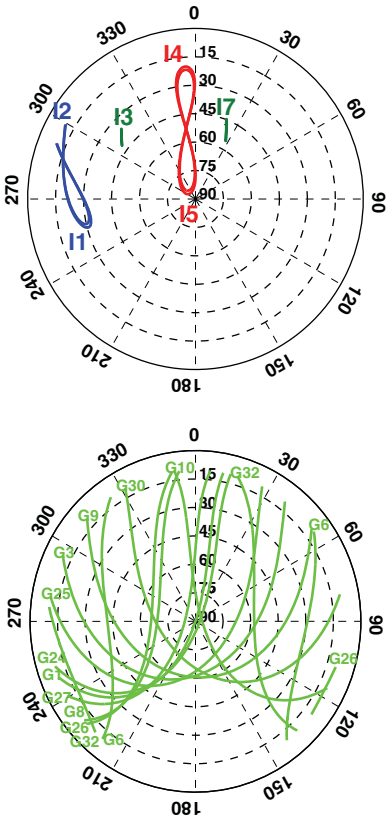

Fig. 2 The 24-h skyplot of IRNSS (*top*) and GPS Block IIF (*bottom*) at Perth, Australia, on DOY 156 of 2016 with cutoff elevation of 10°

multipath. Therefore, it is expected that upon eliminating the unwanted impact of multipath on the data, these values will experience improvement. The impact of multipath is eliminated using the method described in Zaminpardaz et al. (2016a).

Applying the least-squares variance component estimation (LS-VCE) (Teunissen and Amiri-Simkooei 2008; Amiri-Simkooei et al. 2009) to the 1-s original and multipath-corrected data of DOYs 155 and 157 of 2016, the mentioned standard deviations were estimated and the corresponding results are given in Table 2. These estimations are obtained on the basis of baseline-known underlying model. The code precision of the GPS L5 is significantly better than that of the IRNSS L5. This is also in agreement with the signature of the carrier-to-noise density (C/N0) graphs of the two systems in Fig. 3. As it can be seen, the GPS L5-signal has larger values for C/N0 compared to the IRNSS L5, especially for elevations between 30° to 70°. After multipath reduction, both IRNSS and GPS code standard deviations improve significantly. The phase observables of IRNSS L5 and GPS L5 are of comparable precisions, and almost insensitive to the multipath correction. In the sequel, all our empirical analyses are based on the multipath-corrected data of the DOY 156 of 2016. In Table 2, the correlation coefficients of the

Table 2 LS-VCE estimation of the original and multipath-corrected (within brackets) undifferenced code σ_p and phase σ_ϕ zenith-referenced standard deviations and their corresponding correlation coefficient $\rho_{p\phi}$

Frequency	σ_p (cm)	σ_ϕ (mm)	$\rho_{p\phi}$
IRNSS L5	26 (19)	2 (1)	−0.02 (−0.01)
GPS L5	17 (7)	1 (1)	0.02 (0.02)

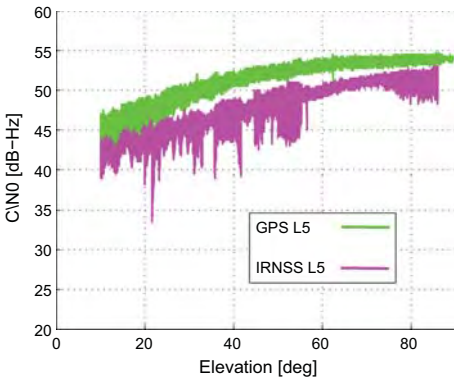

Fig. 3 Carrier-to-noise density (C/N0) for IRNSS L5 and GPS Block IIF L5 signals tracked by a JAVAD TRE_G3TH_8 receiver, connected to a TRM59800.00 SCIS antenna at Perth, Australia, on DOY 156 of 2016

phase and code observables for both IRNSS L5 and GPS L5 are also given. The small values for this quantity confirm that the two types of observations, phase and code, can be considered practically uncorrelated.

3.2 Time correlation

As another aspect of the GNSS signals noise characteristics, here we assess the time correlation of the IRNSS and GPS L5 signals. This would be of importance when one is interested in multi-epoch processing. For this case, not only the correlation of the observations at a single epoch, but also their temporal correlation should properly be taken into account through the stochastic model. Figure 4 (top) shows the graph of the time correlation among the original IRNSS L5 and GPS L5 observations as function of their time difference, while Fig. 4 (bottom) shows the same results for the multipath-corrected data. These graphs are based on applying the LS-VCE method to 1 h of 1-s short-baseline data (Amiri-Simkooei and Tiberius 2007). A significant time correlation of periodic behavior can be recognized among the original data for both the IRNSS and GPS observations. Upon removing the multipath effect however, the time correlation becomes negligible and the periodic signature vanishes. This means that when working with multipath-corrected data, they can safely be considered temporally uncorrelated even if the sampling rate is 1 Hz.

3.3 Satellites visibility and PDOP analysis

Stand-alone IRNSS

The IRNSS constellation consists of seven satellites, three GEOs and four IGSOs. The 24-h visibility of these satellites at Perth, on DOY 156 of 2016 with the cutoff angle of 10° is depicted in Fig. 5 (in *gray*). As is shown, five and sometimes six satellites are visible from Perth. In addition to the number of satellites, Fig. 5 also shows the time series of the corresponding PDOP (Position Dilution of Precision) which is defined as (Teunissen 1998a; Hofmann-Wellenhof et al. 2013)

$$\mathrm{PDOP} = \frac{1}{\sigma_{p_I}}\sqrt{\mathrm{trace}\left(Q_{\hat{b}\hat{b}}\right)}. \tag{6}$$

Since the IRNSS satellite geometry repeats itself every (solar) day 4 min earlier w.r.t. the previous day, the signature of the time series shown in Fig. 5 is representable for any day.

The large values of PDOP during the 24-h period demonstrate the poor IRNSS geometry for positioning. There exists one distinct peak in the PDOP time series at UTC [07:45:50]. Shown in Fig. 6 is the skyplot of the IRNSS satellites at the mentioned time instant. As it can be seen, among the five visible satellites, two occupy the same skyplot position such that all five satellites form a cone-like geometry. Such a satellite

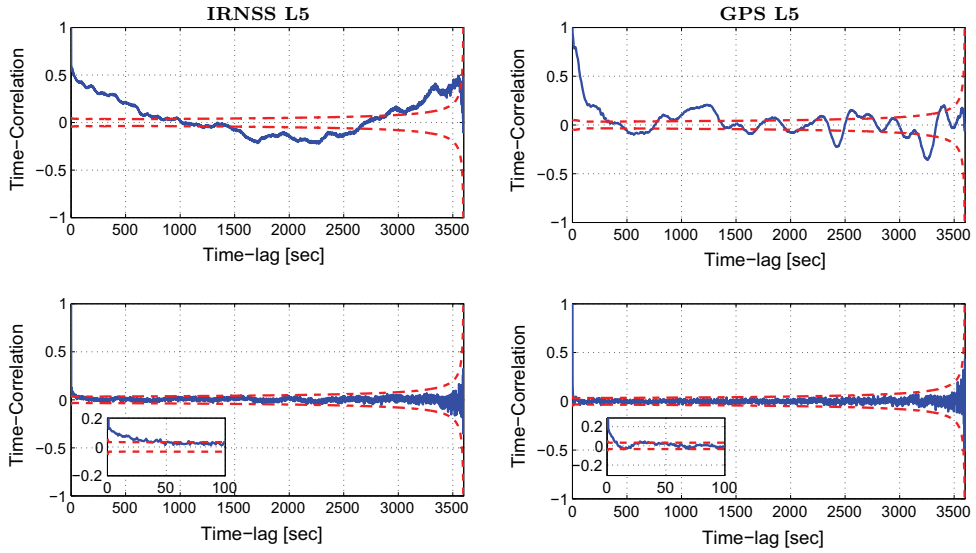

Fig. 4 Time series of the estimated time correlation among the short-baseline IRNSS L5 (*left*) and GPS Block IIF L5 (*right*) observations. (*top*) Original data; (*bottom*) multipath-corrected data. The *red* dashed lines indicate the 95% formal confidence interval

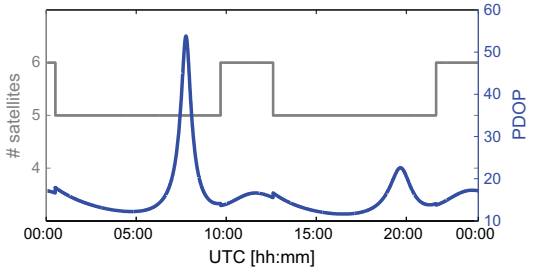

Fig. 5 Time series of the number of visible IRNSS satellites (*gray*) and their corresponding single-epoch PDOP (*blue*) at Perth, Australia, on DOY 156 of 2016 with the cutoff angle of 10°

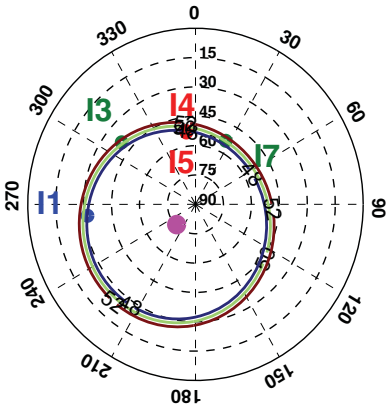

Fig. 6 IRNSS skyplot for Perth on DOY 156 of 2016 at UTC [07:45:50] with the cutoff angle of 10°. The *purple* dot denotes the symmetry axis d of the cone (cf. 8), i.e., the direction in which the receiver position is poorest estimable. The *colored* contour plots show the loci of unit vectors that make a constant angle of 48°, 50° and 52° with d

geometry would in turn lead to the design matrix of the baseline b in (1) becoming rank defect, and PDOP getting large values. The design matrix $D_m^{\mathrm{T}}G$ is rank defect if a vector $d \in \mathbb{R}^3$ can be found such that (Teunissen 1990; Zaminpardaz et al. 2016b)

$$\left(D_m^{\mathrm{T}}G\right) d \;=\; 0 \tag{7}$$

or equivalently

$$u^{s\mathrm{T}}\, d \;=\; \text{const}; \qquad s = 1, \ldots, m \tag{8}$$

implying that all the unit direction vectors from receiver to visible satellites, i.e., u^s $(s = 1, \ldots, m)$, make the same angle with the vector d. From a geometrical point of view, vector d is the symmetry axis of the cone on which the receiver-satellite unit direction vectors lie. The position solution becomes indeterminate in the direction of d. In the

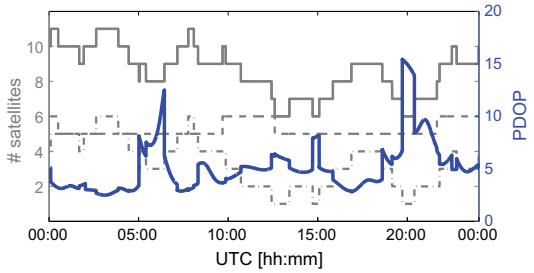

Fig. 7 Time series of the number of visible satellites of IRNSS (*gray* dashed line), of GPS Block IIF (*gray* dashed and dotted line), of both IRNSS and GPS Block IIF (*gray* solid line), and the corresponding single-epoch PDOP of IRNSS + GPS Block IIF (*blue*) at Perth, Australia, on DOY 156 of 2016 with the cutoff angle of 10°

skyplot shown in Fig. 6, the direction d is indicated as *purple* dot, and the corresponding cones as colored contour lines with the angles of 48°, 50° and 52°, respectively.

IRNSS integrated with GPS

Now consider the case when the IRNSS L5 observables are combined with the GPS L5. GPS Block IIF has 12 operational satellites of which the visibility at Perth is illustrated in Fig. 7 (in *gray*). Combining IRNSS with GPS results in the number of visible satellites increasing from 5–6 to 6–11. The IRNSS + GPS PDOP (in *blue*) in Fig. 7 demonstrates a considerable improvement compared to that of the stand-alone IRNSS (see Fig. 5).

4 Ambiguity resolution

In this section, the IRNSS L5 ambiguity resolution performance is investigated. The impact of combining IRNSS L5 with GPS L5 observables on the ambiguity resolution will further be assessed. Our analyses will be based on the unconstrained, as well as height-constrained observational model. Note, the ambiguity resolution in this paper is conducted for the full vector of the DD ambiguities.

4.1 Ambiguity dilution of precision

The ambiguity dilution of precision (ADOP) was introduced in Teunissen (1997) as an easy-to-compute scalar diagnostic to measure the intrinsic model strength for successful ambiguity resolution. It is defined as the square root of the determinant of the ambiguity variance matrix raised to the power of one over the ambiguity dimension. Therefore, the single-baseline ADOP based on (3) is given as

$$\text{ADOP} = \sqrt{|Q_{\hat{a}\hat{a}}|}^{\frac{1}{m-1}}. \tag{9}$$

The closed-form expression for the single-system ADOP, where the observations on the same frequency are of the same quality, has already been provided in Teunissen (1997), Odijk and Teunissen (2008), and the role of different factors such as receiver-satellite geometry and precision of the observables was investigated. As a rule of thumb, an ADOP smaller than about 0.12 cycle corresponds to an ambiguity success rate, also known as the probability of correct integer estimation, larger than 99.9% (Odijk and Teunissen 2008). An increase in the number of satellites would result in an improvement in the ADOP value. The magnitude of this improvement is even larger if the added satellite is from GPS Block IIF since the GPS L5 code observable is more precise than the IRNSS L5 (see Table 2).

Figure 8 shows the single-epoch ADOP time series of IRNSS (top) and IRNSS + GPS (bottom), as well as the corresponding number of visible satellites with the cutoff angle of 10° on DOY 156 of 2016. The horizontal *red* dashed line also indicates the ADOP value of 0.12 cycle. It can be seen that the fluctuations in the ADOP graphs resemble those in the graphs of the number of visible satellites. The stand-alone IRNSS ADOP ranges from 0.3 to 0.7 cycle which is by far more than the target value of 0.12 cycle. When the IRNSS L5 is integrated with the GPS L5, the ADOP experiences

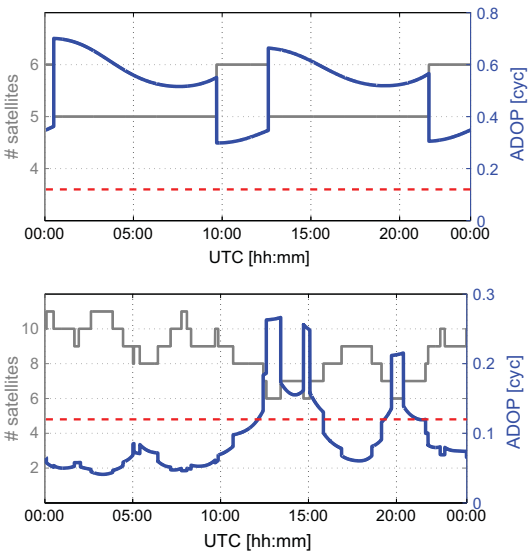

Fig. 8 Time series of the number of visible satellites (*gray*) and their corresponding single-epoch, single-baseline (CUBB–CUCC) ADOP (*blue*) for IRNSS (*top*) and IRNSS + GPS Block IIF (*bottom*) at Perth, Australia, on DOY 156 of 2016 with the cutoff angle of 10°. The *red* dashed line indicates the ADOP value of 0.12 cycle

a dramatic decrease particularly when more than one GPS satellite are in view.

4.2 From unconstrained to height-constrained

Here, we assess, formally and empirically, the impact of (weighted) height-constraining on the ambiguity resolution performance by means of the ADOP and the success rate. Upon height-constraining with the standard deviation of σ_h, the ambiguities variance matrix improves as

$$Q_{\hat{a}\hat{a}|h} = Q_{\hat{a}\hat{a}} - \frac{1}{\sigma_h^2 + \sigma_{\hat{h}}^2} Q_{\hat{a}\hat{h}} Q_{\hat{h}\hat{a}}. \tag{10}$$

Taking the determinant of both sides of the above equation and raising it to the power of $\frac{1}{2(m-1)}$, the weighted height-constrained ambiguity dilution of precision, denoted by $\text{ADOP}_{|h}$, is given by

$$\begin{aligned} \text{ADOP}_{|h} &= \text{ADOP}\, \frac{\sigma_h^2/\sigma_{\hat{h}}^2 + \sigma_{\hat{h}}^2/\sigma_{\hat{h}}^2}{\sigma_h^2/\sigma_{\hat{h}}^2 + 1} \\ &\approx \text{ADOP}\, \left[1 + \sigma_{\hat{h}}^2/\sigma_h^2\right]^{-1} \end{aligned} \tag{11}$$

with $\sigma_{\hat{h}}$ and $\sigma_{\check{h}}$ being the standard deviations of, respectively, unconstrained float and fixed height solutions, and $Q_{\hat{a}\hat{h}}$ the unconstrained float ambiguity-height covariance. The approximation is due to the ratio $\sigma_{\check{h}}^2/\sigma_{\hat{h}}^2$ getting very small values, and is valid as long as $\sigma_{\check{h}}^2/\sigma_{\hat{h}}^2$ is negligible with respect to $\sigma_h^2/\sigma_{\hat{h}}^2$. This is the case when imposing a soft height constraint with relatively large value for σ_h. As (11) shows, the larger the ratio $\sigma_{\hat{h}}^2/\sigma_h^2$, the larger the ADOP improvement will be. Therefore, if $\sigma_{\hat{h}}^2$ is much larger than $\sigma_{\check{h}}^2$, the ambiguity resolution improvement brought by height-constraining would be negligible. Ambiguity resolution can benefit considerably from a weighted height constraint if $\sigma_{\hat{h}}^2$ is large. The larger $\sigma_{\hat{h}}^2$ is, the softer the weighted height constraint can be to still have an impact on ambiguity resolution. Thus, in case of a large $\sigma_{\hat{h}}^2$, soft constraining of the height can still result in a very significant improvement of ambiguity resolution. This is demonstrated in Fig. 9.

The first row of Fig. 9 shows the single-epoch float height standard deviation time series of the unconstrained model with 10° cutoff angle on DOY 156 of 2016, and the second to bottom rows present the corresponding ADOP time series for $\sigma_h = \infty$ (unconstrained), $\sigma_h = 1\,\text{m}$, $\sigma_h = 0.1\,\text{m}$ and $\sigma_h = 0.01\,\text{m}$, respectively. Comparing the results of the stand-alone IRNSS (left column) with those of IRNSS + GPS (right column), the ADOP improvement after applying the weighted height constraint is overall larger for the stand-alone IRNSS. With the above explanation in mind,

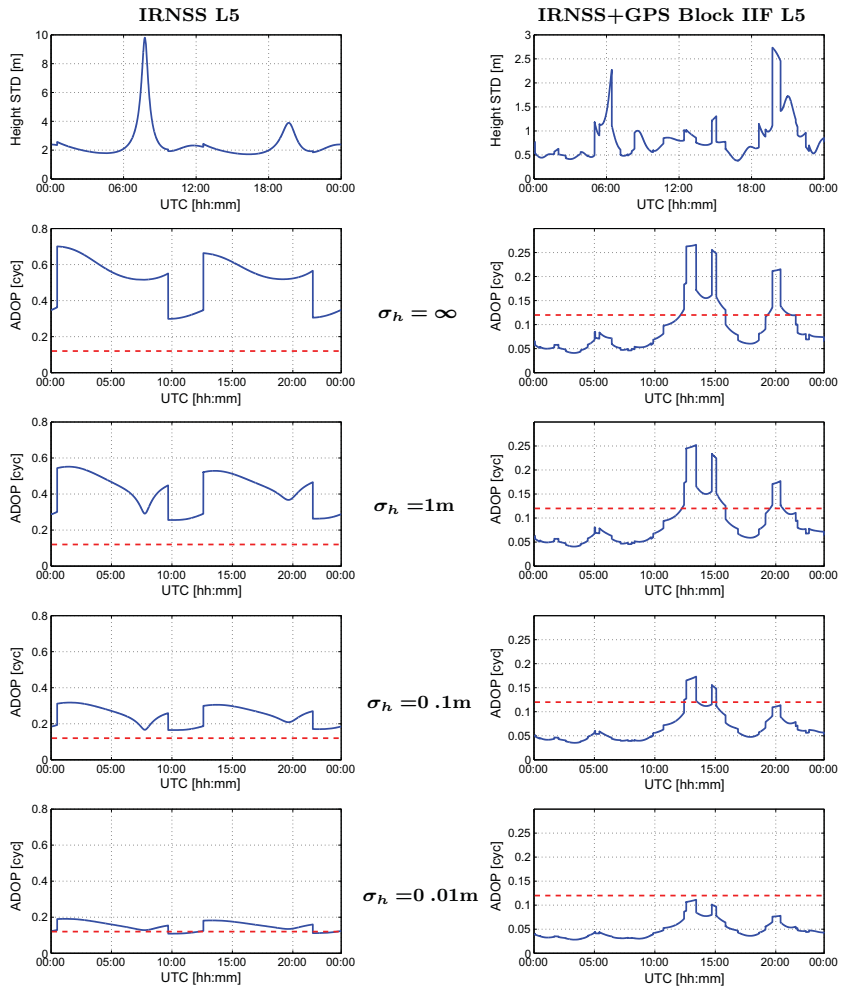

Fig. 9 (*First row*) Time series of the single-epoch unconstrained float height standard deviation of IRNSS L5 (*right*) and IRNSS + GPS Block IIF L5 (*right*) with the receiver pair CUBB–CUCC, on DOY 156 of 2016 with the cutoff angle of 10°. (*From second row to bottom*) The corresponding time series of the single-epoch ADOP based on the unconstrained ($\sigma_h = \infty$) and height-constrained model with the standard deviations of $\sigma_h = 1$ m, $\sigma_h = 0.1$ m and $\sigma_h = 0.01$ m. The *red* dashed line indicates the ADOP value of 0.12 cycle

this is due to the larger values of $\sigma_{\hat{h}}$ of IRNSS compared to IRNSS + GPS. The results in the third row, especially those of stand-alone IRNSS, show that a soft height constraint of $\sigma_h = 1$ m has a notable impact on ambiguity resolution at the time instances for which $\sigma_{\hat{h}}$ is large. Increasing the weight of the height constraint, the results of the fourth and fifth rows of Fig. 9 show that the ambiguity resolution improvements spread over to neighboring time instances. In case of a highly weighted height constraint of $\sigma_h = 0.01$ m, the ADOP of the combined systems is always smaller than 0.12 cycle, whereas the ADOP of the single-system IRNSS is mostly above the target value of 0.12 cycle.

Table 3 gives the single-epoch formal and empirical integer bootstrapped (IB) success rates as well as the empirical integer least-squares (ILS) success rate for the four models of Fig. 9. The formal IB success rate is computed by taking the average of the 24-h time series of the single-epoch IB success rate which is given as Teunissen (1998b)

$$\text{Formal IB } Ps = \prod_{i=1}^{m-1} \left[2\Phi\left(\frac{1}{2\sigma_{\hat{z}_{i|I}}} \right) - 1 \right] \tag{12}$$

Table 3 24-h average single-epoch formal and empirical bootstrapped (IB) and empirical integer least-squares (ILS) success rate, for single- and dual-system scenarios, for the unconstrained model ($\sigma_h = \infty$) and the height-constrained model with different values for σ_h

Model	IRNSS L5 Ps (%)			IRNSS + GPS Block IIF L5 Ps (%)		
	Emp ILS	Emp IB	Form IB	Emp ILS	Emp IB	Form IB
$\sigma_h = \infty$	19.7	19.5	19.9	97.5	97.4	97.1
$\sigma_h = 1\,\text{m}$	31.1	30.7	32.6	98.0	97.9	97.7
$\sigma_h = 0.1\,\text{m}$	70.8	70.3	73.2	99.2	99.2	99.2
$\sigma_h = 0.01\,\text{m}$	91.5	91.4	93.0	>99.9	>99.9	> 99.9

Emp: empirical, Form: formal

where $\Phi(x) = \int_{-\infty}^{x} \frac{1}{\sqrt{2\pi}} \exp\{-\frac{1}{2}v^2\}\mathrm{d}v$ and $\sigma_{\hat{z}_{i|I}}$ ($i = 1, \ldots, m-1$ and $I = 1, \ldots, m-2$) are the conditional standard deviations of the *decorrelated* ambiguities. The reason behind choosing the bootstrapped success rate is twofold. First it is easy to compute, and secondly it is the sharpest lower bound to the ILS success rate which has the highest success rate of all admissible integer estimators (Teunissen 1999; Verhagen and Teunissen 2014). The empirical IB/ILS success rate is given as

$$\text{Empirical } Ps = \frac{\#\,\text{Correct fixed DD ambiguities}}{\#\,\text{Float DD ambiguities}}. \qquad (13)$$

To judge whether a DD ambiguity is correctly fixed, its corresponding IB/ILS solution is compared with the reference integer DD ambiguity computed based on the multi-epoch ILS solution of the baseline-known model. The empirical values in Table 3 are in good agreement with the formal ones, confirming the consistency between model and data. Also, the stronger the model is (from top to bottom), the larger the success rate becomes.

4.3 Ambiguity resolution performance over the IRNSS service area

So far, we have presented the single-epoch ambiguity resolution formal and empirical analyses on the basis of the data collected at Perth. The consistency between our formal outcomes and their empirical counterparts implies that the easy-to-compute formal values can indeed be used to predict the expected ambiguity resolution performance. In this subsection, we conduct a formal analysis of the number of epochs needed to fix the DD ambiguities with the success rate of 99.9% over the IRNSS primary and secondary service area. Our analyses are valid for a short baseline such that the differential orbital and atmospheric errors can be neglected for. Figure 10 depicts the extent of these two areas as well as the locations chosen to be analyzed in terms of ambiguity resolution performance (*red*: primary locations; *black*: secondary locations). Since ambiguities remain constant over time (in case of no loss-of-lock or cycle slip), the ambiguity

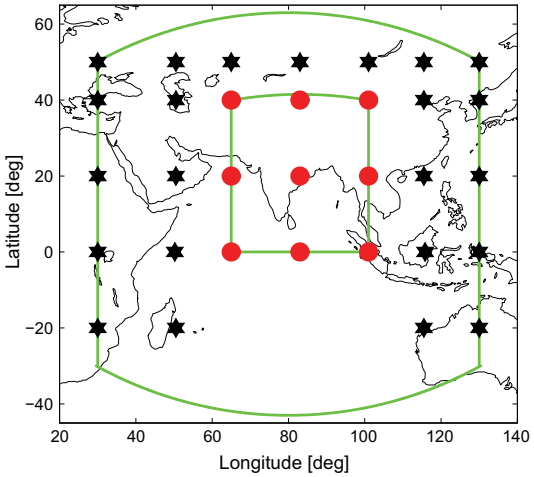

Fig. 10 IRNSS primary (*red* circles) and secondary (*black* hexagrams) service area locations. The inner and outer *green* boundaries indicate the border of the primary and secondary service areas, respectively

resolution performance can improve if this time constancy is taken into account through a Kalman filter. The number of epochs needed to fix the DD ambiguities is then computed as follows

1. Initialize filter with the data of a single epoch.
2. Compute the DD ambiguities variance matrix.
3. Compute the bootstrapped success rate Ps based on the decorrelated DD ambiguities (cf. 12).
4. If $Ps < 99.9\%$, go to step 5, otherwise quit the loop.
5. Accumulate the data of the next epoch and go to step 2.

Providing a 24-h time series of the number of epochs needed to fix the DD ambiguities, we make use of the boxplot concept to give the statistical properties of this time series. Note that as 30-s is the most common sampling rate in GNSS community, our results here are provided on the basis of such a sampling rate. To be conservative, the code standard deviation that we use for GPS L5-signal is

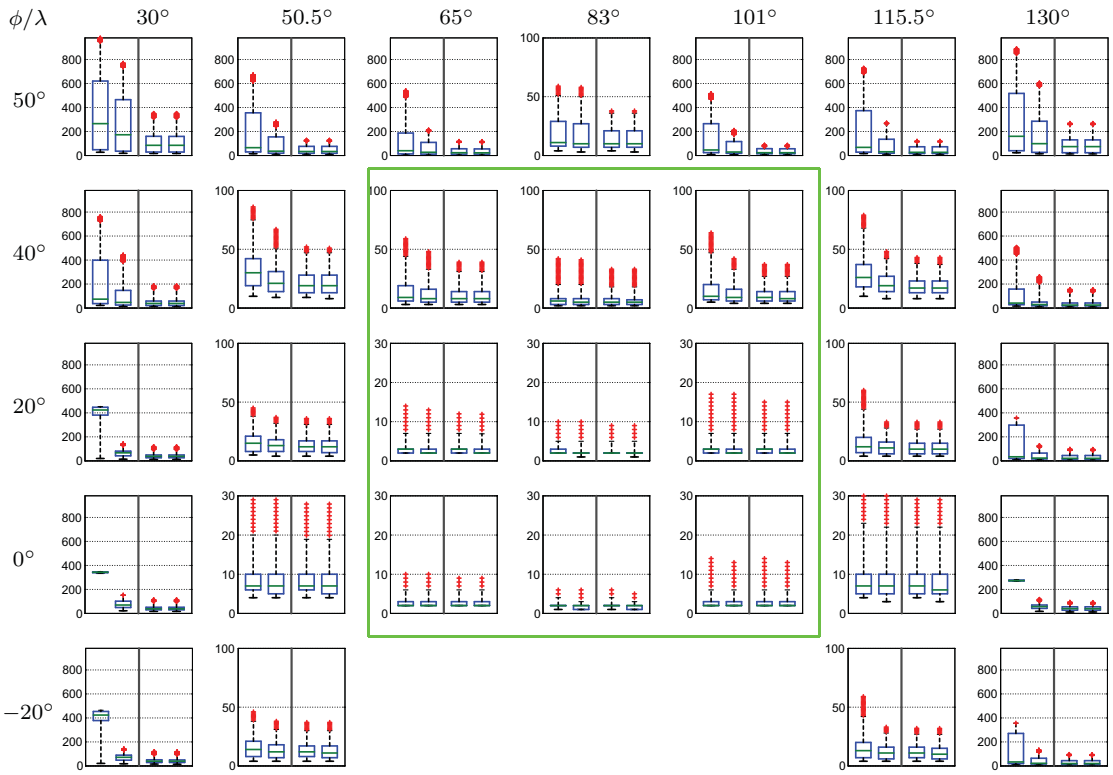

Fig. 11 *Boxplots* of the stand-alone IRNSS L5 time series of the required number of epochs to fix the DD ambiguities with $Ps > 99.9\%$ using 30-s sampling rate over the IRNSS service area, on DOY 156 of 2016 with the cutoff angle of 10°. The primary service area is located within the *green* border. Each panel shows *four boxplots* corresponding with different underlying models: from *left* to *right*, the kinematic unconstrained and height-constrained ($\sigma_h = 1\,\text{m}$) and static unconstrained and height-constrained ($\sigma_h = 1\,\text{m}$) model, respectively. In each boxplot, the horizontal lines from *bottom* to *top* show: 2nd percentile (*black*), 25th percentile (*blue*), 50th percentile (*green*), 75th percentile (*blue*) and 98th percentile (*black*) of the mentioned time series, and *red* pluses show the remaining values thereof. These *boxplots* are computed based on $\sigma_{p_I} = 30\,\text{cm}$ and $\sigma_{\phi_I} = 1\,\text{mm}$

$\sigma_{p_G} = 20\,\text{cm}$ (Nadarajah et al. 2015) and for IRNSS L5-signal is $\sigma_{p_I} = 30\,\text{cm}$, which is considered less precise than the GPS L5-signal (see Table 2). The phase standard deviation for both systems is considered as $\sigma_{\phi_I} = \sigma_{\phi_G} = 1\,\text{mm}$.

Figure 11 for the stand-alone IRNSS L5, and Fig. 12 for the IRNSS + GPS Block IIF L5, show the boxplots of the number of epochs to fix the ambiguities. Each panel contains the results of both kinematic and static scenarios separated with a vertical *gray* line. To the left of this line are shown the unconstrained and height-constrained ($\sigma_h = 1\,\text{m}$) kinematic boxplots, and to the right their static counterparts. In each boxplot, the horizontal lines from bottom to top show: 2nd percentile (*black*), 25th percentile (*blue*), 50th percentile (*green*), 75th percentile (*blue*) and 98th percentile (*black*) of the mentioned time series, and *red* pluses show the remaining values thereof.

We first consider the IRNSS stand-alone results. It can be seen that for those locations on the equator ($\phi = 0°,\ 50.5° < \lambda < 115.5°$), the ambiguity resolution performance is almost independent from the underlying model being kinematic or static, unconstrained or height-constrained. This conclusion is also valid for the locations ($\phi = 20°,\ 65° < \lambda < 101°$). The performance of the unconstrained and height-constrained static ambiguity resolution are similar for all the locations. This is due to the fact that the multi-epoch static height standard deviation $\sigma_{\hat{h}}$ is so small such that a soft height constraint with $\sigma_h = 1\,\text{m}$ does not bring any considerable improvement to the ambiguity resolution performance (see Fig. 9). As one goes further away from the central location ($\phi = 0°,\ \lambda = 83°$), the ambiguity resolution performance gets poorer. Excluding the locations within ($0° < \phi < 20°,\ 65° < \lambda < 101°$), the IRNSS user needs a considerably long time to fix the DD ambiguities with $Ps = 99.9\%$.

We repeated our analysis of the required number of epochs to fix the DD ambiguities for a higher sampling rate of 1s, as well. Although the number of epochs increases, the period

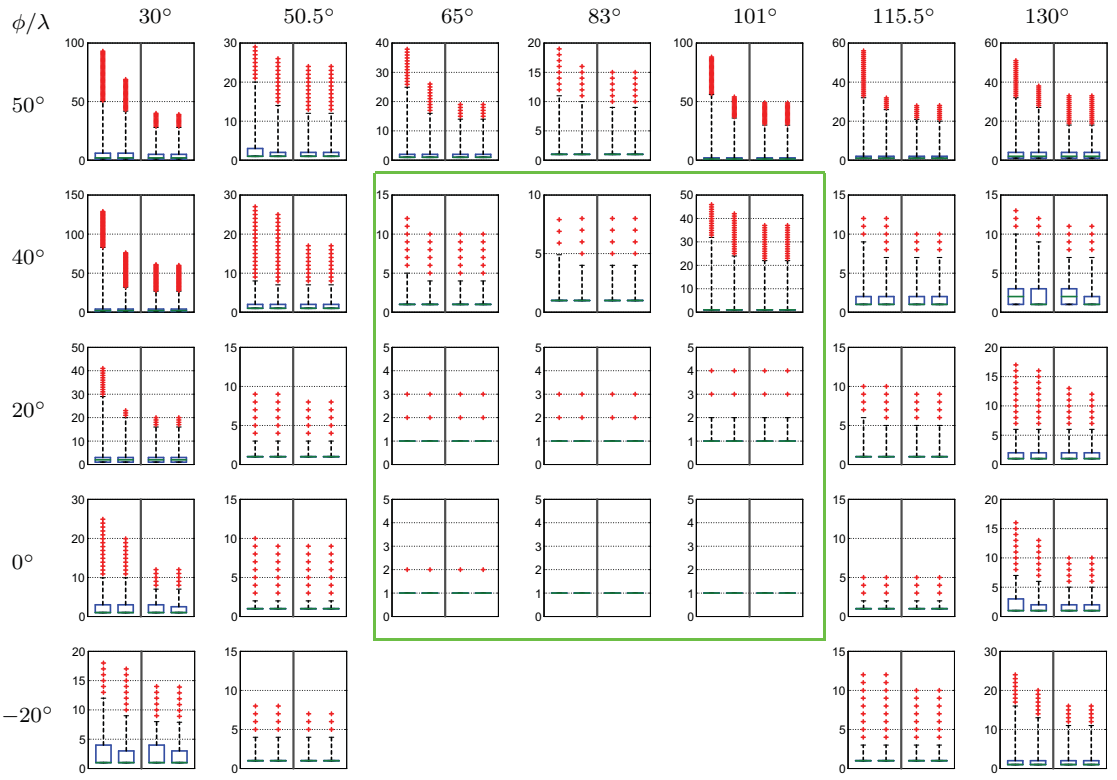

Fig. 12 *Boxplots* of the IRNSS + GPS Block IIF L5 time series of the required number of epochs to fix the DD ambiguities with $Ps > 99.9\%$ using 30-s sampling rate over the IRNSS service area, on DOY 156 of 2016 with the cutoff angle of 10°. The primary service area is located within the *green* border. Each panel shows *four boxplots* corresponding with different underlying models: from left to right, the kinematic unconstrained and height-constrained ($\sigma_h = 1$ m) and static unconstrained and height-constrained ($\sigma_h = 1$ m) model, respectively. In each boxplot, the horizontal lines from bottom to top show: 2nd percentile (*black*), 25th percentile (*blue*), 50th percentile (*green*), 75th percentile (*blue*) and 98th percentile (*black*) of the mentioned time series, and *red* pluses show the remaining values thereof. These *boxplots* are computed based on $\sigma_{p_I} = 30$ cm, $\sigma_{p_G} = 20$ cm and $\sigma_{\phi_I} = \sigma_{\phi_G} = 1$ mm

length needed to achieve a success rate of $Ps = 99.9\%$ decreases dramatically. As an example, we consider the unconstrained kinematic results of the location ($\phi = -20°$, $\lambda = 115.5°$). Switching from 30 s to 1s sampling rate, the 2nd, 25th, 50th, 75th and 98th percentiles experience the following changes, respectively: 4 (120 s) → 5 (5 s), 7 (210 s) → 8 (8 s), 13 (390 s) → 20 (20 s), 20 (600 s) → 29 (29 s) and 42 (1260 s) → 79 (79 s). This means that in case of using the high sampling rate of 1s, one needs a dramatically shorter time period to achieve $Ps = 99.9\%$ w.r.t. using 30-s data.

Integration of IRNSS with the GPS Block IIF brings a huge benefit to the users within the IRNSS service area, especially for those on the border of the secondary service area. The median (50th percentile) for all the locations is now one to two epochs, and the difference between various percentiles reduces, meaning that the variability of the number of epochs over the 24-h period has reduced. As Fig. 12 shows, (almost) instantaneous ambiguity resolution is feasible during the whole day for those locations within ($0° < \phi < 20°$, $65° < \lambda < 101°$).

GPS Block IIF is the first generation of GPS with the capability of transmitting L5 signal, and the next GPS generation, GPS III, will also be transmitting L5 signal as well (Marquis and Shaw 2016). GPS III is planned to become fully operational with a constellation of 32 satellites by 2025 (Lockheed Martin 2013; Bensky 2016), and the first launch thereof is expected in 2017 (GPS World 2016). For the situation when the GPS III has reached its full operational capability, we computed the required number of epochs for fixing the L5 DD ambiguities using single-system GPS III and dual-system IRNSS + GPS III. In case of the single-system GPS III, the 24-h instantaneous ambiguity resolution with $Ps = 99.9\%$ is not feasible for any of the locations within the IRNSS

service area. As to the dual-system IRNSS + GPS III, however, our computations show that for the required success rate of $Ps = 99.9\%$ and even of $Ps = 99.99\%$, *instantaneous ambiguity resolution* becomes always feasible for all the locations within the IRNSS service area. This is also consistent with the results presented by Odolinski and Teunissen (2016). There, the performance of the dual-system single-frequency is compared with that of the single-system dual-frequency, and it is shown that for these scenarios, comparable ambiguity resolution performance are achievable and instantaneous ambiguity-resolved positioning is always feasible. Note that our computations are based on $\sigma_{p_G} = 20\,\text{cm}$. Since the GPS III signals would be three times more accurate than the current GPS signals (Marquis and Shaw 2016), IRNSS + GPS III L5 instantaneous ambiguity resolution even with success rates higher than 99.99% may become achievable.

5 Positioning results

In this section, the single-epoch positioning results for IRNSS and then for IRNSS + GPS are presented. The underlying model ranges from unconstrained to highly weighted height-constrained model.

5.1 Stand-alone IRNSS

Shown in Fig. 13 is the stand-alone IRNSS L5 unconstrained single-epoch float horizontal scatter plot for the CUBB–CUCC baseline on DOY 156 of 2016. As it can be seen, there exist some excursions in the scatter plot which correspond with that time interval with large PDOPs (see Fig. 5). In addition, the formal and empirical 95% confidence ellipses are also illustrated by, respectively, *blue* and *purple* colors, showing a good consistency. Note that the formal and empirical confidence ellipses are computed on the basis of the respective formal and empirical variance matrix. Formal variance matrix is obtained from taking the average of all the single-epoch least-squares baseline variance matrices. Whereas, the empirical variance matrix is obtained from the differences of the estimated baseline and the available ground truth of the CUBB–CUCC baseline.

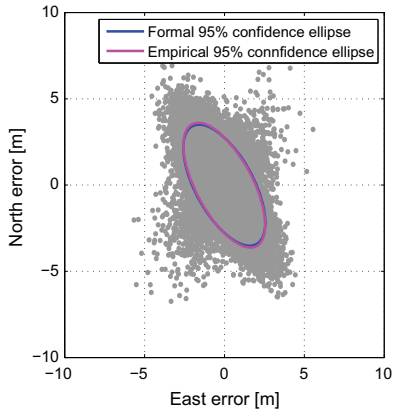

Fig. 13 Stand-alone IRNSS L5 unconstrained single-epoch float horizontal baseline scatter plot corresponding with receiver pair CUBB–CUCC on DOY 156 of 2016 with the cutoff angle of 10°. The *blue* and *purple* ellipses show, respectively, the 95% formal and empirical confidence ellipses

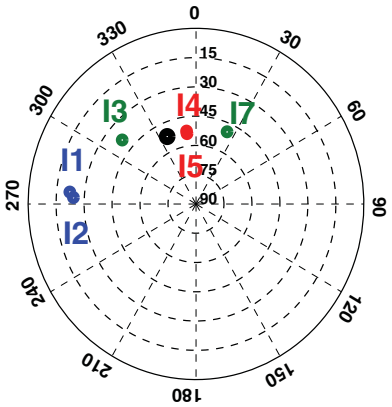

Fig. 14 Day-averaged IRNSS skyplot at Perth for DOY 156 of 2016 with the cutoff angle of 10°. The *black* dot indicates the skyplot position of vector $\bar{u}$ (cf. 15)

Note that the scatter plot and the confidence ellipses are elongated in almost North-Westerly direction. This can be explained by means of the receiver-satellite geometry and its impact on the confidence ellipse of $\hat{b}$,

$$(\hat{b} - b)^{\mathrm{T}}\, Q_{\hat{b}\hat{b}}^{-1}\, (\hat{b} - b) \;=\; r^2 \tag{14}$$

in which the constant r^2 is chosen such that a certain confidence level is reached. As the direction of elongation is given by the direction of the eigenvector of $Q_{\hat{b}\hat{b}}^{-1}$ corresponding to its smallest eigenvalue, it follows with the aid of (3) that this direction is given by

$$\begin{aligned} f &= \underset{\tilde{f}}{\operatorname{argmin}}\; \tilde{f}^{\mathrm{T}} Q_{\hat{b}\hat{b}}^{-1}\, \tilde{f} \\ &= \underset{\tilde{f}}{\operatorname{argmin}} \sum_{s=1}^{m} w^s \left[\tilde{f}^{\mathrm{T}}(u^s - \bar{u})\right]^2 . \end{aligned} \tag{15}$$

Figure 14 depicts the day-averaged skyplot position of the IRNSS satellites as well as that of the weighted-average $\bar{u}$ at Perth on DOY 156 of 2016 with the cutoff angle of 10°. As the differences $(u^s - \bar{u})$ are mainly oriented along the North-East direction, the direction f that minimizes their contribution to (15) will mainly lie in a North-Westerly direction.

Table 4 Stand-alone IRNSS L5 single-epoch empirical and formal standard deviations of the CUBB–CUCC baseline float and fixed estimations on DOY 156 of 2016 with the cutoff elevation angle of 10°

	$\sigma_h = \infty$		$\sigma_h = 1$ m		$\sigma_h = 0.1$ m		$\sigma_h = 0.01$ m	
	Empirical	Formal	Empirical	Formal	Empirical	Formal	Empirical	Formal
Float								
$\sigma_{\hat{n}}$ (m)	1.48	1.44	1.11	1.09	1.01	1.01	1.01	1.01
$\sigma_{\hat{e}}$ (m)	1.04	1.05	0.73	0.74	0.65	0.66	0.65	0.66
$\sigma_{\hat{h}}$ (m)	2.56	2.71	0.89	0.91	0.10	0.10	0.01	0.01
$\rho_{\hat{n}\hat{e}}$	−0.64	−0.62	−0.57	−0.58	−0.49	−0.52	−0.49	−0.52
$\rho_{\hat{n}\hat{h}}$	0.33	0.30	0.33	0.30	0.04	0.04	0.00	0.00
$\rho_{\hat{e}\hat{h}}$	−0.72	−0.72	−0.45	−0.43	−0.05	−0.05	0.00	0.00
Fixed								
$\sigma_{\check{n}}$ (m)	–	–	–	–	0.007	0.005	0.006	0.005
$\sigma_{\check{e}}$ (m)	–	–	–	–	0.005	0.004	0.005	0.003
$\sigma_{\check{h}}$ (m)	–	–	–	–	0.010	0.010	0.007	0.006
$\rho_{\check{n}\check{e}}$	–	–	–	–	−0.70	−0.61	−0.74	−0.65
$\rho_{\check{n}\check{h}}$	–	–	–	–	0.28	0.28	0.44	0.42
$\rho_{\check{e}\check{h}}$	–	–	–	–	−0.67	−0.72	−0.61	−0.64

The underlying models are unconstrained ($\sigma_h = \infty$) and height-constrained for $\sigma_h = 1,\ 0.1,\ 0.01$ m. $\sigma_{\hat{n}}/\sigma_{\check{n}}$: north standard deviation; $\sigma_{\hat{e}}/\sigma_{\check{e}}$: east standard deviation; $\sigma_{\hat{h}}/\sigma_{\check{h}}$: height standard deviation

Table 5 IRNSS + GPS Block IIF L5 single-epoch empirical and formal standard deviations of the CUBB–CUCC baseline float estimations on DOY 156 of 2016 with the cutoff angle of 10°

	$\sigma_h = \infty$		$\sigma_h = 1$ m		$\sigma_h = 0.1$ m		$\sigma_h = 0.01$ m	
	Empirical	Formal	Empirical	Formal	Empirical	Formal	Empirical	Formal
Float								
$\sigma_{\hat{n}}$ (m)	0.30	0.34	0.29	0.31	0.26	0.28	0.26	0.28
$\sigma_{\hat{e}}$ (m)	0.37	0.40	0.31	0.35	0.28	0.31	0.28	0.31
$\sigma_{\hat{h}}$ (m)	0.82	0.93	0.54	0.61	0.10	0.10	0.01	0.01
$\rho_{\hat{n}\hat{e}}$	−0.24	−0.22	−0.17	−0.17	−0.13	−0.15	−0.13	−0.15
$\rho_{\hat{n}\hat{h}}$	0.23	0.23	0.16	0.16	0.03	0.03	0.00	0.00
$\rho_{\hat{e}\hat{h}}$	−0.46	−0.45	−0.23	−0.24	−0.03	−0.03	0.00	0.00

The underlying models are unconstrained ($\sigma_h = \infty$) and height-constrained for $\sigma_h = 1,\ 0.1,\ 0.01$ m. $\sigma_{\hat{n}}$: north standard deviation; $\sigma_{\hat{e}}$: east standard deviation; $\sigma_{\hat{h}}$: height standard deviation

Table 4 lists the stand-alone IRNSS single-epoch formal and empirical standard deviations and correlation coefficients of the CUBB–CUCC baseline components for both ambiguity-float and ambiguity-fixed scenarios. The fixed results are only given for the models with success rates more than 70% (see Table 3). As σ_h gets smaller from $\sigma_h = \infty$ to $\sigma_h = 0.1$ m, the baseline estimation gets better in precision. However, from $\sigma_h = 0.1$ m to $\sigma_h = 0.01$ m no further precision improvement can be achieved for the north and east components.

5.2 IRNSS integrated with GPS

Integrating IRNSS L5 with GPS L5 observations, Table 5 presents the single-epoch empirical and formal standard deviations and correlation coefficients of the CUBB–CUCC baseline components for ambiguity-float scenario. Comparing the results in this table with those in Table 4, the baseline estimation precision improves by a factor of 4–5 horizontally and 2–3 vertically. Imposing a height constraint indeed improves the baseline float solution precision, but not as much as it does for the stand-alone IRNSS. This is due to the fact that the combined system is stronger than the single system, and thus experiencing less improvement caused by height-constraining. Upon fixing the DD ambiguities, the very precise phase observations take the leading role in baseline estimation. In case of $\sigma_{p_I} = \sigma_{p_G}$ and $\sigma_{\phi_I} = \sigma_{\phi_G}$, the fixed baseline standard deviations improve by a factor of $\sigma_{p_I}/\sigma_{\phi_I}$ w.r.t. their float counterparts. However, from Table 2, $\sigma_{p_I} \neq \sigma_{p_G}$, and the ratio of code and phase standard deviations is 190 for IRNSS L5 and 70 for GPS L5. The improvement that is achieved upon fixing the DD ambiguities is around a factor of 150, which lies between 70 and 190. For the chosen values of σ_h, the fixed solutions are

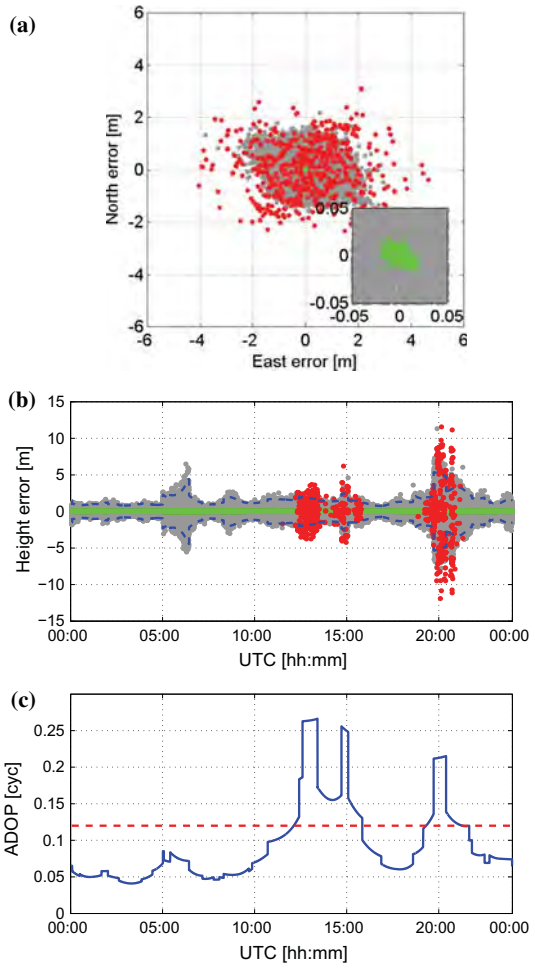

Fig. 15 **a** IRNSS + GPS Block IIF L5 unconstrained single-epoch horizontal baseline scatter plot corresponding with receiver pair CUBB–CUCC on DOY 156 of 2016 with the cutoff angle of 10°. *gray* float solution, *green* correctly fixed solution, *red* wrongly fixed solution. **b** The corresponding time series of the height component. The *blue* dashed lines indicate the 95% formal confidence interval. **c** The corresponding time series of the single-epoch ADOP (*blue*) and the target value of 0.12 cycle (*red* dashed line)

almost insensitive to height-constraining. That is because the height-constraining does not bring any considerable benefit to a model which is already strong enough.

Figure 15 depicts the unconstrained single-epoch 1-s horizontal scatter plot (Fig.15a) and height time series (Fig.15b) of the CUBB–CUCC baseline float solutions (in *gray*), correctly fixed solutions (in *green*), and wrongly fixed solutions (in *red*), and the corresponding ADOP time series (Fig.15c) on the basis of L5 observables of IRNSS and GPS Block IIF collected on DOY 156 of 2016 with the cutoff angle of 10°. The scatter plot is of non-ellipsoidal shape which is due to the significant changes that the receiver-satellite geometry undergoes during the whole day.

Inside the Fig.15b is also shown the 95% formal confidence interval based on the float height standard deviation of which the signature is in good agreement with that of the height error time series, confirming the consistency between data and model. Comparing the time series of the height solution with that of the ADOP, the wrong ambiguity fixing occurs during the periods of large ADOPs. It can also be seen that despite large fluctuations in float height solution during for example UTC [05:00–07:00], DD ambiguities can be correctly fixed. This indicates that while a receiver-satellite geometry can be poor for positioning, it can still be strong enough for ambiguity resolution (Teunissen et al. 2014; Zaminpardaz et al. 2016a).

5.3 Positioning performance over the IRNSS service area

The positioning results presented in the previous subsection reveal that the formal values are indeed reliable representatives for their empirical counterparts. Therefore, in this subsection, we provide a formal analysis of the positioning performance over the IRNSS service area. For our analyses, we chose two stations within the primary service area, namely ($\phi = 0°,\ \lambda = 83°$) and ($\phi = 40°,\ \lambda = 65°$). The rationale behind choosing these two locations is twofold. First, their positioning performance are quite different and secondly, the instantaneous ambiguity resolution is feasible over these two locations when integrating IRNSS with GPS.

Figure 16 shows the number of visible satellites (in *black*) with the cutoff angle of 10°, unconstrained single-epoch north and east standard deviations (in *blue*) and correlation coefficient (in *gray*) time series for ($\phi = 0°,\ \lambda = 83°$) to the top and for ($\phi = 40°,\ \lambda = 65°$) to the bottom. The underlying model varies, from left to right, from stand-alone IRNSS to IRNSS + GPS Block IIF to IRNSS + GPS III. Again to be conservative we set $\sigma_{p_I} = 30\,\text{cm}$, $\sigma_{p_G} = 20\,\text{cm}$ and $\sigma_{\phi_I} = \sigma_{\phi_G} = 1\,\text{mm}$. As the model gets stronger from left to right, the level of standard deviations decreases. The east standard deviation shows a rather stable behavior for all the cases, and this is due to that fact that the IRNSS satellites geometry for the mentioned two locations has a large extent along the East-West direction. The north standard deviation stabilizes as well provided that the IRNSS is integrated with GPS III.

As Fig. 12 shows, ambiguity resolution can be conducted instantaneously always at ($\phi = 0°,\ \lambda = 83°$) and most of the time at ($\phi = 40°,\ \lambda = 65°$), when integrating IRNSS L5-signal with GPS Block IIF L5-signal. The corresponding fixed north and east standard deviations, given $\sigma_{p_I} = 30\,\text{cm}$, $\sigma_{p_G} = 20\,\text{cm}$, $\sigma_{\phi_I} = \sigma_{\phi_G} = 1\,\text{mm}$, become around 250

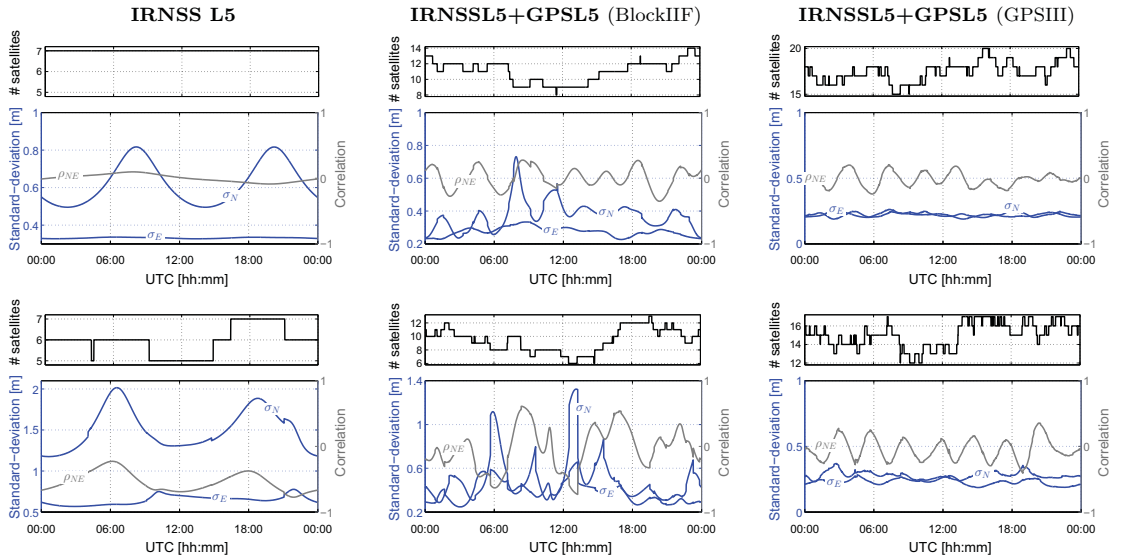

Fig. 16 Time series of the number of visible satellites (*black*), unconstrained single-epoch float east and north standard deviations (*blue* curves) and their corresponding correlation coefficient (*gray* curve) on DOY 156 of 2016 with the cutoff angle of 10° for locations (*top row*) $\phi = 0°$, $\lambda = 83°$ and (*bottom row*) $\phi = 40°$, $\lambda = 65°$. These graphs are computed based on $\sigma_{P_I} = 30\,\text{cm}$, $\sigma_{P_G} = 20\,\text{cm}$ and $\sigma_{\phi_I} = \sigma_{\phi_G} = 1\,\text{mm}$

times better than their float counterparts in Fig. 16 (middle). As was mentioned earlier, when the GPS III with the capability of transmitting L5 signals becomes fully operational, the 24-h instantaneous ambiguity-resolved positioning would be realized for all the locations within the IRNSS service area upon integration of IRNSS with GPS III.

6 Summary and concluding remarks

In this contribution, for the fully operational IRNSS as a stand-alone system and also in combination with GPS, we provided an initial assessment of L5 integer ambiguity resolution and positioning performance. We studied the noise characteristics of the L5-signal for both IRNSS and GPS through carrier-to-noise density, measurement precision and time correlation. The results show that the GPS data have a significantly lower noise level than that of IRNSS, particularly in case of the code data. Also the time correlation of both the constellations can be neglected provided that the multipath impact is corrected for, even if 1-s data are used. We therefore based all our empirical analyses of ambiguity resolution and positioning on the multipath-corrected 1-s data collected by two stations at Perth.

Using real data, single-epoch L5 ambiguity resolution performance was assessed by means of two scalar measures: ambiguity dilution of precision (ADOP) and easy-to-compute bootstrapped success rate, in the framework of unconstrained/height-constrained and single system/dual system. Integrating the IRNSS with GPS Block IIF, ADOP experiences a dramatic decrease particularly when more than one GPS satellite are in view. We also compared empirical and formal success rates for the mentioned underlying models, thereby showing the consistency between data and models.

The agreement between our empirical outcomes and their formal counterparts implies that the easy-to-compute formal values can indeed be used to predict the expected ambiguity resolution performance. We conducted a formal analysis of the number of epochs needed to fix the DD ambiguities with the success rate of 99.9% over the IRNSS primary and secondary service area. Providing a 24-h time series of the number of epochs, we made use of the boxplot concept to give the statistical properties of this time series. The underlying model varied from single-system IRNSS to dual-system IRNSS + GPS, from unconstrained to height-constrained ($\sigma_h = 1\,\text{m}$), and from kinematic to static. As to the stand-alone IRNSS, our results showed that as one goes further away from the IRNSS constellation central location ($\phi = 0°$, $\lambda = 83°$), the ambiguity resolution performance gets poorer. Excluding the locations within ($0° < \phi < 20°$, $65° < \lambda < 101°$), the IRNSS user needs a considerably long time to fix the DD ambiguities with $Ps = 99.9\%$.

This time period can notably decrease if one employs higher sampling rates.

Integration of IRNSS with the GPS Block IIF brings a huge benefit to the users within the IRNSS service area, especially for those on the border of the secondary service area, such that the median for all the locations becomes one to two epochs, and the variability of the number of epochs over the 24-h period reduces. For this case, (almost) instantaneous ambiguity resolution is feasible during the whole day for those locations within ($0° < \phi < 20°$, $65° < \lambda < 101°$). For the case when the fully operational GPS III with the capability of transmitting L5 signal has been realized, we computed the required number of epochs for fixing the DD ambiguities with $Ps = 99.9\%$ and $Ps = 99.99\%$ using IRNSS + GPS III. Our computations showed that instantaneous ambiguity resolution for both the values of success rate becomes always feasible for all the locations within the IRNSS service area.

Next to the ambiguity resolution performance, we also investigated the positioning capability of stand-alone IRNSS (L5) and IRNSS + GPS (L5). All the empirical and formal values were in agreement with each other, further confirming the consistency between data and model. While the scatter plot corresponding with single-system IRNSS looked ellipsoidal, that corresponding with IRNSS + GPS Block IIF (L5) was non-ellipsoidal due to the significant change in receiver-satellite geometry. Integrating IRNSS L5 with GPS Block IIF L5 observations improved the baseline estimation precision considerably w.r.t. stand-alone IRNSS L5. Comparing the time series of the fixed height solution with that of the ADOP, the wrong ambiguity fixing occurs during the periods of large ADOPs. We also showed despite large fluctuations in float height solution, DD ambiguities can be correctly fixed. This indicates that while a receiver-satellite geometry can be poor for positioning, it can be strong enough for ambiguity resolution. Finally, we provided a formal analysis of the positioning performance for two stations within the primary service area. The underlying model varied from IRNSS (L5) to IRNSS + GPS Block IIF (L5) to IRNSS + GPS III (L5). As the model gets stronger, the level of standard deviations decreases and their time series stabilizes.

Acknowledgements This work has been done in the context of the Positioning Program Project 1.19 "Multi-GNSS PPP-RTK Network" of the Cooperative Research Centre for Spatial Information (CRC-SI). The second author is the recipient of an Australian Research Council (ARC) Federation Fellowship (Project number FF0883188). This support is gratefully acknowledged.

References

Amiri-Simkooei AR, Tiberius CCJM (2007) Assessing receiver noise using GPS short baseline time series. GPS Solut 11(1):21–35

Amiri-Simkooei AR, Teunissen PJG, Tiberius CCJM (2009) Application of least-squares variance component estimation to GPS observables. J Surv Eng 135(4):149–160

Babu R, Mula P, Ratnakara SC, Ganeshan AS (2015) IRNSS satellite parameter estimation using combination strategy. Glob J Sci Front Res 15(3):87–95

Bensky A (2016) Wireless positioning technologies and applications. Artech House, London

Chandrasekhar MV, Rajarajan D, Satyanarayana G, Tirmal N, Rathnakara SC, Ganeshan AS (2015) Modernized IRNSS broadcast ephemeris parameters. Control Theory Inf 5(2):1–9

de Bakker PF, Tiberius CCJM, van der Marel H, van Bree RJP (2012) Short and zero baseline analysis of GPS L1 C/A, L5Q, GIOVE E1B, and E5aQ signals. GPS Solut 16(1):53–64

Euler HJ, Goad CC (1991) On optimal filtering of GPS dual frequency observations without using orbit information. Bull Geod 65(2):130–143

Ganeshan AS, Ratnakara SC, Srinivasan N, Rajaram B, Tirmal N, Kartik A (2015) First position fix with IRNSS, Inside GNSS, pp 48–52. http://www.insidegnss.com/node/4545. Accessed 19 Apr 2016

Godha S, Cannon M (2007) GPS/MEMS INS integrated system for navigation in urban areas. GPS Solut 11(3):193–203

GPS Directorate (2011) Navstar GPS space segment/user segment L5 interfaces (IS-GPS-705B). Technical report

GPS World (2016) First GPS III satellite completes critical test. http://gpsworld.com/first-gps-iii-satellite-completes-critical-test/, published 19 Jan 2016, Accessed 9 Aug 2016

Hofmann-Wellenhof B, Lichtenegger H, Collins J (2013) Global positioning system: theory and practice. Springer, Berlin

ISRO (2014a) INDIAN REGIONAL NAVIGATION SATELLITE SYSTEM: signal in space ICD for standard positioning service, version 1.0. ISRO Satellite Centre, June 2014

ISRO (2014b) PSLV-C22/IRNSS-1A. http://www.isro.gov.in/sites/default/files/pdf/pslv-brochures/PSLVC22.pdf. Accessed 1 Sep 2015

ISRO (2014c) PSLV-C24/IRNSS-1B. http://www.isro.gov.in/sites/default/files/pslv-c24-brochure.pdf. Published Mar 2014, Accessed 1 Sept 2015

ISRO (2014d) PSLV-C26/IRNSS-1C. http://www.isro.gov.in/sites/default/files/pdf/pslv-brochures/PSLV-C26

ISRO (2015) PSLV-C27/IRNSS-1D. http://www.isro.gov.in/sites/default/files/pdf/pslv-brochures/PSLV-C27-IRNSS-1D-BROCHURE.pdf. Published Mar 2015, Accessed 1 Sept 2015

ISRO (2016a) PSLV-C31/IRNSS-1E. http://www.isro.gov.in/sites/default/files/pslv-c31brochure.pdf. Published Jan 2016, Accessed 19 Apr 2016

ISRO (2016b) PSLV-C32/IRNSS-1F. http://www.isro.gov.in/sites/default/files/pslv-c32-final.pdf. Published Mar 2016, Accessed 19 Apr 2016

ISRO (2016c) PSLV-C33/IRNSS-1G. http://www.isro.gov.in/sites/default/files/pslv-c33-brochure.pdf. Published Apr 2016, Accessed 1 June 2016

Kumari A, Samal K, Rajarajan D, Swami U, Babu R, Kartik A, Rathnakara SC, Ganeshan AS (2015) Precise modeling of solar radiation pressure for IRNSS satellite. J Nat Sci Res 5(3):35–43

Lockheed Martin (2013) Lockheed Martin powers on the first GPS III satellite. http://www.lockheedmartin.com.au/us/news/press-releases/2013/february/Feb28.html. Published 28 Feb 2013, Accessed 9 Aug 2016

Marquis W, Shaw M (2016) GPS III: bringing new capabilities to the global community. Inside GNSS, pp 34–48. http://www.insidegnss.com/auto/sepoct11-Marquis.pdf. Accessed 9 Aug 2016

Montenbruck O, Steigenberger SR (2015) IRNSS orbit determination and broadcast ephemeris assessment. In: Proceedings of the 2015

international technical meeting of the Institute of Navigation, Dana Point, California, January 2015, pp 185–193
Mozo GA, Piriz R, Lainez SMD, Romay MMM (2010) Multisystem real time precise-point-positioning, today with GPS+GLONASS in the near future also with QZSS, Galileo, Compass, IRNSS. In: International symposium on GPS/GNSS, Taipei, Taiwan, October 2010
Nadarajah N, Khodabandeh A, Teunissen PJG (2015) Assessing the IRNSS L5-signal in combination with GPS, Galileo, and QZSS L5/E5a-signals for positioning and navigation. GPS Solut 20(2):289–297
Odijk D, Teunissen PJG (2008) ADOP in closed form for a hierarchy of multi-frequency single-baseline GNSS models. J Geod 82(8):473–492
Odijk D, Teunissen PJG (2013) Characterization of between-receiver GPS-Galileo inter-system biases and their effect on mixed ambiguity resolution. GPS Solut 17(4):521–533
Odijk D, Teunissen PJG, Huisman L (2012) First results of mixed GPS+GIOVE single-frequency RTK in Australia. J Spat Sci 57(1):3–18
Odijk D, Nadarajah N, Zaminpardaz S, Teunissen PJG (2016) GPS, Galileo, BDS, QZSS and IRNSS differential ISBs estimation and application. GPS Solut. doi:10.1007/s10291-016-0536-y
Odolinski R, Teunissen PJG (2016) Single-frequency, dual-GNSS versus dual-frequency, single-GNSS a low-cost and high-grade receivers GPS-BDS RTK analysis. J Geod. doi:10.1007/s00190-016-0921-x
Rao VG (2013) Proposed LOS fast TTFF signal design for IRNSS. Ph.D thesis. University of Calgary
Rethika T, Mishra S, Nirmala S, Rathnakara SC, Ganeshan AS (2013) Single frequency ionospheric error correction using coefficients generated from regional ionospheric data for IRNSS. Indian J Radio Space Phys 42:125–130
Sarma AD, Sultana Q, Srinivas VS (2010) Augmentation of Indian regional navigation satellite system to improve dilution of precision. J Navig 63(02):313–321
Sekar SB, Sengupta S, Bandyopadhyay K (2012) Spectral compatibility of BOC (5, 2) modulation with existing GNSS signals. In: Position location and navigation symposium (PLANS), 2012 IEEE/ION, IEEE, pp 886–890
Tegedor J, Øvstedal O (2014) Triple carrier precise point positioning (PPP) using GPS L5. Surv Rev 46(337):288–297
Teunissen PJG (1990) GPS op afstand bekeken In: een halve eeuw in de goede richting . Lustrumboek Snellius 1985–1990, DUM Delft pp 215–233
Teunissen PJG (1997) A canonical theory for short GPS baselines. Part I: the baseline precision. J Geod 71(6):320–336
Teunissen PJG (1998a) A proof of Nielsen's conjecture on the relationship between dilution of precision for point positioning and for relative positioning with GPS. IEEE Aerosp Electron Syst 34(2):693–695
Teunissen PJG (1998b) Success probability of integer GPS ambiguity rounding and bootstrapping. J Geod 72(10):606–612
Teunissen PJG (1999) An optimality property of the integer least-squares estimator. J Geod 73(11):587–593
Teunissen PJG, Amiri-Simkooei AR (2008) Least-squares variance component estimation. J Geod 82(2):65–82
Teunissen PJG, Odolinski R, Odijk D (2014) Instantaneous BeiDou+GPS RTK positioning with high cut-off elevation angles. J Geod 88(4):335–350
Thoelert S, Montenbruck O, Meurer M (2014) IRNSS-1A: signal and clock characterization of the Indian regional navigation system. GPS Solut 18(1):147–152
Verhagen S, Teunissen PJG (2014) Ambiguity resolution performance with GPS and BeiDou for LEO formation flying. Adv Space Res 54(5):830–839
Zaminpardaz S, Teunissen PJG, Nadarajah N (2016a) GLONASS CDMA L3 ambiguity resolution and positioning. GPS Solut. doi:10.1007/s10291-016-0544-y
Zaminpardaz S, Teunissen PJG, Nadarajah N (2016) IRNSS stand-alone positioning: first results in Australia. J Spat Sci 61(1):5–27. doi:10.1080/14498596.2016.1142398
Zhu J, Santerre R (2002) Improvement of GPS phase ambiguity resolution using prior height information as a quasi-observation. Geomatica 56(3):211–221

6 IRNSS+GPS L5 RTK performance (Part 2: An analysis of survey-grade and low-cost receivers)

This chapter is covered by the following publication:

Zaminpardaz S., Teunissen P.J.G., Nadarajah N. (2017c) L5 RTK Over India: IRNSS and GPS. Inside GNSS, 12(1):48-55

L5 RTK Over India: IRNSS and GPS

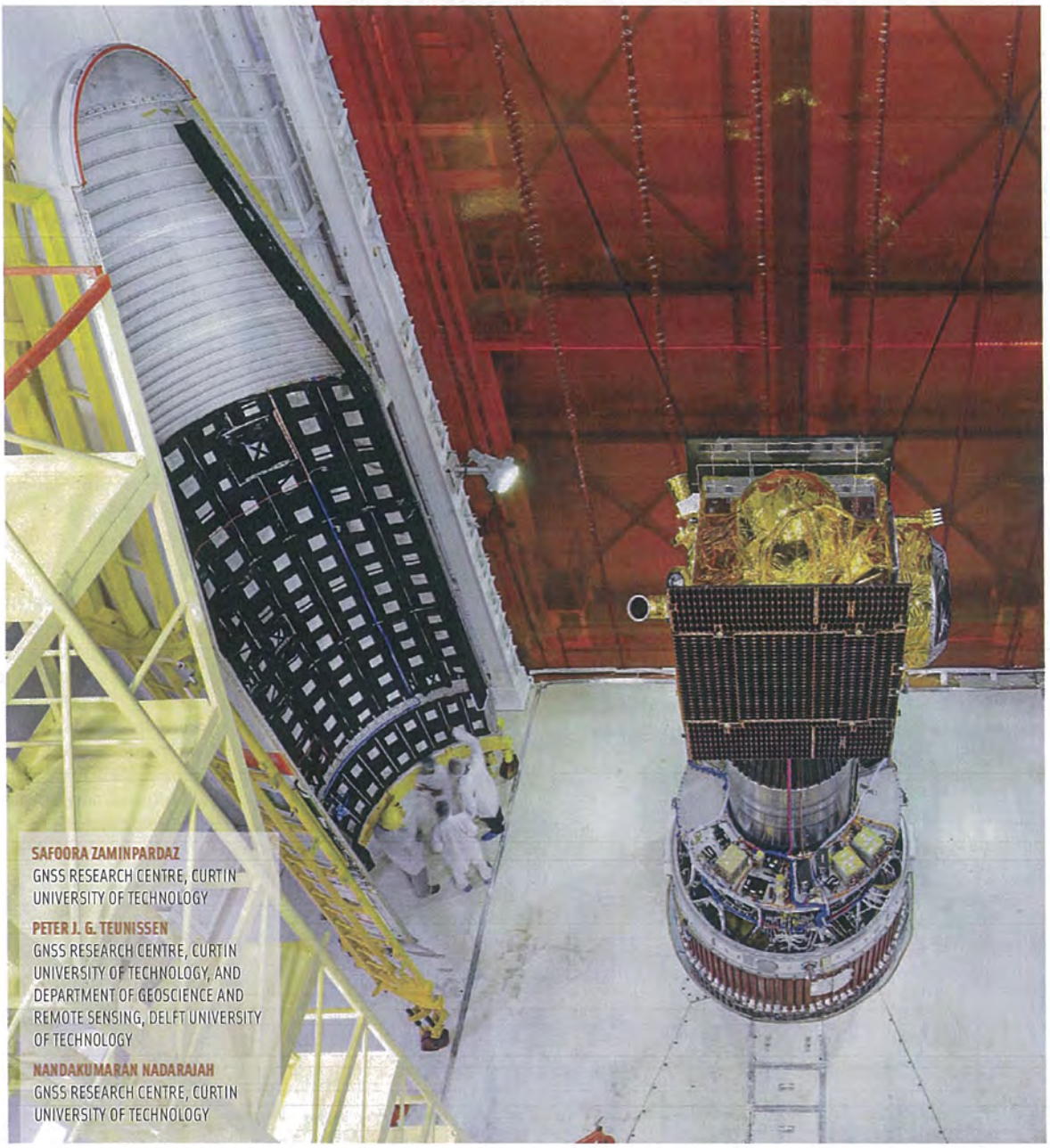

SAFOORA ZAMINPARDAZ
GNSS RESEARCH CENTRE, CURTIN UNIVERSITY OF TECHNOLOGY

PETER J. G. TEUNISSEN
GNSS RESEARCH CENTRE, CURTIN UNIVERSITY OF TECHNOLOGY, AND DEPARTMENT OF GEOSCIENCE AND REMOTE SENSING, DELFT UNIVERSITY OF TECHNOLOGY

NANDAKUMARAN NADARAJAH
GNSS RESEARCH CENTRE, CURTIN UNIVERSITY OF TECHNOLOGY

Indian Space Research Organization

A team of researchers in Australia provide the first assessment of L5 integer ambiguity resolution and positioning performance for the fully operational Indian Regional Navigation Satellite System (IRNSS) as a standalone system and also in combination with GPS. They based empirical analyses on data collected by two GNSS receivers at Curtin University, Perth, Australia, and formal analyses are carried out at several onshore locations within the IRNSS service area. These analyses assessed the feasibility of single-epoch L5 real-time kinematic (RTK) positioning in the framework of different underlying models, varying from standalone IRNSS to standalone GPS to IRNSS+GPS.

The Indian Regional Navigation Satellite System (IRNSS) became fully operational in May 2016 with the operational name of NavIC (Navigation with Indian Constellation). The system consists of three geostationary orbit (GEO) satellites and four inclined geosynchronous orbit (IGSO) satellites (see Table 1). IRNSS has been developed by the Indian Space Research Organization (ISRO) with the objective of offering positioning, navigation and timing (PNT) to the users in its service area. The IRNSS satellites transmit navigation signals on frequency L5 (1176.45 MHz) which is shared by three other GNSSs, i.e., GPS, Galileo and the Quasi-Zenith Satellite System

Satellite	Type	Longitude	Inclination	Launch date
IRNSS-1A (I1)	IGSO	55° E	29.0°	July 2013
IRNSS-1B (I2)	IGSO	55° E	31.0°	April 2014
IRNSS-1C (I3)	GEO	83° E	-	October 2014
IRNSS-1D (I4)	IGSO	111.75° E	30.5°	March 2015
IRNSS-1E (I5)	IGSO	111.75° E	28.1°	January 2016
IRNSS-1F (I6)	GEO	32.5° E	-	March 2016
IRNSS-1G (I7)	GEO	129.5° E	-	April 2016

Table 1 Information on the IRNSS/NavIC satellites (ISRO, 2016).

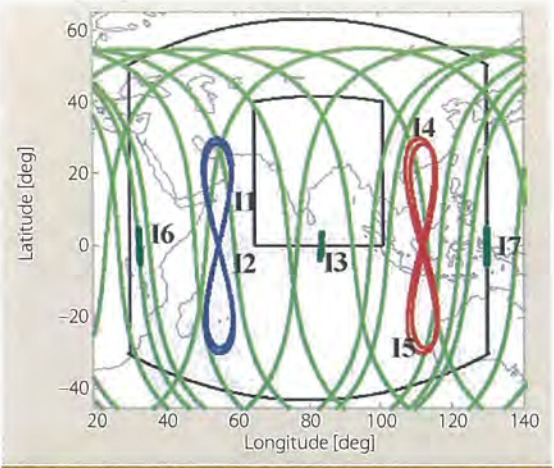

FIGURE 1 Groundtrack of IRNSS and GPS Block IIF (light green) satellites on day of year (DOY) 183 of 2016. The inner and outer black boundaries indicate the border of the IRNSS primary and secondary service areas, respectively.

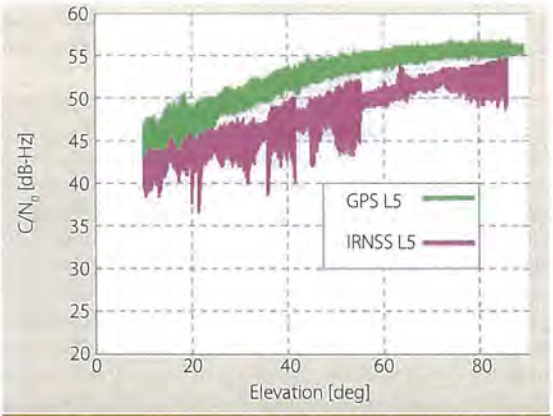

FIGURE 2 Carrier-to-noise-density (C/N_0) for IRNSS L5 and GPS Block IIF L5 signals tracked by a multi-GNSS, multi-frequency receiver, connected to a choke ring antenna at Perth, Australia, on DOY 183 of 2016.

Frequency	σ_p [cm]	σ_φ [mm]
IRNSS L5	26	2
GPS L5	17	1

Table 2 Estimation of the undifferenced code σ_p and phase σ_φ zenith-referenced standard deviations

# antennas	2
Antenna type	choke ring
Receiver type	multi-GNSS, multi-frequencyx
Location	Curtin University, Perth, Australia
Data type	IRNSS L5, GPS L5
Cut-o angle	10°
Date and time	DOY 183 of 2016

Table 3 Characteristics of the experiment conducted for this study

(QZSS), making the IRNSS interoperable with those systems.

All the satellites belonging to the latest generation of GPS, called Block IIF, have been sending out the L5 signal since 2010 as part of the GPS modernization.

With the launch of the last satellite of Block IIF on February 2016, it now has all its 12 satellites operational. The next generation of GPS satellites, GPS III, will also transmit the L5 signal. GPS III is planned to become fully operational with a constellation of 32 satellites by 2025, and the first launch thereof is now expected in spring of 2018.

In this article, we provide the very first empirical and formal L5 ambiguity resolution and corresponding positioning results of the fully operational IRNSS as a standalone system and also in combination with the fully operational GPS Block IIF. For several onshore locations within the IRNSS service area (Figure 1), we investigated the potential of single-frequency (L5) single-epoch real-time kinematic (RTK) positioning. This is carried out for different underlying models, including standalone IRNSS, IRNSS+GPS Block IIF, standalone GPS III and IRNSS+GPS III. With the emergence of low-cost single-frequency RTK receivers and their mass-market applications, our analysis is done for geodetic survey-grade receivers as well as low-cost receivers.

Measurement Experiment

We based our analyses on the IRNSS L5 and GPS L5 data-set recorded by two GNSS receivers of a short baseline between the receiver pair (CUBB-CUCC) at Curtin University, Perth, Australia. Figure 2 shows the observed carrier-to-noise densities (C/N_0) of IRNSS and GPS L5-signal.

As the GPS L5 signal has larger C/N_0 values compared to the IRNSS L5, its precision is expected to be higher with respect to the IRNSS L5. The estimated code and phase standard deviations given in Table 2 confirm this. We used the broadcast ephemeris for both constellations. Table 3 provides further details on the data-set that we used.

Positioning and Ambiguity Resolution Analysis: Empirical and Formal

Here, we concentrate on the L5 positioning performance for both single-system IRNSS and dual-system IRNSS+GPS Block IIF. The data forming the basis of our analysis are one Hertz–sampled on DOY 183 of 2016. Table 4 lists the single-epoch formal and empirical standard deviations of the CUBB-CUCC baseline components.

These results assume that the DD ambiguities are not yet fixed to their integer values, thus being called *float* solutions. Therefore, we obtained them by using the less precise code observations since the phase measurements are fully reserved for the DD ambiguities. Integrating IRNSS L5 with GPS L5 observations, the baseline estimation precision improves by three to four times horizontally and 2.5 times vertically.

Upon fixing the DD ambiguities, the very precise phase observations take the leading role in baseline estimation. The improvement of the ambiguity-resolved

estimations, known as fixed solutions, with respect to their float counterparts, is a factor of 130 in case of standalone IRNSS and 150 in case of IRNSS+GPS Block IIF.

Figure 3 depicts the single-epoch one-second horizontal scatter plot (a) and height time series (b) of the CUBB-CUCC baseline float solutions (in *gray*), correctly fixed solutions (in *green*) and wrongly fixed solutions (in *red*) on the basis of L5 observables of IRNSS+GPS Block IIF collected on DOY 183 of 2016 with the cut-off angle of 10 degrees. The non-ellipsoidal shape of the scatter plot is due to the significant changes that the receiver-satellite geometry experiences during the 24-hour period. The panel (b) also contains the 95 percent formal confidence interval based on the float height standard deviation of which the signature is in good agreement with that of the height error time series, confirming the consistency between data and model.

The occurrence of incorrect ambiguity fixing can be explained by the easy-to-compute scalar diagnostic ADOP (ambiguity dilution of precision) introduced in the article by P. J. G. Teunissen (1997) and referenced in the Additional Resources section near the end of this article. It is defined as the square root of the determinant of the ambiguity variance matrix raised to the power of one over the ambiguity dimension. As a rule of thumb, an ADOP smaller than about 0.12 cycle corresponds to an ambiguity success rate larger than 99.9 percent, as introduced in the article by D. Odijk and P.J. G. Teunissen, (2008) (see Additional Resources). The panel (c) of Figure 3 depicts the time series of the single-epoch ADOP corresponding with IRNSS+GPS Block IIF L5.

Comparing the time series of the ambiguity-fixed height solution with that of the ADOP, the incorrect ambiguity fixing happens during the periods when ADOPs are larger than the value of 0.12 cycle. During some periods such as UTC [03:00-05:00], although the float height solution shows large fluctuations, the DD ambiguities can still be correctly fixed. Therefore, while a receiver-satellite geometry can be poor for positioning, it can still be strong enough for ambiguity resolution.

As our measure to assess the integer ambiguity resolution performance, we made use of the ambiguity resolution success rate, known as the probability of correct integer estimation described in the article by P. J. G. Teunissen (1998). The 24-hour

	IRNSS L5		IRNSS+GPS Block IIF L5	
	empirical	formal	empirical	formal
σ_n [m]	1.56	1.39	0.40	0.40
σ_e [m]	1.02	1.01	0.45	0.46
σ_h [m]	2.43	2.61	1.02	1.07

Table 4 Single-epoch empirical and formal standard deviations of the CUBB-CUCC baseline float estimations on DOY 183 of 2016 with the cut-off angle of 10 degrees. The underlying models are standalone IRNSS L5 and IRNSS+GPS Block IIF L5 with σ_x representing the north standard deviation; σ_e, the east standard deviation; and σ_h, the height standard deviation.

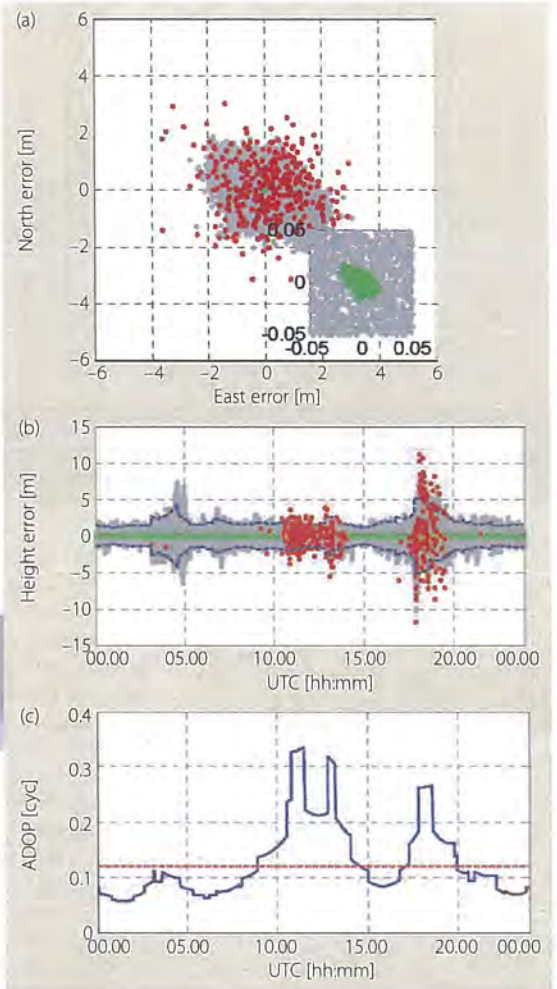

FIGURE 3 (a) IRNSS+GPS Block IIF L5 single-epoch horizontal baseline scatter plot corresponding with receiver pair CUBB-CUCC on DOY 183 of 2016 with the cut-off angle of 10 degrees with *gray* representing a float solution; *green*, a correctly fixed solution; and *red*, an incorrectly fixed solution. (b) The corresponding time series of the height component. The *blue* dashed lines indicate the 95 percent formal confidence interval. (c) The corresponding time series of the single-epoch ADOP (*blue*) and the value of 0.12 cycle (*red* dashed line).

average single-epoch formal and empirical success rates were in good agreement with each other, confirming the consistency between model and data. The results also showed that upon integrating IRNSS with GPS Block IIF, the single-epoch integer ambiguity resolution success rate improves dramatically from about Ps =15% to Ps = 94%.

Ambiguity Resolution Performance for a Kinematic IRNSS User

The demonstrated consistency between our formal results and

their empirical counterparts indicates that the easy-to-compute formal values can indeed predict the expected ambiguity-resolution performance. Here, we turn our focus from a single-epoch scenario to a multi-epoch scenario and conduct a formal analysis of the required number of epochs to fix the DD ambiguities with the success rate of Ps =99.9% . In that regard, we consider several onshore locations over the IRNSS primary and secondary service area (see Figure 4).

Remaining constant over time (in case of no loss-of-lock or cycle slip), the ambiguity resolution performance can improve if this time-constancy is exploited through a kalman filter. For both geodetic survey-grade receivers and low-cost receivers, we compute a 24-hour time series of the number of epochs needed to fix the DD ambiguities with Ps = 99.9% for a *kinematic user* in the framework of different underlying models. In order to show the statistical properties of these time series schematically, we make use of the boxplot concept introduced in the article by John W. Tukey (1997) referenced in the Additional Resources section near the end of this article. Our boxplot results are based on a 30-second sampling rate.

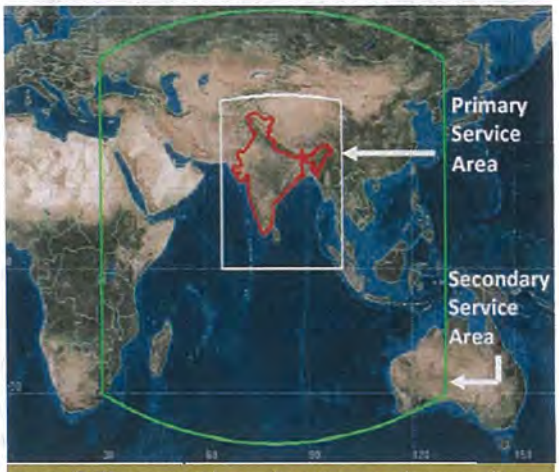

FIGURE 4 IRNSS primary and secondary service area (image credit: Indian Space Research Organization).

Geodetic Survey-Grade Receiver Results. Results presented in this subsection are on the basis of *four* underlying models, i.e., standalone IRNSS, IRNSS+GPS Block IIF, (fully-operational) standalone GPS III, and IRNSS+GPS III. We did not consider the case of standalone GPS Block IIF as this constellation contains only 12 satellites, thus having sometimes fewer than four satellites visible at different locations within the IRNSS service area.

For the geodetic survey-grade receiver, the zenith-referenced code standard deviation that we use for the GPS L5-signal is σ_{P_G} = 20 cm — as introduced in an article by Nandakumaran Nadarajah *et alia* (2015) (Additional Resources) — and for IRNSS L5-signal is σ_{P_I} = 30 cm, which is considered less precise than the GPS L5-signal (see Figure 2). The phase standard deviation for both systems is taken as $\sigma_{\varphi_G} = \sigma_{\varphi_I}$ = 2mm.

Figure 5 shows the boxplots of the number of epochs to fix the ambiguities with Ps = 99.9%. Each

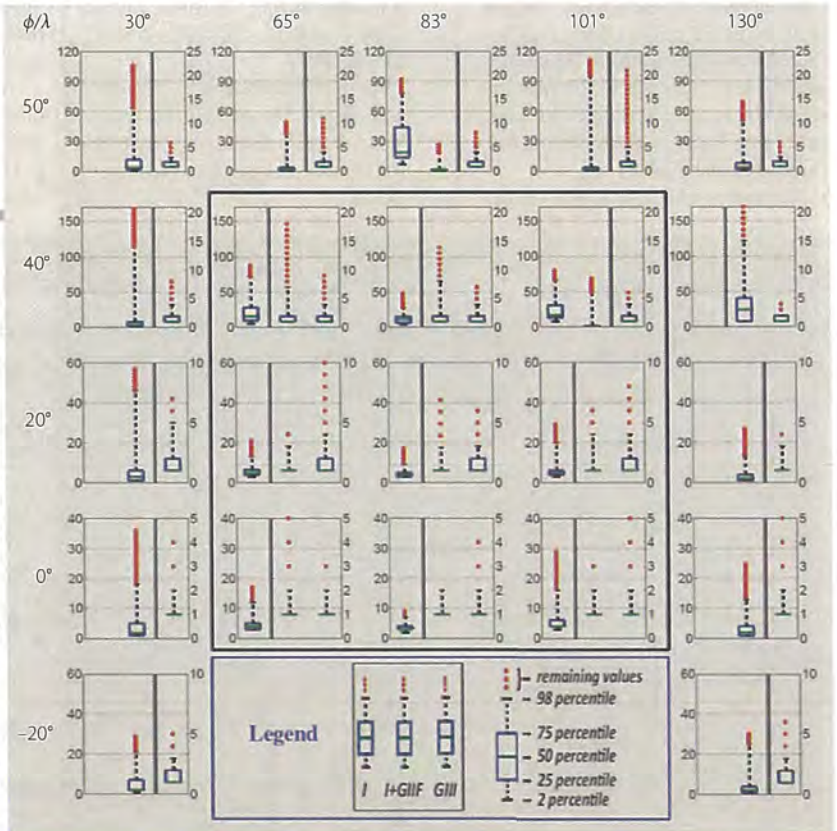

FIGURE 5 Boxplots of the required number of epochs to fix the L5 DD ambiguities with Ps = 99.9% using 30-second sampling rate over the IRNSS service area, on DOY 183 of 2016 with the cut-off angle of 10 degrees. The primary service area is located within the *black* border. Each panel shows *at most* three boxplots corresponding with different underlying models: from left to right, the IRNSS *(I)*, IRNSS+GPS Block IIF *(I+GIIF)* and GPS III *(GIII)* model, respectively. In each panel two vertical axes with different ranges are used. The boxplots to the left of the *gray* line should be read according to the left axis, and those to the right of the *gray* line should be read according to the right axis. These boxplots are computed based on σ_{P_I} = 30 cm, σ_{P_G} = 20 cm and $\sigma_{\varphi_G} = \sigma_{\varphi_I}$ = 2 mm.

panel contains, from left to right, the results of kinematic standalone IRNSS, IRNSS+GPS Block IIF and standalone GPS III, which are abbreviated in the legend to *I*, *I+GIIF* and *GIII*, respectively. Note that the results of the IRNSS+GPS III are not illustrated as this scenario always provides users within the IRNSS service area with the *instantaneous ambiguity resolution* with *Ps* = 99.9%, hence, the single-epoch RTK positioning. Also we did not show the standalone IRNSS results when the 75th percentile is larger than 50 epochs.

In order for our boxplots to be more readable, we used two vertical axes with different ranges in each panel. The boxplots to the le⊠ of the shown *gray* line should be read according to the le⊠ axis, and those to the right of the *gray* line should be read according to the right axis. From Figure 5, the following conclusions can be made:

- Regarding the standalone IRNSS, as one goes further away from the central location (⊠=0°; ⊠=83°), the ambiguity resolution performance gets poorer. Excluding the locations within (0°< ⊠ <20°; 65°< ⊠ <101°), the standalone IRNSS user needs a considerably long time to fix the DD ambiguities with *Ps* = 99.9%.
- Integration of the IRNSS with the GPS Block IIF brings a huge benefit to the users within the IRNSS service area, especially for those on the border of the secondary service area. Nearly instantaneous ambiguity resolution and RTK positioning is feasible during the whole day for those locations within (0°< ⊠ <20°; 65°< ⊠ <101°).
- As to the standalone GPS III performance, one can see that on average fewer than 10 epochs are needed to fix the DD ambiguities with *Ps* = 99.9%.
- Given *Ps* = 99.9%, IRNSS+GPS III always provides the users within the IRNSS service area with the *instantaneous ambiguity resolution* and, hence, single-epoch RTK positioning.

Low-Cost Receiver Results. Thus far, with *Ps* =99.9%, we have shown that the ambiguity resolution can be carried out *almost* instantaneously when using GPS III L5, and instantaneously when using IRNSS+GPS III L5. Now, we will assess the ambiguity resolution performance of these two underlying models when using low-cost single-frequency receivers. For such receivers, the zenith-referenced observation standard deviations are taken as σ_{P_I} = 100 cm, σ_{P_G} = 75 cm and $\sigma_{\varphi_G}=\sigma_{\varphi_I}$ = 3 mm.

Figure 6 shows the boxplots of the number of epochs needed to fix the ambiguities with *Ps* = 99.9%, for GPS III L5 (Le⊠) and IRNSS+GPS III L5 (Right), which are abbreviated in the legend to

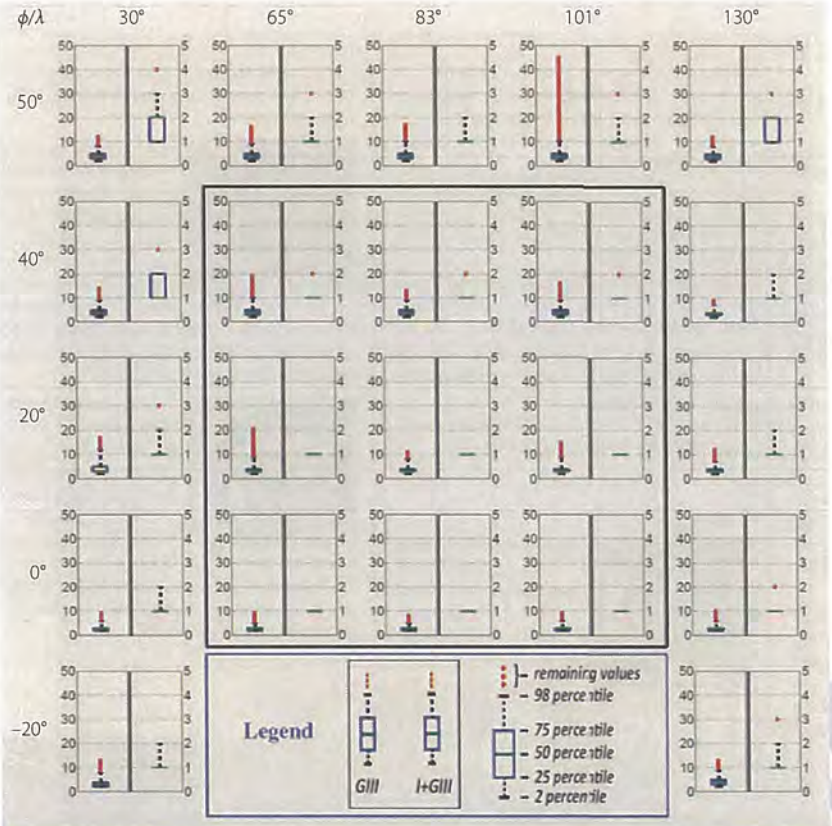

FIGURE 6 Boxplots of the required number of epochs to fix the L5 DD ambiguities with *Ps* = 99.9% using 30-second sampling rate over the IRNSS service area, on DOY 183 of 2016 with the cut-off angle of 10 degrees. The primary service area is located within the *black* border. Each panel shows two boxplots corresponding to different underlying models: from left to right, the GPS III *(GIII)* and IRNSS+GPS III *(I+GIII)* model, respectively. In each panel, two vertical axes with different ranges are used. The boxplots to the left of the *gray* line should be read according to the left axis, and those to the right of the *gray* line should be read according to the right axis. These boxplots are computed based on σ_{η_j} = 100 cm, σ_{I_G} = 75 cm and $\sigma_{\tau_G} = \sigma_{\tau_j}$ = 3 mm.

GIII and *I+GIII*, respectively. From this figure, one can conclude:

- For the single-system GPS III, on average fewer than 20 epochs are required to fix the DD ambiguities.
- Integrating GPS III with IRNSS, almost instantaneous (less than five epochs) ambiguity resolution becomes feasible at all the locations within the IRNSS service area. Therefore, almost instantaneous RTK positioning would become possible.

Summary and Conclusion

For the fully operational IRNSS as a standalone system and also in combination with GPS, we have provided a first assessment of L5 integer ambiguity resolution and positioning performance. Following an empirical analysis and showing the consistency between data and model, we performed a formal analysis of the number of epochs needed to successfully fix the DD ambiguities for a kinematic user within the IRNSS service area for both geodetic survey–grade and low-cost single-frequency receivers.

Given a geodetic survey-grade receiver, the standalone IRNSS user needs quite a long time to fix the DD ambiguities. Meanwhile, the IRNSS+GPS Block IIF as well as the standalone GPS III user can carry out almost instantaneous RTK positioning during the whole day for most of the locations within the IRNSS primary service area. With such a high-grade receiver, single-epoch RTK becomes feasible provided that IRNSS is integrated with GPS III. Switching from geodetic survey-grade to low-cost receivers, this integration can still provide almost instantaneous RTK positioning at all the locations within the IRNSS service area.

Manufacturers

The receivers used to obtain the IRNSS and GPS L5 signals were the TRE_G3TH_8 from **JAVAD GNSS**, San Jose, California USA, and Moscow, Russia. Two TRM59800.00 SCIS antennas from **Trimble**, Sunnyvale, California, were used with the receiver.

Additional Resources

[1] Bensky, A., *Wireless Positioning Technologies and Applications*, Artech House, 2016

[2] GPS Directorate, *Navstar GPS Space Segment/User Segment L5 Interface Specification (IS-GPS-705B)*, 2011

[3] GPS World, "First GPS III Satellite Completes Critical Test," available online at <http://gpsworld.com/first-gps-iii-satellite-completes-critical-test/>, published January 19, 2016, accessed August 9, 2016

[4] Indian Space Research Organization, *Indian Regional Navigation Satellite System: Signal in Space ICD for Standard Positioning Service, Version 1.0*, ISRO Satellite Centre, June 2014

[5] Indian Space Research Organization, *PSLV-C33/IRNSS-1G*, available from <http://www.isro.gov.in/sites/default/files/pslv-c33-brochure.pdf>, published April 2016; accessed June 1, 2016

[6] Lockheed Martin, "Lockheed Martin Powers on the First GPS III Satellite," available from<http://www.lockheedmartin.com.au/us/news/press-releases/2013/february/Feb28.html>, published February 28, 2013; accessed 9 August 2016

[7] Marquis W., and M. Shaw (2016), GPS III: Bringing New Capabilities to the Global Community," September/October 2011, *Inside GNSS*, pp. 34–48, available online at <http://www.insidegnss.com/auto/sepoct11-Marquis.pdf>, accessed August 9, 2016.

[8] Nadarajah N., and A. Khodabandeh, P. J. G. Teunissen PJG, "Assessing the IRNSS L5-Signal in Combination with GPS, Galileo, and QZSS L5/E5a-signals for Positioning and Navigation," *GPS Solutions* 20(2):289–297, 2015

[9] Odijk, D., and P. J. G. Teunissen, "ADOP in Closed Form for a Hierarchy of Multi-Frequency Single-Baseline GNSS Models," *Journal of Geodesy* 82(8):473–492, 2008

[10] Teunissen, P. J. G., (1997), "A Canonical Theory for Short GPS Baselines. Part I: The Baseline Precision. *Journal of Geodesy* 71(6):320–336

[11] Teunissen, P. J. G., (1998), "Success Probability of Integer GPS Ambiguity Rounding and Bootstrapping," *Journal of Geodesy* 72(10):606–612

[12] Tukey, J. W., *Explanatory Data Analysis*, vol 1, Reading, Mass: Addison-Wesley Publishing Co., 1977

Authors

Safoora Zaminpardaz <safoora.zaminpardaz@postgrad.curtin.edu.au> received her M.Sc. in Geodesy from the University of Tehran. She is pursuing her Ph.D. at the GNSS Research Centre, Curtin University, Australia. Her research interests include array-based multi-GNSS positioning, ionosphere sensing, and integrity monitoring.

Peter J. G. Teunissen is a professor of geodesy and navigation and head of Curtin University's GNSS Research Centre and science director of the Cooperative Research Centre for Spatial Information. His current research focuses on multi-GNSS and the modelling of next generation GNSS for high-precision positioning, navigation, and timing applications.

Nandakumaran Nadarajah received his M.A.Sc and Ph.D. in electrical and computer engineering from McMaster University, Canada. Currently, he is working as a research fellow at GNSS Research Centre, Curtin University. His research interests are in multi-GNSS attitude determination and relative navigation, signal processing, and target tracking. IG

7 IRNSS L5 attitude determination

This chapter is covered by the following publication:

Zaminpardaz S., Teunissen P.J.G., Nadarajah N. (2017d) IRNSS/NavIC L5 Attitude Determination. Sensors, MDPI, 17(2), 274, DOI 10.3390/s17020274

sensors

MDPI

Article

IRNSS/NavIC L5 Attitude Determination

Safoora Zaminpardaz [1,*], Peter J.G. Teunissen [1,2] and Nandakumaran Nadarajah [1]

[1] GNSS Research Centre, Department of Spatial Sciences, Curtin University, GPO Box U1987, Perth, WA 6845, Australia; p.teunissen@curtin.edu.au (P.J.G.T.); n.nadarajah@curtin.edu.au (N.N.)

[2] Department of Geoscience and Remote Sensing, Delft University of Technology, PO Box 5048, 2600 GA Delft, The Netherlands

* Correspondence: safoora.zaminpardaz@postgrad.curtin.edu.au

Academic Editor: Assefa M. Melesse

Received: 10 December 2016; Accepted: 25 January 2017; Published: 30 January 2017

Abstract: The Indian Regional Navigation Satellite System (IRNSS) has recently (May 2016) become fully-operational and has been provided with the operational name of NavIC (Navigation with Indian Constellation). It has been developed by the Indian Space Research Organization (ISRO) with the objective of offering positioning, navigation and timing (PNT) to the users in its service area. This contribution provides for the first time an assessment of the IRNSS L5-signal capability to achieve instantaneous attitude determination on the basis of data collected in Perth, Australia. Our evaluations are conducted for both a linear array of two antennas and a planar array of three antennas. A pre-requisite for precise and fast IRNSS attitude determination is the successful resolution of the double-differenced (DD) integer carrier-phase ambiguities. In this contribution, we will compare the performances of different such methods, amongst which the unconstrained and the multivariate-constrained LAMBDA method for both linear and planar arrays. It is demonstrated that the instantaneous ambiguity success rates increase from 15% to 90% for the linear array and from 5% to close to 100% for the planar array, thus showing that standalone IRNSS can realize 24-h almost instantaneous precise attitude determination with heading and elevation standard deviations of 0.05 and 0.10 degrees, respectively.

Keywords: Indian Regional Navigation Satellite System (IRNSS); Navigation with Indian Constellation (NavIC); integer carrier-phase ambiguity resolution; attitude determination; multivariate constrained integer least-squares; MC-LAMBDA

1. Introduction

Developed by the Indian Space Research Organization (ISRO), the Indian Regional Navigation Satellite System (IRNSS) has recently (May 2016) become fully-operational and provided with the operational name of NavIC (Navigation with Indian Constellation). This new addition to Global Navigation Satellite Systems (GNSSs) aims to provide positioning, navigation and timing (PNT) to the users in its service area. The IRNSS satellites transmit navigation signals, based on Code Division Multiple Access (CDMA), on L5 (1176.45 MHz) with a Binary Phase-Shift Key (BPSK (1)) modulation for standard positioning service (SPS) users, and with a Binary Offset Carrier (BOC (5,2)) modulation for restricted service (RS) users [1]. The fully-operational IRNSS constellation consists of three geostationary orbit (GEO) satellites and four inclined geosynchronous orbit (IGSO) satellites (see Table 1).

Table 1. Information on the IRNSS/NavIC satellites [2].

Satellite	Type	Longitude	Inclination	Launch Date
IRNSS-1A (I1)	IGSO	55° E	29.0°	July 2013
IRNSS-1B (I2)	IGSO	55° E	31.0°	April 2014
IRNSS-1C (I3)	GEO	83° E	–	October 2014
IRNSS-1D (I4)	IGSO	111.75° E	30.5°	March 2015
IRNSS-1E (I5)	IGSO	111.75° E	28.1°	January 2016
IRNSS-1F (I6)	GEO	32.5° E	–	March 2016
IRNSS-1G (I7)	GEO	129.5° E	–	April 2016

IRNSS real data have hitherto formed the basis of several studies. The clock stability of I1 is assessed in [3], while the accuracy of a precise model for solar radiation pressure is tested using the I1 and I2 observations in [4]. The data of I1, I2 and I3 are used by [5] for comparison of the orbit determination methods, and by [6] to validate the orbit accuracy with modernized ephemeris parameters. The first positioning results based on the data of I1, I2, I3, and I4 over India are presented in [7], and over Australia in [8]. The observations of I1 and I2 were used by [9] to investigate the quality of the IRNSS navigation messages.

In this contribution, for the first time, an analysis of the *fully-operational* IRNSS L5-signal capability to achieve *instantaneous attitude determination* is carried out. Such an analysis based on only *two* IRNSS satellites, i.e., I1 and I2, was conducted by [10]. Using multiple GNSS antennas rigidly mounted on a platform in known formation, one can determine the attitude of this platform, see e.g., [11–14], which can be a vessel, a land vehicle, an aircraft or a space platform [15–19]. Precise and fast GNSS-based attitude determination would be realized through incorporation of the very precise phase observations, and successful resolution of the double-differenced (DD) integer carrier-phase ambiguities is the key to fully exploit the phase observations. Resulting in the highest possible ambiguity resolution success rate, the Least squares AMBiguity Decorrelation Adjustment (LAMBDA) method developed by [20–22] is the standard method used for the unconstrained mixed-integer GNSS observational model. As for the GNSS attitude model, the local antenna geometry is known in the body (platform) frame, which can be exploited to further improve the ambiguity resolution performance. To realize this, the multivariate constrained (MC-)LAMBDA method has been developed [18,19,23–28]. This method incorporates the known local antenna geometry in a rigorous manner, leading to higher success rates w.r.t. the standard LAMBDA.

In this study, our evaluations are conducted for both a linear array of two antennas and a planar array of three antennas collecting L5 signals of IRNSS at Curtin University, Perth, Australia. We first explain our GNSS-based single-frequency attitude determination method. The performance of the IRNSS L5 observables for the instantaneous attitude determination is presented for both the linear and planar array. It is also shown what improvements are achieved when using MC-LAMBDA instead of standard LAMBDA method. Finally, a summary and conclusions are given.

2. GNSS Observational Model

In this section, the single-frequency GNSS model of observations is described for both the unconstrained and multivariate-constrained scenarios. For the latter, the known body-geometry of the antenna array is taken into account.

2.1. Unconstrained Model

Assume that n antennas, firmly mounted on a platform, are simultaneously tracking m IRNSS satellites on L5 frequency. We further assume that the array is of a small scale such that the differential atmospheric delays (troposphere and ionosphere) and orbital errors between the antennas can be neglected. The multivariate linearized single-epoch DD GNSS array model of observations then reads

$$\begin{aligned} E[(D_m^T \otimes D_n^T)\begin{bmatrix} \phi \\ p \end{bmatrix}] &= \begin{bmatrix} M & A \\ M & 0 \end{bmatrix}\begin{bmatrix} vec(X^T) \\ a \end{bmatrix}, \\ D[(D_m^T \otimes D_n^T)\begin{bmatrix} \phi \\ p \end{bmatrix}] &= \begin{bmatrix} \sigma_\phi^2 Q \otimes P & 0 \\ 0 & \sigma_p^2 Q \otimes P \end{bmatrix}, \end{aligned} \tag{1}$$

where $E[.]$, $D[.]$, $\otimes$ and $vec(.)$ denote the expectation and dispersion operator, Kronecker product and vec-operator [29,30], respectively. The undifferenced *observed-minus-computed* phase and code observations are, respectively, collected in the mn-vectors ϕ and p with the following structure: $y = \{\phi, p\}$, $y = [y^{1^T}, y^{2^T}, \ldots, y^{m^T}]^T$, with $y^s = [y_1^s, y_2^s, \ldots, y_n^s]^T$ and with y_r^s being the phase/code observation between antenna r and satellite s. The $(m-1) \times m$ matrix $D_m^T = [-e_{m-1}, I_{m-1}]$ is the differencing matrix forming the between-satellite single-differencing, while the $(n-1) \times n$ matrix $D_n^T = [-e_{n-1}, I_{n-1}]$ forms the between-receiver single-differencing. e and I are, respectively, the vector of ones and the identity matrix of which the dimension is specified by their subscripts. The unknown baseline components in NED (North–East–Down) frame are included in $3 \times (n-1)$ matrix X, and the unknown integer DD ambiguities, in cycle, in $(m-1)(n-1)$-vector a. Their corresponding design matrices are of the form of $M = D_m^T G \otimes I_{n-1}$ and $A = \lambda I_{m-1} \otimes I_{n-1}$, where G contains the receiver–satellite unit direction vectors as its rows and λ is the wavelength of frequency L5.

The stochastic model is formed by the $(m-1) \times (m-1)$ matrix $Q = D_m^T W^{-1} D_m$ and $(n-1) \times (n-1)$ matrix $P = D_n^T D_n$. $W = \mathrm{diag}(w^1, w^2, \ldots, w^m)$ is an $m \times m$ diagonal matrix of which the diagonal entries w^s $(s = 1, \ldots, m)$ capture the elevation-dependency of the IRNSS observations and are given as [31]

$$w^s = [1 + 10 \exp(-\frac{\theta^s}{10})]^{-2}, \tag{2}$$

where θ^s is the elevation of the satellite s in degrees. The zenith-referenced standard deviation of the undifferenced phase and code observables are denoted as σ_ϕ and σ_p, respectively.

2.2. Multivariate-Constrained Model

Taking into account the known antennas' geometry in the body frame, the model of observations in Equation (1) can be strengthened. The baseline coordinates in the body frame B can be transferred to their counterparts in NED frame X through [32]

$$X = R\,B; \quad X, B \in \mathbb{R}^{3 \times (n-1)}, \; R \in \mathbb{O}^{3 \times 3}, \tag{3}$$

where R is a rotation matrix satisfying $R^T R = I_3$ and $\det(R) = +1$ [33]. Combining Equations (1) and (3), the following replacements are required

$$vec(X^T) \to vec(R^T); \quad D_m^T G \otimes I_{n-1} \to D_m^T G \otimes B^T. \tag{4}$$

Since the rotation matrix R is of full rank, we have $\mathrm{rank}(X) = \mathrm{rank}(B) = q$. The baselines achieve their full span if $q = \min(3, n-1)$ [34]. In case $q < \min(3, n-1)$, the transpose of the baseline matrix B^T forming the design matrix $D_m^T G \otimes B^T$ would be rank deficient. In order to rule this case out, we assume that the body frame axes are formed by the first *three* baselines that are represented in the body frame as [32,34]

$$[b_1, b_2, b_3] = \begin{bmatrix} b_{11} & b_{21} & b_{31} \\ 0 & b_{22} & b_{32} \\ 0 & 0 & b_{33} \end{bmatrix}. \tag{5}$$

Therefore, Equation (3) would be replaced by

$$X = R_q B; \quad , X \in \mathbb{R}^{3\times(n-1)}, B \in \mathbb{R}^{q\times(n-1)}, R_q \in \mathbb{O}^{3\times q} \tag{6}$$

In the sequel, we will work with Equation (6) instead of Equation (3). Our analyses are based on a linear array of one baseline and a planar array of two baselines, for both of which $q = n - 1$.

2.3. Attitude Determination

The aim of the attitude determination is to determine matrix R_q in Equation (6) from which (some of) the attitude parameters, i.e., heading (α), elevation (ϵ) and bank (β), can be extracted. As an example, when $q = 3$, R_3 can be parametrized as

$$R_3 = \begin{bmatrix} c_\alpha c_\epsilon & -s_\alpha c_\beta + c_\alpha s_\epsilon s_\beta & s_\alpha s_\beta + c_\alpha s_\epsilon c_\beta \\ s_\alpha c_\epsilon & c_\alpha c_\beta + s_\alpha s_\epsilon s_\beta & -c_\alpha s_\beta + s_\alpha s_\epsilon c_\beta \\ -s_\epsilon & c_\epsilon s_\beta & c_\epsilon c_\beta \end{bmatrix}, \tag{7}$$

in which $c_{\{.\}} = \cos\{.\}$ and $s_{\{.\}} = \sin\{.\}$.

The least-squares solutions for the orthonormal matrix $\check{R}_q$ and the integer vector $\check{a}$ based on Equations (1) and (4), are obtained through solving the following minimization problems [32]

$$\begin{aligned} \check{R}_q(a) &= \underset{R_q\in\mathbb{O}^{3\times q}}{\operatorname{argmin}} \, ||vec(\hat{R}_q(a) - R_q)||^2_{Q_{vec(\hat{R}_q(a))}}, \\ \check{a} &= \underset{a\in\mathbb{Z}^{(m-1)\times(n-1)}}{\operatorname{argmin}} \left(||\hat{a} - a||^2_{Q_{\hat{a}\hat{a}}} + ||vec(\hat{R}_q(a) - \check{R}_q(a))||^2_{Q_{vec(\hat{R}_q(a))}} \right), \\ \check{R}_q &= \check{R}_q(\check{a}), \end{aligned} \tag{8}$$

where $vec(\hat{R}_q(a)) = vec(\hat{R}_q) - Q_{vec(\hat{R}_q)\hat{a}} Q^{-1}_{\hat{a}\hat{a}}(\hat{a} - a)$. $\hat{R}_q$ and $\hat{a}$ are the least-squares solutions disregarding the orthonormality of the rotation matrix and integerness of the DD ambiguities, and $Q_{vec(\hat{R}_q)}$, $Q_{\hat{a}\hat{a}}$ and $Q_{vec(\hat{R}_q)\hat{a}}$ are their corresponding variance and covariance matrices. The expression to be minimized in the second minimization problem of Equation (8) is the ambiguity objective function, which is nonstandard due to the presence of the second term. To solve this minimization problem, the MC-LAMBDA method has been developed [18,19,23–28,35], incorporating the orthonormality of the rotation matrix in a rigorous manner. This method therefore leads to higher success rates w.r.t. the standard LAMBDA which only takes into account the integerness of the DD ambiguities. In this contribution, the performance of both LAMBDA and MC-LAMBDA is investigated.

As was mentioned, our analyses are based on a linear array of one baseline and a planar array of two baselines satisfying $q = n - 1$. For such a situation, matrix B would become invertible, and Equation (8) can alternatively be written as [34]

$$\begin{aligned} \check{X}(a) &= \underset{X^TX=B^TB}{\operatorname{argmin}} \, ||vec(\hat{X}(a) - X)||^2_{Q_{vec(\hat{X}(a))}}, \\ \check{a} &= \underset{a\in\mathbb{Z}^{(m-1)\times(n-1)}}{\operatorname{argmin}} \left(||\hat{a} - a||^2_{Q_{\hat{a}\hat{a}}} + ||vec(\hat{X}(a) - \check{X}(a))||^2_{Q_{vec(\hat{X}(a))}} \right), \\ \check{X} &= \check{X}(\check{a}). \end{aligned} \tag{9}$$

Therefore, in a single-baseline scenario, the constraint in the first expression of Equation (9) is a constraint on the baseline length, i.e., $||x|| = l$. For such a situation, $\check{x}(a)$ is a vector on the sphere of

radius l that has the smallest distance to $\hat{x}(a)$, where distance is measured with respect to the metric as defined by the variance matrix $Q_{\hat{x}(a)\hat{x}(a)}$ [35].

3. Numerical Analysis

In this section, we present our numerical analysis of IRNSS L5 attitude determination performance.

3.1. Measurement Set-Up

Our evaluations in this study are on the basis of data taken from three stations, namely CUCC, CUBB and CUT3 of short baselines at Curtin University, Perth, Australia (Figure 1a). Each station is equipped with a JAVAD TRE_G3TH_8 receiver and connected to a TRM59800.00 SCIS antenna. The data-set contains the 1-second IRNSS L5 observations collected with a cut-off elevation angle of 10° on DOY (Day Of Year) 166 of 2016. Our analyses are conducted on an epoch-by-epoch basis, using the broadcast ephemeris. Figure 1b illustrates the 24-h skyplot of IRNSS at Perth. Prior to our analyses, we need to consider representative values for the zenith-referenced standard deviations in Equation (1), i.e., $\{\sigma_\phi, \sigma_p\}$. Applying the least-squares variance component estimation (LS-VCE) [36] to the 1-s data of DOYs 155 and 157 of 2016, the mentioned standard deviations were estimated as $\sigma_\phi = 2$ mm and $\sigma_p = 26$ cm.

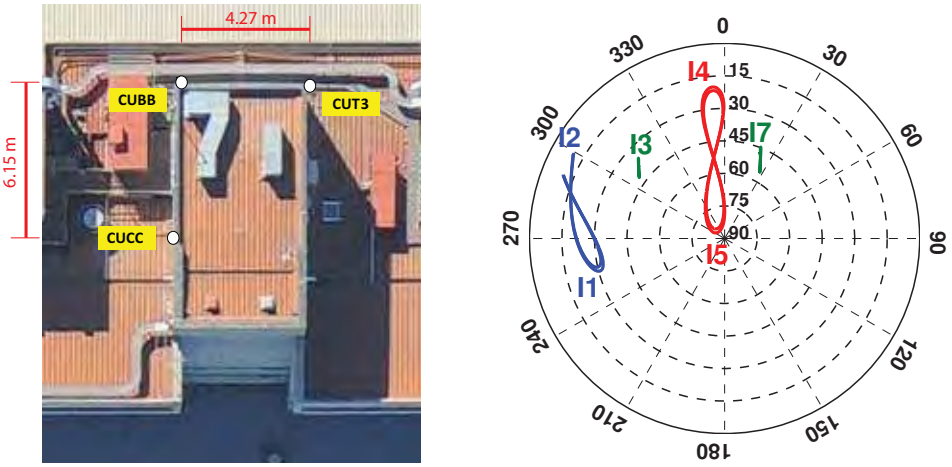

(**a**) (**b**)

Figure 1. (**a**) Stations CUCC, CUBB and CUT3 at Curtin University equipped with JAVAD TRE_G3TH_8 receivers, connected to TRM59800.00 SCIS antennas; (**b**) 24-h IRNSS/NavIC skyplot at Perth on DOY 166 of 2016 with the cut-off elevation of 10°.

3.2. Baseline Solution: From Unconstrained to Constrained

In order to assess the IRNSS L5 attitude determination performance, we first consider a linear array formed by the antenna pair CUCC–CUBB (see Figure 1). Figure 2 for this baseline demonstrates how the constraint on the baseline length affects the baseline solutions. Shown in Figure 2a is a zoom-in of the single-epoch IRNSS L5 solutions (blue dots) for the unconstrained ambiguity–float scenario, as well as the baseline ground truth (black vector). The dispersion in the baseline solutions is governed by the code precision and satellites geometry. The excursions in this three-dimensional scatter plot are due to the significant change that the receiver-satellite geometry undergoes during a 24-h period. Upon constraining the baseline length with e.g., $||x|| = l$, the corresponding solutions can only vary on a sphere with the radius of l.

Figure 2b illustrates the single-epoch IRNSS L5 solutions for the constrained ($||x|| = l$) ambiguity–float scenario (gray dots), the baseline ground truth (gray vector) and the sphere with the radius of l. As it can be seen, the baseline solutions all lie on the shown sphere. Resolving the integer DD ambiguities, Figure 2c shows the single-epoch IRNSS L5 solutions for the constrained ($||x|| = l$) ambiguity–fixed scenario (green dots: correctly-fixed; red dots: wrongly-fixed), the baseline ground truth (gray vector) and the sphere with the radius of l. In order to have a better view of the correctly-fixed solutions, this panel has been rotated with respect to the first two panels. For this scenario, there are different clusters of the baseline solutions that correspond to different estimated integer values for the DD ambiguities. The green cluster associates with the correct integer value comprising 89.2% of the fixed solutions, while the red clusters correspond to the wrong integer values. To judge whether a DD ambiguity is correctly fixed, its corresponding integer solution is compared with the reference integer DD ambiguity computed based on the multi-epoch solution of the baseline-known model.

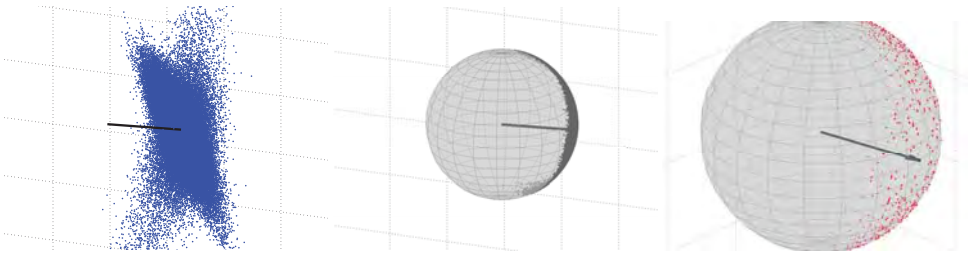

(**a**) (**b**) (**c**)

Figure 2. Single-epoch IRNSS L5 solutions of the CUCC–CUBB baseline at Curtin University on DOY 166 of 2016 with the cut-off elevation of 10°. (**a**) unconstrained ambiguity–float scenario; (**b**) constrained ($||x|| = l$) ambiguity–float scenario using MC-LAMBDA (multivariate-constrained LAMBDA); (**c**) constrained ($||x|| = l$) ambiguity–fixed scenario using MC-LAMBDA. The vector shown in all the three panels denotes the baseline ground truth. The sphere in panels (**b**) and (**c**) is zero-centered with a radius of the CUCC–CUBB baseline length. In panel (**c**), green and red dots show the correctly-fixed and wrongly-fixed solutions, respectively.

Shown in Figure 3a is the horizontal scatter plot of the single-epoch IRNSS L5 solutions for all the scenarios depicted in Figure 2, corrected for the baseline ground truth. Note that the blue scatter plot is elongated in an almost North–Westerly direction, which can be explained by means of the receiver-satellite geometry. Since confidence ellipse is the formal representative of the empirical scatter plot, we concentrate on the confidence ellipse. Denoting the unconstrained ambiguity–float baseline solution as $\hat{x}$ with mean and covariance matrix of, respectively, x and $Q_{\hat{x}\hat{x}}$, its confidence ellipse reads

$$(\hat{x} - x)^T Q_{\hat{x}\hat{x}}^{-1} (\hat{x} - x) = k^2, \tag{10}$$

in which the constant k^2 is chosen such that a certain confidence level is reached. As the direction of elongation is given by the direction of the eigenvector of $Q_{\hat{x}\hat{x}}^{-1}$ corresponding to its smallest eigenvalue, it follows with the aid of Equation (1) that this direction is given by

$$\begin{aligned} f &= \underset{\tilde{f}}{\operatorname{argmin}}\ \tilde{f}^T Q_{\hat{b}\hat{b}}^{-1} \tilde{f} \\ &= \underset{\tilde{f}}{\operatorname{argmin}} \sum_{s=1}^{m} w^s [\tilde{f}^T (u^s - \bar{u})]^2, \end{aligned} \tag{11}$$

with u^s being the unit direction vector from receiver to satellite s, and $\bar{u}$ being the weighted average of the vectors u^s $(s = 1, \ldots, m)$. Figure 3b depicts the day-averaged skyplot position of the IRNSS satellites as well as that of the weighted-average at Perth on DOY 166 of 2016 with the cut-off elevation of 10°. As the differences are mainly oriented along the North–East direction, the direction f that minimizes their contribution to Equation (11) will mainly lie in a North–Westerly direction.

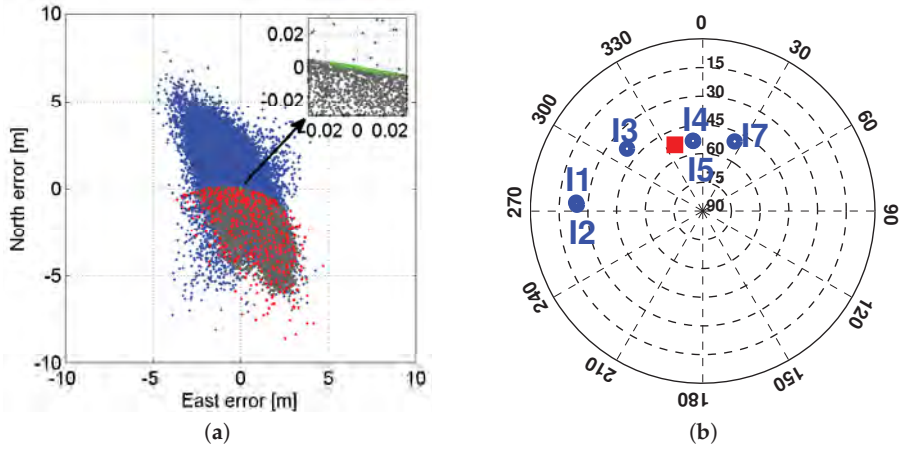

Figure 3. (**a**) Single-epoch IRNSS L5 solutions of the CUCC–CUBB baseline at Curtin University corrected for the ground truth, on DOY 166 of 2016 with the cut-off elevation of 10°. blue: unconstrained ambiguity–float solutions; gray: constrained ($||x|| = l$) ambiguity–float solutions; red: constrained ($||x|| = l$) wrongly-fixed solutions using MC-LAMBDA; green: constrained ($||x|| = l$) correctly-fixed solutions using MC-LAMBDA. A zoom-in is also depicted in the upper-right of the figure; (**b**) Day-averaged IRNSS skyplot at Perth for DOY 166 of 2016 with the cut-off elevation of 10°. The red square indicates the skyplot position of vector $\bar{u}$ (cf. Equation (11))

Now, we turn our focus onto the constrained scenario. The gray dots in Figure 3a show the horizontal scatter plot of the constrained ambiguity–float baseline solutions, while the red and green dots show that of the constrained correctly- and wrongly-fixed baseline solutions. A zoom-in is also provided in the upper-right of the figure to show the correctly-fixed results more clearly. As it can be seen, while the ambiguity–float results are biased, the correctly-fixed results are unbiased. This can be attributed to the precision of the contributing observations and the nonlinearity of the baseline length constraint. For the single-epoch ambiguity–float scenario, the precision of the baseline solution is only dependent on the less precise code observables, whereas, for the ambiguity–fixed scenario, it are the very precise phase observations that play the leading role in the baseline estimation. In the following, we give a two-dimensional example to elaborate how the poor precision of the observations may lead to a bias in the constrained baseline solution.

Suppose that we have a two-dimensional baseline with the length of $l = 3$ m and azimuth of $\alpha = 0°$. The corresponding baseline North–East coordinates then read $b = [3 \quad 0]^T$ m. By the use of normal distribution, we simulate 10^5 samples of baseline north and east components with the mean of $b = [3 \quad 0]^T$ m and the variance matrix of $Q = I_2$ (identity matrix). These samples are shown as blue dots in Figure 4a. In this figure, the true position of the baseline is shown as the black vector. Now, if we impose a constraint on the baseline length, the blue dots are mapped onto a circle with the radius equal to the baseline length $l = 3$ m. This circle is also shown in black in Figure 4a. Due to the poor precision of the baseline samples, they are mapped onto a large part of the circle circumference.

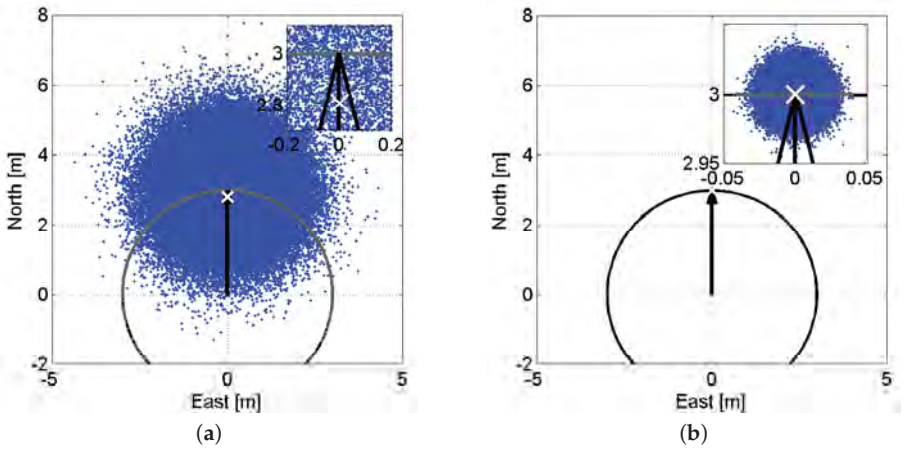

Figure 4. Visualization of the baseline-length constraint nonlinearity as function of data precision. Blue dots are samples of a two-dimensional baseline simulated from a normal distribution with the mean of $b = [3 \quad 0]^T$ m and variance matrix of $Q = \sigma^2 \, I_2$. Gray dots show the baseline-length-constrained counterparts ($||b|| = 3$ m) of blue dots. The black vector indicates the baseline ground truth position and the black circle is centred at $b = [0 \quad 0]^T$ with the radius of 3 m. The white cross shows the mean value of the gray scatter plot. In each panel, a zoom-in is also provided in the upper-right of the panel. (**a**) $\sigma = 1$ m; (**b**) $\sigma = 0.01$ m.

The non-negligible curvature of the area onto which the samples are mapped makes the constrained solutions biased. The mean value of the constrained solutions is depicted as the white cross. This bias is called the *nonlinearity bias* [37]. Now, we switch to a second scenario where the precision of the samples are 100 times better, i.e., $Q = 10^{-4} \, I_2$. Figure 4b illustrates the counterparts of Figure 4a for $Q = 10^{-4} \, I_2$. For this scenario, due to the very small variability of the simulated samples, they are mapped, upon constraining the baseline length, onto a very small part of the circle circumference, which, as the figure shows, can be considered a straight line. Therefore, the nonlinearity bias for this scenario becomes negligible.

3.3. Attitude Determination Performance

In this section, we analyse the IRNSS L5 single-epoch attitude determination performance for the linear array of CUCC–CUBB and the planar array formed by CUCC, CUBB and CUT3 (see Figure 1). The body frame coordinate matrix B for the planar array is given by

$$B = \begin{bmatrix} 6.15 & 6.78 \\ 0 & 4.22 \end{bmatrix}.$$

Table 2, for the mentioned linear and planar arrays, presents the IRNSS L5 single-epoch empirical and formal standard deviations of the attitude angles for both the ambiguity–float and ambiguity–fixed scenarios. The ambiguity–fixed solutions are obtained through applying MC-LAMBDA. Formal values are obtained from taking the average of all the single-epoch *linearized* formal least-squares standard deviations, whereas the empirical values are obtained from the single-epoch least-squares estimations of the attitude angles. In the case of the planar array, in addition to heading and elevation, bank is also estimable. Upon fixing the DD ambiguities, the attitude angles improve in precision by almost a factor of 120.

Table 2. IRNSS L5 single-epoch empirical and linearized formal standard deviations of the attitude angles for the linear array of CUBB–CUCC and the planar array of CUBB–CUCC–CUT3 (see Figure 1), for both the ambiguity–float and ambiguity–fixed scenarios based on the data collected on DOY 166 of 2016 with the cut-off elevation angle of 10°. The ambiguity–fixed solutions are obtained through applying MC-LAMBDA (multivariate-constrained LAMBDA). emp: empirical; form: formal; STD: standard deviation.

Scenario	Ambiguity-Float				Ambiguity-Fixed			
	Linear Array		Planar Array		Linear Array		Planar Array	
	Emp	Form	Emp	Form	Emp	Form	Emp	Form
heading STD [deg]	13.36	7.27	12.66	6.33	0.04	0.05	0.04	0.05
elevation STD [deg]	19.73	17.91	20.41	16.46	0.09	0.14	0.09	0.13
bank STD [deg]	–	–	25.99	21.21	–	–	0.11	0.16

According to this table, in contrast to the ambiguity–fixed results, ambiguity–float outcomes show inconsistency between (linearized) formal and empirical values. This can be attributed to the nonlinearity of the model of observations. The formal standard deviations in Table 2 are obtained through the linear approximation of the model of observations w.r.t. the attitude angles and then applying the error propagation law. Now, by means of Figure 4, we explain how well this linear approximation can describe the uncertainty of the constrained solutions of the baseline and the attitude angles. Applying a linear approximation around $b = [3 \quad 0]^T$ m in Figure 4 would map all the blue dots onto a line, which touches the shown circle at $b = [3 \quad 0]^T$ m. In that case, the constrained baseline uncertainty in the North direction would be zero. This indeed can well describe the uncertainty of the constrained baseline in Figure 4b, where the precision of the simulated samples is very high. However, for Figure 4a with samples of poor precision, the constrained baseline uncertainty in the North direction is far larger than zero due to the non-negligible curvature of the area onto which the samples are mapped. This can also explain the inconsistency between the empirical and the (linearized) formal results of the ambiguity–float scenario, where the solutions are achieved on the basis of less precise code observations.

Denoting the standard deviations of heading, elevation and bank by, respectively, $\sigma_{\hat{\alpha}}$, $\sigma_{\hat{\epsilon}}$, and $\sigma_{\hat{\beta}}$, Table 2 shows that $\sigma_{\hat{\alpha}} \leq \sigma_{\hat{\epsilon}} \leq \sigma_{\hat{\beta}}$. This can be explained through the baselines orientation along with the IRNSS satellites geometry. As an example, here we consider the linear array of the single-baseline CUCC–CUBB. By the aid of linear approximation, the heading–elevation covariance matrix is given as

$$Q_{\hat{\gamma}\hat{\gamma}} = \frac{\sigma_p^2}{l^2} \left(\sum_{s=1}^{m} w^s [J^T(u^s - \bar{u})][J^T(u^s - \bar{u})]^T \right)^{-1} \tag{12}$$

with $\gamma = [\alpha \quad \epsilon]^T$ and J being the Jacobian matrix of the following form

$$J = [J_\alpha \quad J_\epsilon] = \begin{bmatrix} -s_\alpha c_\epsilon & -c_\alpha s_\epsilon \\ c_\alpha c_\epsilon & -s_\alpha s_\epsilon \\ 0 & -c_\epsilon \end{bmatrix}. \tag{13}$$

From Equations (12) and (13), if $J_\alpha^T(u^s - \bar{u})$ is larger than $J_\epsilon^T(u^s - \bar{u})$, then the heading estimation would be more precise than the elevation and vice versa. For the CUCC–CUBB baseline with almost the South–North orientation, we have $J_\alpha \approx [0, \ 1, \ 0]^T$ (East direction) and $J_\epsilon \approx [0, \ 0, \ -1]^T$ (Up direction). Figure 5 depicts the projection of the day-averaged u^s $(s = 1, \ldots, m)$ and $\bar{u}$ onto the plane spanned by J_α and J_ϵ. As the differences $(u^s - \bar{u})$ have larger projections onto J_α w.r.t. J_ϵ, heading is expected to have better precision than elevation. Equation (12) in addition reveals that the longer the baseline, the more precise the attitude angles estimations.

Our ambiguity–fixed results are in good consistency with the GPS L1-based ones presented in [38]. There, an almost South–North oriented 8-meter baseline is used and the phase standard deviation is considered to be 1 mm. Given that the CUCC–CUBB baseline has almost the South–North orientation and the length of almost 6 m, and also that the IRNSS L5 phase precision is 2 mm, it is expected that the attitude precision in [38] be better by a factor of $\frac{8}{3}$ compared to those listed in Table 2. Such superiority is indeed confirmed by the presented results.

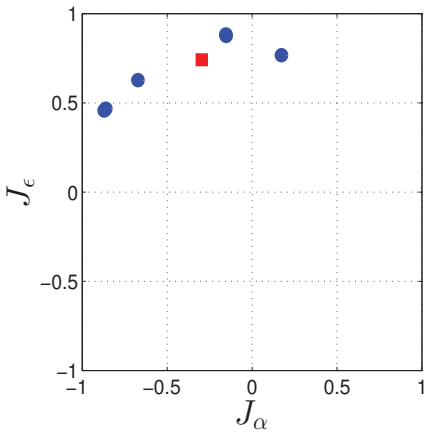

Figure 5. The projection of the day-averaged IRNSS satellites unit direction vectors at Perth onto the plane spanned by $J_\alpha \approx [0,\ 1,\ 0]^T$ and $J_\epsilon \approx [0,\ 0,\ -1]^T$ (cf. Equation (13)) for DOY 166 of 2016 with the cut-off elevation of 10°. The red square indicates the position of vector $\bar{u}$ projected on J_α and J_ϵ (cf. Equations (11) and (12)).

3.4. Ambiguity Resolution Performance

Having investigated the IRNSS L5 attitude determination performance, we now concentrate on the ambiguity resolution performance. To do so, we consider both the aforementioned linear and planar arrays and make use of both the standard LAMBDA and MC-LAMBDA method. As was explained in Introduction, MC-LAMBDA was developed for attitude determination and is advantageous over LAMBDA due to the inclusion of the rotation matrix orthonormality. Figure 6 shows the 24-h time series of the IRNSS L5 single-epoch solutions for the attitude angles for linear array of CUCC–CUBB (a and b) and planar array of CUCC–CUBB–CUT3 (c and d). The fixed solutions on the left are estimated through LAMBDA, while those on the right are estimated through MC-LAMBDA.

From Figure 6, switching from LAMBDA to MC-LAMBDA, the number of wrongly-fixed solutions decreases dramatically. The percentage of correctly fixed solutions, known as the ambiguity resolution success rate, increases from 14.6% to 89.2% for the linear array, and from 4.8% to 99.8% for the planar array. Higher success rates would be achievable if we include the data of more than one epoch. Since the MC-LAMBDA success rate is already large, only a few number of epochs are needed to achieve higher success rates. This indicates that, upon using MC-LAMBDA, standalone IRNSS can realize 24-h almost instantaneous precise attitude determination.

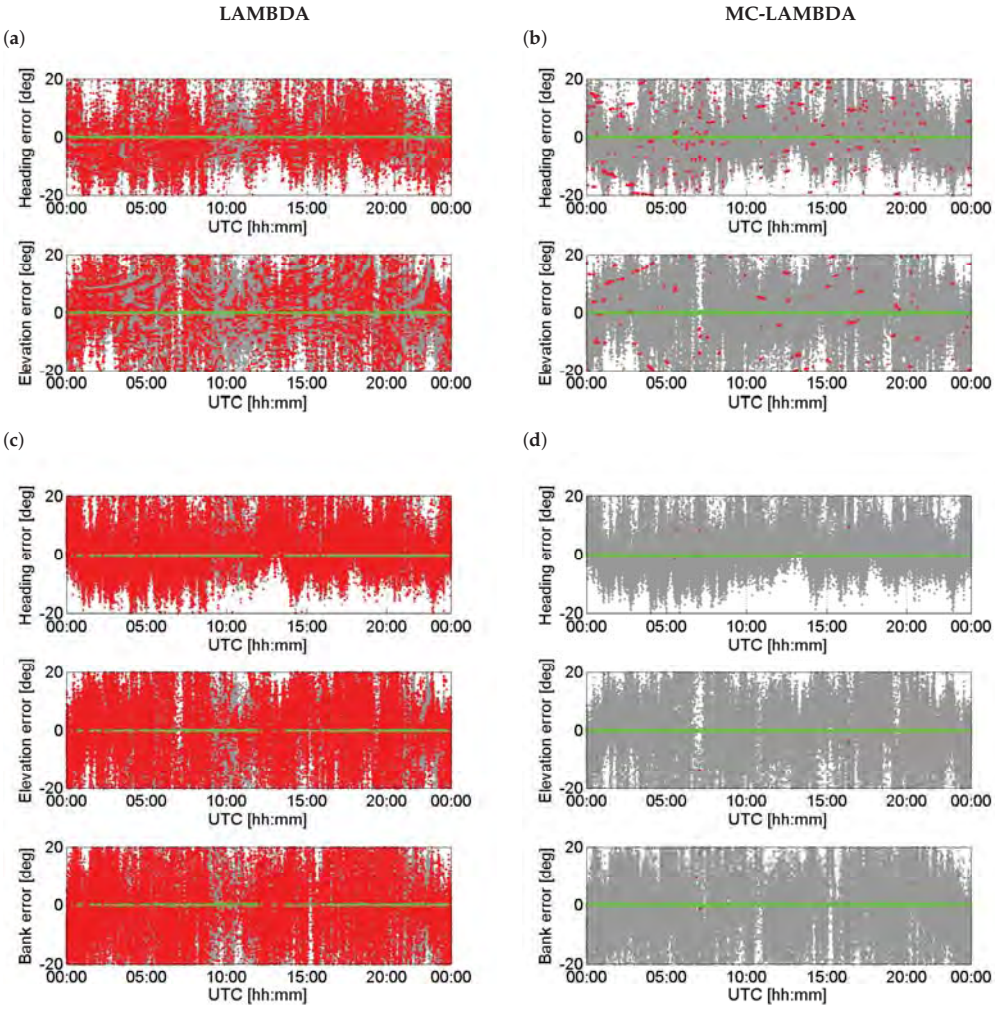

Figure 6. Time series of the IRNSS L5 single-epoch solutions for the attitude angles based on the data collected on DOY 166 of 2016 at Perth with the cut-off elevation of 10°. Each panel shows three types of solutions: gray—ambiguity–float solutions; red—wrongly-fixed solutions; green—correctly-fixed solutions. The fixed solutions on the left are estimated through LAMBDA, while those on the right are estimated through MC-LAMBDA. (**a**,**b**) correspond to the linear array formed by CUCC–CUBB; (**c**,**d**) correspond to the planar array formed by CUCC–CUBB–CUT3.

From linear array to planar array, while the ambiguity success rate of LAMBDA decreases, that of MC-LAMBDA increases. In the case of MC-LAMBDA, which takes into account the constraint $X^T X = B^T B$, the model gets stronger from linear array to planar array due to the inclusion of a larger number of constraints, which, in turn, leads to ambiguity resolution improvements. The LAMBDA-based success rate Ps for single-frequency DD ambiguities, corresponding with n antennas and m satellites, can be well approximated by [39,40]

$$Ps \approx \left[2\Phi\left(\frac{1}{\mathrm{ADOP}}\right) - 1\right]^{(m-1)(n-1)}, \tag{14}$$

where $\Phi(x) = \int_{-\infty}^{x} \frac{1}{\sqrt{2\pi}} \exp\{-\frac{1}{2}v^2\}dv$. ADOP (Ambiguity Dilution Of Precision) was introduced in [21], defined as the square root of the determinant of the ambiguity variance matrix raised to the power of one over the ambiguity dimension. Considering the model of observations in Equation (1), it can be shown that the ADOP corresponding with $n = 2$ is only 1.07 times larger than the ADOP corresponding with $n = 3$. Therefore, the ADOP of $n = 2$ is almost the same as the ADOP of $n = 3$. For a given value of ADOP, the success rate in Equation (14) decreases as n increases. Thus, the LAMBDA-based success rate is indeed expected to decrease as one switches from the linear array ($n = 2$) to the planar array ($n = 3$).

4. Conclusions

In this contribution, we provided an initial assessment of the *fully-operational* IRNSS L5-signal capability to achieve the *instantaneous attitude determination*. We first studied the noise characteristics of the IRNSS L5-signal through the LS-VCE method, and estimated the code and phase zenith-referenced standard deviations as 26 cm and 2 mm, respectively. Our evaluations of IRNSS attitude determination performance were conducted for both a linear array of two antennas and a planar array of three antennas located at Curtin University, Perth, Australia. For a linear array, we showed schematically in a stepwise manner how the inclusion of the baseline length constraint and then the integerness of the DD ambiguities affect the baseline least-squares solutions.

It was shown that, for the single-epoch constrained ambiguity–float scenario, where only the less precise code observations contribute to the baseline estimation, due to the nonlinearity of the baseline length constraint and poor precision of the observations, a large bias, called nonlinearity bias, affects the solution of the attitude angles and hence the constrained baseline solutions. However, if one takes into account the integerness of the DD ambiguities, the very precise phase observations will play the leading role in estimation of attitude angles, thus making the corresponding bias negligible.

A pre-requisite for precise attitude determination is the successful resolution of the DD integer ambiguities. The performance of LAMBDA and MC-LAMBDA was compared for both the linear and planar array. The ambiguity success rate was shown to increase from 14.6% to 89.2% for the linear array, and from 4.8% to 99.8% for the planar array. Higher success rates would be achievable if we include the data of more than one epoch. Since the MC-LAMBDA success rate is already large, only a small number of epochs are needed to achieve higher success rates. This indicates that, upon using MC-LAMBDA, standalone IRNSS can realize 24-h almost instantaneous precise attitude determination. Upon fixing the integer ambiguities, it was shown for the linear array oriented in the South–North direction, with the length of around $l = 6$ m, that heading and elevation are estimable with the standard deviations of 0.05 and 0.10 degrees. The higher precision of heading compared to the elevation was explained through the baseline orientation and IRNSS satellites geometry. Since IRNSS satellites are mainly located in the North–West quadrant of the Perth skyplot, the mentioned precisions are also obtained if the baseline is oriented in the East–West direction. This is also confirmed by the results we obtained using real data.

Acknowledgments: The second author is the recipient of an Australian Research Council Federation Fellowship (project number FF0883188). This support is gratefully acknowledged.

Author Contributions: Safoora Zaminpardaz: Processing the data and analysing the results; Peter J.G. Teunissen: Analysing the results; Nandakumaran Nadarajah: Analysing the results.

Conflicts of Interest: The authors declare no conflict of interest.

References

1. Indian Space Research Organisation (ISRO). *Indian Regional Navigation Satellite System: Signal in Space ICD for Standard Positioning Service*, Version 1.0; ISRO Satellite Centre: Bengaluru, India, 2014.
2. Indian Space Research Organisation (ISRO). PSLV-C33/IRNSS-1G. Available online: http://www.isro.gov.in/sites/default/files/pslv-c33-brochure.pdf (accessed on 1 June 2016).

3. Thoelert, S.; Montenbruck, O.; Meurer, M. IRNSS-1A: Signal and clock characterization of the Indian regional navigation system. *GPS Solut.* **2014**, *18*, 147–152.
4. Kumari, A.; Samal, K.; Rajarajan, D.; Swami, U.; Babu, R.; Kartik, A.; Rathnakara, S.C.; Ganeshan, A.S. Precise Modeling of Solar Radiation Pressure for IRNSS Satellite. *J. Nat. Sci. Res.* **2015**, *5*, 35–43.
5. Babu, R.; Mula, P.; Ratnakara, S.C.; Ganeshan, A.S. IRNSS Satellite Parameter Estimation Using Combination Strategy. *Glob. J. Sci. Front. Res.* **2015**, *15*, 3.
6. Chandrasekhar, M.V.; Rajarajan, D.; Satyanarayana, G.; Tirmal, N.; Rathnakara, S.C.; Ganeshan, A.S. Modernized IRNSS Broadcast Ephemeris Parameters. *Control Theory Inform.* **2015**, *5*, 1–9.
7. Ganeshan, A.S.; Ratnakara, S.C.; Srinivasan, N.; Rajaram, B.; Tirmal, N.; Anbalagan, K. First position fix with IRNSS. *Inside GNSS*, July 2015, pp. 48–52. Available online: http://www.insidegnss.com/node/4545 (accessed on 19 April 2016).
8. Zaminpardaz, S.; Teunissen, P.J.G.; Nadarajah, N. IRNSS stand-alone positioning: First results in Australia. *J. Spat. Sci.* **2016**, *61*, 5–27.
9. Montenbruck, O.; Steigenberger, S.R. IRNSS orbit determination and broadcast ephemeris assessment. In Proceedings of the 2015 International Technical Meeting of The Institute of Navigation, Dana Point, CA, USA, 26–28 January 2015; pp. 185–193.
10. Nadarajah, N.; Khodabandeh, A.; Teunissen, P.J.G. Assessing the IRNSS L5-signal in combination with GPS, Galileo, and QZSS L5/E5a-signals for positioning and navigation. *GPS Solut.* **2016**, *20*, 289–297.
11. Cohen, C. Attitude Determination Using GPS. Ph.D. Thesis, Stanford University, Stanford, CA, USA, 1992.
12. Lu, G. Development of a GPS Multi-Antenna System for Attitude Determination. Ph.D. Thesis, University of Calgary, Calgary, AB, Canada, 1995.
13. Madsen, J.; Lightsey, E.G. Robust spacecraft attitude determination using global positioning system receivers. *J. Spacecr. Rockets* **2004**, *41*, 635–644.
14. Psiaki, M.L. Batch algorithm for global-positioning-system attitude determination and integer ambiguity resolution. *J. Guid. Control Dyn.* **2006**, *29*, 1070–1079.
15. Hodgart, M.S.; Purivigraipong, S. New approach to resolving instantaneous integer ambiguity resolution for spacecraft attitude determination using GPS signals. In Proceedings of the IEEE Position Location and Navigation Symposium, San Diego, CA, USA, 13–16 March 2000; pp. 132–139.
16. Li, Y.; Zhang, K.; Roberts, C.; Murata, M. On-the-Fly GPS-Based Attitude Determination Using Single- and Double-Differenced Carrier Phase Measurements. *GPS Solut.* **2004**, *8*, 93–102.
17. Wang, B.; Miao, L.; Wang, S.; Shen, J. A constrained LAMBDA method for GPS attitude determination. *GPS Solut.* **2009**, *13*, 97–107.
18. Giorgi, G.; Teunissen, P.J.G.; Verhagen, S.; Buist, P.J. Testing a new multivariate GNSS carrier phase attitude determination method for remote sensing platforms. *Adv. Space Res.* **2010**, *46*, 118–129.
19. Teunissen, P.J.; Giorgi, G.; Buist, P.J. Testing of a new single-frequency GNSS carrier phase attitude determination method: land, ship and aircraft experiments. *GPS Solut.* **2011**, *15*, 15–28.
20. Teunissen, P.J. The least-squares ambiguity decorrelation adjustment: A method for fast GPS integer ambiguity estimation. *J. Geod.* **1995**, *70*, 65–82.
21. Teunissen, P.J.G. A canonical theory for short GPS baselines. Part I: The baseline precision. *J. Geod.* **1997**, *71*, 320–336.
22. Teunissen, P.J.G. An optimality property of the integer least-squares estimator. *J. Geod.* **1999**, *73*, 587–593.
23. Park, C.; Teunissen, P.J.G. A new carrier phase ambiguity estimation for GNSS attitude determination systems. In Proceedings of International GPS/GNSS Symposium, Tokyo, Japan, 15–18 November 2003; Volume 8, pp. 283–290.
24. Park, C.; Teunissen, P.J.G. Integer least squares with quadratic equality constraints and its application to GNSS attitude determination systems. *Int. J. Control Autom. Syst.* **2009**, *7*, 566–576.
25. Teunissen, P. The LAMBDA method for the GNSS compass. *Artif. Satell.* **2006**, *41*, 89–103.
26. Buist, P.J. The baseline constrained LAMBDA method for single epoch, single-frequency attitude determination applications. In Proceedings of the 20th International Technical Meeting of the Satellite Division of The Institute of Navigation (ION GNSS 2007), Fort Worth, TX, USA, 25–28 September 2007; pp. 2962–2973.

27. Giorgi, G.; Teunissen, P.J.G.; Buist, P.J. A search and shrink approach for the baseline constrained LAMBDA method: Experimental results. In Proceedings of the International Symposium on GPS/GNSS, Tokyo, Japan, 11–14 November 2008; Yasuda, A., Ed.; Tokyo University of Marine Science and Technology: Tokyo, Japan, 2008; pp. 797–806.
28. Giorgi, G.; Buist, P.J. Single-epoch, single-frequency, standalone full attitude determination: Experimental results. In Proceedings of the Fourth ESA Workshop on Satellite Navigation User Equipment Technologies (NAVITEC), Noordwijk, The Netherlands, 10–12 December 2008.
29. Harville, D.A. *Matrix Algebra From A Statistician's Perspective*; Springer: New York, NY, USA, 1997.
30. Magnus, J.R.; Neudecker, H. *Matrix Differential Calculus with Applications in Statistics and Econometrics*; John Wiley & Sons: Hoboken, NJ, USA, 1995.
31. Euler, H.J.; Goad, C.C. On optimal filtering of GPS dual frequency observations without using orbit information. *Bull. Geod.* **1991**, *65*, 130–143.
32. Teunissen, P. A general multivariate formulation of the multi-antenna GNSS attitude determination problem. *Artif. Satell.* **2007**, *42*, 97–111.
33. Kuipers, J.B. *Quaternions and Rotation Sequences*; Princeton University Press: Princeton, NJ, USA, 2002.
34. Teunissen, P.J.G. The affine constrained GNSS attitude model and its multivariate integer least-squares solution. *J. Geod.* **2012**, *86*, 547–563.
35. Teunissen, P.J. Integer least-squares theory for the GNSS compass. *J. Geod.* **2010**, *84*, 433–447.
36. Teunissen, P.J.G.; Amiri-Simkooei, A.R. Least-squares variance component estimation. *J. Geod.* **2008**, *82*, 65–82.
37. Teunissen, P.J.G. Estimation in Nonlinear Models. In Proceedings of the II Hotine-Marussi Symposium on Mathematical Geodesy, Pisa, Italy, 5–8 June 1989.
38. Nadarajah, N.; Teunissen, P. Instantaneous GPS/Galileo/QZSS/SBAS Attitude Determination: A Single-Frequency (L1/E1) Robustness Analysis under Constrained Environments. *Navigation* **2014**, *61*, 65–75.
39. Teunissen, P.J.G. Success probability of integer GPS ambiguity rounding and bootstrapping. *J. Geod.* **1998**, *72*, 606–612.
40. Verhagen, S. On the reliability of integer ambiguity resolution. *Navigation* **2005**, *52*, 99–110.

8 IRNSS+GPS L5 attitude determination

This chapter is covered by the following publication:

Zaminpardaz S., Teunissen P.J.G., Nadarajah N. (2017e) Single-frequency L5 attitude determination from IRNSS/NavIC and GPS: a single- and dual-system analysis. Journal of Geodesy, Springer, 91(12):1415-1433

J Geod (2017) 91:1415–1433
DOI 10.1007/s00190-017-1033-y

ORIGINAL ARTICLE

Single-frequency L5 attitude determination from IRNSS/NavIC and GPS: a single- and dual-system analysis

S. Zaminpardaz[1] · **P. J. G. Teunissen**[1,2] · **N. Nadarajah**[1]

Received: 12 December 2016 / Accepted: 19 April 2017 / Published online: 3 May 2017

Abstract The Indian Regional Navigation Satellite System (IRNSS) has recently (May 2016) reached its full operational capability. In this contribution, we provide the very first L5 attitude determination analyses of the fully operational IRNSS as a standalone system and also in combination with the fully operational GPS Block IIF along with the corresponding ambiguity resolution results. Our analyses are carried out for both a linear array of two antennas and a planar array of three antennas at Curtin University, Perth, Australia. We study the noise characteristics (carrier-to-noise density, measurement precision, time correlation), the integer ambiguity resolution performance (LAMBDA, MC-LAMBDA) and the attitude determination performance (ambiguity float and ambiguity fixed). A prerequisite for precise and fast IRNSS attitude determination is the successful resolution of the double-differenced integer carrier-phase ambiguities. In this contribution, we will compare the performance of the unconstrained and the multivariate-constrained LAMBDA method. It is therefore also shown what improvements are achieved when the known body geometry of the antenna array is rigorously incorporated into the ambiguity objective function. As our ambiguity-fixed outcomes show consistency between empirical and formal results, we also formally assess the precise attitude determination performance for several locations within the IRNSS service area.

✉ S. Zaminpardaz
safoora.zaminpardaz@curtin.edu.au

[1] GNSS Research Centre, Department of Spatial Sciences, Curtin University, Perth, Australia

[2] Department of Geoscience and Remote Sensing, Delft University of Technology, Delft, The Netherlands

Keywords IRNSS · NavIC · GPS Block IIF · Integer carrier-phase ambiguity resolution · Attitude determination · Multivariate-constrained integer least squares · MC-LAMBDA

1 Introduction

Reaching the full operational capability recently (May 2016), the Indian Regional Navigation Satellite System (IRNSS) has been provided with the operational name of NavIC (Navigation with Indian Constellation). This new addition to GNSSs (Global Navigation Satellite Systems) has been developed by the Indian Space Research Organization (ISRO) with the objective of offering positioning, navigation and timing (PNT) to the users in its service area. Based on Code Division Multiple Access (CDMA), the IRNSS satellites transmit navigation signals on L5 (1176.45 MHz) with a binary phase shift key (BPSK (1)) modulation for standard positioning service (SPS) users, and with a binary offset carrier (BOC (5,2)) modulation for restricted service (RS) users (ISRO 2014). The fully operational IRNSS constellation consists of three geostationary orbit (GEO) satellites and four inclined geosynchronous orbit (IGSO) satellites (see Table 1), with the orbital period of one sidereal day (23 h and 56 min).

Transmission of L5 frequency by IRNSS makes it interoperable with three other GNSSs, i.e., GPS Block IIF, Galileo and QZSS, which share this frequency. At different stages of the IRNSS development, several studies have been published on the basis of IRNSS real data. Thoelert et al. (2014) assess the clock stability of satellite I1. Using the I1 and I2 observations, Kumari et al. (2015) test the accuracy of a precise model for solar radiation pressure, while Montenbruck and Steigenberger (2015) investigate the quality of the IRNSS navigation messages. The data of I1, I2 and I3 are used by

Table 1 Information on the IRNSS/NavIC satellites (ISRO 2016)

Satellite	Type	Longitude	Inclination	Launch date
IRNSS-1A (I1)	IGSO	55° E	29.0°	July 2013
IRNSS-1B (I2)	IGSO	55° E	31.0°	April 2014
IRNSS-1C (I3)	GEO	83° E	–	October 2014
IRNSS-1D (I4)	IGSO	111.75° E	30.5°	March 2015
IRNSS-1E (I5)	IGSO	111.75° E	28.1°	January 2016
IRNSS-1F (I6)	GEO	32.5° E	–	March 2016
IRNSS-1G (I7)	GEO	129.5° E	–	April 2016

Babu et al. (2015) for comparison of the orbit determination methods and by Chandrasekhar et al. (2015) to validate the orbit accuracy with modernized ephemeris parameters. The first positioning results based on the data of I1, I2, I3 and I4 over India are presented in Ganeshan et al. (2015) and over Australia in Zaminpardaz et al. (2016b). In 2010, following the launch of the first GPS Block IIF satellite, GPS started transmitting L5 signals as part of the GPS modernization (GPS Directorate 2011). With the launch of the last satellite of Block IIF on February 2016, it now has all its 12 satellites operational. There exist a few studies making use of the GPS L5 real data. An analysis of the GPS L5 stochastic properties through different GNSS observables combinations is provided by de Bakker et al. (2012), and the GPS L5-based precise point positioning (PPP) results are presented in Tegedor and Øvstedal (2014). The DISBs (differential inter-system biases) between GPS L5 and the same signal of the other systems including IRNSS are characterized in Odijk and Teunissen (2013) and Odijk et al. (2016).

In this contribution, we aim to investigate the L5-signal instantaneous attitude determination capability using the IRNSS as a standalone system and also in combination with the GPS Block IIF. Since L5 signal is a quite new addition to the GNSS signals, it is important to gain an understanding of its performance from the viewpoint of different applications like attitude determination. The attitude of a platform can be determined using multiple GNSS antennas which are rigidly mounted on it (Cohen 1992; Lu 1995; Madsen and Lightsey 2004; Psiaki 2006). Depending on the application at hand, this platform can be a vessel, a land vehicle, an aircraft or a space platform (Hodgart and Purivigraipong 2000; Li et al. 2004; Hide et al. 2007; Hauschild et al. 2008; Wang et al. 2009; Giorgi et al. 2010; Teunissen et al. 2011). Precise and fast GNSS-based attitude determination can be realized through incorporation of the very precise phase observations and hence requires the successful resolution of the double-differenced (DD) integer carrier-phase ambiguities. The Least-squares AMBiguity Decorrelation Adjustment (LAMBDA) method developed by Teunissen (1995, 1997, 1999) is the standard method used for solving the unconstrained mixed-integer GNSS models, which also results in the highest possible ambiguity resolution success rate (percentage of correctly fixed solutions).

However, if the local antenna geometry in the body frame is known, one can further improve the ambiguity resolution performance. To realize this, the multivariate-constrained (MC-)LAMBDA method has been developed (Park and Teunissen 2003, 2009; Teunissen 2006; Buist 2007; Giorgi et al. 2008; Giorgi and Buist 2008; Giorgi et al. 2010; Teunissen et al. 2011). This method incorporates the known local antenna geometry in a rigorous manner into the ambiguity objective function, leading to higher success rates as compared to the standard LAMBDA. The attitude determination performance of the L5 signal of IRNSS, GPS, Galileo and QZSS was assessed by Nadarajah et al. (2015). Their assessment was based on *two* IRNSS and *seven* GPS Block IIF satellites. Our attitude evaluations in the current study, however, employ, for the first time, the *fully operational* IRNSS and GPS Block IIF.

This contribution is organized as follows. In Sect. 2, the unconstrained and multivariate-constrained single-frequency GNSS model of observations is formulated. The measurement setup is explained in Sect. 3, while the noise characteristics of the IRNSS and GPS L5 signal are presented in Sect. 4 through the carrier-to-noise density, the estimated measurement precision and time correlation. Section 5 compares the ambiguity resolution performance on the basis of LAMBDA and MC-LAMBDA for both a linear and a planar array of GNSS antennas at Curtin University, Perth, Australia. In Sect. 6, an empirical and formal analysis of the instantaneous attitude determination performance at Perth is provided for the mentioned arrays. We then extend this study with formal analysis to the IRNSS service area. Finally, a summary and conclusions are given in Sect. 7.

2 GNSS model of observations

In this section, the dual-system (IRNSS + GPS) single-frequency GNSS model of observations for an array of antennas is formulated from which the single-system (IRNSS) model follows as a special case. We assume the array is

of small scale such that the differential atmospheric delays (troposphere and ionosphere) and orbital errors between the antennas can be neglected. Due to the close proximity of the antennas, the satellites elevations are considered to be the same for all the antennas. We further assume that all the receivers are of the same manufacturer (make, type and firmware), thus allowing us to assume that the IRNSS-GPS ISBs are zero (Odijk et al. 2012, 2016). Therefore, instead of classical double differencing per constellation, inter-system double differencing can be used, resulting in a higher level of redundancy. In the sequel, we refer to the IRNSS-specific parameters and the GPS-specific parameters using the subscripts $_I$ and $_G$, respectively.

2.1 Unconstrained model

Suppose that n antennas, firmly mounted on a platform, are simultaneously tracking m_I IRNSS plus m_G GPS satellites on L5 frequency with the wavelength of λ. With $m = m_I + m_G$, the multivariate linearized single-epoch DD GNSS array model of observations then reads

$$E\left[(D_m^T \otimes D_n^T)\begin{bmatrix}\phi\\ p\end{bmatrix}\right] = \begin{bmatrix}D_m^T G \otimes I_{n-1} & \lambda I_{m-1} \otimes I_{n-1}\\ D_m^T G \otimes I_{n-1} & 0\end{bmatrix}\begin{bmatrix}vec(X^T)\\ a\end{bmatrix}$$
$$D\left[(D_m^T \otimes D_n^T)\begin{bmatrix}\phi\\ p\end{bmatrix}\right] = \begin{bmatrix}D_m^T Q_{\phi\phi} D_m \otimes D_n^T D_n & 0\\ 0 & D_m^T Q_{pp} D_m \otimes D_n^T D_n\end{bmatrix} \quad (1)$$

where $E[.]$ and $D[.]$ denote the expectation and dispersion operator and $\otimes$ and $vec(.)$ denote Kronecker product and vec-operator (Harville 1997; Magnus and Neudecker 1995), respectively. The $(m-1)\times m$ matrix $D_m^T = [-e_{m-1},\ I_{m-1}]$ is the differencing matrix forming the between-satellite single differencing, while the $(n-1)\times n$ matrix $D_n^T = [-e_{n-1},\ I_{n-1}]$ forms the between-receiver single differencing. e and I are, respectively, the vector of ones and the identity matrix the dimension thereof is specified by their subscripts. The combined vectors and matrices can be split into system-specific parts as

$$\phi = \left[\phi_I^T, \phi_G^T\right]^T,\ p = \left[p_I^T, p_G^T\right]^T,\ G = \left[G_I^T, G_G^T\right]^T$$
$$Q_{\phi\phi} = \text{blkdiag}\left(\sigma_{\phi_I}^2 W_I^{-1},\ \sigma_{\phi_G}^2 W_G^{-1}\right)$$
$$Q_{pp} = \text{blkdiag}\left(\sigma_{p_I}^2 W_I^{-1},\ \sigma_{p_G}^2 W_G^{-1}\right)$$

With $* = \{I, G\}$, ϕ_* and p_* denote, respectively, the $m_* n$-vectors of the undifferenced "observed-minus-computed" phase and code observations of the following structure: $y_* = \{\phi_*, p_*\}$, $y_* = [y^{1T}_*,\ y^{2T}_*, \ldots, y^{m_*^T}_*]^T$, with $y^{s_*}_* = [y_1^{s_*},\ y_2^{s_*}, \ldots, y_n^{s_*}]^T$ and with $y_r^{s_*}$ being the phase/code observation between antenna r and satellite s_*. The $m_* \times 3$ matrix $G_* = [-u^{1}_*, \ldots, -u^{m_*}_*]^T$ includes the undifferenced receiver-satellite unit direction vectors $u^{s_*^T}_*$ as its rows. The unknown baseline components in NED (North–East–Down) frame are included in the $3 \times (n-1)$ matrix X, and the unknown integer DD ambiguities, in cycle, in the $(m-1)(n-1)$-vector a. The zenith-referenced standard deviation of the undifferenced phase and code observables are denoted as σ_{ϕ_*} and σ_{p_*}, respectively. The $m_* \times m_*$ diagonal matrix $W_* = \text{diag}(w^{1}_*, \ldots, w^{m_*})$ captures the satellite elevation dependency of the GNSS observables. In this contribution, the satellite elevation-dependent weight w^{s_*} takes the form of the exponential weighting function as

$$w^{s_*} = \left[1 + 10\exp\left(-\frac{\theta^{s_*}}{10}\right)\right]^{-2} \quad (2)$$

where θ^{s_*} is the elevation of the satellite s_* in degrees (Euler and Goad 1991). To obtain the standalone IRNSS observational model from (1), it is enough to put $m_G = 0$. Since, in the case of a single epoch, the number of DD ambiguities equals that of the DD phase observables, uncorrelated with the DD code observables, the DD phase observables are fully reserved for the ambiguities estimation. Therefore, the single-epoch estimation of the baselines components does not benefit from the high precision phase observables unless the DD ambiguities are resolved to their integer values. Upon fixing the DD ambiguities, the phase observations act as the very precise code observations and improve the baseline estimation and precision. In the following, we use the system-specific indexes only when working with the dual-system model of observations.

2.2 Multivariate-constrained model

In the model of observations given by (1), the known antennas' geometry in the body frame is disregarded. Such information, if taken into account, can strengthen the GNSS observational model considerably. The baseline coordinates in the body frame B are linked to their counterparts in NED frame X through the following transformation (Teunissen 2007)

$$X = R\,B;\quad X,\ B \in \mathbb{R}^{3\times(n-1)},\ R \in \mathbb{O}^{3\times 3} \quad (3)$$

where $\mathbb{O}^{3\times 3}$ denotes the set of 3×3 matrices of which the column vectors form an orthonormal span. R is a rotation matrix satisfying $R^T R = I_3,\ \det(R) = +1$ (Kuipers 2002). Substituting (3) in (1), the unknown parameters and their corresponding design matrix change accordingly as

$$vec(X^T) \to vec(R^T);\quad D_m^T G \otimes I_{n-1} \to D_m^T G \otimes B^T \quad (4)$$

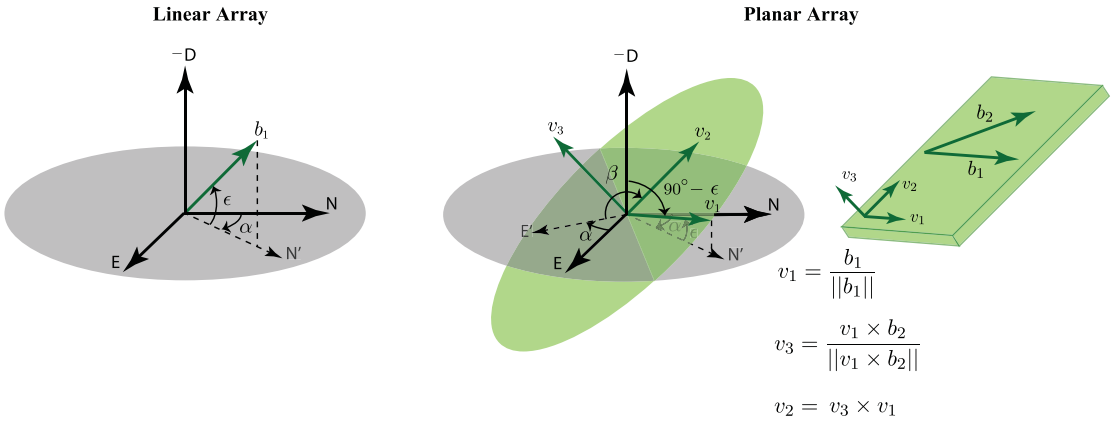

Fig. 1 Transformation between North–East–Down frame and the body frame of a linear array (b_1) and a planar array ($v_1,\ v_2,\ v_3$)

In (3), since the matrix R is of full rank, the matrices X and B are also of the same rank, namely $\text{rank}(X) = \text{rank}(B) = q$ which is the dimension of the space spanned by the baselines. The baselines achieve their full span if $q = \min(3, n-1)$ (Teunissen 2012). If $q < \min(3, n-1)$, the transpose of the baseline matrix B^T forming the design matrix $D_m^T G \otimes B^T$ would be rank deficient. In order to rule this case out, we assume that the body frame axes are formed by the first *three* baselines which are represented in the body frame as (Teunissen 2007, 2012)

$$[b_1,\ b_2,\ b_3] = \begin{bmatrix} b_{11} & b_{21} & b_{31} \\ 0 & b_{22} & b_{32} \\ 0 & 0 & b_{33} \end{bmatrix} \tag{5}$$

Therefore, (3) would be replaced by

$$X = R_q\, B; \quad X \in \mathbb{R}^{3\times(n-1)},\ B \in \mathbb{R}^{q\times(n-1)},\ R_q \in \mathbb{O}^{3\times q} \tag{6}$$

In which $R_q^T R_q = I_q$, and $\mathbb{O}^{3\times q}$ denotes the set of $3 \times q$ matrices of which the q column vectors form an orthonormal span. In the sequel, we will work with (6) instead of (3).

2.3 Ambiguity resolution and attitude determination

The aim of the attitude determination is to determine matrix R_q in (6) from which (some of) the attitude parameters, i.e., heading (α), elevation (ε) and bank (β), can be extracted. As an example, when $q = 3$, R_3 can be parametrized as

$$R_3 = \begin{bmatrix} c_\alpha c_\varepsilon & -s_\alpha c_\beta + c_\alpha s_\varepsilon s_\beta & s_\alpha s_\beta + c_\alpha s_\varepsilon c_\beta \\ s_\alpha c_\varepsilon & c_\alpha c_\beta + s_\alpha s_\varepsilon s_\beta & -c_\alpha s_\beta + s_\alpha s_\varepsilon c_\beta \\ -s_\varepsilon & c_\varepsilon s_\beta & c_\varepsilon c_\beta \end{bmatrix} \tag{7}$$

in which $c_{\{.\}} = \cos\{.\}$ and $s_{\{.\}} = \sin\{.\}$. For $q = 1,\ 2$, R_q is formed by the first column and the first two columns of R_3, respectively. Our analyses in this contribution are conducted for a linear array of one baseline and a planar array of two baselines. Figure 1 schematically shows how the body frame and therefore the attitude angles are defined for these two types of array. With the aid of this figure, (6) can be worked out for the *linear array* as

$$x_1 = ||b_1|| \begin{bmatrix} c_\alpha c_\varepsilon \\ s_\alpha c_\varepsilon \\ -s_\varepsilon \end{bmatrix} \tag{8}$$

and for the *planar array* as

$$[x_1\ \ x_2] = \begin{bmatrix} c_\alpha c_\varepsilon & -s_\alpha c_\beta + c_\alpha s_\varepsilon s_\beta \\ s_\alpha c_\varepsilon & c_\alpha c_\beta + s_\alpha s_\varepsilon s_\beta \\ -s_\varepsilon & c_\varepsilon s_\beta \end{bmatrix} \begin{bmatrix} ||b_1|| & \langle b_2, v_1\rangle \\ 0 & \langle b_2, v_2\rangle \end{bmatrix} \tag{9}$$

where $||.||$ and $\langle .,. \rangle$ denote the Euclidean norm and inner product, respectively.

Solving (1) in a least-squares sense considering the constraint in (6), the solutions for the integer ambiguity vector $\check{a}$ and the orthonormal matrix $\check{R}_q$ are given by Teunissen (2007)

$$\begin{aligned} \check{R}_q(a) &= \underset{R_q\in\mathbb{O}^{3\times q}}{\text{argmin}} \left|\left|vec(\hat{R}_q(a) - R_q)\right|\right|^2_{Q_{vec(\hat{R}_q(a))}} \\ \check{a} &= \underset{a\in\mathbb{Z}^{(m-1)\times(n-1)}}{\text{argmin}} \left(||\hat{a} - a||^2_{Q_{\hat{a}\hat{a}}} + \left|\left|vec(\hat{R}_q(a) - \check{R}_q(a))\right|\right|^2_{Q_{vec(\hat{R}_q(a))}} \right) \\ \check{R}_q &= \check{R}_q(\check{a}) \end{aligned} \tag{10}$$

where $vec(\hat{R}_q(a)) = vec(\hat{R}_q) - Q_{vec(\hat{R}_q)\hat{a}} Q^{-1}_{\hat{a}\hat{a}}(\hat{a} - a)$. $\hat{R}_q$ and $\hat{a}$ are the least-squares solutions disregarding the orthonormality of the rotation matrix and integerness of

the DD ambiguities, and $Q_{vec(\hat{R}_q)}$, $Q_{\hat{a}\hat{a}}$ and $Q_{vec(\hat{R}_q)\hat{a}}$ are their corresponding variance and covariance matrices. In the sequel, depending on which constraints are taken into account, we distinguish between the following scenarios

$R_q \in \mathbb{R}^{3\times q}$: unconstrained scenario;
$R_q \in \mathbb{O}^{3\times q}$: constrained scenario;
$a \in \mathbb{R}^{(m-1)\times(n-1)}$: ambiguity-float scenario;
$a \in \mathbb{Z}^{(m-1)\times(n-1)}$: ambiguity-fixed scenario.

The expression to be minimized in the second minimization problem of (10) is the ambiguity objective function which is nonstandard due to the presence of the second term. This term would disappear provided the orthonormality of the rotation matrix is disregarded. To solve the minimization problem in (10), the MC-LAMBDA method has been developed (Park and Teunissen 2003, 2009; Teunissen 2006, 2010; Buist 2007; Giorgi et al. 2008, 2010; Giorgi and Buist 2008; Teunissen et al. 2011), incorporating the orthonormality of the rotation matrix in a rigorous manner. This method therefore leads to higher success rates w.r.t. the standard LAMBDA which only takes into account the integerness of the DD ambiguities. The performance of both LAMBDA and MC-LAMBDA is investigated in Sect. 5.

As was mentioned, our evaluations in this study are conducted for a linear array of one baseline and a planar array of two baselines. For such a situation, matrix B would become invertible, and (10) can alternatively be written as (Teunissen 2012)

$$\begin{aligned}
\check{X}(a) &= \underset{\substack{X^TX = B^TB \\ X\in\mathbb{R}^{3\times(n-1)}}}{\operatorname{argmin}} \left\| vec\left(\hat{X}(a) - X\right)\right\|^2_{Q_{vec(\hat{X}(a))}} \\
\check{a} &= \underset{a\in\mathbb{Z}^{(m-1)\times(n-1)}}{\operatorname{argmin}} \left(||\hat{a} - a||^2_{Q_{\hat{a}\hat{a}}} + \left\| vec\left(\hat{X}(a) - \check{X}(a)\right)\right\|^2_{Q_{vec(\hat{X}(a))}} \right) \\
\check{X} &= \check{X}(\check{a})
\end{aligned} \tag{11}$$

For the single-baseline scenario, the constraint in the first expression of (11) is a constraint on the baseline length, i.e., $||x|| = l$. For such a situation, $\check{x}(a)$ is the vector on the sphere of radius l that has the smallest distance to $\hat{x}(a)$, where distance is measured with respect to the metric defined by the variance matrix $Q_{\hat{x}(a)\hat{x}(a)}$ (Teunissen 2010).

3 Measurement experiment

In this contribution, we investigate the L5-signal attitude determination performance based on standalone IRNSS and IRNSS + GPS Block IIF, for both the linear and planar arrays. The data are taken from three stations CUCC, CUBB and CUT3 of short baselines at Curtin University, Perth, Australia (Fig. 2a). Each station is equipped with a JAVAD TRE_G3TH_8 receiver and connected to a TRM59800.00 SCIS antenna. The dataset contains the 1-s (1Hz) IRNSS and GPS Block IIF L5 observations collected with a cutoff elevation angle of 10° on DOY (Day Of Year) 167 of 2016.

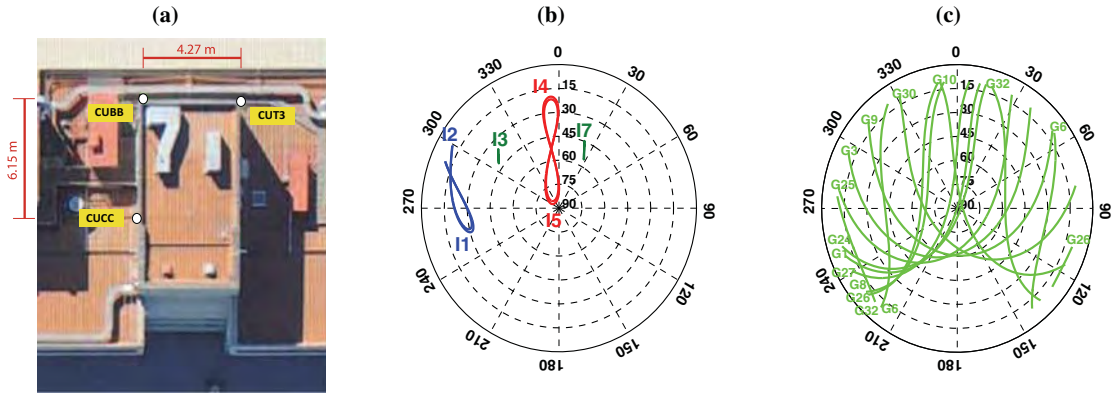

Fig. 2 Curtin University stations used with the corresponding skyplots. **a** CUCC, CUBB and CUT3 are equipped with JAVAD TRE_G3TH_8 receivers, connected to TRM59800.00 SCIS antennas. The 24-h skyplot of **b** IRNSS and **c** GPS Block IIF at Perth, Australia, on DOY 167 of 2016 with the cutoff elevation of 10°

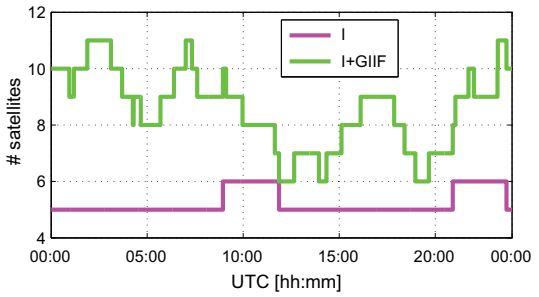

Fig. 3 Time series of the number of visible satellites of IRNSS (I) and IRNSS + GPS Block IIF (I + GIIF) at Perth, Australia, on DOY 167 of 2016 with the cutoff elevation of 10°

Figure 2b, c illustrates the 24-h skyplot of IRNSS and GPS Block IIF at Perth, respectively. Our analyses are conducted on an *epoch-by-epoch* basis, and since the satellites geometry has a low rate of change over time, our conclusions would be valid even for lower sampling rates, like 30 s. For both constellations, the broadcast ephemeris is used. Figure 3 shows the number of visible satellites for both the standalone IRNSS and IRNSS + GPS Block IIF. Combining IRNSS with GPS results in the number of visible satellites increasing from 5–6 to 6–11.

4 Noise characteristics

In this subsection, the noise characteristics of the L5 signal of IRNSS and GPS are assessed through the estimation of measurement precision, the carrier-to-noise density and time correlation. The zenith-referenced standard deviations in (1), i.e., $\{\sigma_{p_I}, \sigma_{\phi_I}, \sigma_{p_G}, \sigma_{\phi_G}\}$, capture the precision of the undifferenced phase and code observables and, if present, any remaining mis-modeled effects like multipath. Therefore upon eliminating the unwanted impact of multipath on the data, it is expected that these values experience improvement. In this study, the impact of multipath is eliminated through the method described in Zaminpardaz et al. (2016a). In order to see the impact of multipath, we apply the least-squares variance component estimation (LS-VCE) (Teunissen and Amiri-Simkooei 2008) to the 1-s L5 data of IRNSS and GPS collected on DOYs 175 and 176 of 2016 before and after applying multipath corrections. The mentioned standard deviations were estimated and the corresponding results are given in Table 2.

The code precision of the GPS L5 is significantly better than that of the IRNSS L5. This is also in agreement with the signature of the carrier-to-noise-density (C/N0) graphs of the two systems in Fig. 4. As it can be seen, the GPS L5 signal has larger values for C/N0 compared to the IRNSS L5. Upon multipath reduction, both IRNSS and GPS code standard deviations improve significantly. The phase observables of IRNSS L5 and GPS L5 are of comparable precisions and almost insensitive to the multipath correction. In the sequel, our analyses are based on both the original and the multipath-corrected data.

Table 2 LS-VCE estimation of the multipath-corrected and the original (within brackets) undifferenced phase σ_ϕ and code σ_p zenith-referenced standard deviations

Frequency	σ_p (cm)	σ_ϕ (mm)
IRNSS L5	19 (26)	1 (2)
GPS L5	7 (17)	1 (1)

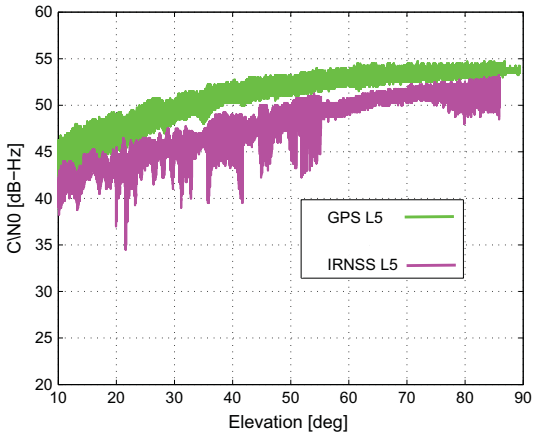

Fig. 4 Carrier-to-noise density (C/N0) for L5 signal of IRNSS and GPS Block IIF tracked by a JAVAD TRE_G3TH_8 receiver, connected to a TRM59800.00 SCIS antenna at Perth, Australia, on DOY 167 of 2016 with the cutoff elevation of 10°

Since 1-s data form the basis of our analyses, we assess the presence of time correlation in our data. Here we investigate the level of time correlation of the IRNSS and GPS L5 signals after and before applying multipath correction. Figure 5 (top) shows the graph of the time correlation among the original IRNSS L5 and GPS L5 observations as function of their time difference, while Fig. 5 (bottom) shows the same results for the multipath-corrected data. These graphs are based on applying the LS-VCE method (Amiri-Simkooei and Tiberius 2007) to 1 h of 1-s short-baseline data of CUCC–CUBB. A significant periodic time correlation among the original data is recognizable for both the IRNSS and GPS observations. Upon removing the multipath effect, however, the time correlation decreases dramatically and the periodic signature vanishes.

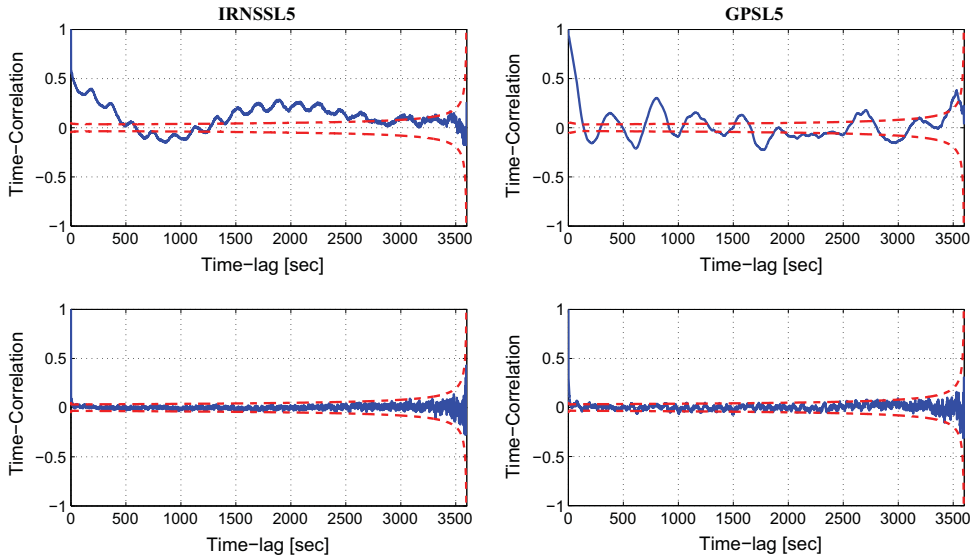

Fig. 5 Time correlation of the L5 signal of IRNSS and GPS Block IIF. Time series of the estimated time correlation among the 1-s short-baseline observations of the IRNSS L5 (*left*) and GPS Block IIF L5 (*right*). *Top* original data; *bottom* multipath-corrected data. The *red dashed lines* indicate the 95% formal confidence interval. The data were collected with the cutoff elevation of 10° by the stations CUCC and CUBB at Curtin University, Perth, Australia, on DOYs 175 and 176 of 2016

5 Ambiguity resolution performance

A prerequisite for precise and fast attitude determination is the successful resolution of the DD ambiguities. In this section, we will compare the performances of the standard LAMBDA and the MC-LAMBDA method, for both the standalone IRNSS L5 and IRNSS + GPS Block IIF L5. It is therefore also shown what improvements are achieved when the known body geometry of the antenna array is rigorously incorporated into the ambiguity objective function through MC-LAMBDA method. We consider two types of array: linear array formed by CUCC–CUBB and planar array formed by CUCC–CUBB–CUT3 (see Fig. 2). The body frame coordinate matrix B for the planar array is given by

$$B = \begin{bmatrix} 6.15 & 6.78 \\ 0 & 4.22 \end{bmatrix} \text{ m}$$

5.1 Standalone IRNSS

Figure 6 shows the 24-h time series of the IRNSS L5 single-epoch ambiguity-float and ambiguity-fixed solutions of the attitude angles corresponding to the linear array of CUCC–CUBB (a and b) and planar array of CUCC–CUBB–CUT3 (c and d). The fixed solutions on the left are estimated through LAMBDA, while those on the right are estimated through MC-LAMBDA. These results are computed based on the multipath-corrected GNSS data. In Table 3, however, we give the corresponding ambiguity resolution success rates on the basis of both the original and the multipath-corrected data. From this table, through either LAMBDA or MC-LAMBDA, multipath correction indeed improves the ambiguity resolution success rate for both the linear and planar array. This enhancement is, however, negligible (0.1%) in case of using the MC-LAMBDA method to resolve the planar array ambiguities. The advantage of MC-LAMBDA over LAMBDA is quite clear from the results in Table 3 and Fig. 6. Switching from LAMBDA to MC-LAMBDA, the success rate increases from 20.4 to 94.3% for the linear array and from 9.3 to 99.9% for the planar array. Higher MC-LAMBDA success rates would be achievable if we include the data of more than one epoch. Since the MC-LAMBDA success rate is already large, only a few number of epochs are needed to achieve higher success rates. This indicates that upon using MC-LAMBDA, standalone IRNSS can realize 24-h almost instantaneous precise attitude determination.

As the dimension of the array increases from one (linear) to two (planar), the LAMBDA success rate decreases while that of MC-LAMBDA increases. This is also shown in Fig. 6. The density of the red dots (wrongly fixed solutions) increases from panel (a) to (c), while it decreases from panel (b) to (d). In case of MC-LAMBDA which takes into account the constraint $X^T X = B^T B$, the model gets stronger from linear array to planar array due to the inclusion of larger

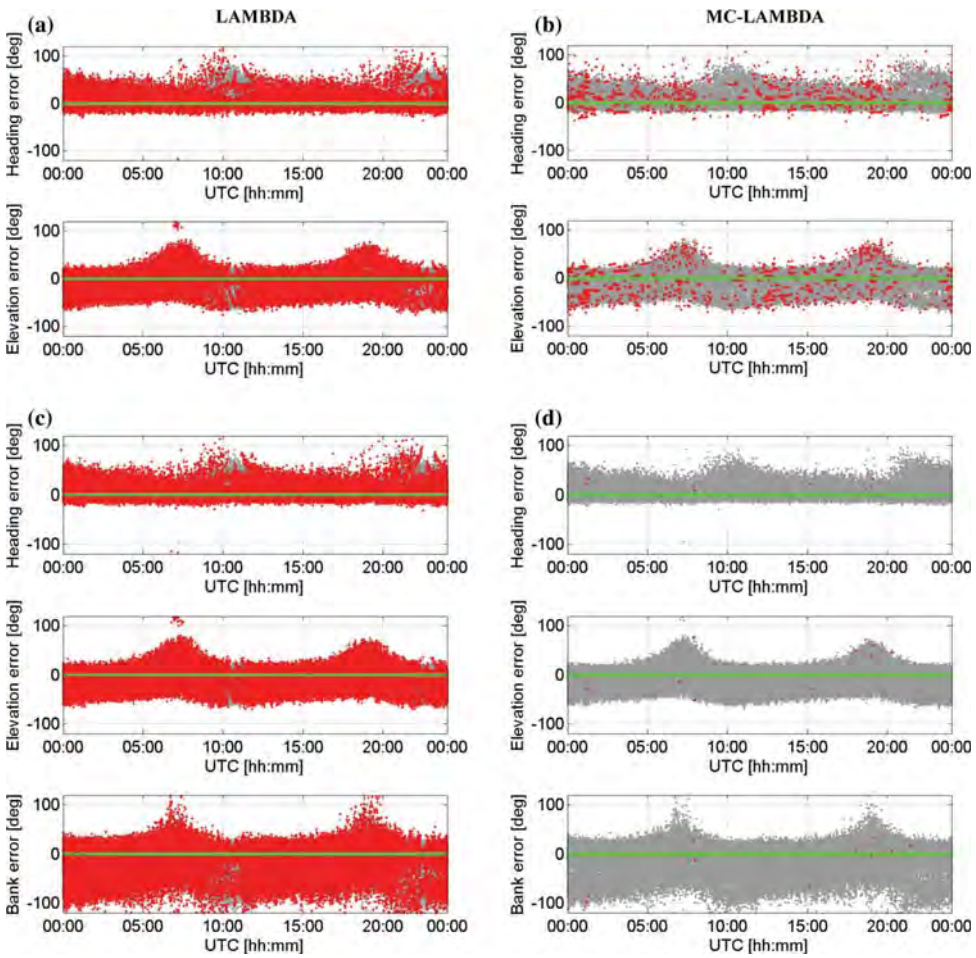

Fig. 6 Standalone IRNSS L5 instantaneous ambiguity resolution performance. Time series of the single-epoch solutions for the attitude angles based on the data collected on DOY 167 of 2016 at Perth with the cutoff elevation of 10°. *Each panel* shows three types of solution: *gray* ambiguity-float solutions; *red* wrongly fixed solutions; *green* correctly fixed solutions. The fixed solutions on the left are estimated through LAMBDA, while those on the right are estimated through MC-LAMBDA. **a**, **b** Correspond to the linear array formed by CUCC–CUBB. **c**, **d** Correspond to the planar array formed by CUCC–CUBB–CUT3

number of constraints which in turn leads to the ambiguity resolution improvements. The LAMBDA success rate for the single-frequency DD ambiguities corresponding to n antennas and m satellites can be well approximated by Teunissen (1998)

$$Ps \approx \left[2\Phi\left(\frac{1}{\mathrm{ADOP}}\right) - 1\right]^{(m-1)(n-1)} \tag{12}$$

where $\Phi(x) = \int_{-\infty}^{x} \frac{1}{\sqrt{2\pi}} \exp\{-\frac{1}{2}v^2\}\mathrm{d}v$. ADOP (ambiguity dilution of precision) is defined as the square root of the determinant of the ambiguity variance matrix raised to the power of one over the ambiguity dimension, and is the geometric average of the conditional ambiguities standard deviations (Teunissen 1997). For the observational model in (1), it can be shown that the ADOP corresponding to $n = 2$ is only 1.07 times larger than the ADOP corresponding to $n = 3$, which can be considered almost the same. Moreover, for a given value of ADOP, the success rate in (12) decreases as n increases. Therefore, from the linear array of two antennas to the planar array of three antennas, where ADOP remains almost unchanged but n increases from 2 to 3, the LAMBDA success rate is indeed expected to experience a reduction.

Table 3 Instantaneous L5 ambiguity resolution empirical success rate (%) for attitude observational model using the multipath-corrected data and the original data (within brackets)

Scenario	IRNSS L5		IRNSS + GPS Block IIF L5	
	LAMBDA	MC-LAMBDA	LAMBDA	MC-LAMBDA
Linear array	20.4 (15.2)	94.3 (89.8)	97.4 (95.1)	99.8 (99.8)
Planar array	9.3 (5.8)	99.9 (99.8)	97.1 (93.7)	>99.9 (>99.9)

The results are given for the linear array of CUBB–CUCC and the planar array of CUBB–CUCC–CUT3 (see Fig. 2)

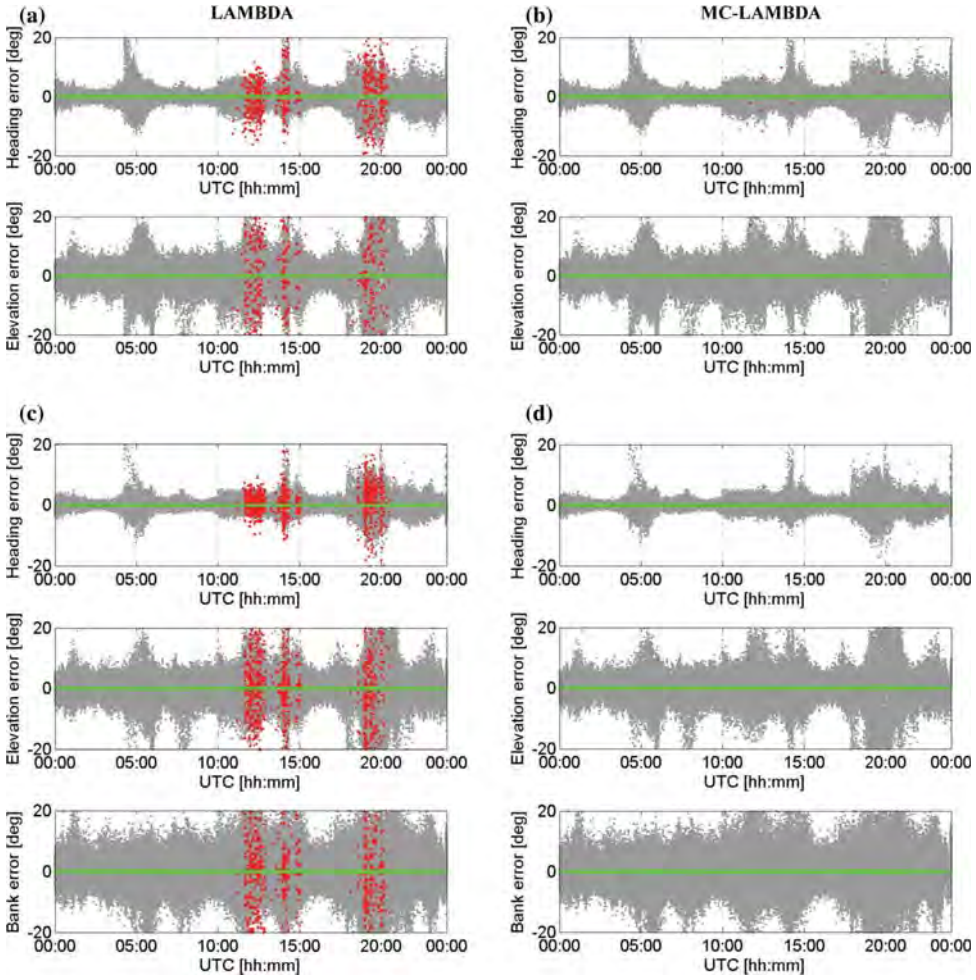

Fig. 7 IRNSS + GPS Block IIF L5 instantaneous ambiguity resolution performance. Time series of the single-epoch solutions for the attitude angles based on the data collected on DOY 167 of 2016 at Perth with the cutoff elevation of 10°. *Each panel* shows three types of solution: *gray* ambiguity-float solutions; *red* wrongly fixed solutions; *green* correctly fixed solutions. The fixed solutions on the left are estimated through LAMBDA, while those on the right are estimated through MC-LAMBDA. **a**, **b** Correspond to the linear array formed by CUCC–CUBB. **c**, **d** Correspond to the planar array formed by CUCC–CUBB–CUT3

5.2 IRNSS combined with GPS

Now we consider the dual-system scenario, i.e., IRNSS + GPS Block IIF. Figure 7 shows the corresponding dual-system counterparts of Fig. 6, for which the empirical ambiguity resolution success rates are also given in Table 3. According to this table, the impact of multipath correction on the ambiguity resolution performance is not very consider-

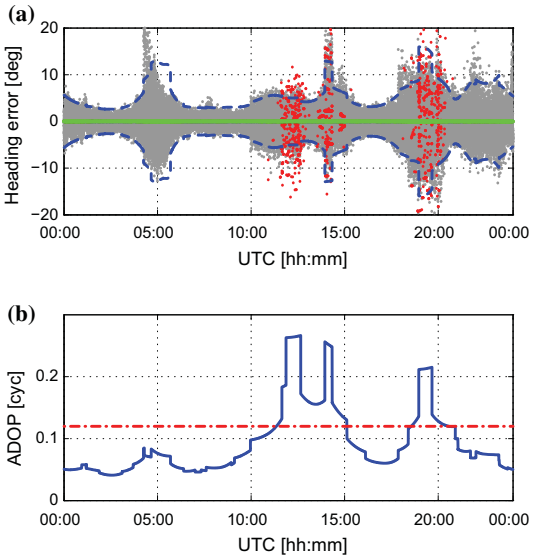

Fig. 8 **a** Time series of IRNSS + GPS Block IIF L5 instantaneous heading solutions based on the data of CUCC–CUBB collected on DOY 167 of 2016 at Perth with the cutoff elevation of 10°. *gray* ambiguity-float solution; *green* LAMBDA-based correctly fixed solution; *red* LAMBDA-based wrongly fixed solution. The *blue dashed lines* indicate the 95% formal confidence interval. **b** The corresponding time series of the single-epoch unconstrained ADOP (*blue*) and the value of 0.12 cycle (*red dashed line*)

able, particularly in case of MC-LAMBDA. As a result of the integration of the IRNSS with GPS Block IIF, the number of wrongly fixed solutions decreases dramatically particularly using the standard LAMBDA method. It can be seen that using MC-LAMBDA method, a success rate of 99.8% for the linear array and higher than 99.9% for the planar array can be attained.

In Figs. 6 and 7, the fluctuations in the ambiguity-float solutions (gray dots) and the variability of the wrongly fixed solutions (red dots) density can be explained through, respectively, the (linearized) formal standard deviations and the ADOP. Here, as an example, we explain the behavior of the heading dual-system estimations based on the linear array. The information depicted in Fig. 8a are those in the top panel of Fig. 7a plus the 95% formal confidence interval based on the linearized formal ambiguity-float heading standard deviation (blue dashed lines). The signature of the blue lines is in agreement with that of the ambiguity-float heading error time series. Comparing the time series of the ambiguity-fixed heading solutions with that of the ADOP (blue graph) shown in Fig. 8b, the wrong ambiguity fixing occurs during the periods of large ADOPs. The red dashed line in this figure indicates the ADOP value of 0.12 cycle. As a rule of thumb, an ADOP smaller than about 0.12 cycle corresponds to a LAMBDA success rate of larger than 99.9% (Odijk and Teunissen 2008).

6 Attitude determination performance

Having investigated the ambiguity resolution performance, we now turn our focus onto the attitude determination performance. In this section, we present our numerical evaluations of the L5-signal attitude determination performance for standalone IRNSS and IRNSS integrated with GPS Block IIF, for the aforementioned linear and planar array.

6.1 Standalone IRNSS

We start our attitude determination analysis with the linear array of CUCC–CUBB. Figure 9 illustrates for this array in a stepwise manner how the baseline solutions are built up from unconstrained ambiguity-float scenario to the constrained ambiguity-fixed scenario. The gray vector and sphere shown in all the panels of this figure are the baseline ground truth and the sphere with the radius of the baseline (CUCC–CUBB) length l, respectively. Figure 9a shows the single-epoch IRNSS L5 baseline solutions as blue dots for the unconstrained ambiguity-float scenario. The dispersion in the baseline solutions is governed by the code precision and satellites geometry. The excursions in this three-dimensional scatter plot are due to the significant change that the receiver-satellite geometry undergoes during a 24-h period.

Shown in Fig. 9b are the single-epoch IRNSS L5 baseline solutions for the constrained ambiguity-float scenario (gray dots). As is shown, upon constraining the baseline length $||x|| = l$, the corresponding solutions can only vary on a sphere with the radius of l. Incorporating the integerness of the DD ambiguities, Fig. 9c illustrates the single-epoch IRNSS L5 solutions for the constrained ambiguity-fixed scenario (green dots: correctly fixed; red dots: wrongly fixed). For this scenario, there are different clusters of the baseline solutions which correspond to different estimated integer values for the DD ambiguities. The green cluster associates with the correct integer value comprising 94.3% of the fixed solutions, while the red clusters correspond to the wrong integer values. To judge whether a DD ambiguity is correctly fixed, its corresponding integer solution is compared with the reference integer DD ambiguity computed based on the multi-epoch solution of the baseline-known model.

Figure 10a shows the horizontal scatter plot of the single-epoch IRNSS L5 baseline solutions, corrected for the baseline ground truth, for all the scenarios depicted in Fig. 9. Looking at the blue scatter plot, a Northwest elongation can be recognized which is due to a specific receiver-satellite geometry. In order to explain this, we make use of the confidence ellipse concept as it is the formal representative

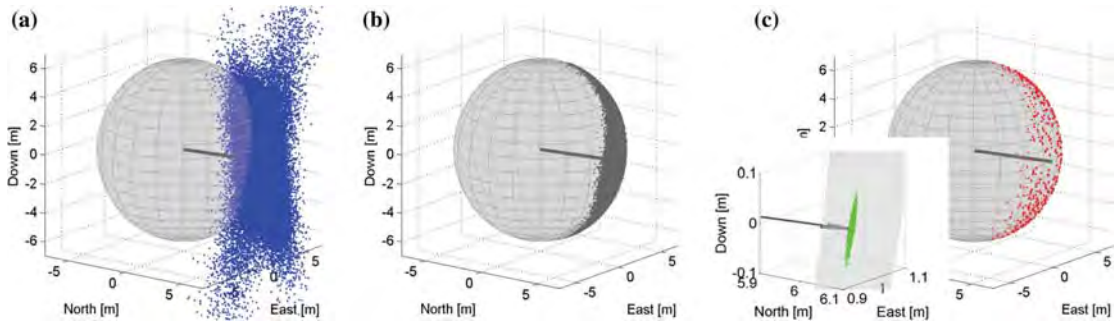

Fig. 9 Single-epoch IRNSS L5 solutions of the CUCC–CUBB baseline at Curtin University on DOY 167 of 2016 with the cutoff elevation of 10°. **a** Unconstrained ambiguity-float scenario; **b** Constrained ($||x|| = l$) ambiguity-float scenario; **c** Constrained ($||x|| = l$) ambiguity-fixed scenario (with a zoom-in in the lower left). *The gray vector* and the sphere shown in all the three panels denote, respectively, the baseline ground truth and the sphere with the radius of the CUCC–CUBB baseline length l. In panel **c**, *green and red dots* show the correctly fixed and wrongly fixed solutions, respectively

of the empirical scatter plot. Denoting the unconstrained ambiguity-float baseline solution as $\hat{x}$ with mean and covariance matrix of, respectively, x and $Q_{\hat{x}\hat{x}}$, its confidence ellipse reads

$$(\hat{x} - x)^T Q_{\hat{x}\hat{x}}^{-1} (\hat{x} - x) = k^2 \tag{13}$$

in which the constant k^2 is chosen such that a certain confidence level, e.g., 95%, is reached. As the direction of elongation is given by the direction of the eigenvector of $Q_{\hat{x}\hat{x}}^{-1}$ corresponding to its smallest eigenvalue, it follows with the aid of (1) that this direction is given by

$$\begin{aligned} f &= \underset{\tilde{f}}{\text{argmin}}\ \tilde{f}^T Q_{\hat{x}\hat{x}}^{-1} \tilde{f} \\ &= \underset{\tilde{f}}{\text{argmin}} \sum_{s=1}^{m} w^s \left[\tilde{f}^T \left(u^s - \bar{u} \right) \right]^2 \end{aligned} \tag{14}$$

with u^s being the unit direction vector from receiver to satellite s and $\bar{u}$ being the weighted average of the vectors u^s $(s = 1, \ldots, m)$. Note that here for simplicity, we drop the index $_I$ from those IRNSS-specific parameters. Figure 10b depicts the day-averaged skyplot position of the IRNSS satellites as well as that of the weighted average at Perth on DOY 167 of 2016 with the cutoff elevation of 10°. The differences $(u^s - \bar{u})$ are mainly oriented along the West–East direction. However, they have a non-negligible projection onto the North–South direction for satellites I1 and I2 such that the direction f that minimizes the contribution of all $(u^s - \bar{u})$ to (14) will mainly lie in an almost Northwesterly direction. This explains the Northwesterly elongation of the blue horizontal scatter plot in Fig. 10a.

The gray dots in Fig. 10a show the horizontal scatter plot of the constrained ambiguity-float baseline solutions, while the green and red dots show that of the constrained correctly and wrongly fixed baseline solutions, respectively. A zoom-in is also provided on the lower left of the figure to show the correctly fixed results more clearly. As it can be seen, the gray dots mainly take negative values along the North direction revealing that the constrained ambiguity-float baseline solutions are biased. This bias is due to the nonlinearity involved in the model of observations, called *nonlinearity bias* (Teunissen 1989). The nonlinearity of our model of observations stems from the orthonormality constraint of the rotation matrix R_q in (6). In "Appendix", we have elaborated more on this type of bias. The level of nonlinearity of the observational model depends on the baseline length and the GNSS data precision. The more precise the GNSS data and/or the longer the baseline, the less the impact of the constraint nonlinearity. Consider, as an example, the ambiguity-fixed scenario where the DD ambiguities are successfully fixed to their integer values. Then it is the very precise phase observations which take the leading role in baseline estimation. Therefore, the nonlinearity bias in the constrained correctly fixed solutions is expected to be negligible. This is indeed confirmed by the correctly fixed solutions scatter plot (green dots) in Fig. 10a.

Table 4, for the linear and planar array, lists the IRNSS L5 single-epoch empirical and formal standard deviations of the attitude angles based on the multipath-corrected data. In Sect. 5, it was shown that the instantaneous MC-LAMBDA ambiguity resolution using the standalone IRNSS is feasible with a notably high success rate. Therefore, Table 4 shows, in addition to the ambiguity-float results, the corresponding MC-LAMBDA ambiguity-fixed results as well. The empirical values are obtained from the single-epoch least-squares estimations of the attitude angles, whereas the formal values are obtained from taking the average of all the single-epoch

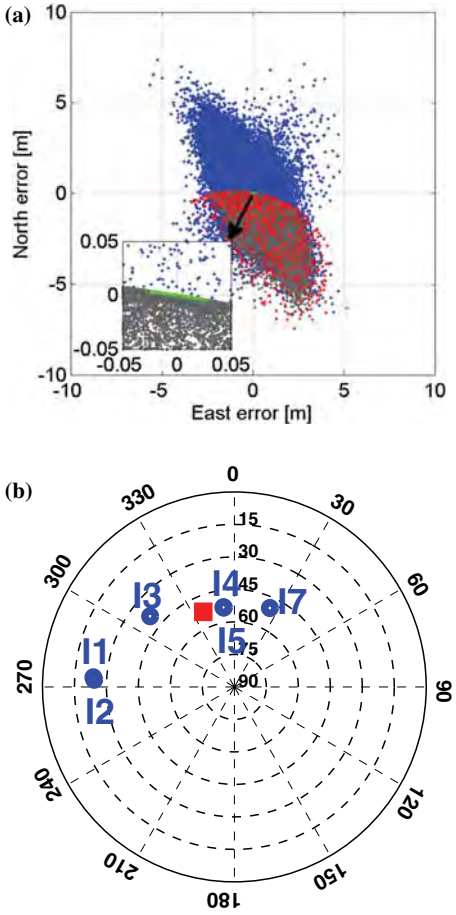

Fig. 10 **a** Single-epoch IRNSS L5 horizontal scatter plot of the CUCC–CUBB baseline at Curtin University corrected for the corresponding ground truth, on DOY 167 of 2016 with the cutoff elevation of 10°. *Blue* unconstrained ambiguity-float solutions; *gray* constrained ambiguity-float solutions; *red* constrained wrongly fixed solutions; *green* constrained correctly fixed solutions. A zoom-in is also depicted in the lower left of the figure. **b** Day-averaged IRNSS skyplot at Perth for DOY 167 of 2016 with the cutoff elevation of 10°. The *red square* indicates the skyplot position of vector $\bar{u}$ (cf. 14)

formal least-squares standard deviations based on the *linearized* observational model (w.r.t. the attitude angles). In case of the planar array, in addition to heading and elevation, bank is also estimable.

Comparing the empirical and the linearized formal results of the ambiguity-float scenario, an inconsistency is recognizable between them which can be attributed to the nonlinearity of the observational model. More explanation is provided in "Appendix". Upon fixing the DD ambiguities, however, the discrepancy between the empirical and the linearized formal outcomes disappears. The attitude angles standard deviations increase from heading to elevation to bank. This can be explained through the baselines orientation along with the IRNSS satellites geometry. Here, as an example, we consider the linear array of CUCC–CUBB with the baseline length of l. Through the linear approximation of (1) w.r.t. the attitude angles $\gamma = [\alpha \quad \varepsilon]^T$, the heading–elevation covariance matrix is given by

$$Q_{\hat{\gamma}\hat{\gamma}} = \frac{\sigma_p^2}{l^2}\left(\sum_{s=1}^{m} w^s \left[J^T\left(u^s - \bar{u}\right)\right]\left[J^T\left(u^s - \bar{u}\right)\right]^T\right)^{-1} \tag{15}$$

with J being the Jacobian matrix of the following form

$$J = [J_\alpha \quad J_\varepsilon] = \begin{bmatrix} -s_\alpha c_\varepsilon & -c_\alpha s_\varepsilon \\ c_\alpha c_\varepsilon & -s_\alpha s_\varepsilon \\ 0 & -c_\varepsilon \end{bmatrix} \tag{16}$$

From (15) and (16), if $J_\alpha^T(u^s - \bar{u})$ is larger than $J_\varepsilon^T(u^s - \bar{u})$, then the heading estimation would be more precise than the elevation and vice versa. For the CUCC–CUBB baseline with almost the South–North orientation, we have $J_\alpha \approx [0,\ 1,\ 0]^T$ (East direction) and $J_\varepsilon \approx [0,\ 0,\ -1]^T$ (Up direction). Since the GNSS satellites have a larger extension along the horizontal plane than the vertical, heading is expected to have better precision than elevation. Equation (15) in addition reveals that the longer the baseline, the more precise the attitude angles estimation.

Note, in case of working with the original data (without multipath correction), the ambiguity-fixed attitude angles standard deviations in Table 4 change as follows. The value of σ_{ϕ_I} for the original phase data is larger than that of the multipath-corrected phase data by a factor of 2 (see Table 2).

Table 4 Instantaneous IRNSS L5 attitude precision

Scenario	Ambiguity float (°)			Ambiguity fixed (°)		
	$\sigma_{\hat{\alpha}}$	$\sigma_{\hat{\varepsilon}}$	$\sigma_{\hat{\beta}}$	$\sigma_{\check{\alpha}}$	$\sigma_{\check{\varepsilon}}$	$\sigma_{\check{\beta}}$
Linear array						
emp	12.06	18.55	–	0.04	0.08	–
form	7.51	18.52	–	0.04	0.09	–
Planar array						
emp	11.77	18.97	27.64	0.03	0.07	0.10
form	6.54	17.01	21.92	0.03	0.08	0.10

Empirical and linearized formal standard deviations of the attitude angles in degrees for the linear array of CUBB–CUCC and the planar array of CUBB–CUCC–CUT3 (see Fig. 2), based on the multipath-corrected data collected on DOY 167 of 2016 with the cutoff elevation of 10°. The ambiguity-fixed solutions are obtained through applying MC-LAMBDA. emp, empirical; form, formal. $\sigma_{\hat{\alpha}}/\sigma_{\check{\alpha}}$, $\sigma_{\hat{\varepsilon}}/\sigma_{\check{\varepsilon}}$, $\sigma_{\hat{\beta}}/\sigma_{\check{\beta}}$, ambiguity-float/ambiguity-fixed standard deviation of heading, elevation and bank, respectively

Table 5 Instantaneous IRNSS + GPS Block IIF L5 attitude precision

Scenario	Ambiguity-float (°)			Ambiguity-fixed (°)		
	$\sigma_{\hat{\alpha}}$	$\sigma_{\hat{\varepsilon}}$	$\sigma_{\hat{\beta}}$	$\sigma_{\check{\alpha}}$	$\sigma_{\check{\varepsilon}}$	$\sigma_{\check{\beta}}$
Linear array						
emp	2.78	6.06	–	0.02	0.05	–
form	3.36	7.46	–	0.02	0.05	–
Planar array						
emp	1.93	5.69	8.76	0.01	0.04	0.06
form	2.07	6.28	9.15	0.01	0.04	0.06

Empirical and linearized formal standard deviations of the attitude angles in degrees for the linear array of CUBB–CUCC and the planar array of CUBB–CUCC–CUT3 (see Fig. 2), based on the multipath-corrected data collected on DOY 167 of 2016 with the cutoff elevation of 10°. The ambiguity-fixed solutions are obtained through applying MC-LAMBDA. emp, empirical; form, formal. $\sigma_{\hat{\alpha}}/\sigma_{\check{\alpha}}$, $\sigma_{\hat{\varepsilon}}/\sigma_{\check{\varepsilon}}$, $\sigma_{\hat{\beta}}/\sigma_{\check{\beta}}$, ambiguity-float/ambiguity-fixed standard deviation of heading, elevation and bank, respectively

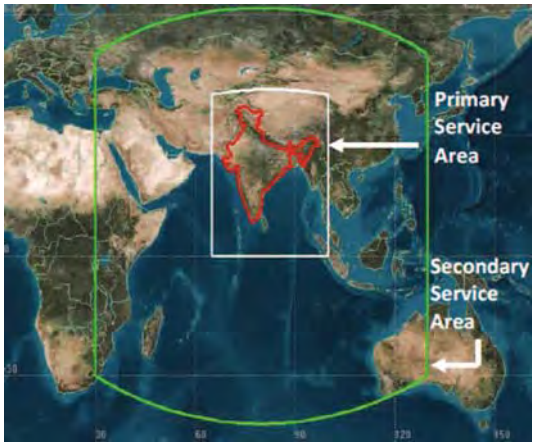

Fig. 11 IRNSS primary and secondary service area (image credit: ISRO)

However, the weight matrix corresponding to the multipath-corrected data is 2 times larger than that of the original data due to the adding multipath corrections based on the previous day data. Therefore, multiplying the ambiguity-fixed entries of Table 4 by $\sqrt{2}$ gives their counterparts on the basis of the original data.

6.2 IRNSS combined with GPS

Now we analyze the IRNSS L5 attitude determination capability when combined with GPS L5. Table 5 displays the dual-system counterparts of the entries in Table 4. Upon integrating IRNSS with GPS Block IIF, the attitude angles precisions improve by 3–4 times in case of ambiguity-float scenario and 1.5–2 times in case of ambiguity-fixed scenario. This improvement is due to the increase in number of visible satellites and, in case of ambiguity-float scenario, to the higher precision of the GPS L5 code observations w.r.t the IRNSS. As was explained for the standalone IRNSS scenario, following successful fixing of the ambiguities, the empirical and the linearized formal results become consistent with each other.

6.3 Attitude determination over the IRNSS service area

So far, we have presented the single-epoch formal and empirical analyses on the basis of the data collected at Perth. For the ambiguity-fixed scenario, a good consistency was shown between our empirical outcomes and their linearized formal counterparts (see Tables 4, 5). This agreement implies that the easy-to-compute (linearized) formal values can indeed be used to predict the expected attitude determination performance. Therefore, in this subsection, we perform a formal analysis of the ambiguity-fixed attitude angles standard deviations for a linear array of two antennas over the IRNSS primary and secondary service area, i.e., locations within $(-30° < \phi < 50°, 30° < \lambda < 130°)$. The extent of these two service areas is depicted in Fig. 11.

Prior to our ambiguity-fixed analyses, it is important to first investigate whether high instantaneous MC-LAMBDA success rates are achievable for the locations inside the IRNSS service area. To do so, we first compare the instantaneous LAMBDA formal success rate at these locations with that at Perth. If for a location, instantaneous LAMBDA success rate not lower than that at Perth can be achieved, then it can be concluded that the instantaneous MC-LAMBDA success rate at this location would also not be lower than its counterpart at Perth, which is as high as 90% for a linear array of two antennas (see Table 3). With this in mind, the standalone IRNSS ambiguity-fixed results are then given only for the locations with the larger instantaneous LAMBDA success rate than that at Perth.

Integration of the IRNSS with the GPS Block IIF results in the instantaneous LAMBDA success rate becoming higher than 70% for all the locations within $(-30° < \phi < 50°, 30° < \lambda < 130°)$. This means that these locations are expected to have the instantaneous MC-LAMBDA success rate higher than *at least* 70%. Therefore, the IRNSS + GPS Block IIF ambiguity-fixed results are given for all these locations.

Our ambiguity-fixed evaluations in this section are based on the variance matrix given in (15), albeit with σ_p being replaced by σ_ϕ. The precision with which the attitude angles can be estimated depends on the phase data precision [σ_ϕ], satellites geometry [u^s (receiver-satellite unit direction vector), w^s (satellite elevation-dependent weight)], baseline length [l] and orientation [α (heading), ε (elevation)]. For our analyses, we consider the following setup:

$\sigma_{\phi_I} = \sigma_{\phi_G} = 2$mm, baseline length $l = 1$m, baseline orientations ($\alpha = 0°$, $\varepsilon = 0°$), ($\alpha = 90°$, $\varepsilon = 0°$) and ($\alpha = 0°$, $\varepsilon = 45°$). For such a setup, Figs. 12 and 13 provide the color map of the day-averaged single-epoch ambiguity-resolved L5-based heading and elevation standard deviations on the basis of standalone IRNSS and IRNSS + GPS Block IIF, respectively. For other values of phase data precision and baseline length, the results of these figures will change according to (15). The white areas in Fig. 12 denote those locations excluded from our computations, due to having the poorer instantaneous MC-LAMBDA success rate than that of Perth. In order for the color maps to be readable, we use the same color to show all the elevation standard deviations not lower than 1.3°, and also the same color to illustrate all the heading standard deviations not lower than 0.9°.

The results in Figs. 12 and 13 show that the heading and elevation precision at a given location varies with changing baseline orientation. As was explained earlier, what drives the heading and elevation precision is the satellites extension along the vectors J_α and J_ε in (16), respectively. For the baseline orientations of ($\alpha = 0°$, $\varepsilon = 0°$) and ($\alpha = 90°$, $\varepsilon = 0°$), vector J_ε will always points toward Up direction, while vector J_α points toward East and South direction, respectively. Therefore, if the satellites have a larger extension along West–East compared to South–North, the heading corresponding to the baseline ($\alpha = 0°$, $\varepsilon = 0°$) will be more precise than that of ($\alpha = 90°$, $\varepsilon = 0°$). For example, for the location ($\phi = -30°$, $\lambda = 115.5°$) which is close to Perth, the standalone IRNSS heading associated with the baseline orientation ($\alpha = 0°$, $\varepsilon = 0°$) is about 1.4 times more precise than that of the baseline orientation ($\alpha = 90°$, $\varepsilon = 0°$). This is due to the fact that the IRNSS satellites extension at this location is a bit larger in West–East direction compared to the South–North direction.

Integrating the IRNSS with GPS Block IIF, both the heading and elevation increase in precision. The improvement in heading standard deviation is more significant for the baseline orientation of ($\alpha = 90°$, $\varepsilon = 0°$) compared to ($\alpha = 0°$, $\varepsilon = 0°$). This can be explained as follows. The IRNSS satellites, for almost all the locations, have a stronger extension along the West–East direction than the South–North direction. As a result, the baseline orientation ($\alpha = 0°$, $\varepsilon = 0°$) has already a heading estimation with high precision which is not the case with the baseline orientation

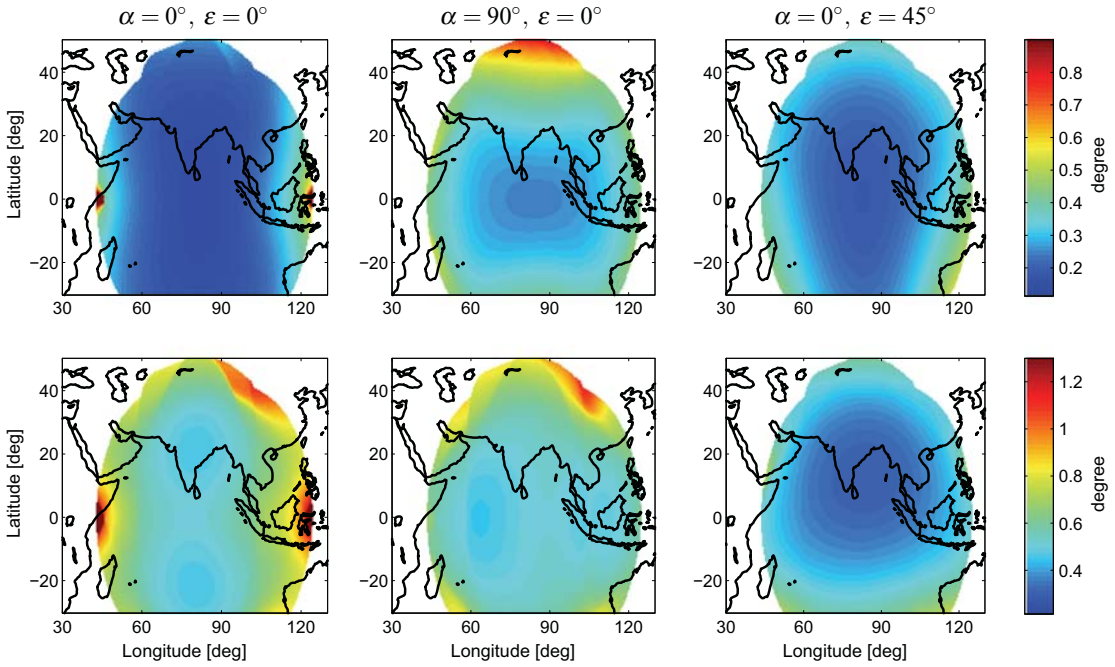

Fig. 12 Color map of day-averaged single-epoch ambiguity-resolved attitude angles standard deviation based on the standalone IRNSS L5, on DOY 167 of 2016 with 10° cutoff elevation. The results are computed assuming $\sigma_{\phi_I} = 2$mm and baseline length $l = 1$m, for the baseline orientations of, from left to right, ($\alpha = 0°$, $\varepsilon = 0°$), ($\alpha = 90°$, $\varepsilon = 0°$) and ($\alpha = 0°$, $\varepsilon = 45°$), respectively. *top* heading; *bottom* elevation. The *white areas* denote those locations excluded from our computations, due to having the poorer instantaneous MC-LAMBDA success rate than that of Perth

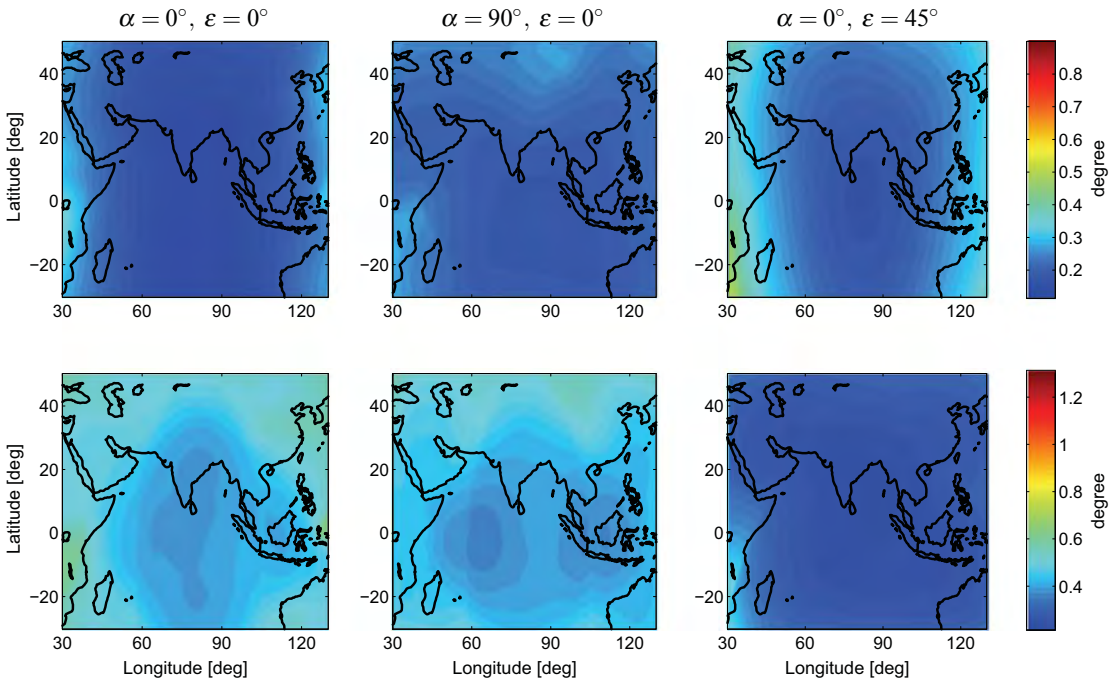

Fig. 13 Color map of day-averaged single-epoch ambiguity-resolved attitude angles standard deviation based on the IRNSS + GPS Block IIF L5, on DOY 167 of 2016 with 10° cutoff elevation. The results are computed assuming $\sigma_{\phi_I} = \sigma_{\phi_G} = 2$mm and baseline length $l = 1$m, for the baseline orientations of, from left to right, ($\alpha = 0°,\ \varepsilon = 0°$), ($\alpha = 90°,\ \varepsilon = 0°$) and ($\alpha = 0°,\ \varepsilon = 45°$), respectively. *top* heading; *bottom* elevation

($\alpha = 90°,\ \varepsilon = 0°$). Adding GPS Block IIF constellation to IRNSS enhances the South–North satellites extension, thus considerably improving heading precisions for the baseline orientation ($\alpha = 90°,\ \varepsilon = 0°$).

7 Conclusion

In this contribution, we presented the very first L5 attitude determination analyses of the fully operational IRNSS as a standalone system and also in combination with the fully operational GPS Block IIF. The noise characteristics of the L5 signal for both the IRNSS and GPS were assessed through the carrier-to-noise density, measurement precision and time correlation. It was shown that the GPS data have a significantly lower noise level than that of the IRNSS, particularly in case of the code data. The time correlation of both the constellations was shown to be negligible providing that the multipath impact is corrected for, even if 1-s data are used. Our analyses were conducted on an epoch-by-epoch basis, using both the multipath-corrected and original 1-s data collected by three stations at Curtin University, Perth, Australia.

A prerequisite for precise and fast attitude determination is the successful resolution of the DD ambiguities. Employing real data, we compared the performance of standard LAMBDA and MC-LAMBDA method for both a linear array of two antennas and a planar array of three antennas with the following body frames

$$\text{Lineararray:} B = 6.15 \text{ m}$$

$$\text{Planararray:} B = \begin{bmatrix} 6.15 & 6.78 \\ 0 & 4.22 \end{bmatrix} \text{ m}$$

Based on the multipath-corrected data, when switching from LAMBDA to MC-LAMBDA, the standalone IRNSS instantaneous ambiguity resolution success rate was shown to increase significantly from 20.4 to 94.3% for the linear array and from 9.3 to 99.9% for the planar array. Upon integrating IRNSS with GPS Block IIF, the instantaneous MC-LAMBDA success rates of 99.8% and larger than 99.9% were achieved for the mentioned linear and planar array, respectively. For the original data, the mentioned success rates are marginally smaller.

Having investigated the ambiguity resolution performance, we then assessed the attitude angles precision for both the ambiguity-float and ambiguity-fixed scenarios. The orthonormality constraint of the rotation matrix, involved in the attitude observational model, is a nonlinear constraint of which the impact on the constrained baseline and attitude angles estimation was explained. The larger the standard deviation of the GNSS data and/or the shorter the baselines length, the more considerable the impact of the constraint nonlinearity, and the poorer the linear approximation will be.

Our ambiguity-fixed results showed that for the linear array oriented in South–North direction with the length of around $l = 6$ m, heading and elevation are estimable with the standard deviations of 0.04 and 0.09 degrees in case of standalone IRNSS and 0.02 and 0.05 degrees in case of IRNSS + GPS Block IIF. The higher precision of heading compared to the elevation was explained through the baseline orientation and satellites geometry. For the planar array, the ambiguity-fixed standard deviations for heading, elevation and bank were 0.03, 0.08 and 0.10 degrees in case of standalone IRNSS and 0.01, 0.04 and 0.06 degrees in case of IRNSS + GPS Block IIF.

For the ambiguity-fixed scenario, a good consistency was shown between our empirical outcomes and their *linearized* formal counterparts, implying that the easy-to-compute (linearized) formal values can indeed be used to predict the expected attitude determination performance. Therefore, we performed a formal analysis of the ambiguity-fixed attitude angles standard deviations over the IRNSS primary and secondary service area. Such an analysis was provided for those locations where the high instantaneous MC-LAMBDA success rates are guaranteed.

Our evaluations were based on the following setup: phase standard deviations $\sigma_{\phi_I} = \sigma_{\phi_G} = 2$mm, baseline length $l = 1$m, baseline orientations ($\alpha = 0°$, $\varepsilon = 0°$), ($\alpha = 90°$, $\varepsilon = 0°$) and ($\alpha = 0°$, $\varepsilon = 45°$). For such a setup, we illustrated the L5-based heading and elevation standard deviations on the basis of standalone IRNSS and IRNSS + GPS Block IIF. For other values of phase data precision and baseline length, these results will change according to (15). It was shown that the heading and elevation precision at a given location varies with changing baseline orientation, which was explained through the satellites geometry extension.

Switching from standalone IRNSS to IRNSS + GPS Block IIF, both the heading and elevation increase in precision. The improvement in heading standard deviation was shown to be more significant for the South–North-oriented baseline compared to the West–East-oriented baseline. This is due to the IRNSS satellites having a stronger extension along the West–East direction than the South–North direction for almost all the locations within its service area. As a result, the South–North-oriented baseline has already a heading estimation with high precision which is not the case with the West–East-oriented baseline. Adding GPS Block IIF to IRNSS enhances the South–North satellites extension, thus considerably improving heading precision for the West–East-oriented baseline.

Acknowledgements The second author is the recipient of an Australian Research Council (ARC) Federation Fellowship (Project Number FF0883188). This support is gratefully acknowledged.

Appendix: Nonlinearity of the GNSS attitude model

The orthonormality constraint of the rotation matrix R_q in (6) is a nonlinear constraint. Here, through simulation, we explain the impact of this nonlinearity on the estimation of the attitude angles. Considering the linear array of CUCC–CUBB, we simulated two sets of 10^4 baseline solutions, corresponding to the unconstrained ambiguity-float and ambiguity-fixed scenarios. They were generated from the normal distribution with the same mean (CUCC–CUBB baseline ground truth $\bar{b}$), but different variances. The variance matrix of the first set Q_1 is equal to the average formal variance matrix of the blue dots in Fig. 9a over the first 15,000 epochs, while the variance matrix of the second set is given by $Q_2 = \frac{\sigma_{\phi_I}}{\sigma_{p_I}} Q_1$.

As was previously mentioned, for the single-baseline scenario, the orthonormality constraint of the rotation matrix is equivalent to the length constraint on the baseline vector, i.e., $||x|| = l$. It indicates that the baseline vector is constrained to lie on a sphere with known radius of l. Imposing the baseline-length constraint, we estimated the heading and elevation of the CUCC–CUBB baseline based on the two sets of simulated data. Figure 14 shows the corresponding histograms of the estimated attitude angles, corrected for the ground truth, on the basis of the samples with the variance matrix Q_1 (a) and samples with the variance matrix Q_2 (b). Given the *linearized* formal standard deviations of the estimated angles, we computed the corresponding zero-mean normal PDF (probability density function) which are indicted by the red curves in Fig. 14.

The histograms in Fig. 14a demonstrate an asymmetric behavior. From these two histograms, it can be seen that the empirical density of the errors of the estimated angles at negative values is not the same as that at positive values, implying that the estimated angles are biased. This bias is called the nonlinearity bias which was already recognized, in the baseline domain, in the gray scatter plots in Fig. 10. Also, the deviation of these histograms from the red normal curve indicates that looking at only the standard deviations of the attitude angles is not enough to find out the complete probabilistic behavior of their estimators. The histograms in Fig. 14b, in contrast, show a very good consistency with

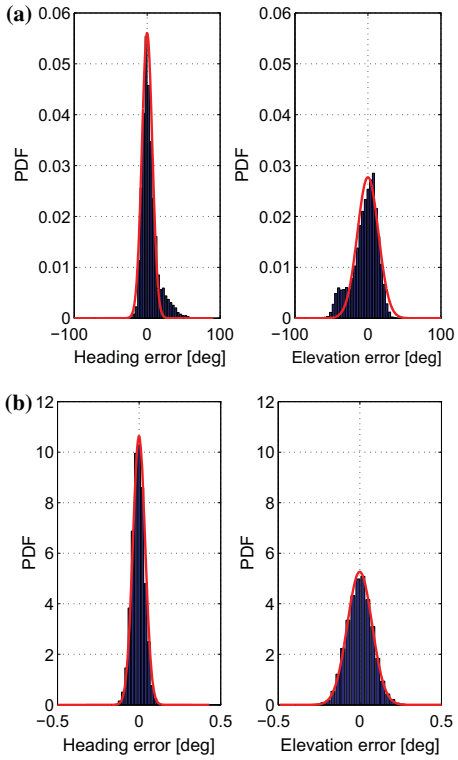

Fig. 14 *Histograms* of the heading (*left*) and elevation (*right*) estimation errors (*blue*) and their linearized formal counterparts (*red*). These results are computed based on 10^4 normally distributed baseline samples with the mean value of the CUCC–CUBB baseline ground truth and with two variance matrices Q_1 (**a**) and $Q_2 = \frac{\sigma_{\phi_I}}{\sigma_{p_I}} Q_1$ (**b**). Q_1 is equal to the average formal variance matrix of the *blue dots* in Fig. 9a over the first 15,000 epochs

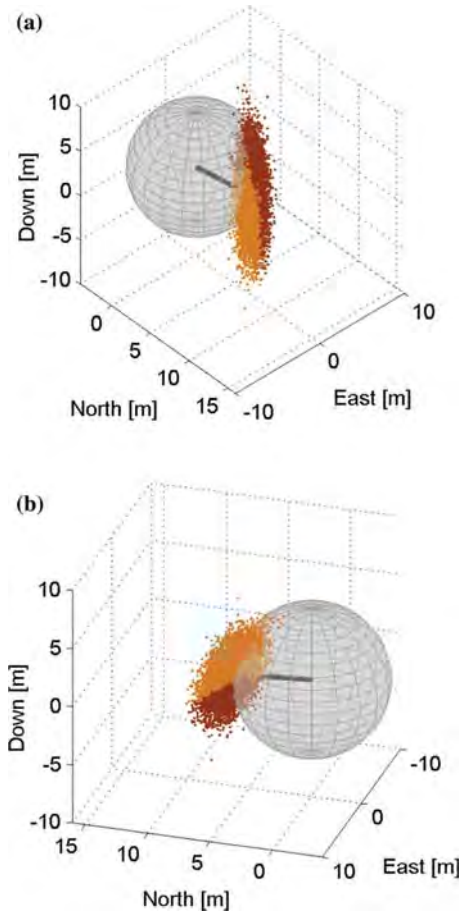

Fig. 15 Mapping the unconstrained ambiguity-float baseline solutions to their baseline-length-constrained counterparts. The scatter plot of 10^4 normally distributed baseline samples with the mean value of the CUCC–CUBB baseline ground truth and with the variance matrix of Q_1 (the average formal variance matrix of the blue dots in Fig. 9a over the first 15,000 epochs). The *gray vector* and the *sphere* denote, respectively, the baseline ground truth and the sphere with the radius of the CUCC–CUBB baseline length l. The *scatter plot* is split into two clusters. *light brown*/*dark brown* the points that upon constraining the baseline length result in negative/positive $\{*\}$ estimation errors. $\{*\}$: heading (**a**); elevation (**b**)

their corresponding normal PDF. This is due to the fact that these estimations are based on the very precise samples with the precision (Q_2) at the level of phase precision, where the nonlinearity of the attitude model can be neglected.

The signature of the attitude angles histograms is driven by the variance matrix of the simulated samples, hence the size, shape and orientation of their scatter plot. The asymmetric signature in Fig. 14a can therefore be explained through the specific orientation of the first set of simulated data scatter plot. Figure 15a, b shows the scatter plot of the first set of the simulated samples each of which is split into two clusters (*light/dark brown*) based on two different criteria. Clusters in panel (a), upon constraining the baseline length, result in heading estimation errors either of negative (light brown) or positive (dark brown) values, while clusters in panel (b) are the counterparts of those in panel (a) for the elevation estimation errors. It can be seen that the two clusters are not symmetric in any of the two panels. This explains the asymmetric behavior of the histograms in Fig. 14a.

In Fig. 15a/b, the light brown and the dark brown clusters are separated by a two-dimensional manifold being the locus of the points which, upon constraining the baseline length, result in the heading/elevation estimation errors equal to zero. The intersection of these two manifolds then accommodates the points which, upon constraining the baseline length, are mapped to the baseline ground truth $\bar{b}$. This intersection is described by a straight line given by

$$b_o = \left(I_3 + k\, Q_{\hat{b}\hat{b}}\right)\, \bar{b};$$

$$k \in \mathbb{R}: \ \left|\left|b_o - \bar{b}\right|\right|^2_{Q_{\hat{b}\hat{b}}} \leq ||b_o - b||^2_{Q_{\hat{b}\hat{b}}} \qquad \forall\, b \in \mathbb{S}^3(l) \tag{17}$$

where $\mathbb{S}^3(l)$ is the set of points on the circumference of a three-dimensional zero-centered sphere with the radius of l. Proof is as follows. Given the unconstrained ambiguity-float baseline solution $\hat{b}$, its baseline-length-constrained counterpart is given by

$$\hat{\hat{b}} = \underset{\substack{||b|| = l \\ b \in \mathbb{R}^3}}{\operatorname{argmin}} \ \left|\left|\hat{b} - b\right|\right|^2_{Q_{\hat{b}\hat{b}}} \tag{18}$$

which, from geometrical point of view, is the point where the ellipsoid $\mathbb{E}^3 = \{b \in \mathbb{R}^3 |\ ||\hat{b} - b||^2_{Q_{\hat{b}\hat{b}}} = \text{constant}\}$ just touches the sphere $\mathbb{S}^3(l)$ (Teunissen 2010). This indicates that the gradient vectors of the mentioned ellipsoid and sphere will be parallel at point $\hat{\hat{b}}$. Therefore to find the locus of the points $b_o \in \mathbb{R}^3$ for which $\hat{\hat{b}} = \bar{b}$, the gradient vector of the corresponding ellipsoid $\mathbb{E}^3$ and sphere $\mathbb{S}^3(l)$ at $\bar{b}$ should be set parallel to each other, i.e.,

$$Q^{-1}_{\hat{b}\hat{b}}\left(b_o - \bar{b}\right) = k\, \bar{b} \tag{19}$$

where k is a scalar. Equation (19) can be worked out to

$$b_o = \left(I_3 + k\, Q_{\hat{b}\hat{b}}\right)\, \bar{b} \tag{20}$$

With changing k, (20) describes a straight line which is parallel to $Q_{\hat{b}\hat{b}}\bar{b}$ and passes through $\bar{b}$. Note the values of k should result in $\bar{b}$ being the solution of (18) for $\hat{b} = b_o$ given by (20). Therefore, k follows from

$$k \in \mathbb{R}: \ \left|\left|b_o - \bar{b}\right|\right|^2_{Q_{\hat{b}\hat{b}}} \leq ||b_o - b||^2_{Q_{\hat{b}\hat{b}}} \qquad \forall\, b \in \mathbb{S}^3(l) \tag{21}$$

□

References

Amiri-Simkooei AR, Tiberius CCJM (2007) Assessing receiver noise using GPS short baseline time series. GPS Solut 11(1):21–35

Babu R, Mula P, Ratnakara SC, Ganeshan AS (2015) IRNSS satellite parameter estimation using combination strategy. Glob J Sci Front Res 15(3):87–95

de Bakker PF, Tiberius CCJM, van der Marel H, van Bree RJP (2012) Short and zero baseline analysis of GPS L1 C/A, L5Q, GIOVE E1B, and E5aQ signals. GPS Solut 16(1):53–64

Buist PJ (2007) The baseline constrained LAMBDA method for single epoch, single-frequency attitude determination applications. In: Proceedings of the 20th international technical meeting of the satellite division of The Institute of Navigation (ION GNSS 2007), ION, pp 2962–2973

Chandrasekhar MV, Rajarajan D, Satyanarayana G, Tirmal N, Rathnakara SC, Ganeshan AS (2015) Modernized IRNSS broadcast ephemeris parameters. Control Theory Inform 5(2):1–9

Cohen C (1992) Attitude determination using GPS. Ph D Thesis Stanford University

Euler HJ, Goad CC (1991) On optimal filtering of GPS dual frequency observations without using orbit information. Bull Geod 65(2):130–143

Ganeshan AS, Ratnakara SC, Srinivasan N, Rajaram B, Tirmal NKA (2015) First position fix with IRNSS. Inside GNSS 10(4):48–52

Giorgi G, Buist PJ (2008) Single-epoch, single-frequency, standalone full attitude determination: experimental results. In: Proceedings of the fourth ESA workshop on satellite navigation user equipment technologies, NAVITEC. ESA-ESTEC, The Netherlands

Giorgi G, Teunissen PJG, Buist PJ (2008) A search and shrink approach for the baseline constrained LAMBDA method: experimental results. In: Yasuda A (ed) Proceedings of international symposium on GPS/GNSS, Tokyo University of Marine Science and Technology, pp 797–806

Giorgi G, Teunissen PJG, Verhagen S, Buist PJ (2010) Testing a new multivariate GNSS carrier phase attitude determination method for remote sensing platforms. Adv Space Res 46(2):118–129

GPS Directorate (2011) Navstar GPS space segment/user segment L5 interfaces (IS-GPS-705B). Technical report

Harville DA (1997) Matrix algebra from A statistician's perspective. Springer, New York

Hauschild A, Grillmayer G, Montenbruck O, Markgraf M, Vörsmann P (2008) GPS based attitude determination for the flying laptop satellite. In: Small satellites for earth observation, Springer, pp 211–220

Hide C, Pinchin J, Park D (2007) Development of a low cost multiple GPS antenna attitude system. In: Proceedings of ION GNSS, pp 88–95

Hodgart MS, Purivigraipong S (2000) New approach to resolving instantaneous integer ambiguity resolution for spacecraft attitude determination using GPS signals. In: Proceedings of IEEE position location and navigation symposium, IEEE, pp 132–139

ISRO (2014) INDIAN REGIONAL NAVIGATION SATELLITE SYSTEM: signal in space ICD for standard positioning service, Version 1.0. ISRO Satellite Centre, June 2014

ISRO (2016) PSLV-C33/IRNSS-1G. http://www.isro.gov.in/sites/default/files/pslv-c33-brochure.pdf, published April 2016. Accessed 1 June 2016

Kuipers JB (2002) Quaternions and rotation sequences. Princeton University Press, Princeton

Kumari A, Samal K, Rajarajan D, Swami U, Babu R, Kartik A, Rathnakara SC, Ganeshan AS (2015) Precise modeling of solar radiation pressure for IRNSS satellite. J Nat Sci Res 5(3):35–43

Li Y, Zhang K, Roberts C, Murata M (2004) On-the-fly GPS-based attitude determination using single- and double-differenced carrier phase measurements. GPS Solut 8(2):93–102

Lu G (1995) Development of a GPS multi-antenna system for attitude determination. Ph.D. Thesis University of Calgary

Madsen J, Lightsey EG (2004) Robust spacecraft attitude determination using global positioning system receivers. J Spacecr Rockets 41(4):635–644

Magnus JR, Neudecker H et al (1995) Matrix differential calculus with applications in statistics and econometrics. Wiley, New York

Montenbruck O, Steigenberger SR (2015) IRNSS orbit determination and broadcast ephemeris assessment. In: Proceedings of the 2015 international technical meeting of the institute of navigation, Dana Point, California, January 2015, pp 185–193

Nadarajah N, Khodabandeh A, Teunissen PJG (2015) Assessing the IRNSS L5-signal in combination with GPS, Galileo, and

QZSS L5/E5a-signals for positioning and navigation. GPS Solut 20(2):289–297
Odijk D, Teunissen PJG (2008) ADOP in closed form for a hierarchy of multi-frequency single-baseline GNSS models. J Geod 82(8):473–492
Odijk D, Teunissen PJ (2013) Characterization of between-receiver GPS-Galileo inter-system biases and their effect on mixed ambiguity resolution. GPS Solut 17(4):521–533
Odijk D, Teunissen PJG, Huisman L (2012) First results of mixed GPS + GIOVE single-frequency RTK in Australia. J Spat Sci 57(1):3–18
Odijk D, Nadarajah N, Zaminpardaz S, Teunissen PJG (2016) GPS, Galileo, BDS, QZSS and IRNSS differential ISBs: estimation and application. GPS Solut. doi:10.1007/s10291-016-0536-y
Park C, Teunissen PJG (2003) A new carrier phase ambiguity estimation for GNSS attitude determination systems. In: Proceedings of international GPS/GNSS symposium, Tokyo, vol 8, pp 283–290
Park C, Teunissen PJG (2009) Integer least squares with quadratic equality constraints and its application to GNSS attitude determination systems. Int J Control Autom 7(4):566–576
Psiaki ML (2006) Batch algorithm for global-positioning-system attitude determination and integer ambiguity resolution. J Guid Control Dyn 29(5):1070–1079
Tegedor J, Øvstedal O (2014) Triple carrier precise point positioning (ppp) using gps l5. Surv Rev 46(337):288–297
Teunissen P (2006) The LAMBDA method for the GNSS compass. Artif Satell 41(3):89–103
Teunissen P (2007) A general multivariate formulation of the multi-antenna GNSS attitude determination problem. Artif Satell 42(2):97–111
Teunissen PJ (1995) The least-squares ambiguity decorrelation adjustment: a method for fast GPS integer ambiguity estimation. J Geod 70(1–2):65–82
Teunissen PJ (2010) Integer least-squares theory for the GNSS compass. J Geod 84(7):433–447
Teunissen PJ, Giorgi G, Buist PJ (2011) Testing of a new single-frequency GNSS carrier phase attitude determination method: land, ship and aircraft experiments. GPS Solut 15(1):15–28
Teunissen PJG (1989) Estimation in nonlinear models, II. Hotine-Marussi symposium on mathematical geodesy, Pisa, Italy, June 5–8
Teunissen PJG (1997) A canonical theory for short GPS baselines. Part I: the baseline precision. J Geod 71(6):320–336
Teunissen PJG (1998) Success probability of integer gps ambiguity rounding and bootstrapping. J Geod 72(10):606–612
Teunissen PJG (1999) An optimality property of the integer least-squares estimator. J Geod 73(11):587–593
Teunissen PJG (2012) The affine constrained GNSS attitude model and its multivariate integer least-squares solution. J Geod 86(7):547–563
Teunissen PJG, Amiri-Simkooei AR (2008) Least-squares variance component estimation. J Geod 82(2):65–82
Thoelert S, Montenbruck O, Meurer M (2014) IRNSS-1A: signal and clock characterization of the Indian regional navigation system. GPS Solut 18(1):147–152
Wang B, Miao L, Wang S, Shen J (2009) A constrained LAMBDA method for GPS attitude determination. GPS Solut 13(2):97–107
Zaminpardaz S, Teunissen PJG, Nadarajah N (2016a) GLONASS CDMA L3 ambiguity resolution and positioning. GPS Solut. doi:10.1007/s10291-016-0544-y
Zaminpardaz S, Teunissen PJG, Nadarajah N (2016b) IRNSS standalone positioning: first results in Australia. J Spat Sci 61(1):5–27

9 GLONASS CDMA L3 performance (Part 1: Ambiguity resolution and positioning in comparison with GPS L1)

This chapter is covered by the following publication:

Zaminpardaz S., Teunissen P.J.G., Nadarajah N. (2017f) GLONASS CDMA L3 ambiguity resolution and positioning. GPS Solutions, Springer, 21(2):535-549

GPS Solut (2017) 21:535–549
DOI 10.1007/s10291-016-0544-y

ORIGINAL ARTICLE

GLONASS CDMA L3 ambiguity resolution and positioning

Safoora Zaminpardaz[1] · Peter J. G. Teunissen[1,2] · Nandakumaran Nadarajah[1]

Received: 7 March 2016 / Accepted: 12 April 2016 / Published online: 18 May 2016

Abstract A first assessment of GLONASS CDMA L3 ambiguity resolution and positioning performance is provided. Our analyses are based on GLONASS L3 data from the satellite pair SVNs 755-801, received by two JAVAD receivers at Curtin University, Perth, Australia. In our analyses, four different versions of the two-satellite model are applied: the geometry-free model, the geometry-based model , the height-constrained geometry-based model, and the geometry-fixed model. We study the noise characteristics (carrier-to-noise density, measurement precision), the integer ambiguity resolution performance (success rates and distribution of the ambiguity residuals), and the positioning performance (ambiguity float and ambiguity fixed). The results show that our empirical outcomes are consistent with their formal counterparts and that the GLONASS data have a lower noise level than that of GPS, particularly in case of the code data. This difference is not only seen in the noise levels but also in their onward propagation to the ambiguity time series and ambiguity residuals distribution.

Keywords GLONASS · CDMA · Integer ambiguity resolution · GPS · PDOP · ADOP

✉ Peter J. G. Teunissen
P.Teunissen@curtin.edu.au

[1] GNSS Research Centre, Curtin University, GPO Box U1987, Perth, WA 6845, Australia

[2] Department of Geoscience and Remote Sensing, Delft University of Technology, PO Box 5048, 2600 GA Delft, The Netherlands

Introduction

A first assessment of GLONASS CDMA L3 ambiguity resolution and positioning performance is provided. The navigation signals of the GLONASS system are traditionally transmitted on the basis of the frequency division multiple access (FDMA) technique (ICD-GLONASS 2008). As a consequence of the FDMA technique, inter-frequency biases are present that impede a straightforward integer resolution of the double-differenced (DD) ambiguities (Leick et al. 2015; Hofmann-Wellenhof et al. 2013). To resolve this issue, special calibration procedures have been proposed aimed at realizing GLONASS FDMA integer ambiguity resolution (Takac 2009; Yamada et al. 2010; Reussner and Wanninger 2011; Wanninger 2009). With the advent, however, of the GLONASS code division multiple access (CDMA) signals, double differences of the carrier-phase ambiguities become integer themselves and standard methods of integer ambiguity resolution can directly be applied to realize ambiguity-resolved precise positioning.

In February 2011, following the launch of the first GLONASS-K1 satellite, SVN 801 (R26) (IAC 2016), the Russian satellite system commenced transmitting CDMA signals on L3 (1202.025 MHz) (Urlichich et al. 2010; Thoelert et al. 2011; Oleynik 2012). The current constellation (March 2016) consists of 28 satellites of which 26 are of GLONASS-M series, and two are of GLONASS-K series, subseries GLONASS-K1 (IAC 2016). This constellation has *four* CDMA-transmitting satellites, i.e., SVNs 801 (R26) and 802 (R17) of series K, 755 (R21) and the newly launched 751 of series M, among which SVN 801 is undergoing a flight test (IAC 2016). All the satellites of the GLONASS-K series as well as the last seven satellites of the GLONASS-M series will be capable of

transmitting CDMA signals on the L3 frequency (Oleynik 2012; Montenbruck et al. 2015).

It is expected that the last satellites of the GLONASS-M series will be launched by 2017 and that of the GLONASS-K1 series, 11 satellites will be launched through 2020. The GLONASS-K2 satellites will be launched in early 2017 (GPS World 2015). All these satellites will be able to transmit CDMA signals. Providing signals on the frequencies used by the other GNSSs (GPS L5 and L1) is also part of the future plan (Karutin 2012). An overview of these signals was presented in Urlichich et al. (2010, 2011) and Karutin (2012), and Thoelert et al. (2011) assessed the signal quality and the modulation quality of the L3 CDMA civil signal of SVN 801 received by a high-gain antenna.

We provide for the first time an analysis of the GLONASS L3 ambiguity resolution and corresponding positioning performance. Our analyses are based on L3 data of the GLONASS satellite pair R21–R26, received by two JAVAD receivers at Curtin University, Perth, Australia. We also compare our results with corresponding results obtained for the GPS L1 observables from the satellite pair G21–G29, having almost the same trajectories as those of R21–R26 for the periods considered in this contribution. We start first with the formulation of the four versions of the two-satellite models used in our analyses. These four versions are the geometry-free model, the geometry-based model, the height-constrained geometry-based model and the geometry-fixed model. We then study the noise characteristics of the GLONASS CDMA data and compare it to their GPS L1 counterparts. We present results on the carrier-to-noise density and on the estimated zenith-referenced measurement precision. Next, double-differenced (DD) ambiguity resolution is taken up. This is done for all four models, both for GLONASS and GPS. In this analysis, we present the empirical results and compare them for consistency with their formal counterparts. Following the ambiguity resolution analyses, the positioning performance is discussed. This is done both for the ambiguity float case as well as for the ambiguity fixed case. Besides, we illustrate a case of a near rank-deficiency and demonstrate that the PDOP and ADOP characteristics can be quite distinct and that one therefore should not confuse a poor PDOP with poor ambiguity resolution capabilities. Finally, a summary and conclusions are provided.

Two-satellite observational model

As our analyses are based on data from the GLONASS satellites R21 and R26, we first formulate the underlying two-satellite model. In the following, this formulation will be presented for four different models of different strengths, i.e., geometry-free, geometry-based, height-constrained geometry-based, and geometry-fixed model.

From geometry-free to geometry-fixed

With the expectation $E\{.\}$ and dispersion $D\{.\}$, the corresponding two-satellite double-differenced (DD) system of observation equations reads

$$E\{\begin{bmatrix} p \\ \varphi \end{bmatrix}\} = \begin{bmatrix} 1 & 0 \\ 1 & \lambda \end{bmatrix}\begin{bmatrix} \rho \\ a \end{bmatrix}$$
$$D\{\begin{bmatrix} p \\ \varphi \end{bmatrix}\} = \frac{1}{w}\begin{bmatrix} \sigma_p^2 & 0 \\ 0 & \sigma_\varphi^2 \end{bmatrix} \quad (1)$$

with p and φ being the DD code and phase observable, respectively, ρ the DD receiver-satellite range and a the DD integer ambiguity in cycles. The ambiguity a is linked to the DD phase observable through the signal wavelength λ. With the elevation-dependent weighting functions, $w_{\theta 1}$ and $w_{\theta 2}$ (see 4), for the first and the second satellite with elevation angles θ_1 and θ_2, respectively, the final weight becomes $w = \frac{1}{2}[w_{\theta 1}^{-1} + w_{\theta 2}^{-1}]^{-1}$. The zenith-referenced standard deviations of the undifferenced code and phase observables are denoted as σ_p and σ_φ, respectively.

We will be working with four different models (Teunissen 1997). They are arranged in ascending order of strength:

1. Geometry-free model (GFr): This is the model as formulated in (1). As it is parametrized in ρ, it is free from the receiver-satellite geometry;
2. Geometry-based model (GB): This model follows from linearizing (1) with respect to the unknown receiver coordinates. The receiver-satellite geometry is then taken into account through the parametrization

$$\delta\rho = -c^T \delta b \quad (2)$$

with $\delta\rho$ being the receiver-satellite range increment, c the 3-vector containing the between-satellite single-differenced (SD) receiver-satellite unit direction vectors, and $\delta b = [\delta N, \delta E, \delta H]^T$ the unknown between-receiver baseline increment vector;
3. Height-constrained geometry-based model (H-GB): This model follows if one adds the (weighted) height constraint to the geometry-based model,

$$E\{\delta h\} = [0, 0, 1]\delta b; \quad D\{\delta h\} = \sigma_h^2 \quad (3)$$

4. Geometry-fixed model (GFi): In this model the positions of the receiver and the satellite, and thus receiver-satellite range ρ, are assumed known.

Note that both the geometry-free and geometry-fixed model are solvable on an epoch-by-epoch basis, i.e., instantaneously. This is, however, not the case for the unconstrained and height-constrained geometry-based models. Two or more epochs are then needed for these models to be solvable.

Two-satellite positioning

Our solutions of the unconstrained and height-constrained geometry-based models are based on data from three epochs each. To realize a sufficient change of receiver-satellite geometry, the three epochs are every time chosen from three distinct segments of the satellite trajectories. In the skyplot of Fig. 1, this process is schematically shown for the satellites R21–R26. In this figure, the location of the satellites over the stated sub-periods is distinguished using different colors. Each position solution makes use of *one* pair of the DD observable (phase and code) over the *red* period, *one* pair over the *blue* period and *one* pair over the *green* period. For example, the satellites location indicated with the same markers in Fig. 1 are associated with those instants of which the observables are used in one position solution. Thus, each solution computed is in fact a triple-epoch solution, for which the ambiguities as well as baseline coordinates are assumed constant. As the sampling rate of the epoch-triples is 1 s, the so obtained ambiguity and position time series also has a 1 Hz rate.

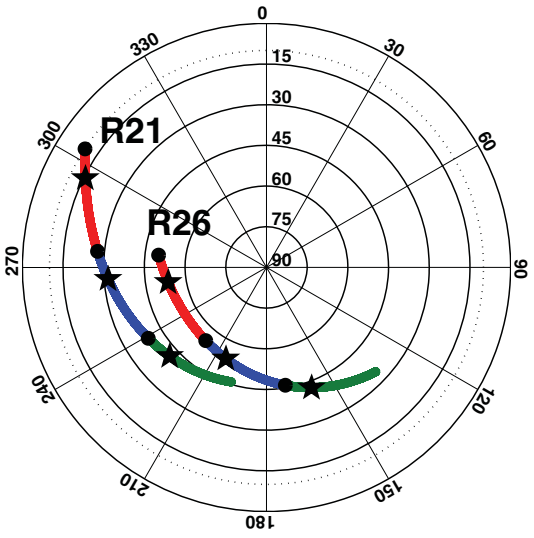

Fig. 1 Skyplot of the GLONASS CDMA-transmitting satellites at Perth, Australia, during UTC [04:47:00–06:55:00] on DOY 21 of 2016, with the cutoff elevation angle of 10°. The whole period is divided into three sub-periods distinguished using different colors. The *black circles* indicate the satellite positions at the first epoch of each sub-period, whereas the *black pentagrams* indicate them at 1000th epoch of each sub-period

Noise characteristics

In this section, we study the noise characteristics of the GLONASS CDMA data and compare it to their GPS L1 counterparts. We present results on the carrier-to-noise density, the estimated zenith-referenced measurement precision and on the influence of multipath.

Measurement experiment

The data used in our analyses were collected by the two stations CUT3 and CUCC of an eight-meter baseline at Curtin University. Each station is equipped with a JAVAD receiver, capable of tracking GLONASS L3 CDMA signals as well as GPS L1 signals. The signals of the GLONASS satellite pair R21–R26 and of the GPS satellite pair G21–G29 were tracked. Their receiver-satellite geometry over the observation time span is shown in the skyplot of Fig. 2. For both the GLONASS and the GPS satellites, the broadcast ephemeris data are used. Further information is

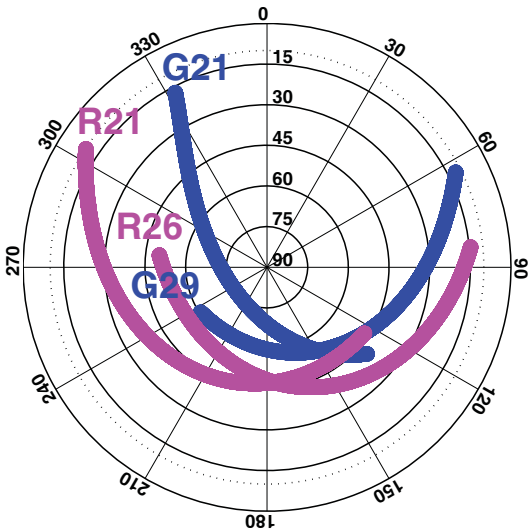

Fig. 2 Skyplot of the GLONASS CDMA-transmitting satellites (*purple*) and GPS satellites (*blue*) at Perth, Australia, during UTC [04:47:00–09:31:00] on DOY 21 of 2016, with the cutoff elevation angle of 10°

Table 1 Characteristics of the experiment conducted for this study

# antennas	2
Antenna type	TRM59800.00 SCIS
Receiver type	JAVAD TRE_G3TH_8
Location	Curtin University, Perth, Australia
Data type	GLONASS L3, GPS L1
Satellites	R21–R26, G21-G29
Cutoff angle	10°
Date and time	UTC [05:20:00–10:03:00] on DOY 13 of 2016
	UTC [04:47:00–09:31:00] on DOY 21 of 2016
	UTC [03:42:00–08:26:00] on DOY 37 of 2016

provided in Table 1. Note that the observation time spans are listed in three different days (DOYs 13, 21, 37). They were chosen such that the receiver-satellite geometries of GPS and of GLONASS repeat.

Carrier-to-noise density

To get insight into the noise characteristics of the GLONASS CDMA L3 signal, we first consider its carrier-to-noise density (C/N0). Figure 3 shows the observed C/N0 of the GLONASS L3 and GPS L1 (all the visible satellites) signals. While the GLONASS L3 signal has a BPSK(10) modulation (Urlichich et al. 2011), the GPS L1 (C/A) signal has a BPSK(1) modulation (GPSD 2013). The C/N0 graph of the GLONASS L3 signal has a similar signature to that of GPS L5-signal (see Nadarajah et al. (2015)), which also has a BPSK(10) modulation.

Estimated precision (time correlation)

As another step to characterize the noise of the GLONASS L3 and the GPS L1 observables, we apply the least-squares variance component estimation (LS-VCE) method (Teunissen and Amiri-Simkooei 2008). The LS-VCE is applied to the short-baseline phase and code observables of the CUT3-CUCC receiver pair. Use was made of the exponential weighting function

$$w_\theta = \left[1 + 10\exp\left(-\frac{\theta}{10}\right)\right]^{-2} \tag{4}$$

so as to capture the elevation dependency, where θ is the elevation of the satellite in degrees (Euler and Goad 1991). Incorporation of this elevation dependency in the LS-VCE allows one to estimate the zenith-referenced standard deviations of the undifferenced code and phase observables, σ_p and σ_φ. The corresponding VCE results are shown in Table 2. Note that the precision of the GLONASS L3 signal is significantly better than its GPS L1 counterpart.

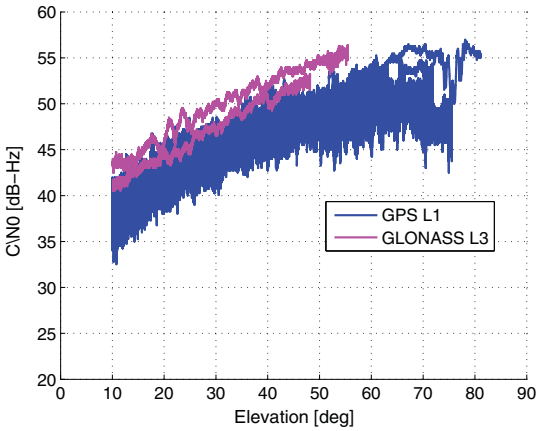

Fig. 3 Carrier-to-noise density (C/N0) for GPS L1 and GLONASS L3 signals tracked by JAVAD TRE_G3TH_8 receiver, connected to TRM59800.00 SCIS antenna at Perth, Australia, on DOY 21 of 2016 during UTC [04:47:00–09:31:00]

Table 2 Estimated zenith-referenced standard deviations of the undifferenced original (multipath-corrected) code σ_p and phase σ_φ observables

Frequency	σ_p[m]	σ_φ[mm]
GPS L1	0.25 (0.22)	1 (1)
GLONASS L3	0.11 (0.05)	2 (1)

This is consistent with what was concluded from the C/N0 graph of Fig. 3. Also note that the table shows results for multipath-corrected standard deviations. The more detailed information on multipath correction is given in the next section. The so-obtained improvement is significant for both the GLONASS and GPS code observables, but most pronounced for GLONASS.

Multipath

We now describe how the above-mentioned multipath was determined and how it was used as a means to correct the data. Consider the code-phase vector

$$\begin{bmatrix} m_p \\ m_\varphi \end{bmatrix} = \begin{bmatrix} p \\ \varphi \end{bmatrix} - \begin{bmatrix} 1 & 0 \\ 1 & \lambda \end{bmatrix} \begin{bmatrix} \rho \\ a \end{bmatrix} \tag{5}$$

This vector is a zero-mean noise vector in case model (1) is correct, e.g., in case multipath is absent. In the presence of multipath, however, it captures the multipath on code, m_p, as well as the multipath on phase m_φ.

In our case, the epoch-by-epoch time series of the DD multipath vector $[m_p, m_\varphi]^T$ was determined by computing

ρ from the known receiver and satellite positions, while the reference integer a was computed using the very strong multi-epoch geometry-fixed model. Figure 4 displays the so-obtained DD code and phase multipath time series for the GLONASS L3 (R21–R26) and the GPS L1 (G21–G29) signals over the three time periods given in Table 1. Note that in all cases the time series of the three periods on DOYs 13, 21 and 37 indeed completely overlap each other.

As a further confirmation that the time series of the three DOYs 13, 21 and 37 capture the same phenomena, we now consider their day differences. These should then be showing zero-mean noise behavior with a variability that reflects the measurement precision. To do so, we first form the day-differenced DD code and phase multipaths, dm_p and dm_φ, by subtracting the DD multipath of DOY 37 from those of DOYs 13 and 21. Since the observables are highly dependent on the elevation of the satellites, the day-differenced DD multipaths are then normalized using the weight $dw = \frac{w}{2}$. While w captures the DD observable weight of (1), the factor 2 in the denominator takes care of the differencing between the 2 days.

Figure 5 shows, for the 2 day pairs DOY 37-DOY 13 and DOY 37-DOY 21, the histograms obtained from the epoch-by-epoch time series of $\sqrt{dw}\,dm_p$ and $\sqrt{dw}\,dm_\varphi$ for both GLONASS and GPS. The red curve in each panel shows the normal probability density function (PDF) with its standard deviation given by the values of Table 2 and with its mean equal to the mean of the histogram. For both GLONASS and GPS, the 2 day pairs show a good consistency between the histograms and the formal PDFs. This consistency supports the conclusion that the time series of (5) indeed captures the mentioned multipath. Also note that Fig. 5 illustrates again the difference in measurement precision between the GLONASS and GPS signals.

For the results of Table 2, as well as for the results in the sections following, the data of DOYs 13 and 21 have been multipath-corrected on an epoch-by-epoch basis using the multipath time series of DOY 37. This epoch-by-epoch correction ensures that no time correlation enters. The doubling in noise that enters through the correction is accounted for in the analyses that follow.

Ambiguity resolution

In this section, the ambiguity resolution performance of the GLONASS L3 observables will be assessed and compared with that of the GPS L1 observables. Our assessment will be carried out using four different models: the geometry-free model, the unconstrained and height-constrained geometry-based model, and the geometry-fixed model.

From geometry-free to geometry-fixed

The data used for our analysis is that of DOY 21 of 2016 over the time period UTC [04:47:00-06:55:00]. The solutions computed are triple-epoch solutions as explained earlier (see Fig. 1). Each of these solutions are obtained with a 1 Hz sampling rate, thus producing a time series of 3500 solutions. As there is only one unknown DD ambiguity in each case, the ambiguity resolution can be done through simple integer rounding. We denote the float

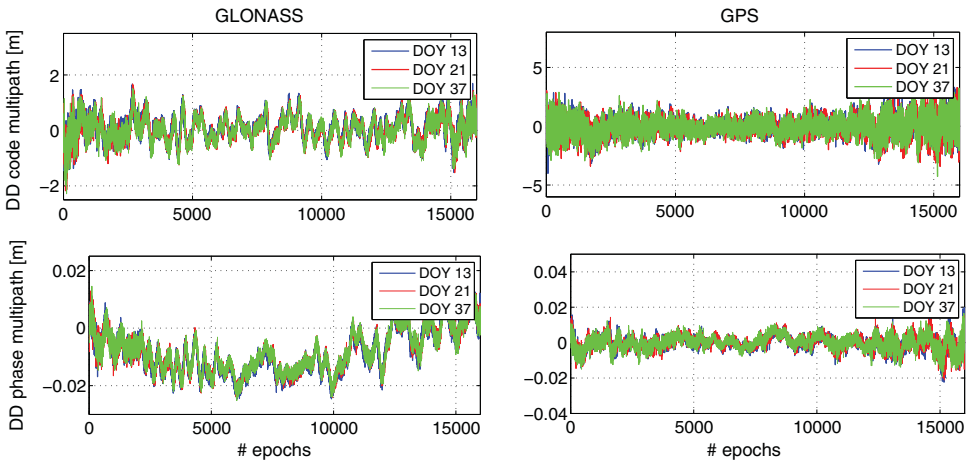

Fig. 4 DD code multipath (*top*) and DD phase multipath (*bottom*) for receiver pair CUT3-CUCC on DOY 13 during UTC [05:20:00–10:03:00] (*blue*), DOY 21 during UTC [04:47:00-09:31:00] (*red*) and DOY 37 during UTC [03:42:00–08:26:00] (*green*). Also, L3-signal of R21–R26 (*left*) and L1-signal of G21–G29 (*right*)

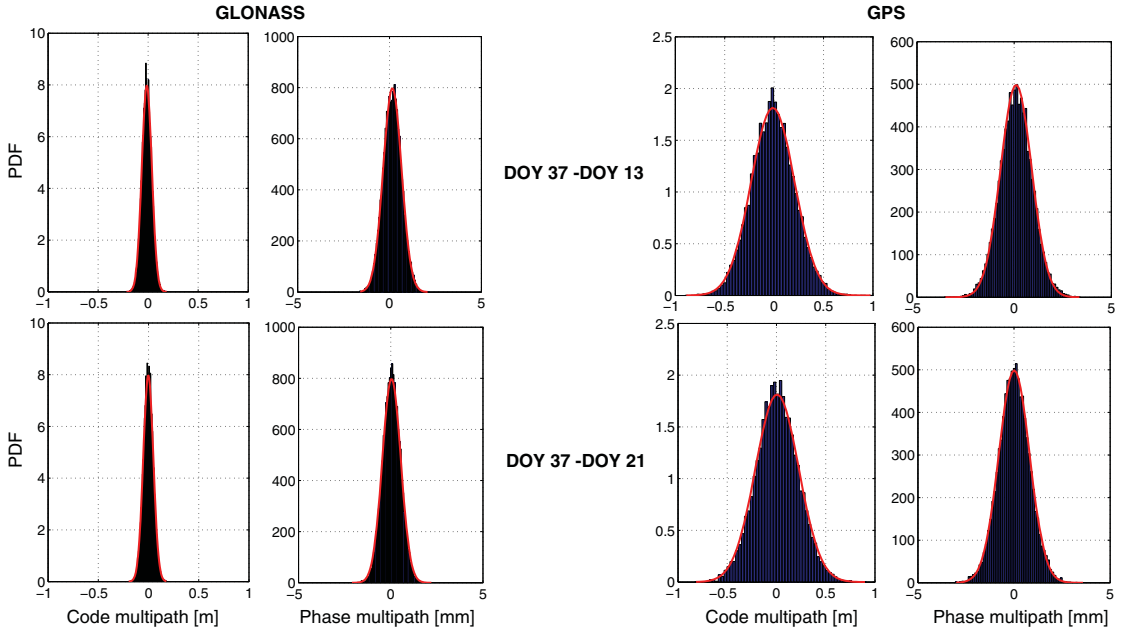

Fig. 5 Histograms (*blue*) and formal PDF (*red*) of the weighted day-differenced DD code and phase multipath for GLONASS (*left*) and GPS (*right*)

ambiguity as $\hat{a}$, the fixed (integer rounded) ambiguity as $\check{a}$, and the reference ambiguity as a. The reference DD ambiguity a has been obtained, as mentioned earlier, through the multi-epoch solution of the geometry-fixed model.

Figure 6 shows, for the receiver pair CUT3-CUCC, the time series of $\hat{a} - a$ and $\check{a} - a$ for both the GLONASS satellite pair R21–R26 (left column) and the GPS satellite pair G21-G29 (right column). Float solutions are shown in *gray*, correctly fixed solutions in *green*, and incorrectly fixed solutions in *red*. These time series are given, from top to bottom, for the geometry-free model, the geometry-based model, the height-constrained geometry-based models using $\sigma_h = 0.2$ m and $\sigma_h = 0.15$ m, respectively, and the geometry-fixed model.

The results clearly show a much better ambiguity resolution performance for the GLONASS data than for the GPS data. This is due to the lower noise level of the GLONASS code data and the longer wavelength of L3. If we start with the geometry-free model (top in Fig. 6), we observe many incorrectly fixed solutions, both for GLONASS and GPS. The geometry-free model is simply too weak for successful ambiguity resolution. The variation in incorrectly fixed solutions is, however, much smaller for GLONASS than it is for GPS. In case of GLONASS, the range is only $\check{a} - a \in \{-2, -1, 1, 2\}$.

The ambiguity resolution performance improves if we switch to the stronger (unconstrained) geometry-based model (second row in Fig. 6). The incorrectly fixed GPS ambiguities do, however, still vary over a much larger range than their GLONASS counterparts. The performance improves further if we include a weighted height constraint (3rd and 4th row in Fig. 6). Now GLONASS and GPS have the same range of incorrectly fixed ambiguities, although the number of incorrectly fixed GLONASS solutions is of course still smaller than that of GPS. Finally, with the strongest model of all, being the geometry-fixed model (bottom row in Fig. 6), both GLONASS and GPS have all ambiguities correctly fixed. Thus, despite the larger noise level of the GPS ambiguities (compare the variability in the GLONASS and GPS float time series), all fixed ambiguities are now correct.

Distribution of the ambiguity residuals

So far we considered the float and fixed time series $\hat{a} - a$ and $\check{a} - a$, respectively (Fig. 6). We now consider the ambiguity residual, i.e., the difference between the float and corresponding fixed solution, $\check{\varepsilon} = \hat{a} - \check{a}$. The ambiguity residuals form the basis for ambiguity validation (Verhagen and Teunissen 2013). Figure 7 displays the histograms of the DD ambiguity residuals for the five

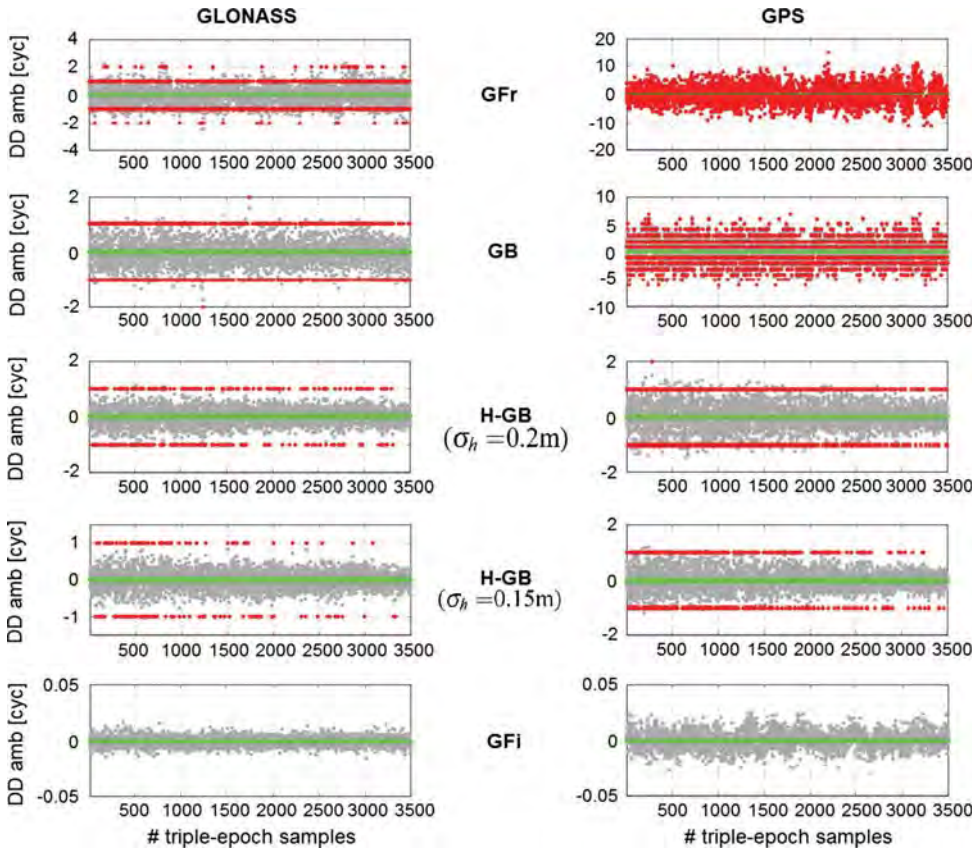

Fig. 6 DD ambiguity time series of $\hat{a} - a$ and $\check{a} - a$ for both the GLONASS satellite pair R21–R26 (*left*) and the GPS satellite pair G21-G29 (*right*) using data from the receiver pair CUT3-CUCC on DOY 21 during UTC [04:47:00-06:55:00]. Float solutions $\hat{a} - a$ are shown in *gray*, correctly fixed solutions in *green*, and incorrectly fixed solutions in *red*. The time series are given, from *top* to *bottom*, for the geometry-free (GFr) model, the geometry-based (GB) model, the height-constrained geometry-based (H-GB) models using $\sigma_h = 0.2$ m and $\sigma_h = 0.15$ m, respectively, and the geometry-fixed (GFi) model

different models considered. The domain of the histograms is $[-0.5, +0.5]$. Note that the shape of the histograms changes when one goes from the weaker model (geometry-free) to the stronger model (geometry-fixed). Hence, the ambiguity residuals are not normally distributed, i.e., they are not normally distributed even if the data are.

Assuming the data to be normally distributed, the ambiguity residuals have the distribution given by Teunissen (2002) as

$$f_{\breve{a}}(x) = \sum_{z\in\mathbb{Z}} \frac{1}{\sqrt{2\pi}\sigma_{\hat{a}}} \exp\{-\frac{1}{2}\left(\frac{x-z}{\sigma_{\hat{a}}}\right)^2\} \qquad (6)$$

with $x \in [-0.5, 0.5]$. This distribution has also been shown (red curve) for the five cases in Fig. 7. It demonstrates the consistency between the empirical and formal distributions. The distribution (6) has two limiting cases. The distribution tends to the uniform distribution when $\sigma_{\hat{a}}$ gets larger and it tends to the impulse function when $\sigma_{\hat{a}}$ gets smaller. This behavior is indeed clearly present in Fig. 7 when one goes from the rather weak geometry-free model toward the much stronger geometry-fixed model.

The ambiguity success rates

We computed the ambiguity success rates for the above five cases for GLONASS L3, GPS L1 and GPS L2, both formally as well as empirically. Being the probability of correct integer estimation, the formal ambiguity success rate is computed as (Teunissen 1998),

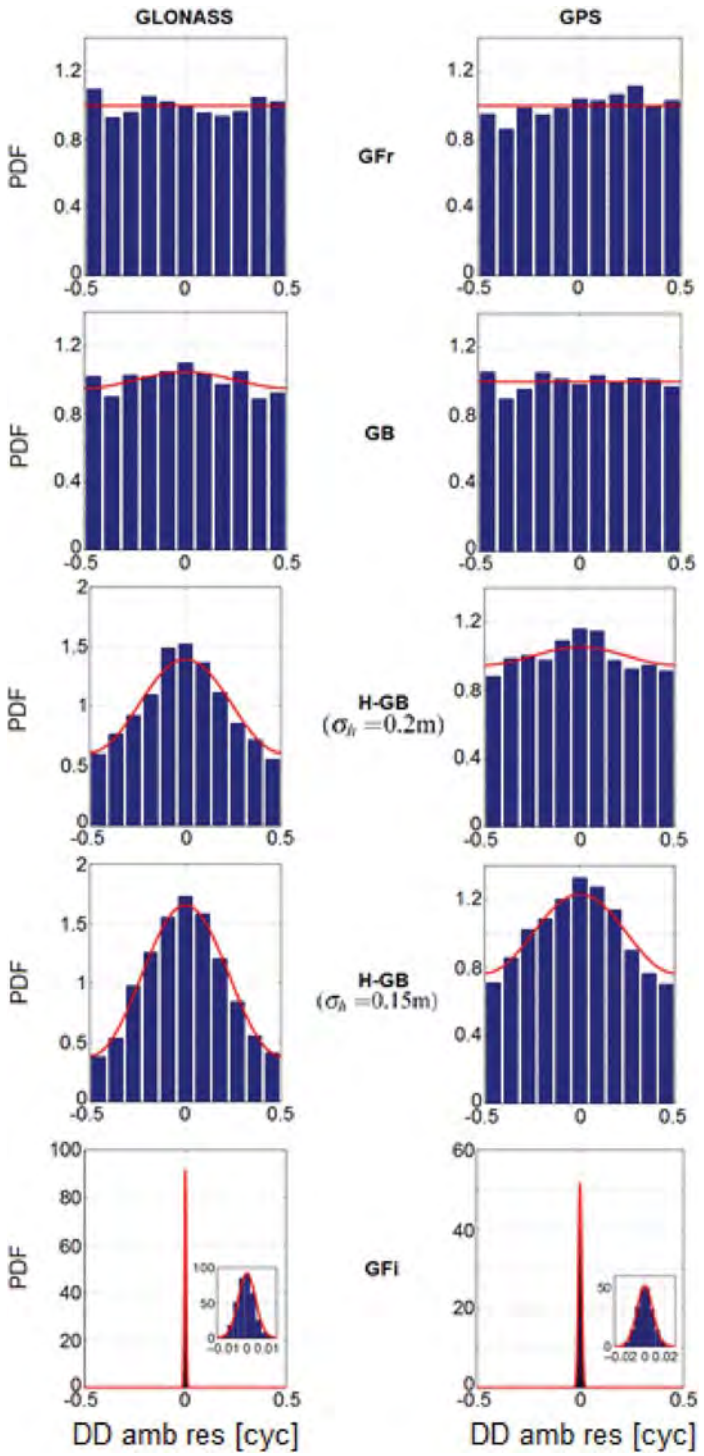

Fig. 7 Histograms (*blue*) and formal PDFs (*red*) of the DD ambiguity residuals $\breve{\varepsilon} = \hat{a} - \breve{a}$ that correspond with the time series of Fig. 6, for GLONASS (*left*) and GPS (*right*). The formal PDF of the ambiguity residual is given by (6)

$$\text{Formal } Ps = 2\Phi\left(\frac{1}{2\sigma_{\hat{a}}}\right) - 1 \quad (7)$$

with $\sigma_{\hat{a}}$ being the ambiguity standard deviation and $\Phi(x) = \int_{-\infty}^{x} \frac{1}{\sqrt{2\pi}} \exp\{-\frac{1}{2}v^2\}dv$. The empirical success rate is computed as

$$\text{Empirical } Ps = \frac{\#\text{ correct fixed DD ambiguities}}{\#\text{ float DD ambiguities}} \quad (8)$$

The results of the empirical and formal success rates for the above five cases are given in Table 3. For the computation of the formal success rate, the ambiguity standard deviation was taken as an average of the formal standard deviations, thus $\sigma_{\hat{a}} = \sqrt{\frac{1}{s}\sum_{j=1}^{s} \sigma_{\hat{a}}^2(j)}$, with $\sigma_{\hat{a}}^2(j)$ being the variance of the float DD ambiguity of the jth solution. As the results of Table 3 show, the empirical values are in good agreement with the formal ones. Also, the stronger the model is (from top to bottom), the larger the success rates become. Similarly, we see an increase in success rate with wavelength.

Positioning performance

In this section, we assess the GLONASS L3 observables performance in positioning. All results belong to the triple-epoch geometry-based model without any height constraint.

Two-satellite positioning: float solution

As discussed above, we make use of the 3500 triple-epoch solutions over the time period UTC [04:47:00-06:55:00] on DOY 21. Shown in Fig. 8 is the horizontal scatter plot for both the unconstrained float (gray) and correctly fixed (green) position solutions. Note that although the scatter plot of the fixed solutions has an ellipsoidal shape, the float scatter plot does not. The explanation lies in the significant change that the receiver-satellite geometry undergoes in the observational time span. This becomes clearer if we partition the time span in smaller time intervals and then assign different colors to these different time intervals, see Fig. 9. Now, we do recognize the ellipsoidal shapes in the scatter plot.

As the confidence ellipses are the formal representatives of the scatter plots, the change in orientation that the float scatter plot undergoes from time interval to time interval can be explained by means of the properties of the confidence ellipses. The confidence ellipsoid of $\hat{b}$, having mean $E(\hat{b}) = b$, is given as

Table 3 GLONASS L3, GPS L1, and GPS L2 ambiguity success rates, empirical and (formal), for the geometry-free (GFr) model, the geometry-based (GB) model, the height-constrained geometry-based (H-GB) model, and the geometry-fixed (GFi) model

Model	GLONASS L3 *Ps*	GPS L1 *Ps*	GPS L2 *Ps*
GFr	0.60 (0.55)	0.12 (0.11)	0.25 (0.20)
GB	0.77 (0.75)	0.20 (0.19)	0.34 (0.32)
H-GB (σ_h=0.2 m)	0.92 (0.92)	0.76 (0.75)	0.87 (0.87)
H-GB (σ_h=0.15 m)	0.96 (0.96)	0.87 (0.87)	0.95 (0.95)
GFi	1.00 (1.00)	1.00 (1.00)	1.00 (1.00)

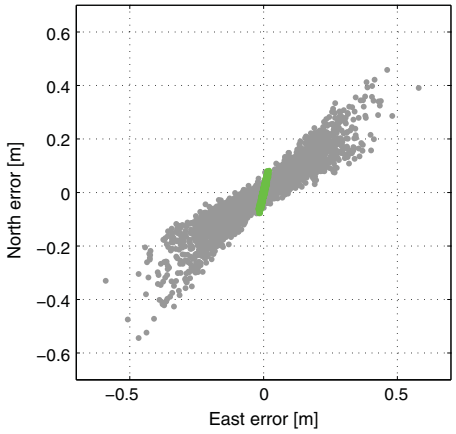

Fig. 8 GLONASS R21–R26 horizontal position scatter plot (triple-epoch based) collected by the receiver pair CUT3-CUCC on DOY 21 during UTC [04:47:00–06:55:00]. Float solutions are shown in *gray* and correctly fixed solutions are shown in *green*

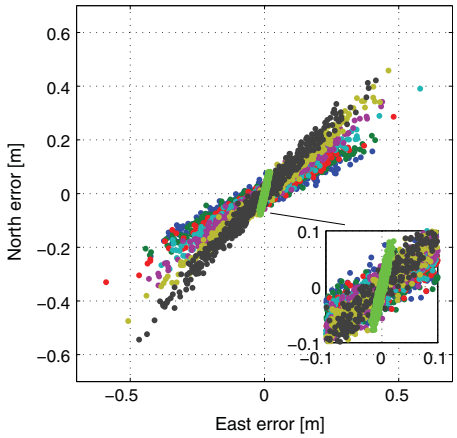

Fig. 9 GLONASS R21–R26 horizontal position scatter plot (triple-epoch based) collected by the receiver pair CUT3-CUCC on DOY 21 during UTC [04:47:00–06:55:00]. Float solutions are shown in *blue*, *dark green*, *red*, *cyan*, *purple*, *beige*, *dark gray*, each of which has a specific orientation. Correctly fixed solutions are shown in *green*

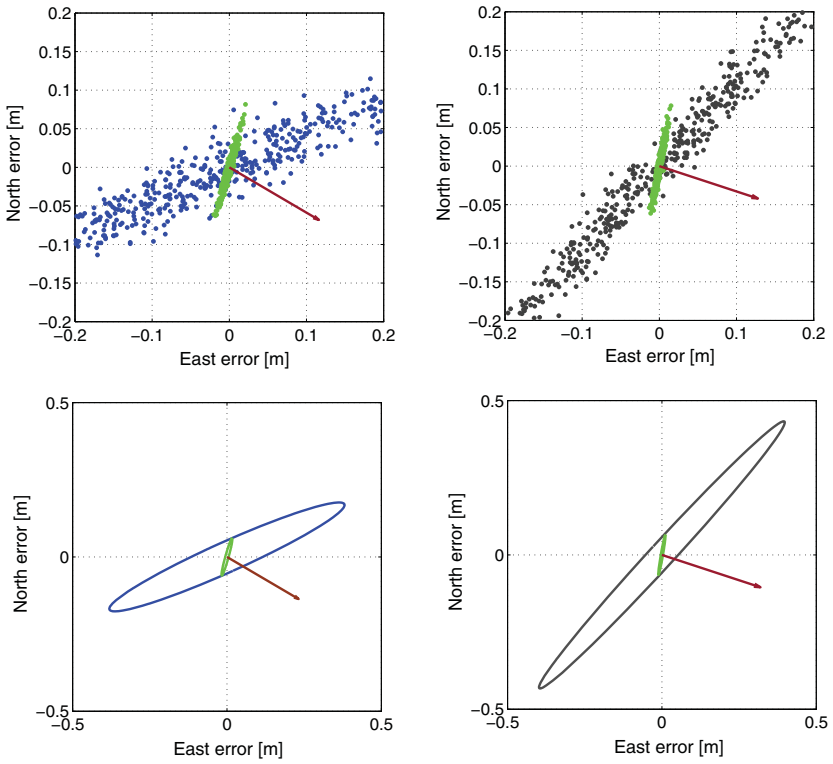

Fig. 10 [*Top*] GLONASS R21–R26 horizontal position scatter plots (triple-epoch based) collected by the receiver pair CUT3-CUCC on DOY 21 during UTC [04:47:00–06:55:00], *left* first 500 solutions; *right* last 500 solutions. Float solutions are illustrated in *blue* and *dark gray*, each having a specific orientation. Correctly fixed solutions are shown in *green*. [*Bottom*] The corresponding float and fixed confidence ellipses with the same *color* as their scatter plots. The *brown* vector indicates the direction of $\bar{c}$ in (10)

$$(\hat{b}-b)^T Q_{\hat{b}\hat{b}}^{-1}(\hat{b}-b) = r^2 \tag{9}$$

With $Q_{\hat{b}\hat{b}}$ the variance matrix of $\hat{b}$ and constant r^2 chosen such that a certain confidence level is reached (e.g., 95 %). The confidence ellipsoid of the fixed solution is obtained by replacing $\hat{b}$ and $Q_{\hat{b}\hat{b}}$ by $\check{b}$ and $Q_{\check{b}\check{b}}$, respectively.

The difference in shape between the float and fixed confidence ellipsoids is determined by the difference in the corresponding variance matrices. When solving the triple-epoch geometry-based model, the inverse variance matrices of the float and fixed solution can be shown to be related as

$$Q_{\hat{b}\hat{b}}^{-1} = Q_{\check{b}\check{b}}^{-1} - \frac{k\bar{w}}{\sigma_\varphi^2}\bar{c}\bar{c}^T \qquad (k=3) \tag{10}$$

in which $\bar{w} = \frac{1}{3}\sum_{i=1}^{3}\frac{w(i)}{2}$ and $\bar{c} = \frac{1}{3\bar{w}}\sum_{i=1}^{3}\frac{w(i)}{2}c(i)$. It is the second term on the right-hand side of (10) that determines the difference in orientation between the float and fixed scatter plots. Because of the very small value of the phase variance in the denominator of this second term, any change over time in the rank-1 matrix $\bar{c}\bar{c}^T$ will be amplified and thus play an important role in the determination of the orientation of the float confidence ellipsoid.

From (9) and (10), it follows that the maximum and minimum differences between the float and fixed ellipsoids are realized in a direction parallel and orthogonal to the vector $\bar{c}$, respectively. This is demonstrated in Fig. 10 by the horizontal scatter plots and corresponding ellipses. Figure 10 (top) shows the two float scatter plots (blue and gray) for two different orientations along with their correctly fixed counterparts, and Fig. 10 (bottom) shows their corresponding confidence ellipses. These ellipses are computed using the average float and fixed variance matrices over the period associated with the shown scatter plots. The brown colored vectors indicate the corresponding direction of the vector $\bar{c}$, thus indeed pointing in the direction of maximum difference between the fixed and float ellipses. It is the change over time of this direction that makes the float scatter plot take the shape shown in Fig. 8.

Two-satellite positioning: fixed solution

Now, we consider the scatter plot of the fixed solutions. In Fig. 11 (top), the unconstrained correctly fixed horizontal scatter plot along with the formal and empirical confidence ellipses (in red and blue) are shown, while Fig. 11 (bottom)

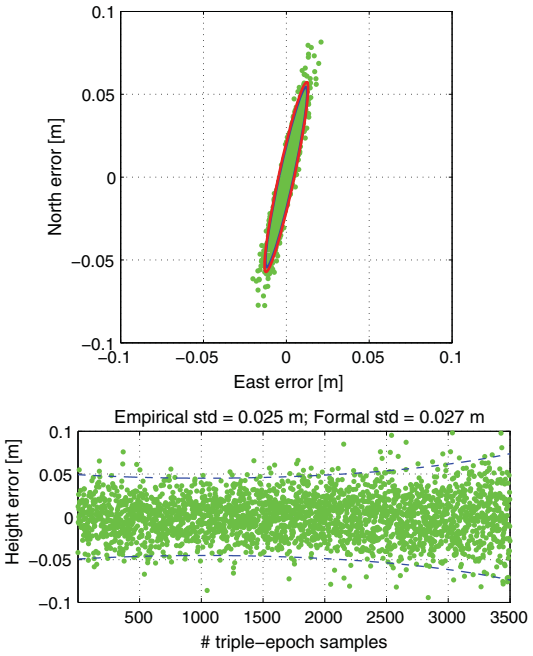

Fig. 11 (*Top*) GLONASS R21–R26 horizontal position scatter plot (triple-epoch based) of the correctly fixed solutions collected by the receiver pair CUT3-CUCC on DOY 21 during UTC [04:47:00–06:55:00]. The 95 % formal and empirical confidence ellipses are shown in *blue* and *red*, respectively. (*Bottom*) Time series of the correctly fixed height solutions. The *blue dashed curves* indicate the 95 % confidence interval

displays the time series of the corresponding fixed height solutions. Both graphs show a good agreement between formal and empirical values. According to these values, the North and Height components are estimable with a standard deviation of about 25 mm, while the standard deviation of the East component is much smaller and around 5 mm.

That the East component can be determined so much better than the other two components can be explained by the behavior of the difference of the line-of-sight vectors to the two satellites R21 and R29. Figure 12 shows the absolute values of the weighted SD lines-of-sight $\sqrt{\frac{w}{2}} \times c$ North, East, Height components for the satellites R21 and R29 over the observational period. The larger such component is, the better this component can be estimated. It therefore follows from Fig. 12 that one can indeed expect the North and Height components to be estimable with almost equal precision (see *blue* and *red* curves), while the East component would be much more precisely estimable (see *green* curve).

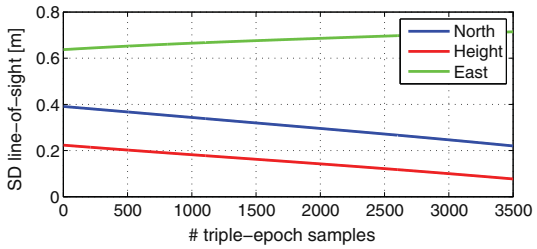

Fig. 12 Time series of the weighted SD lines-of-sight components corresponding with the satellites R21 and R29 over UTC [04:47:00–06:55:00] on DOY 21 of 2016

Interaction of positioning and ambiguity resolution

So far, the geometries of the triple-epoch geometry-based models have been such that the corresponding PDOP (Position Dilution of Precision) time series showed rather stable values over the chosen observational time periods. When we extend this time window, however, we note a period in which the PDOPs dramatically increase in value, see Fig. 13 (*blue* curve). This dramatic increase in PDOP must be due to a very poor relative receiver-satellite geometry. To explain the situation, we first show under which condition the multi-epoch geometry-based model becomes rank defect.

Almost rank defect positioning geometry

When solving the multi-epoch geometry-based model, its k-epoch design matrix is formed by stacking the SD receiver-satellite unit vectors $-c^T(i)$ for $i = 1, \ldots, k$ (see 2). Such a design matrix is rank defect if a vector $d \in \mathbb{R}^3$ can be found such that

$$c^T(i)d = 0, \quad i = 1, \ldots, k \tag{11}$$

According to the definition of the vector $c(i)$, the condition (11) means that at each epoch the two line-of-sight vectors make the *same angle* with the direction vector d. Geometrically this means that the rank deficiency occurs when the receiver-satellite unit line-of-sight vectors lie, at each epoch, on a cone having d as its symmetry axis (Fig. 14). The symmetry axis of the cone, i.e., the vector d, is then the direction in which the baseline solution becomes indeterminate. It is precisely this situation that explains the dramatic increase in PDOP values of Fig. 13.

Figure 15 (top) shows the skyplot positions of the two GLONASS satellites R21 and R26 at the three epochs associated with the peak in the PDOP time series of Fig. 13 which is clearly depicted in Fig. 15 (bottom). The location of the satellites at the same epoch is shown with the same color. As the figure shows, the red and green satellite

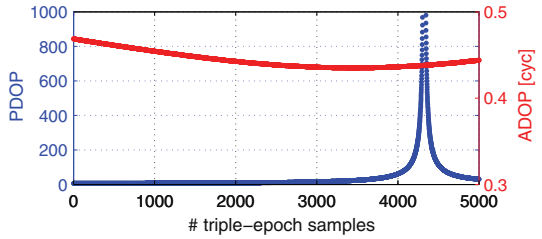

Fig. 13 Triple-epoch time series of the unconstrained PDOP (*blue*) and ADOP (*red*), corresponding with the receiver pair CUT3-CUCC and GLONASS satellite pair R21–R26 on DOY 21 during UTC [04:47:00–08:10:00]

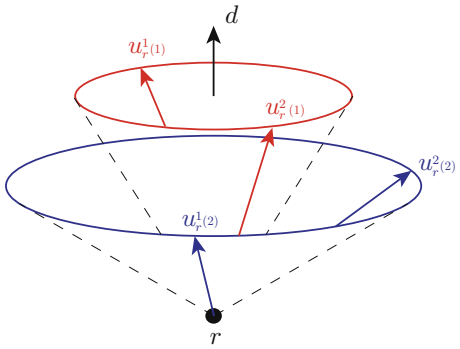

Fig. 14 Multi-epoch two-satellite positioning is indeterminate in direction d if the receiver-satellite unit directions $u_r^1(i)$ and $u_r^2(i)$ at each epoch lie on a cone having d as its symmetry axis (Teunissen 1990). The *red* and *blue* cones around d are formed by the receiver-satellite unit vectors at epoch 1 and epoch 2, respectively

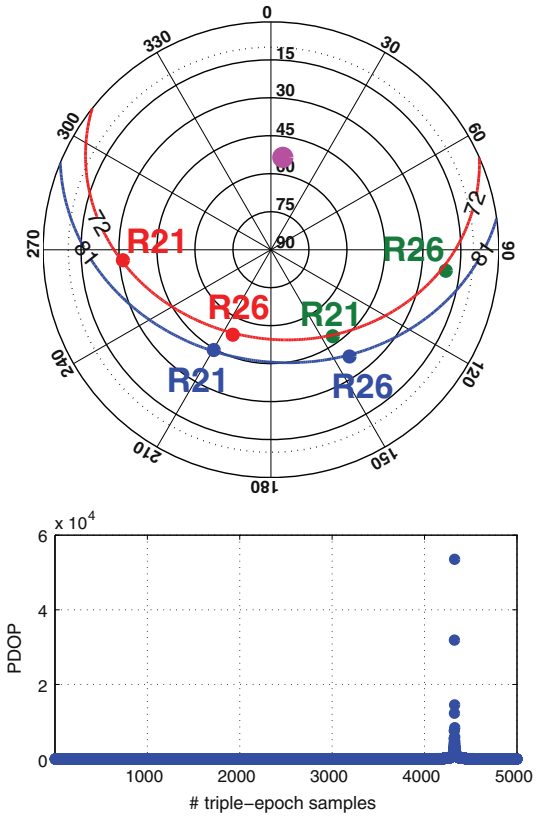

Fig. 15 (*Top*) GLONASS CDMA-transmitting skyplot for Perth, on DOY 21 of 2016 at three epochs, namely 05:59:25 (*red*), 06:22:45 (*blue*) and 07:46:05 (*green*) UTC. The purple circle illustrates the direction d along which the receiver position is poorest estimable. The *two colored contour lines* show the loci of the unit vectors that make the same 72 respective 81 degree angle with d. (*Bottom*) Triple-epoch time series of the unconstrained PDOP corresponding with the receiver pair CUT3-CUCC and GLONASS satellite pair R21–R26 on DOY 21 during UTC [04:47:00–08:10:00]

locations of R21 and R26 all lie on the same (*red* and *green*) cone having direction d (see 11), indicated as a *purple* circle, as its symmetry axis. Although the blue satellite locations of R21 and R26 lie on a different cone, this (blue) cone has again the same symmetry axis d. Hence, the geometry as shown in Fig. 15 is one in which the design matrix of the geometry-based model becomes (near) rank defect such that the baseline component in the direction of vector d becomes very poorly estimable. It is the very poor precision of this component that drives the PDOP to such large values.

Poor PDOP, good ADOP

Although the PDOP is often used as a quick diagnostic to infer whether the receiver-satellite geometry is favorable for positioning, one should be aware of the fact that the PDOP does not reveal whether or not one can expect ambiguity resolution to be successful (Teunissen et al. 2014). For that one needs the ADOP (Ambiguity Dilution of Precision). The ADOP is an easy-to-compute scalar diagnostic that measures the intrinsic model strength for successful ambiguity resolution. It is defined as the square-root of the determinant of the ambiguity variance matrix raised to the power of one over the ambiguity dimension (Teunissen 1997). The ADOP has several important properties. First, it is invariant against the choice of ambiguity parametrization. Second, it is a measure of the volume of the ambiguity confidence ellipsoid. And third, the ADOP equals the geometric mean of the standard deviations of the ambiguities, in case the ambiguities are completely decorrelated. Hence, in the one-dimensional case it simply reduces to the ambiguity standard deviation itself.

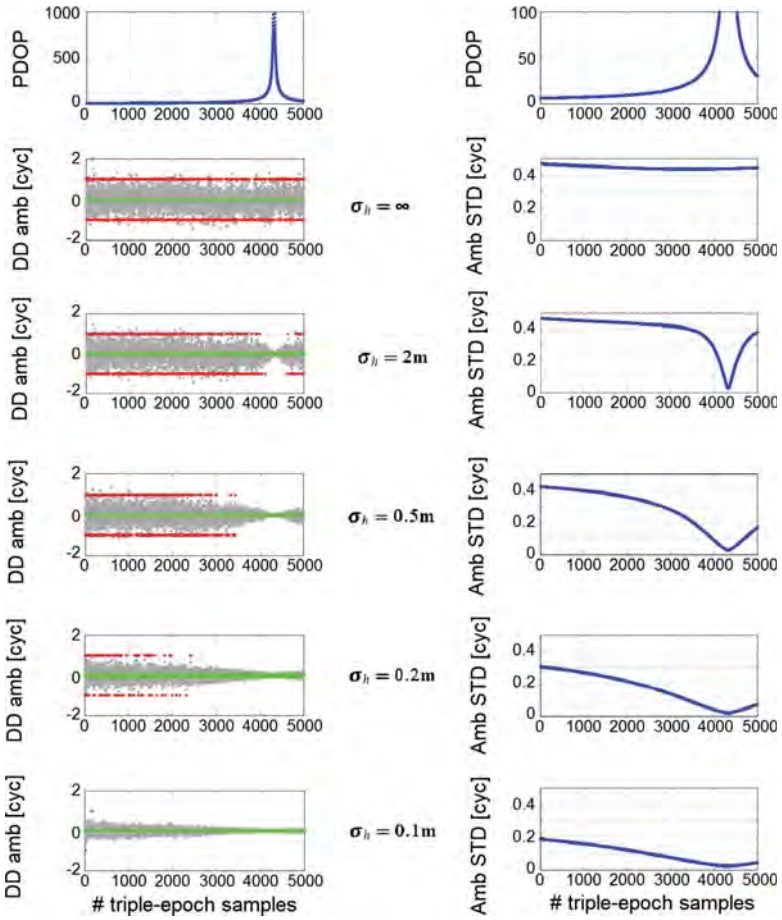

Fig. 16 [*Top row*] Triple-epoch time series of the unconstrained PDOP (*left*) and a zoom-in of it (*right*), corresponding with the receiver pair CUT3-CUCC and GLONASS satellites R21–R26 on DOY 21 during UTC [04:47:00–08:10:00]. [From second to the bottom row] The corresponding time series of the DD ambiguity estimations using the multipath-corrected observations (*left*) and DD ambiguity standard deviations (*right*), based on the unconstrained and height-constrained geometry-based model with the standard deviations of 2, 0.5, 0.2 and 0.1 m. Further, float solution (*gray*), correctly fixed solution (*green*), and incorrectly fixed solution (*red*)

That the PDOP and ADOP can have a very different behavior over time is shown in Fig. 13. There where the PDOP increases dramatically in value, due to the near rank defect in the geometry-based design matrix, the time series of the ADOP still shows rather stable behavior over time. This difference between PDOP and ADOP has an interesting consequence for ambiguity resolution when weighted height-constraining is enforced. When a weighted height constraint is imposed on the geometry-based model, the variance of the float DD ambiguity can be shown to improve from its unconstrained value $\sigma^2_{\hat{a}}$to its weighted height-constrained value

$$\sigma^2_{\hat{a}|h} = \sigma^2_{\hat{a}} - [1 + \sigma^2_h/\sigma^2_{\hat{h}}]^{-1}\sigma^2_{\hat{a}\hat{h}}\sigma^{-2}_{\hat{h}} \tag{12}$$

with $\sigma_{\hat{a}\hat{h}}$ being the ambiguity-height covariance, σ_h the a priori standard deviation of the height constraint, and $\sigma^2_{\hat{h}}$ the variance of the unconstrained estimator of the height component. It can be seen that the ratio $\sigma^2_h/\sigma^2_{\hat{h}}$ governs the benefit brought by the height constraint. One has the most benefit when $\sigma^2_h = 0$ and the least benefit when $\sigma^2_h = \infty$.

If σ^2_h is chosen much larger than $\sigma^2_{\hat{h}}$, then the bracketed term of (12) becomes small. This means that if the receiver-satellite geometry is so strong that $\sigma^2_{\hat{h}}$ is small, constraining the height with a variance σ^2_h much larger than $\sigma^2_{\hat{h}}$ would have a negligible impact on ambiguity resolution. On the other hand, however, ambiguity resolution can benefit considerably from a weighted height constraint if $\sigma^2_{\hat{h}}$ is large. The larger $\sigma^2_{\hat{h}}$ is, the softer the weighted height constraint can be to still have an impact on ambiguity resolution. Thus, in case of a large PDOP, soft constraining of the height can still result in a very significant improvement of ambiguity resolution. The following examples shown in Fig. 16 make this clear.

The first row of Fig. 16 shows the PDOP time series (and a zoom-in) of the triple-epoch, two-satellite geometry-

based model of the GLONASS satellites R21–R26 for the period UTC [04:47:00-08:10:00] of DOY 21 in 2016. The second row of Fig. 16 shows in the left column the unconstrained DD ambiguity float and fixed time series, $\hat{a} - a$ (in gray) and $\check{a} - a$ (in green and red), and in the right column the corresponding time series of the unconstrained ambiguity standard deviation. Similar time series are also shown in the third to bottom row of Fig. 16, but now as a result of imposing a weighted height constraint with increasing weight.

The results in the third row show that a soft height constraint of only $\sigma_h = 2$ m already has a significant impact on ambiguity resolution at the time instances for which the PDOPs are large. At these instances, the formal float ambiguity standard deviation has become much smaller, the variability in the float time series has reduced dramatically, and the ambiguity fixed solutions are now all correct. When we further increase the weight of the height-constraint, the results of the fourth to sixth row of Fig. 16 show that the ambiguity resolution improvements flow over to neighboring time instances such that finally in case of the bottom row now almost all of the 5000 ambiguity fixed solutions are correct.

Summary and conclusions

We provided an initial assessment of GLONASS CDMA L3 double-differenced integer ambiguity resolution and corresponding positioning performance. Our analyses are based on GLONASS L3 data from the satellite pair R21–R26 and on GPS L1 data from the satellite pair G21–G29. We studied the noise characteristics (carrier-to-noise density, measurement precision), the integer ambiguity resolution performance (success rates and distribution of the ambiguity residuals) and the corresponding ambiguity float and ambiguity fixed positioning performance. The results show that the GLONASS data have a significantly lower noise level than that of GPS, particularly in case of the code data. This difference is not only seen in the noise levels but also in their onward propagation to ambiguity time series and ambiguity residuals distribution. We also compared all our empirical results with their formal counterparts, thereby showing the consistency between data and models. The four different versions of the two-satellite model that were applied are as following: the geometry-free model, the geometry-based model, the height-constrained geometry-based model, and the geometry-fixed model. Finally, we demonstrated that PDOP and ADOP characteristics can be quite distinct and that one therefore should not confuse a poor PDOP with poor ambiguity resolution capabilities.

Acknowledgments Part of this work has been done in the context of the Positioning Program Project 1.19 "Multi-GNSS PPP-RTK Network" of the Cooperative Research Centre for Spatial Information (CRC-SI). The second author is the recipient of an Australian Research Council (ARC) Federation Fellowship (Project Number FF0883188).

References

Euler HJ, Goad CC (1991) On optimal filtering of GPS dual frequency observations without using orbit information. Bulletin Geodesique 65(2):130–143

GPS World (2015) Final GLONASS-M satellite passes tests. Available from: http://gpsworld.com/final-glonass-m-satellite-passes-tests/. Accessed 2 Feb, 2016

GPSD (2013) Navstar GPS space segment/navigation user segment interface, Revision F (IS-GPS-200H:24-Sep-2013), global positioning system directorate

Hofmann-Wellenhof B, Lichtenegger H, Collins J (2013) Global positioning system: theory and practice. Springer Science & Business Media

IAC (2016) GLONASS constellation status. Available from: https://www.glonass-iac.ru/en/GLONASS/, accessed 2 February 2016

ICD-GLONASS (2008) Global Navigation Satellite System GLONASS Interface Control Document, version 5.1, Moscow

Karutin S (2012) GLONASS signals and augmentations. In: Proceeding of ION GNSS 2012, Institute of Navigation, Nashville, TN, 17–21 September, pp 3878–3911

Leick A, Rapoport L, Tatarnikov D (2015) GPS satellite surveying. Wiley, New York

Montenbruck O, Schmid R, Mercier F, Steigenberger P, Noll C, Fatkulin R, Kogure S, Ganeshan AS (2015) GNSS satellite geometry and attitude models. Adv Space Res 56(6):1015–1029

Nadarajah N, Khodabandeh A, Teunissen PJG (2015) Assessing the IRNSS L5-signal in combination with GPS, Galileo, and QZSS L5/E5a-signals for positioning and navigation. GPS Solutions 20(2):289–297. doi:10.1007/s10291-015-0450-8

Oleynik E (2012) GLONASS Status and Modernization. United Nations/Latvia Workshop on the Applications of Global Navigation Satellite Systems, Riga

Reussner N, Wanninger L (2011) GLONASS interfrequency biases and their effects on RTK and PPP carrier-phase ambiguity resolution. In: Proceedings of ION GNSS 2011, Institute of Navigation, Portland, OR, 20–23 September, pp 712–716

Takac F (2009) GLONASS inter-frequency biases and ambiguity resolution. Inside GNSS 4(2):24–28

Teunissen PJG (1990) GPS op afstand bekeken In: een halve eeuw in de goede richting. Lustrumboek Snellius 1985-1990, DUM Delft pp 215–233

Teunissen PJG (1997) A canonical theory for short GPS baselines. Part I: The baseline precision. Journal of Geodesy 71(6):320–336

Teunissen PJG (1998) Success probability of integer GPS ambiguity rounding and bootstrapping. J Geodesy 72(10):606–612

Teunissen PJG (2002) The parameter distributions of the integer GPS model. J Geodesy 76(1):41–48

Teunissen PJG, Amiri-Simkooei AR (2008) Least-squares variance component estimation. J Geodesy 82(2):65–82
Teunissen PJG, Odolinski R, Odijk D (2014) Instantaneous BeiDou + GPS RTK positioning with high cut-off elevation angles. J Geodesy 88(4):335–350
Thoelert S, Erker S, Furthner J, Meurer M, Gao GX, Heng L, Walter T, Enge P (2011) First signal in space analysis of GLONASS K-1. In: Proceedings of ITM 2011, Institute of Navigation, Portland, OR, 19–23 September, pp. 3076–3082
Urlichich Y, Subbotin V, Stupak G, Dvorkin V, Povaliaev A, Karutin S (2010) GLONASS Developing Strategy. In: Proceedings of the 23rd ITM 2010, ION, pp 1566–1571
Urlichich Y, Subbotin V, Stupak G, Dvorkin V, Povaliaev A, Karutin S (2011) A new data processing strategy for combined GPS/GLONASS carrier phase-based positioning. In: Proceedings of ION GNSS 2011, Institute of Navigation, Portland, OR, 20-23 September, pp 3125–3128
Verhagen S, Teunissen P (2013) The ratio test for future GNSS ambiguity resolution. GPS Solutions 17(4):535–548
Wanninger L (2009) Carrier-phase inter-frequency biases of GLONASS receivers. J Geodesy 86(2):139–148
Yamada Y, Takasu T, Kubo N, Yasuda A (2010) Evaluation and calibration of receiver inter- channel biases for RTK-GPS/GLONASS. In: Proceedings of ION GNSS 2010, Institute of Navigation, Portland, OR, 21–24 September, pp 1580–1587

Safoora Zaminpardaz received her M.Sc. in Geodesy from University of Tehran. She has been pursuing her Ph.D. since July 2014 at the GNSS Research Centre, Curtin University, Australia. Her research interests include array-based multi-GNSS positioning, ionosphere sensing and integrity monitoring.

Peter J. G. Teunissen is Professor of Geodesy and Navigation, Head of CUT's GNSS Research Centre and Science Director of the Cooperative Research Centre for Spatial Information. His current research focuses on multi-GNSS and the modelling of next generation GNSS for high-precision positioning, navigation and timing applications.

Nandakumaran Nadarajah received his M.A.Sc. and Ph.D. in electrical and computer engineering from McMaster University, Canada. Currently, he is working as a research fellow at GNSS Research Centre, Curtin University. His research interests are in multi-GNSS attitude determination and relative navigation, signal processing, and target tracking.

10 GLONASS CDMA L3 performance (Part 2: Ambiguity resolution in comparison with GPS L5)

This chapter is covered by the following publication:

Zaminpardaz S., Teunissen P.J.G., Nadarajah N. (2016b) GLONASS CDMA L3 Ambiguity Resolution. Inside GNSS, 11(4):44-47

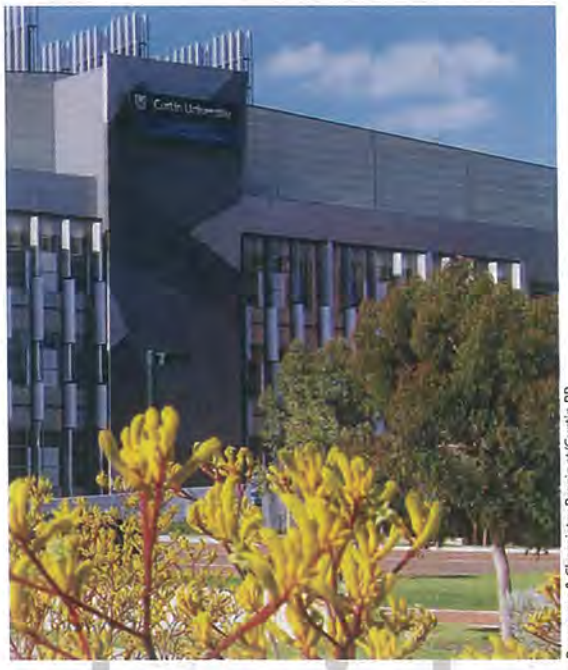

Resources & Chemistry Precinct/Curtin PR

First Results
GLONASS CDMA L3 Ambiguity Resolution

Researchers in Australia present their first results of GLONASS CDMA L3 ambiguity resolution. Based on the observations from two GLONASS satellites that were collected at Curtin University, this article assesses the performance of geometry-free and geometry-fixed L3 ambiguity resolution methods and compares the outcomes with their GPS L5 counterparts.

In February 2011, Russia launched the first satellite of the GLONASS-K1 series, i.e., SVN (space vehicle number) 801 (R26), which in addition to the legacy frequency division multiple access (FDMA) signals, for the first time was enabled to transmit code division multiple access (CDMA) signals on the GLONASS L3 frequency (1202.025 MHz). Later in 2014, the GLONASS program added SVNs 802 (R17) of series K1 and 755 (R21) of series M, and in 2016, SVN 751 of series M, with the capability of transmitting CDMA L3 signals to the constellation.

The GLONASS FDMA double-differenced (DD) ambiguity resolution is known to be hampered by the inherent inter-frequency biases. Several calibration procedures have been proposed to deal with this impediment. With GLONASS-CDMA however, the inter-frequency biases are absent, and standard methods of integer ambiguity resolution can be applied to resolve the integer DD ambiguities. The goal of this article is to provide a first assessment of this L3 ambiguity resolution performance.

SAFOORA ZAMINPARDAZ, PETER J. G. TEUNISSEN, NANDAKUMARAN NADARAJAH
GNSS RESEARCH CENTRE, DEPARTMENT OF SPATIAL SCIENCES, CURTIN UNIVERSITY OF TECHNOLOGY, PERTH, AUSTRALIA

Measurement Setup

Our analysis is based on the GLONASS L3 data of the satellite pair R21-R26, collected by two multi-frequency GPS/GLONASS receivers on an eight-meter baseline at Curtin University, Perth, Australia (Figure 1). We also compare these results with their GPS L5 counterparts for the satellite pair G10-G26. The rationale behind making this comparison is that both these modern signals have close frequencies (see Table 1) and the same BPSK(10) modulation.

Figure 2 shows their observed carrier-to-noise densities (C/N_0). As their C/N_0 graphs show a similar signature, their signals are expected to have similar noise characteristics. Figure 1 also shows the skyplot of the mentioned satellite pairs at Perth. For both the GLONASS and the GPS satellites, we used the broadcast ephemeris data. Table 2 provides further information on the dataset that we used.

Model of Observations

Because our analysis is based on satellite pairs, we first formulate the two-satellite observational model. With the expectation $E\{.\}$ and dispersion $D\{.\}$, the corresponding double-differenced (DD) system of observation equations reads

$$E\left\{\begin{bmatrix} p \\ \varphi \end{bmatrix}\right\} = \begin{bmatrix} 1 & 0 \\ 1 & \lambda \end{bmatrix}\begin{bmatrix} \rho \\ a \end{bmatrix} \qquad (1)$$

$$D\left\{\begin{bmatrix} p \\ \varphi \end{bmatrix}\right\} = \frac{1}{w}\begin{bmatrix} \sigma_p^2 & 0 \\ 0 & \sigma_\varphi^2 \end{bmatrix}$$

in which p and φ are the DD code and phase observable, respectively, ρ the DD receiver-satellite range and a the DD integer ambiguity in cycles. The ambiguity a is linked to the DD phase observable through the signal wavelength λ. With the elevation-dependent weighting function w_{θ^s} ($s = 1, 2$) for the s^{th} satellite with elevation angle θ^s, respectively, the final weight becomes

$$w = \frac{1}{2}[w_{\theta 1}^{-1} + w_{\theta 2}^{-1}]^{-1}.$$

Here w_{θ^s} is taken as

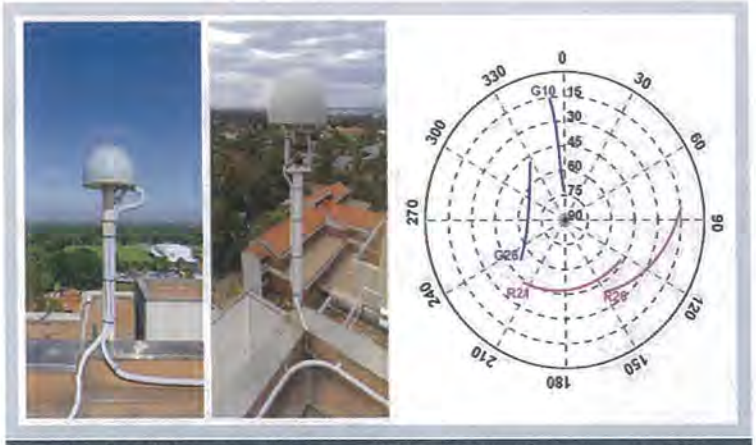

FIGURE 1 At left, GLONASS L3-enabled stations (CUCC and CUT3) at Curtin University GPS/GLONASS receivers connected to choke ring antennas. At right, skyplot of the GLONASS CDMA-transmitting satellites *(purple)* and GPS satellites *(blue)* at Perth, Australia, during UTC [07:16:59–09:31:38] on DOY 21 of 2016, with the cut-off elevation angle of 10 degrees.

Signal	Frequency [MHz]	Wavelength [cm]
GLONASS L3	1202.025	24.94
GPS L5	1176.45	25.48

Table 1 Frequency and wavelength of GLONASS L3 and GPS L5 signal.

# antennas	2
Location	Curtin University, Perth, Australia
Data type	GLONASS L3, GPS L5
Satellites	R21-R26, G10-G26
Cut-off angle	10°
Date and time	UTC [07:16:59-09:13:38] on DOY 21 of 2016

Table 2 Characteristics of the experiment conducted for this study.

$$w_{\theta^s} = [1 + 10\exp(-\frac{\theta^s}{10})]^{-2} \quad (2)$$

where θ^s is in degrees. The zenith-referenced standard deviations of the undifferenced code and phase observables are denoted as σ_p and σ_φ. In our analysis we considered *two* different models. These are arranged in ascending order of strength as:

1. *Geometry-free* model (GFr): This is the model as formulated in (1). As it is parametrized in ρ, it is free from the receiver-satellite geometry. The single-epoch DD ambiguity is then estimated as
$$\hat{a} = \frac{1}{\lambda}(\varphi - p);\ \sigma^2_{\hat{a}} = \frac{1}{w\lambda^2}(\sigma^2_\varphi + \sigma^2_p) \quad (3)$$
with $\sigma_{\hat{a}}$ being the ambiguity standard deviation;
2. *Geometry-fixed* model (GFi): In this model, the information on receiver position, from e.g. surveying, and satellite position, from navigation file, is available and thus ρ is assumed known. The single-epoch DD ambiguity is then estimated as
$$\check{a} = \frac{1}{\lambda}(\varphi - \rho);\ \sigma^2_{\check{a}} = \frac{1}{w\lambda^2}\sigma^2_\varphi \quad (4)$$

Note that although the observations of only two satellites are used, both the geometry-free and geometry-fixed models are instantaneously solvable, i.e., based on data of only a single epoch. See the article by P. J. G. Teunissen (1997) listed in the Additional Resources section near the end of this article for a more detailed discussion of these models.

Ambiguity Resolution

The data used for our L3 and L5 ambiguity resolution performance analysis were one hertz sampled on DOY 21 of 2016 over the time period UTC [07:16:59-09:13:38]. As the observations of a satellite pair and a receiver pair result in only one unknown DD ambiguity, simple integer rounding can be used for integer ambiguity resolution. We denote the float ambiguity by $\hat{a}$, the fixed (integer rounded) ambiguity by $\check{a}$, and the reference ambiguity by a. The reference DD ambiguity a is computed based on the multi-epoch solution of the geometry-fixed model.

In **Figure 3**, the time series of $\hat{a} - a$ and $\check{a} - a$ are shown for the receiver pair CUT3-CUCC, for both the GLONASS satellite pair R21-R26 (left column) and the GPS satellite pair G10-G26 (right column).

While the geometry-fixed results of the two signals are comparable, the GPS L5 geometry-free ambiguity resolution outperforms that of the GLONASS L3, which can be explained by means of the satellites' elevations: the higher the elevation, the lower the noise level, thus the better the ambiguity resolution performance (cf. 2, 3 and 4).

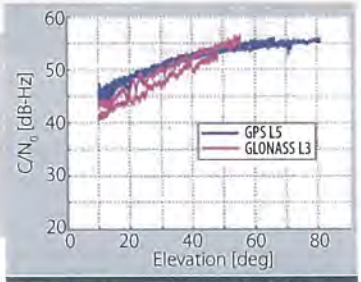

FIGURE 2 Carrier-to-noise-density (C/N_0) for GLONASS L3 and GPS L5 signals tracked by our receiver, connected to a choke-ring antenna at Perth, Australia, on DOY 21 of 2016 during UTC [07:16:59–09:31:38].

The bottom set of graphs in Figure 3 also illustrates the elevation time series of the chosen satellite pair (in blue) in addition to the geometry-fixed DD ambiguities. Here we can see that the elevations of the GPS satellite pair is higher than those of the GLONASS satellite pair. Also, the low elevation of R26 at the end of the period and the low elevation of G10 at the beginning of the period describe the larger fluctuations of, respectively, the GLONASS DD ambiguities and the GPS DD ambiguities at those time instants.

For both the geometry-free and the geometry-fixed scenario, we computed the formal and empirical ambiguity

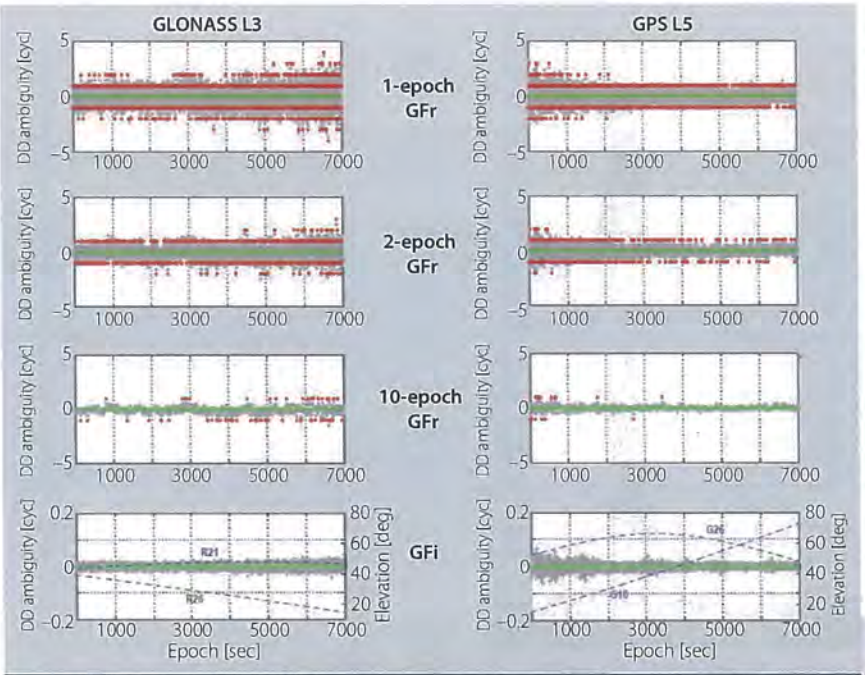

FIGURE 3 DD ambiguity time series of $\hat{a}-a$ and $\check{a}-a$ for both the GLONASS satellite pair R21-R26 (left column) and the GPS satellite-pair G10-G26 (right column) using data from the receiver pair CUT3-CUCC on DOY 21 during UTC [07:16:59-09:13:38]. Float solutions are shown in *grey*, correctly fixed solutions in *green*, and wrongly fixed solutions in *red*. The time series are given (from top to bottom) for the 1-epoch, 2-epoch and 10-epoch geometry-free (GFr) model and the geometry-fixed (GFi) model. The *blue* curves in the panels of geometry-fixed model are the time series of satellite pairs elevation.

success-rates, defined as the probability of correct integer estimation. The formal ambiguity success-rate can be computed, as discussed in the article by P. J. G. Teunissen, (1998) cited in Additional Resources, as

$$\text{Formal } Ps = 2\Phi\left(\frac{1}{2\sigma_{\hat{a}}}\right) - 1 \qquad (5)$$

with

$$\Phi(x) = \int_{-\infty}^{x} \frac{1}{\sqrt{2\pi}} \exp\{-\tfrac{1}{2}v^2\} dv$$

being the standard normal probability density function (PDF).

For the computation of the formal success-rate, the ambiguity standard deviation was taken as the square-root of an average of the formal variances, i.e., as

$$\sigma_{\hat{a}} = \sqrt{\frac{1}{k}\sum_{i=1}^{k}\sigma_{\hat{a}}^2(i)}$$

with $\sigma_{\hat{a}}^2(i)$ being the variance of the float DD ambiguity of the i^{th} epoch. The empirical success-rate is given as

$$\text{Empirical } Ps = \frac{\#\text{correct fixed DD ambiguities}}{\#\text{float DD ambiguities}} \qquad (6)$$

Table 3 lists the empirical and formal success-rates for both GLONASS and GPS corresponding with Figure 3. Based on these results, the empirical values are consistent with their formal counterparts. Moreover, as the model gets stronger from one-epoch geometry-free to geometry-fixed, the ambiguity resolution success-rates experience a significant improvement. In case of the one-epoch geometry-free model, $\sigma_{\hat{a}}$ is governed by the code precision σ_p. Including the observations of k epochs, the corresponding $\sigma_{\hat{a}}$ of k-epoch geometry-free model is improved by almost $\sqrt{k}$ times.

Switching from geometry-free to geometry-fixed model, $\sigma_{\hat{a}}$ is then governed by the phase precision σ_φ which is much better than the code precision. For the geometry-free model to achieve a success-rate of more than 0.999, 40 epochs of observation in the case of GLONASS L3 and 10 epochs in the case of GPS L5 are required.

To further confirm the consistency between the data and models, we compare, for both the geometry-free and the geometry-fixed model, the formal PDF with the histogram of the estimated DD ambiguity. Normalizing the estimated DD ambiguity by means of the elevation weighting function results in a new quantity, i.e., $\sqrt{w}(\hat{a}-a)$ which, assuming the data to be normally distributed, has a central normal distribution with the standard deviation of $\sqrt{w}\sigma_{\hat{a}}$. Depending on whether the underlying model is geometry-free or geometry-fixed, the value of $\sqrt{w}\sigma_{\hat{a}}$ can be obtained from (3) or (4), respectively.

Figure 4 displays the histograms of the normalized DD ambiguity $\sqrt{w}(\hat{a}-a)$, for geometry-free and geometry-fixed model. The corresponding formal distribution is also shown by the *red* curve. It demonstrates the consistency between the empirical and formal distributions.

Conclusion

We have presented a first assessment of GLONASS CDMA L3 double-differenced integer ambiguity resolution.

Model	GLONASS	GPS
1-epoch GFr	0.49(0.43)	0.73(0.76)
2-epoch GFr	0.63(0.57)	0.85(0.85)
10-epoch GFr	0.89(0.93)	0.98(1.00)
GFi	1.00(1.00)	1.00(1.00)

Table 3 GLONASS L3 and GPS L5 ambiguity resolution success-rates, empirical and formal (in parentheses), for the 1-epoch, 2-epoch and 10-epoch geometry-free (GFr) model and the geometry-fixed (GFi) model.

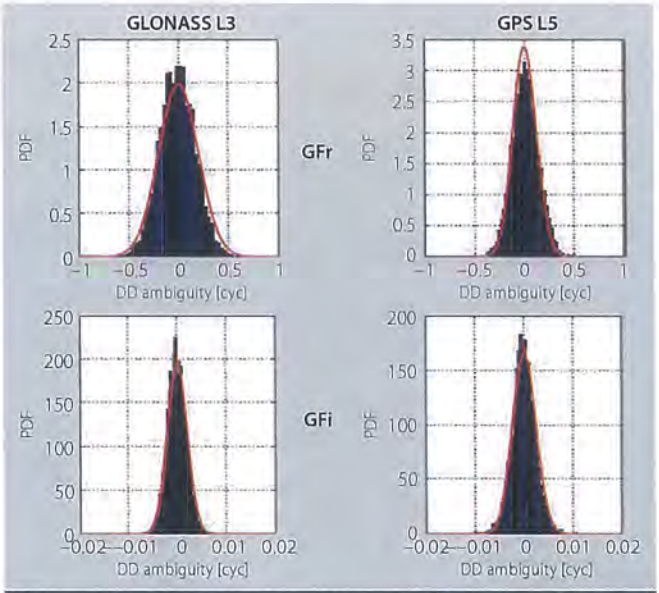

FIGURE 4 The histograms *(blue)* and formal PDFs *(red)* of the normalized DD ambiguities $\sqrt{w}(\hat{a}-a)$ that correspond with the time series of Figure 3.

For our analyses, we made use of the GLONASS L3 signal transmitted by the satellite pair R21-R26 and of the GPS L5 signal from the satellite pair G10-G26. The carrier-to-noise densities of both signals were shown to have similar signatures.

The integer ambiguity resolution performance in the framework of geometry-free and geometry-fixed observational model was demonstrated. As the model gets stronger from geometry-free to geometry-fixed model, the ambiguity resolution improves significantly.

Our empirical results (in the form of success-rates and normalized ambiguity PDF) showed a good agreement with their formal counterparts, thereby showing the consistency between data and models. The ambiguity resolution of GPS L5 was better than that of the GLONASS L3, which was attributed to the higher elevation of the GPS satellites w.r.t the GLONASS satellites during the considered period.

Manufacturers

The GPS/GLONASS receivers used to observe satellite signals were JAVAD TRE_G3TH_8 receivers from **Javad GNSS**, San Jose, California USA. They were connected with TRM59800.00 SCIS antennas from **Trimble Navigation Ltd.**, Sunnyvale, California USA.

Additional Resources

[1] Euler, H.J., and C. C. Goad, "On Optimal Filtering of GPS Dual Frequency Observations without Using Orbit Information," *Bulletin Geodesique* 65(2):130-143, 1991

[2] Global Positioning Systems Directorate, NAVSTAR GPS space segment/navigation user segment Interface Specification, Revision F (IS-GPS-200H:24-Sep-2013)

[3] Hofmann-Wellenhof, B., and H. Lichtenegger and J. Collins, *Global Positioning System: Theory and Practice*, Springer Science & Business Media, 2013

[4] Information and Analytisis Center for Positioning, Navigation, and Timing, GLONASS constellation status, available from <https://www.glonass-iac.ru/en/GLONASS>, accessed February 2, 2016

[5] Leick, A., *GPS Satellite Surveying*, John Wiley and Sons, 2003

[6] Oleynik, E., "GLONASS Status and Modernization," United Nations/Latvia Workshop on the Applications of Global Navigation Satellite Systems, Riga, Latvia, 2012

[7] Reussner, N., and L. Wanninger, GLONASS Inter-frequency Biases and Their Rffects on RTK and PPP Carrier-Phase Ambiguity Resolution," Proceedings of ION GNSS 2011, Institute of Navigation, pp. 712-716, 2011

[8] Takac, F., "GLONASS Inter-Frequency Biases and Ambiguity Resolution, *Inside GNSS*, 4(2):24-28, 2009

[9] Teunissen, P. J. G., (1997) "A Canonical Theory for Short GPS baselines. Part I: The Baseline Precision," *Journal of Geodesy*, 71(6):320-336, 1997

[10] Teunissen, P. J. G.,(1998) Success probability of integer GPS ambiguity rounding and bootstrapping. *Journal of Geodesy*, 72(10):606-612, 1998

[11] Thoelert, S., and S. Erker, J. Furthner, M. Meurer, G. X. Gao, L. Heng, Walter, and P. Enge, "First Signal in Space Analysis of GLONASS K-1," Proceedings of ION ITM 2011, pp. 3076-3082, 2011

[12] Urlichich, Y., and V. Subbotin, G. Stupak, V. Dvorkin, A Povaliaev and S. Karutin,(2010) GLONASS Developing Strategy," Proceedings of the 23rd ION ITM 2010, Institute of Navigation, pp. 1566-1571, 2010

[13] Urlichich, Y., and V. Subbotin, G. Stupak, V. Dvorkin, A Povaliaev and S. Karutin, (2011), "A New Data Processing Strategy for Combined GPS/GLONASS Carrier Phase-Based Positioning," Proceedings of the ION GNSS 2011, Institute of Navigation, pp. 3125-3128, 2011

[14] Wanninger, L., "Carrier-Phase Inter-Frequency Biases of GLONASS Receivers," *Journal of Geodesy*, 86(2):139-148, 2009

[15] Yamada, Y., and T. Takasu, N. Kubo, and A. Yasuda, "Evaluation and Calibration of Receiver Inter-Channel Biases for RTK-GPS/GLONASS," Proceedings of ION GNSS 2010, Institute of Navigation, pp. 1580-1587, 2010

Authors

Safoora Zaminpardaz <safoora.zaminpardaz@curtin.edu.au> received her M.Sc. in Geodesy from the University of Tehran. She is pursuing her Ph.D. at the GNSS Research Centre, Curtin University, Australia. Her research interests include array-based multi-GNSS positioning, ionosphere sensing, and integrity monitoring.

Peter J. G. Teunissen is a professor of geodesy and navigation and head of Curtin University's GNSS Research Centre and science director of the Cooperative Research Centre for Spatial Information. His current research focuses on multi-GNSS and the modelling of next generation GNSS for high-precision positioning, navigation, and timing applications. He is also head of the Department of Earth Observation and Space Systems of the Delft University of Technology, Delft, The Netherlands.

Nandakumaran Nadarajah received his M.A.Sc. and Ph.D. in electrical and computer engineering from McMaster University, Canada. Currently, he is working as a research fellow at the GNSS Research Centre, Curtin University. His research interests are in multi-GNSS attitude determination and relative navigation, signal processing, and target tracking.

11 Galileo IOV+FOC signal analysis

This chapter is covered by the following publication:

Zaminpardaz S., Teunissen P.J.G. (2017) Analysis of Galileo IOV+FOC Signals and E5 RTK performance. GPS Solutions, Springer, 21(4):1855-1870

GPS Solut (2017) 21:1855–1870
DOI 10.1007/s10291-017-0659-9

ORIGINAL ARTICLE

Analysis of Galileo IOV + FOC signals and E5 RTK performance

Safoora Zaminpardaz[1] · **Peter J. G. Teunissen**[1,2]

Received: 14 July 2017 / Accepted: 11 August 2017 / Published online: 29 August 2017

Abstract The current Galileo constellation in April 2017 comprises both in-orbit validation and full operational capability satellites transmitting signals on five frequencies, i.e., E1, E5a, E5b, E5, and E6. We analyze the power, multipath and noise of these signals using the data collected by four short baselines of various lengths and receiver/antenna types in Perth, Australia, as well as the Netherlands. In our analysis, the Galileo signals, except E5, show different relative noise and multipath performance for different receiver/antenna types. The E5 signal, with a weak dependency on the type of receiver/antenna, shows a significantly lower level of multipath and noise with respect to the other signals. Estimations of the E5 code standard deviation based on the data of each of the mentioned baselines gives a value of about 6 cm, which is further reduced to about 1 cm once the data are corrected for multipath. Due to the superior stochastic properties of E5 signal compared to the other Galileo signals, we further analyze the short-baseline real-time kinematic performance of the Galileo standalone E5 observations. Our findings confirm that the Galileo E5 data, if corrected for the multipath effect, can make (almost) instantaneous ambiguity resolution feasible already based on the current constellation.

✉ Safoora Zaminpardaz
safoora.zaminpardaz@postgrad.curtin.edu.au

[1] GNSS Research Centre, Curtin University, GPO Box U1987, Perth, WA 6845, Australia

[2] Department of Geoscience and Remote Sensing, PO Box 5048, 2600 GA Delft, The Netherlands

Keywords Galileo · IOV · FOC · E5AltBOC · Signal power · Multipath · Noise characteristics · Integer ambiguity resolution · RTK

Introduction

Galileo, Europe's global navigation satellite system, has been under development through the collaboration of the European Commission (EC) and the European Space Agency (ESA), with the aim of providing highly accurate global positioning services (ESA 2016). Upon validating the Galileo design, two experimental Galileo in-orbit validation element (GIOVE) satellites, i.e., GIOVE-A and -B, were launched in 2005 and 2008, respectively. These satellites were put into orbit with the purpose of characterizing the performance of the novel Galileo signals and were later on decommissioned in 2012. The last two phases of the Galileo program are the in-orbit validation (IOV) phase and the full operational capability (FOC) phase. The former was planned to conduct the initial validation of the Galileo system based on four satellites and became finalized by 2014, while the latter is still ongoing to realize the fully operational system such that a minimum of four satellites is always visible at any location (http://www.esa.int/).

The full constellation of Galileo will comprise 24 satellites plus at most six spares, expected to be realized by 2020. They orbit in three medium earth orbit (MEO) planes, at an altitude of 23,222 km and with an inclination angle of 56° with respect to the equator (European Union 2015). The navigation signals of these satellites are transmitted on five frequencies E1, E5a, E5b, E5 and E6 (Table 1). Having alternative binary offset carrier (AltBOC) modulation, the Galileo E5 signal is a wideband

Table 1 Galileo frequencies and wavelengths

Signal	Carrier frequency (MHz)	Wavelength (cm)
E1	1575.420	19.03
E5a	1176.450	25.48
E5b	1207.140	24.83
E5	1191.795	25.15
E6	1278.750	23.44

signal consisting of two subcarriers, i.e., E5a and E5b, which can be tracked either as two independent BPSK(10) (binary phase shift keying) modulations at respective center frequencies of 1176.45 and 1207.14 MHz, or coherently as one signal centered at 1191.795 MHz, leading to the E5 signal (Simsky et al. 2006). Figure 1 illustrates how these frequencies are distributed with respect to the GPS L1, L2, and L5 frequencies.

The first analyses of the power, tracking noise and multipath performance of the Galileo signals based on the GIOVE-A and -B data were provided in Simsky et al. (2006, 2008a, b). Applying a geometry-free short- and zero-baseline analysis method to the measurements of GIOVE-A and -B, deBakker et al. (2009, 2012) analyzed the code and phase noise of E1 and E5a signals. Such zero-baseline analysis was also carried out by Cai et al. (2016) but on the basis of the four IOV satellites data at E1, E5a, E5b, and E5 frequencies. The code noise and the cross-correlation of these frequencies were assessed in Odijk et al. (2014).

Throughout different phases of the Galileo development, its data have been studied for a variety of GNSS applications either in Galileo-only mode or in Galileo plus other GNSSs mode. Examples of such studies are Langley et al. (2012), Tegedor et al. (2014, 2015), Afifi and El-Rabbany (2014), Cai et al. (2015), Li et al. (2015), Lou et al. (2016) and Guo et al. (2017), who presented the precise point positioning (PPP) results, Odijk et al. (2012, 2014) and Odolinski et al. (2015), who provided the short-baseline real-time kinematic (RTK) positioning results, Steigenberger et al. (2013), Cai et al. (2014), Gioia et al. (2015), Gaglione et al. (2015), Steigenberger and Montenbruck (2016), Pan et al. (2017) and Liu et al. (2017), who analyzed the single point positioning (SPP) performance, and Nadarajah et al. (2013, 2015) and Nadarajah and Teunissen (2014), who provided the attitude determination results.

The Galileo constellation in April 2017 consists of four IOV and 14 FOC satellites. The first two FOC satellites (PRNs E14 and E18) were launched in August 2014, albeit into wrong orbits (Hellemans 2014). By early 2015, they were moved to an improved orbit, such that the Galileo ground segment is now able to produce the navigation messages for these two satellites (GSA 2017). The fourth IOV satellite (PRN E20) experienced a power anomaly on May 27, 2014, which led to the shutdown of the E1 signal. Although this signal recovered within seconds, E5 and E6 signals suffered a permanent loss of power. Since then, PRN E20 has been flagged as 'NOT AVAILABLE' (Langley 2014). Among the 14 FOC satellites, four are newly launched and not operational yet. Therefore, in total, 13 Galileo satellites are currently providing data to the GNSS users. In the sequel, we refer to the constellation of these 13 satellites as the current Galileo constellation.

We analyze the multipath performance and the noise characteristics of all the five Galileo signals. For the former, the multipath combinations (Estey and Meertens 1999) are formed while for the latter use is made of the least-squares variance component estimation (LS-VCE) method (Teunissen and Amiri-Simkooei 2008; Amiri-Simkooei et al. 2009). These assessments are on the basis of the data of the current Galileo constellation–excluding E14 and E18–collected by baselines of various lengths and different receiver/antenna types in Perth, Australia, and in the Netherlands. This is the first time that the stochastic properties of the Galileo signals are assessed using both IOV and FOC satellites measurements. Our outcomes, in agreement with the previous studies (Simsky et al. 2006, 2008a), show a significantly lower level of noise and multipath for the E5 signal. This gives us the motivation to further investigate the E5 instantaneous RTK positioning

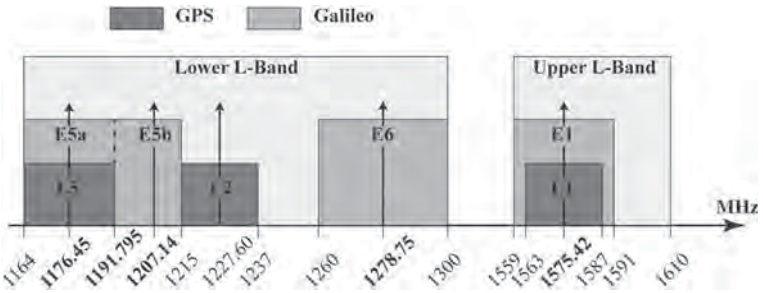

Fig. 1 Distribution of the Galileo frequencies versus GPS frequencies

performance. We then provide the Galileo standalone single-frequency E5-based RTK results. The understanding provided by such single-frequency analysis would also be useful for multifrequency analysis when integrating E5 with other frequencies. The detailed information on the data used in this study can be found in Table 2. Note the antennas used in this study do not offer, at the moment, the phase center calibrations for the Galileo E5, E5a, E5b and E6 signals. However, our analyses employing the short baselines of identical antennas are not affected by the lack of such calibrations (Mader 2002; EL-Hattab 2013).

Galileo signals characteristics

In this section, our aim is to characterize the Galileo signals stochastic properties. To do so, we investigate their power through C/N0 (carrier-to-noise density ratio), multipath performance through the code multipath combinations, and code and phase noise by means of the LS-VCE method.

Signal power

Shown in Fig. 2 are the graphs of the carrier-to-noise density ratio C/N0 of the Galileo signals with respect to the satellites elevation. The top two panels correspond to the measurements of station CUBS (Septentrio PolaRx5) while the bottom two panels correspond to those of station ADR2 (Leica GR50). The ground track of the Galileo constellation, except the two FOC satellites E14 and E18, repeats every 10 sidereal days, and therefore the Galileo satellites do not reach the whole range of elevations during one single day. Therefore, the C/N0 measurements were taken during a period of 10 days in 2017, which are days of year (DOYs) 54–63 in the case of CUBS, and DOYs 12–21 in the case of ADR2. For each station, the left panel corresponds to the FOC satellites while the right panel corresponds to the three IOV satellites. Each panel shows the average of the C/N0 data over elevation bins of 10°. Note that E6 signal is tracked only by Septentrio PolaRx5 receiver.

Comparing the C/N0 of Galileo signals, E5 shows the highest level of the carrier-to-noise density ratio for all the elevation angles, for both the FOC and IOV satellites and for both stations. In the case of CUBS, E1 and E5a have almost the same C/N0 for the range of elevations between 25° and 75°. For the elevation angles out of this range, E5a reaches a higher level of carrier-to-noise density ratio compared to the E1 particularly for the elevations higher than 75°. It can also be seen that the C/N0 of E1 experiences a drop at high elevations which was also reported in Simsky et al. (2006) using the space engineering antenna tracking the E1 data of GIOVE-A. The C/N0 of E6 lies above that of the E5b with almost the same difference for all the elevation angles. These two signals have a higher level of C/N0 with respect to the E1 and E5a. As to ADR2, the C/N0 signature of E5a coincides with that of E5b, both having higher levels than C/N0 of E1.

The observed carrier-to-noise density ratio depends on several factors such as the signal path, satellite hardware and antenna, receiving equipment including receiver, antenna, splitter and cable (Simsky et al. 2006; Hauschild

Table 2 Characteristics of the data set used for this study

Receiver—firmware Antenna—radome	Location	Station name
Septentrio PolaRx5—5.1.1 TRM 59800.00—SCIS	Curtin University, Perth, Australia	CUBS, CUCS SP01, UWA0
Leica GR50—4.00/7.001 LEIAR20 + S10—LEIM	The Netherlands	ADR2
Leica GR50—4.00/7.001 LEIAR25.R4—LEIT	The Netherlands	APEL
Data type	Galileo E1, E5a, E5b, E5, E6 (E6 is tracked only by Septentrio PolaRx5)	
Satellites	FOC (E01, E02, E08, E09, E22, E24, E26, E30) IOV (E11, E12, E19)	
Sampling interval	1 s (1 Hz)	
Baselines	CUBS-CUCS (6 m) CUBS-SP01 (350 m) ADR2-APEL (3.6 km) CUBS-UWA0 (7.9 km)	

All the antennas are survey grade and of choke-ring type

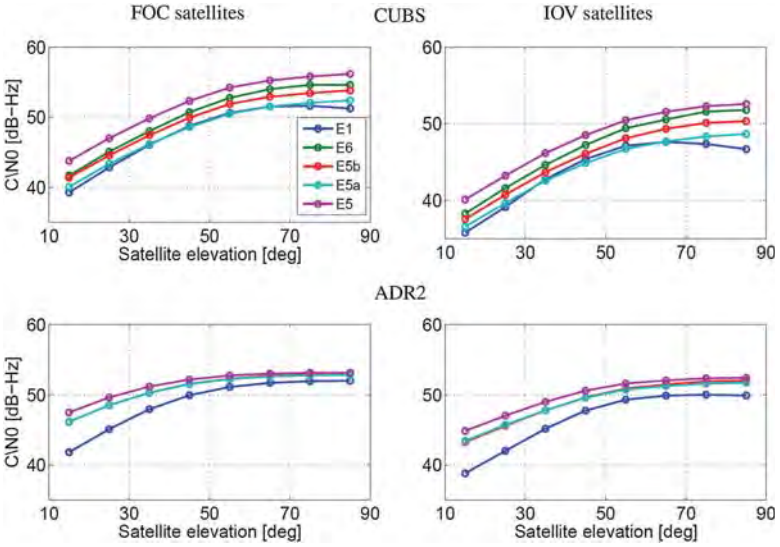

Fig. 2 Carrier-to-noise density ratio C/N0 of the Galileo signals on different frequencies as function of satellite elevation. The *top two panels* correspond to the measurements collected by station CUBS during DOYs 54-63 of 2017. The *bottom two panels* correspond to the measurements collected by station ADR2 during DOYs 12–21 of 2017. *Each panel* shows the average of C/N0 over elevation bins of 10°

et al. 2012). Such dependencies are well reflected in our observations in Fig. 2. The signals transmitted by the IOV satellites show a lower level of C/N0 in comparison with their FOC counterparts. This difference probably stems from the FOC and IOV satellites being different in transmit antenna patterns and transmit power levels. In addition, in 2014, following the fourth IOV (E20) sudden power loss and failure in transmission of the E5 and E6 signal, ESA imposed a reduction of 1.5 dB in the signal power of all the four IOV satellites (Langley 2014; Steigenberger and Montenbruck 2016). Beside the discrepancy between the IOV and FOC signals C/N0, we also noticed a difference between the C/N0 of IOV satellite pair E11/E12 and IOV satellite E19, being more pronounced in the case of Septentrio PolaRx5 receiver. According to our observations, the carrier-to-noise density ratio for E19 lies below that of the other two IOV satellites for the elevations higher than 60°.

Multipath performance

The Galileo code modulations are theoretically expected to suppress the long-delay multipath. In this sense, E5AltBOC not only outperforms the other signals, but it is also expected to have a high level of short-delay multipath rejection (Simsky et al. 2006, 2008a). In order to assess the multipath impact on Galileo signals, we form the code multipath combinations using the data collected by stations CUBS, SP01, and ADR2. The first two stations are equipped with the same receiver and antenna type, but have a different multipath environment (Table 2). The antennas deployed at all these three stations are of choke-ring type with low gain at low and negative elevation angles (Tranquilla et al. 1994). The code multipath combination is given as follows (Estey and Meertens 1999)

$$\begin{aligned}\eta^s_{r,j} &= p^s_{r,j} - \varphi^s_{r,j} + 2\frac{\lambda_j^2}{\lambda_i^2-\lambda_j^2}\left(\varphi^s_{r,i} - \varphi^s_{r,j}\right)\\ &= \xi_{p^s_{r,j}} + c^s_{r,\{j,i\}} + \epsilon^s_{r,\{j,i\}},\end{aligned} \tag{1}$$

where $p^s_{r,j}$ and $\varphi^s_{r,j}$ denote the code and the phase observation from receiver r to satellite s on frequency j, respectively. λ_j is the wavelength of the frequency j. The code multipath combination $\eta^s_{r,j}$ is composed of code multipath, $\xi_{p^s_{r,j}}$, receiver/satellite hardware delays and integer-valued ambiguities on both frequency j and i, $c^s_{r,\{j,i\}}$, and the phase noise and multipath on both frequency j and i and the code noise on frequency j, $\epsilon^s_{r,\{j,i\}}$. The contribution of the multipath and noise of the phase observations $\varphi^s_{r,i}$ and $\varphi^s_{r,j}$ is amplified through the factor $\frac{2\lambda_j^2}{\lambda_i^2-\lambda_j^2}$ of which the absolute value in case j is set to E1, E5a, E5b, E5 and E6 can, respectively, reach up to 3.9 (i: E6), 78.2 (i: E5), 77.2 (i: E5), 76.2/79.2 (i: E5a/E5b) and 16.4 (i: E5b). The significance of this contribution for a given j is then governed by the choice of i and the relative magnitude of the multipath and noise of $p^s_{r,j}$ compared to those of $\varphi^s_{r,i}$ and $\varphi^s_{r,j}$. As will be discussed in the next subsection, the multipath and noise of the code observations of E1, E5a, E5b, and E6 frequencies are by far greater than those of the phase observations, such that when j is set to one of these frequencies, the contribution of the phase noise and multipath to (1) can practically be neglected for any choice of

i. As to E5, however, due to having centimeter-level code precision, one should avoid i: E5a/E5b since the phase noise and multipath contribution to (1) would be as large as code noise and multipath. In the following, for the cases j: E5a, E5b, E5 and E6, we set i: E1, and for the case j: E1, we set i: E5.

Figure 3 (Left) depicts the time series of the code multipath combination of the Galileo signals observed between station-satellite (from top to bottom) CUBS-E26 on DOY 118 of 2017, SP01-E26 on DOY 118 of 2017 and ADR2-E11 on DOY 21 of 2017. The satellite elevation is also shown as a gray dashed line. During the considered periods, the receiver/satellite hardware delays can be assumed constant over time, and since there was no loss of lock, the ambiguities are also constant over time. Therefore the term $c^s_{r,\{j,i\}}$ in (1) can be eliminated if the mean value of $\eta^s_{r,j}$ time series during the mentioned periods, denoted by $\bar{\eta}^s_{r,j}$, is subtracted from the $\eta^s_{r,j}$ time series. Shown in Fig. 3 (Left) are then the time series of $\eta^s_{r,j} - \bar{\eta}^s_{r,j}$. The differences in the multipath signature between these three panels stem from the differences in multipath environment and, in case of the bottom panel, the receiver/antenna type. As the satellite elevation decreases, the code multipath fluctuates more rapidly and with higher amplitudes. The Galileo signals in terms of the severity of this behavior can be ordered as E1 > E5a > E5b > E6 > E5 for the stations CUBS and SP01, and as E5a > E5b > E1 > E5 for the station ADR2. As to the E5, this behavior is mitigated considerably such that the E5 code multipath can be assumed to a large extent independent of the satellite elevation. The high performance of the E5 signal lies in its wide bandwidth and AltBOC modulation (Simsky et al. 2006; Diessongo et al. 2014).

Figure 3 (Right) provides the standard deviation of the code multipath combination over elevation bins of 10° for the Galileo signals. These graphs are obtained based on all the Galileo observations recorded by the corresponding stations during 10 days. The multipath performance of three signals E5a, E5b and E6 are similar to each other, poorer than E1 in the case of station ADR2 and better than E1 in the case of stations CUBS and SP01. The graphs corresponding with E5AltBOC shows a much flatter signature, revealing a small difference between high-elevation and low-elevation multipath for this signal. This observation is also consistent with the results presented by Simsky et al. (2006) based on the observations of GIOVE-A.

Measurement noise

The GNSS underlying observational model consists of two parts: functional model and stochastic model. The former describes how the parameters of interest, e.g., receiver-satellite range, ionospheric delay, receiver clock error, are related to the GNSS observations, while the latter describes the noise characteristics of the GNSS observables. In order to assess the noise characteristics of the Galileo signals, we employ the Galileo data of the short baselines CUBS-CUCS, CUBS-SP01, ADR2-APEL, and CUBS-UWA0 (Table 2), for which the differential ionospheric and tropospheric delays can be assumed negligible. With the covariance $C(.,.)$ operator, we consider the following stochastic model for the undifferenced code and phase observations on frequency j,

$$C\left(p^s_{r,j}, p^v_{u,j}\right) = \delta_{ru}\delta_{sv}\sigma^2_{p_j} w^s, \quad C\left(\varphi^s_{r,j}, \varphi^v_{u,j}\right) = \delta_{ru}\delta_{sv}\sigma^2_{\varphi_j} w^s, \quad C\left(p^s_{r,j}, \varphi^v_{u,j}\right) = 0, \tag{2}$$

where δ_{ru} is the Kronecker delta ($\delta_{ru} = 1$ for $r = u$ and zero otherwise), and δ_{sv} is defined likewise. w^s captures the satellite elevation dependency of the Galileo data through the exponential weighting function as

$$w^s = \left(1 + 10\exp\left(-\frac{\theta^s}{10}\right)\right)^{-2}, \tag{3}$$

where θ^s is the elevation of satellite s in degrees (Euler and Goad 1991). Note we have dropped the receiver index from θ^s and w^s since the elevation of satellite s can be assumed the same for the considered station pairs which are separated at a short distance. σ_{p_j} and σ_{φ_j} denote the zenith-referenced standard deviations of the undifferenced code and phase observations on frequency j, respectively.

Our aim is to find representative values for $\{\sigma_{p_j}, \sigma_{\varphi_j}\}(j = 1, \ldots, 5)$. To do so, we apply the LS-VCE method (Teunissen and Amiri-Simkooei 2008; Amiri-Simkooei et al. 2009) to the 1-s (1 Hz) double-differenced (DD) code and phase observations which are corrected for the DD ranges and, in case of phase observations, the integer DD ambiguities. The DD ranges were computed from the known receiver and satellite positions. Whereas the reference integer ambiguities were computed using the very strong multiepoch baseline-known model in which the observations of multiple epochs are incorporated, the ambiguities are assumed to be constant over time and the baseline components are assumed known. These corrected DD observations and the so estimated variances, will capture the combined effect of the transmitted signal quality, the receiver architecture like correlator and loops, as well as any remaining mis-modeled effects like multipath. The impact of multipath can be largely mitigated through the method explained in the following. Since the stations in use are static and their surrounding environment almost remains unchanged over time, the multipath influence on a signal of a specific frequency is expected

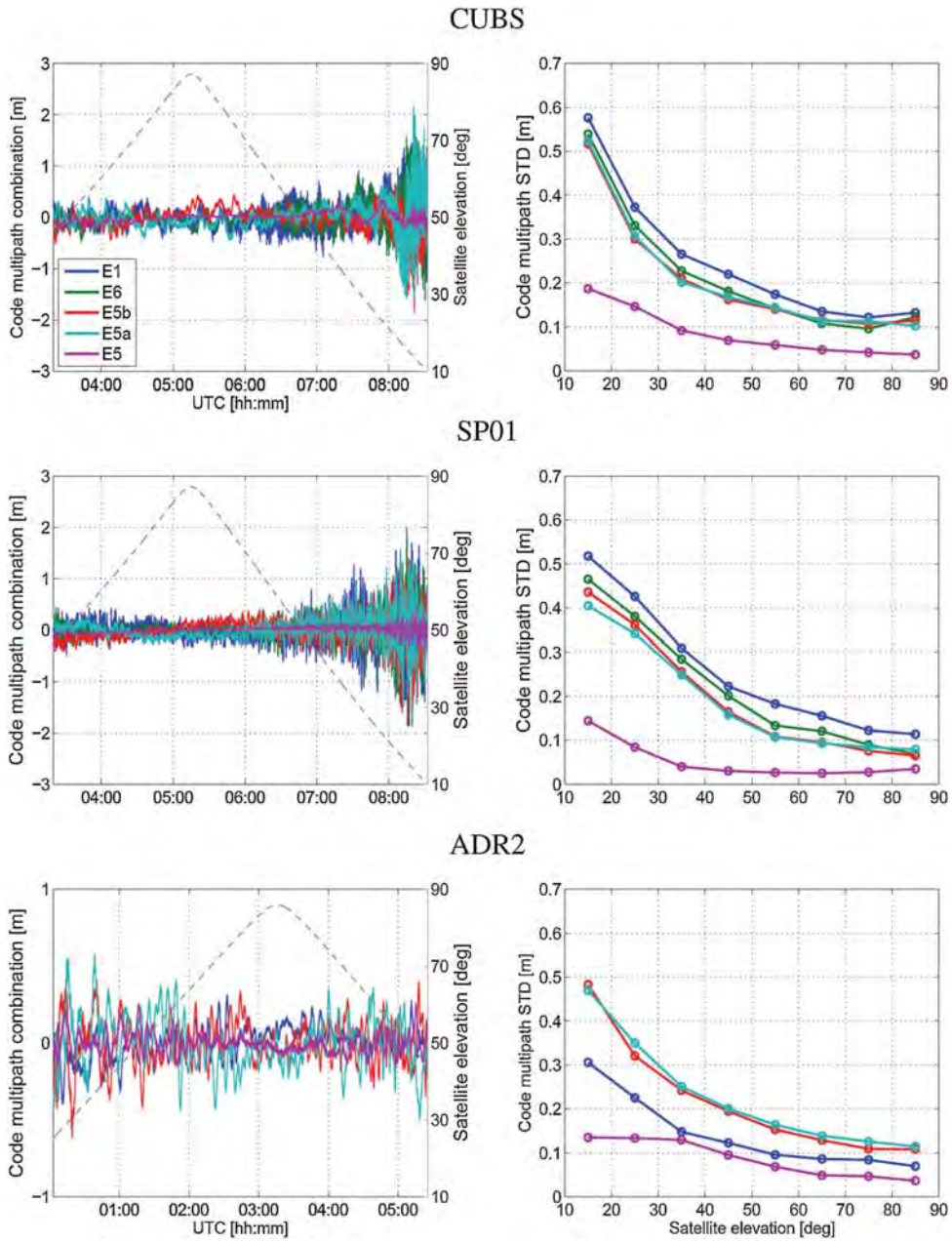

Fig. 3 Galileo code multipath behavior. (*Left*) code multipath combination time series based on the observations of station-satellite (from *top* to *bottom*) CUBS-E26 on DOY 118 of 2017, SP01-E26 on DOY 118 of 2017 and ADR2-E11 on DOY 21 of 2017. The satellite elevation is indicated by the dashed line. (*Right*) the standard deviation of the code multipath combination over elevation bins of 10°, based on all the Galileo observations recorded by (from *top* to *bottom*) station CUBS and SP01 during DOYs 118–127 of 2017 and station ADR2 during DOYs 12–21 of 2017

Table 3 LS-VCE estimation of the undifferenced code σ_p and phase σ_φ zenith-referenced standard deviations of the Galileo data

	Signal	CUBS-CUCS	CUBS-SP01	ADR2-APEL	CUBS-UWA0
σ_p (cm)	E1	21.2, 10.8	18.9, 9.8	17.5, 3.2	16.4, 9.8
	E5a	15.3, 5.6	14.9, 5.5	19.6, 3.7	13.7, 5.5
	E5b	16.3, 5.6	15.1, 5.6	18.8, 3.7	14.1, 5.6
	E5	6.4, 1.1	5.1, 1.1	6.8, 1.0	5.1, 1.2
	E6	16.5, 7.5	16.6, 7.6	–, –	13.1, 7.9
σ_φ (mm)	E1	1.4, 0.5	3.0, 0.8	3.8, 0.9	5.7, 3.2
	E5a	1.5, 0.5	3.1, 0.9	3.8, 1.3	6.8, 4.5
	E5b	1.4, 0.5	3.1, 0.8	3.6, 1.3	6.7, 4.4
	E5	1.1, 0.4	3.0, 0.8	3.6, 1.3	6.7, 4.4
	E6	1.4, 0.5	3.0, 0.8	–, –	5.6, 4.1

For each frequency and each baseline, two values are given for σ_p and σ_φ which, from left to right, correspond to the original and multipath-corrected data

to repeat when the Galileo receiver-satellite geometry repeats after 10 sidereal days. Therefore, by subtracting the corrected DD observations corresponding with the same satellite geometry (obtained every 10 sidereal days), the adverse multipath impact can be largely eliminated (Bock 1991; Genrich and Bock 1992; Zaminpardaz et al. 2016).

Table 3 lists the estimated standard deviations of the Galileo code σ_{p_j} and phase σ_{φ_j} observations with and without multipath corrections. For static stations, as used in this study, the multipath pattern for the Galileo constellation is expected to repeat every 10 sidereal days. This indicates that for every 10-day period, the multipath signature differs from day to day. Therefore, the standard deviations estimations of the original observations in Table 3 are obtained based on 10-day data sets. Prior to applying the multipath corrections to these data sets using the data of 10 days later as explained above, we first checked whether the multipath pattern indeed repeats after 10 sidereal days. Our observations showed that, in spite of the multipath environment remaining unchanged over time, for some of the satellites during some time intervals the multipath signature does not show a good repeatability. As an example, Fig. 4 for the station-satellite CUBS-E12 shows the E1 code multipath combination time series during a 48-min period on DOY pairs (blue-red) 123–133 (top) and 124–134 (bottom). The satellite elevations during the considered periods in top and bottom panels are similar. The UTC labels given in the top/bottom panel are on DOY 133/134, and therefore the UTC for the blue graphs are obtained by adding 2420 s ($\approx 10 \times 4$ min) to the shown UTC labels. It can be seen that while the multipath pattern shows consistent signature for DOY pair 123–133, its behavior differs from DOY 124 to DOY 134. A possible explanation for this discrepancy is as follows. The time shift that we use for DOY pairs 123–133 and 124–134 is

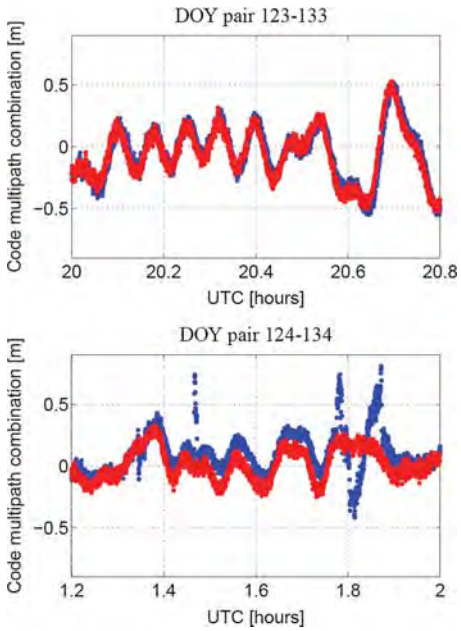

Fig. 4 Code multipath combination time series based on the E1 observations of station-satellite CUBS-E12 on (*top*) DOYs 123 (*blue*) and 133 (*red*) of 2017 (*bottom*) DOYs 124 (*blue*) and 134 (*red*) of 2017

2420 s which has been computed through cross-correlation of the corresponding baseline (CUBS-CUCS) estimation time series on DOYs 53 and 63 of 2017. However, our observations show that the repeat cycle varies among different Galileo satellites. Even for a given specific satellite, the repeat cycle changes from time to time. Any variation in the satellite geometry would then result in the variation in multipath signature. Thus, for estimating the multipath-corrected standard deviations in Table 3, we only chose

data of those days showing very similar multipath signature to that of their counterparts 10 days later, with the purpose of providing values one could achieve in case the multipath could have been eliminated. Note for multipath-corrected estimations, due to day-differencing, we have taken the doubling of the noise level into account through replacing w^s by $2w^s$.

Despite having the same receiver and antenna type, baselines CUBS-CUCS, CUBS-SP01 and CUBS-UWA0 show differences in their estimations of the original data standard deviations which can be attributed to the differences in the multipath environment of the stations CUCS, SP01 and UWA0. These discrepancies would vanish though, were the multipath effect be completely eliminated. This is also confirmed comparing the corresponding outcomes based on the original and multipath-corrected data. It can be seen that upon applying multipath corrections, the differences between the estimations of the mentioned three baselines get smaller. The stations forming the baseline ADR2-APEL have different antenna types (Table 2). The results presented in Table 3 for this station pair thus capture the combined effect of different antenna types involved. Comparing the standard deviation estimations of a specific signal based on the data of different baselines, one notes that the ordering would change if the multipath corrections are applied. For example, the code precision of the E5a original data improves from ADR2-APEL to CUBS-CUCS to CUBS-SP01 to CUBS-UWA0, whereas on the basis of E5a multipath-corrected data, the code precision improves from CUBS-CUCS to CUBS-SP01/CUBS-UWA0 to ADR2-APEL.

The order in which the signals can be arranged in terms of their precision is different for various receiver/antenna types. The code standard deviation of the E5 signal, however, shows lower dependency on the receiver/antenna type and the multipath environment, and significantly smaller values with respect to that of the other signals. Upon applying the multipath correction, the code standard deviations of all the signals experience a dramatic reduction which is a factor of five in the case of E5. The phase precision estimations either with or without multipath corrections, in contrast to their code counterparts, do not show any dependency on the signal type.

The results presented in Table 3 have been obtained combining the observations of the IOV and FOC satellites. We also carried out the LS-VCE estimations based on the IOV-only and FOC-only observations. The estimated code standard deviations of the FOC satellites are generally smaller than those of the IOV satellites. The phase observations of these two types of satellites, however, show similar precisions.

E5AltBOC RTK analysis

It was shown in the previous section that among the five Galileo signals, E5AltBOC shows a significantly higher signal power and lower level of multipath and noise. Such characteristics give us the motivation to further analyze the high-performance E5 signal for its potential capability in RTK positioning. In this section, we present the results of the Galileo E5-based instantaneous RTK performance. Our assessments are carried out based on the Galileo data collected by CUBS-CUCS (6-day data set; DOYs 54, 56–60 of 2017), CUBS-SP01 (5-day data set; DOYs 123–127 of 2017), ADR2-APEL (1-day data set; DOY 17 of 2017) and CUBS-UWA0 (2-day data set; DOYs 173–174 of 2017), once without multipath correction and once with multipath correction provided by the Galileo data 10 days later. With the current Galileo constellation, there exist time intervals with less than four visible satellites, accounting for 41 and 51% of a repeat cycle of 10 days at Perth and the Netherlands, respectively. These percentages increase further to 78% upon excluding E14 and E18, which is the case with our analyses in this contribution. The periods considered for our RTK evaluations accommodate time intervals with four to five visible satellites. In case of the first two baselines, there is a very short time interval with six satellites being visible. Given the limited number of visible Galileo satellites, the corresponding position dilution of precision (PDOP) reaches extremely large values, thus making positioning almost infeasible. In order to leave out these extreme values, in the sequel, we consider various PDOP thresholds when presenting RTK results.

GNSS single-frequency observational model

Let us assume that two receivers are simultaneously tracking m Galileo satellites on a single frequency, say E5. The corresponding multivariate DD observation equations can be cast in (Teunissen and Montenbruck 2017, Chap. 1; Hofmann-Wellenhof et al. 2008, Chap. 5)

$$E\begin{bmatrix} D_m^T p \\ D_m^T \varphi \end{bmatrix} = \begin{bmatrix} D_m^T G & 0 \\ D_m^T G & \lambda I_{m-1} \end{bmatrix}\begin{bmatrix} b \\ a \end{bmatrix}, \quad D\begin{bmatrix} D_m^T p \\ D_m^T \varphi \end{bmatrix} = \begin{bmatrix} \sigma_p^2 Q & 0 \\ 0 & \sigma_\varphi^2 Q \end{bmatrix}, \tag{4}$$

where $E[.]$ and D $[.]$ denote, respectively, the expectation and dispersion operator. The observations are formed by the vectors of the DD code and phase measurements, obtained by applying the between-satellite differencing operator D_m^T to the m-vector of between-receiver single-differenced (SD) code p and phase φ measurements. The $(m-1)\times m$ differencing operator can be formed as, e.g., $D_m^T = [-e_{m-1}, I_{m-1}]$ where e_{m-1} and I_{m-1} denote the

vector of ones and the identity matrix, respectively. The unknowns to be estimated are the 3-vector of the baseline increments b, linked to the observations through the $m \times 3$ geometry matrix G, and the $(m-1)$-vector of the DD ambiguities a, linked to the phase observations through the signal wavelength λ. The noise of the measurements is characterized through three factors, i.e., σ_p, σ_φ and $Q = 2 \times D_m^T W^{-1} D_m$. σ_p and σ_φ denote the zenith-referenced standard deviation of the undifferenced code and phase measurements (cf. 2), and W is the $m \times m$ diagonal matrix having the satellite elevation-dependent weights w^s (cf. 3) as its diagonal entries. Note our analyses are based on the short-baseline data where the differential ionospheric and tropospheric delays can be neglected.

As (4) suggests, for the single-epoch analyses, the phase observations are fully reserved for the estimation of the DD ambiguities. The estimation of the baseline would then be governed by the code observations only. The so obtained solutions for the baseline and the DD ambiguities are called float solutions. Upon resolving the DD ambiguities to their integer values, the phase observations would take the leading role in the baseline estimation. The so obtained solutions for the baseline and the DD ambiguities are called fixed solutions.

Ambiguity resolution results

Successful phase ambiguity resolution is a prerequisite to the realization of RTK positioning. As a measure to analyze the Galileo E5 ambiguity resolution performance in the framework of the model given in (4), we make use of the integer bootstrapped (IB) success rate as it is easy to compute, and also the sharpest lower bound to the integer least-squares (ILS) success rate which has the highest success rate of all admissible integer estimators (Teunissen 1999; Verhagen and Teunissen 2014). The formal IB success rate is computed as (Teunissen 1998)

$$\text{Formal IB Ps} = \prod_{i=1}^{m-1} \left[2\phi\left(\frac{1}{2\sigma_{\hat{z}_{i|I}}} \right) - 1 \right], \tag{5}$$

with $\phi(x) = \int_{-\infty}^{x} \frac{1}{\sqrt{2\pi}} \exp\{-\frac{1}{2}\upsilon^2\} \mathrm{d}\upsilon$ and $\sigma_{\hat{z}_{i|I}} (i = 1, \ldots, m-1$ and $I = 1, \ldots, i-1)$ being the conditional standard deviations of the decorrelated ambiguities. As the formal IB success rate is model-driven, to check the consistency between our data and the assumed underlying model, we also compute the empirical IB success rate which is data-driven and given as

$$\text{Empirical IB Ps} = \frac{\#\,\text{Correct fixed DD ambiguities}}{\#\text{Float DD ambiguities}}, \tag{6}$$

Table 4 Average single-epoch formal and empirical bootstrapped (IB) success rate (%), for the original and the multipath-corrected Galileo E5 data, collected by several baselines with the cutoff elevation of 10°

Baseline	PDOP < 30		PDOP < 20		PDOP < 10	
	emp	form	emp	form	emp	form
CUBS-CUCS	32.2	28.0	33.1	28.5	40.2	34.6
	95.2	92.1	95.5	92.3	97.6	95.0
CUBS-SP01	32.1	27.0	33.1	27.9	30.4	26.9
	89.6	93.0	89.7	93.4	87.3	94.2
ADR2-APEL	23.2	19.9	20.9	19.5	14.1	13.6
	95.6	93.7	95.2	93.7	96.9	91.0
CUBS-UWA0	29.3	29.5	29.2	29.8	27.0	29.4
	85.1	91.4	85.1	91.9	81.4	91.4

For each baseline and each PDOP threshold, two rows of values are given; the first row corresponds to original data, while the second row corresponds to the multipath-corrected data

emp empirical, *form* formal

To judge whether a float DD ambiguity $(\hat{a})$ is correctly fixed, its corresponding IB solution $(\breve{a})$ is compared with the reference integer DD ambiguity (a) computed based on the multiepoch ILS solution of the baseline-known model. Table 4 shows the empirical and formal single-epoch IB success rates for both the original and multipath-corrected data of the mentioned four baselines. The formal values in this table are obtained through averaging the formal IB success rates over the period in use. In addition, since for the positioning results, coming in the next subsection, we consider various thresholds for PDOP value, we apply them here as well. One should, nevertheless, have in mind that the ambiguity resolution performance is not characterized through PDOP (Zaminpardaz et al. 2016, p. 546).

The results in Table 4 state that upon applying the multipath corrections, the IB success rates increase dramatically such that (almost) instantaneous ambiguity resolution becomes feasible. For example, if an ambiguity resolution success rate of 99.9% is sought for RTK positioning, our computation shows that, on average, four epochs of 1-s data are required. However, there still remains some inconsistencies between empirical and formal outcomes which can be attributed to the existence of the multipath residuals as explained in the following. As was mentioned previously, applying the multipath corrections cannot fully eliminate the multipath impact on our data sets, thereby leaving some residuals. The multipath-corrected standard deviations in Table 3, based on which the multipath-corrected formal success rates are computed, also, in turn, capture the impact of the multipath residuals

of the underlying data sets. The multipath-corrected empirical success rates in Table 4 are also affected by the multipath residuals of the corresponding data sets. The difference of the multipath residuals existing in the data sets used in Table 3 and those employed in Table 4, if non-negligible, can lead to disagreement between empirical and formal success rates. Note that the differences between the formal success rates of different baselines stem from the differences in the corresponding code/phase standard deviation (Table 3) and the satellite geometry.

Now, through visualization, we elaborate more on how applying the multipath correction improves the ambiguity resolution performance. For this purpose, we choose a period of 7000 s of the CUBS-CUCS data set, over which four Galileo satellites are visible from these stations, which in turn, results in three DD ambiguities. During this period, there was no loss of lock, and therefore the DD ambiguities remained constant. Figure 5 shows the corresponding three-dimensional scatter plot of the single-epoch solutions of $\hat{a} - a$ (gray) and $\check{a} - a$ (green: correctly fixed; red: wrongly fixed). While the left panel depicts the estimations based on the original data, the right panel shows those based on the multipath-corrected data. It can be seen that once the multipath corrections are applied to our data, the scatter plot of $\hat{a} - a$ shrinks considerably, and the number of incorrectly fixed solutions decreases from 29 to 3.

RTK positioning results

In this subsection, we discuss the single-epoch baseline estimation results based on the Galileo E5 observations. Setting the thresholds of 30, 20 and 10 for PDOP, Table 5 gives the empirical and formal single-epoch standard deviations of the estimated components of the baselines CUBS-CUCS, CUBS-SP01, ADR2-APEL, and CUBS-UWA0. The first two rows for each baseline give the ambiguity-float results on the basis of original and multipath-corrected data, respectively. The multipath-corrected results in Table 5 can be considered of practical relevance for kinematic users in a low multipath environment or for static baselines like, e.g., for deformation monitoring. As was shown in the previous subsection, the multipath-corrected Galileo E5 data can provide (almost) instantaneous successful ambiguity resolution. Therefore, the third row for each baseline gives the multipath-corrected ambiguity-fixed results, which are computed based on only the correctly fixed solutions. The formal and empirical standard deviations are computed on the basis of the respective formal and empirical variance matrix. The formal variance matrix is obtained from taking the average of all the single-epoch least-squares baseline variance matrices, whereas the empirical variance matrix is obtained from the differences of the estimates and the available ground truth of the mentioned baselines. Comparing the ambiguity-float results from the original data with those from the multipath-corrected data, the precision improvement achieved upon applying the multipath correction is a factor of about 4.24 which is the ratio of σ_p of the original data to $\sqrt{2} \times \sigma_p$ of the multipath-corrected data. The empirical results show consistency with the formal outcomes, particularly in case of the ambiguity-fixed scenario. Also, the positioning precisions depend on the receiver/antenna type as well as the extent to which the multipath impact can be mitigated (Table 3).

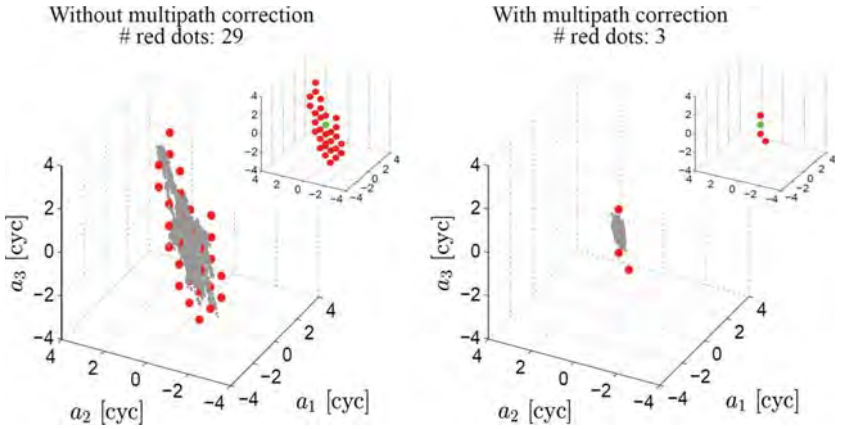

Fig. 5 Three-dimensional scatter plot of the single-epoch DD ambiguities in float mode $\hat{a} - a$ (*gray*) and fixed mode $\check{a} - a$ (*green* correctly fixed; *red* incorrectly fixed), corresponding with the Galileo E5 data collected by CUBS-CUCS over a period of 7000 s on DOY 54 of 2017. Given on *top* of *each panel* is the number of integers which were incorrectly determined by the IB estimator to be the DD ambiguities solution. Also, in the *upper right* of each panel, the *scatter plot* of only the fixed solutions is depicted. (*Left*) without multipath correction; (*right*) with multipath correction

Table 5 Single-epoch standard deviations of the estimated components of the baselines CUBS-CUCS, CUBS-SP01, ADR2-APEL and CUBS-UWA0 based on the Galileo E5 measurements collected with the cutoff angle of 10°

Baseline	PDOP < 30			PDOP < 20			PDOP < 10		
	North	East	Height	North	East	Height	North	East	Height
CUBS-CUCS									
	0.268, 0.305	0.225, 0.262	0.735, 0.804	0.235, 0.268	0.213, 0.238	0.593, 0.656	0.150, 0.165	0.185, 0.179	0.412, 0.423
	0.064, 0.076	0.044, 0.065	0.170, 0.201	0.053, 0.067	0.040, 0.059	0.143, 0.164	0.030, 0.041	0.034, 0.045	0.083, 0.106
	0.002, 0.003	0.002, 0.002	0.006, 0.007	0.002, 0.002	0.002, 0.002	0.005, 0.006	0.001, 0.001	0.002, 0.002	0.003, 0.004
CUBS-SP01									
	0.233, 0.260	0.197, 0.217	0.607, 0.662	0.200, 0.226	0.181, 0.191	0.505, 0.534	0.172, 0.168	0.165, 0.145	0.376, 0.339
	0.085, 0.077	0.071, 0.064	0.196, 0.196	0.077, 0.067	0.066, 0.056	0.158, 0.158	0.060, 0.050	0.060, 0.043	0.134, 0.100
	0.006, 0.006	0.005, 0.005	0.016, 0.015	0.004, 0.005	0.004, 0.004	0.012, 0.012	0.004, 0.004	0.003, 0.003	0.008, 0.008
ADR2-APEL									
	0.386, 0.387	0.226, 0.260	0.746, 0.799	0.397, 0.378	0.224, 0.248	0.715, 0.690	0.252, 0.305	0.225, 0.205	0.346, 0.503
	0.062, 0.081	0.051, 0.054	0.162, 0.167	0.062, 0.079	0.046, 0.052	0.143, 0.144	0.045, 0.063	0.035, 0.043	0.086, 0.105
	0.011, 0.010	0.006, 0.007	0.024, 0.022	0.010, 0.010	0.005, 0.006	0.019, 0.019	0.007, 0.008	0.003, 0.005	0.012, 0.014
CUBS-UWA0									
	0.229, 0.258	0.153, 0.170	0.614, 0.577	0.197, 0.224	0.143, 0.156	0.562, 0.511	0.166, 0.171	0.126, 0.138	0.364, 0.368
	0.071, 0.087	0.053, 0.058	0.180, 0.195	0.065, 0.076	0.050, 0.053	0.166, 0.173	0.052, 0.058	0.049, 0.047	0.125, 0.124
	0.029, 0.029	0.020, 0.019	0.070, 0.067	0.024, 0.025	0.018, 0.017	0.062, 0.060	0.017, 0.020	0.016, 0.015	0.050, 0.040

For each baseline and each PDOP threshold, six values per coordinate components are given on three rows. The first row contains the ambiguity-float results without multipath correction; the second contains the multipath-corrected ambiguity-float results and the third contains the multipath-corrected ambiguity-fixed results. On each row, from left to right, empirical and formal values are presented

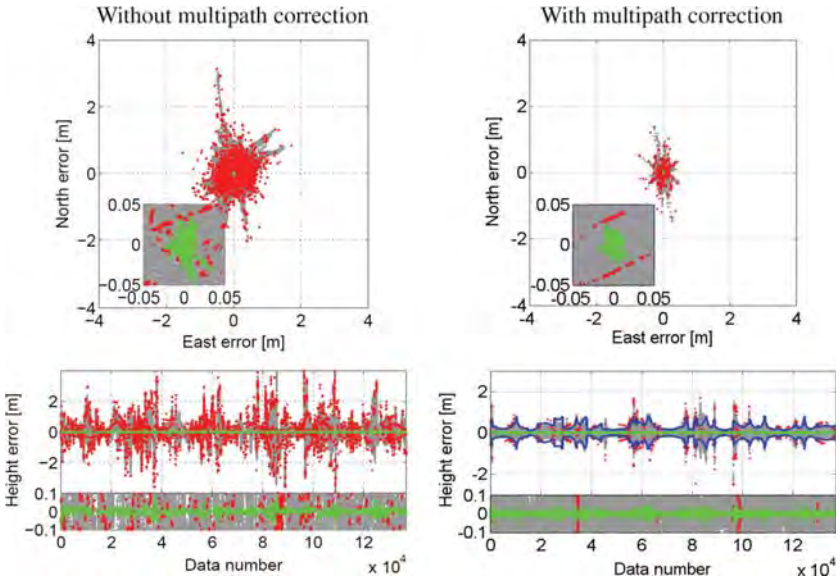

Fig. 6 CUBS-CUCS baseline solutions based on the Galileo E5 measurements collected on DOYs 54 and 56–60 of 2017 with the cutoff angle of 10°. These solutions correspond to PDOP values smaller than 30. (*Top*) *horizontal scatter plot* with a zoom-in in the lower left. (*Bottom*) height estimation errors time series with a zoom-in in the *bottom*. *Gray* float solutions; *green* correctly fixed solutions; *red* incorrectly fixed solutions. The *blue lines* in the *lower right panel* indicate the 95% formal confidence interval

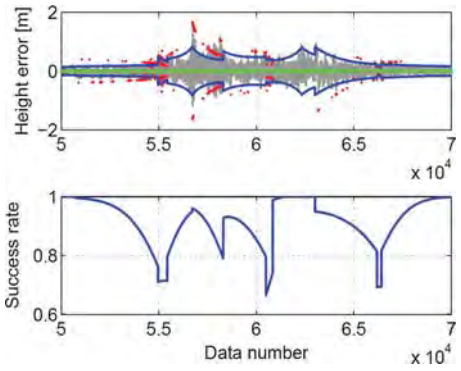

Fig. 7 Ambiguity resolution performance. (*Top*) a zoom-in of the height estimation errors time series illustrated in the *lower right panel* of Fig. 6. (*Bottom*) the corresponding time series of the single-epoch formal IB success rate

In the following, the positioning results of the baseline CUBS-CUCS are visualized and further discussed. Shown in Fig. 6 are the scatter plot of the CUBS-CUCS baseline horizontal components estimation errors (top) and the time series of the baseline height estimation error (bottom). Note, in this figure, we have stacked all the periods on DOYs 54 and 56–60 of 2017, during which a minimum of four Galileo satellites are visible, and the corresponding PDOP is less than 30. The estimation errors are computed by subtracting the baseline ground truth from the baseline single-epoch estimations. Different colors in this figure have the following meanings; gray: float solution, green: correctly fixed solution, and red: incorrectly fixed solution. The two left panels are based on the original data, whereas the two right panels correspond with the multipath-corrected data. In the lower right panel is also shown the 95% formal confidence interval (blue lines) based on the float height standard deviation. To obtain these results, a threshold of 30 was imposed on the PDOP.

In Fig. 6, the scatter plots do not show an ellipsoidal shape which is due to the significant changes that the receiver-satellite geometry undergoes during the mentioned six days. It can also be seen that the variation of the float solutions (gray) significantly decreases upon applying the multipath correction. This is due to the improvement of the E5 code precision following the elimination of the multipath effect from the code data (Table 3). The density of the red and green dots can be explained by means of the formal IB success rate. Figure 7 shows a zoom-in of the multipath-corrected height estimation error time series between (50,000, 70,000) (top) and the corresponding time series of the single-epoch formal IB success rate (bottom). The distribution of the red and green dots is in good agreement with the behavior of the formal IB success rate. When the success rate gets smaller, the density of red dots increases and vice versa.

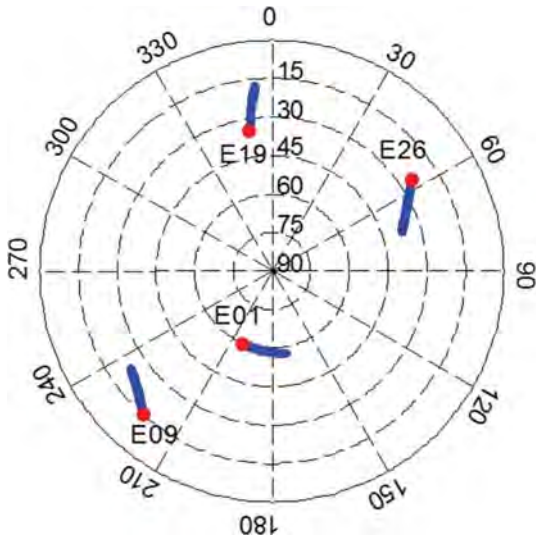

Fig. 8 Skyplot of Galileo at Perth, Australia, during UTC(18:35:11–19:21:51) on DOY 56 of 2017 with a cutoff elevation of 10°. The *red dots* show the location of the visible satellites at the first epoch of this time interval

The time series of the multipath-corrected height estimation errors, except for some intervals, shows a consistent signature with its formal counterpart (blue lines). The inconsistencies between the formal and empirical float solutions can be attributed to the fact that the multipath corrections that we apply to our data cannot eliminate the multipath effect completely. Instead, they capture largely the multipath trend (low-frequency multipath components) and partly the high-frequency multipath components which are of higher amplitudes in the satellite signals received at low elevations (Fig. 3, left).

Looking at the ambiguity-fixed solutions presented in the right panel of Fig. 6, during some time interval, different clusters of fixed solutions can be recognized, indicating that the DD ambiguities are resolved to different integer vectors during these periods. As an example, we consider the interval (30,200, 33,000) through which there exist three (two red and one green) clusters of fixed solutions, thus three different integer estimations of the ambiguities. Shown in Fig. 8 is the skyplot of the Galileo satellites at Perth during this period. According to this figure, four satellites are visible among which satellite E09 is just rising from the elevation of 15°. Figure 9 (right) shows the time series of the float and fixed DD ambiguities over the mentioned period, from top to bottom, for the satellite pairs E01–E09, E01–E19, and E01–E26, respectively. It can be seen that while the DD ambiguities of E01–E19 and E01–E26 are correctly fixed to 0, those corresponding with E01–E09 are varying between −1, 0 and 1 which is obviously due to the residuals of the high-frequency multipath components. Figure 9 (left) shows the three-dimensional scatter plot of the float DD ambiguities during the first 100 epochs of the interval (30,200, 33,000), where a_1: E01–E09, a_2: E01–E19 and a_3: E01–E26. The zero IB pull-in region (black parallelepiped), computed based on the average DD ambiguities variance matrix over the mentioned 100 epochs, is also illustrated in this figure. The ambiguities solutions inside the pull-in region are indicated by the green dots and those outside the pull-in region by the red dots. It can be seen that the scatter plot of the DD ambiguities deviates from the zero IB pull-in region along a_1 direction, corresponding with E01–E09.

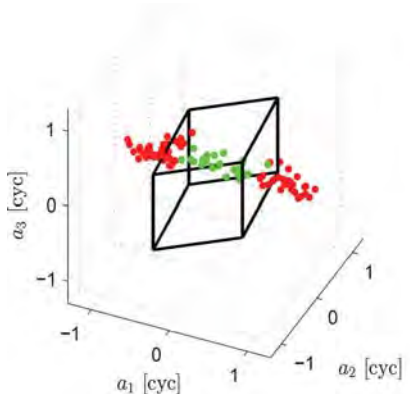

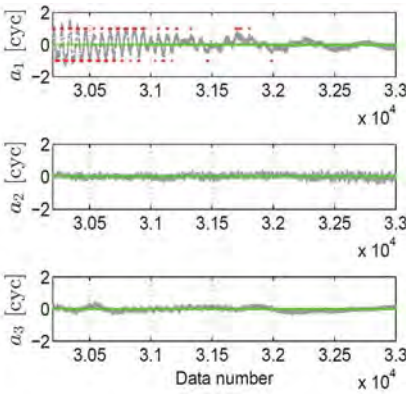

Fig. 9 (*Left*) Three-dimensional scatter plot of the float DD ambiguities corresponding with the satellite geometry shown in Fig. 8 during the interval (30200, 30300). The *black parallelepiped* is the IB pull-in region. The float DD ambiguities inside the IB pull-in regions are denoted by *green dots* and those outside the IB pull-in region by *red dots*. a_1: E01–E09, a_2: E01–E19 and a_3: E01–E26. (*Right*) time series of the float and fixed DD ambiguities over the mentioned interval. *Gray* float solutions; *green* correctly fixed solutions; *red* incorrectly fixed solutions

Summary and conclusion

We provided the results of the Galileo signals stochastic properties employing 1-s data collected by four short baselines of different lengths and receiver/antenna types. The assessments included the observations of both the IOV and FOC satellites in the constellation in April 2017 excluding E14 and E18. We analyzed the signal power, multipath performance and the noise level of the Galileo E1, E5a, E5b, E5 and E6 signals. The carrier-to-noise density ratio C/N0 measurements of the Galileo FOC satellites demonstrated higher values than those of the IOV satellites. This can be attributed to different transmit antenna patterns and transmit power levels of these two types of satellites, and also the signal power reduction of all the IOV satellites imposed by ESA in 2014. For two types of receiver/antenna in use, i.e., Septentrio PolaRx5/TRM 59800.00 SCIS (CUBS) and Leica GR50/LEI AR20 (ADR2), our C/N0 observations revealed the following ordering $E5 > E6 > E5b > E5a \approx E1$ and $E5 > E5b \approx E5a > E1$, respectively.

To analyze the multipath performance of the Galileo signals, the corresponding code multipath combinations were formed based on the observations of three stations (CUBS and SP01 at Perth and ADR2 in the Netherlands) with different multipath environment and receiver/antenna type. The standard deviations of the code multipath combination as a function of satellite elevation were illustrated. The multipath performance of three signals E5a, E5b and E6 were similar to each other, poorer than E1 in the case of station ADR2 and better than E1 in the case of stations CUBS and SP01. A strong satellite elevation dependency was visible in the code multipath of all these four signals. Taking considerably smaller values, E5 signal multipath showed a weak dependency on the satellite elevation.

Having investigated the multipath performance of the Galileo signals, we then turned our attention into the assessment of the measurement noise. To do so, we made use of the LS-VCE method to estimate the zenith-referenced variance of the signals on different frequencies. Our estimations are combinations of the transmitted signal quality, the receiver architecture including correlator and loops, and any remaining mis-modeled effects like multipath. Describing a multipath mitigation method, we presented the LS-VCE estimations of the mentioned variances for both the original and the multipath-corrected data of several short baselines of different lengths and receiver/antenna types. The order in which the signals can be arranged in terms of their precision is different for various receiver/antenna types. Upon applying the multipath correction, the code standard deviations of all the signals experienced a dramatic reduction. The code standard deviation of the E5 signal showed significantly smaller values with respect to that of the other signals, with low dependency on the receiver/antenna type and the multipath environment. Estimations based on the data of all four short baselines confirmed a standard deviation of about 6 cm without multipath correction and about 1 cm with multipath correction for the E5 code observations. The phase precision estimations either with or without multipath corrections did not show any dependency on the signal type.

Showing a significantly lower level of multipath and noise and higher signal power irrespective of the receiver/antenna type, E5 signal was further investigated for its capability in instantaneous RTK positioning. For this purpose, we made use of the observations recorded by all the mentioned baselines. It was shown that the Galileo E5 single-epoch ambiguity resolution IB success rate of about 90% is achievable for all the station pairs upon applying the multipath correction to the E5 data. This means that the Galileo E5 data, if corrected for the multipath effect, can make (almost) instantaneous ambiguity resolution feasible already based on the current constellation. The resultant ambiguity-fixed positioning precision varied as a function of the receiver/antenna type and the extent to which the multipath impact can be mitigated.

We showed that the multipath corrections, generated as described in this paper, capture largely the low-frequency multipath components and partly the high-frequency multipath components which are of higher amplitudes and mainly present in the satellite signals received at low elevations. Our results revealed that the residuals of these high-frequency multipath components after applying the multipath corrections can still lead to incorrect fixing of the DD ambiguities.

Acknowledgements The second author is the recipient of an Australian Research Council (ARC) Federation Fellowship (Project Number FF0883188). The Netherlands data were provided by Mr. Lennard Huisman from Kadaster, the Netherlands. This support is greatly acknowledged. We are also thankful to Dr. Nandakumaran Nadarajah and Dr. Mohammad Choudhury from Curtin University GNSS Research Center, Perth, Australia, for providing the data of UWA0 station.

References

Afifi A, El-Rabbany A (2014) Single frequency GPS/Galileo precise point positioning using un-differenced and between-satellite single difference measurements. GEOMATICA 68:195–205

Amiri-Simkooei AR, Teunissen PJG, Tiberius CCJM (2009) Application of least-squares variance component estimation to GPS observables. J Surv Eng 135(4):149–160

Bock Y (1991) Continuous monitoring of crustal deformation. GPS World 2(6):40–47

Cai C, Luo X, Liu Z, Xiao Q (2014) Galileo signal and positioning performance analysis based on four IOV satellites. Navigation 67:810–824

Cai C, Gao Y, Pan L, Zhu J (2015) Precise point positioning with quad-constellations: GPS, BeiDou, GLONASS and Galileo. Adv Space Res 56:133–143

Cai C, He C, Santerre R, Pan L, Cui X, Zhu J (2016) A comparative analysis of measurement noise and multipath for four constellations: GPS, BeiDou, GLONASS and Galileo. Surv Rev 48:287–295

de Bakker PF, van der Marel H, Tiberius CC (2009) Geometry-free undifferenced, single and double differenced analysis of single frequency GPS, EGNOS and GIOVE-A/B measurements. GPS Solut 13(4):305–314

de Bakker PF, Tiberius CC, Van Der Marel H, van Bree RJ (2012) Short and zero baseline analysis of GPS L1 C/A, L5Q, GIOVE E1B, and E5aQ signals. GPS solut 16(1):53–64

Diessongo TH, Schüler T, Junker S (2014) Precise position determination using a Galileo E5 single-frequency receiver. GPS Solut 18(1):73–83

EL-Hattab AI (2013) Influence of GPS antenna phase center variation on precise positioning. NRIAG J Astron Geophys 2:272–277

ESA (2016) Galileo fact sheet. http://esamultimedia.esa.int/docs/galileo/Galileo-factsheet-2016.pdf

Estey LH, Meertens CM (1999) TEQC: the multi-purpose toolkit for GPS/GLONASS data. GPS Solut 3(1):42–49

Euler HJ, Goad CC (1991) On optimal filtering of GPS dual frequency observations without using orbit information. Bull Geodes 65(2):130–143

European Union (2015) European GNSS (Galileo) open service signal in space interface control document, OS SIS ICD, Issue 1.2, Nov 2015

Gaglione S, Angrisano A, Castaldo G, Freda P, Gioia C, Innac A, Troisi S, Del Core G (2015) The first Galileo FOC satellites: from useless to essential. In: 2015 IEEE international on geoscience and remote sensing symposium (IGARSS), IEEE, pp 3667–3670. doi:10.1109/IGARSS.2015.732661814

Genrich JF, Bock Y (1992) Rapid resolution of crustal motion at short ranges with the global positioning system. J Geophys Res 97:3261–3269

Gioia C, Borio D, Angrisano A, Gaglione S, Fortuny-Guasch J (2015) A Galileo IOV assessment: measurement and position domain. GPS Solut 19:187–199

GSA (2017) Galileo programme. https://www.gsc-europa.eu/galileo-gsc-overview/programme

Guo F, Li X, Zhang X, Wang J (2017) Assessment of precise orbit and clock products for Galileo, BeiDou, and QZSS from IGS multi-GNSS experiment (MGEX). Surv Rev 21:279–290

Hauschild A, Montenbruck O, Sleewaegen JM, Huisman L, Teunissen PJ (2012) Characterization of compass M-1 signals. GPS Solut 16(1):117–126

Hellemans A (2014) A simple plumbing problem sent Galileo satellites into wrong orbits. http://spectrum.ieee.org/tech-talk/aerospace/satellites/a-simple-plumbing-problem-sent-galileo-satellites-into-wrong-orbits

Hofmann-Wellenhof B, Lichtenegger H, Wasle E (2008) GNSS-global navigation satellite systems, GPS, GLONASS, Galileo and more. Springer, Berlin

Langley R (2014) ESA discusses Galileo satellite power loss, upcoming launch. http://gpsworld.com/esa-discusses-galileo-satellite-power-loss-upcoming-launch/. Published 20 Aug 2014

Langley RB, Banville S, Steigenberger P (2012) First results: precise positioning with Galileo prototype satellites. GPS World 23:45–49

Li X, Ge M, Dai X, Ren X, Fritsche M, Wickert J, Schuh H (2015) Accuracy and reliability of multi-GNSS real-time precise positioning: GPS, GLONASS, BeiDou, and Galileo. J Geod 89:607–635

Liu T, Yuan Y, Zhang B, Wang N, Tan B, Chen Y (2017) Multi-GNSS precise point positioning (MGPPP) using raw observations. J Geod 91(3):253–268

Lou Y, Zheng F, Gu S, Wang C, Guo H, Feng Y (2016) Multi-GNSS precise point positioning with raw single-frequency and dual-frequency measurement models. GPS Solut 20:849–862

Mader G (2002) GPS antenna calibration at the national geodetic survey. National Geodetic Survey, NOS, NOAA, Silver Spring, MD

Nadarajah N, Teunissen PJG (2014) Instantaneous GPS/Galileo/QZSS/SBAS attitude determination: a single-frequency (L1/E1) robustness analysis under constrained environments. Navigation 61(1):65–75

Nadarajah N, Teunissen PJG, Raziq N (2013) Instantaneous GPS–Galileo attitude determination: single-frequency performance in satellite-deprived environments. IEEE Trans Veh Technol 62(7):2963–2976

Nadarajah N, Khodabandeh A, Teunissen PJG (2015) Assessing the IRNSS L5-signal in combination with GPS, Galileo, and QZSS L5/E5a-signals for positioning and navigation. GPS Solut 20(2):289–297

Odijk D, Teunissen PJG, Huisman L (2012) First results of mixed GPS + GIOVE single-frequency RTK in Australia. J Spat Sci 57(1):3–18

Odijk D, Teunissen PJG, Khodabandeh A (2014) Galileo IOV RTK positioning: standalone and combined with GPS. Surv Rev 46:267–277

Odolinski R, Odijk D, Teunissen PJG (2015) Combined BDS, Galileo, QZSS and GPS single-frequency RTK. GPS Solut 19:151–163

Pan L, Cai C, Santerre R, Zhang X (2017) Performance evaluation of single-frequency point positioning with GPS, GLONASS, BeiDou and Galileo. Surv Rev. doi:10.1080/00396265.2016.1151628

Simsky A, Sleewaegen JM, Hollreiser M, Crisci M (2006) Performance assessment of galileo ranging signals transmitted by GSTB-V2 satellites. In: Proceedings of ION GNSS 2006, Institute of Navigation, Fort Worth, TX, USA, 26–29 Sept, pp 1547–1559

Simsky A, Mertens D, Sleewaegen JM, Hollreiser M, Crisci M (2008a) Experimental results for the multipath performance of galileo signals transmitted by GIOVE—a satellite. Int J Navig Observ. doi:10.1155/2008/416380

Simsky A, Sleewaegen JM, Wilde WD, Hollreiser M, Crisci M (2008b) Multipath and tracking performance of galileo ranging signals transmitted by GIOVE-B. In: Proceedings of ION GNSS 2008, Institute of Navigation, Savannah, Georgia, USA, 16–19 Sept, pp 1525–1536

Steigenberger P, Montenbruck O (2016) Galileo status: orbits, clocks, and positioning. GPS Solut 21(2):319–331

Steigenberger P, Hugentobler U, Montenbruck O (2013) First demonstration of Galileo-only positioning. GPS World 24:14–15

Tegedor J, Øvstedal O, Vigen E (2014) Precise orbit determination and point positioning using GPS, Glonass, Galileo and BeiDou. J Geod Sci 4:65–73

Tegedor J, Øvstedal O, Vigen E (2015) Estimation of Galileo uncalibrated hardware delays for ambiguity-fixed precise point positioning. Navigation 63:173–179

Teunissen PJG (1998) Success probability of integer GPS ambiguity rounding and bootstrapping. J Geod 72(10):606–612

Teunissen PJG (1999) An optimality property of the integer least-squares estimator. J Geod 73(11):587–593

Teunissen PJG, Amiri-Simkooei AR (2008) Least-squares variance component estimation. J Geod 82(2):65–82

Teunissen PJG, Montenbruck O (eds) (2017) Springer handbook of global navigation satellite systems. Springer, Berlin

Tranquilla JM, Cam JP, Al-Rizzo HM (1994) Analysis of a choke ring groundplane for multipath control in global positioning system (GPS) applications. IEEE Trans Antennas Propag 42(7):905–911

Verhagen S, Teunissen PJG (2014) Ambiguity resolution performance with GPS and BeiDou for LEO formation flying. Adv Space Res 54(5):830–839

Zaminpardaz S, Teunissen PJG, Nadarajah N (2016) GLONASS CDMA L3 ambiguity resolution and positioning. GPS Solut 21(2):535–549

Safoora Zaminpardaz received her M.Sc. in Geodesy from University of Tehran. She has been pursuing her Ph.D. since July 2014 at the GNSS Research Centre, Curtin University, Australia. Her research interests include array-based multi-GNSS positioning, ionosphere sensing and integrity monitoring.

Peter J. G. Teunissen is professor of Geodesy and Navigation and Head of CUT's GNSS Research Centre. His current research focuses on multi-GNSS and the modeling of next-generation GNSS for high-precision positioning, navigation and timing applications.

12 Array-based ionospheric gradient monitoring

This chapter is covered by the following publication:

Zaminpardaz S., Teunissen P.J.G., Nadarajah N., Khodabandeh A. (2015) GNSS Array-Based Ionospheric Spatial Gradient Monitoring: Precision and Integrity Analysis. ION Pacific PNT 2015, pp. 799-814. The Institute of Navigation, Honolulu, Hawaii

GNSS Array-Based Ionospheric Spatial Gradient Monitoring: Precision and Integrity Analysis

S. Zaminpardaz[1], P.J.G. Teunissen[1,2], N. Nadarajah[1] and A. Khodabandeh[1]
[1]*GNSS Research Centre, Curtin University of Technology, Perth, Australia*
[2]*Geoscience and Remote Sensing, Delft University of Technology, The Netherlands*

Biography

Safoora Zaminpardaz is a PhD student at Curtin's GNSS Research Centre. Her research interests comprise array-based multi-GNSS, ionosphere sensing and precise point positioning. Peter J.G. Teunissen is Professor of Geodesy and Navigation, and Head of Curtin's GNSS Research Centre. Nandakumaran Nadarajah and Amir Khodabandeh are, respectively, a postdoc research fellow and a PhD student at the GNSS Research Centre of Curtin University. Their research focus is on modeling next-generation GNSSs for precise positioning, navigation and attitude determination.

Abstract

Integrity monitoring and reliable detection of the ionospheric spatial gradient is of importance for various fields including total electron content modeling, radio communication and radar, and differential GNSS applications such as landing, departure and surface operations at an airport. In this contribution, we investigate the precision and the integrity of the ionospheric spatial gradient estimation upon the double-differenced (DD) array-based GNSS model of observations. Closed-form expressions for the variance matrix of the ionospheric spatial gradient and the corresponding uniformly most powerful invariant (UMPI) minimal detectable biases (MDBs) are provided for different scenarios, through which we assess the importance of several contributing factors. The closed-form expressions will show that the precision of the ionospheric spatial gradient estimator and its detectability are independent of our choice for the reference receiver and the reference satellite when forming the DD equations.

In this contribution it will be shown how the precision of the estimated ionospheric spatial gradient and its MDB depend on and benefit from the number of receivers, number of satellites, number of frequencies, and the size and geometry of the array.

1 Introduction

Acting as a dispersive environment, the ionosphere affects the GNSS measurements through introducing a delay in the code signals and an advance in the carrier-phase signals, see e.g. [1, 2]. Since the ionosphere varies in both space and time, the affected GNSS signals would therefore also experience spatial and temporal variations. Large values for the ionospheric spatial gradient are expected when an ionospheric front occurs. The possible undesirable impact of the ionospheric spatial gradients needs therefore to be properly taken into account. Indeed, integrity monitoring and reliable detection of the ionospheric spatial gradient have recently been given growing attention in various disciplines such as estimating and modeling total electron content [3–5], radio communication and radar [6], and differential GNSS applications such as landing, departure and surface operations at an airport [7–10]. In case of the aviation applications for instance, a single Ground Facility (GF), comprising multiple spatially-separated GNSS receivers, is meant to ensure safe flight operations through monitoring signal-in-space failures, e.g. ionospheric spatial gradient that are potentially hazardous for the user (aircraft) positioning.

In this contribution, we study the precision and integrity of the ionospheric spatial gradient estimation using an array of GNSS antennas. Our study characterizes the role of contributing factors including number of antennas, number of frequencies, range of frequencies, configuration of the GF antennas, number of satellites, and satellites elevation. Of many detailed studies regarding the ionospheric spatial gradient monitoring techniques, there are quite recent contributions that are also dedicated to the array-based estimation/detection of the ionospheric spatial gradient, see e.g. [7, 11–14]. Our study differs from those contributions in the following four aspects:

1) While multiple baselines are utilized, our approach to the precision and reliability analysis of the ionospheric

spatial gradient remains invariant for the choice of reference antenna, thereby being independent of how receiver pairs are selected to form the baselines, see e.g. [12, 14].

2) Although GBAS is currently operational on a single frequency $L1$, it is going to be modernized to multiple frequencies [15, 16]. Therefore, our analysis is not restricted to the single-frequency GBAS scenario, providing an opportunity to characterize the impact of the number/structure of frequencies on the detection of the ionospheric spatial gradient.

3) In the previous studies, attention is focused on the estimation/detection of the ionospheric spatial gradient based on the observations of a single satellite pair [12–14]. In this study, we relax this assumption by considering the contribution of multiple satellites to the detection of ionospheric spatial gradient. The gradient detection of a single satellite pair would then follow as a special case.

4) We assess how including the observations of more than one epoch contributes to the detection procedure of the ionospheric spatial gradient, for both *ambiguity-float* case and *ambiguity-fixed* case. The impact of the aforementioned contributing factors on integer ambiguity resolution success rate will be investigated as well.

In the present contribution, the precision of the array-based ionospheric spatial gradient estimator will be studied through the analytical structure of its variance matrix, whereas its integrity will be studied by means of its minimal detectable bias (MDB) [17, 18]. The MDBs in this contribution are associated with the uniformly most powerful invariant (UMPI) test [19, 20]. Closed-form expressions of the stated variance matrix and MDBs will be presented as functions of the contributing factors, e.g. number of antennas and number of frequencies. This gives further insights into the role of these contributing factors and allows one to conduct an a-priory analysis before an actual measurement campaign is launched. Our analytical formulation will be accompanied by numerical results.

2 Ionospheric spatial gradient monitoring

2.1 Array-based GNSS model of observations

We assume that the GNSS signals transmitted by m satellites on f frequencies, are tracked by n receivers. If the relative receivers positions and tropospheric delays are known, the multivariate double-differenced (DD) GNSS observation equations can be written in the compact form,

$$E\begin{bmatrix} \underline{p}_R^S \\ \underline{\phi}_R^S \end{bmatrix} = \begin{bmatrix} I_{m-1}\otimes\mu\otimes I_{n-1} & 0 \\ -I_{m-1}\otimes\mu\otimes I_{n-1} & I_{m-1}\otimes\Lambda\otimes I_{n-1} \end{bmatrix}\begin{bmatrix} \iota_R^S \\ z_R^S \end{bmatrix} \quad (1)$$

where $E[.]$ is the expectation operator, and $\otimes$ denotes the Kronecker product [21]. Considering p and q as, respectively, the pivot receiver and the pivot satellite, the DD 'observed-minus-computed' code observations associated with n receivers, satellite s and satellite q on frequency j are stacked in the $(n-1)$-vector $p_{R,j}^{qs} = [p_{p1,j}^{qs}, \ldots, p_{pn,j}^{qs}]^T$. The $f(n-1)$-vector $p_R^{qs} = [p_{R,1}^{qs^T}, \ldots, p_{R,f}^{qs^T}]^T$ then contains all the DD code observations associated with satellites s and q. The $f(n-1)(m-1)$-vector of the DD code observations is structured as $p_R^S = [p_R^{q1^T}, \ldots, p_R^{qm^T}]^T$. The $f(n-1)(m-1)$-vector of phase observations is obtained likewise. The $f(n-1)(m-1)$-vector of integer-valued DD ambiguities z_R^S, in cycles, has the same order as $\underline{p}_R^S/\underline{\phi}_R^S$. ι_R^S is the $(n-1)(m-1)$-vector of the DD first-order ionospheric delays on the first frequency. I_f is the identity matrix of size f. $\Lambda = \mathrm{diag}(\lambda_1, \ldots, \lambda_f)$ with λ_j the wavelength of frequency f_j. The f-vector μ includes the frequency-dependent ratios $\mu_j = \lambda_j^2/\lambda_1^2$.

The stochastic model is assumed given as

$$D\begin{bmatrix} \underline{p}_R^S \\ \underline{\phi}_R^S \end{bmatrix} = \begin{bmatrix} \sigma_p^2 & 0 \\ 0 & \sigma_\phi^2 \end{bmatrix} \otimes D_m^T W^{-1} D_m \otimes I_f \otimes D_n^T D_n \quad (2)$$

where $D[.]$ is the dispersion operator. The $(m-1)\times m$ matrix D_m^T and $(n-1)\times n$ matrix D_n^T are the differencing operators. σ_p and σ_ϕ are, respectively, the zenith-referenced standard deviation of the undifferenced code and phase observables. $W = \mathrm{diag}(w^1, \ldots, w^m)$ contains the satellite-elevation-dependent weights w^s. In this paper, we use the following form [22]

$$w^s = [1 + 10\exp(-\frac{\varepsilon^s}{10^\circ})]^{-2} \quad (3)$$

with ε^s being the elevation of satellite s in degrees. If $\varepsilon^s = 90^\circ$, then w^s is in agreement with 1 up to 2 digits after the decimal point.

Our aim, in this study, is to detect the ionospheric spatial gradient using an array of GNSS antennas. When we speak of an array of antennas, it means that the antennas are located within few kilometers of each other. For such a small-size array, one can make some assumptions leading to a more simplified model of observations to work with. One of the possible suppositions is that signals from a particular GNSS satellite to all the antennas existing in the array experience almost the same ionospheric delays under nominal ionosphere condition (no ionospheric front or storm), leading to the ionospheric delays becoming independent of the receiver location. Under these circumstances, the DD ionospheric delays are zero. Hence, with $\iota_R^S = 0$, our working hypothesis H_o follows then from Eq. (1) as

$$E\begin{bmatrix} \underline{p}_R^S \\ \underline{\phi}_R^S \end{bmatrix}_{H_o} = \begin{bmatrix} 0 \\ I_{m-1}\otimes\Lambda\otimes I_{n-1} \end{bmatrix} z_R^S \quad (4)$$

In the single-epoch case, the number of observations, number of unknowns and the redundancy of the model of observations under H_o are, respectively, $2f(m-1)(n-1)$, $f(m-1)(n-1)$ and $f(m-1)(n-1)$.

In case an ionospheric front affects the signals of one or more satellites, the assumption that the ionospheric delays do not depend on the location of the receivers will not be valid anymore for the contaminated satellites. In previous studies, only the GPS system has been considered, and it is asserted that the probability of a large gradient affecting more than one satellite is sufficiently low, see e.g. [14, 23]. However, when other GNSS systems, e.g. GLONASS and Galileo, are involved, the likelihood of having more than one satellite influenced by the ionospheric front, would increase. Here, in line with previous studies, we consider the case that only one satellite, say c, is contaminated by the ionospheric front.

Many studies have considered that the impact of ionospheric fronts on the GNSS signals changes almost linearly with the distance between two points [8, 24]. Therefore, the ionospheric delay experienced by a signal from satellite c to antenna r in the array can be approximated by its first-order Taylor expansion around an arbitrary point (located within few kilometers with respect to the array) as

$$\imath_r^c \approx \imath_0^c + g^T b_r \tag{5}$$

with b_r being the baseline vector of receiver r with respect to the mentioned arbitrary point, and $\imath_0^c$ being the ionospheric delay on the signal between satellite c and the mentioned arbitrary point. g is the 3-vector of the first-order partial derivative of the ionospheric delay with respect to the receiver position, which is referred to as the *ionospheric spatial gradient*. As mentioned before, ionospheric delays have both spatial and temporal variations. In Eq. (5), the temporal variation has not been modeled. Figure 1 shows the impact of the ionospheric front on the signals of one of the GNSS satellites as function of the between-antennas baseline vector.

In order to see how the ionospheric spatial gradient affects the DD GNSS observables, we start with the undifferenced level. The ionospheric delays on the first frequency associated with n receivers and satellite s are stacked in the n-vector $\tilde{\imath}_R^s = [\tilde{\imath}_1^s, \ldots, \tilde{\imath}_n^s]^T$. The nm-vector of the undifferenced ionospheric delays is structured as $\tilde{\imath}_R^S = [\tilde{\imath}_R^{1^T}, \ldots, \tilde{\imath}_R^{c^T}, \ldots, \tilde{\imath}_R^{m^T}]^T$. Applying the DD operator $D_m^T \otimes D_n^T$ on to the both sides of the last equation, those ionospheric delays associated with the uncontaminated satellites will disappear. Therefore we have

$$\imath_R^S = (D_m^T u_m^c \otimes D_n^T)\tilde{\imath}_R^c \tag{6}$$

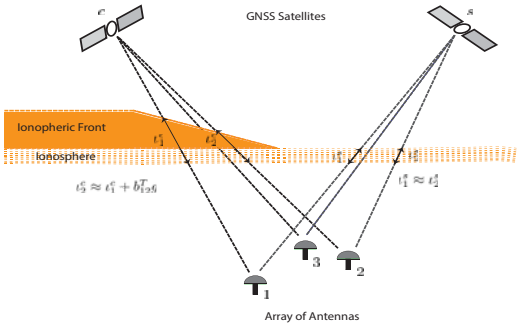

Figure 1. An ionospheric front affects the signals from satellite c to the array of antennas. The ionospheric delays experienced by the signals from satellite s can be considered the same. The ionospheric delays experienced by the signals from satellite c are related to each other through the ionospheric spatial gradient g and the baseline vector between them b_{12}.

in which the m-vector u_m^c is a canonical unit vector with 1 as its c^{th} element and zeros elsewhere. $\tilde{\imath}_R^c$ can be parametrized using Eq. (5) as

$$\tilde{\imath}_R^c = e_n \imath_0^c + B g \tag{7}$$

where the $n \times 3$ matrix B includes the vectors b_r^T ($r = 1, \ldots, n$) as its rows, and e_n is the n-vector of ones. Combining Eqs. (6) and (7), we get

$$\imath_R^S = (D_m^T u_m^c \otimes D_n^T B) g \tag{8}$$

Since $D_n^T e_n = 0$, $\imath_0^c$ is eliminated in Eq. (8). Substituting Eqs. (8) into (1), we obtain the alternative model H_a as

$$E\left[\begin{array}{c} \underline{p}_R^S \\ \underline{\phi}_R^S \end{array}\right]_{H_a} = \left[\begin{array}{cc} D_m^T u_m^c \otimes \mu \otimes D_n^T B & 0 \\ -D_m^T u_m^c \otimes \mu \otimes D_n^T B & I_{m-1} \otimes \Lambda \otimes I_{n-1} \end{array}\right] \left[\begin{array}{c} g \\ z_R^S \end{array}\right] \tag{9}$$

If matrix B satisfies $D_n^T B = 0$, it means that all the antennas are in the same place. The ionospheric spatial gradient will then not be estimable. As a result, the DD observation equations will only contain the DD ambiguities as the unknown parameters, which is desirable for the estimation of the DD ambiguities since only the highly precise phase observables contribute to their estimation and precision. The number of observations, number of unknowns and the redundancy of the model of observations under H_a are, respectively, $2f(m-1)(n-1)$, $f(m-1)(n-1)+l$ and $f(m-1)(n-1)-l$, with l being the dimension of the array (the number of estimable components of the ionospheric spatial gradient).

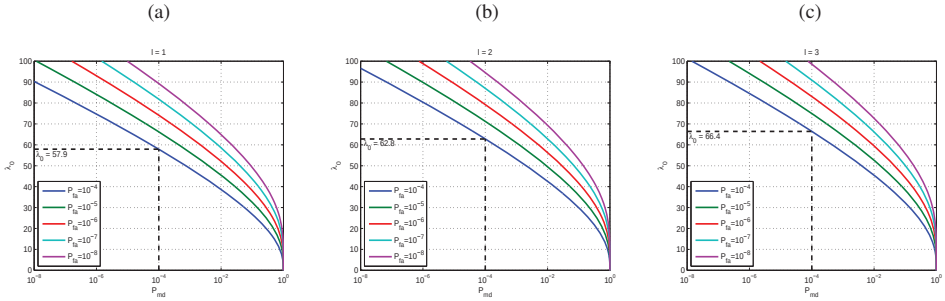

Figure 2. Chi-square non-centrality parameter λ_0 versus probability of missed detection P_{md} for different values of probability of false alarm P_{fa} when the degrees of freedom is (a) $l = 1$; (b) $l = 2$; (c) $l = 3$.

2.2 *Testing procedure*

To detect the ionospheric spatial gradient, we employ the UMPI test [20], as it results in the highest probability of the detection for a class of critical regions. The UMPI test statistic formed to detect and identify the ionospheric bias g reads [20, 25]

$$\underline{T}_l = \underline{\hat{g}}^T Q_{\hat{g}\hat{g}}^{-1} \underline{\hat{g}} \tag{10}$$

where $\underline{\hat{g}}$ and $Q_{\hat{g}\hat{g}}$ are, respectively, the best linear unbiased estimator (BLUE) of g and its corresponding variance matrix, computed under H_a (that is Eq. (9)). The subscript l shows the number of (functions of) estimable components of vector g. If the GNSS phase and code observables are normally distributed, $\underline{\hat{g}}$ as a linear function of them is also normally distributed, i.e. $\underline{\hat{g}} \sim N(g, Q_{\hat{g}\hat{g}})$. The distribution of $\underline{T}_l$ under H_o is then the central Chi-square with l degrees of freedom, i.e. $\underline{T}_l \sim \chi^2(l,0)$, and under H_a the Chi-square with l degrees of freedom and the non-centrality parameter λ, i.e. $\underline{T}_l \sim \chi^2(l,\lambda)$, where $\lambda = g^T Q_{\hat{g}\hat{g}}^{-1} g$. Given the false alarm rate P_{fa}, if $\underline{T}_l > \chi^2_{P_{fa}}(l,0)$, then H_o is rejected in favor of H_a. Here $\chi^2_{P_{fa}}(l,0)$ is the critical value obtained from the distribution $\chi^2(l,0)$ and chosen false alarm rate P_{fa}. The probability of missed detection can be determined by the use of P_{fa}, λ and l [20]. The reverse procedure can also be followed, which means that based on P_{fa}, P_{md} and l, the non-centrality parameter can be computed as $\lambda_0 = \lambda(P_{fa}, P_{md}, l)$ visualized in Figure 2 [17, 20]. For example, when $P_{fa} = 10^{-4}$ and $P_{md} = 10^{-4}$, the non-centrality parameter would be $\lambda_0 = 57.9$, $\lambda_0 = 62.8$ and $\lambda_0 = 66.4$ for, respectively, $l = 1$, $l = 2$ and $l = 3$.

The boundary of the ellipsoidal MDB region is defined as $\lambda_0 = g^T Q_{\hat{g}\hat{g}}^{-1} g$ [20]. Parametrizing the MDB-vector as $g = ||g||d$, with unit l-vector d, the MDB can be computed as

$$||g|| = \sqrt{\frac{\lambda_0}{d^T Q_{\hat{g}\hat{g}}^{-1} d}} \tag{11}$$

If the unit vector d sweeps the surface of the unit sphere in $\mathbb{R}^l$, the whole MDB region is obtained. The shape and the orientation of the MDB region is governed by $Q_{\hat{g}\hat{g}}$, and its size is determined by λ_0. The MDB region is an interval when $l = 1$, an ellipse when $l = 2$, and an ellipsoid when $l = 3$.

The variance matrix $Q_{\hat{g}\hat{g}}$, and, as a result, the MDB depend on several contributing factors like number of receivers, number of satellites, array configuration etc. Before conducting the actual measurements, one can decide on these contributing factors such that the requirements of the application at hand are satisfied. For instance, civil aviation precision approach needs to detect ionospheric spatial gradient greater than 300 mm/km with the probability of 0.9999 [14, 23, 26].

In the following, we will present analytical expressions for $Q_{\hat{g}\hat{g}}$ and the corresponding MDB. Numerical evidence will also be provided to support closed-form formulas.

3 Ionospheric spatial gradient UMPI MDB

3.1 *Single-epoch ambiguity-float scenario*

To obtain closed-form expressions for $Q_{\hat{g}\hat{g}}$ and the corresponding MDB-vector $||g||d$, we start with the single-epoch ambiguity-float scenario. It can be shown that the variance matrix of the ionospheric spatial gradient estimator and its corresponding MDB, for 3-dimensional, 2-dimensional and 1-dimensional arrays read

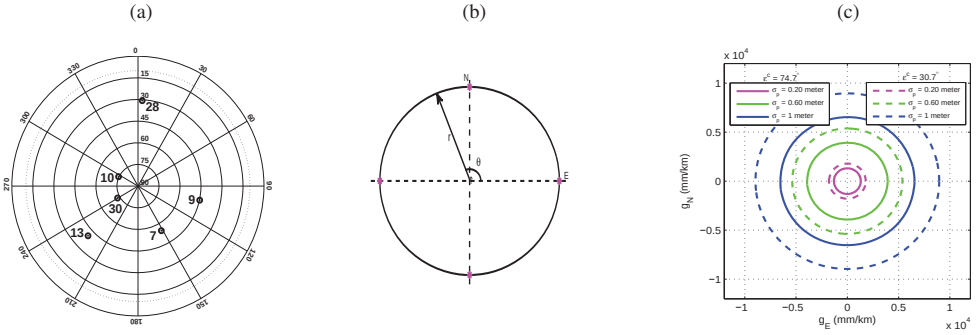

Figure 3. (a) GPS satellites configuration; (b) Positions of the receivers (purple points) in a circular array with the radius of $r = 500$ meter and with the angles $\theta = 0°,\ 90°,\ 180°,\ 270°$; (c) The ellipses showing the corresponding single-epoch ambiguity-float MDBs, with $f = 2$ $(L1 + L2)$, $m = 6$, $n = 4$, $P_{fa} = 10^{-4}$ and $P_{md} = 10^{-4}$ for different values of σ_p. Solid and dashed curves are associated with when, respectively, the highest satellite PRN10 with the elevation $\varepsilon^c = 74.7°$ and the lowest satellite PRN28 with the elevation $\varepsilon^c = 30.7°$ are contaminated by the ionospheric front.

3-dimensional array

$$Q_{\hat{g}\hat{g}} = \frac{\sigma_p^2}{c_f^2 \times c_s^2} \times C_r^{-1} \tag{12}$$

$$||g||d = \frac{\sigma_p}{c_f \times c_s} \sqrt{\frac{\lambda_0}{d^T C_r d}} d,\ \ d \in \mathbb{R}^3 \tag{13}$$

2-dimensional array

$$Q_{\hat{\tilde{g}}\hat{\tilde{g}}} = \frac{\sigma_p^2}{c_f^2 \times c_s^2} \times \tilde{\tilde{C}}_r^{-1} \tag{14}$$

$$||\tilde{\tilde{g}}||d = \frac{\sigma_p}{c_f \times c_s} \sqrt{\frac{\lambda_0}{d^T \tilde{\tilde{C}}_r d}} d,\ \ d \in \mathbb{R}^2 \tag{15}$$

1-dimensional array

$$\sigma_{\tilde{g}}^2 = \frac{\sigma_p^2}{c_f^2 \times c_s^2} \times \tilde{C}_r^{-1} \tag{16}$$

$$|\tilde{g}| = \frac{\sigma_p}{c_f \times c_s} \sqrt{\frac{\lambda_0}{\tilde{C}_r}} \tag{17}$$

where

$$c_f = \sqrt{f(\bar{\mu}^2 + \sigma_\mu^2)}\ ,\ c_s = \sqrt{w^c (1 - \frac{w^c}{m\overline{w}})} \tag{18}$$

$$C_r = (B - e_n b_r^T)^T (B - e_n b_r^T) \tag{19}$$

$$\tilde{\tilde{C}}_r = [u, v]^T C_r [u, v]\ ,\ \tilde{C}_r = [u]^T C_r [u] \tag{20}$$

with $b_r^T = \frac{1}{n} e_n^T B$, $\bar{\mu} = \frac{1}{f} \sum_{j=1}^{f} \mu_j$, $\sigma_\mu^2 = \frac{1}{f} \sum_{j=1}^{f} (\mu_j - \bar{\mu})^2$, $\overline{w} = \frac{1}{m} \sum_{s=1}^{m} w^s$, and u, v forming an orthonormal basis of the array-plane such that u spans the linear array. $||\tilde{\tilde{g}}||$ is the norm of the projection of g onto the array-plane spanned by u, v, and $|\tilde{g}|$ is the absolute value of the projection of g onto the linear-array spanned by u. Be aware that the ionospheric spatial gradient component(s) orthogonal to the array is (are) not estimable.

Eq. (19) shows that both the variance matrix and the corresponding MDBs are invariant for our choice of the reference receiver, and hence how receiver pairs are selected to form the baselines. From Eqs. (12), (14) and (16), we do see that the precision of the ionospheric spatial gradient is dominated by code observables. That is because in single-epoch ambiguity-float scenario, all the DD phase observables are preserved for the DD ambiguities. Therefore, the estimator of the ionospheric spatial gradient, the so-called *float-solution*, does not benefit from the high phase precision.

The main difference between the MDB regions of different types of arrays lies in λ_0 (because of different values for l) and the array configuration. Based on the analytical expressions derived above, we conduct a pre-analysis on the role played by various contributing factors in the MDB region of ionospheric spatial gradient. All the conclusions are valid for all types of arrays. We also present our conclusions visually for a planar array, which can also be illustrated for other types of arrays in a similar way. Only for simplicity, we consider a circle to put antennas over and make use of polar coordinates with respect to its center.

Code-precision-specific contribution: There is a direct relation between the MDB and σ_p, such that an increment in σ_p will result in MDB region growing. Figure 3 depicts the impact of σ_p on the MDB region, for the shown planar array and satellite geometry. The coordinates of antennas with respect to the center of circle have the form of $b_r = [r\cos\theta\ ,\ r\sin\theta]^T$. Since the geometry of the array is symmetric, the MDB region would be of circle shape. The use is made of frequencies $L1$ and $L2$. P_{fa} and P_{md} should be set based on the requirements of the specific application at hand. For civil aviation applications, '*however, a standardized way of determining such a probability has not yet been developed and needs to be investigated*' [23]. Here, we choose $P_{fa} = 10^{-4}$ and $P_{md} = 10^{-4}$, consistent with the previous works [13, 14, 27]. The graphs in this figure have been plotted for two extreme cases, namely the signals from the highest PRN10 and the lowest PRN28 satellites are contaminated by the ionospheric front. The linear dependency between the MDB size and σ_p is visible in this figure.

g_E and g_N in Figure 3 (and all the figures coming after) are, respectively, the projection of g on the East and North direction.

Non-centrality-specific contribution: The MDB is proportional to the square-root of λ_0. From Figure 2, for a given P_{fa}, λ_0 will get higher values for smaller P_{md} and larger p. Larger λ_0 would result in larger MDBs.

Satellite-specific contribution: GNSS satellites effect has three aspects, which are number of satellites m, satellites elevation through the mean elevation-dependent weight $\overline{w}$, and elevation of the contaminated satellite through the elevation-dependent weight w^c. Assuming that $w^1 \approx \ldots \approx w^m \approx \overline{w}$, it can be seen that the number of satellites affects the MDB by approximately $\sqrt{m/(m-1)}$. Since the growth speed of $\sqrt{m/(m-1)}$ is much less than that of m, the rate of change of MDB as function of number of satellites will not be very considerable after adding a particular number of satellites. Figure 4 shows the behavior of MDB for different numbers of satellites, for the planar array and satellite geometry in Figure 3. The MDB region experiences a notable decrease when going from $m = 2$ to $m = 4$. As more other satellites are included, the improvement of MDB decreases.

Satellite elevations manifest themselves through the elevation-weighting $\overline{w}, w^c$, which are reversely related to the satellite elevation. Two questions may be asked here: 1) what is the best constellation to detect ionospheric spatial gradient? 2) given a specific constellation, on which satellite, ionospheric spatial gradient can be detected the best? To answer the first question, we consider the follow-

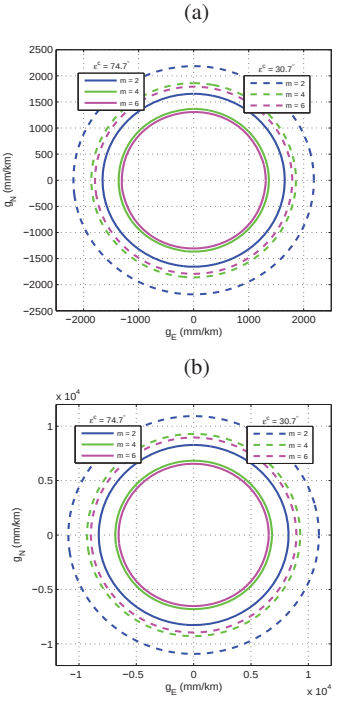

Figure 4. The single-epoch ambiguity-float MDBs corresponding with the planar array and satellite geometry in Figure 3, with $f = 2$ $(L1 + L2)$, $n = 4$, $P_{fa} = 10^{-4}$ and $P_{md} = 10^{-4}$ for different values of m and (a) $\sigma_p = 0.2$ meter; (b) $\sigma_p = 1$ meter. For plotting solid and dashed curves, satellites are, respectively, sorted in a descending and ascending order in terms of their elevations. Then, we start from first 2 satellites and add more other ones. For each ordering, the first satellite is considered to be contaminated by the ionospheric front, for descending order the highest satellite PRN10 with the elevation $\varepsilon^c = 74.7^\circ$ and for ascending order the lowest satellite PRN28 with the elevation $\varepsilon^c = 30.7^\circ$.

ing equivalent expression for c_s

$$c_s = \left(\frac{1}{w^c} + \frac{1}{\sum_{s=1, s\neq c}^{m} w^s}\right)^{-\frac{1}{2}} \tag{21}$$

based on which, one can easily conclude that the maximum value for c_s is obtained when all the visible satellites are in zenith, i.e. $\varepsilon^s = 90^\circ$ $(s = 1, \ldots, m)$. Therefore, the best satellite configuration in terms of ionospheric spatial gradient detectability is the one containing zenith-elevated satellites.

When it comes to the second question, $m\overline{w}$ in c_s formula-

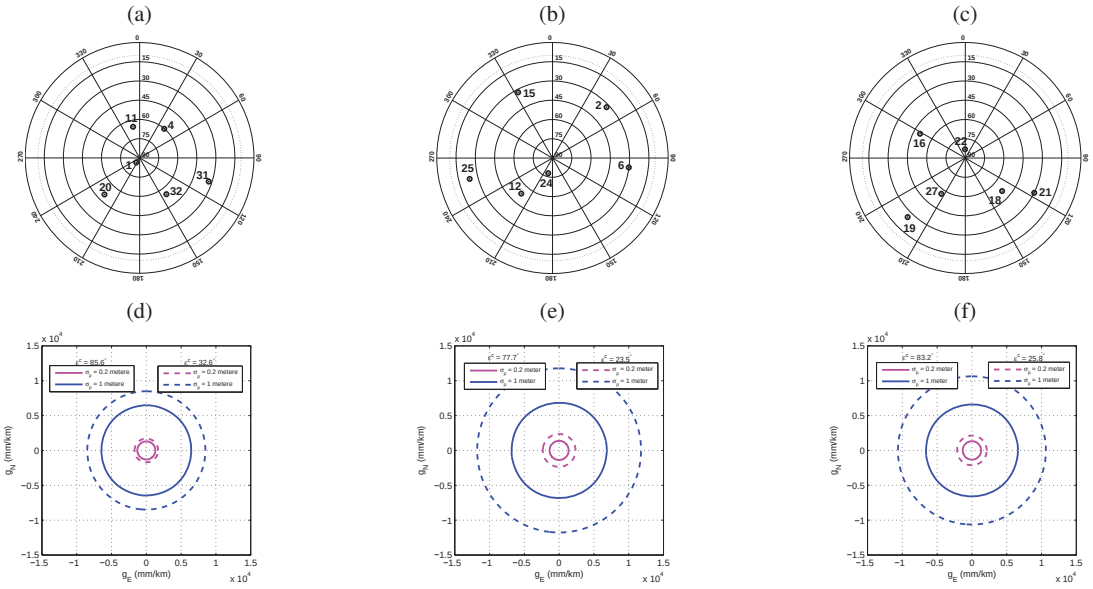

Figure 5. GPS satellites configurations where (a) most of the satellites have almost high elevations; (b) most of the satellites have low elevations; (c) some of the satellites have high elevations and some low elevations. The ellipses showing the single-epoch ambiguity-float MDBs corresponding with the planar array in Figure 3 and (d) satellite configuration in (a); (e) satellite configuration in (b); (f) satellite configuration in (c), with $f = 2$ $(L1+L2)$, $m = 6$, $n = 4$, $P_{fa} = 10^{-4}$ and $P_{md} = 10^{-4}$. Solid and dashed curves are associated with when, respectively, the highest satellites, PRN1 with the elevation $\varepsilon^c = 85.6^\circ$ in (a), PRN24 with the elevation $\varepsilon^c = 77.7^\circ$ in (b), PRN22 with the elevation $\varepsilon^c = 83.2^\circ$ in (c), and the lowest satellites, PRN31 with the elevation $\varepsilon^c = 32.6^\circ$ in (a), PRN25 with the elevation $\varepsilon^c = 23.5^\circ$ in (b), PRN19 with the elevation $\varepsilon^c = 25.8^\circ$ in (c), are contaminated by the ionospheric front.

tion is constant. In that case, the behavior of c_s with respect to changes in w^c is parabolic. It can be shown that c_s reaches its maximum value when $w^c = \sum_{s=1,s\neq c}^{m} w^s$. Therefore, the best detectability of the ionospheric spatial gradient would be realized when the ionospheric front affects, among the satellites in view, that satellite of which the elevation-dependent weight is the closest to $\sum_{s=1,s\neq c}^{m} w^s$. The worst detectability is associated with those satellites of which the elevation-dependent weights are the furthest from $\sum_{s=1,s\neq c}^{m} w^s$.

Figure 5 illustrates 3 GPS satellite configurations when (a) most of the satellites have almost high elevations, (b) most of the satellites have almost low elevations, (c) some of the satellites have high elevations and some low elevations. Table 1 shows the values of $\frac{w^c}{\sum_{s=1,s\neq c}^{m} w^s}$ and c_s for these configurations when the lowest and highest satellites are contaminated. We can see that within each satellite configuration, $\frac{w^c}{\sum_{s=1,s\neq c}^{m} w^s}$ gets its largest value when the highest satellite is corrupted by the ionospheric front. Moreover, the higher the elevations of the satellites in view, the better the ionospheric spatial gradient would be detectable.

Frequency-specific contribution: Three parameters represent the influence of the GNSS signal frequencies on the MDB, which are number of frequencies f, squared mean of the frequencies ratios $\bar{\mu}^2$, and the dispersion of the frequencies ratios σ_μ^2. The more frequencies are used, the MDB region will decrease more. If we go from single-frequency $(L1)$ to dual-frequency $(L1+L2)$ model of observations, then $\bar{\mu}^2$ increases from 1 to almost 1.7, and σ_μ^2 grows from 0 to almost 1. Therefore, the MDB region corresponding with the dual-frequency scenario is nearly 2 times smaller than that corresponding with the single-frequency scenario. It is shown in Figure 6.

Array-specific contribution: The contribution of the array is characterized through the number of receivers n and the array configuration B. As the number of receivers increases, the MDB region gets smaller in all or some particular directions depending on the array geometry. Figure 7 illustrates the MDB regions as function of number of receivers for the satellite geometry in Figure 3. When

Table 1. The values of $\frac{w^c}{\sum_{s=1,s\neq c}^{m} w^s}$ and c_s for the satellite configurations in Figure 5.

	Satellite configuration (a)		Satellite configuration (b)		Satellite configuration (c)	
	PRN1	PRN31	PRN24	PRN25	PRN22	PRN19
$\frac{w^c}{\sum_{s=1,s\neq c}^{m} w^s}$	0.234	0.110	0.375	0.078	0.287	0.078
c_s	0.898	0.685	0.849	0.494	0.879	0.547

the green receiver is added to the existing 4 blue receivers in the North-East direction, the detectability in the same direction improves. The change of MDB region due to including other receivers can be interpreted likewise.

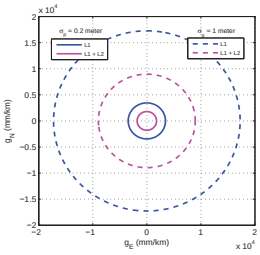

Figure 6. The ellipses showing the single-epoch ambiguity-float MDBs corresponding with the planar array and satellite geometry in Figure 3, with $m = 6$, $n = 4$, $P_{fa} = 10^{-4}$ and $P_{md} = 10^{-4}$ for different number of frequencies. Solid and dashed curves are, respectively, associated with $\sigma_p = 0.2$ meter and $\sigma_p = 1$ meter. The lowest satellite PRN28 with the elevation $\varepsilon^c = 30.7°$ has been considered to be contaminated by the ionospheric front.

If the length of the array increases, then the term C_r^{-1} decreases, so does the MDB region. In Figure 8, the MDB region has been plotted for different lengths of array for the array configuration and satellite geometry in Figure 3. An equivalent form for C_r^{-1} can be obtained as

$$C_r^{-1} = (B^T B)^{-1} + \frac{(B^T B)^{-1} B^T e_n e_n^T B (B^T B)^{-1}}{n - e_n^T P_B e_n} \qquad (22)$$

with $P_B = B(B^T B)^{-1} B^T$. The smaller $e_n^T B$ (the projection of matrix B onto the vector e_n), the smaller C_r^{-1}. If $e_n^T B = 0$, then the second term in Eq. (22) will disappear. A symmetric array geometry satisfies $e_n^T B = 0$, hence being desirable in terms of the MDB region size. The vector e_n is the orthogonal complement of the space formed by the columns of differencing matrix D_n, i.e. $D_n^T e_n = 0$.

(a)

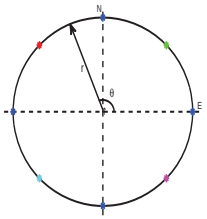

(b)

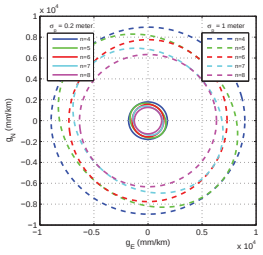

Figure 7. (a) Positions of the receivers (colored points) in a circular array with the radius of $r = 500$ meter and with the angles $\theta = 0°$, $45°$, $90°$, $135°$, $180°$, $225°$, $270°$, $315°$; (b) The ellipses showing the single-epoch ambiguity-float MDBs corresponding with the satellite geometry in Figure 3 and for 4 blue receivers (*blue*), 5 blue+green receivers (*green*), 6 blue+green+red receivers (*red*), 7 blue+green+red+cyan receivers (*cyan*), and 8 blue+green+red+cyan+purple receivers (*purple*), with $f = 2$ $(L1 + L2)$, $m = 6$, $P_{fa} = 10^{-4}$ and $P_{md} = 10^{-4}$. Solid and dashed curves are, respectively, associated with $\sigma_p = 0.2$ meter and $\sigma_p = 1$ meter. The lowest satellite PRN28 with the elevation $\varepsilon^c = 30.7°$ has been considered to be contaminated by the ionospheric front.

Therefore, the smaller $D_n^T B$ (the projection of matrix B

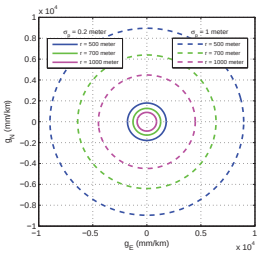

Figure 8. The ellipses showing the single-epoch ambiguity-float MDBs corresponding with the planar array and the satellite geometry in Figure 3, with $f = 2$ $(L1 + L2)$, $m = 6$, $n = 4$, $P_{fa} = 10^{-4}$ and $P_{md} = 10^{-4}$ for various lengths of the array. Solid and dashed curves are, respectively, associated with $\sigma_p = 0.2$ meter and $\sigma_p = 1$ meter. The lowest satellite PRN28 with the elevation $\varepsilon^c = 30.7°$ has been considered to be contaminated by the ionospheric front.

onto the range space of D_n), the larger $e_n^T B$, and the larger C_r^{-1}. The term $D_n^T B$ gets its small values when the baseline vectors b_r $(r = 1, \ldots, n)$ are close to each other. In Figure 9, the MDB regions for different geometries of 4 antennas, and the satellite configuration in Figure 3 are illustrated. In Figure 9 (b), the shape of antennas is almost aligned with the East direction, which is why the corresponding ionospheric spatial gradient MDB ellipse has its minor axis parallel to the East direction. In fact, this shape of array enables the user to find smaller gradients in East direction. The MDB area associated with Figure 9 (c) can be interpreted analogously.

From Figures 3 to 9, it can be seen that achieving small MDBs for the ionospheric spatial gradient with test in Eq. (10) with $P_{fa} = 10^{-4}$ and $P_{md} = 10^{-4}$ based on the single-epoch code observables (ambiguity-float scenario) would require a large number of receivers or long distances between antennas. The above MDBs might be desirable for some special applications, but not for civil aviation precision approach. For such an application, due to the airport geometry and the high price of the receivers, increasing the number of receivers or the length of the array may not always be possible. So, does it mean it is impossible to detect ionospheric spatial gradient at the level of 300 mm/km upon the single-epoch observations? We answer this question in the following.

3.2 Single-epoch ambiguity-fixed scenario

Once the DD ambiguities are fixed, the phase observables would also contribute to the estimation of the ionospheric spatial gradient, hence improving its precision and reducing the MDB region size. The variance matrix of the ionospheric spatial gradient estimator after fixing the DD ambiguities, the so-called *fixed solution*, and the corresponding MDB can be shown to have the following form for the 3-dimensional array

$$Q_{\check{g}\check{g}} = \frac{\varepsilon}{1+\varepsilon} Q_{\hat{g}\hat{g}} \tag{23}$$

$$||g||d = \sqrt{\frac{\varepsilon}{1+\varepsilon}} [\frac{\sigma_p}{c_f \times c_s} \sqrt{\frac{\lambda_0}{d^T C_r d}} d], \; d \in \mathbb{R}^3 \tag{24}$$

where $\varepsilon = \sigma_\phi^2 / \sigma_p^2 \approx 10^{-4}$. For other types of array, the same relationship between float and fixed parameters holds true. Comparing Eqs. (23)/(24) and (12)/(13), if one can fix the DD ambiguities successfully at a single epoch, then the precision of ionospheric spatial gradient estimator improves by 10^4, and the size of the corresponding MDB region reduces by 10^2. Therefore, it is important to know how it would be possible to fix the DD ambiguities with an acceptable success rate at only one epoch. The success rate of the integer DD ambiguity resolution depends on their variance matrix. It can be shown that the variance matrix of the DD ambiguities for single-epoch scenario based on Eqs. (9) (fault-affected model H_a) and (2) reads

$$\begin{aligned} Q_{\hat{z}_R^S \hat{z}_R^S} \;=\; & \underbrace{\sigma_\phi^2 D_m^T W^{-1} D_m \otimes \Lambda^{-2} \otimes D_n^T D_n}_{C_\phi} \\ & + \underbrace{D_m^T u_m^c u_m^{c\,T} D_m \otimes \Lambda^{-1} \mu \mu^T \Lambda^{-1} \otimes D_n^T B Q_{\hat{g}\hat{g}} B^T D_n}_{C_p} \end{aligned} \tag{25}$$

This variance matrix of order $f(m-1)(n-1)$ has two terms. The first term C_ϕ is dominated by high phase precision, while the second one C_p is dominated by poor code precision. C_p is due to the presence of the ionospheric spatial gradient in model H_a. In other words, based on the model of observations in Eq. (4) (fault-free model H_o), C_p would disappear. In that case, the precision of the DD ambiguities would be at the level of the DD phase precision.

Based on Eq. (25), we can analyze the efficacy of various factors on the precision of the DD ambiguities estimators and the consequent integer ambiguity resolution success rate. But, since the only purpose of fixing the ambiguities is to improve the precision of the ionospheric spatial gradient, it is important to know how setting these factors in favor of the ambiguity resolution, affects the variance matrix of the fixed ionospheric spatial gradient estimator $Q_{\check{g}\check{g}}$.

Looking at Eqs. (23) and (25), $Q_{\hat{z}_R^S \hat{z}_R^S}$ and $Q_{\check{g}\check{g}}$ are both dependent on $Q_{\hat{g}\hat{g}}$. The variance matrix of the fixed solution $Q_{\check{g}\check{g}}$ is a ratio of that of the float solution $Q_{\hat{g}\hat{g}}$, and

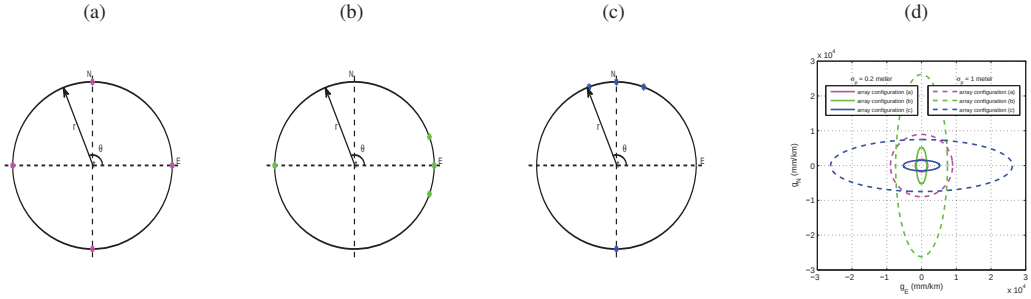

Figure 9. Positions of the receivers (colored points) in a circular array with the radius of $r = 500$ meter and with the angles (a) $\theta = 0°, 90°, 180°, 270°$; (b) $\theta = 0°, 20°, 180°, 340°$; (c) $\theta = 70°, 90°, 110°, 270°$; (d) The ellipses showing the single-epoch ambiguity-float MDBs corresponding with the planar arrays in (a), (b) and (c) and the satellite geometry in Figure 3, with $f = 2$ $(L1+L2)$, $m = 6$, $n = 4$, $P_{fa} = 10^{-4}$ and $P_{md} = 10^{-4}$. Solid and dashed curves are, respectively, associated with $\sigma_p = 0.2$ meter and $\sigma_p = 1$ meter. The lowest satellite PRN28 with the elevation $\epsilon^c = 30.7°$ has been considered to be contaminated by the ionospheric front.

therefore all the influencing factors mentioned in Subsection 3.1 have the same impact on both of them. $Q_{\hat{z}^S_R \hat{z}^S_R}$ like $Q_{\hat{g}\hat{g}}$ will also benefit from increasing the number of frequencies, and number of satellites. If the ionospheric front contaminates those satellites of which the elevation-dependent weights are near to $\sum_{s=1,s\neq c}^{m} w^s$, then $Q_{\hat{g}\hat{g}}$ and, consequently, $Q_{\hat{z}^S_R \hat{z}^S_R}$ would improve.

If in Eq. (25) we expand $Q_{\hat{g}\hat{g}}$, we will see that the array configuration (B and n) affects $Q_{\hat{z}^S_R \hat{z}^S_R}$ through the term $D_n^T B C_r^{-1} B^T D_n$, which can be extended as

$$D_n^T B C_r^{-1} B^T D_n = D_n^T P_B D_n + \frac{(D_n^T P_B e_n)(D_n^T P_B e_n)^T}{n - e_n^T P_B e_n} \quad (26)$$

Comparing Eqs. (22) and (26), the first observation is that in contrast to $Q_{\check{g}\check{g}}$, $Q_{\check{z}^S_R \check{z}^S_R}$ is independent of the total length of the array. It means that if the receivers positions in the array are all scaled by the same factor, it would have no result on the precision of the DD ambiguities. The second observation is that if $e_n^T B = 0$, the second term in Eq. (26) will disappear. If the design of the array is such that $D_n^T B \to 0$ (b_r's are close to each other), Eq. (26) will get very small values, but the second term in Eq. (22), as was previously described, will get its large values. However, because of the very small value of $\varepsilon = 10^{-4}$ in the formulation of $Q_{\check{g}\check{g}}$, designing the array geometry to the benefit of ambiguity resolution ($D_n^T B \to 0$), should not be an obstacle to achieve the desirable values for the precision of $\underline{\check{g}}$ and the size of the corresponding MDB.

Table 2 lists the integer least-squares (ILS) [28, 29] success rate, for the satellite configurations in Figure 5 and the illustrated array configurations, for different number of frequencies and different elevations of the contaminated satellite when $\sigma_p = 0.2$ meter. It can be seen when the GNSS observations are made on 2 frequencies ($L1+L2$), the DD ambiguities can be fixed by 100% regardless of array and satellite configuration, if the elevation of the contaminated satellite is sufficiently high. When the elevation of the contaminated satellite is low, then both array and satellite configurations become important. If the GNSS observations are available on only 1 frequency ($L1$), it is impossible to fix the ambiguities successfully at a single epoch.

Figure (10) (a) and (b) shows MDB regions corresponding to array configurations (2) and (1) in Table 2, respectively, for dual-frequency ambiguity-float scenario. MDB region associated with the array configuration (1) is indeed better than the one corresponding to the array configuration (2), since it is symmetric and its maximum boundary is 10 times smaller. Based on the results in Table 2, it is possible to fix the DD ambiguities associated with the array configuration (2) and satellite configuration (a) at one epoch. Figure (10) (c) illustrates the fixed MDB region. Although it is not symmetric, its maximum boundary is 10 times smaller than that of the float MDB region associated with the array configuration (1). This figure tells us , for some special satellite geometries, it is possible to detect the ionospheric spatial gradient even smaller than 300 mm/km at one single epoch when the shape of the array is to the benefit of the successful ambiguity resolution and the GNSS observables are available on 2 frequencies. For other satellite geometries that the high success rates are not achievable at one epoch, only a few number of epochs are needed to reach a desirable success rate.

Table 2. DD ambiguity resolution ILS success rate $Ps\ (\%)$ as function of the satellite configurations in Figure 5 and the array configurations shown, number of frequencies f, and the elevation of the contaminated satellite ε^c for $\sigma_p = 0.2$ meter.

	Array configuration	ε^c		Satellite configuration (a)		Satellite configuration (b)		Satellite configuration (c)	
				$f=1$	$f=2$	$f=1$	$f=2$	$f=1$	$f=2$
	$r = 500$ meter	Highest	$Ps\ (\%)$	10.921	**100**	9.962	99.999	10.737	**100**
	$\theta = 0°,\ 90°,\ 180°,\ 270°$								
(1)	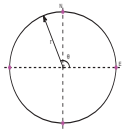	Lowest	$Ps\ (\%)$	6.511	99.926	3.383	97.427	4.289	98.964
	$r = 500$ meter	Highest	$Ps\ (\%)$	65.660	**100**	61.135	**100**	64.325	**100**
	$\theta = 0°,\ 10°,\ 20°,\ 70°$								
(2)	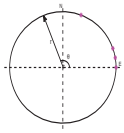	Lowest	$Ps\ (\%)$	44.210	**100**	22.724	99.907	28.058	99.978

Table 3. DD ambiguity resolution ILS success rate $Ps\ (\%)$ as function of the satellite configurations in Figure 5 and the array configurations shown, and the elevation of the contaminated satellite ε^c for $f = 2\ (L1 + L2)$ and $\sigma_p = 1$ meter.

	Array configuration	ε^c		Satellite configuration (a)	Satellite configuration (b)	Satellite configuration (c)
	$r = 500$ meter	Highest	Ps (%)	20.014	16.903	18.836
	$\theta = 0°,\ 90°,\ 180°,\ 270°$					
(1)	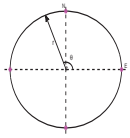	Lowest	Ps (%)	8.689	2.619	3.870
	$r = 500$ meter	Highest	Ps (%)	50.578	44.726	48.171
	$\theta = 0°,\ 10°,\ 20°,\ 70°$					
(2)	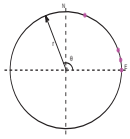	Lowest	Ps (%)	23.83	6.471	10.142

Table 3 contains the ILS success rate for the satellite configurations in Figure 5 and the illustrated array configurations, for $f = 2\ (L1 + L2)$ and different elevations of the contaminated satellite when $\sigma_p = 1$ meter. It shows that for such a large value of σ_p, it would be impossible to reach high values for ILS success rate even if the GNSS observables are available on 2 frequencies.

Up to now, we have assessed the case of detecting iono-

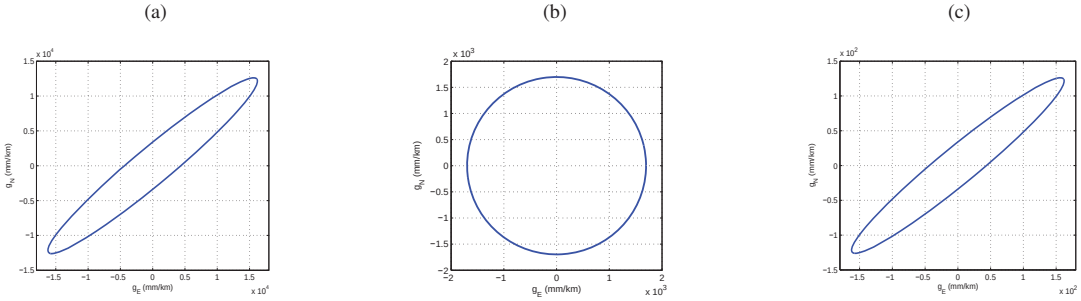

Figure 10. The ellipses showing the (a) single-epoch ambiguity-float MDB corresponding with the planar array (2) in Table 2, (b) single-epoch ambiguity-float MDB corresponding with the planar array (1) in Table 2, (c) single-epoch ambiguity-fixed MDB corresponding with the planar array (2) in Table 2, and the satellite geometry in Figure 5 (a), $f = 2$ $(L1 + L2)$, $m = 6$, $n = 4$, $P_{fa} = 10^{-4}$ and $P_{md} = 10^{-4}$. The lowest satellite PRN31 with the elevation $\varepsilon^c = 32.6°$ has been considered to be contaminated by the ionospheric front.

spheric spatial gradient upon the single-epoch GNSS observables. From the results we obtained above, fixing the DD ambiguities for single-epoch scenario to achieve the desirable MDB regions depends on some factors like the satellite geometry and the elevation of the contaminated satellite which are uncontrollable and probably hinder having acceptable DD ambiguity resolution success rate. It is also known that, since the ambiguities are considered constant over time, if we let the time go on and collect GNSS observables over a particular number of epochs, more precise estimations for the DD ambiguities will be obtained, giving rise to larger success rates. In the following subsection we will address the multi-epoch scenario.

3.3 Multi-epoch scenario

When it comes to multi-epoch scenario, one can think of two cases: 1) ionospheric spatial gradient is time-invariant; 2) ionospheric spatial gradient is time-variant. In Table 4, the variance matrices of the ionospheric spatial gradient estimator corresponding with epoch i are illustrated as function of $Q_{\hat{g}\hat{g}}$ in Eq. (12) specified for epoch i, for several scenarios and the two cases time-invariant and time-variant ionospheric spatial gradient. The closed-form formulations for the MDB can be easily found by substituting the variance matrices into Eq. (11). Although the variance matrix notation in this table is the one used for the 3-dimensional array, the results in this table holds true for all types of array.

Table 4. Variance matrix of the ionospheric spatial gradient vector corresponding with epoch i (ε is the phase-code variance ratio).

Scenario	Iono. gradient	Ambiguity	Variance matrix
Single-epoch	-	float	$Q_{\hat{g}\hat{g}}(i)$
Single-epoch	-	fixed	$\frac{\varepsilon}{1+\varepsilon} Q_{\hat{g}\hat{g}}(i)$
multi-epoch	time-invariant	float	$[\sum_{h=1}^{k} Q_{\hat{g}\hat{g}}^{-1}(h)]^{-1}$
multi-epoch	time-invariant	fixed	$\frac{\varepsilon}{1+\varepsilon} [\sum_{h=1}^{k} Q_{\hat{g}\hat{g}}^{-1}(h)]^{-1}$
multi-epoch	time-variant	float	$\frac{\varepsilon}{1+\varepsilon} (1 + \frac{1}{k\varepsilon}) Q_{\hat{g}\hat{g}}(i)$
multi-epoch	time-variant	fixed	$\frac{\varepsilon}{1+\varepsilon} Q_{\hat{g}\hat{g}}(i)$

3.3.1 Time-invariant ionospheric spatial gradient

First we consider the case when the ionospheric spatial gradient is time-invariant. When the ambiguities are still float, including the observations of more than one epoch, say k epochs, improves the variance matrix of $\hat{g}$ by almost k factor, and the MDB region by $\sqrt{k}$. Phase observables have no contribution to the variance matrix of $\hat{g}$ unless the integer DD ambiguities are successfully fixed. The reason for this can be explained as follows. We have assumed that both g and z_R^S are constant over time. Therefore, the *time-averaged* DD phase observations are reserved for the integer-valued DD ambiguities, and only the *time-differenced* DD phase observations remain to contribute to the solution of the ionospheric spatial gradient. This contribution would, however, be zero since the *time-differenced* design matrix of the ionospheric spatial gradient is zero, and also phase observables are uncorrelated with the code ones. When the ambiguities are fixed, DD phase observables act as if they are highly precise DD code observables. Hence, both phase and code observables would contribute to the estimation and the corre-

Table 5. Number of epochs needed for the DD ambiguity resolution ILS success rate to reach 99.9999%, as function of the satellite configurations and the array configurations shown, for $f = 2$ $(L1 + L2)$ and $\sigma_p = 1$ meter. The data sampling-rate is 30 seconds.

	Array configuration	ε^c	Ionospheric spatial gradient	Satellite configuration (a)	Satellite configuration (b)	Satellite configuration (c)
(1)	$r = 500$ meter $\theta = 0°, 90°, 180°, 270°$	Highest	time-invariant	24	28	24
			time-variant	23	29	25
	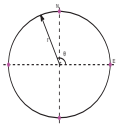	Lowest	time-invariant	44	55	44
			time-variant	43	54	45
(2)	$r = 500$ meter $\theta = 0°, 10°, 20°, 70°$	Highest	time-invariant	14	16	17
			time-variant	13	15	15
	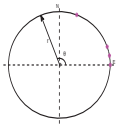	Lowest	time-invariant	25	39	29
			time-variant	25	37	29

sponding variance matrix of the ionospheric spatial gradient. Therefore, the variance matrix of the ionospheric spatial gradient and its associated MDB region will decrease by, respectively, ε and $\sqrt{\varepsilon}$ compared to when the ambiguities are float.

The precision of the DD ambiguities would benefit from the number of epochs. It can be shown that the variance matrix of the DD ambiguities after k epochs has the following form

$$\begin{aligned} Q_{\hat{z}^S_R \hat{z}^S_R} &= \sigma_\phi^2 [\textstyle\sum_{i=1}^k (D_m^T W^{-1}(i) D_m)^{-1}]^{-1} \otimes \Lambda^{-2} \otimes D_n^T D_n \\ &\quad + D_m^T u_m^c u_m^{c\,T} D_m \otimes \Lambda^{-1} \mu \mu^T \Lambda^{-1} \otimes D_n^T B [\textstyle\sum_{i=1}^k Q^{-1}_{\hat{g}\hat{g}}(i)]^{-1} B^T D_n \end{aligned} \tag{27}$$

This shows that $Q_{\hat{z}^S_R \hat{z}^S_R}$ will improve by almost k factor after k epochs. This means that if the values of some uncontrollable factors such as satellites configuration and the number of satellites does not provide us with the required single-epoch precision for the DD ambiguities, then letting the time go on would be of help in that sense.

From Table 3, we saw that when $\sigma_p = 1$ meter, it is impossible to reach high ILS success rates for the ambiguity resolution based on single-epoch observables. In Table 5, one can see the number of epochs (with the sampling-rate of 30 seconds) needed for $Ps = 99.9999\%$ when the ionospheric spatial gradient is time-invariant, for the satellite configurations in Figure 5 and the illustrated array configurations, for $f = 2$ $(L1 + L2)$ and different elevations of the contaminated satellite when $\sigma_p = 1$ meter.

3.3.2 Time-variant ionospheric spatial gradient

Now we consider the case where the ionospheric spatial gradient is assumed to change over time. In order to derive closed-form expressions for this case, we have made the assumption that over a limited number of epochs, say k, $w^s(1) \approx \ldots \approx w^s(k) \approx w^s$. The variance matrix of $\hat{g}(i)$ will not be improved by including other epochs observables, in case only code observables are taken into account. That is because, according to Eq. (9), the ionospheric spatial gradient vectors are estimated based on the time-uncorrelated DD code observables and observation models with no common parameters. When the phase observables are also included and the ambiguities are float, the variance matrix of the ionospheric spatial gradient and the corresponding MDB drops by k and $\sqrt{k}$, respectively. When the ambiguities are successfully fixed, DD phase observables act as highly precise DD code observables. In this case, the ionospheric spatial gradient vectors are estimated based on the time-uncorrelated code and phase observables and observation models with no common parameters. So, there would be no correlation among the estimators of the ionospheric spatial gradient associated with various epochs.

Assuming that $w^s(1) \approx \ldots \approx w^s(k) \approx w^s$, the variance matrix of the DD ambiguities after k epochs can be approxi-

mated by

$$Q_{\hat{z}^S_R \hat{z}^S_R} \approx \frac{\sigma_\phi^2}{k} D_m^T W^{-1} D_m \otimes \Lambda^{-2} \otimes D_n^T D_n + \frac{1}{k} D_m^T u_m^c u_m^{c\,T} D_m \otimes \Lambda^{-1} \mu \mu^T \Lambda^{-1} \otimes D_n^T B Q_{\hat{g}\hat{g}}(i) B^T D_n \quad (28)$$

which clearly shows $Q_{\hat{z}^S_R \hat{z}^S_R}$ will decrease by almost k after k epochs.

Table 5 shows the number of epochs needed for the DD ambiguity resolution ILS success rate to reach $Ps = 99.9999\%$ when the ionospheric spatial gradient is time-variant, for $f = 2$ ($L1 + L2$) and $\sigma_p = 1$ meter, as function of the array configurations, the satellite configurations, and the elevation of the contaminated satellite.

According to Table 5, fixing the DD ambiguities does not have a dependency on whether the ionospheric spatial gradient is time-invariant or time-variant. This conclusion has already been confirmed by comparing Eqs. (27) and (28). The reason for this can be explained as follows. In both cases, ambiguities at epoch k are estimated based on the time-averaged phase observables, corrected for the ionospheric spatial gradient estimator at epoch k. Looking at Table 4, one can see that the variance matrices associated with epoch k of the time-invariant ionospheric spatial gradient and the time-variant one are approximately the same. as long as the ambiguities are float, time-variant ionospheric spatial gradient is estimated using code observables (uncorrelated with the phase measurements), and time-invariant ionospheric spatial gradient is estimated using code and time-differenced phase observables (uncorrelated with the time-averaged phase measurements). Therefore, the precisions of the ambiguities are almost the same for both cases.

4 Summary and conclusions

The detectability of the ionospheric spatial gradient using the test in Eq. (10) depends on various factors summarized below in bullets.

- Increasing the number of receivers and the length of the array would lead to detecting smaller ionospheric spatial gradients with the test in Eq. (10). Regarding the array geometry, we showed that configurations fulfilling $e_n^T B = 0$ will decrease the size of the UMPI MDB. However, if one aims at fixing the DD ambiguities with a high success rate at only one epoch, this array geometry would not be of much help. High ILS success rates will be obtained if the array geometry satisfies $D_n^T B \to 0$, which is not desirable for the MDB size. At the same time, one should keep in mind that if the DD ambiguities are successfully fixed, then the highly precise phase observables will contribute to the precision of the ionospheric spatial gradient, making the MDB size very small.

- Both the variance matrix and the MDB region of the ionospheric spatial gradient are independent of our choice of the reference receiver and reference satellite.

- Increasing the number of satellites will give rise to enhancing the ability to detect smaller ionospheric spatial gradients. The higher the elevation of the satellites in view, the better the detectability of the ionospheric spatial gradient will be. Given a satellite configuration, the best ionospheric spatial gradient detectability will be obtained when the ionospheric front affects satellite c of which the elevation-dependent weight w^c is the closest to $\sum_{s=1, s\neq c}^{m} w^s$. The behavior of the precision of the DD ambiguities with respect to the number of satellites and the satellites elevation can be explained the same way.

- Having GNSS observables on more than one frequency available would be of much help in terms of reducing the minimal detectable ionospheric spatial gradient.

- Involving the observables of more than one epoch, say k epochs, has different effects for different scenarios. When the ionospheric spatial gradient is considered to be time-invariant, as long as the ambiguities are float, only the code observable of k epochs contribute to the estimation of the ionospheric spatial gradient, improving its precision by almost k factor and reducing the corresponding MDB size by $\sqrt{k}$. Once the DD ambiguities are successfully fixed, phase observables also play role in the precision of the ionospheric spatial gradient, and enhance it by $\varepsilon = 10^{-4}$ and the associated MDB by $\sqrt{\varepsilon}$ compared with the ambiguity-float scenario.

- When the ionospheric spatial gradient is assumed to change over time, its precision at each epoch will not benefit from observables of other epochs, if only the code observables are included. As the phase measurements are taken into account, and ambiguities are float, the precision and the MDB improve by k and $\sqrt{k}$, respectively. Once the ambiguities are fixed, the precision and the MDB region enhance by, respectively, ε and $\sqrt{\varepsilon}$ with respect to multi-epoch code-only scenario.

Based on the numerical results obtained, when the ambiguities are still float, even if there are 8 symmetrically-distributed receivers with the length of 500 meter, and GNSS observables are available on 2 ($L1$ and $L2$) frequencies, the ionospheric spatial gradient smaller than 6000 mm/km and 1260 mm/km can not be detected with $P_{fa} = 10^{-4}$ and $P_{md} = 10^{-4}$ at single epoch when, respectively, $\sigma_p = 1$ meter and $\sigma_p = 0.2$ meter. The MDB region can become desirable by making the array larger. For example, if the length of the array (the radius of the array circle) reaches 2000 meter, then the previous numbers would reduce to 1500 mm/km and 315 mm/km.

Our outcomes showed that for an array configuration with 4 antennas satisfying $D_n^T B \to 0$, the DD ambiguities could be fixed during a few number of epochs for dual-frequency scenario and $\sigma_p = 0.2$ meter. When $\sigma_p = 1$ meter, however, a large number of epochs are needed for the ILS success rate to reach a desirable value. For example, for a satellite geometry with highly-elevated satellites, when the data sampling-rate is 30 seconds, it would be 25 epochs, and for a satellite geometry with low-elevated satellites, it would be 37 epochs, to get ILS success rate more than 99.9999% when the ionospheric spatial gradient is assumed to change over time. If the ambiguities, by choosing an appropriate array configuration, could be fixed during a few number of epochs, the MDB size would reach values at the level of a few hundred mm/km.

Acknowledgements

This work has been done in the context of the Positioning Program Project 1.19 "Multi-GNSS PPP-RTK Network" of the Cooperative Research Centre for Spatial Information (CRC-SI).

References

[1] G. Seeber, "Satellite geodesy: foundations, methods, and applications," *Berlin; New York: W. de Gruyter, 1993.*, vol. 1, 1993.

[2] B. Hofmann-Wellenhof, H. Lichtenegger, and E. Wasle, *GNSS–global navigation satellite systems: GPS, GLONASS, Galileo, and more*. Springer Science & Business Media, 2007.

[3] H. Bourne and Y. Morton, "GPS receiver ionosphere error correction based on spatial gradients and IGS satellite DCBs," in *Proceedings of the ION 2013 Pacific PNT Meeting, Honolulu, Hawaii, April 2013*, pages 685–693, 2013.

[4] C. Wang and Y. Morton, "Ionosphere TEC and TEC gradients estimation using a regional GNSS network," in *Proceedings of the 26th International Technical Meeting of The Satellite Division of the Institute of Navigation (ION GNSS+ 2013), Nashville, TN, September 2013*, pages 1875–1880, 2013.

[5] C. Wang, J. Wang, and Y. Morton, "Regional ionospheric TEC gradients estimation using a single GNSS receiver," in *China Satellite Navigation Conference (CSNC) 2014 Proceedings: Volume II*, pages 363–373, Springer, 2014.

[6] N. Blaunstein and E. Plohotniuc, *Ionosphere and applied aspects of radio communication and radar*. CRC Press, 2008.

[7] L. Gratton and B. Pervan, "Airborne and ground monitors for ionospheric front detection for the local area augmentation system using carrier phase measurements," in *Proceedings of the 18th International Technical Meeting of the Satellite Division of The Institute of Navigation (ION GNSS 2005), Long Beach, CA, September 2005*, pages 748–757, 2005.

[8] M. Luo, S. Pullen, J. Dennis, H. Konno, G. Xie, T. Walter, P. Enge, S. Datta-Barua, and T. Dehel, "LAAS ionosphere spatial gradient threat model and impact of LGF and airborne monitoring," *Proceedings of ION GPS 2003*, pages 9–12, 2003.

[9] S. Pullen, Y. S. Park, and P. Enge, "Impact and mitigation of ionospheric anomalies on ground-based augmentation of GNSS," *Radio Science*, vol. 44, no. 1, 2009.

[10] D. Simili and B. Pervan, "Code-carrier divergence monitoring for the GPS local area augmentation system," in *Position, Location, And Navigation Symposium, 2006 IEEE/ION*, pages 483–493, 2006.

[11] B. Belabbas, P. Remi, M. Meurer, and S. Pullen, "Absolute slant ionosphere gradient monitor for GAST-D: Issues and opportunities," in *Proceedings of the 24th International Technical Meeting of The Satellite Division of the Institute of Navigation (ION GNSS 2011), Portland, OR, September 2011*, pages 2993–3002, 2011.

[12] G. Giorgi, P. Henkel, and C. Gunther, "Testing of a statistical approach for local ionospheric disturbances detection," in *Proceedings of the IEEE-ION PLANS, Myrtle Beach, SC, USA*, pages 167–173, 2012.

[13] J. Jing, S. Khanafseh, F.-C. Chan, S. Langel, and B. Pervan, "Detecting ionospheric gradients for

GBAS using a null space monitor," in *Proceedings of the IEEE-ION PLANS, Myrtle Beach, SC, USA,*, pages 1125–1133, 2012.

[14] S. Khanafseh, S. Pullen, and J. Warburton, "Carrier phase ionospheric gradient ground monitor for GBAS with experimental validation," *Journal of The Institute of Navigation*, vol. 59, no. 1, pages 51–60, 2012.

[15] M.-S. Circiu, M. Felux, P. Remi, L. Yi, B. Belabbas, and S. Pullen, "Evaluation of dual frequency GBAS performance using flight data," in *Proceedings of the 2014 International Technical Meeting of The Institute of Navigation, San Diego, California*, pages 645–656, 2014.

[16] W. T., "The future of satellite navigation for aviation," *Stanford's 2011 PNT Challenges and Opportunities Symposium*, 2011.

[17] P. J. G. Teunissen and P. F. De Bakker, "Single-receiver single-channel multi-frequency GNSS integrity: outliers, slips, and ionospheric disturbances," *Journal of Geodesy*, vol. 87, no. 2, pages 161–177, 2013.

[18] A. Khodabandeh and P. J. G. Teunissen, "Single-Epoch GNSS Array Integrity: an Analytical Study," *IAG Symp*, vol. 142, 2015. Accepted for publication.

[19] W. Baarda, "A testing procedure for use in geodetic networks," *Publications on geodesy (ISSN 0165-1706*, vol. 2, no. 5, 1968.

[20] P. J. G. Teunissen, *Testing theory, an introduction*. Delft University Press, Delft, The Netherlands, 2001.

[21] J. Magnus, "Linear structures. London School of Economics and Political Science, Charles Griffin & Company LTD," 1988.

[22] H. J. Euler and C. C. Goad, "On optimal filtering of GPS dual frequency observations without using orbit information," *J. Geod.*, vol. 65, no. 2, pages 130–143, 1991.

[23] M. Felux, J. Lee, and F. Holzapfel, "GBAS ground monitoring requirements from an airworthiness perspective," *GPS Solutions*, pages 1–9, 2014.

[24] J. R. Christie, P.-Y. Ko, A. Hansen, D. Dai, S. Pullen, B. S. Pervan, and B. W. Parkinson, "The effects of local ionospheric decorrelation on LAAS: theory and experimental results," pages 769–777, 1999.

[25] P. J. G. Teunissen and A. Kleusberg, *GPS for Geodesy*. Berlin; New York: Springer, second ed., 1998.

[26] T. Murphy, M. Harris, S. Pullen, B. Pervan, S. Saito, and M. Brenner, "Validation of ionospheric anomaly mitigation for GAST-D," *ICAO NSP Working Group of the Whole (WGW) Meeting, Montreal, Canada, WGW/WP 14*, 2010.

[27] B. Belabbas and M. Meurer, "Carrier phase and code based absolute slant ionosphere gradient monitor for GBAS," in *Proceedings of the Institute of Navigation, Nashville, TN, USA*, pages 2201–2208, 2012.

[28] P. J. G. Teunissen, "The least-squares ambiguity decorrelation adjustment: a method for fast GPS integer ambiguity estimation," *Journal of Geodesy*, vol. 70, no. 1-2, pages 65–82, 1995.

[29] P. J. G. Teunissen, "An optimality property of the integer least-squares estimator," *Journal of Geodesy*, vol. 73, pages 587–593, 1999.

13 The potential benefit of the horizon-to-elevation mask data to the ionospheric gradient detectability

This chapter is covered by the following publication:

Zaminpardaz S. (2016) Horizon-to-elevation Mask: A Potential Benefit to Ionospheric Gradient Monitoring. ION GNSS+ 2016, pp. 1764-1779. The Institute of Navigation, Portland, Oregon. ***Best Student Paper Award***

Horizon-to-Elevation Mask: a Potential Benefit to Ionospheric Gradient Monitoring

Safoora Zaminpardaz
GNSS Research Centre, Curtin University, Perth, Australia

Biography

Safoora Zaminpardaz has been pursuing her PhD since July 2014 at the GNSS Research Centre, Curtin university, Australia. Her research interests include array-based multi-GNSS positioning, ionosphere sensing and integrity monitoring.

Abstract

Monitoring and detecting signif cant ionospheric spatial gradients are of importance for safety-critical aviation applications. During the period a satellite is above the elevation mask, Ground Based Augmentation System (GBAS) monitors must be capable of instantaneously detecting hazardous ionospheric gradients that affect the signals of that satellite. At the time the satellite rises above the elevation mask, the GBAS monitors ability to detect hazardous ionospheric spatial gradients depends on the data of *only* that epoch since no observations were recorded beforehand. The detection ability of the monitors would, however, be improved if the receivers could collect the data during the period when the satellite elevation is increasing from horizon to elevation mask. In this paper, we explore the potential benef ts of using such data in terms of ionospheric spatial gradient detectability. We show how and under which circumstances this data can be employed to successfully detect a signif cant ionospheric gradient. Supported by simulation results, our analytical investigations demonstrate that reliable detection gets realized upon applying integer ambiguity resolution (IAR). The IAR success rate, based on the single-frequency GPS data, can attain high values of $1 - 10^{-6}$ before the satellite elevation reaches the value of 5°, if *at least* 8 antennas are utilized. This number of antennas can be reduced to even less than 4 in case the IAR is carried out on the basis of dual-frequency data. Resolving the double-difference (DD) ambiguities, the Minimal Detectable Biases (MDBs) for the ionospheric spatial gradient experience a dramatic decrease so that they can reach the required values before the elevation of the satellite reaches 5°, even when the baselines between antennas are shorter than 500 meters.

1 Introduction

Ground Based Augmentation System (GBAS) is a safety-critical system developed with the aim of improving the satellite system performance for civil aviation users. It provides differential corrections and integrity monitoring to an aircraft f ying at a distance of tens of kilometers w.r.t. the GBAS reference receivers [1, 2].

The positioning accuracy of the user is vulnerable to several error sources among which ionosphere is one of the most challenging. Observations during ionospheric storms have conf rmed the occurrence of ionospheric spatial gradients as large as 412 mm/km and 460 mm/km which can pose a threat to user positioning accuracy [3, 4]. In the case of GBAS approach service type D supporting CAT-III operations, for instance, gradients larger than 300 mm/km are considered to be hazardous [5, 6]. GBAS monitors are then required to detect such failures and warn the user within a period of 2-3 seconds from the beginning of the failure occurrence (almost instantaneously), see e.g. [7].

To realize the aforementioned requirement, a considerable number of contributions have been hitherto devoted to designing a proper gradient monitor [6–12]. Making use of both the phase and code observables, an ionospheric spatial gradient detector was formulated in [12] based on the concept of Uniformly Most Powerful Invariant (UMPI) test [13] (see Sect. 2.4). In this contribution, we follow the same concept as employing the code observations along

with the phase ones would provide enough information such that the ionospheric spatial gradient does not lump with the double-difference (DD) phase ambiguities.

A signif cant ionospheric front may affect the signals of a satellite before the satellite rises above the *elevation mask*. The elevation mask is def ned as the elevation below which if a GNSS satellite elevation lies, GBAS does not provide differential corrections for that satellite, see e.g. [14]. To guarantee the civil-aviation user safety with specif c false-alarm and missed-detection rates, the UMPI test should be capable of detecting the minimum hazardous value for the gradient at the time that an arbitrary satellite rises above the elevation mask. Due to the lack of time history for this case, the UMPI test performance should therefore be assessed based on the observations of a *single* epoch.

The UMPI test *single-epoch* performance can be considered under two scenarios: *ambiguity-float* and *ambiguity-fixed* scenarios. For the f rst one, the DD ambiguities are estimated as real-valued parameters preventing the phase data from contributing to the gradient detection. The ionospheric spatial gradient is therefore estimated and tested based on the less precise code observables. The corresponding numerical results, presented in this paper, will show that obtaining a single-epoch *float* minimal detectable bias (MDB) of 300 mm/km for the ionospheric spatial gradient, would not practically be feasible.

Under the ambiguity-f xed scenario, the DD ambiguities are resolved, and the very precise phase observables would in turn make a signif cant contribution to the ionospheric gradient detectability. Thus, the single-epoch *fixed* MDB of 300 mm/km for the gradient would be achievable, provided that successful integer ambiguity resolution (IAR) is carried out. Conducting successful IAR may, however, need more than one epoch.

The UMPI MDB may therefore not reach the desirable value when the satellite elevation reaches the elevation mask. To tackle this issue, one could try to take advantage of the observations that could be recorded prior to rise of the satellite above the elevation mask, i.e. the *horizon-to-elevation mask data*. This paper, therefore, aims to explore how and under which circumstances the horizon-to-elevation mask data can be used to successfully detect a signif cant ionospheric spatial gradient.

We f rst discuss the GNSS array-aided model based on which our methodology will be developed. Then, the testing procedure to detect the ionospheric gradient through the UMPI test statistic will be described. Under different circumstances, our methodology will be assessed analytically using the closed-form expressions for the ionospheric spatial gradient MDB. Promising analytical results will f nally be validated by employing a simulated GPS data-set.

2 Array-aided ionospheric gradient detection

2.1 Small-scale array's observation equations

Let $p^s_{r,j}$ and $\phi^s_{r,j}$ be, respectively, the undifferenced GNSS code and phase observations on frequency j ($j = 1,\ldots,f$) of satellite s ($s = 1,\ldots,m$) that are collected by antenna r ($r = 1,\ldots,n$). Also assume that the position of the antennas and satellites are precisely known, giving the antenna-to-satellite geometric ranges ρ^s_r. The corresponding full-rank double-difference (DD) observation equations read then [15]

$$\begin{aligned} \mathsf{E}(p^{1s}_{1r,j} - \rho^{1s}_{1r}) &= \tau^{1s}_{1r} + \mu_j\, \iota^{1s}_{1r} \\ \mathsf{E}(\phi^{1s}_{1r,j} - \rho^{1s}_{1r}) &= \tau^{1s}_{1r} - \mu_j\, \iota^{1s}_{1r} + \lambda_j\, z^{1s}_{1r,j} \end{aligned} \tag{1}$$

where $(.)^{1s}_{1r} = [(.)^s_r - (.)^s_1] - [(.)^1_r - (.)^1_1]$ is the DD operator in which the f rst antenna and satellite are taken as the pivot. $\mathsf{E}(.)$ is the expectation operator. The term τ^{1s}_{1r} denotes the DD slant tropospheric delay, while ι^{1s}_{1r} denotes the DD f rst-order slant ionospheric delay on the f rst frequency. The ionospheric delays ι^{1s}_{1r} are linked to the observations through the frequency-dependent ratios $\mu_j = (\lambda_j/\lambda_1)^2$ with λ_j being the wavelength of j^{th} frequency. The integer-valued DD ambiguity $z^{1s}_{1r,j}$, in cycles, is linked to the phase observables by means of the wavelengths λ_j ($j = 1,\ldots,f$). Apart from the DD ambiguity term $z^{1s}_{1r,j}$, the remaining parameters are all expressed in units of range.

Observations' stochastic model. In our analysis, an elevation-dependent model is adopted to model the randomness of the GNSS measurements. Let σ_{p_j} and σ_{ϕ_j} be the undifferenced zenith-referenced standard deviations of the code and phase observations on the j^{th} frequency, respectively. The variances of the *undifferenced* code and phase observations $p^s_{r,j}$ and $\phi^s_{r,j}$ can then be expressed as

$$\sigma^2_{p^s_{r,j}} = \frac{1}{w^s_r}\,\sigma^2_{p_j}, \qquad \sigma^2_{\phi^s_{r,j}} = \frac{1}{w^s_r}\,\sigma^2_{\phi_j}, \tag{2}$$

in which the following sinusoidal elevation-dependent weights are taken [16]

$$w_r^s = (\frac{1.02}{\sin e_r^s + 0.02})^{-2} \tag{3}$$

with e_r^s being the elevation of satellite s with respect to the antenna r. According to the elevation weighting strategy, given in (3), the higher the elevation of the satellites, the more precise the observations become. In the extreme case, when the elevation of the satellites reaches its zenith (i.e. $e_r^s = 90°$), the weight w_r^s attains its maximum value, i.e. $w_r^s = 1$, thereby leading the variances $\sigma^2_{p^s_{r,j}}$ and $\sigma^2_{\phi^s_{r,j}}$ to attain their minimum values $\sigma^2_{p_j}$ and $\sigma^2_{\phi_j}$, respectively. The stochastic model of the DD setup (1) follows by applying the error propagation law to the DD operator.

Atmospheric delays of the small-scale array. In cases where the antennas r ($r = 1,\ldots,n$) are spatially separated by *less* than a few kilometers, one can assume that *almost* the same atmospheric delays are experienced by all the antennas. In that case, the atmospheric delays τ_r^s and $\imath_r^s$, introduced in (1), can be approximated as

$$\begin{aligned} &(i): \quad \tau_r^s \approx \tau_1^s, \quad \text{for all} \quad r = 2,\ldots,n \\ &(ii): \quad \imath_r^s \approx \imath_1^s, \quad \text{for all} \quad r = 2,\ldots,n \end{aligned} \tag{4}$$

Throughout this contribution, we assume that the f rst condition of (4), i.e. (i), holds valid. Thus, the unknown parameters τ_{1r}^{1s} ($r = 2,\ldots,n$; $s = 2,\ldots,m$) vanish in (1). In case of the second condition (ii) however, we take recourse to *hypotheses testing* which decides us whether to reject (ii) or not. This is indeed the topic of this contribution and will be discussed in following.

2.2 Fault-free scenario

Under nominal ionosphere condition (null hypothesis), we assume that the second condition (ii), in (4), holds true, i.e. that the ionospheric delays are *equally* experienced by all the antennas r ($r = 1,\ldots,n$). Therefore, the null hypothesis H_o is expressed as

$$H_o: \quad \imath_r^s = \imath_1^s, \qquad r = 2,\ldots,n; \quad s = 1,\ldots,m \tag{5}$$

Under H_o, *no* ionospheric front is assumed present. The null hypothesis H_o is therefore here referred to as the *fault-free scenario*.

2.3 Fault-affected scenario

When the signals of the satellites are affected by an ionospheric front (alternative hypothesis), the second condition (ii), in (4), does *not* hold true anymore. In that case, the signals of one or more satellites are assumed to be contaminated by an ionospheric front. In accordance with the literature stating that the probability of a large gradient affecting more than one satellite is believed to be suff ciently low, see e.g. [17], here we assume only one of the satellites in view, say satellite c, is affected by the ionospheric front. With this in mind, let ∇_r^c be the bias that the ionospheric front imposes on the signals transmitted by satellite c. The alternative hypothesis H_a can then be expressed as

$$H_a: \quad \begin{cases} \imath_r^s = \imath_1^s & r = 2,\ldots,n;\ s \neq c \\ \imath_r^c = \imath_1^c + \nabla_r^c & r = 2,\ldots,n \end{cases} \tag{6}$$

Under H_a, a signif cant ionospheric front is assumed present. The alternative hypothesis H_a is therefore here referred to as the *fault-affected scenario*.

Modeling the ionospheric front's bias ∇_r^c. In agreement with the previous research into the ionospheric fronts, the corresponding bias ∇_r^c can be assumed to *linearly* change with the distance between two spatially-separated points, see e.g. [18, 19]. While some studies make use of the distance between the ground points [6, 10, 11, 20], other studies focus on the distance between the corresponding Ionospheric Pierce Points (IPPs) based on the thin-shell model [21, 22]. Depending on whether a ground baseline or a baseline between two IPPs is chosen, the interpretation of the estimable ionospheric spatial gradient would be different. Here, our preference is to work with the ground baselines since the validity of the thin-shell model, under severe ionosphere activities, is not always guaranteed (Sam Pullen, personal communication, Dec 8, 2015). The bias ∇_r^c, given in (6), can then be parametrized as follows

$$\nabla_r^c = b_{1r}^T g \tag{7}$$

with $b_{1r} = b_r - b_1$ denoting the baseline between the pivot antenna 1 and antenna r. The unknown parameter vector g (of dimension l) is referred to as the *ionospheric spatial gradient*. As shown in [12], the dimension of g, i.e. l, is governed by the *dimension* of the array. In case of the 1-dimensional (linear) arrays, the stated dimension becomes $l = 1$. This parameter becomes equal to $l = 2$ and $l = 3$, respectively, for the 2-dimensional (planar) and 3-dimensional arrays.

Substituting (7) into (1) gives the full-rank DD observation equations under H_a as

$$H_a: \quad \begin{aligned} \mathsf{E}(p_{1r,j}^{1s} - \rho_{1r}^{1s}) &= +\mu_j \eta^c (b_{1r}^T g) \\ \mathsf{E}(\phi_{1r,j}^{1s} - \rho_{1r}^{1s}) &= -\mu_j \eta^c (b_{1r}^T g) + \lambda_j z_{1r,j}^{1s} \end{aligned} \tag{8}$$

in which the indicator function η^c is def ned as

$$\eta^c = \begin{cases} +1 & c = s,\ c \neq 1 \\ -1 & c = 1 \\ 0 & \text{otherwise} \end{cases} \tag{9}$$

2.4 *Testing procedure*

Let $\hat{g}$ be the least-squares solution of the ionospheric gradient g obtained by (8) under H_a. Its variance matrix is denoted by $Q_{\hat{g}\hat{g}}$. The task is to check whether or not the magnitude of $\hat{g}$ is signif cant in a statistical sense. Upon performing the testing procedure, two unwanted, but possible, outcomes may occur. First, the magnitude of $\hat{g}$ is not signif cant, but the test incorrectly considers the magnitude to be *significant*. The probability of such outcomes is referred to as the *probability of false-alarm* and denoted by P_{fa}. Second, the magnitude of $\hat{g}$ is signif cant, but the test wrongfully considers the magnitude to be *insignificant*. The probability of such outcomes is referred to as the *probability of missed-detection* and denoted by P_{md}. In order to have an eff cient testing procedure, both of these probabilities must be small.

For a given P_{fa}, the probability P_{md} is minimized, if the Uniformly Most Powerful Invariant (UMPI) test is applied [13]. The UMPI test statistic T_l can be computed as

$$T_l = \hat{g}^T Q_{\hat{g}\hat{g}}^{-1} \hat{g} \tag{10}$$

Assuming normally-distributed GNSS data, the test statistic T_l follows the Chi-square distribution with l degrees of freedom and the noncentrality parameter λ, i.e. $\chi^2(l,\lambda)$. The noncentrality parameter λ is different for the hypotheses H_o and H_a. It is zero ($\lambda = 0$) for H_o and non-zero ($\lambda \neq 0$) for H_a.

Fig. 1 presents a schematic diagram showing how the testing procedure is carried out. Given a probability of false-alarm P_{fa} (depicted by the blue area), the corresponding critical value $\chi^2_{P_{fa}}(l,0)$ is obtained from the distribution $H_o:\ \chi^2(l,0)$. The null hypothesis is rejected if T_l exceeds the critical value $\chi^2_{P_{fa}}(l,0)$, that is

$$\text{reject} \quad H_o \quad \text{if} \quad T_l > \chi^2_{P_{fa}}(l,0)$$

In this case, the alternative hypothesis H_a is assumed as the correct model, meaning that a signif cant ionospheric spatial gradient is considered to occur.

The corresponding probability of missed detection P_{md} is highlighted by the red area in Fig. 1. Given the probabilities P_{fa} and P_{md}, one can compute the corresponding

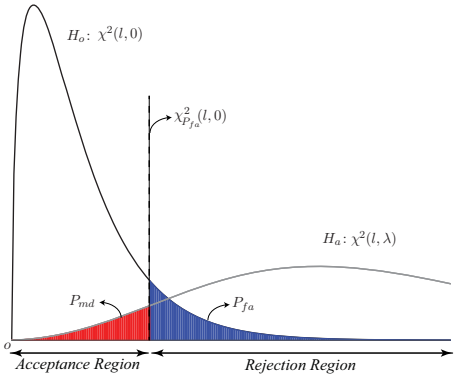

Figure 1. Schematic diagram showing how the UMPI testing procedure is carried out. The given probability of false-alarm P_{fa} (the blue area) determines the critical value $\chi^2_{P_{fa}}(l,0)$ (dashed line), separating the acceptance region from the rejection region. The probability of missed detection P_{md} is depicted by the red area.

noncentrality parameter $\lambda = \lambda_o$, thereby determining the minimal detectable bias (MDB) that the test can detect.

Let the gradient g be parametrized, in terms of its magnitude $||g||$ and its unit direction vector d, as $g = ||g||d$. Then the MDB of the ionospheric spatial gradient g is given by [12]

$$||g|| = \sqrt{\frac{\lambda_0}{d^T Q_{\hat{g}\hat{g}}^{-1} d}};\ d \in \mathbb{R}^l \tag{11}$$

The *region* of the whole MDB is formed when the unit vector d sweeps the surface of the unit sphere in $\mathbb{R}^l$. The shape and the orientation of the MDB region is governed by the variance matrix $Q_{\hat{g}\hat{g}}$, and its size is determined by λ_0. The MDB region is an interval when $l = 1$, an ellipse when $l = 2$, and an ellipsoid when $l = 3$.

3 Methodology

The GBAS monitors must be able to detect hazardous ionospheric fronts as soon as a contaminated satellite just rises above the elevation mask. In this section, we investigate the potential capacity of the test statistic in (10) to meet the following requirement

$$\text{maximum MDB} = 300\ \text{mm/km};\quad P_{fa} = P_{md} = 10^{-4} \tag{12}$$

Since the MDB region would be an ellipse (ellipsoid) when using planar (3-dimensional) arrays, the maximum

MDB is the semi-major axis of the stated ellipse (ellipsoid). As to the linear array, the MDB region is an interval of which the maximum and minimum values are the same. The value of 300 mm/km is taken from GBAS approach service type D requirement supporting CAT-III operations [5, 6]. $P_{fa} = 10^{-4}$ and $P_{md} = 10^{-4}$ are chosen in agreement with previous works [6, 10]. In the sequel, we distinguish between *ambiguity-float* and *ambiguity-fixed* scenarios.

3.1 Ambiguity-float scenario

Let us first consider the ambiguity-float scenario, in which the integerness of the DD ambiguities $z^{ls}_{1r,j}$ in (8) is not taken into account. Thus, they are estimated as real-valued parameters. Assuming that the ionospheric spatial gradient is unlinked in time, its corresponding MDB after k epochs can be shown to be approximated as [12]

$$||g||_{float}(k) \approx \sqrt{\frac{\varepsilon}{1+\varepsilon}(1+\frac{1}{k\varepsilon})} \times ||g|| \qquad (13)$$

where $\varepsilon \approx 10^{-4}$ is the ratio of the phase variance to that of code, and $||g||$ is the single-epoch ambiguity-float ionospheric spatial gradient MDB, i.e. $||g|| = ||g||_{float}(1)$.

Table 1 presents numerical values of the single-epoch ionospheric spatial gradient MDB $||g||$ as a function of the number of antennas n, number of frequencies, and the array length a, for a GPS dual-frequency (L1/L2) dataset. In addition to mentioned factors, $||g||$ has a large dependency on the satellite configuration and the elevation of the ionospheric front-affected satellite. The lower the satellites in view, the larger the MDB $||g||$ becomes. Therefore, a configuration containing low-elevated satellites would be weak in terms of ionospheric gradient detectability. Since the satellite configuration is not controllable, we consider a weak configuration of seven satellites where the elevation of most of them is below 35°. The contaminated satellite is considered the lowest one with the elevation of 5°. Setting 5° as the elevation mask [6, 14], this satellite therefore just rose above the elevation mask.

As shown in Table 1, using a symmetric circular array with the radius of $a = 200$ m, no MDB smaller than 19600 mm/km is achievable. Enlarging the array length by a factor of 10, i.e. $a = 2000$ m, the single-epoch MDB gets 10 times smaller such that the single-epoch MDB one can reach at, provided 8 antennas track dual-frequency GPS data, is around 1960 mm/km.

Table 1. Single-epoch ionospheric spatial gradient MDBs $||g||$ (mm/km) for GPS single-frequency (L1) and dual-frequency (L1+L2) scenarios, on the basis of a configuration of seven satellites most of which are below 35°, and the lowest satellite at the elevation of 5° is affected by the ionospheric front. These values follow by setting, n antennas located symmetrically on a circle with radius a, and with $P_{fa} = 10^{-4}$, $P_{md} = 10^{-4}$ and the undifferenced standard-deviations $\sigma_{p_1} = \sigma_{p_2} = 0.2$ m.

		$a = 200$ m		$a = 2000$ m	
		$n = 4$	$n = 8$	$n = 4$	$n = 8$
L1	$\|\|g\\|\|$ (mm/km)	53452	37796	5345	3780
L1+L2	$\|\|g\\|\|$ (mm/km)	27742	19616	2774	1962

These observations therefore reveal that obtaining (12) when satellite elevation reaches the elevation mask of 5° is not feasible, unless a large number of antennas (i.e. $n > 8$) and/or a long separation between the antennas (i.e. $a > 2000$ m) are considered. For example, deploying $n = 50$ dual-frequency antennas on a circular array with the radius of $a = 5000$ m would realize attaining (12) at elevation mask of 5°. Such a solution is, however, not always practical due to e.g. restrictions imposed on the antennas' location. The expression given in (13) suggests an alternative approach to reducing the MDB to the required value, i.e. involving the GNSS data of more than one epoch (i.e. $k > 1$).

3.2 Ambiguity-fixed scenario

Now consider the case where the integerness of the DD ambiguities $z^{ls}_{1r,j}$ is imposed as a constraint on (8). Thus, the estimated ambiguities solutions are fixed to their integers. The corresponding fixed MDB of the ionospheric spatial gradient after k epochs, can be approximated as [12]

$$||g||_{fixed}(k) \approx \sqrt{\frac{\varepsilon}{1+\varepsilon}} \times ||g|| \qquad (14)$$

Since the phase observables are about 100 times more precise than the code ones, the fixed MDB of the ionospheric spatial gradient in (14) is 100 times smaller than its single-epoch float counterpart. Therefore, it is worth exploring how to reach a high *probability of fixing the DD ambiguities to their correct integers*, known as the *success rate*. In this contribution, fixing the ambiguities to their inte-

gers through *Integer Ambiguity Resolution* (IAR), is conducted by the LAMBDA method on the basis of integer least-squares principle [23, 24].

To gain a better understanding of the typical values of the single-epoch IAR success rates on the basis of the model of observations in (8), an example is presented here. Consider the array conf gurations and satellites geometry given in Table 1. Having $n = 4$ antennas, the single-frequency and dual-frequency success rates are 0.0015 and 0.0332, respectively. Including extra antennas, i.e. $n = 8$, the single-frequency and dual-frequency success rates increase to 0.0394 and 0.8424. Such values of the success rate are far from being acceptable, especially for the safety critical applications requiring high levels of reliability. Being constant over time, the DD ambiguities can, however, improve in precision, leading to high values for the success rate if one collects the data of multiple epochs (i.e. $k > 1$).

3.3 Benefits of horizon-to-elevation mask data

At the time a satellite just rises above the elevation mask, the signals of that satellite may be contaminated by a signif cant ionospheric front. In that case, the GBAS monitors ability to detect the stated hazardous ionospheric front depends on the data of *only* that epoch since no observations were recorded beforehand. However, as discussed above, to get (12), one should involve the GNSS observations of more than one epoch. The question then naturally arises whether full advantage of the horizon-to-elevation mask observations can be taken. But, how to deal with the large ionospheric delays and multipath corresponding to such low elevations? The effect of large atmospheric delays can be captured by a proper elevation-dependent weighting as was presented in (3). As to the multipath, its unwanted effect can be mitigated through employing multipath limiting antennas and choosing a proper location (free of ground ref ections) for antennas [17].

Motivated by [25], the present contribution aims to address the following research question:

How and under which circumstances can the horizon-to-elevation mask data be used to successfully detect a significant ionospheric spatial gradient?

We will f rst assess how the f oat MDB of (12) can be timely achieved using the horizon-to-elevation mask data. Then, the possibility of successful IAR, hence achievement of f xed MDB of (12) between horizon and elevation mask will be investigated.

Noise characteristics. The randomness of the GNSS data plays a key role in computing reliable ionospheric spatial gradient MDBs and ambiguities success rates. Thus, prior to any qualitative and quantitative analyses, it is of importance to characterize the stochastic behavior of the GNSS data which depends on the receiver type and constellation (GPS, Galileo, GLONASS, etc.), through $\sigma^2_{p_j}$ and $\sigma^2_{\phi_j}$ given in (2). In this study, a GPS data-set collected by receivers of JAVAD TRE_G3TH_8 type, are employed. Applying the Least-Squares Variance Component Estimation (LS-VCE) [26, 27] to 1Hz GPS DD code observations recorded by our receivers, the *undifferenced* zenith-referenced code standard-deviations for the frequencies L1 and L2 were, respectively, estimated as $\sigma_{p_1} = 21$ cm and $\sigma_{p_2} = 16$ cm. For the phase measurements, the *undifferenced* zenith-referenced standard deviation is set to $\sigma_{\phi_1} = \sigma_{\phi_2} = 2$ mm on both the frequencies. This corresponds to setting the standard-deviation of the DD phase measurements to 4 mm.

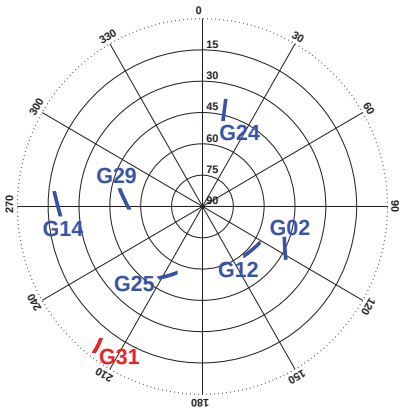

Figure 2. GPS skyplot at Perth for the time interval when the ionospheric front-affected satellite G31 (red) is traveling from 2° to 10° of elevation.

4 Analytical assessment

The analytical results presented here are only based on the closed-form expressions in (13) and (14), and the DD ambiguities variance matrix. In order to form the elevation-dependent weight function in (3), elevations of the satellites are taken from the broadcast ephemeris, sampled every second (1Hz).

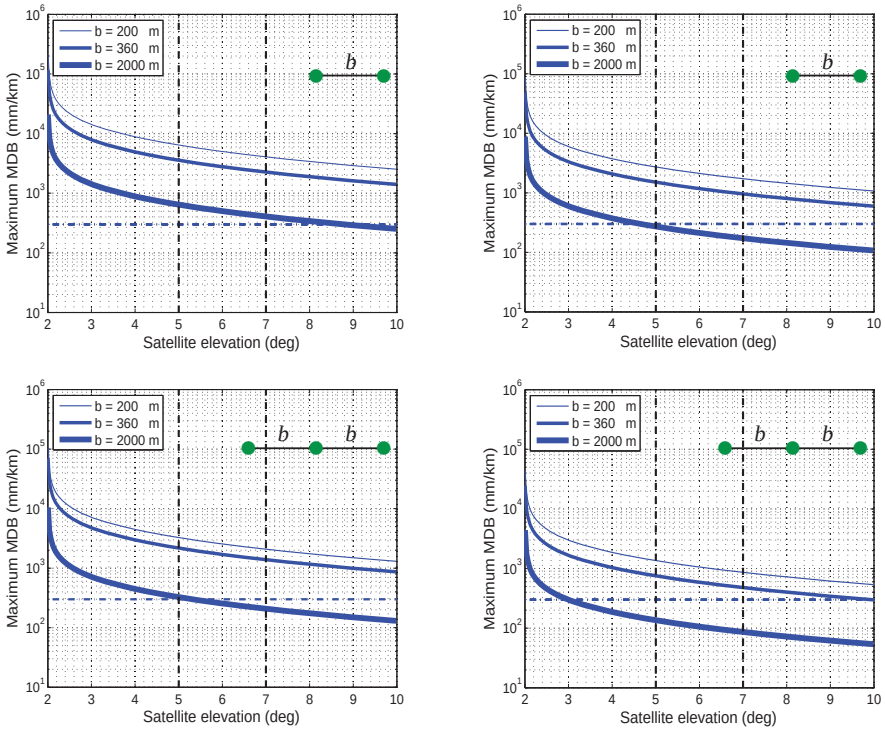

Figure 3. Linear array ionospheric spatial gradient MDB (*blue* solid lines), with $P_{fa} = 10^{-4}$ and $P_{md} = 10^{-4}$, as function of number of epochs (represented as the rising elevation of satellite G31), number of antennas, number of frequencies and length of between-antennas baselines b. The ionospheric front is assumed to affect G31 in the skyplot in Fig. 2. Left column corresponds to single-frequency scenario (L1), while the right column corresponds to dual-frequency scenario (L1+L2). Array conf guration is shown with antennas as *green* circles. The *blue* horizontal dashed line indicates the desirable MDB value of 300 mm/km. The *black* vertical dashed lines indicate the elevation angles of 5° and 7°.

4.1 Float MDB from horizon to elevation mask

In this subsection we analytically assess the possibility of achieving (12), under ambiguity-f oat scenario, during the period between horizon and elevation mask. To do so, satellite G31 of GPS constellation is considered during the time when its elevation changes form 2° to 5°, 7° and 10° w.r.t. the local horizon at Curtin University, Perth, Australia. Fig. 2 depicts the corresponding skyplot, in which satellite G31, considered for evaluation of our methodology, is shown by *red*.

Fig. 3 for linear array, and Fig. 4 for planar array, give the MDBs of the ionospheric gradient affecting satellite G31, during its pass from elevation of 2° to 10° (see Fig. 2). The horizontal axis shows the rising elevation of the satellite G31. The MDB graphs are depicted, with $P_{fa} = 10^{-4}$ and $P_{md} = 10^{-4}$, as a function of number of antennas, baselines length, array dimension and number of frequencies. From these f gures, the following observations can be made:

- *Linear array, single-frequency (L1).* With two antennas separated at $b = 2000$ m, MDB can reach 300 mm/km just before 9° of elevation. Including one more antenna aligned with the other two and setting baselines to $b = 2000$ m, the elevation associated with the MDB of 300 mm/km, is pushed back to just above 5°. This, namely, means that if the elevation

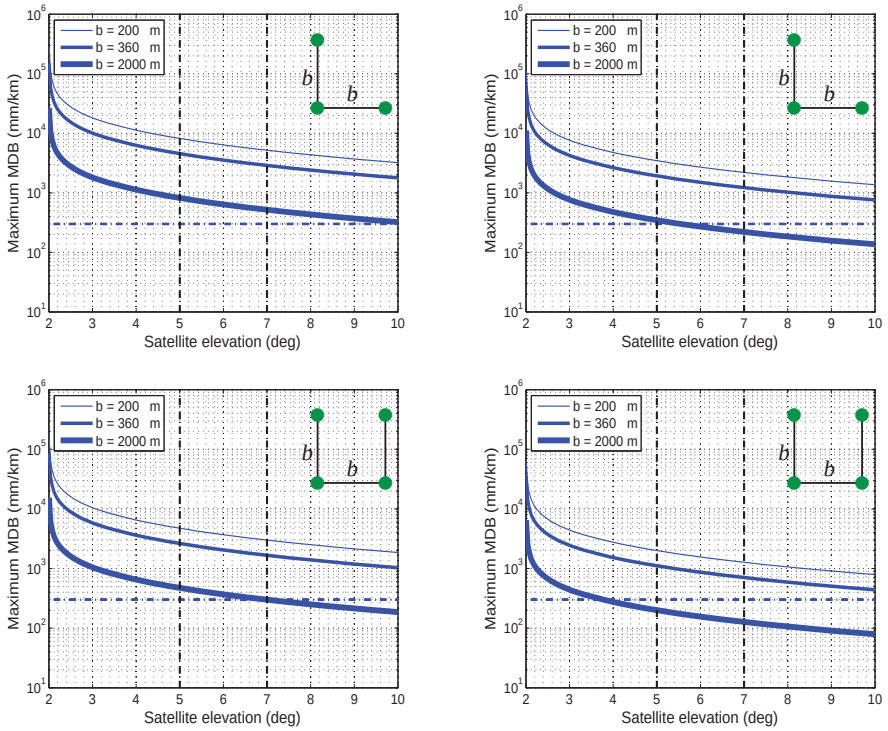

Figure 4. Planar array ionospheric spatial gradient MDB (*blue* solid lines), with $P_{fa} = 10^{-4}$ and $P_{md} = 10^{-4}$, as function of number of epochs (represented as the rising elevation of satellite G31), number of antennas, number of frequencies and length of between-antennas baselines b. The ionospheric front is assumed to affect G31 in the skyplot in Fig. 2. Left column corresponds to single-frequency scenario (L1), while the right column corresponds to dual-frequency scenario (L1+L2). Array conf guration is shown with antennas as *green* circles. The *blue* horizontal dashed line indicates the desirable MDB value of 300 mm/km. The *black* vertical dashed lines indicate the elevation angles of 5° and 7°.

mask is given larger values, even shorter baselines than 2000 m can lead to MDBs of 300 mm/km when satellite elevation reaches the elevation mask. For example, with 3 receivers aligned, baselines of 1350 m and 850 m would serve getting desirable MDBs at the respective elevations of 7° and 10°.

- *Linear array, dual-frequency (L1+L2).* Employing a single baseline of $b = 2000$ m results in MDB of 300 mm/km around 4.5°. This indicates, in case of higher allowable elevation masks of 7° and 10°, shorter baselines of 1150 m and 720 m can serve the purpose. Increasing the number of antennas from two to three, the 2000m-baselines MDB reaches 300 mm/km around 3°. The baselines of 360 m also achieve MDB of 300 mm/km just before 10°. If the elevation mask is set to 7°, then baselines of 550 m would be suff cient to get the desirable MDBs as soon as the satellite elevation reaches the elevation mask.

- *Planar array, single-frequency (L1).* With three antennas forming an isosceles right triangle, MDB can reach 300 mm/km just below 10° would the equal sides are chosen to be $b = 2000$ m. Changing the array conf guration from a triangle to a square with sides of $b = 2000$ m, by adding one more antenna, 300 mm/km MDB becomes achievable at 7°. Given the elevation mask of 10°, baselines of $b = 1250$ m

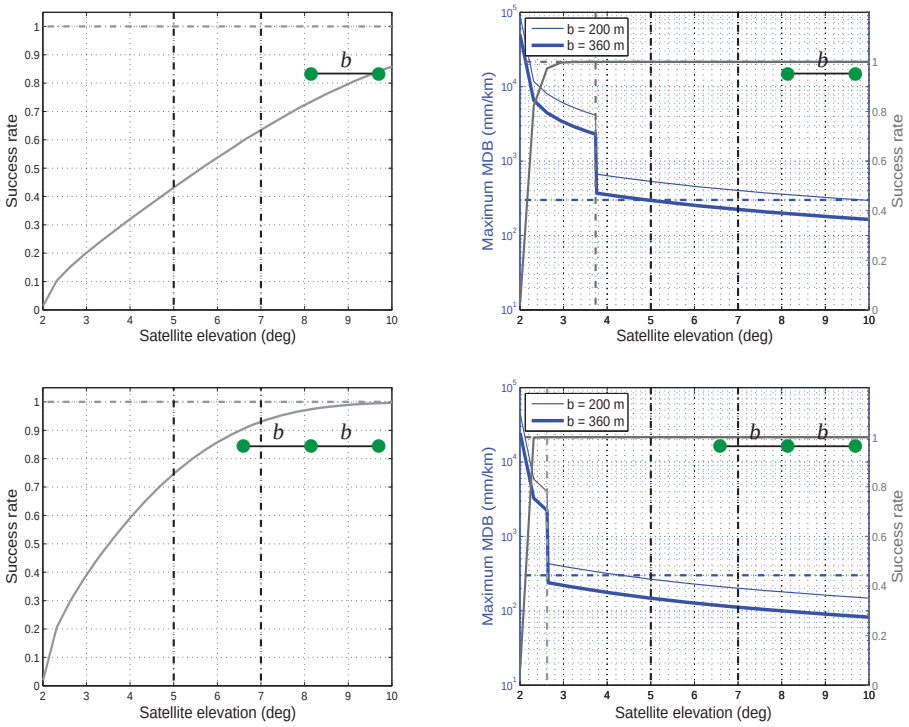

Figure 5. Linear array IAR success-rate (*gray* solid line) and ionospheric spatial gradient MDB (*blue* solid line), with $P_{fa} = 10^{-4}$ and $P_{md} = 10^{-4}$ as function of number of epochs (represented as the rising elevation of satellite G31), number of antennas, number of frequencies and length of between-antennas baselines b. The ionospheric front is assumed to affect G31 in skyplot in Fig. 2. Left column corresponds to single-frequency scenario (L1), while the right column corresponds to dual-frequency scenario (L1+L2). Array conf guration is shown with antennas as *green* circles. The *gray* and the *blue* horizontal dashed lines indicate the success rate of $1 - 10^{-6}$ and the desirable MDB of 300 mm/km, respectively. The *black* vertical dashed lines indicate the elevation angles of 5° and 7°. The *gray* vertical dashed line indicates the epoch at which the IAR achieves the success rate of $1 - 10^{-6}$ and DD ambiguities are f xed. After this epoch, MDB graphs show a marked drop due to f xing the DD ambiguities (cf. (13) and (14)).

would then be needed to obtain the desirable MDB.

- *Planar array, dual-frequency (L1+L2).* Three antennas on an isosceles right triangle with equal sides of $b = 2000$ m make MDB reach 300 mm/km around 5.6°. If higher elevation masks like 7° and 10° are chosen, then baselines of 1500 m and 920 m would, respectively, be suff cient to achieve MDBs of 300 mm/km as satellite elevation reaches the elevation mask. Replacing the triangular array with a square-shaped one with sides of $b = 2000$ m, MDB would reach 300 mm/km around 3.8°. Baselines of 850 m and 530 m would do this if the elevation mask is chosen as 7° and 10°, respectively.

The above observations reveal that in order to get the required MDB of (12) prior to the satellite elevation reaching the angle of 5°, one should indeed make use of long baselines between 1 km to 5 km depending on the number of frequencies, number of antennas and array dimension. These limitations can, however, be mitigated if the integerness of the DD ambiguities is taken into consideration,

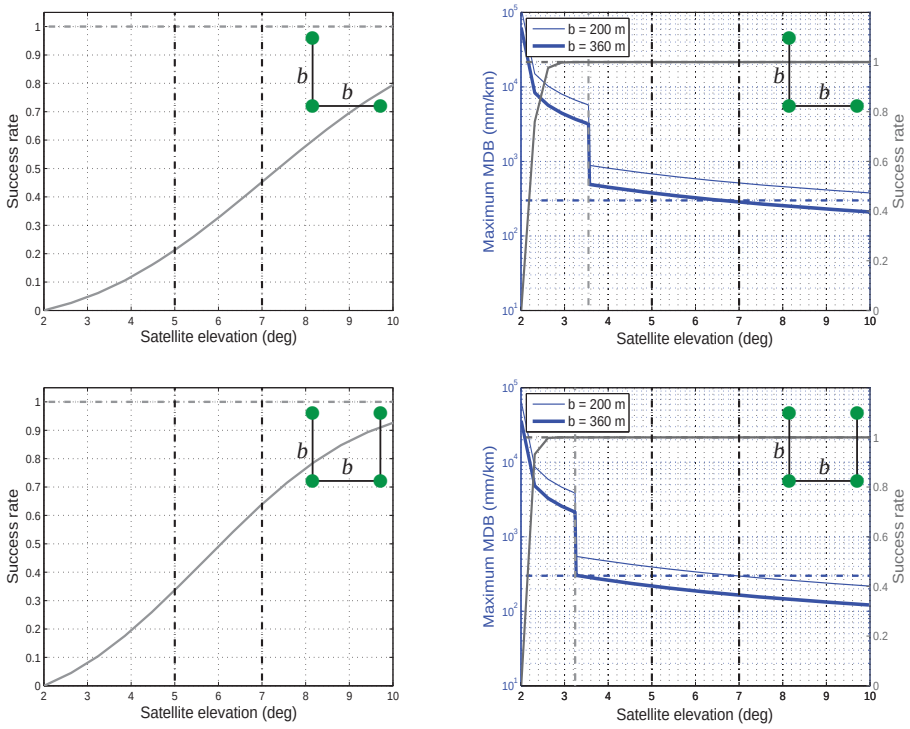

Figure 6. Planar array IAR success-rate (*gray* solid line) and ionospheric spatial gradient MDB (*blue* solid line), with $P_{fa} = 10^{-4}$ and $P_{md} = 10^{-4}$ as function of number of epochs (represented as the rising elevation of satellite G31), number of antennas, number of frequencies and length of between-antennas baselines *b*. The ionospheric front is assumed to affect G31 in skyplot in Fig. 2. Left column corresponds to single-frequency scenario (L1), while the right column corresponds to dual-frequency scenario (L1+L2). Array conf guration is shown with antennas as *green* circles. The *gray* and the *blue* horizontal dashed lines indicate the success rate of $1 - 10^{-6}$ and the desirable MDB of 300 mm/km, respectively. The *black* vertical dashed lines indicate the elevation angles of 5° and 7°. The *gray* vertical dashed line indicates the epoch at which the IAR achieves the success rate of $1 - 10^{-6}$ and DD ambiguities are f xed. After this epoch, MDB graphs show a marked drop due to f xing the DD ambiguities (cf. (13) and (14)).

which is the concern of the following subsection.

4.2 IAR success rate and fixed MDB from horizon to elevation mask

This subsection is devoted to investigating whether it would be possible to resolve the DD ambiguities reliably (with success rate of $1 - 10^{-6}$), hence getting small MDBs (cf. 14) between horizon and elevation mask. The analytical results to be presented are again based on the skyplot in Fig. 2, Eqs. (13), (14), and ambiguities variance matrix.

Note that the DD ambiguities precision and hence success rate, in contrast with the MDB, are independent of the total length of the array [12]. In other words, if all the existing baselines are scaled by the same factor, the ambiguities variance matrix remains unchanged, so does the success rate.

Fig. 5 for linear array, and Fig. 6 for planar array, display the IAR LAMBDA success rate and MDB graph ($P_{fa} = 10^{-4}$ and $P_{md} = 10^{-4}$) for the ionospheric spatial gradient contaminating satellite G31, while it is elevating from 2° to 10°. The results are provided for different number of

antennas, baselines length, array dimension and number of frequencies. The conclusions based on these results can be summarized as follows:

- *Linear array, single-frequency (L1).* Either with two or three antennas, success rate cannot reach the value of $1-10^{-6}$ even if the elevation mask is set to be 10°. To acquire success rate of $1-10^{-6}$ prior to the satellite G31 rising above the elevations of 5°, 7° and 10°, one needs at least 8, 6, and 4 antennas, respectively.
- *Linear array, dual-frequency (L1+l2).* Single-baseline success rate reaches $1-10^{-6}$ well before elevation angle of 5°. After fixing the DD ambiguities, the graph of MDBs show marked drops. The baseline of 360 m reaches 300 mm/km for MDB just before the elevation of 5°, while the 200 m baseline has to wait up until the elevation of 10° is captured. Increasing the number of antennas from two to three, not only a faster successful IAR is realized, even a short baseline of 200 m can achieve MDB of 300 mm/km before 5°.
- *Planar array, single-frequency (L1).* Either with three or four antennas, single-frequency success rate cannot reach acceptable high values even if the elevation mask is set to be 10°. In case of using 8 antennas, the success rate can achieve the value of $1-10^{-6}$ before the elevation of 5°.
- *Planar array, dual-frequency (L1+l2).* With three antennas on an isosceles right triangle, success rate reaches $1-10^{-6}$ well before elevation angle of 5°, i.e. around 3.8°. Setting the equal sides of isosceles right triangle to be 360 m, the fixed MDB reaches 300 mm/km just before the elevation of 7°. In order to speed up getting desirable MDBs, longer baselines should be chosen. Going from triangular to square-shaped array expedites the successful IAR, and baselines of 360 m and 200 m can achieve MDB of 300 mm/km around 3.2° and 7°, respectively.
- Comparing the results of three-antenna planar array with the three-antenna linear array, it can be observed that the success rate gets smaller if the dimension of the array increases while preserving the number of antennas.

The above conclusions reveal that the IAR success rate, based on the single-frequency GPS data, can attain high values of $1-10^{-6}$ before the satellite elevation reaches the value of 5°, if *at least* 8 antennas are utilized. This number of antennas will reduce to even less than 4 in case the IAR is carried out on the basis of dual-frequency data. Resolving the DD ambiguities, the MDBs for the ionospheric spatial gradient experience a dramatic decrease so that they can reach the required values before the elevation of the satellite reaches 5°, even when the baselines between antennas are shorter than 500 meters.

5 Simulation-based assessment

Having presented analytical results based on our methodology, here we aim at providing simulation-based results to support some of the promising analytical outcomes. To do so, a single-baseline (two antennas) simulated dual-frequency GPS data-set (L1 and L2) is employed. The information on this data-set is given in Table 2. The two antennas in use, called CUT3 and SPA7, are located at the distance of 357.59 meter from each other, at Curtin University in Perth, Australia.

By this simulation, our aim is to validate the analytical IAR LAMBDA success rate and the ionospheric spatial gradient UMPI MDB. In this regard, three satellite configurations are considered, shown in Fig. 7 (a) in which *red* satellites G31, G15, and G2 are passing from 2° to 5° of elevation.

Table 2. Characteristics of the simulation conducted for this study.

Receiver type	JAVAD TRE_G3TH_8
Number of antennas	2
location	Curtin University (Lat: 32.01° S, Long: 115.89° E)
Data type	GPS dual-frequency (L1 and L2)
Date and time	8 July 2015 (00:00:00-23:59:59 UTC)
Sampling interval	1 second (1 Hz)

The code and phase observations are simulated through the following *3 steps*:

1. The elevation of the satellites with respect to the antennas are computed using the known position of the antennas and the position of the satellites available in broadcast navigation files. These elevations are then given as inputs to (3) and (2) to form the variance matrix of the DD observations.

2. The DD code and phase observations are generated from a zero-mean normal distribution with the variance matrix determined in the previous step.

3. Finally, an ionospheric spatial gradient with the magnitude of 300 mm/km is introduced to the DD observations corresponding with the *red* satellites in Fig. 7 (a).

In the sequel, *formal* results refers to as the analytical results, while *empirical* results refers to as the simulation-based results.

5.1 Ionospheric spatial gradient detectability

The empirical UMPI test missed-detection rates, denoted by P_{md}, to detect an ionospheric spatial gradient of 300 mm/km with $P_{fa} = 10^{-4}$ for the dual-frequency data of the station-pair CUT3–SPA7, is computed and then compared to their formal counterparts. To obtain the empirical UMPI test missed-detection rate after a certain number of epochs, say k, the DD observations are simulated over k epochs through the aforementioned 3-step procedure, for 10^6 times. Each time, the UMPI test statistic in (10) is applied to detect the imposed ionospheric spatial gradient on the observations of the lowest satellite (*red* satellites in Fig. 7 (a)). The number of times where the test fails to detect the ionospheric spatial gradient, is then divided by 10^6. The outcome would be the empirical UMPI test missed-detection rate.

Shown in Fig. 7 (b) are the diagrams of formal success rate and the ionospheric spatial gradient MDB as function of epoch numbers. The horizontal axis covers the period where the *red* satellites in Fig. 7 (a) are increasing in elevation from 2° to 5°. All three graphs indicate that both high acceptable success rate and the ionospheric gradient MDB of (12) are attained before elevation of 5°.

Fig. 7 (c) depicts the tables of empirical and formal UMPI test missed-detection rate to detect an ionospheric spatial gradient of 300 mm/km with $P_{fa} = 10^{-4}$, after different number of epochs. A good agreement between the empirical and formal UMPI test missed-detection rates in all three cases can be seen. This means that the formal values can indeed be used to predict the expected UMPI test missed-detection rate. Empirical values for probability of missed-detection at elevation of 5° (last epoch), similar to their respective formal ones, indeed confirms that ionospheric spatial gradient of 300 mm/km is detectable with $P_{fa} = 10^{-4}$ and $P_{md} = 10^{-4}$ just before the elevation of the contaminated satellite reaches 5°.

5.2 IAR reliability

Now, we compute the empirical success rate, denoted by Ps, for the dual-frequency data of the station-pair CUT3–SPA7 and then compare them to their formal counterparts. To obtain the empirical success rate after a certain number of epochs, say k, the DD observations are simulated for k epochs through the 3-step procedure mentioned above, for 10^6 times. Each time, the float ambiguities are resolved. The number of times where the DD float ambiguities are fixed to the correct integer values (here the zero vector) is then divided by 10^6. The outcome would be the empirical success rate.

Fig. 7 (d) gives the tables of empirical and formal success rates after different number of epochs. It can be seen that all the three cases show a good consistency between empirical and formal IAR success rates, especially after larger number of epochs. This means that the formal values can indeed be used to predict the expected IAR success rate. For the empirical success rates to reach the value of $Ps = 1 - 10^{-6}$, almost the same number of epochs takes as for their formal counterparts.

6 Summary and Conclusion

GBAS monitors are required to instantaneously detect hazardous ionospheric fronts. Therefore, the GBAS monitors should be capable of detecting hazardous ionospheric gradients at the time the elevation of a satellite reaches the elevation mask, using only the data of that single epoch since there is no time history available. The detectability of the monitors would, however, be improved if the receivers collect the *horizon-to-elevation mask data* as well. In this contribution, we therefore assessed the advantage of using the *horizon-to-elevation mask data* in terms of UMPI-based ionospheric spatial gradient detectability.

We described the *small-scale array* model which formed the basis of our analysis. The UMPI testing procedure, through which the significance of the ionospheric spatial gradient is tested, was then described. Our requirement was formulated in (12) stating that the ionospheric gradient MDB must be equal or smaller than 300 mm/km for the probabilities $P_{fa} = P_{md} = 10^{-4}$. We first focused on the *single-epoch* performance of the UMPI test, and in that regard, discriminated between the *ambiguity-float*

a)

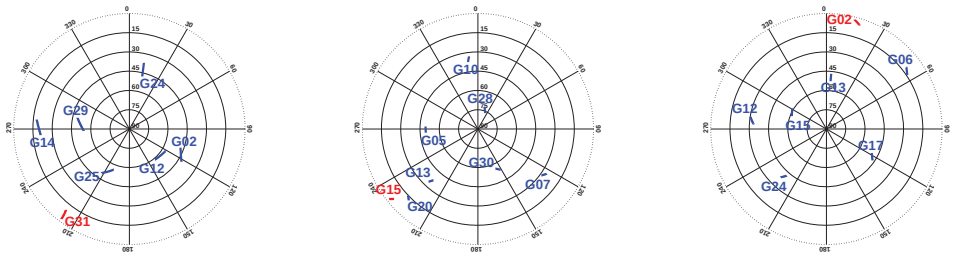

b)

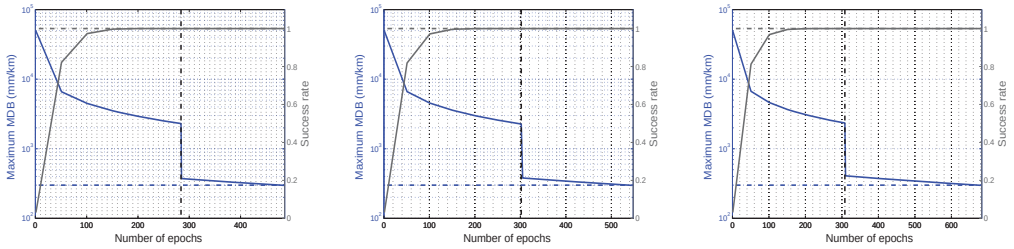

c)

Epoch #	Empirical P_{md}	Formal P_{md}
290	0.011443	0.011593
410	0.000733	0.000709
480	0.000085	0.000097

Epoch #	Empirical P_{md}	Formal P_{md}
310	0.015584	0.015933
450	0.001012	0.000955
540	0.000090	0.000099

Epoch #	Empirical P_{md}	Formal P_{md}
310	0.044145	0.044218
500	0.002962	0.002983
675	0.000090	0.000095

d)

Epoch #	Empirical *Ps*	Formal *Ps*
1	0.031030	0.030983
50	0.814949	0.821717
200	0.999691	0.999727
284	0.999997	0.999999

Epoch #	Empirical *Ps*	Formal *Ps*
1	0.031024	0.031293
50	0.812332	0.818546
200	0.999594	0.999631
302	0.999996	0.999999

Epoch #	Empirical *Ps*	Formal *Ps*
1	0.031027	0.031270
50	0.805605	0.812559
200	0.999339	0.999382
308	0.999998	0.999999

Figure 7. (a) GPS skyplots seen from stations CUT3 and SPA7 at Curtin University. (b) Formal IAR success rate (*gray* solid line) and ionospheric spatial gradient UMPI MDB (*blue* solid line), with $P_{fa} = 10^{-4}$ and $P_{md} = 10^{-4}$, as function of number of epochs, obtained under the dual-frequency scenario (L1+L2). The horizontal axis covers the period where the *red* satellites in Fig. 7 (a) are increasing in elevation from 2° to 5°. The ionospheric front is assumed to affect G31, G15, and G02 (shown in red) in the skyplots (from left to right). The *gray* and the *blue* horizontal dashed lines indicate the success rate of $1 - 10^{-6}$ and the desirable MDB of 300 mm/km, respectively. The *black* vertical dashed line indicates the epoch at which the IAR achieves the success rate of $1 - 10^{-6}$. (c) Tables showing the empirical and formal values of the UMPI test missed-detection rate (P_{md}) to detect ionospheric spatial gradient of 300 mm/km with $P_{fa} = 10^{-4}$ for different number of epochs. (c) Tables showing the empirical and formal IAR success rates (*Ps*) for different number of epochs.

and *ambiguity-fixed* scenarios. For both scenarios, it was shown that at the time when a satellite rises above the elevation mask, the requirement (12) would not practically be achievable, if use is made of the single-epoch data only. Therefore, we focused our attention on the role of the *horizon-to-elevation mask* data in getting the required MDB as soon as the satellite rises above the elevation mask.

The corresponding analytical results were presented for the single-frequency and dual-frequency scenarios as well as for linear arrays and planar arrays. For the ambiguity-f oat scenario, to meet the requirement (12) before the elevation angle of 5°, the observations revealed that one should make use of long baselines between 1 km to 5 km depending on the number of frequencies, number of antennas and array dimension. Such practical limitations can be mitigated though if the integerness of the DD ambiguities is taken into account. To achieve the very small MDBs brought by the ambiguity-f xed scenario, the DD ambiguities need to be f xed with a high success rate. The IAR success rate, based on the single-frequency GPS data, can attain high values of $1 - 10^{-6}$ before the satellite elevation reaches the value of 5°, if *at least* 8 antennas are utilized. This number of antennas will reduce to even less than 4 in case the IAR is carried out on the basis of dual-frequency data. Resolving the DD ambiguities, the MDBs for the ionospheric spatial gradient experience a dramatic decrease so that they can reach the required value of 300 mm/km before the elevation of the satellite reaches 5°, even when the baselines between antennas are shorter than 500 meters.

In order to support the promising analytical results, simulation-based results based on a pair of stations at Curtin University, were also presented. The dual-frequency empirical success rate and the UMPI test missed-detection rate were computed and compared with their analytical counterparts. The results demonstrate a consistency between the analytical and simulation-based values, thereby showing the potential of the proposed methodology at work.

Acknowledgements

This study has benef ted from constructive comments of Prof Peter Teunissen and Dr Amir Khodabandeh from the Curtin GNSS Research Center. Their support is gratefully acknowledged.

References

[1] P. Enge, "Local area augmentation of GPS for the precision approach of aircraft," in *Proceedings of the IEEE*, vol. 87, pages 111–132, 1999.

[2] S. Datta-Barua, T. Walter, S. Pullen, M. Luo, J. Blanch, and P. Enge, "Ionospheric Threat Parameterization for Local Area Global-Positioning-System-Based Aircraft Landing Systems," in *Proceedings of the 2002 National Technical Meeting of The Institute of Navigation, San Diego, CA, January 2002*, pages 523–530, 2002.

[3] S. Pullen, Y. S. Park, and P. Enge, "Impact and mitigation of ionospheric anomalies on ground-based augmentation of GNSS," *Radio Science*, vol. 44, no. 1, 2009.

[4] V. S. Srinivas, A. D. Sarma, A. S. Reddy, and D. K. Reddy, "Investigation of the effect of ionospheric gradients on GPS signals in the context of LAAS," *Progress In Electromagnetics Research B*, vol. 57, pages 191–205, 2014.

[5] T. Murphy, M. Harris, S. Pullen, B. Pervan, S. Saito, and M. Brenner, "Validation of ionospheric anomaly mitigation for GAST-D," *ICAO NSP Working Group of the Whole (WGW) Meeting, Montreal, Canada, WGW/WP 14*, 2010.

[6] S. Khanafseh, S. Pullen, and J. Warburton, "Carrier phase ionospheric gradient ground monitor for GBAS with experimental validation," *Journal of The Institute of Navigation*, vol. 59, no. 1, pages 51–60, 2012.

[7] G. Xie, S. Pullen, M. Luo, P. L. Normark, D. Akos, J. Lee, P. Enge, and B. Pervan, "Integrity design and updated test results for the Stanford LAAS integrity monitor testbed," in *Proceedings of the 57th Annual Meeting of The Institute of Navigation (2001), Albuquerque, NM, June 2001*, pages 681–693, 2001.

[8] B. Pervan, "A review of LGF code-carrier divergence issues," *Illinois Institute of Technology, MMAE Dept, May 29, 2001*, 2001.

[9] M. Luo, S. Pullen, D. Akos, G. Xie, S. Datta-Barua, T. Walter, and P. Enge, "Assessment of ionospheric impact on LAAS using WAAS supertruth data," in

Proceedings of the 58th Annual Meeting of The Institute of Navigation and CIGTF 21st Guidance Test Symposium (2002), Albuquerque, NM, June 2002, pages 175–186, 2002.

[10] J. Jing, S. Khanafseh, F. C. Chan, S. Langel, and B. Pervan, "Detecting ionospheric gradients for GBAS using a null space monitor," in *Proceedings of IEEE/ION PLANS 2012, Myrtle Beach, South Carolina , April 2012*, pages 1125–1133, IEEE, 2012.

[11] G. Giorgi, P. Henkel, and C. Gunther, "Testing of a statistical approach for local ionospheric disturbances detection," in *Proceedings of IEEE/ION PLANS 2012, Myrtle Beach, South Carolina , April 2012*, pages 167–173, IEEE, 2012.

[12] S. Zaminpardaz, P. J. G. Teunissen, N. Nadarajah, and A. Khodabandeh, "GNSS Array-Based Ionospheric Spatial Gradient Monitoring: Precision and Integrity Analysis," in *Proceedings of the ION 2015 Pacific PNT Meeting, Honolulu, Hawaii, April 2015*, pages 799–814, 2015.

[13] P. J. G. Teunissen, *Testing theory, an introduction*. Delft University Press, Delft, The Netherlands, 2000.

[14] G. Xie, *Optimal on-airport monitoring of the integrity of GPS-based landing systems*. PhD thesis, Stanford University, 2004.

[15] P. J. G. Teunissen and A. Kleusberg, *GPS for Geodesy*. Berlin; New York: Springer, second ed., 1998.

[16] R. Odolinski, P. J. G. Teunissen, and D. Odijk, "First combined COMPASS/BeiDou-2 and GPS positioning results in Australia. Part I: single-receiver and relative code-only positioning," *Journal of Spatial Science*, vol. 59, no. 1, pages 3–24, 2014.

[17] M. Felux, J. Lee, and F. Holzapfel, "GBAS ground monitoring requirements from an airworthiness perspective," *GPS Solutions*, vol. 19, no. 3, pages 1–9, 2014.

[18] J. R. I. Christie, P. Y. Ko, A. Hansen, D. Dai, S. Pullen, B. S. Pervan, and B. W. Parkinson, "The effects of local ionospheric decorrelation on LAAS: theory and experimental results," in *Proceedings of the 1999 National Technical Meeting of The Institute of Navigation, San Diego, CA, January 1999*, pages 769–777, 1999.

[19] M. Luo, S. Pullen, J. Dennis, H. Konno, G. Xie, T. Walter, P. Enge, S. Datta-Barua, and T. Dehel, "LAAS ionosphere spatial gradient threat model and impact of LGF and airborne monitoring," *Proceedings of ION GPS/GNSS 2003, Portland, OR, September 2003*, pages 9–12, 2003.

[20] B. Belabbas, M. Dautermann, M. Fluex, M. Rippl, S. Schulter, V. Wilken, A. Hornbostel, and M. Meurer, "A GBAS testbed to support new monitoring algorithms development for CAT III precision approach," in *ENC GNSS, Braunschweig, Germany, November 2010*, 2010.

[21] T. Walter, A. Hansen, J. Blanch, P. Enge, T. Mannucci, X. Pi, L. Sparks, B. Iijima, B. El-Arini, R. Lejeune, and M. Hagen, "Robust detection of ionospheric irregularities," *Navigation*, vol. 48, no. 2, pages 89–100, 2001.

[22] O. Osechas and J. Rife, "Distributed ionosphere monitoring by collaborating mobile receivers," *IEEE Transactions on Aerospace Electronic Systems*, vol. 50, no. 4, pages 2860–2869, 2014.

[23] P. J. G. Teunissen, "The least-squares ambiguity decorrelation adjustment: a method for fast GPS integer ambiguity estimation," *Journal of Geodesy*, vol. 70, no. 1-2, pages 65–82, 1995.

[24] P. J. G. Teunissen, "An optimality property of the integer least-squares estimator," *Journal of Geodesy*, vol. 73, no. 11, pages 587–593, 1999.

[25] L. Gratton, S. Khanafseh, B. Pervan, S. Pullen, J. Warburton, and W. J. Hughes, "Experimental observations and integrity monitor applications of LAAS IMLA carrier phase measurements," in *Proceedings of ION GNSS 2004, Long Beach, CA, September 2004*, pages 2259–2270, 2004.

[26] P. J. G. Teunissen, "Towards a least-squares framework for adjusting and testing of both functional and stochastic model, Internal research memo.," *Geodetic Computing Centre, Delft, reprint of original 1988 report (2004)*, no. 26, 1988.

[27] A. R. Amiri-Simkooei and C. C. J. M. Tiberius, "Assessing receiver noise using GPS short baseline time series," *GPS solutions*, vol. 11, no. 1, pages 21–35, 2007.

REFRENCES

Afifi A, El-Rabbany A (2014) Single Frequency GPS/Galileo Precise Point Positioning Using Un-Differenced and Between-Satellite Single Difference Measurements. GEOMATICA 68:195–205

Amiri-Simkooei AR, Tiberius CCJM (2007) Assessing receiver noise using GPS short baseline time series. GPS Solutions 11(1):21–35

Amiri-Simkooei AR, Teunissen PJG, Tiberius CCJM (2009) Application of least-squares variance component estimation to GPS observables. Journal of Surveying Engineering 135(4):149–160

Baarda W (1968) A testing procedure for use in geodetic networks. Publications on geodesy (ISSN 0165-1706 2(5)

Baarda W (1973) S-transformations and criterion matrices. Publications on geodesy/Netherlands geodetic commission NS 5(1)

BaardaW, Commission NG, et al (1967) Statistical concepts in geodesy, vol 2. Rijkscommissie voor Geodesie

Babu R,Mula P, Ratnakara SC, Ganeshan AS (2015) IRNSS Satellite Parameter Estimation using Combination Strategy. Global Journal of Science Frontier Research 15(3)

de Bakker PF, Tiberius CCJM, van der Marel H, van Bree RJP (2012) Short and zero baseline analysis of GPS L1 C/A, L5Q, GIOVE E1B, and E5aQ signals. GPS Solutions 16(1):53–64

Basseville M, Nikiforov IV, et al (1993) Detection of abrupt changes: theory and application, vol 104. Prentice Hall Englewood Cliffs

Belabbas B, Meurer M (2012) Carrier phase and code based absolute slant ionosphere gradient monitor for GBAS. In: Proceedings of the Institute of Navigation, Nashville, TN, USA, pp 2201–2208

Belabbas B, Dautermann M, Fluex M, Rippl M, Schulter S, Wilken V, Hornbostel A, Meurer M (2010) A GBAS testbed to support new monitoring algorithms development for CAT III precision approach. In: ENC GNSS

Belabbas B, Remi P, Meurer M, Pullen S (2011) Absolute slant ionosphere gradient monitor for GAST-D: Issues and opportunities. In: Proceedings of the 24th

International Technical Meeting of The Satellite Division of the Institute of Navigation (ION GNSS 2011), Portland, OR, September 2011, pp 2993–3002

Bensky A (2016) Wireless positioning technologies and applications. Artech House

Blaunstein N, Plohotniuc E (2008) Ionosphere and applied aspects of radio communication and radar. CRC Press

Bourne H, Morton Y (2013) GPS receiver ionosphere error correction based on spatial gradients and IGS satellite DCBs. In: Proceedings of the ION 2013 Pacific PNT Meeting, Honolulu, Hawaii, April 2013, pp 685–693

Buist PJ (2007) The baseline constrained LAMBDA method for single epoch, single-frequency attitude determination applications. In: Proceedings of the 20th International Technical Meeting of the Satellite Division of The Institute of Navigation (ION GNSS 2007), ION, pp 2962–2973

Cameron A, Reynolds T (2014) Power loss created trouble aboard Galileo satellite. http://www.gpsworld.com/trouble-aboard-galileo-satellite/

Cai C, Luo X, Liu Z, Xiao Q (2014) Galileo Signal and Positioning Performance Analysis Based on Four IOV Satellites. Navigation 67:810–824

Cai C, Gao Y, Pan L, Zhu J (2015) Precise point positioning with quad-constellations: GPS, BeiDou, GLONASS and Galileo. Advances in Space Research 56:133–143

Cai C, He C, Santerre R, Pan L, Cui X, Zhu J (2016) A comparative analysis of measurement noise and multipath for four constellations: GPS, BeiDou, GLONASS and Galileo. Survey Review 48:287–295

Cameron A, Reynolds T (2014) Power Loss Created Trouble Aboard Galileo Satellite. Available from Available from: http://gpsworld.com/trouble-aboard-galileo-satellite/, published 8 July 2014, accessed 18 April 2017

Chandrasekhar MV, Rajarajan D, Satyanarayana G, Tirmal N, Rathnakara SC, Ganeshan AS (2015) Modernized IRNSS Broadcast Ephemeris Parameters. Control Theory and Informatics 5(2):1–9

Christie J, Pervan B, Enge P, Powell J, Parkinson B, Ko P (1998) Analytical and experimental observations of ionospheric and tropospheric decorrelation effects for differential satellite navigation during precision approach. In: Proceedings of ION GPS, Institute of Navigation, vol 11, pp 739–748

Christie JR, Ko PY, Hansen A, Dai D, Pullen S, Pervan BS, Parkinson BW (1999) The effects of local ionospheric decorrelation on LAAS: theory and experimental results pp 769–777

Circiu MS, Felux M, Remi P, Yi L, Belabbas B, Pullen S (2014) Evaluation of dual frequency GBAS performance using flight data. In: Proceedings of the 2014 International Technical Meeting of The Institute of Navigation, San Diego, California, pp 645–656

CODE (2015) Global ionosphere maps produced by CODE. URL ftp://ftp.unibe.ch/aiub/CODE/2015/

CODE (2016) Global ionosphere maps produced by CODE. Available from : ftp://ftp.unibe.ch/aiub/CODE/2016, accessed 11 July 2016

Cohen C (1992) Attitude determination using GPS, Ph.D. Thesis. Stanford University

CSNO (2013) Report on the Development of BeiDou Navigation Satellite System, Version 2.2, China Satellite Navigation Office. Technical report

Damen MO (2003) On maximum-likelihood detection and the search for the closest lattice point. IEEE Transaction on Information Theory 49(10)

Datta-Barua S, Walter T, Pullen S, Luo M, Blanch J, Enge P (2002) Ionospheric Threat Parameterization for Local Area Global-Positioning-System-Based Aircraft Landing Systems. In: Proceedings of the 2002 National Technical Meeting of The Institute of Navigation, San Diego, CA, January 2002, pp 523–530

de Bakker PF, van der Marel H, Tiberius CC (2009) Geometry-free undifferenced, single and double differenced analysis of single frequency GPS, EGNOS and GIOVE-A/B measurements. GPS Solutions 13(4):305–314

de Bakker PF, Tiberius CC, Van Der Marel H, van Bree RJ (2012) Short and zero baseline analysis of GPS L1 C/A, L5Q, GIOVE E1B, and E5aQ signals. GPS Solutions 16(1):53–64

Diessongo TH, Schüler T, Junker S (2014) Precise position determination using a Galileo E5 single-frequency receiver. GPS Solutions 18(1):73–83

Dvorkin VV, Nosenko YI, Urlichich YM, Finkel'shtein AM (2009) The Russian Global Navigation Satellite Program. Herald of the Russian Academy of Sciences 79:7–13

ESA (2016a) Galileo Fact Sheet. Available from: http://esamultimedia.esa.int/docs/galileo/Galileo-factsheet-2016.pdf, accessed 15 March 2017

ESA (2016b) What is Galileo? Available from http://www.esa.int/Our_Activities/Navigation/Galileo/What_is_Galileo

Enge P (1999) Local area augmentation of GPS for the precision approach of aircraft. In: Proceedings of the IEEE, vol 87, pp 111–132

Estey LH, Meertens CM (1999) TEQC: the multi-purpose toolkit for GPS/GLONASS data. GPS Solutions 3(1):42–49

Euler HJ, Goad CC (1991) On optimal filtering of GPS dual frequency observations without using orbit information. Bulletin Geodesique 65(2):130–143

European Commission (2015) European GNSS (Galileo) Open Service Signal In Space Interface Control Document (OS SIS ICD)

Felux M, Lee J, Holzapfel F (2014) GBAS ground monitoring requirements from an airworthiness perspective. GPS Solutions 19(3): 393–401

Gaglione S, Angrisano A, Castaldo G, Freda P, Gioia C, Innac A, Troisi S, Del Core G (2015) The first Galileo FOC satellites: From useless to essential. In: Geoscience and Remote Sensing Symposium (IGARSS), 2015 IEEE International, IEEE, pp 3667–3670, DOI 10.1109/IGARSS.2015.7326618

Ganeshan AS (2012) Overview of GNSS and Indian Navigation Program. In: GNSS User Meeting, 23 Feb. 2012, ISRO Satellite Center, Bangalore

Ganeshan AS (2015) The complete constellation of 7 satellites of IRNSS will be deployed by 2016. http://mycoordinates.org/?cat=15

Ganeshan AS, Ratnakara SC, Srinivasan N, Rajaram B, Tirmal N, K A (2015) First Position Fix with IRNSS. Available from: http://www.insidegnss.com/node/4545, accessed 19 April 2016. Inside GNSS pp 48–52

Gioia C, Borio D, Angrisano A, Gaglione S, Fortuny-Guasch J (2015) A Galileo IOV assessment: measurement and position domain. GPS Solutions 19:187–199

Giorgi G (2014) On ionosphere-induced error detection for gnss integrity monitoring. In: Aerospace Conference, 2014 IEEE, pp 1–9

Giorgi G, Buist PJ (2008) Single-epoch, single-frequency, standalone full attitude determination: experimental results. In: Proceedings of the Fourth ESA Workshop on Satellite Navigation User Equipment Technologies, NAVITEC. ESA-ESTEC, The Netherlands

Giorgi G, Teunissen PJG, Buist PJ (2008) A search and shrink approach for the baseline constrained LAMBDA method: experimental results. In: Yasuda A (ed) Proceedings of International Symposium on GPS/GNSS, Tokyo University of Marine Science and Technology, pp 797–806

Giorgi G, Teunissen PJG, Verhagen S, Buist PJ (2010) Testing a new multivariate GNSS carrier phase attitude determination method for remote sensing platforms. Advance in Space Research 46(2):118–129

Giorgi G, Henkel P, Gunther C (2012) Testing of a statistical approach for local ionospheric disturbances detection. In: Proceedings of the IEEE-ION PLANS, Myrtle Beach, SC, USA, pp 167–173

Godha S, Cannon M (2007) GPS/MEMS INS integrated system for navigation in urban areas. GPS Solutions 11(3):193–203

GPS (2017) Space Segment. Available from: http://www.gps.gov/systems/gps/space/#orbits, published 6 June 2017, accessed 4 July 2017

GPS Directorate (2011) Navstar GPS Space Segment/User Segment L5 interfaces (IS-GPS-705B). Technical report.

GPS World (2015a) Final GLONASS-M Satellite Passes Tests. Available from: http://gpsworld.com/final-glonassm-satellite-passes-tests/, accessed 2 February 2016.

GPS World (2015b) ISRO: All 7 IRNSS Satellites in Orbit by March. Available from: http://gpsworld.com/isroall-7-irnss-satellites-in-orbit-by-march, published 8 October 2015, accessed 2 November 2015

GPS World (2016) First GPS III satellite completes critical test. Available from: http://gpsworld.com/first-gpsiii-satellite-completes-critical-test/, published 19 January 2016, accessed 9 August 2016

GPSD (2013) Navstar GPS space segment/navigation user segment interface, Revision F (IS-GPS-200H:24-Sep-2013), global positioning system directorate

Gratton L, Pervan B (2005) Airborne and ground monitors for ionospheric front detection for the local area augmentation system using carrier phase measurements.

In: Proceedings of the 18th International Technical Meeting of the Satellite Division of The Institute of Navigation (ION GNSS 2005), Long Beach, CA, September 2005, pp 748–757

Gratton L, Khanafseh S, Pervan B, Pullen S, Warburton J, Hughes WJ (2004) Experimental observations and integrity monitor applications of LAAS IMLA carrier phase measurements. In: Proceedings of the 17th International Technical Meeting of the Satellite Division of The Institute of Navigation (ION GNSS 2004), Long Beach, CA, September 2004, pp 2259–2270

GSA (2017) Galileo Programme. https://www.gsc-europa.eu/galileo-gsc-overview/programme

Guo F, Li X, Zhang X, Wang J (2017) Assessment of precise orbit and clock products for Galileo, BeiDou, and QZSS from IGS Multi-GNSS Experiment (MGEX). Survey Review 21:279–290

Harde H, Shahade MR, Badnore D (2015) INDIAN REGIONAL NAVIGATION SATELLITE SYSTEM. International Journal of Research In Science & Engineering 1:36–42

Harville DA (1997) Matrix Algebra From A Statistician's Perspective. Springer, New York

Hatch R (1983) The synergism of GPS code and carrier measurements. In: International geodetic symposium on satellite doppler positioning, vol 1, pp 1213–1231

Hatch R (1986) Dynamic differential GPS at the centimetre level. In: Proceedings of the Fourth International Geodetic Symposiumon Satellite Positioning, vol 2, pp 1287–98

Hauschild A, Grillmayer G, Montenbruck O, Markgraf M, V¨orsmann P (2008) GPS based attitude determination for the flying laptop satellite. In: Small Satellites for Earth Observation, Springer, pp 211–220

Hauschild A, Montenbruck O, Sleewaegen JM, Huisman L, Teunissen PJ (2012) Characterization of compass M-1 signals. GPS Solutions 16(1):117–126

Hegarty C, Powers E, Fonville B (2004) Accounting for timing biases between GPS, modernized GPS, and Galileo signals. In: Proceedings of 36th annual Precise Time and Time Interval (PTTI) meeting, Washington, DC, 7–9 Dec, pp. 307–317

Hellemans A (2014) A simple plumbing problem sent Galileo satellites into wrong orbits. http://spectrum.ieee.org/tech-talk/aerospace/satellites/a-simple-plumbing-problem-sent-galileo-satellites-into-wrong-orbits

Henderson H, Pukelsheim F, Searle S (1983) On the history of the Kronecker product. Linear Multilinear Algebra 14(2):113–120

Hide C, Pinchin J, Park D (2007) Development of a low cost multiple GPS antenna attitude system. In: Proceedings of ION GNSS, pp 88–95

Hodgart MS, Purivigraipong S (2000) New Approach to Resolving Instantaneous Integer Ambiguity Resolution for Spacecraft Attitude Determination Using GPS Signals. In: Proceedings of IEEE Position Location and Navigation Symposium, IEEE, pp 132–139

Hofmann-Wellenhof B, Lichtenegger H, Wasle E (2008) GNSS-Global Navigation Satellite Systems, GPS, GLONASS, Galileo and more. Springer-Verlag

Hofmann-Wellenhof B, Lichtenegger H, Collins J (2013) Global positioning system: theory and practice. Springer Science & Business Media

IAC (2016) GLONASS constellation status. Available from: https://www.glonass-iac.ru/en/GLONASS/, accessed 2 February 2016.

ICD-GLONASS (2008) Global Navigation Satellite System GLONASS Interface Control Document, version 5.1, Moscow

IGS and RTCM-SC104 (2015) RINEX—The receiver independent exchange format, Version 3.03, 14 July. International GNSS Service (IGS), RINEX Working Group and Radio Technical Commission for Maritime Services Special Committee

ISRO (2014a) INDIAN REGIONAL NAVIGATION SATELLITE SYSTEM: signal in space ICD for standard positioning service, Version 1.0. ISRO Satellite Centre, June 2014

Jiang N, Xu Y, Xu T, Xu G, Sun Z, Schuh H (2016) GPS/BDS short-term ISB modelling and prediction. GPS Solutions. doi:10.1007/s10291-015-0513-x

Jing J, Khanafseh S, Chan FC, Langel S, Pervan B (2012) Detecting ionospheric gradients for GBAS using a null space monitor. In: Proceedings of the IEEE-ION PLANS, Myrtle Beach, SC, USA,, pp 1125–1133

Julien O, Alves P, Cannon ME, Zhang W (2003) A tightly coupled GPS/GALILEO combination for improved ambiguity resolution. In: Proceedings of ENC-GNSS 2003, Graz, Austria, 22–25 April

Karutin S (2012) GLONASS signals and augmentations. In: Proc. ION GNSS 2012, ION, pp 3878–3911

Khanafseh S, Pullen S, Warburton J (2012) Carrier phase ionospheric gradient ground monitor for GBAS with experimental validation. Journal of The Institute of Navigation

Khodabandeh A, Teunissen PJG (2014) Array-based satellite phase bias sensing: theory and GPS/BeiDou/QZSS results. Measurement Science and Technology 25(9):095,801

Khodabandeh A, Teunissen PJG (2015) Single-Epoch GNSS Array Integrity: an Analytical Study. IAG Symp 142, accepted for publication

Kim D, Langley RB (2000) The multipath divergence problem in GPS carrier-smoothed code pseudorange. In: Proceedings of 47th Annual Conference of the Canadian Aeronautics and Space, pp 161–163

Klobuchar J (1996) Ionospheric effects on GPS. Global Positioning System: Theory and applications 1:485–515

Kuipers JB (2002) Quaternions and rotation sequences. Princeton University Press, Princeton

Kumari A, Samal K, Rajarajan D, Swami U, Babu R, Kartik A, Rathnakara SC, Ganeshan AS (2015) Precise Modeling of Solar Radiation Pressure for IRNSS Satellite. Journal of Natural Sciences Research 5(3):35–43

Langley R (2014) ESA Discusses Galileo Satellite Power Loss, Upcoming Launch. Available from Available from: http://gpsworld.com/esa-discusses-galileo-satellite-power-loss-upcoming-launch/, published 20 August 2014, accessed 18 April 2017

Langley RB, Banville S, Steigenberger P (2012) First results: precise positioning with Galileo prototype satellites. GPS World 23:45–49

Leick A (2003) GPS Satellite Surveying. Wiley, New York

Leick A, Rapoport L, Tatarnikov D (2015) GPS satellite surveying. Wiley, New York

Li Y, Zhang K, Roberts C, Murata M (2004) On-the-Fly GPS-Based Attitude Determination Using Single- and Double-Differenced Carrier Phase Measurements. GPS Solutions 8(2):93–102

Li X, Ge M, Dai X, Ren X, Fritsche M, Wickert J, Schuh H (2015) Accuracy and reliability of multi-GNSS real-time precise positioning: GPS, GLONASS, BeiDou, and Galileo. Journal of Geodesy 89:607–635

Liu T, Yuan Y, Zhang B, Wang N, Tan B, Chen Y (2017) Multi-GNSS precise point positioning (MGPPP) using raw observations. Journal of Geodesy 91(3):253–268

Lockheed Martin (2013) Lockheed Martin Powers on the First GPS III Satellite. Available from: http://www.lockheedmartin.com.au/us/news/pressreleases/2013/february/Feb28.html , published 28 February 2013, accessed 9 August 2016

Lou Y, Zheng F, Gu S, Wang C, Guo H, Feng Y (2016) Multi-GNSS precise point positioning with raw single-frequency and dual-frequency measurement models. GPS Solutions 20:849–862

Lu G (1995) Development of a GPS multi-antenna system for attitude determination, Ph.D. Thesis. University of Calgary

Luo M, Pullen S, Akos D, Xie G, Datta-Barua S, Walter T, Enge P (2002) Assessment of ionospheric impact on LAAS using WAAS supertruth data. In: Proceedings of the 58th Annual Meeting of The Institute of Navigation and CIGTF 21st Guidance Test Symposium, Albuquerque, NM, pp 175–186

Luo M, Pullen S, Dennis J, Konno H, Xie G,Walter T, Enge P, Datta-Barua S, Dehel T (2003) LAAS ionosphere spatial gradient threat model and impact of LGF and airborne monitoring. Proceedings of ION GPS 2003 pp 9–12

Madsen J, Lightsey EG (2004) Robust spacecraft attitude determination using global positioning system receivers. Journal of Spacecraft and Rockets 41(4):635–644 Magnus JR (1988) Linear structures. London School of Economics and Political Science, Charles Griffin & Company LTD

Magnus JR, Neudecker H, et al (1995) Matrix differential calculus with applications in statistics and econometrics. John Wiley & Sons

Marquis W, Shaw M (2016) GPS III: Bringing new capabilities to the global community. Available from: http://www.insidegnss.com/auto/sepoct11-Marquis.pdf, accessed 9 August 2016. Inside GNSS pp 34–48

Melgard T, Tegedor J, Jong K de, Lapucha D, Lachapelle G (2013) Interchangeable integration of GPS and Galileo by using a common system clock in PPP. In: Proceedings of ION GNSS + 2013, Nashville, TN, 16–20 Sept, pp. 1198–1206

Montenbruck O, Steigenberger SR (2015) IRNSS orbit determination and broadcast ephemeris assessment. In: Proceedings of the 2015 International Technical Meeting of The Institute of Navigation, Dana Point, California, January 2015, pp 185–193

Montenbruck O, Hauschild A, Hessels U (2011) Characterization of GPS/GIOVE sensor stations in the CONGO network. GPS Solutions 15(3):193–205

Montenbruck O, Schmid R, Mercier F, Steigenberger P, Noll C, Fatkulin R, Kogure S, Ganeshan AS (2015) GNSS satellite geometry and attitude models. Advances in Space Research 56(6):1015–1029

Mozo Garcia A, Piriz R, Lainez Samper MD, Romay Merino MM (2010) Multisystem Real Time Precise-Point-Positioning, today with GPS+GLONASS in the near future also with QZSS, Galileo, Compass, IRNSS. In: International Symposium on GPS/GNSS, Taipei, Taiwan, October 2010

Murai Y (2015) Project Overview of the Quasi-Zenith Satellite System, In: Proceedings of ION GNSS+ 2015, Tampa, FL, 14 – 18 September, pp. 1291-1332

Murphy T, Harris M, Pullen S, Pervan B, Saito S, Brenner M (2010) Validation of ionospheric anomaly mitigation for GAST-D. ICAO NSP Working Group of the Whole (WGW) Meeting, Montreal, Canada, WGW/WP 14

Nadarajah N, Teunissen PJG (2014) Instantaneous GPS/Galileo/QZSS/SBAS Attitude Determination: A Single-Frequency (L1/E1) Robustness Analysis under Constrained Environments. Navigation 61(1):65–75

Nadarajah N, Teunissen PJG, Buist PJ, Steigenberger P (2012) First results of instantaneous GPS/Galileo/COMPASS attitude determination. In: Satellite Navigation Technologies and European Workshop on GNSS Signals and Signal Processing, (NAVITEC), 2012 6th ESA Workshop on, IEEE, pp 1–8

Nadarajah N, Teunissen PJG, Raziq N (2013) Instantaneous GPS–Galileo attitude determination: single-frequency performance in satellite-deprived environments. IEEE Transactions on Vehicular Technology 62(7):2963–2976

Nadarajah N, Teunissen PJG, Raziq N (2014) Instantaneous BeiDou–GPS attitude determination: a performance analysis. Advances in Space Research 54(5):851–862

Nadarajah N, Khodabandeh A, Teunissen PJG (2015) Assessing the IRNSS L5-signal in combination with GPS, Galileo, and QZSS L5/E5a-signals for positioning and navigation. GPS Solutions 20(2):289–297

Niell AE (1996) Global mapping functions for the atmosphere delay at radio wavelengths. Journal of Geophysical Research: Solid Earth (1978–2012) 101(B2):3227–3246

Odijk D, Teunissen PJG, Huisman L (2012) First results of mixed GPS+GIOVE single-frequency RTK in Australia. Journal of Spatial Science 57:3–18

Odijk D, Teunissen PJ (2013a) Characterization of between-receiver GPS-Galileo inter-system biases and their effect on mixed ambiguity resolution. GPS Solutions 17(4):521–533

Odijk D, Teunissen PJ (2013b) Estimation of differential inter-system biases between the overlapping frequencies of GPS, Galileo, BeiDou and QZSS. In: Proceedings of the 4th International Colloquium Scientific and Fundamental Aspects of the Galileo Programme. 4–6 December, Prague, Czech Republic

Odijk D, Teunissen PJG (2008) ADOP in closed form for a hierarchy of multi-frequency single-baseline GNSS models. Journal of Geodesy 82(8):473–492

Odijk D, Teunissen PJG, Huisman L (2012) First results of mixed GPS+GIOVE single-frequency RTK in Australia. Journal of Spatial Science 57(1):3–18

Odijk D, Nadarajah N, Zaminpardaz S, Teunissen PJG (2017) GPS, Galileo, QZSS and IRNSS differential ISBs: estimation and application. GPS Solutions, Springer, 21(2):439-450

Odijk D, Teunissen PJG, Khodabandeh A (2014) Galileo IOV RTK positioning: standalone and combined with GPS. Survey Review 46:267–277

Odolinski R, Teunissen PJG (2016) Single-frequency, dual-GNSS versus dual-frequency, single-GNSS: a low-cost and high-grade receivers GPS-BDS RTK analysis. Journal of Geodesy pp 1–24, DOI 10.1007/s00190-016-0921-x

Odijk D, Zhang B, Khodabandeh A, Odolinski R, Teunissen PJG (2016) On the estimability of parameters in undifferenced, uncombined GNSS network and PPP-RTK user models by means of S-system theory. Journal of Geodesy 90(1):15–44

Odolinski R, Teunissen PJG, Odijk D (2014) First combined COMPASS/BeiDou-2 and GPS positioning results in Australia. Part I: single-receiver and relative code-only positioning. Journal of Spatial Science 59(1):3–24

Odolinski R, Teunissen PJG, Odijk D (2015) Combined BDS, Galileo, QZSS and GPS single-frequency RTK. GPS Solutions 19(1):151–163

Oleynik E (2012) GLONASS Status and Modernization. United Nations/Latvia Workshop on the Applications of Global Navigation Satellite Systems. Riga, Latvia

Osechas O, Rife J (2014) Distributed ionosphere monitoring by collaborating mobile receivers. IEEE Transactions on Aerospace Electronic Systems 50(4):2860–2869

Pan L,CaiC,Santerre R,Zhang X(2017) Performance evaluation of single-frequency point positioning with GPS, GLONASS, BeiDou and Galileo. Survey Review pp 1–9, DOI 10.1080/00396265.2016.1151628

Park B, Sohn K, Kee C (2008) Optimal Hatch filter with an adaptive smoothing window width. Journal of Navigation 61(03):435–454

Park C, Teunissen PJG (2003) A new carrier phase ambiguity estimation for GNSS attitude determination systems. In: Proceedings of international GPS/GNSS symposium, Tokyo, vol 8, pp 283–290

Park C, Teunissen PJG (2009) Integer least squares with quadratic equality constraints and its application to GNSS attitude determination systems. International Journal of Control, Automation and Systems 7(4):566–576

Paziewski J, Wielgosz P (2015) Accounting for Galileo-GPS intersystem biases in precise satellite positioning. Journal of Geodesy 89(1):81–93

Pervan B (2001) A review of LGF code-carrier divergence issues. Illinois Institute of Technology, MMAE Dept, May 29, 2001

Psiaki ML (2006) Batch algorithm for global-positioning system attitude determination and integer ambiguity resolution. Journal of guidance, control, and dynamics 29(5):1070–1079

Pullen S, Park YS, Enge P (2009a) Impact and mitigation of ionospheric anomalies on ground-based augmentation of GNSS. Radio Science 44(1)

Ran C (2011) Development of the BeiDou Navigation Satellite System, Global Navigation Satellite Systems: Report of a Joint Workshop of the National Academy of Engineering and the Chinese Academy of Engineering, Shanghai 24-25 May 2011, ed. By L. A. Davis, P. K. Enge, G. X. Gao (National Academies Press, Washington, DC 2012) 83–94

Rao CR (1973) Linear statistical inference and its applications Rao VG (2013) Proposed LOS fast TTFF signal design for IRNSS. University of Calgary

Rao VG, Lachapelle G, Vijaykumar SB (2001) Analysis of IRNSS over Indian subcontinent. In: Proceedings of the 2011 International Technical Meeting of The Institute of Navigation, San Diego, CA, January 2011, pp 1150–1162

Rethika T, Mishra S, Nirmala S, Rathnakara SC, Ganeshan AS (2013) Single frequency ionospheric error correction using coefficients generated from regional ionospheric data for IRNSS. Indian Journal of radio & Space Physics 42:125–130

Reussner N, Wanninger L (2011) GLONASS interfrequency biases and their effects on RTK and PPP carrier-phase ambiguity resolution. In: Proc. ION GNSS 2011, ION, pp 712 – 716

Saastamoinen J (1972) Atmospheric correction for the troposphere and stratosphere in radio ranging satellites. The use of artificial satellites for geodesy pp 247–251

Saikiran B, Vikram V (2013) IRNSS architecture and applications. Journal of Comm & Electron 1(3):21–27

Sarma AD, Sultana Q, Srinivas VS (2010) Augmentation of Indian regional navigation satellite system to improve dilution of precision. Journal of Navigation 63(02):313–321

Seeber G (1993) Satellite geodesy: foundations, methods, and applications. Berlin; New York: W de Gruyter, 19931

Sekar SB, Sengupta S, Bandyopadhyay K (2012) Spectral compatibility of BOC (5, 2) modulation with existing GNSS signals. In: Position Location and Navigation Symposium (PLANS), 2012 IEEE/ION, IEEE, pp 886–890

Simili D, Pervan B (2006) Code-carrier divergence monitoring for the GPS local area augmentation system. In: Position, Location, And Navigation Symposium, 2006 IEEE/ION, pp 483–493

Simsky A, Sleewaegen JM, Hollreiser M, Crisci M (2006) Performance Assessment of Galileo Ranging Signals Transmitted by GSTB-V2 Satellites. In: Proceedings of the 19th International Technical Meeting of the Satellite Division of The Institute of Navigation (ION GNSS 2006), ION, pp 1547–1559

Simsky A, Mertens D, Sleewaegen JM, Hollreiser M, Crisci M (2008a) Experimental Results for the Multipath Performance of Galileo Signals Transmitted by GIOVE-A Satellite. International Journal of Navigation and Observation pp 1–13, DOI 10.1155/2008/416380

Simsky A, Sleewaegen JM, Wilde WD, Hollreiser M, Crisci M (2008b) Multipath and Tracking Performance of Galileo Ranging Signals Transmitted by GIOVE-B. In: Proceedings of the 21th International Technical Meeting of the Satellite Division of The Institute of Navigation (ION GNSS 2008), ION, pp 1525–1536

Srinivas VS, Sarma AD, Reddy AS, Reddy DK (2014) Investigation of the effect of ionospheric gradients on GPS signals in the context of LAAs. Progress In Electromagnetics Research B 57:191–205

Steigenberger P, Montenbruck O (2016) Galileo status: orbits, clocks, and positioning. GPS Solutions 21(2):319–331

Steigenberger P, Hugentobler U, Montenbruck O (2013) First demonstration of Galileo-only positioning. GPS World 24:14–15

Suryanarayana Rao KN (2007) Indian Regional Navigation Satellite System. In: IEEE Seminar on Global Satellite Navigation and Applications, Hyderabad, India

T W (2011) The future of satellite navigation for aviation. Stanford's 2011 PNT Challenges and Opportunities Symposium

Takac F (2009) GLONASS inter-frequency biases and ambiguity resolution. Inside GNSS 4(2):24–28

Tegedor J, Øvstedal O (2014) Triple carrier precise point positioning (PPP) using GPS L5. Survey Review 46(337):288–297

Tegedor J, Øvstedal O, Vigen E (2014) Precise orbit determination and point positioning using GPS, Glonass, Galileo and BeiDou. Journal of Geodetic Science 4:65–73

Tegedor J, Øvstedal O, Vigen E (2015) Estimation of Galileo Uncalibrated Hardware Delays for Ambiguity-Fixed Precise Point Positioning. Navigation 63:173–179

Teunissen P (1997a) A canonical theory for short GPS baselines. Part IV: Precision versus reliability. Journal of Geodesy 71(9):513–525

Teunissen PJ (2010) Integer least-squares theory for the GNSS compass. Journal of Geodesy 84(7):433–447

Teunissen PJG (1988) Towards a least-squares framework for adjusting and testing of both functional and stochastic models. internal research memo, geodetic computing centre, delft (26)

Teunissen PJG (1989) Estimation in Nonlinear Models, II Hotine-Marussi Symposium on Mathematical Geodesy, Pisa, Italy, June 5-8

Teunissen PJG (1990a) GPS op afstand bekeken In: een halve eeuw in de goede richting . Lustrumboek Snellius 1985-1990, DUM Delft pp 215–233

Teunissen PJG (1990b) Quality control in integrated navigation systems. In: Position Location and Navigation Symposium, 1990. Record. The 1990's-A Decade of Excellence in the Navigation Sciences. IEEE PLANS'90., IEEE, IEEE, pp 158–165

Teunissen PJG (1991) The GPS phase-adjusted pseudorange. In: Proceedings of the 2nd international workshop on high precision navigation Stuttgart/Freudenstadt, Germany, pp 115–125

Teunissen PJG (1995) The least-squares ambiguity decorrelation adjustment: a method for fast GPS integer ambiguity estimation. Journal of geodesy 70(1-2):65–82

Teunissen PJG (1997b) A canonical theory for short GPS baselines. Part I: The baseline precision. Journal of Geodesy 71(6):320–336

Teunissen PJG (1998a) A proof of Nielsen's conjecture on the relationship between dilution of precision for point positioning and for relative positioning with GPS. IEEE on Aerospace and Electronic Systems 34(2):693–695

Teunissen PJG (1998b) On the integer normal distribution of the GPS ambiguities. Artificial satellites 33(2):49–64

Teunissen PJG (1998c) Success probability of integer GPS ambiguity rounding and bootstrapping. Journal of Geodesy 72(10):606–612

Teunissen PJG (1999) An optimality property of the integer least-squares estimator. Journal of Geodesy 73(11):587–593

Teunissen PJG (2000) ADOP based upperbounds for the bootstrapped and the least-squares ambiguity success rates. Artificial Satellites 35(4):171–179

Teunissen PJG (2001) Testing theory, an introduction. Delft University Press, Delft, The Netherlands

Teunissen PJG (2002) The parameter distributions of the integer GPS model. Journal of Geodesy 76(1):41–49

Teunissen PJG (2006) The LAMBDA method for the GNSS compass. Artificial Satellites 41(3):89–103

Teunissen PJG (2007) A general multivariate formulation of the multi-antenna GNSS attitude determination problem. Artificial Satellites 42(2):97–111

Teunissen PJG (2012) The affine constrained GNSS attitude model and its multivariate integer least-squares solution. Journal of Geodesy 86(7):547–563

Teunissen PJG, Amiri-Simkooei AR (2008) Least-squares variance component estimation. Journal of Geodesy 82(2):65–82

Teunissen PJG, De Bakker PF (2013) Single-receiver single-channel multi-frequency GNSS integrity: outliers, slips, and ionospheric disturbances. Journal of Geodesy 87(2):161–177

Teunissen PJG, Kleusberg A (1998) GPS for Geodesy, 2nd edn. Springer, Berlin; New York

Teunissen PJG, Odijk D (1997) Ambiguity dilution of precision: definition, properties and application. Proceedings of ION GPS-1997 pp 16–19

Teunissen PJG, Simons DG, Tiberius CCJM (2004) Probability and observation theory. Lecture Notes Delft University of Technology

Teunissen PJG, Giorgi G, Buist PJ (2011) Testing of a new single-frequency GNSS carrier phase attitude determination method: land, ship and aircraft experiments. GPS Solutions 15(1):15–28

Teunissen PJG, Huisman L, Hu C (2012) Real-time precise point positioning in NAD83: global and regional broadcast corrections compared. Journal of Surveying Engineering 139(1):1–10

Teunissen PJG, Odolinski R, Odijk D (2014) Instantaneous BeiDou+ GPS RTK positioning with high cut-off elevation angles. Journal of geodesy 88(4):335–350

Teunissen PJG, Khodabandeh A, Zhang B (2016) Multi-GNSS PPP-RTK: mixed-receiver network and user scenarios. In: International association of geodesy (IAG) symposia series, 26th IUGG General Assembly 2015, Prague, Czech Republic, 22 June–2 July

Thoelert S, Erker S, Furthner J, Meurer M, Gao GX, Heng L,Walter T, Enge P (2011) First Signal in Space Analysis of GLONASS K-1. In: Proc. ITM 2011, ION, pp 3076–3082

Thoelert S, Montenbruck O, Meurer M (2014) IRNSS-1A: signal and clock characterization of the Indian regional navigation system. GPS Solutions 18(1):147–152

Torre AD, Caporali A (2015) An analysis of intersystem biases for multi-GNSS positioning. GPS Solutions 19(2):297–307

Tranquilla JM, Cam JP, Al-Rizzo HM (1994) Analysis of a Choke Ring Groundplane for Multipath Control in Global Positioning System (GPS) Applications. IEEE Transactions on Antennas and Propagation 42(7):905–911

Tukey JW (1977) Explanatory Data Analysis, vol 1. Reading, Mass: Addison-Wesley Publishing Co

Urlichich Y, Subbotin V, Stupak G, Dvorkin V, Povaliaev A, Karutin S (2010) GLONASS Developing Strategy. In: Proc. 23rd ITM 2010, ION, pp 1566–1571

Urlichich Y, Subbotin V, Stupak G, Dvorkin V, Povaliaev A, Karutin S (2011) A new data processing strategy for combined GPS/GLONASS carrier phase-based positioning. In: Proc. ION GNSS 2011, ION, pp 3125–3128

Y. Urlichich, V. Subbotin, G. Stupak, V. Dvorkin, A. Povaliaev, S. Karutin: GLONASS Modernization, ION GNSS 2011, Portland, OR 20-23 Sep 2011 (ION, Virginia 2011) 3125–3128

Verhagen S, Teunissen PJG (2013) The ratio test for future GNSS ambiguity resolution. GPS Solutions 17(4):535–548

Verhagen S, Li B, Teunissen PJG (2013) Ps-LAMBDA: Ambiguity success rate evaluation software for interferometric applications. Computers & Geosciences 54:361–376

Verhagen S, Teunissen PJG (2014) Ambiguity resolution performance with GPS and BeiDou for LEO formation flying. Advances in Space Research 54(5):830–839

Walter T, Hansen A, Blanch J, Enge P, Mannucci T, Pi X, Sparks L, Iijima B, El-Arini B, Lejeune R, et al (2001) Robust detection of ionospheric irregularities. NAVIGATION, Journal of The Institute of Navigation 48(2):89–100

Wang B, Miao L, Wang S, Shen J (2009) A constrained LAMBDA method for GPS attitude determination. GPS Solutions 13(2):97–107

Wang C, Morton Y (2013) Ionosphere TEC and TEC gradients estimation using a regional GNSS network. In: Proceedings of the 26th International Technical Meeting

of The Satellite Division of the Institute of Navigation (ION GNSS+ 2013), Nashville, TN, September 2013, pp 1875–1880

Wang C, Wang J, Morton Y (2014) Regional ionospheric TEC gradients estimation using a single GNSS receiver. In: China Satellite Navigation Conference (CSNC) 2014 Proceedings: Volume II, Springer, pp 363–373 Wang J (1999) Stochastic modeling for real-time kinematic GPS/GLONASS positioning. Navigation 46(4):297–305

Wanninger L (2009) Carrier-phase inter-frequency biases of GLONASS receivers. Journal of Geodesy 86(2):139–148

Xie G (2004) Optimal on-airport monitoring of the integrity of GPS-based landing systems. PhD thesis, Stanford University

Xie G, Pullen S, Luo M, Normark PL, Akos D, Lee J, Enge P, Pervan B (2001) Integrity design and updated test results for the Stanford LAAS integrity monitor testbed. In: Proceedings of the 57th Annual Meeting of The Institute of Navigation (2001), Albuquerque, NM, June 2001, pp 681–693

Yamada Y, Takasu T, Kubo N, Yasuda A (2010) Evaluation and calibration of receiver inter-channel biases for RTK-GPS/GLONASS. In: Proc. ION GNSS 2010, ION, pp 1580–1587

Yuan Y, Zhang B (2014) Retrieval of inter-system biases (ISBs) using a network of multi-GNSS receivers. J Glob Position Syst 13(1):22–29

Zaminpardaz S (2016) Horizon-to-elevation Mask: A Potential Benefit to Ionospheric Gradient Monitoring. ION GNSS+2016, pp. 1764-1779. The Institute of Navigation, Portland, Oregon

Zaminpardaz S, Teunissen PJG, Nadarajah N, Khodabandeh A (2015) GNSS Array-Based Ionospheric Spatial Gradient Monitoring: Precision and Integrity Analysis. ION Pacific PNT 2015, pp. 799-814. The Institute of Navigation, Honolulu, Hawaii

Zaminpardaz S, Teunissen PJG, Nadarajah N (2016a) IRNSS stand-alone positioning: first results in Australia. Journal of Spatial Science, Taylor & Francis, 61(1):5-27

Zaminpardaz S, Teunissen PJG, Nadarajah N (2016b) GLONASS CDMA L3 Ambiguity Resolution. Inside GNSS, 11(4):44-47

Zaminpardaz S, Teunissen PJG (2017) Analysis of Galileo IOV+FOC Signals and E5 RTK performance. GPS Solutions, Springer, 21(4):1855-1870

Zaminpardaz S, Teunissen PJG, Nadarajah N (2017a) IRNSS/NavIC Single-Point Positioning: A Service Area Precision Analysis. Marine Geodesy, Taylor & Francis, 40(4):259-274

Zaminpardaz S, Teunissen PJG, Nadarajah N (2017b) IRNSS/NavIC and GPS: A Single and Dual System L5 Analysis. Journal of Geodesy, Springer, 91(8):915-931

Zaminpardaz S, Teunissen PJG, Nadarajah N (2017c) L5 RTK Over India: IRNSS and GPS. Inside GNSS, 12(1):48-55

Zaminpardaz S, Teunissen PJG, Nadarajah N (2017d) IRNSS/NavIC L5 Attitude Determination. Sensors, MDPI, 17(2), 274, DOI 10.3390/s17020274

Zaminpardaz S, Teunissen PJG, Nadarajah N (2017e) Single-frequency L5 attitude determination from IRNSS/NavIC and GPS: a single- and dual-system analysis. Journal of Geodesy, Springer, 91(12):1415-1433

Zaminpardaz S, Teunissen PJG, Nadarajah N (2017f) GLONASS CDMA L3 ambiguity resolution and positioning. GPS Solutions, Springer, 21(2):535-549

Zhang B, Teunissen PJG (2015) Characterization of multi-GNSS between-receiver differential code biases using zero and short baselines. Sci Bull 60(21):1840–1849

Zhao L, Li L, Zhao X (2009) An adaptive Hatch filter to minimize the effects of ionosphere and multipath for GPS single point positioning. In: Mechatronics and Automation, 2009. ICMA 2009. International Conference on, IEEE, pp 4167–4172

Zhu J, Santerre R (2002) Improvement of GPS phase ambiguity resolution using prior height information as a quasi-observation. Geomatica 56(3):211–221

APPENDIX A COPYRIGHT PERMISSION STATEMENTS

I warrant that I have obtained, where necessary, permission from the copyright owners to use any third-party copyright material reproduced in this thesis, or to use any of my own published work (e.g. journal articles) in which the copyright is held by another party (e.g. publisher, co-author). These permissions are all attached below.

Safoora Zaminpardaz

Permissions of the following **Springer** publications are attached in the forthcoming pages:

1) Odijk D., Nadarajah N., Zaminpardaz S., Teunissen P.J.G (2017) GPS, Galileo, QZSS and IRNSS differential ISBs: estimation and application. GPS Solutions, **Springer**, 21(2):439-450

2) Zaminpardaz S., Teunissen P.J.G, Nadarajah N. (2017b) IRNSS/NavIC and GPS: A Single and Dual System L5 Analysis. Journal of Geodesy, **Springer**, 91(8):915-931

3) Zaminpardaz S., Teunissen P.J.G, Nadarajah N. (2017e) Single-frequency L5 attitude determination from IRNSS/NavIC and GPS: a single- and dual-system analysis. Journal of Geodesy, **Springer**, 91(12):1415-1433

4) Zaminpardaz S., Teunissen P.J.G (2017) Analysis of Galileo IOV+FOC Signals and E5 Single-frequency RTK performance. GPS Solutions, **Springer**, 21(4):1855-1870

SPRINGER LICENSE
TERMS AND CONDITIONS

Jul 01, 2017

This Agreement between Safoora Zaminpardaz ("You") and Springer ("Springer") consists of your license details and the terms and conditions provided by Springer and Copyright Clearance Center.

License Number	4140090302428
License date	Jul 01, 2017
Licensed Content Publisher	Springer
Licensed Content Publication	GPS Solutions
Licensed Content Title	GPS, Galileo, QZSS and IRNSS differential ISBs: estimation and application
Licensed Content Author	Dennis Odijk
Licensed Content Date	Jan 1, 2016
Licensed Content Volume	21
Licensed Content Issue	2
Type of Use	Book/Textbook
Requestor type	Publisher
Publisher	N/A
Portion	Full text
Format	Print and Electronic
Will you be translating?	No
Print run	20
Author of this Springer article	Yes and you are the sole author of the new work
Order reference number	
Title of new book	New Generation GNSS\RNSS: Algorithms, Numerical Analyses and Applications
Publisher	N/A
Author of new book	Safoora Zaminpardaz
Expected publication date of new book	Feb 2018
Estimated size of new book (pages)	100
Requestor Location	Safoora Zaminpardaz GPO Box U1987, Curtin University Department of Spatial Sciences GNSS Research Center Perth, WA 6845 Australia Attn:
Billing Type	Invoice
Billing Address	Safoora Zaminpardaz GPO Box U1987, Curtin University

Department of Spatial Sciences
GNSS Research Center
Perth, Australia 6845
Attn:

Total 0.00 USD

Terms and Conditions

Introduction
The publisher for this copyrighted material is Springer. By clicking "accept" in connection with completing this licensing transaction, you agree that the following terms and conditions apply to this transaction (along with the Billing and Payment terms and conditions established by Copyright Clearance Center, Inc. ("CCC"), at the time that you opened your Rightslink account and that are available at any time at http://myaccount.copyright.com).
Limited License
With reference to your request to reuse material on which Springer controls the copyright, permission is granted for the use indicated in your enquiry under the following conditions:
- Licenses are for one-time use only with a maximum distribution equal to the number stated in your request.
- Springer material represents original material which does not carry references to other sources. If the material in question appears with a credit to another source, this permission is not valid and authorization has to be obtained from the original copyright holder.
- This permission
• is non-exclusive
• is only valid if no personal rights, trademarks, or competitive products are infringed.
• explicitly excludes the right for derivatives.
- Springer does not supply original artwork or content.
- According to the format which you have selected, the following conditions apply accordingly:
• **Print and Electronic:** This License include use in electronic form provided it is password protected, on intranet, or CD-Rom/DVD or E-book/E-journal. It may not be republished in electronic open access.
• **Print:** This License excludes use in electronic form.
• **Electronic:** This License only pertains to use in electronic form provided it is password protected, on intranet, or CD-Rom/DVD or E-book/E-journal. It may not be republished in electronic open access.
For any electronic use not mentioned, please contact Springer at permissions.springer@spi-global.com.
- Although Springer controls the copyright to the material and is entitled to negotiate on rights, this license is only valid subject to courtesy information to the author (address is given in the article/chapter).
- If you are an STM Signatory or your work will be published by an STM Signatory and you are requesting to reuse figures/tables/illustrations or single text extracts, permission is granted according to STM Permissions Guidelines: http://www.stm-assoc.org/permissions-guidelines/
For any electronic use not mentioned in the Guidelines, please contact Springer at permissions.springer@spi-global.com. If you request to reuse more content than stipulated in the STM Permissions Guidelines, you will be charged a permission fee for the excess content.
Permission is valid upon payment of the fee as indicated in the licensing process. If permission is granted free of charge on this occasion, that does not prejudice any rights we might have to charge for reproduction of our copyrighted material in the future.
-If your request is for reuse in a Thesis, permission is granted free of charge under the following conditions:

This license is valid for one-time use only for the purpose of defending your thesis and with a maximum of 100 extra copies in paper. If the thesis is going to be published, permission needs to be reobtained.
- includes use in an electronic form, provided it is an author-created version of the thesis on his/her own website and his/her university's repository, including UMI (according to the definition on the Sherpa website: http://www.sherpa.ac.uk/romeo/);
- is subject to courtesy information to the co-author or corresponding author.

Geographic Rights: Scope

Licenses may be exercised anywhere in the world.

Altering/Modifying Material: Not Permitted

Figures, tables, and illustrations may be altered minimally to serve your work. You may not alter or modify text in any manner. Abbreviations, additions, deletions and/or any other alterations shall be made only with prior written authorization of the author(s).

Reservation of Rights

Springer reserves all rights not specifically granted in the combination of (i) the license details provided by you and accepted in the course of this licensing transaction and (ii) these terms and conditions and (iii) CCC's Billing and Payment terms and conditions.

License Contingent on Payment

While you may exercise the rights licensed immediately upon issuance of the license at the end of the licensing process for the transaction, provided that you have disclosed complete and accurate details of your proposed use, no license is finally effective unless and until full payment is received from you (either by Springer or by CCC) as provided in CCC's Billing and Payment terms and conditions. If full payment is not received by the date due, then any license preliminarily granted shall be deemed automatically revoked and shall be void as if never granted. Further, in the event that you breach any of these terms and conditions or any of CCC's Billing and Payment terms and conditions, the license is automatically revoked and shall be void as if never granted. Use of materials as described in a revoked license, as well as any use of the materials beyond the scope of an unrevoked license, may constitute copyright infringement and Springer reserves the right to take any and all action to protect its copyright in the materials.

Copyright Notice: Disclaimer

You must include the following copyright and permission notice in connection with any reproduction of the licensed material:
"Springer book/journal title, chapter/article title, volume, year of publication, page, name(s) of author(s), (original copyright notice as given in the publication in which the material was originally published) "With permission of Springer"
In case of use of a graph or illustration, the caption of the graph or illustration must be included, as it is indicated in the original publication.

Warranties: None

Springer makes no representations or warranties with respect to the licensed material and adopts on its own behalf the limitations and disclaimers established by CCC on its behalf in its Billing and Payment terms and conditions for this licensing transaction.

Indemnity

You hereby indemnify and agree to hold harmless Springer and CCC, and their respective officers, directors, employees and agents, from and against any and all claims arising out of your use of the licensed material other than as specifically authorized pursuant to this license.

No Transfer of License

This license is personal to you and may not be sublicensed, assigned, or transferred by you without Springer's written permission.

No Amendment Except in Writing

This license may not be amended except in a writing signed by both parties (or, in the case of Springer, by CCC on Springer's behalf).

Objection to Contrary Terms
Springer hereby objects to any terms contained in any purchase order, acknowledgment, check endorsement or other writing prepared by you, which terms are inconsistent with these terms and conditions or CCC's Billing and Payment terms and conditions. These terms and conditions, together with CCC's Billing and Payment terms and conditions (which are incorporated herein), comprise the entire agreement between you and Springer (and CCC) concerning this licensing transaction. In the event of any conflict between your obligations established by these terms and conditions and those established by CCC's Billing and Payment terms and conditions, these terms and conditions shall control.
Jurisdiction
All disputes that may arise in connection with this present License, or the breach thereof, shall be settled exclusively by arbitration, to be held in the Federal Republic of Germany, in accordance with German law.
Other conditions:
V 12AUG2015

Questions? customercare@copyright.com or +1-855-239-3415 (toll free in the US) or +1-978-646-2777.

SPRINGER LICENSE
TERMS AND CONDITIONS

Jul 01, 2017

This Agreement between Safoora Zaminpardaz ("You") and Springer ("Springer") consists of your license details and the terms and conditions provided by Springer and Copyright Clearance Center.

License Number	4140081277709
License date	Jul 01, 2017
Licensed Content Publisher	Springer
Licensed Content Publication	Journal of Geodesy
Licensed Content Title	IRNSS/NavIC and GPS: a single- and dual-system L5 analysis
Licensed Content Author	S. Zaminpardaz
Licensed Content Date	Jan 1, 2017
Type of Use	Book/Textbook
Requestor type	Publisher
Publisher	N/A
Portion	Full text
Format	Print and Electronic
Will you be translating?	No
Print run	20
Author of this Springer article	Yes and you are the sole author of the new work
Order reference number	
Title of new book	New Generation GNSS\RNSS: Algorithms, Numerical Analyses and Applications
Publisher	N/A
Author of new book	Safoora Zaminpardaz
Expected publication date of new book	Feb 2018
Estimated size of new book (pages)	100
Requestor Location	Safoora Zaminpardaz GPO Box U1987, Curtin University Department of Spatial Sciences GNSS Research Center Perth, WA 6845 Australia Attn:
Billing Type	Invoice
Billing Address	Safoora Zaminpardaz GPO Box U1987, Curtin University Department of Spatial Sciences GNSS Research Center Perth, Australia 6845 Attn:

Total 0.00 USD

Terms and Conditions

Introduction
The publisher for this copyrighted material is Springer. By clicking "accept" in connection with completing this licensing transaction, you agree that the following terms and conditions apply to this transaction (along with the Billing and Payment terms and conditions established by Copyright Clearance Center, Inc. ("CCC"), at the time that you opened your Rightslink account and that are available at any time at http://myaccount.copyright.com).
Limited License
With reference to your request to reuse material on which Springer controls the copyright, permission is granted for the use indicated in your enquiry under the following conditions:
- Licenses are for one-time use only with a maximum distribution equal to the number stated in your request.
- Springer material represents original material which does not carry references to other sources. If the material in question appears with a credit to another source, this permission is not valid and authorization has to be obtained from the original copyright holder.
- This permission
• is non-exclusive
• is only valid if no personal rights, trademarks, or competitive products are infringed.
• explicitly excludes the right for derivatives.
- Springer does not supply original artwork or content.
- According to the format which you have selected, the following conditions apply accordingly:
• **Print and Electronic:** This License include use in electronic form provided it is password protected, on intranet, or CD-Rom/DVD or E-book/E-journal. It may not be republished in electronic open access.
• **Print:** This License excludes use in electronic form.
• **Electronic:** This License only pertains to use in electronic form provided it is password protected, on intranet, or CD-Rom/DVD or E-book/E-journal. It may not be republished in electronic open access.
For any electronic use not mentioned, please contact Springer at permissions.springer@spi-global.com.
- Although Springer controls the copyright to the material and is entitled to negotiate on rights, this license is only valid subject to courtesy information to the author (address is given in the article/chapter).
- If you are an STM Signatory or your work will be published by an STM Signatory and you are requesting to reuse figures/tables/illustrations or single text extracts, permission is granted according to STM Permissions Guidelines: http://www.stm-assoc.org/permissions-guidelines/
For any electronic use not mentioned in the Guidelines, please contact Springer at permissions.springer@spi-global.com. If you request to reuse more content than stipulated in the STM Permissions Guidelines, you will be charged a permission fee for the excess content.
Permission is valid upon payment of the fee as indicated in the licensing process. If permission is granted free of charge on this occasion, that does not prejudice any rights we might have to charge for reproduction of our copyrighted material in the future.
-If your request is for reuse in a Thesis, permission is granted free of charge under the following conditions:
This license is valid for one-time use only for the purpose of defending your thesis and with a maximum of 100 extra copies in paper. If the thesis is going to be published, permission needs to be reobtained.
- includes use in an electronic form, provided it is an author-created version of the thesis on

his/her own website and his/her university’s repository, including UMI (according to the definition on the Sherpa website: http://www.sherpa.ac.uk/romeo/);
- is subject to courtesy information to the co-author or corresponding author.

Geographic Rights: Scope

Licenses may be exercised anywhere in the world.

Altering/Modifying Material: Not Permitted

Figures, tables, and illustrations may be altered minimally to serve your work. You may not alter or modify text in any manner. Abbreviations, additions, deletions and/or any other alterations shall be made only with prior written authorization of the author(s).

Reservation of Rights

Springer reserves all rights not specifically granted in the combination of (i) the license details provided by you and accepted in the course of this licensing transaction and (ii) these terms and conditions and (iii) CCC's Billing and Payment terms and conditions.

License Contingent on Payment

While you may exercise the rights licensed immediately upon issuance of the license at the end of the licensing process for the transaction, provided that you have disclosed complete and accurate details of your proposed use, no license is finally effective unless and until full payment is received from you (either by Springer or by CCC) as provided in CCC's Billing and Payment terms and conditions. If full payment is not received by the date due, then any license preliminarily granted shall be deemed automatically revoked and shall be void as if never granted. Further, in the event that you breach any of these terms and conditions or any of CCC's Billing and Payment terms and conditions, the license is automatically revoked and shall be void as if never granted. Use of materials as described in a revoked license, as well as any use of the materials beyond the scope of an unrevoked license, may constitute copyright infringement and Springer reserves the right to take any and all action to protect its copyright in the materials.

Copyright Notice: Disclaimer

You must include the following copyright and permission notice in connection with any reproduction of the licensed material:

"Springer book/journal title, chapter/article title, volume, year of publication, page, name(s) of author(s), (original copyright notice as given in the publication in which the material was originally published) "With permission of Springer"

In case of use of a graph or illustration, the caption of the graph or illustration must be included, as it is indicated in the original publication.

Warranties: None

Springer makes no representations or warranties with respect to the licensed material and adopts on its own behalf the limitations and disclaimers established by CCC on its behalf in its Billing and Payment terms and conditions for this licensing transaction.

Indemnity

You hereby indemnify and agree to hold harmless Springer and CCC, and their respective officers, directors, employees and agents, from and against any and all claims arising out of your use of the licensed material other than as specifically authorized pursuant to this license.

No Transfer of License

This license is personal to you and may not be sublicensed, assigned, or transferred by you without Springer's written permission.

No Amendment Except in Writing

This license may not be amended except in a writing signed by both parties (or, in the case of Springer, by CCC on Springer's behalf).

Objection to Contrary Terms

Springer hereby objects to any terms contained in any purchase order, acknowledgment, check endorsement or other writing prepared by you, which terms are inconsistent with these terms and conditions or CCC's Billing and Payment terms and conditions. These terms and conditions, together with CCC's Billing and Payment terms and conditions (which are

incorporated herein), comprise the entire agreement between you and Springer (and CCC) concerning this licensing transaction. In the event of any conflict between your obligations established by these terms and conditions and those established by CCC's Billing and Payment terms and conditions, these terms and conditions shall control.

Jurisdiction

All disputes that may arise in connection with this present License, or the breach thereof, shall be settled exclusively by arbitration, to be held in the Federal Republic of Germany, in accordance with German law.

Other conditions:

V 12AUG2015

Questions? customercare@copyright.com or +1-855-239-3415 (toll free in the US) or +1-978-646-2777.

SPRINGER ORDER DETAILS

Jul 21, 2017

This Agreement between ("You") and Springer ("Springer") consists of your order details and the terms and conditions provided by Springer and Copyright Clearance Center.

Order Number	501289368
Order date	Jul 18, 2017
Licensed Content Publisher	Springer
Licensed Content Publication	Journal of Geodesy
Licensed Content Title	Single-frequency L5 attitude determination from IRNSS/NavIC and GPS: a single- and dual-system analysis
Licensed Content Author	S. Zaminpardaz
Licensed Content Date	Jan 1, 2017
Type of Use	Book/Textbook
Requestor type	Publisher
Publisher	N/A
Portion	Full text
Format	Print and Electronic
Will you be translating?	No
Print run	20
Author of this Springer article	Yes and you are the sole author of the new work
Order reference number	
Title of new book	New Generation GNSS\RNSS: Algorithms, Numerical Analyses and Applications
Publisher	N/A
Author of new book	Safoora Zaminpardaz
Expected publication date of new book	Feb 2018
Estimated size of new book (pages)	100
Requestor Location	Safoora Zaminpardaz GPO Box U1987, Curtin University Department of Spatial Sciences GNSS Research Center Perth, WA 6845 Australia Attn:
Billing Type	Invoice
Billing Address	Safoora Zaminpardaz GPO Box U1987, Curtin University Department of Spatial Sciences GNSS Research Center Perth, Australia 6845 Attn: Safoora Zaminpardaz
Total	0.00 USD

Terms and Conditions

Introduction
The publisher for this copyrighted material is Springer. By clicking "accept" in connection with completing this licensing transaction, you agree that the following terms and conditions apply to this transaction (along with the Billing and Payment terms and conditions established by Copyright Clearance Center, Inc. ("CCC"), at the time that you opened your Rightslink account and that are available at any time at http://myaccount.copyright.com).
Limited License
With reference to your request to reuse material on which Springer controls the copyright, permission is granted for the use indicated in your enquiry under the following conditions:
- Licenses are for one-time use only with a maximum distribution equal to the number stated in your request.
- Springer material represents original material which does not carry references to other sources. If the material in question appears with a credit to another source, this permission is not valid and authorization has to be obtained from the original copyright holder.
- This permission
• is non-exclusive
• is only valid if no personal rights, trademarks, or competitive products are infringed.
• explicitly excludes the right for derivatives.
- Springer does not supply original artwork or content.
- According to the format which you have selected, the following conditions apply accordingly:
• **Print and Electronic:** This License include use in electronic form provided it is password protected, on intranet, or CD-Rom/DVD or E-book/E-journal. It may not be republished in electronic open access.
• **Print:** This License excludes use in electronic form.
• **Electronic:** This License only pertains to use in electronic form provided it is password protected, on intranet, or CD-Rom/DVD or E-book/E-journal. It may not be republished in electronic open access.
For any electronic use not mentioned, please contact Springer at permissions.springer@spi-global.com.
- Although Springer controls the copyright to the material and is entitled to negotiate on rights, this license is only valid subject to courtesy information to the author (address is given in the article/chapter).
- If you are an STM Signatory or your work will be published by an STM Signatory and you are requesting to reuse figures/tables/illustrations or single text extracts, permission is granted according to STM Permissions Guidelines: http://www.stm-assoc.org/permissions-guidelines/
For any electronic use not mentioned in the Guidelines, please contact Springer at permissions.springer@spi-global.com. If you request to reuse more content than stipulated in the STM Permissions Guidelines, you will be charged a permission fee for the excess content.
Permission is valid upon payment of the fee as indicated in the licensing process. If permission is granted free of charge on this occasion, that does not prejudice any rights we might have to charge for reproduction of our copyrighted material in the future.
-If your request is for reuse in a Thesis, permission is granted free of charge under the following conditions:
This license is valid for one-time use only for the purpose of defending your thesis and with a maximum of 100 extra copies in paper. If the thesis is going to be published, permission needs to be reobtained.
- includes use in an electronic form, provided it is an author-created version of the thesis on his/her own website and his/her university’s repository, including UMI (according to the

definition on the Sherpa website: http://www.sherpa.ac.uk/romeo/);
- is subject to courtesy information to the co-author or corresponding author.

Geographic Rights: Scope

Licenses may be exercised anywhere in the world.

Altering/Modifying Material: Not Permitted

Figures, tables, and illustrations may be altered minimally to serve your work. You may not alter or modify text in any manner. Abbreviations, additions, deletions and/or any other alterations shall be made only with prior written authorization of the author(s).

Reservation of Rights

Springer reserves all rights not specifically granted in the combination of (i) the license details provided by you and accepted in the course of this licensing transaction and (ii) these terms and conditions and (iii) CCC's Billing and Payment terms and conditions.

License Contingent on Payment

While you may exercise the rights licensed immediately upon issuance of the license at the end of the licensing process for the transaction, provided that you have disclosed complete and accurate details of your proposed use, no license is finally effective unless and until full payment is received from you (either by Springer or by CCC) as provided in CCC's Billing and Payment terms and conditions. If full payment is not received by the date due, then any license preliminarily granted shall be deemed automatically revoked and shall be void as if never granted. Further, in the event that you breach any of these terms and conditions or any of CCC's Billing and Payment terms and conditions, the license is automatically revoked and shall be void as if never granted. Use of materials as described in a revoked license, as well as any use of the materials beyond the scope of an unrevoked license, may constitute copyright infringement and Springer reserves the right to take any and all action to protect its copyright in the materials.

Copyright Notice: Disclaimer

You must include the following copyright and permission notice in connection with any reproduction of the licensed material:

"Springer book/journal title, chapter/article title, volume, year of publication, page, name(s) of author(s), (original copyright notice as given in the publication in which the material was originally published) "With permission of Springer"

In case of use of a graph or illustration, the caption of the graph or illustration must be included, as it is indicated in the original publication.

Warranties: None

Springer makes no representations or warranties with respect to the licensed material and adopts on its own behalf the limitations and disclaimers established by CCC on its behalf in its Billing and Payment terms and conditions for this licensing transaction.

Indemnity

You hereby indemnify and agree to hold harmless Springer and CCC, and their respective officers, directors, employees and agents, from and against any and all claims arising out of your use of the licensed material other than as specifically authorized pursuant to this license.

No Transfer of License

This license is personal to you and may not be sublicensed, assigned, or transferred by you without Springer's written permission.

No Amendment Except in Writing

This license may not be amended except in a writing signed by both parties (or, in the case of Springer, by CCC on Springer's behalf).

Objection to Contrary Terms

Springer hereby objects to any terms contained in any purchase order, acknowledgment, check endorsement or other writing prepared by you, which terms are inconsistent with these terms and conditions or CCC's Billing and Payment terms and conditions. These terms and conditions, together with CCC's Billing and Payment terms and conditions (which are incorporated herein), comprise the entire agreement between you and Springer (and CCC)

concerning this licensing transaction. In the event of any conflict between your obligations established by these terms and conditions and those established by CCC's Billing and Payment terms and conditions, these terms and conditions shall control.

Jurisdiction

All disputes that may arise in connection with this present License, or the breach thereof, shall be settled exclusively by arbitration, to be held in the Federal Republic of Germany, in accordance with German law.

Other conditions:

V 12AUG2015

SPRINGER LICENSE
TERMS AND CONDITIONS

Aug 31, 2017

This Agreement between Safoora Zaminpardaz ("You") and Springer ("Springer") consists of your license details and the terms and conditions provided by Springer and Copyright Clearance Center.

License Number	4179400808127
License date	Aug 31, 2017
Licensed Content Publisher	Springer
Licensed Content Publication	GPS Solutions
Licensed Content Title	Analysis of Galileo IOV + FOC signals and E5 RTK performance
Licensed Content Author	Safoora Zaminpardaz
Licensed Content Date	Jan 1, 2017
Type of Use	Book/Textbook
Requestor type	Publisher
Publisher	N/A
Portion	Full text
Format	Print and Electronic
Will you be translating?	No
Print run	20
Author of this Springer article	Yes and you are the sole author of the new work
Order reference number	
Title of new book	New Generation GNSS\RNSS: Algorithms, Numerical Analyses and Applications
Publisher	N/A
Author of new book	Safoora Zaminpardaz
Expected publication date of new book	Feb 2018
Estimated size of new book (pages)	100
Requestor Location	Safoora Zaminpardaz GPO Box U1987, Curtin University Department of Spatial Sciences GNSS Research Center Perth, WA 6845 Australia Attn:
Billing Type	Invoice
Billing Address	Safoora Zaminpardaz GPO Box U1987, Curtin University Department of Spatial Sciences GNSS Research Center Perth, Australia 6845 Attn: Safoora Zaminpardaz
Total	0.00 USD
Terms and Conditions	

Introduction

The publisher for this copyrighted material is Springer. By clicking "accept" in connection with completing this licensing transaction, you agree that the following terms and conditions apply to this transaction (along with the Billing and Payment terms and conditions established by Copyright Clearance Center, Inc. ("CCC"), at the time that you opened your Rightslink account and that are available at any time at http://myaccount.copyright.com).

Limited License

With reference to your request to reuse material on which Springer controls the copyright, permission is granted for the use indicated in your enquiry under the following conditions:

- Licenses are for one-time use only with a maximum distribution equal to the number stated in your request.
- Springer material represents original material which does not carry references to other sources. If the material in question appears with a credit to another source, this permission is not valid and authorization has to be obtained from the original copyright holder.
- This permission
• is non-exclusive
• is only valid if no personal rights, trademarks, or competitive products are infringed.
• explicitly excludes the right for derivatives.
- Springer does not supply original artwork or content.
- According to the format which you have selected, the following conditions apply accordingly:
• **Print and Electronic:** This License include use in electronic form provided it is password protected, on intranet, or CD-Rom/DVD or E-book/E-journal. It may not be republished in electronic open access.
• **Print:** This License excludes use in electronic form.
• **Electronic:** This License only pertains to use in electronic form provided it is password protected, on intranet, or CD-Rom/DVD or E-book/E-journal. It may not be republished in electronic open access.

For any electronic use not mentioned, please contact Springer at permissions.springer@spi-global.com.

- Although Springer controls the copyright to the material and is entitled to negotiate on rights, this license is only valid subject to courtesy information to the author (address is given in the article/chapter).
- If you are an STM Signatory or your work will be published by an STM Signatory and you are requesting to reuse figures/tables/illustrations or single text extracts, permission is granted according to STM Permissions Guidelines: http://www.stm-assoc.org/permissions-guidelines/

For any electronic use not mentioned in the Guidelines, please contact Springer at permissions.springer@spi-global.com. If you request to reuse more content than stipulated in the STM Permissions Guidelines, you will be charged a permission fee for the excess content.

Permission is valid upon payment of the fee as indicated in the licensing process. If permission is granted free of charge on this occasion, that does not prejudice any rights we might have to charge for reproduction of our copyrighted material in the future.

-If your request is for reuse in a Thesis, permission is granted free of charge under the following conditions:

This license is valid for one-time use only for the purpose of defending your thesis and with a maximum of 100 extra copies in paper. If the thesis is going to be published, permission needs to be reobtained.

- includes use in an electronic form, provided it is an author-created version of the thesis on his/her own website and his/her university’s repository, including UMI (according to the definition on the Sherpa website: http://www.sherpa.ac.uk/romeo/);
- is subject to courtesy information to the co-author or corresponding author.

Geographic Rights: Scope

Licenses may be exercised anywhere in the world.

Altering/Modifying Material: Not Permitted

Figures, tables, and illustrations may be altered minimally to serve your work. You may not

alter or modify text in any manner. Abbreviations, additions, deletions and/or any other alterations shall be made only with prior written authorization of the author(s).

Reservation of Rights

Springer reserves all rights not specifically granted in the combination of (i) the license details provided by you and accepted in the course of this licensing transaction and (ii) these terms and conditions and (iii) CCC's Billing and Payment terms and conditions.

License Contingent on Payment

While you may exercise the rights licensed immediately upon issuance of the license at the end of the licensing process for the transaction, provided that you have disclosed complete and accurate details of your proposed use, no license is finally effective unless and until full payment is received from you (either by Springer or by CCC) as provided in CCC's Billing and Payment terms and conditions. If full payment is not received by the date due, then any license preliminarily granted shall be deemed automatically revoked and shall be void as if never granted. Further, in the event that you breach any of these terms and conditions or any of CCC's Billing and Payment terms and conditions, the license is automatically revoked and shall be void as if never granted. Use of materials as described in a revoked license, as well as any use of the materials beyond the scope of an unrevoked license, may constitute copyright infringement and Springer reserves the right to take any and all action to protect its copyright in the materials.

Copyright Notice: Disclaimer

You must include the following copyright and permission notice in connection with any reproduction of the licensed material:

"Springer book/journal title, chapter/article title, volume, year of publication, page, name(s) of author(s), (original copyright notice as given in the publication in which the material was originally published) "With permission of Springer"

In case of use of a graph or illustration, the caption of the graph or illustration must be included, as it is indicated in the original publication.

Warranties: None

Springer makes no representations or warranties with respect to the licensed material and adopts on its own behalf the limitations and disclaimers established by CCC on its behalf in its Billing and Payment terms and conditions for this licensing transaction.

Indemnity

You hereby indemnify and agree to hold harmless Springer and CCC, and their respective officers, directors, employees and agents, from and against any and all claims arising out of your use of the licensed material other than as specifically authorized pursuant to this license.

No Transfer of License

This license is personal to you and may not be sublicensed, assigned, or transferred by you without Springer's written permission.

No Amendment Except in Writing

This license may not be amended except in a writing signed by both parties (or, in the case of Springer, by CCC on Springer's behalf).

Objection to Contrary Terms

Springer hereby objects to any terms contained in any purchase order, acknowledgment, check endorsement or other writing prepared by you, which terms are inconsistent with these terms and conditions or CCC's Billing and Payment terms and conditions. These terms and conditions, together with CCC's Billing and Payment terms and conditions (which are incorporated herein), comprise the entire agreement between you and Springer (and CCC) concerning this licensing transaction. In the event of any conflict between your obligations established by these terms and conditions and those established by CCC's Billing and Payment terms and conditions, these terms and conditions shall control.

Jurisdiction

All disputes that may arise in connection with this present License, or the breach thereof, shall be settled exclusively by arbitration, to be held in the Federal Republic of Germany, in accordance with German law.

Other conditions:

V 12AUG2015

Permissions of the following **'The Institute of Navigation'** publications are attached in the forthcoming pages:

1) Zaminpardaz S., Teunissen P.J.G., Nadarajah N., Khodabandeh A. (2015) GNSS Array-Based Ionospheric Spatial Gradient Monitoring: Precision and Integrity Analysis. ION Pacific PNT 2015, pp. 799-814. **The Institute of Navigation**, Honolulu, Hawaii

2) Zaminpardaz S. (2016) Horizon-to-elevation Mask: A Potential Benefit to Ionospheric Gradient Monitoring. ION GNSS+ 2016, pp. 1764-1779. **The Institute of Navigation**, Portland, Oregon

THE INSTITUTE OF NAVIGATION

COPYRIGHT RELEASE FORM

ION PROCEEDINGS

Signing of "Statement A" or "Statement B" is required except that employees of governments other than the U.S. Government may submit equivalent statements. It is essential that the Institute of Navigation (ION) and its agents or assignees have the right of publication and reproduction.

Proceedings to Appear in: **ION Pacific PNT 2015 Meeting**

Session Number & Title: Session C4: Ground Based Augmentation System Technology

Paper Title *(exactly as it appears on the paper)*: GNSS Array-Based Ionospheric Spatial Gradient Monitoring: Precision and Integrity Analysis

Author(s) & Affiliation(s) *(in the exact order they appear on the paper)*: S.Zaminpardaz, P.J.G Teunissen, N. Nadarajah, A. Khodabandeh

GNSS Research Centre, Curtin University of Technology, Perth, Australia

Primary Author Address: Department of Spatial Sciences ,Curtin University, Perth, WA, 6845

Phone/Fax/E-Mail: (+61) 8-9266-3157/s.zaminpardaz@curtin.edu.au

STATEMENT A:
The undersigned "Copyright Owner," desiring to publish a paper (the "Paper") in ION Proceedings and/or through other publications of The Institute of Navigation ("ION"), hereby grants to ION the following rights in exchange for good and valuable consideration:

1.) the exclusive, royalty-free right of first publication of the above Paper throughout the world as part of the proceedings named above and;
2.) a non-exclusive, perpetual, royalty-free, worldwide license to reprint and/or provide in electronic format the above Paper, either in excerpt, in summary, or in completed form, for free or in exchange for a fee.

Copyright Owner reserves all rights not specifically granted to ION herein and has the right after the Paper has been published, to reprint the Work in any publication, provided that the terms of such republication do not conflict with this license. Copyright Owner agrees to include the proper credit to ION for prior publication of the Paper in any reprint of the Paper in a publication, including date (month and year) and location (city and state) of the meeting at which the paper was presented.

Copyright Owner warrants that the Paper is original with him/her, that its publication will not infringe the rights of others, that the Paper is factually accurate and contains no defamatory or otherwise unlawful material, and that Copyright Owner has full power to make this agreement. Copyright Owner further warrants that the Paper has not been published elsewhere in whole or in part (except as set out in a rider attached thereto if applicable) and that no agreement to publish the Paper or any part or version thereof is outstanding. Should the Paper contain any material which requires permission for inclusion in the Paper, Copyright Owner agrees to obtain such permission in writing and provide a copy of such permission to ION.

1. Zahoora Zaminpardaz — Curtin University
PRIMARY AUTHOR'S SIGNATURE — EMPLOYER FOR WHOM WORK WAS PERFORMED

TEUNISSEN — 27/02/2015
AUTHORIZED SIGNATURE — DATE FORM SIGNED

STATEMENT B:
This will certify that all authors of the above Paper are employees of the U.S. Government and that the authors created the Paper as part of their employment and that the Paper is therefore not subject to U.S. Copyright protection.

2. _____ _____
PRIMARY AUTHOR'S SIGNATURE — EMPLOYER FOR WHOM WORK WAS PERFORMED

_____ _____
AUTHORIZED SIGNATURE — DATE FORM SIGNED

Crown Copyright Certification (where applicable)

This will certify that all authors of the Work are employees of the British or applicable Commonwealth Government and prepared the Work in connection with their official duties. As such, the Work is subject to Crown Copyright and is not assigned to the ION as set forth above. The Undersigned acknowledges, however, that the ION has the right to publish, distribute and reprint the Work in all forms and media.

3. _____ _____
AUTHORIZED SIGNATURE — DATE FORM SIGNED

(Authors who are British or applicable Commonwealth Government employees should also sign line (1) above to indicate their acceptance of all terms other than the copyright transfer.)

THE INSTITUTE OF NAVIGATION

COPYRIGHT RELEASE FORM

ION PROCEEDINGS

Signing of "Statement A" or "Statement B" is required except that employees of governments other than the U.S. Government may submit equivalent statements. It is essential that the Institute of Navigation (ION) and its agents or assignees have the right of publication and reproduction.

Proceedings to Appear in: **ION Pacific PNT 2015 Meeting**

Session Number & Title: Session C4: Ground Based Augmentation System Technology

Paper Title *(exactly as it appears on the paper)*: GNSS Array-Based Ionospheric Spatial Gradient Monitoring: Precision and Integrity Analysis

Author(s) & Affiliation(s) *(in the exact order they appear on the paper)*: S.Zaminpardaz, P.J.G Teunissen, N. Nadarajah, A. Khodabandeh

GNSS Research Centre, Curtin University of Technology, Perth, Australia

Primary Author Address: Department of Spatial Sciences ,Curtin University, Perth, WA, 6845

Phone/Fax/E-Mail: (+61) 8-9266-3157/s.zaminpardaz@curtin.edu.au

STATEMENT A:
The undersigned "Copyright Owner," desiring to publish a paper (the "Paper") in ION Proceedings and/or through other publications of The Institute of Navigation ("ION"), hereby grants to ION the following rights in exchange for good and valuable consideration:

1.) the exclusive, royalty-free right of first publication of the above Paper throughout the world as part of the proceedings named above and;
2.) a non-exclusive, perpetual, royalty-free, worldwide license to reprint and/or provide in electronic format the above Paper, either in excerpt, in summary, or in completed form, for free or in exchange for a fee.

Copyright Owner reserves all rights not specifically granted to ION herein and has the right after the Paper has been published, to reprint the Work in any publication, provided that the terms of such republication do not conflict with this license. Copyright Owner agrees to include the proper credit to ION for prior publication of the Paper in any reprint of the Paper in a publication, including date (month and year) and location (city and state) of the meeting at which the paper was presented.

Copyright Owner warrants that the Paper is original with him/her, that its publication will not infringe the rights of others, that the Paper is factually accurate and contains no defamatory or otherwise unlawful material, and that Copyright Owner has full power to make this agreement. Copyright Owner further warrants that the Paper has not been published elsewhere in whole or in part (except as set out in a rider attached thereto if applicable) and that no agreement to publish the Paper or any part or version thereof is outstanding. Should the Paper contain any material which requires permission for inclusion in the Paper, Copyright Owner agrees to obtain such permission in writing and provide a copy of such permission to ION.

1. Zahoora Zaminpardaz — Curtin University
PRIMARY AUTHOR'S SIGNATURE — EMPLOYER FOR WHOM WORK WAS PERFORMED

TEUNISSEN — 27/02/2015
AUTHORIZED SIGNATURE — DATE FORM SIGNED

STATEMENT B:
This will certify that all authors of the above Paper are employees of the U.S. Government and that the authors created the Paper as part of their employment and that the Paper is therefore not subject to U.S. Copyright protection.

2. _____ _____
PRIMARY AUTHOR'S SIGNATURE — EMPLOYER FOR WHOM WORK WAS PERFORMED

_____ _____
AUTHORIZED SIGNATURE — DATE FORM SIGNED

Crown Copyright Certification (where applicable)

This will certify that all authors of the Work are employees of the British or applicable Commonwealth Government and prepared the Work in connection with their official duties. As such, the Work is subject to Crown Copyright and is not assigned to the ION as set forth above. The Undersigned acknowledges, however, that the ION has the right to publish, distribute and reprint the Work in all forms and media.

3. _____ _____
AUTHORIZED SIGNATURE — DATE FORM SIGNED

(Authors who are British or applicable Commonwealth Government employees should also sign line (1) above to indicate their acceptance of all terms other than the copyright transfer.)

Permission of the following '**MDPI'** publication can be found in (http://www.mdpi.com/about/openaccess), which is attached in the forthcoming pages:

Zaminpardaz S., Teunissen P.J.G., Nadarajah N. (2017d) IRNSS/NavIC L5 Attitude Determination. Sensors, **MDPI**, 17(2), 274, DOI 10.3390/s17020274

MDPI Contact

MDPI AG
St. Alban-Anlage 66,
4052 Basel, Switzerland
Support contact
Tel. +41 61 683 77 34
Fax: +41 61 302 89 18

For more contact information, see here.

MDPI Open Access Information and Policy

All articles published by MDPI are made immediately available worldwide under an open access license. This means:

- everyone has free and unlimited access to the full-text of *all* articles published in MDPI journals, and
- everyone is free to re-use the published material if proper accreditation/citation of the original publication is given.
- open access publication is supported by the authors' institutes or research funding agencies by payment of a comparatively low Article Processing Charge (APC) for accepted articles.

External Open Access Resources

MDPI is a RoMEO green publisher — RoMEO is a database of Publishers' copyright and self-archiving policies hosted by the University of Nottingham

Those who are new to the concept of open access might find the following websites or 'Open Access 101' video informative:

Wikipedia article on 'Open Access'
Peter Suber's 'Open Access Overview'
Information Platform Open Access [in English, in German]
SHERPA's 'Authors and Open Access'

Meaning of Open Access

In accordance with major definitions of open access in scientific literature (namely the Budapest, Berlin, and Bethesda declarations), MDPI defines *open access* by the following conditions:

- peer-reviewed literature is freely available without subscription or price barriers,
- literature is immediately released in open access format (no embargo period), and
- published material can be re-used without obtaining permission as long as a correct citation to the original publication is given.

Open Access Explained!

Until 2008, most articles published by MDPI contained the note: "© *year* by MDPI (http://www.mdpi.org). Reproduction is permitted for noncommercial purposes". During 2008, MDPI journals started to publish articles under the Creative Commons Attribution License and are now using the latest version of the CC BY license, which grants authors the most extensive rights. All articles published by MDPI before and during 2008 should now be considered as having been released under the post-2008 Creative Commons Attribution License.

This means that all articles published in MDPI journals, including data, graphics, and supplements, can be linked from external sources, scanned by search engines, re-used by text mining applications or websites, blogs, *etc.* free of charge under the sole condition of proper accreditation of the source and original publisher. MDPI believes that open access publishing fosters the exchange of research results amongst scientists from different disciplines, thus facilitating interdisciplinary research. Open access publishing also provides access to research results to researchers worldwide, including those from developing countries, and to an interested general public. Although MDPI publishes all of its journals under the open access model, we believe that open access is an enriching part of the scholarly communication process that can and should co-exist with other forms of communication and publication, such as society-based publishing and conferencing activities.

Important Note: some articles (especially *Reviews*) may contain figures, tables or text taken from other publications, for which MDPI does not hold the copyright or the right to re-license the published material. Please note that you should inquire with the original copyright holder (usually the original publisher or authors), whether or not this material can be re-used.

Advantages of Open Access for Authors

The High Availability and Visibility of our open access articles is guaranteed through the free and unlimited accessibility of the publication over the Internet. Everyone can freely access and download the full text of all articles published with MDPI: readers of open access journals, *i.e.*, mostly other researchers, do not need to pay any subscription or pay-per-view charges to read articles published by MDPI. Open access publications are also more likely to be included in search engines and indexing databases.

The Higher Citation Impact of open access articles results from their high publicity and availability. Open access publications are demonstrably more frequently cited [1,2].

Lower Publishing Costs: Open access publishers cover their costs for editorial handling and editing of a paper by charging authors' institutes or research funding agencies. The cost of handling and producing an article is covered through the one-time payment of an article processing charge (APC) for each accepted article. The APCs of open access publishers are only a fraction of the average income per paper earned by traditional, subscription-based publishers. MDPI's article processing charge (APC) is the same, irrespective of article length, because we wish to encourage publication of long papers with complete results and full experimental or computational details [3].

Faster Publication in MDPI's open access journals is achieved by online-only availability. Accepted articles are typically published online more rapidly in MDPI journals than those of traditional, subscription-based and printed journals are [4].

Links and Notes

1. Open access citation impact advantage: http://en.wikipedia.org/wiki/Open_access#Authors_and_researchers. For example, a standard research paper "Shutalev, A.D.; Kishko, E.A.; Sivova, N.V.; Kuznetsov, A.Y. *Molecules* **1998**, *3*, 100-106" has been cited 51 times, the highest number among all the papers published so far by the same author.
2. Lin, S.-K. *Editorial*: Non-Open Access and Its Adverse Impact on Molecules. *Molecules* **2007**, *12*, 1436-1437 (PDF format 16 K, HTML format).
3. Recently a research paper of 30 pages has been published: *Molecules* **2008**, *13*(5), 1081-1110.
4. Some well written papers have been peer reviewed and published in less than two weeks from manuscript submission, see e.g.: *Molecules* **2006**, *11*(4), 212-218.

Permissions of the following '**Taylor & Francis'** publications can be found in (http://journalauthors.tandf.co.uk/copyright/#link4), which are attached in the forthcoming pages:

1) Zaminpardaz S., Teunissen P.J.G., Nadarajah N. (2016a) IRNSS stand-alone positioning: first results in Australia. Journal of Spatial Science, **Taylor & Francis**, 61(1):5-27

2) Zaminpardaz S., Teunissen P.J.G., Nadarajah N. (2017a) IRNSS/NavIC Single-Point Positioning: A Service Area Precision Analysis. Marine Geodesy, **Taylor & Francis**, 40(4):259-274

Browse:

Author guides

Preparation
Submission
Review
Production
Copyright and you
- Publishing agreements and your options
- Sharing your work
- Using third party material
- Author rights pilot

Publication
Beyond publication

Resources

Benefits for authors
News and events
Author feedback

You are in: Home > Copyright > Copyright and you

Copyright and you

What is copyright?

Copyright gives the copyright holder exclusive rights over how others use their work.

As an author, this means that which copyright option you choose defines how researchers, scientists, policy makers, journalists, corporations, or anyone else who has an interest in your research can use your work.

Copyright has a time limit (usually life of the author plus 50–70 years for a journal article) and the level and type of protection offered varies between countries. Local and international laws and conventions mean that the copyright is recognized and protected, to varying degrees, in almost every country in the world.

In a digital world, how others want to read and reuse content is evolving rapidly. Understanding what your copyright options are is becoming ever more important, especially with the growth of open access publishing.

back to top

What does it mean for you?

Copyright allows you to protect your original material and stop others from using your work without your permission. It means others will generally need to credit you and your work properly, increasing its impact.

back to top

Copyright at Taylor & Francis

When publishing in a subscription journal published by Taylor & Francis, we ask you to assign copyright to us. Alternatively, any author publishing with us can also opt to retain their own copyright and sign a License to Publish (sample).

If you choose to assign copyright to us, as part of the publication process, you will be asked to sign a publishing agreement. This will be after your manuscript has been through the peer review process, has been accepted, and moves into production. Details will be sent to you via email, from the journal's Production Editor.

Sample publishing agreement

Find out more about what defines a conflict of interest and how to declare it

back to top

Why do we ask you to assign copyright to us?

Asking you to assign copyright means we are showing our commitment to:

- Act as **stewards** of the scholarly record of your work
- **Defend** your article against plagiarism and copyright infringement
- Enable you to **share** your article (using your free eprints and Green Open Access at Taylor & Francis)
- Assure attribution of your work, by making sure you are **identified** as the author

We encourage you to:

- Share your work
- Make **printed copies** of your article to use for lecture or classroom purposes
- Include your article in a thesis or dissertation
- **Present your article at a meeting or conference** and distribute printed copies of the article
- Republish the article (making sure you cite the original article)
- Adapt and expand your published journal article to make it suitable for your thesis or dissertation

Alternatively, any author publishing with us can opt to retain their own copyright and sign a License to Publish.

back to top

Page content

View the page content by selecting any of the links below

- What is copyright?
- What does it mean for you?
- Copyright at Taylor & Francis
- Why do we ask you to assign copyright to us?
- Useful definitions
- Useful links

Useful definitions

Version of Record (VoR)

"A fixed version of a journal article that has been made available by ... a publisher by formally and exclusively declaring the article 'published.'

This includes any 'early release' article that is formally identified as being published even before the compilation of a volume issue and assignment of associated metadata, as long as it is citable via some permanent identifier(s).

This does not include any 'early release' article that has not yet been 'fixed' by processes that are still to be applied, such as copy-editing, proof corrections, layout, and typesetting."

(Defined by National Information Standards Organization, in partnership with the Association of Learned and Professional Society Publishers.)

back to top

Useful links

- Creative Commons licenses
- UK Intellectual Property Office's What is copyright?" guide
- US Government's Copyright Office guide to copyright
- World Intellectual Property Organization guide to copyright

back to top

Permissions of the following '**Inside GNSS'** publications are attached in the forthcoming pages:

1) Zaminpardaz S., Teunissen P.J.G., Nadarajah N. (2017c) L5 RTK Over India: IRNSS and GPS. **Inside GNSS**, 12(1):48-55

2) Zaminpardaz S., Teunissen P.J.G., Nadarajah N. (2016b) GLONASS CDMA L3 Ambiguity Resolution. **Inside GNSS**, 11(4):44-47

Safoora Zaminpardaz

From: Safoora Zaminpardaz
Sent: Tuesday, 18 July 2017 10:46 PM
To: 'Glen Gibbons'
Subject: Permission request

Dear Mr Gibbons,

I am the first author of the following publications in Inside GNSS Magazine:

1) **Zaminpardaz S.**, Teunissen P.J.G, Nadarajah N. (2017) L5 RTK Over India: IRNSS and GPS. Inside GNSS, 12(1):48-55

2) **Zaminpardaz S.**, Teunissen P.J.G, Nadarajah N. (2016) GLONASS CDMA L3 Ambiguity Resolution. Inside GNSS, 11(4):44-47

I am writing to ask your permission to use the material of these two papers in my thesis entitled "New Generation GNSS\RNSS: Algorithms, Numerical Analyses and Applications" at Curtin University. As my thesis is by publication, the full content of the aforementioned papers will be used in the thesis.

Could you please advise me to obtain the permission in that regard?

Thank you and best regards,
Safoora

From: Glen Gibbons [mailto:glen@insidegnss.com]
Sent: Wednesday, 19 July 2017 12:32 AM
To: Safoora Zaminpardaz
Subject: Re: Permission request

Dear Safoora,

You have our permission to use the material from these articles in your thesis. We would appreciate a citation or reference to their publication in Inside GNSS.

Best regards,
Glen

Glen Gibbons
Editor, *Inside GNSS*
Managing Partner, Gibbons Media & Research LLC
1574 Coburg Rd. #233
Eugene, OR 97401-4802

Tel: 408-216-7561

Fax: 408-216-7525
E-mail: glen@insidegnss.com

APPENDIX B STATEMENT OF CONTRIBUTIONS BY OTHERS

This thesis presents 1 single-author, 10 first-author, and 1 third-author papers that have been published in journals, conference proceedings and professional magazines. In this Appendix, author's and co-authors' contributions for these papers are stated and signed.

To Whom It May Concern,

I, Safoora Zaminpardaz, wrote the manuscripts, derived the analytical expressions, and provided the numerical multi-GNSS analyses. The numerical results were obtained using either my own software or the extended version of an existing software originally developed by Dr Nandakumaran Nadarajah. For the co-authored publications, Prof Peter J.G. Teunissen and Dr Nandakumaran Nadarajah provided their comments as to improve the manuscripts for submission. All the above holds for the following publications:

1) Zaminpardaz S., Teunissen P.J.G., Nadarajah N. (2016a) IRNSS stand-alone positioning: first results in Australia. Journal of Spatial Science, Taylor & Francis, 61(1):5-27

2) Zaminpardaz S., Teunissen P.J.G., Nadarajah N. (2016b) GLONASS CDMA L3 Ambiguity Resolution. Inside GNSS, 11(4):44-47

3) Zaminpardaz S., Teunissen P.J.G., Nadarajah N. (2017a) IRNSS/NavIC Single-Point Positioning: A Service Area Precision Analysis. Marine Geodesy, Taylor & Francis, 40(4):259-274

4) Zaminpardaz S., Teunissen P.J.G., Nadarajah N. (2017b) IRNSS/NavIC and GPS: A Single and Dual System L5 Analysis. Journal of Geodesy, Springer, 91(8):915-931

5) Zaminpardaz S., Teunissen P.J.G., Nadarajah N. (2017c) L5 RTK Over India: IRNSS and GPS. Inside GNSS, 12(1):48-55

6) Zaminpardaz S., Teunissen P.J.G., Nadarajah N. (2017d) IRNSS/NavIC L5 Attitude Determination. Sensors, MDPI, 17(2), 274, DOI 10.3390/s17020274

7) Zaminpardaz S., Teunissen P.J.G., Nadarajah N. (2017e) Single-frequency L5 attitude determination from IRNSS/NavIC and GPS: a single- and dual-system analysis. Journal of Geodesy, Springer, 91(12):1415-1433

8) Zaminpardaz S., Teunissen P.J.G., Nadarajah N. (2017f) GLONASS CDMA L3 ambiguity resolution and positioning. GPS Solutions, Springer, 21(2):535-549

And, I, Safoora Zaminpardaz, wrote the main material of the following publications, including the underlying theory and analytical derivations. For the co-authored publication, Prof Peter J.G. Teunissen, Dr Amir Khodabandeh and Dr Nandakumaran Nadarajah provided their comments as to improve the manuscript for submission:

9) Zaminpardaz S. (2016) Horizon-to-elevation Mask: A Potential Benefit to Ionospheric Gradient Monitoring. ION GNSS+ 2016, pp. 1764-1779. The Institute of Navigation, Portland, Oregon

10) Zaminpardaz S., Teunissen P.J.G., Nadarajah N., Khodabandeh A. (2015) GNSS Array-Based Ionospheric Spatial Gradient Monitoring: Precision and Integrity Analysis. ION Pacific PNT 2015, pp. 799-814. The Institute of Navigation, Honolulu, Hawaii

And, I, Safoora Zaminpardaz, wrote the manuscript of the following publication and provided the analytical and numerical results. Prof Peter J.G. Teunissen provided his comments as to improve the manuscript for submission:

11) Zaminpardaz S., Teunissen P.J.G. (2017) Analysis of Galileo IOV+FOC Signals and E5 RTK performance. GPS Solutions, Springer, 21(4):1855-1870

And, I, Safoora Zaminpardaz, contributed to a part of initial numerical analyses of the following publication. The first author is Dr Dennis Odijk who wrote the manuscript. Dr Nandakumaran Nadarajah provided the data and the initial numerical analyses, and Prof Peter J.G. Teunissen provided his comments to the manuscript before submission:

12) Odijk D., Nadarajah N., Zaminpardaz S., Teunissen P.J.G. (2017) GPS, Galileo, QZSS and IRNSS differential ISBs: estimation and application. GPS Solutions, Springer, 21(2):439-450

Safoora Zaminpardaz

I, as a Co-Author, endorse that this level of contributions by the candidate indicated above is appropriate.

Peter J.G. Teunissen

Nandakumaran Nadarajah

Amir Khodabandeh

Dennis Odijk

APPENDIX C PROOF OF PEER-REVIEWED AND ACCEPTED PUBLICATIONS

Provided below is the proof that the conference publications:

1) Zaminpardaz S., Teunissen P.J.G., Nadarajah N., Khodabandeh A. (2015) GNSS Array-Based Ionospheric Spatial Gradient Monitoring: Precision and Integrity Analysis. ION Pacific PNT 2015, pp. 799-814. The Institute of Navigation, Honolulu, Hawaii

2) Zaminpardaz S. (2016) Horizon-to-elevation Mask: A Potential Benefit to Ionospheric Gradient Monitoring. ION GNSS+ 2016, pp. 1764-1779. The Institute of Navigation, Portland, Oregon

and the technical articles:

1) Zaminpardaz S., Teunissen P.J.G., Nadarajah N. (2017c) L5 RTK Over India: IRNSS and GPS. Inside GNSS, 12(1):48-55

2) Zaminpardaz S., Teunissen P.J.G., Nadarajah N. (2016b) GLONASS CDMA L3 Ambiguity Resolution. Inside GNSS, 11(4):44-47

were published in peer-reviewed conference proceedings/professional magazines and accepted respectively.

Safoora Zaminpardaz

From: meetings@ion.org
Sent: Thursday, 4 December 2014 1:19 AM
To: Amir Khodabandeh
Subject: Acceptance of your ION Pacific PNT Abstract

Dear Amir:

Your abstract, "GNSS Array-Based Ionospheric Spatial Gradient Monitoring: Precision and Integrity Analyses" has been accepted for the ION Pacific PNT 2015 Conference, April 20-23, 2015, at the Marriott Waikiki Beach Resort and Spa in Honolulu, Hawaii. Your session, Ground Based Augmentation System Technology, will take place on Wednesday, April 22, 2015. The program is now online at https://www.ion.org/pnt/program.cfm.

Please confirm that you have received this notice by clicking on the link below. You can also sign in to the Abstract Management Portal at https://www.ion.org/abstracts to acknowledge the acceptance of your abstract.

Click here to confirm that you have received this message.

Your completed manuscript is due no later than March 1. Papers not submitted electronically by March 1 will be withdrawn from the conference program.

Note that abstracts submitted to your session are currently listed in alphabetical order. **The final determination as to which papers will be guaranteed a presentation time in the session, and which papers will be designated as alternate presentations, will be based upon the session chairs' review of full technical papers.**

Please look at your paper title and author list carefully to determine if all of the information is correct. You can update the title of your paper, author list, your abstract, upload your conference paper and make changes to your conference paper directly through the ION's Abstract Management Portal at https://www.ion.org/abstracts. Changes made before March 1 will be reflected in the printed on-site conference program.

The Author Resource Center is available at https://www.ion.org/pnt/author-resource-center.cfm. The resource center contains the following information:

- Important dates and deadlines
- Speaker Breakfast information (your attendance is mandatory on the day of your presentation)
- Presentation instructions
- Paper layout and preparation instructions
- Instructions for uploading your files
- Helpful tips on Promoting Your Presentation
- Copyright Release Form and Document Templates

You are encouraged to contact your session chairs, preferably by e-mail, at your earliest opportunity. Please keep them current on your status. They are your first points of contact for any questions you might have. If for any reason you are not able to make contact with your session chair, please do not hesitate to contact me.

Miriam Lewis
ION Author Liaison
E-mail: meetings@ion.org

C4: Ground Based Augmentation System Technology
Date: Wednesday, April 22, 2015
Time: 1:30 PM - 5:00 PM
Room: Kona Moku Ballroom, Salon C

Chairs:
Dr. Tung Hai Ta, *Hanoi University of Science & Technology, Vietnam*
Dr. Stuart Riley, *Trimble Navigation*

- **Flight Evaluations of INS-Aided GPS Performance under Strong Ionospheric Scintillation,** *T. Tsujii, T. Fujiwara, Y. Shimizu, Japan Aerospace Exploration Agency (JAXA), Japan*
- **GBAS Availability Assessment and Modeling of Ionospheric Scintillation Effects,** *Takeshi Fujiwara and Toshiaki Tsujii, Aviation Program Group, Japan Aerospace Exploration Agency, Japan*
- **GBAS CAT II/III Validation for Business Aircraft – Final Flight Tests and Simulations,** *J. Dvorska, L. Podivin, L. Zaviralova, M. Musil, M. Kren, Honeywell International, Czech Republic*
- **GNSS Array-Based Ionospheric Spatial Gradient Monitoring: Precision and Integrity Analyses,** *S. Zaminpardaz, Curtin University, Australia; P.J.G. Teunissen, Curtin University, Perth, Australia and Delft University of Technoloty, The Netherlands; N. Nadarajah and A. Khodabandeh, Curtin University, Australia*
- **Localized Ionospheric Threat Validation using Time-Step Method for GBAS Ionospheric Anomaly Threat Model in the Brazilian Region,** *Moonseok Yoon, Dongwoo Kim, and Jiyun Lee, Korea Advanced Institute of Science and Technology, South Korea*
- **Performance of GAST-D Ionospheric Gradient Monitor Studied with Low Latitude Ionospheric Disturbance Data Obtained in a Real Airport Environment,** *Susumu Saito, Electronic Navigation Research Institute, Japan; Hiroaki Nakahara, The University of Electro-Communications, Japan; Takayuki Yoshihara, Electronic Navigation Research Institute, Japan*
- **Total System Performance in GBAS-based Landings,** *Michael Felux, German Aerospace Center (DLR), Germany; Jiyun Lee, Korea Advanced Institute of Science and Technology, South Korea; Florian Holzapfel, Technische Universität München, Germany*
- **Troposphere Reassessment in the scope of MC/MF Ground Based Augmentation System (GBAS),** *Alizé Guilbert , Carl Milner, Christophe Macabiau, Ecole Nationale de l'Aviation Civile, France*

Safoora Zaminpardaz

From: meetings@ion.org
To: Safoora Zaminpardaz
Subject: GNSS+ 2016 Abstract Acceptance Notification
Date: Thursday, 28 April 2016 4:23:21 AM

Dear Safoora Zaminpardaz:

Your abstract, titled Horizon-to-elevation Mask: A Potential Benefit to Ionospheric Gradient Monitoring, has been accepted for the ION GNSS+ 2016 Conference, taking place September 12-16, 2016, at the Portland Convention Center, Portland, Oregon.
Your abstract has been assigned to Session C6: GNSS Augmentation Systems and Integrity (Research and Innovations) 2, scheduled for Friday, September 16, 2016.
You can view the full program online at: https://www.ion.org/gnss/program.cfm
Please confirm that you have been notified of the acceptance of your abstract.

Click here to confirm that you have received this acceptance notice:
https://www.ion.org/abstracts/confirmNotification.cfm?abstractkey=F6DA64F09AF4F3EDD67C2299249E73FD

Please review your paper title and authors list carefully to ensure that all of the information is correct. You may use the ION Abstract Management Portal at www.ion.org/abstracts to make edits to the title of your paper, the authors listed, and your abstract text. You can also upload your conference paper and/or make changes to it any times. Any changes made online before August 12, 2016 will be reflected in the on-site printed conference program. NOTE: Papers not representative of the original abstract submitted will NOT be included in the conference proceedings, regardless of whether or not they were presented at the conference and may affect the acceptance of future abstracts.

Submission of Completed Paper for Publication

Research and Innovations Tracks

If your paper has been accepted in one of the sessions in the Research and Innovations Tracks and you chose the option to be peer reviewed at the time of abstract submission, you must upload your completed paper to the Abstract Management Portal (AMP) no later than June 30. Papers not uploaded by June 30 will not be eligible for peer review. Authors will be notified of peer-review results through AMP by the end of August. Papers that fail to pass peer review will still be presented and published in the conference proceedings but without the peer reviewed designation. Authors who pass peer review will be able to upload a final revision of your paper that address small updates or corrections by the final deadline of September 23, 2016.

Applications and Advances Tracks

If your paper has been accepted in the Systems and Applications Tracks, please be aware that presentations will be included in the published proceedings if submitted through AMP no later than September 23. A full technical paper is optional and will be included in the conference proceedings if submitted by the author. Presentations and/or paper submitted in these tracks are not eligible for peer-review.

The Author's Kit with all necessary information for authors is available online at the GNSS+ Author Resource Center at: http://www.ion.org/gnss/author-resource-center.cfm. This online format gives you 24/7 access to all the information you need to carefully prepare your paper for submission, and to create a dynamic presentation at your session. The Author Resource Center includes:

- Important Dates and Deadlines
- Speaker Breakfast Information (attendance is mandatory)
- Presentation Instructions
- Paper Preparation Instructions for Compliant Files
- Instructions for Uploading Your Final Paper Electronically
- Helpful Tips on Promoting Your Presentation
- Forms, Documents and Templates

Corrected manuscripts will be accepted through September 23, 2016. Papers submitted after September 23 will not be accepted.

You are encouraged to contact your session chairs, preferably by e-mail, at your earliest opportunity. Please keep them updated on your status; they are your first points of contact for any questions you might have (Session chairs e-mail addresses will send to you by e-mail early next week). If for any reason you are not able to make contact with your session chair, please do not hesitate to contact me.

Best Regards,

Miriam Lewis
ION Author Liaison
Phone: 703-366-2723
E-mail: meetings@ion.org

RESEARCH AND INNOVATIONS SESSIONS
APPLICATIONS AND ADVANCES SESSIONS

Friday Afternoon, September 16, 1:45 p.m.–4:50 p.m.

Room B113/114/115/116
1:45 p.m.–4:00 p.m.
A6a: PANEL: High-Accuracy GNSS–How Good Does it Get?

Dr. Anna Jensen, *KTH Royal Institute of Technology, Sweden*

Dr. Paul Alves, *Hemisphere GNSS, Canada*

The state of the art research related to real time kinematic positioning (RTK), and to precise point positioning (PPP) in real time and post mission. Factors limiting improvement in position accuracy and in convergence / initialization time will be discussed including ambiguity resolution. Panelists will also present their views on future performance considering multi constellation multi frequency methodologies for next generation high-accuracy GNSS positioning.

1. **The NRCan PPP Service: Towards Fast Convergence:** Dr. Simon Banville, Natural Resources Canada
2. **Some Issues Still in the Way to Ultimate Precision:** Dr. Oscar Colombo, USRA/NASA Goddard Space Flight Center
3. **Think Globally, Act Locally: Challenges of an Australian PPP-RTK Service:** Dr. Stavros Melachroinos, Geoscience Australia
4. **The Ascent and Realities of PPP:** Dr. Sunil Bisnath, York University, Canada
5. **Increasing the Availability of High Accuracy Positioning:** Sandra Kennedy, NovAtel, Inc., Canada
6. **Galileo and High Accuracy Services:** Alvaro Mozo, European GNSS Agency, Czech Republic
7. **HIgh-accuracy Positioning Solutions and Services–Techonology and Applications:** Dr. Rodrigo Leandro, Hemisphere GNSS
8. **High Accuracy GNSS Positioning: Ubi Sumus? Quo Vadimus?:** Dr. Richard Langley, University of New Brunswick, Canada

Room B110/111/112
3:20 p.m.–4:50 p.m.
A6b: Atmospheric Science 2

Dr. Gary Bust, *The Johns Hopkins University/APL*

Dr. Susumu Saito, *Electronic Navigation Research Institute (ENRI), Japan*

3:20 **DCB Estimation Based on Uncombined PPP:** Y. Xiang, University of Calgary, Canada

3:42 **Ionospheric Storms of Solar Cycle 24 and Their Impact on the WAAS Ionospheric Threat Model:** L. Sparks, JPL California Institute of Technology; E. Altshuler, Sequoia Research

4:04 **Ionosphere Ray-Tracing of RF Signals and Solution Sensitivities to Model Parameters:** M.L. Psiaki, Virginia Tech

4:26 **Real-time Ionosphere Monitoring by Three-dimensional Tomography Over Japan:** S. Saito, ENRI, Japan; S. Suzuki, M. Yamamoto, Kyoto University, Japan; C-H. Chen, National Cheng Kung University, Taiwan; A. Saito, Kyoto University, Japan

Alternate

1. **Assessing Ionospheric Scintillation Effects for Future GNSS Radio Occultation Missions:** M. Najmafshar and S. Skone, University of Calgary, Canada

Room C120/121/122
1:45 p.m.–4:50 p.m.
B6: Navigation Using Environmental Features

Dr. Paul D. Groves, *University College London*

Dr. Kyle Kauffman, *Air Force Institute of Technology*

1:50 **Validation of a Magnetic Anomaly Navigation Model with Fight Test Data:** A. Canciani and J. Raquet, Air Force Institute of Technology

2:12 **Gaussian Mixture Filter for Multipath Assisted Positioning:** M. Ulmschneider, C. Gentner, German Aerospace Center (DLR), Germany; R. Faragher, Focal Point Positioning, UK; T. Jost, DLR, Germany

2:35 **Smartphone Navigation Using Barometric Altitude and Topographic Maps:** P. Smagowski, Military Institute of Armament Technology, Poland; J. Raquet, Air Force Institute of Technology; K. Kauffman, VRA/ANT Center

2:58 **Direct Positioning Utilizing Non Line of Sight (NLOS) GPS Signals:** Y. Ng and G.X. Gao, University of Illinois at Urbana-Champaign

3:20 **Sensitivity Analysis of 3D Building Model-assisted Snapshot Positioning:** R. Kumar and M.G. Petovello, University of Calgary, Canada

3:42 **Integration of GNSS Positioning and 3D Map using Particle Filter:** T. Suzuki, Waseda University, Japan

4:04 **Real-Time Implementation of Vision-Aided Monocular Navigation for Small Fixed-Wing Unmanned Aerial Systems:** T. Machin, J. Raquet, D. Jacques, J. Pecarina, Air Force Institute of Technology; D. Venable, Air Force Research Laboratory

4:26 **Integrating Vision Based Navigation with INS and GPS for Land Vehicle Navigation in Challenging GNSS Environments:** Y. Sun, Harbin Engineering University, China & Queen's University, Canada; M.T. Rahman, Queen's University, Canada; T.B. Karamat, Royal Military College of Canada; A. Noureldin, RMC & Queen's University, Canada; Y. Gao, Harbin Engineering University, China

Alternates

1. **Analysis of a New Navigation System Based on Partially Tight Integration of IMU-Visual Odometry with Loosely Coupled GPS:** M. Sahmoudi and R. Navya, ISAE-SUPAERO, Toulouse University, France
2. **Tightly Coupled Kinematics Visual Odometry /PPP System for Land Vehicle Navigation:** F. Liu and Y. Gao, University of Calgary, Canada

Room B117/118/119
1:45 p.m.–4:50 p.m.
C6: GNSS Augmentation Systems and Integrity 3

Victoria Kropp, University FAF Munich, Germany

Dr. Andriy Konovaltsev, German Aerospace Center (DLR), Germany

1:50 **Mitigation of Short Duration Satellite Outages for Advanced RAIM and other GNSS Integrity Systems:** J. Blanch, T. Walter, P. Enge, Stanford University

2:12 **Exploiting Satellite Motion in ARAIM: Measurement Error Model Refinement Using Experimental Data:** M. Joerger and B. Pervan, Illinois Institute of Technology

2:35 **Requirements and Performance of Horizontal and Vertical ARAIM Exclusion Algorithm:** Y. Zhai, M. Joerger, B. Pervan, Illinois Institute of Technology

2:58 **Nominal Range Error Analysis to Support ARAIM:** S. Perea, M. Meurer, German Aerospace Center, DLR & RWTH Aachen, Germany; I. Martini, M. Rippl, DLR, Germany; M. Joerger, B. Pervan, Illinois Institute of Technology

3:20 **Kalman Filter-Based GNSS Integrity Monitoring:** S. Bhattacharyya, Indian Institute of Technology, India; D. Gebre-Egziabher, University of Minnesota, Twin Cities

3:42 **Signal Quality Monitoring for New GNSS Signals:** J-B. Pagot, P. Thevenon, O. Julien, ENAC, France; F. Amarillo-Fernandez, ESA, the Netherlands; D. Maillard, Cap Gemini, France

4:04 **Horizon-to-elevation Mask: A Potential Benefit to Ionospheric Gradient Monitoring:** S. Zaminpardaz, Curtin University, Australia

4:26 **Robust Chi-Square Monitor Performance with Noise Covariance of Unknown Aspect-Ratio:** J. Rife, Tufts University

Alternates

1. **Experimental Evaluation in Multipath Scenarios of a Novel Framework for GNSS Integrity Based on the Transient Change Detection Theory:** D. Egea-Roca, G. Seco-Granados, J.A. López-Salcedo, Universitat Autònoma de Barcelona, Spain
2. **Automated GPS Signal-in-Space Anomalies Monitoring Over More than 11 Years:** C. López de Echazarreta, ESA, GNSS Regional Augmentation Systems Division, France; A. Pandele, Romanian Institute of Space Science (ISS), Romania; J. Sanz, J.M. Juan, Universitat Politécnica de Catalunya, Spain
3. **GPS SISRE/URA Integrity Analysis for ARAIM:** F. Mistrapau, B. Bija, G. Cueto-Felgueroso, M. Odriozola, M. Azaola, A. Cezón, GMV, Spain; F. Amarillo, ESA
4. **A Frequency Domain-based Detection Technique for Digital Distortion on GNSS Signals:** C. Sun, H. Zhao, C. Zhuang, W. Feng, Beihang University, China

Blue Text Indicates Student Paper Award Winner

12:15 p.m. –1:30 p.m., ION GNSS+ Awards Luncheon, Oregon Ballroom

Safoora Zaminpardaz

From: Miriam Lewis <mlewis@ion.org>
To: Safoora Zaminpardaz
Cc: Peter Teunissen
Subject: ION GNSS+ 2016 Student Paper Award
Date: Thursday, 3 March 2016 4:35:13 AM

Mr./Ms. Safoora Zaminpardaz
Curtin University
Dept. of Spatial Sciences
GPO Box U1987
Perth WA 6845 Australia

Sent Via E-mail (Original will be sent via air mail)

Dear Mr./Ms. Zaminpardaz,

It is my pleasure to inform you that your paper "***Horizon-to-Elevation Mask: A Potential Benefit to Ionospheric Gradient Monitoring***" have been selected by the ION GNSS+ 2016 Student Award Committee to be presented at the ION GNSS+ 2016 Conference, September 12-16, 2016 in Portland, Oregon. Details for the presentation and travel sponsorship are as follows:

Paper Title: ***Horizon-to-Elevation Mask: A Potential Benefit to Ionospheric Gradient Monitoring***
Session: **TBD**

Below are some important details concerning the meeting, your travel arrangements, and final paper publication guidelines. I would encourage you to get an early start of making your arrangements to attend the conference and pay special attention to the mandatory deadlines.

WHAT YOU RECEIVE:

Your award includes:

1. Travel award funds (according to the published schedule and based on the country in which the school resides) upon the Institute's receipt of valid visa copy.
2. A complimentary **FULL** conference registration that includes all conference meals and a copy of the proceedings.
3. Publication of your technical paper in the conference proceedings.
4. Awards certificate and acknowledgement of your accomplishment at the ION GNSS+ Awards Luncheon.

Travel Award Funds: Student travel awards provide a flat rate of travel subsidy based on the country in which the sponsoring school is located as follows:

U.S. Schools:	*$1,300*

Canadian Schools: *$1,500*
U.K./Western European Schools: *$2,000*
Brazilian Schools: *$2,200*
Chinese/Korean/Japanese Schools *$2,300*
Australian Schools: *$2,500*
Other: qualify for special arrangements

You, or your school, is responsible to make ALL travel arrangements (including airline and individual hotel reservations). Due to U.S. tax laws travel funds will NOT be payable to an individual. Travel funds shall be remitted directly to the sponsored student's academic institution after the ION National Office receives proof of visa/passport (if applicable). There will be no exceptions made to this policy. Travel costs that exceed the published amount shall be borne by the student. The university shall retain funds in excess of actual student's travel. **Funds are not transferable and shall be returned to the ION if for any reason the student winner named on this letter is unable to attend**. Failure to do so would affect the acceptance of future papers submitted for consideration under the student awards program.

ION GNSS+ Meeting Registration:

You will be receiving a **full complimentary meeting registration**. This includes all sessions, conference events, meals served at the conference, and a copy of the proceedings. You will receive an electronic registration confirmation letter from our meeting registration department this summer.

Publication of Your Paper in GNSS+ Meeting Proceedings:

You will receive a link to the online authors' kit via e-mail from Miriam Lewis. Please review it thoroughly as it contains information on the formatting of your paper for publication in the official ION GNSS+ conference proceedings. Your final formatted paper must be received at the National Office in proper form no later than August 12, 2016.

The author's kit also contains additional requirements for the publication of your paper. Note that your paper must be presented to be included in the proceedings. You will also find information on what audio-visual equipment will be made available to you for your oral presentation and you will be provided information on the speaker's breakfast (which you are required to attend the morning of your presentation).

YOU ARE RESPONSIBLE FOR/TO:

As a GNSS student award winner you are responsible for/required to:

1. E-mail a copy of your visa or valid passport to my attention at the National Office at +1-703-366-2724.
2. Attend the **Speakers Breakfast** on the morning of your presentation.
3. Present your paper at the time scheduled per the published conference program.
4. Participate in all three days of the conference's technical program/commercial exhibit.
5. You are **REQUIRED** to attend the **Friday Awards Luncheon**. Failure to attend this event will jeopardize future student papers being accepted from your school.

Obtain a Visa:

We recommend that you apply for your visa at least three months in advance. Currently there is a mandatory security check period of 30 days for people whose passports are issued from several countries. U.S. consular offices now interview most applicants as part of the application process. Please ensure you arrive at the embassy with all required documentation at the time of your interview.

You will find an original visa letter for use in making your visa application enclosed. Please take this visa letter with you to the embassy when making your visa application.

IMPORTANT!!! A copy of your visa must be received no later than August 30. If your visa is not received by August 30 your travel award will be terminated and your paper will be automatically canceled and withdrawn from the conference. If you are not a U.S./Canadian citizen, you are required to obtain a visa prior to the Institute issuing you any sponsorship funds. No exceptions will be made to this policy. After your visa has been issued please e-mail a copy to meetings@ion.org. Once the copy of your visa has been received you will be eligible to receive travel funds.

To Whom Travel Award Funds Shall Be Sent:

All travel award funds will be made payable to your university. Please provide your university department's full mailing address. All checks will be mailed via standard airmail. Travel funds shall be issued with a check written in U.S. dollars and drawn on a U.S. bank. There will be no exceptions made to these policies.

At the GNSS Meeting YOU are REQUIRED to:

- Attend the **Speakers Breakfast** on the morning of your presentation.
- Present your paper at the original time in which it has been scheduled per the conference program.
- Participate in all three days of the conference's technical program/commercial exhibit (Wednesday through Friday).
- Attend the **Friday Awards Luncheon on Friday, September 16** from noon-2 p.m.

I hope this memo has answered most of your questions. **Remember to make your visa application right away and e-mail valid visa no later than August 30** to avoid the cancellation of your paper and discontinuation of your sponsorship. Let us know if you have any questions.

Sincerely,
Miriam Lewis
Program/Author Liaison
The Institute of Navigation
8551 Rixlew Lane, Ste. 360
Manassas, VA 20109
Ph: 703-366-2723

Safoora Zaminpardaz

From: Safoora Zaminpardaz
To: Glen Gibbons < glen@insidegnss.com>
Cc: Peter Teunissen; Nandakumaran Nadarajah
Subject: Article submission
Date: Saturday, 15 October 2016 5:31:00 PM
Attachments: IRNSS_InsideGNSS.pdf

Dear Mr Gibbons,

Herein, I have attached an article entitled "L5 RTK Over India: IRNSS and GPS", in which we provide the very first L5 ambiguity resolution and corresponding positioning results of the fully-operational IRNSS as a standalone system and also in combination with the fully-operational GPS Block IIF and the future GPS III. Our analyses cover several onshore locations within the IRNSS service area, and are conducted for both the geodetic survey-grade receivers as well as the low-cost receivers.

As we would like to submit this article to the INSIDE GNSS magazine, we would greatly appreciate it if you could give us your valuable feedback.

We are looking forward to hearing from you.
Best regards,
Safoora Zaminpardaz On behalf of
Safoora Zaminpardaz, Peter JG Teunissen, Nandakumaran Nadarajah

---

From: Glen Gibbons < glen@insidegnss.com>
Sent: Tuesday, 18 October 2016 6:54 AM
To: Safoora Zaminpardaz
Cc: Peter Teunissen; Nandakumaran Nadarajah
Subject: Re: Article submission

Dear Ms. Zaminpardaz,

Thanks you for sending the manuscript for consideration. We will review the article and get back in touch soon.

Best regards,
Glen

Glen GIbbons, editor
Inside GNSS

From: Safoora Zaminpardaz
To: Glen Gibbons <glen@insidegnss.com>
Cc: Peter Teunissen
Subject: Re: Article submission
Sent: Wednesday, 16 November 2016 10:07:00 AM

Dear Mr Gibbons,

Could you please update us on the status of our paper? I was wondering how long the review procedure would take.

We are looking forward to hearing from you.

Best regards,
Safoora Zaminpardaz

From: Glen Gibbons <glen@insidegnss.com>
Sent: Thursday, 17 November 2016 3:11 AM
To: Safoora Zaminpardaz
Cc: Peter Teunissen
Subject: Re: Article submission

Dear Ms. Zaminpardaz,

Thank you for your email. Yes, we would like to use this manuscript as the basis for an article in an upcoming issue of Inside GNSS. Could you please provide us with a version of the manuscript in MS Word format?

Best regards,
Glen

Glen GIbbons
Editor, Inside GNSS

From: Glen Gibbons <glen@insidegnss.com>
Sent: Friday, 2 December 2016 3:55 AM
To: Safoora Zaminpardaz
Cc: Peter Teunissen
Subject: Re: Article submission

Dear Safoora,

We would like to prepare the manuscript for publication as an article in the January/February 2017 issue of Inside GNSS. If that is acceptable, we will begin processing the manuscript in the near future and will send you a copyedited/annotated version for review as with your previous article in Inside GNSS.

Best regards,
Glen

From: Glen Gibbons <glen@insidegnss.com>
Sent: Thursday, 5 January 2017 10:32 AM
To: Safoora Zaminpardaz
Cc: Peter Teunissen; Stan Goff
Subject: Re: Article submission

Dear Safoora,

Attached you will find our copyedited/annotated version of your article for review. A few changes have been left highlighted for your special attention. We have one Question to Author (Q/A) regarding the type of low-cost receiver used in your project.

Please let us know of any corrections or changes, leaving those highlighted using the Track Changes tool. When we have those, we will prepare a page layout of the article for you to review. Also, in future communications, please copy Stan Goff, our managing editor who will handle further processing of the article with our art director.

Best regards,
Glen

Glen Gibbons
Editor, Inside GNSS

From: Safoora Zaminpardaz
Sent: Thursday, 13 January 2017 4:55 AM
To: Glen Gibbons
Cc: Peter Teunissen; Stan Goff
Subject: Re: Article submission

Dear Mr Gibbons,

Please find attached the annotated version of the article and the photo of Dr Nandakumaran Nadarajah. There are a few corrections highlighted throughout the manuscript. In the following, I have also addressed your question regarding the low-cost receiver.

Q/A: what were the receivers used in the “low-cost receiver” analysis?

As is mentioned in the article, in the section "Ambiguity Resolution Performance for a Kinematic IRNSS User", we have provided only the formal analyses (model-driven results) and therefore we did not make use of the real-world data of a low-cost receiver. In order to provide the corresponding results, we only considered high values for the zenith-referenced code and phase standard deviations. Such values for GPS were taken from Odolinski and Teunissen (2016). The values associated with the IRNSS data were chosen based on the fact that our precision analysis shows lower code precision for IRNSS L5 than GPS L5 (see Table 2).

Should more information be required, please let me know.

Best regards,

Safoora

From: Glen Gibbons <glen@insidegnss.com>
Sent: Thursday, 13 January 2017 5:10 AM
To: Safoora Zaminpardaz
Cc: Peter Teunissen; Stan Goff
Subject: Re: Article submission

Dear Safoora,

Many thanks for returning your revised manuscript as well as the photo of Dr. Nadarajah. We will prepare a page layout based on this version and send you a PDF of that for another review.

Best regards,
Glen

Safoora Zaminpardaz

From: Safoora Zaminpardaz
To: glen@insidegnss.com; Guenter.Hein@unibw-muenchen.de
Subject: Article submission
Date: Sunday, 24 April 2016 3:19:00 PM
Attachments: GLONASS.pdf

Dear Editor,

Herein, I have attached an article entitled "GLONASS CDMA L3 Ambiguity Resolution", which presents the first results of the ambiguity resolution performance of GLONASS CDMA L3 in comparison with GPS L5.

We would like to submit this article to the INSIDE GNSS magazine. Could you please inform us which steps need to be taken to do so?

We are looking forward to hearing from you.

Best regards,
Safoora Zaminpardaz On behalf of
Safoora Zaminpardaz, Peter JG Teunissen, Nandakumaran Nadarajah

---

From: Glen Gibbons <glen@insidegnss.com>
Sent: Monday, 25 April 2016 5:00 AM
To: Safoora Zaminpardaz
Cc: Guenter.Hein@unibw-muenchen.de
Subject: Re: Article submission

Dear Ms. Zaminpardaz,

Thank you very much for sending the manuscript, which deals with a very interesting and timely subject.

I will read the paper and get back in touch with you soon.

Best regards,
Glen

Glen Gibbons
Editor, *Inside GNSS*
Managing Partner, Gibbons Media & Research LLC
1574 Coburg Rd. #233
Eugene, OR 97401-4802

Tel: 408-216-7561
Fax: 408-216-7525
E-mail: glen@insidegnss.com

From: Safoora Zaminpardaz
To: Glen Gibbons < glen@insidegnss.com>
Cc: Peter Teunissen
Subject: Re: Article submission
Sent: Friday, 29 April 2016 5:56:00 PM

Dear Glen Gibbons,

Could you please let us know how long it would take to get feedback on our paper? We are looking forward to hearing from you.

Best regards,
Safoora Zaminpardaz

From: Glen Gibbons <glen@insidegnss.com>
Sent: Saturday, 30 April 2016 12:43 AM
To: Safoora Zaminpardaz
Cc: Peter Teunissen
Subject: Re: Article submission

Dear Ms. Zaminpardaz,

I should have the opportunity to review the paper carefully and provide a reply next week, but I am very favorably inclined toward publishing an article based on the it given the subject and authorship alone.

Would it be possible for you to send me the paper in a Word.docx format?

Best regards,
Glen

Glen Gibbons
Editor, *Inside GNSS*
Managing Partner, Gibbons Media & Research LLC
1574 Coburg Rd. #233
Eugene, OR 97401-4802

Tel: 408-216-7561
Fax: 408-216-7525
E-mail: glen@insidegnss.com

From: Glen Gibbons <glen@insidegnss.com>
Sent: Wednesday, 4 May 2016 12:17 AM
To: Safoora Zaminpardaz
Cc: Peter Teunissen
Subject: Re: Article submission

Dear Ms. Zaminpardaz,

Thank you for sending the Word version of the document. After reviewing your paper more closely, I am pleased to confirm its acceptance for publication as an article in Inside GNSS -- tentatively in the July/August 2016 issue. We will be back in touch as we begin its preparation -- copyediting and annotation -- in June.

Best regards,
Glen

Glen Gibbons
Editor, *Inside GNSS*
Managing Partner, Gibbons Media & Research LLC
1574 Coburg Rd. #233
Eugene, OR 97401-4802

Tel: 408-216-7561
Fax: 408-216-7525
E-mail: glen@insidegnss.com